



HAL
open science

Stereocomplex PLA: from synthesis to biomedical applications

Carmen Moya Lopez-Pelaez

► **To cite this version:**

Carmen Moya Lopez-Pelaez. Stereocomplex PLA: from synthesis to biomedical applications. Material chemistry. Université de Lorraine, 2022. English. NNT : 2022LORR0270 . tel-04065861

HAL Id: tel-04065861

<https://hal.univ-lorraine.fr/tel-04065861>

Submitted on 12 Apr 2023

HAL is a multi-disciplinary open access archive for the deposit and dissemination of scientific research documents, whether they are published or not. The documents may come from teaching and research institutions in France or abroad, or from public or private research centers.

L'archive ouverte pluridisciplinaire **HAL**, est destinée au dépôt et à la diffusion de documents scientifiques de niveau recherche, publiés ou non, émanant des établissements d'enseignement et de recherche français ou étrangers, des laboratoires publics ou privés.

Thèse

Présentée et soutenue publiquement pour l'obtention du titre de

DOCTEUR DE L'UNIVERSITE DE LORRAINE

Mention : Sciences des matériaux

par **Carmen MOYA LOPEZ-PELAEZ**

PLA stéréo-complexes à blocs : de la synthèse aux applications biomédicales

18 Novembre 2022 à Metz

Membres du jury :

Rapporteurs:	Mme. Valérie GAUCHER	Professeure, Université de Lille-Lille
	M. Maurice BROGLY	Professeur, Université de Haute Alsace-Mulhouse
Président de jury:	Mme. Isabelle ROYAUD	Professeure, Université de Lorraine-Nancy
Examineurs:	Mme. Maria J.VINCENT	Responsable du Laboratoire Polymères Thérapeutiques, Centro de Investigacion Principe Felipe-Valencia
	Mme. Nadège BRUN	Responsable du laboratoire, Total Energies-Rogerville
Membres invités:	Mme. Cécile Nouvel	Professeure, Université de Lorraine-Nancy
	M. Carlos ALONSO-MORENO	Professeur, Université de Castilla-La Mancha-Albacete
Directeur:	M. Patrice BOURSON	Professeur, Université de Lorraine-Metz
Co-directeur:	M. David CHAPRON	Maître de Conf., Université de Lorraine-Metz
Co-encadrant:	M. Daniel HERMIDA-MERINO	Assistant Professeur, Université de Vigo-Vigo

*« Chaque effort ajoute un peu d'or à ce
trésor que rien au monde ne peut ravir »*

Simone Weil

A Pío Baroja, 6

ACKNOWLEDGEMENT

“If you want to go fast, go alone. If you want to go far, go together”

Certainly, there are many people involved in this thesis, to whom I am more grateful than I can herein express.

First, I would like to thank my supervisors for their continuous support and help during these three years. Thanks to Prof. Patrice Bourson and Dr David Chapron for trusting me from the beginning, for allowing me to do this work and for the freedom to trace the pathway of this thesis. Particularly, thanks to Patrice for bringing that closeness that everyone needs when you are far from home, for brightening up the days with good humour and jokes, and for all the baby-foot after lunch. You have become my French father. Many thanks also to Dr Daniel for the close follow-up of my work despite the distance, for every lesson I have learned from you, both personally and academically, and especially, for all the fun along this years working together. *Estoy muerto/vivo, pero todo ok* José Luis.

During my thesis, I had the opportunity to work in different laboratories and research facilities. My base camp was LMOPS, at the University of Lorraine. I would like to thank Thomas, Jean Claude and Maryne for your scientific and technical help, and especially thanks to Sarah for being my big sister without asking for anything in return, always with good humour and care. Thanks also to all the students I met at LMOPS, mainly Christelle, Sadaqat, Waqar, Sourav and Rodolph, for welcoming me with you despite my sporadic presence in the laboratory. I also wanted to dedicate a few words to the memory of Chrystives, who was one of the first people I met at LMOPS and always had a piece of good advice to give or a suggestion for a weekend plan.

I also worked for some time at the University of Castilla La Mancha and I would like to thank Prof. Carlos Alonso Moreno, Prof. Ivan Bravo Perez, Prof. Jose Antonio Castro Osma and Prof. Agustin Lara Sanchez, for supporting me and helping me, especially in the first stage of the thesis. Special thanks to Prof. Carlos Alonso Moreno and Prof. Ivan Bravo Perez, for that phone call in December 2018 that would change the course of my life. Furthermore, I would also like to thank all the students and technicians with whom I worked during my stay in Albacete and Ciudad Real, for welcoming me as if I was one of the team, Felipe, Marc, Alberto, Elena, Enrique, Murillo, Rosario, and also thanks to Fernando, Victor, Sergio, Maria and Diego for those months pre- and post-confinement.

I had also the opportunity to work at the University of Maastricht on several occasions. I would like to thank Prof. Karel Wilsens and Prof. Jules Harings for your willingness to welcome me and help me in any way you could. Furthermore, I would also like to thank Nils, Gijs and Francesca for your scientific collaboration in this work, and of course

the group of friends that I met there and who welcomed me immediately, Varun, Geert, Andrea, Gijs and especially Manta, for taking me in your home from minute 1.

I have also spent a lot of time at the ESRF, and I would like to thank Dr Dipaanjan Banerjee for facilitating all the administrative arrangements for my stay and the financial support. I would also like to thank Dr Martin Rosenthal for all the work done on ID13, as well as Florian and Dirk for the technical support.

Besides the ESRF, I had also the opportunity to go many times to the ALBA synchrotron radiation facility, in Barcelona, where Dr Eduardo Soriano always had an incredible predisposition to help me and make me autonomous in the line, in addition to his human quality and closeness. There, I also met Prof. Manuel Piñeiro and Dr Carolina Hermida Merino, from the University of Vigo, to whom I am very grateful for the work done together and in particular to Carolina, for the connection since the very first moment and for making the beam-times much more pleasant.

Finally, in addition to the scientific support of all the people mentioned above, many people have been emotionally supporting me during these three years so that I could do my best.

First of all, I would like to thank my lifelong friends, Maria, Maite, Inma, Juancar, Luis and Mañas, for their interest in what I was doing, for their constant support, but especially thanks for getting my mind away from the thesis with lots of laughs. We are such a good team! I also wanted to thank my girls from Albacete, Angela, Ahijon, Cris, Clara, Santos, and Raquel, for trusting me and always having a hug and a smile no matter how much time has passed since the last time. I also wanted to thank my more recent friends, Pablo, Shere, Sonia, Judoka and Chechu, thank you for welcoming me into your group once and a thousand times, also, no matter how much time has passed. You are all my chosen family.

I also wanted to thank my non-chosen family for bringing me and accompanying me here, the Moyas and the Lopeh-Pelaeh, but especially, thanks to my father, for your persistence since I was a child on the importance of working "el musculo", to my mother for your endless care and for teaching me how to study the green boxes of "conocimiento del medio", and to my sister for being the best example of effort and perseverance that I could have had as a reference, I admire you very much. I am who I am thanks to you. I love you.

Last but not least, Vilches, thank you for getting involved in this adventure from the beginning without hesitation. Thank you for the confidence, the freedom, and for being there no matter what. Thanks for slicing the elephant for me when I was exhausted. Yetem!

PREFACE

Since Berzelius coined the word *polymeric* in 1833, the study of the behaviour of such “long molecules” brought about new insights such as the vulcanization of caoutchouc (Goodyear, 1839) and the synthesis of nitrocellulose (Schönbein, 1845) or the celluloid (Brothers Hyatt, 1869), setting the onset of plastics revolution. Since then, plastics have burst into our daily life due to their versatility, cheapness, lightness, and excellent thermal properties, with packaging use accounting for the largest plastic sector on the market (39,7%). Moreover, the application of synthetic polymers in medicine was firstly reported during the Second World War, when Nicholas Harold used poly(methyl methacrylate) (PMMA) as an artificial corneal substitute, which was followed by the employ of polyethylene terephthalate (PET) for vascular grafts, polydimethylsiloxane (PDMS) for breast implants, and polyethylene (PE) for hip joint replacements. The design of novel polymeric materials must fulfil the environmental and societal demands to diminish the carbon footprint required to adopt manufacturing strategies that meet the European policies such as “A European Strategy for Plastics in a Circular Economy”, which was launched in 2018 to address how plastics are designed, used, and recycled. Likewise, the European Parliament has recently recognised the potential role of bioplastics and compostable plastics in the circular economy and sustainability. Consequently, bio-based plastics synthesised from renewable resources such as Poly-(lactic acid) (PLA) are promising environmentally friendly candidates for the development of biomedical and pharmaceutical applications whilst contributing to the circular economy. However, the clinical application of PLA-based materials is limited despite the research abundance on both its structural characterization and potential applications which might be due to the lack of know-how transfer between the fundamental research and clinical trials.

In this context, the University of Castilla-La Mancha (Spain) and the University of Lorraine (France), as well as different collaborators in Spain, France and the Netherlands (**Figure 1**), developed a global project with an interdisciplinary approach consisting of the synthesis in a controlled manner of biocompatible polymers obtained from renewable sources and the establishment of the structure-processing-properties relationship to tailor polymeric materials from the genesis for biomedical applications aiming at the end-user requirements. This thesis, focused on PLA and particularly on stereocomplex PLA (SC-PLA), is the foundation stone of this project.

The state-of-the-art of PLA as a biomaterial for its medical application is reviewed from a global approach by highlighting the interconnections among the architectural designing parameters with the desired applications. Moreover, special emphasis has been placed on the stereocomplex phase and the problems encountered so far to obtain pure stereocomplex phase (**Chapter 1**).



Figure 1. Map summarising the collaborators of the project.

Moreover, the synthesis of the long desired- HM_w stereo-diblock copolymer of PLA (PLA-SBC) is described by using a Zn-based heteroscorpionate catalyst synthesized by the Inorganic group of the University of Castilla-La Mancha (UCLM), in Spain. The living character of the catalyst selected as well as the high stereochemical control achieved enable the customisation of block copolymers of PLA (tri-, tetra-, penta-block copolymers) as well as hetero-block copolymers in combination with polymers presenting complementary physico-chemical properties to PLA such as Poly-caprolactone (PCL), Poly-ethylenglicol (PEG), etc. However, in this chapter, the synthesis of symmetric block copolymers exhibiting different molecular weight has been established as the main objective (**Chapter 2**).

In addition, the crystallization mechanism from the melt of the PLA-SBC under different thermal conditions is studied at different length scales, in collaboration with the beamline 26 of the European Synchrotron Radiation Facility (ESRF), in France. Likewise, the crystallization mechanism of the PLA-SBC blended with different nucleating agents (NA) is also analysed in collaboration with the University of Maastricht, as a strategy to overcome one of the main drawback of PLA, the low crystallization rate (**Chapter 3**).

The selection of a trace element-based catalyst to accomplish the synthesis of PLA stereoblock copolymers was aimed to apply the PLA-derivatives in the biomedical field.

During my studies of pharmacy, I was introduced to the world of nanocarriers through the collaboration with the Neuroscience research group of the faculty of Pharmacy at the UCLM. Moreover, there is a gap between material research, preclinical test, clinical requirements and regulatory aspects that hamper the translation of PLA nanoparticles research to the clinical level. Likewise, gelatin-based drug delivery systems (DDS) containing nanoparticles formulated from PLA-derivatives presenting different stereoregularities are designed as well as the release rate and local applicability of the bionanocomposites, in collaboration with the Universities of Vigo and Castilla-La Mancha, in Spain (**Chapter 4**).

ABSTRACT

The pharmaceutical industry demands constantly the development of drug delivery systems that improve therapeutic efficacy and reduce side effects. The traditional strategy of manufacturing standardised drug doses is ineffective for 70% of patients, creating the need to replace mass production with personalised medicine. In particular, nanoparticles (NP) and generally from polymeric sources were largely investigated as drug nanocarriers to improve the stability and solubility of the encapsulated molecules. In addition, NP formulations improve safety and efficacy. However, the current gap between the characterisation of the physicochemical properties of polymeric NP and their performance under physiological conditions hampers the translation from research to the clinical level. Typically, Poly-(lactic acid) (PLA) is an aliphatic and synthetic polyester obtained from renewable sources that was extensively employed to generate NPs as drug carriers due to its bioresorbable nature related to its hydrolysis in physiological media into non-toxic products.

Likewise, the current thesis aims to establish from a global approach the design of tailored PLA block-copolymers with defined nanostructures to target materials with specific structure-processing-properties relationship that enable to obtain personalised biomedical and pharmaceutical solutions from the genesis aiming at the end-user requirements.

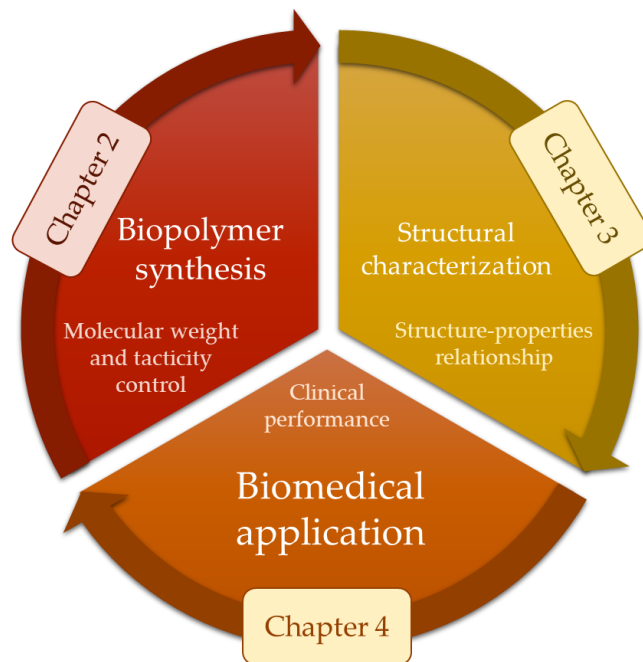
The rich PLA nanostructure together with the polymorphic nature offers the possibility to twitch the desired physicochemical properties. Particularly, the stereocomplex (SC) phase has been largely aimed due to the exhibited promising physicochemical properties featuring higher melting temperature, mechanical performance and hydrolysis resistance compared to the enantiomeric counterparts. Likewise, biomedical and pharmaceutical applications have been extensively designed with SC-PLA such as drug delivery systems. However, the typical SC crystallization by the blend of enantiomer (PLLA and PDLA) derivatives diminishes for high molecular weight (HM_w) PLA and enantiomeric homocrystals (HC) are obtained instead. In addition, the synthesis of PLA stereo-block copolymers (PLA-SBC) exhibiting HM_w and high stereocontrol requires catalysts with stereocontrol for both enantiomers that are extremely rare.

Herein, a novel series of PLA derivatives comprising different nanostructures were synthesized by Ring-Opening Polymerization through a novel biocompatible heteroscorpionate catalyst with high control of the chain stereochemistry. Particularly, the long-desired HM_w PLA-SBC presenting high tacticity has been synthesized for the first time without the use of a co-initiator. Moreover, the analysis of the mechanism of crystallization of the PLA-SBC proved the prevalence of the SC-phase, avoiding the typical HC- and SC-phase separation that occurs in the enantiomeric blends. Furthermore, the PLA industrial drawback related to its slow crystallization rate has been tackled by the addition of an organic nucleating

agent that increases the crystallization rate of PLA-SBC whilst preserving its biocompatibility with a significant impact on the new processing technologies.

NP-PLA with different nanostructures were then formulated with 2 antitumoral compounds. However, the NP-PLA so generated exhibited an amorphous structure upon formulation, erasing the designed nanostructures and their different release rate. Therefore, a straightforward synthetic approach was designed to generate bionanocomposites of gelating hydrogels with embedded NP-PLA with the aimed crystal phase and degree of crystallinity by its post-formulation thermal annealing step. Likewise, the gelatin hydrogel network acts thereby as a mechanical sustain for both the storage and local administration of the therapeutic agent as well as avoiding the aggregation of nanoparticles upon annealing whilst offering support to complementary drugs with different profile releases.

Graphical ABSTRACT



RESUME

L'industrie pharmaceutique exige constamment le développement de systèmes d'administration de médicaments qui améliorent l'efficacité thérapeutique et réduisent les effets secondaires. La stratégie traditionnelle consistant à fabriquer des médicaments à dose médicamenteuse standardisée est inefficace pour 70 % des patients, créant le besoin de substituer la production en masse par une médecine personnalisée. En plus, les nanoparticules (NP) formulées normalement à partir de polymères permettent d'améliorer la stabilité et la solubilité des molécules encapsulées, ce qui améliore la sécurité et leur efficacité. Néanmoins, il existe un écart entre la caractérisation des propriétés physico-chimiques de NP polymériques et ses performances dans des conditions physiologiques qui limite l'application au niveau clinique. L'acide polylactique (PLA) est un polyester synthétique et biosourcé qui présente des caractéristiques biorésorbables grâce à son hydrolyse en milieu physiologique en produits non toxiques.

Cette thèse vise à établir les relations structure-traitement-propriétés des matériaux polymères, et en particulier du PLA stéréocomplexe (SC) à blocs, pour concevoir des solutions biomédicales personnalisées depuis la synthèse jusqu'aux exigences du patient final.

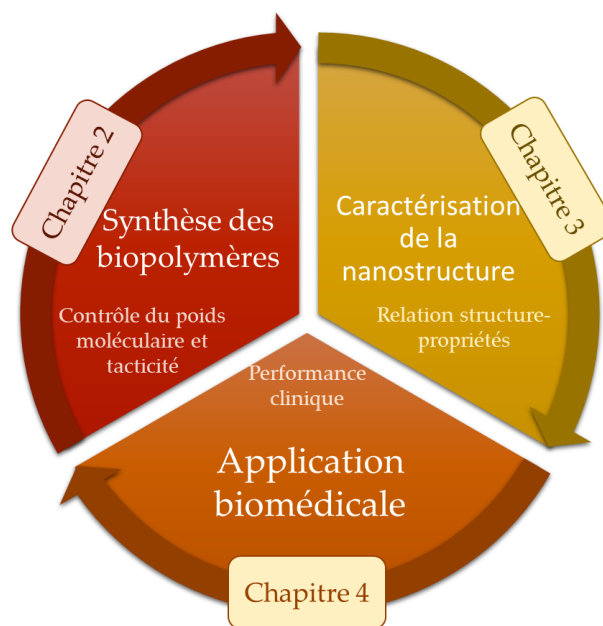
La richesse de la nanostructure du PLA associée à sa nature polymorphe, offrent la possibilité de modifier les propriétés physicochimiques en fonction de l'application souhaitée. En particulier, la phase SC est une solution en raison des propriétés physico-chimiques prometteuses qu'elle présente, notamment une température de fusion, des performances mécaniques et une résistance à l'hydrolyse plus élevées que celles de ses homologues énantiomères. De même, les applications biomédicales et pharmaceutiques ont été largement conçues avec des PLA SC, comme les systèmes d'administration de médicaments. Cependant, la cristallisation typique des SC par le mélange de dérivés énantiomères (PLLA et PDLA) diminue pour les PLA à haut poids moléculaire (HMw) et des homocristaux énantiomères (HC) sont obtenus à la place. En outre, la synthèse de copolymères stéréoblocs de PLA (PLA-SBC) présentant une masse moléculaire élevée et un contrôle stéréochimique élevé nécessite des catalyseurs avec un contrôle stéréochimique pour les deux énantiomères, qui sont extrêmement rares.

Dans ce travail, une nouvelle série de dérivés de PLA comprenant différentes nanostructures a été synthétisée par polymérisation par ouverture de cycle à l'aide d'un nouveau catalyseur hétéroscorpionate biocompatible avec un contrôle élevé de la stéréochimie. En particulier, le HMw PLA-SBC présentant une tacticité élevée, a été synthétisé pour la première fois sans l'utilisation d'un coinitiateur. De plus, l'analyse du mécanisme de cristallisation du PLA-SBC à différentes échelles a prouvé la prévalence de la phase SC, évitant la séparation des phases HC et SC qui se produit dans les mélanges d'énantiomères. En outre,

l'inconvénient industriel du PLA lié à sa vitesse de cristallisation lente a été résolu par l'ajout d'un agent de nucléation organique qui augmente la vitesse de cristallisation du PLA-SBC tout en préservant sa biocompatibilité.

Des nanoparticules de PLA (NP-PLA) avec différentes nanostructures ont ensuite été formulées avec 2 composés anti-tumoraux. Cependant, les NP-PLA ainsi générées présentaient une structure amorphe lors de la formulation, effaçant les nanostructures conçues. Par conséquent, une approche simple a permis de générer des bionanocomposites d'hydrogels gélifiants avec des NP-PLA. Le taux de cristallinité a été ensuite contrôlé par une étape de recuit thermique après formulation. De même, la matrice d'hydrogel de gélatine agit ainsi comme un support mécanique pour le stockage et l'administration locale de l'agent thérapeutique, tout en évitant l'agrégation des NP lors du recuit et en offrant un support à des médicaments complémentaires ayant des profils de libération différents.

RESUME graphique



LIST OF PUBLICATIONS

1. Naffakh, M.; Rica, P.; Moya-Lopez, C.; Castro-osma, J.A.; Alonso-moreno, C.; Moreno, D.A. The Effect of WS 2 Nanosheets on the Non- I Sothermal Cold- and Melt-Crystallization Kinetics of Poly (L -Lactic Acid) Nanocomposites. **2021**, 1–19.
2. Hermida-Merino, C.; Valcarcel, J.; Vázquez, J.A.; Cabaleiro, D.; Moya-Lopez, C.; Piñeiro, M.M.; Hermida-Merino, D. Combined Gelatin-Chondroitin Sulfate Hydrogels with Graphene Nanoparticles. *Emergent Mater.* **2021**, doi:10.1007/s42247-021-00303-5.
3. Moya-Lopez, C.; Valcarcel, J.; Vázquez, J.A.; Bourson, P.; Chapron, D.; Solano, E.; Piñeiro, M.M.; Hermida-Merino, C.; Hermida-Merino, D. Biocompatibility Enhancement of PLA by the Generation of Bionanocomposites with Fish Collagen Derivatives. *Emergent Mater.* **2022**, 5, 695–702, doi:10.1007/s42247-021-00340-0.
4. Moya-Lopez, C.; Bravo, I.; Castro-Osma, J.A.; Chapron, D.; Bourson, P.; Vagner, C.; Cochez, M.; Leon, N.; Alonso-Moreno, C.; Hermida-Merino, D. Synthesis of High Molecular Weight Stereo-Di-Block Copolymers Driven by a Co-Initiator Free Catalyst. *Polymers (Basel)*. **2022**, 14, 1–16, doi:10.3390/polym14020232.
5. Moya-Lopez, C.; Juan, A.; Donizeti, M.; Valcarcel, J.; Vazquez, J.A.; Solano, E.; Chapron, D.; Bourson, P.; Bravo, I.; Alonso-Moreno, C.; et al. Multifunctional PLA/Gelatin Bionanocomposites for Tailored Drug Delivery Systems. *Pharmaceutics* **2022**, 14, 1138, doi:10.3390/pharmaceutics14061138.
6. Moya-Lopez, C.; González-Fuentes, J.; Bravo, I.; Chapron, D.; Bourson, P.; Alonso-Moreno, C.; Hermida-Merino, D. Polylactide Perspectives in Biomedicine: From Novel Synthesis to the Application Performance. *Pharmaceutics* **2022**, 14, 1673, doi:10.3390/pharmaceutics14081673.
7. Hermida-Merino, C.; Cabaleiro, D.; Gracia-Fernández, C.; Valcarcel, J.; Vazquez, J.A.; Sanz, N.; Arenas-Moreira, M.; Banerjee, D.; Longo, A.; Moya-Lopez, C.; et al. Ionogels Derived from Fluorinated Ionic Liquids to Enhance Aqueous Drug Solubility for Local Drug Administration. *Gels* **2022**, 8, 594.

LIST OF ABBREVIATIONS

3DP	Three-dimensional printing
DDS	Drug delivery system
D-LA	D-Lactide
DSC	Differential Scanning Calorimetry
FDA	Food and Drug Administration
FTIR	Fourier-Transformed Infrared Spectroscopy
g	Growth rate
G	Spherulites growth rate
G₀	Front factor
GPC	Gel Permeation Chromatography
HC	Homocrystals
HP-PLA	Homopolymer Polylactide
HM_w	High molecular weight
HP	Homopolymer
i	Nucleation rate
i-PP	Isotactic polypropylene
k	Boltzmann constant
K_g	Nucleation constant
k_h	Hydrolysis constant
k_H	Degradation constant catalysed by protons
k_o	Degradation constant in water
k_{OH}	Degradation constant catalysed by hydroxyl ions
LA	Lactide
L-LA	L-Lactide
LM_w	Low molecular weight
M_n	Number averaged molecular weight
M_w	Weight averaged molecular weight
NA	Nucleating agent
NP	Nanoparticles
PCL	Poly (ε-caprolactone)
PCM	Polymer of chiral acetylenic
PDLA	Poly (D-lactide)
PE	Polyethylene
PEG	Polyethylene glycol
PET	Polyethylene terephthalate
PEVA	Poly (ethylene-co-vinyl acetate)
PGA	Polyglycolic acid
PHA	Polyhydroxyalkanoate
PLA	Polylactide or poly (lactic acid)

PLA-SBC	Poly lactide stereoblock copolymers
PLGA	Poly (lactic- <i>co</i> -glycolic) acid
PLLA	Poly (L-lactide)
PLLA-<i>b</i>-PDLA	Poly (L-lactide- <i>co</i> -D-lactide)
PMMA	Poly (methyl methacrylate)
POM	Polarized Optical Microscopy
PP	Polypropylene
PS	Polystyrene
r	Spherulite growth radius
R	Gas constant
<i>Rac</i>-LA	Racemic-lactide
ROP	Ring-opening polymerization
SAXS	Small Angle X-Ray Scattering
SBC	Stereo-block copolymers
SC	Stereocomplex
SC-PLA	Poly lactide Stereocomplexed
SEM	Scanning Electron Microscopy
SMP	Shape memory polymer
t	Time
T⁰_m	Equilibrium melting temperature
T_c	Crystallization temperature
TE	Tissue engineering
TEM	Transmission Electron Microscopy
T_g	Glass transition temperature
TGA	Thermo-Gravimetric Analysis
T_h	Hydrolytic degradation temperature
T_{i-c}	Isothermal crystallization temperature
T_m	Melting temperature
U*	Activation energy
WAXS	Wide Angle X-Ray Scattering
X_c	Crystallinity
ΔH_c	Crystallization enthalpy
ΔH_{cc}	Cold-crystallization enthalpy
ΔH_m	Melting enthalpy

TABLE OF CONTENTS

Chapter 1. Introduction

1.1 Introduction	5
1.2 Poly-(lactic acid)	7
1.3 Synthesis of PLA	11
1.4 PLA processing	15
1.5 PLA properties	19
1.5.1 Mechanical properties	19
1.5.2 Degradation	20
1.5.2.1 Polymer factors	21
1.5.2.2 Media factors	21
1.6 Medical applications	25
1.6.1 Pharmaceutical applications	25
1.6.1.1 Nanoparticles	25
1.6.1.2 Hydrogels	27
1.6.1.3 Perspectives	28
1.6.1.3.1 Pharmaceutical design	28
1.6.1.3.2 Chiral drugs	29
1.6.1.3.3 Antibacterial applications	31
1.6.1.3.4 Polymer therapeutics	31
1.6.2 Biomedical applications	33
1.6.2.1 Stents	33
1.6.2.2 Tissue engineering	34
1.6.2.2.1 Bone regeneration	36
1.6.2.2.2 Tendon regeneration	37
1.6.2.2.3 Nerve regeneration	38
1.6.2.2.4 Cartilage regeneration	38
1.6.2.3 Perspectives	39
1.6.2.3.1 Piezoelectric activity	39
1.6.2.3.2 Shape memory polymers	40
1.7 Conclusions	43
1.8 Aims and objectives of the thesis	45
1.9 References	47

3.3.2	<i>Effect of Mw in the PLA-SBC crystallization</i>	109
3.3.3	<i>Spherulite growth rate of stereo-block copolymers (PLA-SBC) and PLLA and PDLA enantiomers (PLA-HP)</i>	111
3.3.4	<i>Isothermal crystallization</i>	115
3.3.4.1	Avrami model.....	122
3.3.5	<i>Non-isothermal crystallization</i>	126
3.3.5.1	Avrami modified model.....	131
3.3.5.2	Ozawa model.....	133
3.3.5.3	Avrami-Ozawa model.....	133
3.3.6	<i>Crystallization of SBC with nucleating agents</i>	135
3.3.6.1	Nucleating agent efficacy survey	136
3.3.6.1.1	BHET	136
3.3.6.1.2	OXA.....	137
3.3.6.2	Morphology of the crystallized NA/SC-PLA derivatives.....	140
3.4	Conclusion	151
3.5	Experimental section	153
3.5.1	<i>Materials</i>	153
3.5.2	<i>Methods</i>	153
3.5.2.1	Polymerizations.....	153
3.5.2.2	Films preparation	153
3.5.3	<i>Instrumentations and measurements</i>	153
3.5.3.1	Thermogravimetric analysis (TGA).....	153
3.5.3.2	Gel permeation chromatography (GPC)	153
3.5.3.3	Polarized Optical Microscopy (POM)	154
3.5.3.4	Differential Scanning Calorimetry (DSC)	154
3.5.3.5	Modulated-Differential Scanning Calorimetry (M-DSC)	155
3.5.3.6	Wide-Angle X-Ray Scattering (WAXS) and Small-Angle X-Ray Scattering (SAXS)	155
3.5.3.7	Scanning X-ray micro-diffraction (micro-beam)	156
3.5.3.8	Nanocalorimeter.....	156
3.6	References	159

Chapter 4. Multifunctional PLA/Gelatin Bionanocomposites for Tailored Drug Delivery Systems

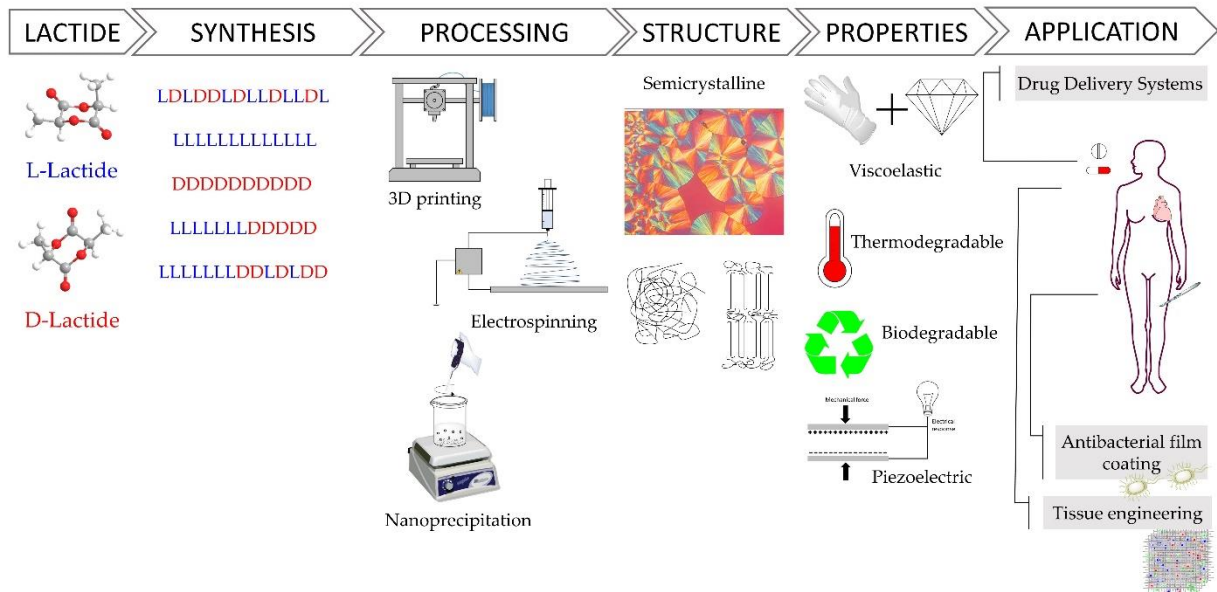
4.1	Introduction	173
4.2	Aims and objectives	175
4.3	Results and discussion	177

4.3.1 Selection and characterization of PLA-derivatives	178
4.3.2 Nanoparticles formulation	181
4.3.3 Nanoparticles characterization	182
4.3.4 Bionanocomposite formation.....	186
4.3.5 Rheological properties of the bionanocomposite.....	189
4.3.6 Drug release analysis.....	191
4.4 Conclusions	193
4.5 Experimental section	195
4.5.1 Materials.....	195
4.5.2 Methods	195
4.5.2.1 Gelatin extraction	195
4.5.2.2 Polymerizations.....	195
4.5.2.3 Nanoparticles formulations	195
4.5.2.4 Bionanocomposites generation	196
4.5.3 Instrumentation and measurements	196
4.5.3.1 ¹ H NMR	196
4.5.3.2 GPC analysis	196
4.5.3.3 Optical rotation.....	196
4.5.3.4 DLS technique.....	196
4.5.3.5 SEM	197
4.5.3.6 Cryo-SEM	197
4.5.3.7 DSC measurements	197
4.5.3.8 Raman spectroscopy	198
4.5.3.9 Small-angle X-ray scattering (SAXS) and wide-angle X-ray scattering (WAXS).....	198
4.5.3.10 Rheological experiments	198
4.5.3.11 Release studies.....	199
4.6 References	201
Conclusions and perspectives	207
Appendix	211
Resumé Français	279

CHAPTER 1

INTRODUCTION

In this Chapter the state of the art of the synthesis, processing, and properties of PLA is summarized, as well as its application in the biomedical and pharmaceutical field. Particularly, the influence of PLA synthesis and processing on its nanostructure is emphasised to correlate it with its thermo-mechanical properties that in turn, will define the suitability of the generated end-product for the desired application (**Scheme 1.1**).



Scheme 1.1 Summary of the state-of-the-art of PLA as a material for its application in the biomedical and pharmaceutical field, considering the correlation of the synthesis-processing-structure-properties relationship.

Table of contents

1.1 Introduction	5
1.2 Poly-(lactic acid)	7
1.3 Synthesis of PLA	11
1.4 PLA processing	15
1.5 PLA properties	19
1.5.1 Mechanical properties.....	19
1.5.2 Degradation.....	20
1.5.2.1 Polymer factors.....	21
1.5.2.2 Media factors.....	21
1.6 Medical applications	25
1.6.1 Pharmaceutical applications.....	25
1.6.1.1 Nanoparticles.....	25
1.6.1.2 Hydrogels.....	27
1.6.1.3 Perspectives.....	28
1.6.1.3.1 Pharmaceutical design.....	28
1.6.1.3.2 Chiral drugs.....	29
1.6.1.3.3 Antibacterial applications.....	31
1.6.1.3.4 Polymer therapeutics.....	31
1.6.2 Biomedical applications.....	33
1.6.2.1 Stents.....	33
1.6.2.2 Tissue engineering.....	34
1.6.2.2.1 Bone regeneration.....	36
1.6.2.2.2 Tendon regeneration.....	37
1.6.2.2.3 Nerve regeneration.....	38
1.6.2.2.4 Cartilage regeneration.....	38
1.6.2.3 Perspectives.....	39
1.6.2.3.1 Piezoelectric activity.....	39
1.6.2.3.2 Shape memory polymers.....	40
1.7 Conclusions	43
1.8 Aims and objectives of the thesis	45
1.9 References	47

1.1 Introduction

Poly-(lactic acid) or Polylactide (PLA), classified as an aliphatic polyester, is the biopolymer most employed in industrial fields such as fibre manufacturing, food handling, or textile industry [1] and it accounts for 24% of the global production capacity for biodegradable polymers [2]. PLA is derived from renewable sources such as corn sugar, potato, and sugar cane [3], is compostable [4], and its properties are comparable to those of petroleum-based polymers, such as polyethylene, polypropylene, polystyrene, polycarbonate and polyethylene terephthalate [5]. Furthermore, PLA hydrolyses in physiological media, yielding lactic acid, a non-toxic component that is eliminated via Krebs cycle as water and carbon dioxide [6]. Moreover, PLA is a polymorphic polyester comprising a chiral carbon in its structure that yields a wide variety of nanostructured derivatives (isotactic, atactic, syndiotactic, stereocomplexed, etc.) [7–9] featuring different physicochemical properties. Particularly, the stereocomplex (SC) phase, which is formed upon blending enantiomeric poly(L-lactide) (PLLA) and poly(D-lactide) (PDLA) or by synthesizing stereo-block copolymers (PLLA-*b*-PDLA), exhibits higher melting temperature, mechanical performance and hydrolysis resistance compared to the enantiomeric counterparts, and has been extensively investigated for biomedical and pharmaceutical applications, as well as commodity and industrial applications [7,10]. However, the SC crystallization of the blended enantiomers (PLLA and PDLA) diminishes for high molecular weight (HM_w) PLA and enantiomeric homocrystals (HC) are obtained instead [11]. In addition, the synthesis of PLA stereo-block copolymers (PLA-SBC) exhibiting HM_w and high stereocontrol requires catalyst extremely rare and has only been reported twice [12,13].

The biocompatibility, biodegradability, and resorbability characteristics of PLA have promoted its use in the biomedical field for a wide range of applications (suture threads, bone fixation screws, drug delivery systems, etc.), offering an alternative to conventional biocompatible materials such as metals and ceramics [14]. In addition, the ability to tailor the mechanical, thermal, and degradation properties of PLA derivatives due to the range of afforded nanostructures depending on the chemical architecture and processing conditions allows for designing personalised medical solutions. Indeed, the novel available synthetic PLA approaches to generate multiblock copolymers as well as the advent of current processing technologies broaden its suitability to advance into the customisation of the generated end-products to minimise the side effects. In particular, several highly cutting-edge PLA-based therapeutic applications have recently attained the clinical phase, such as drug-eluting stents [15–18] as well as personalised pharmaceutical agents that were designed from an interdisciplinary approach to avoid the serendipitous progress, emphasising the beneficial interaction between the materials and the biomedical fields. Likewise, the frequent dismissed PLA nanostructure of the designed biomedical solutions hamper the systematic advance by correlating the structure–property relationship of the system with the application

performance. Several reviews about PLA have been published covering a wide range of topics, such as the PLA synthesis [9,19], the physicochemical and mechanical properties of PLA [1], the crystallisation and structure–properties relationship of PLA [20], the characteristics of the promising stereocomplex PLA phase [7,10], and PLA applications in widespread fields [3,14,21–25].

Herein, the state-of-the-art of PLA-based biomedical applications is reviewed from a global approach by highlighting the interconnections among the architectural designing parameters with the desired applications, with an emphasis on the stereocomplex phase of PLA.

1.2 Poly-(lactic acid)

Poly-(lactic acid) is a poly- α -hydroxy acid synthesized from lactic acid (LA; 2-hydroxypropanoic acid), which exists in two optically active stereoisomers, namely L-LA and D-LA (S and R in absolute configuration, respectively) [26]. Approximately 90% of the total lactic acid produced worldwide is made by bacterial fermentation, which offers the advantages in both utilization of a renewable source and the production of optically pure L- and D-lactic acid, depending on the strain selected (the chemical synthesis of lactic acid always results in a racemic mixture). The dehydrated cyclic dimer of lactic acid is commonly called lactide (3,6-dimethyl-1,4-dioxane-2,5-dione). Lactide exists in three different forms due to the presence of two asymmetric carbon atoms in the molecule: L-lactide, D-lactide, and *meso*-lactide (**Figure 1.1**). In addition, a racemate of D-lactide and L-lactide exists as *rac*-lactide [26].

The polymerization of optically pure L- and D- lactide yields *isotactic* homopolymers of Poly-(L-lactide) (PLLA) and Poly-(D-Lactide) (PDLA) respectively (Figure 1.1). Both PLLA and PDLA are semicrystalline polymers, showing a melting temperature (T_m) around 170°C [8,9] and a thermal degradation temperature around 200°C [27]. The PLA derivative crystallinity as well as their melting and glass transition temperatures (T_g) usually decrease with diminishing optical purity of the lactate units [1,28]. PLLA polymers with D-lactide

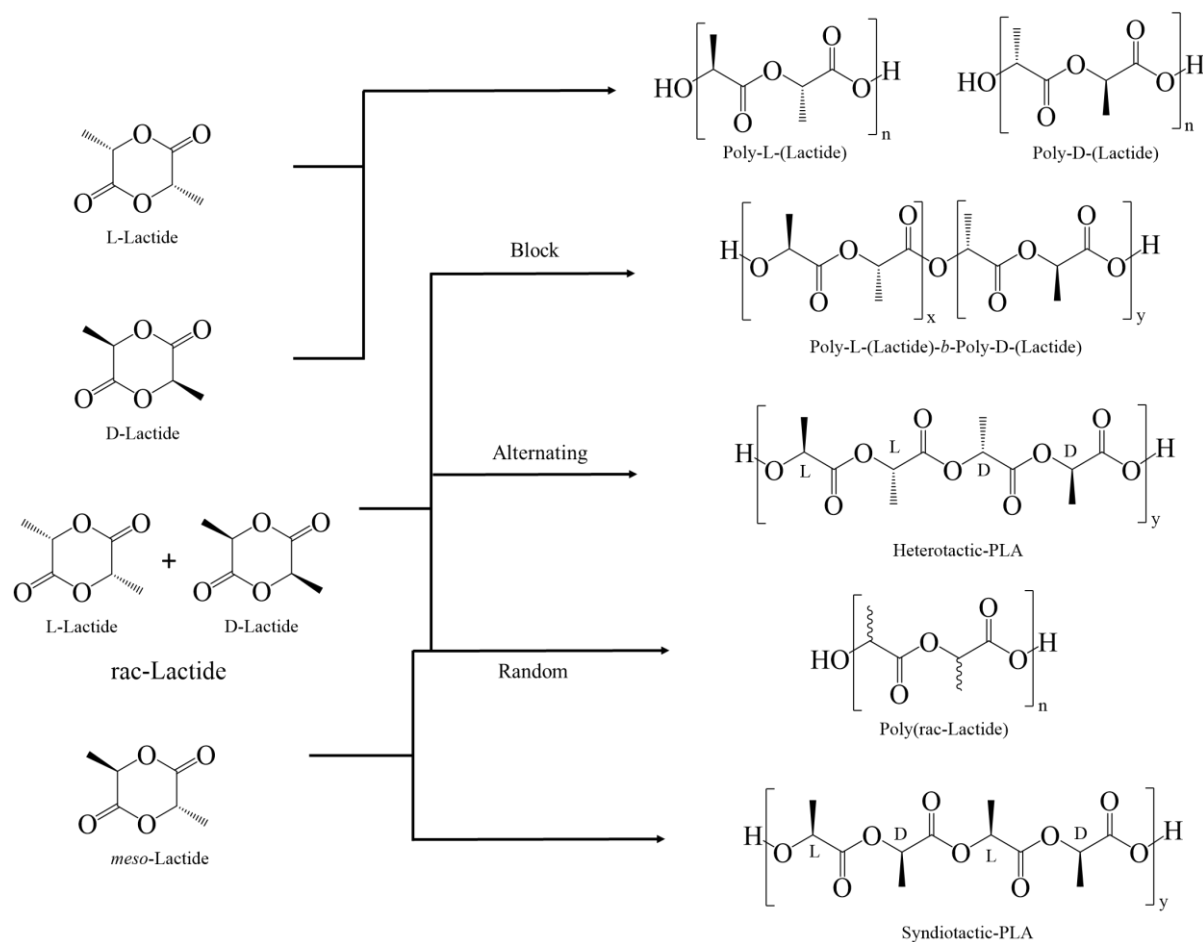


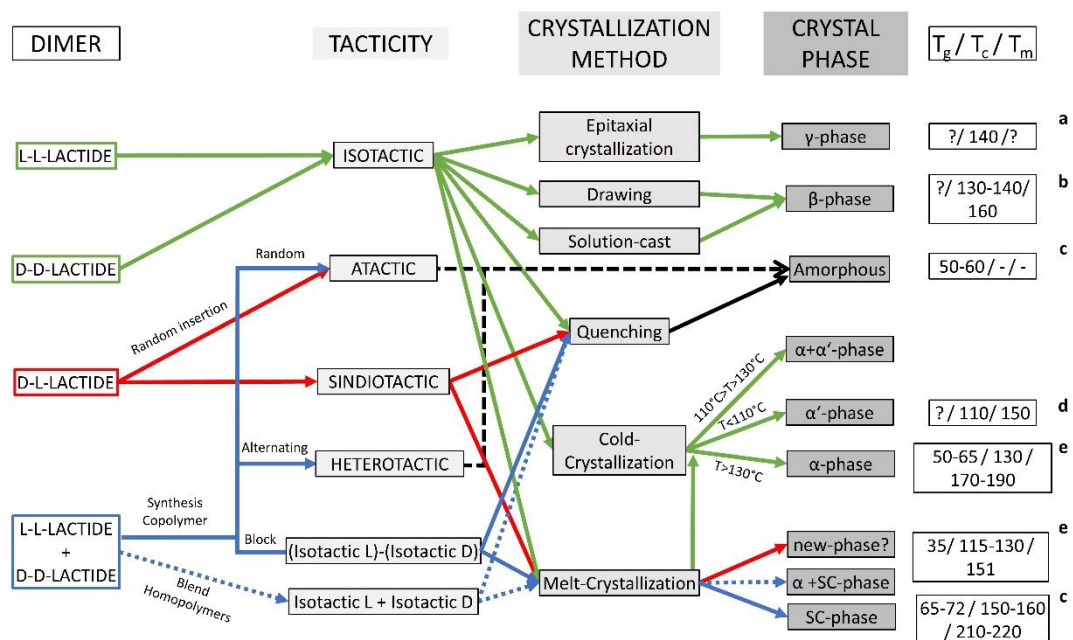
Figure 1.1. PLA microstructures.

content lower than 10% tend to be crystalline (or PDLA with L-lactide content), whilst homopolymers with lower optical purity are amorphous [29]. Besides, the random insertion during the polymerization of D- and L-LA units of both *rac*- and *meso*-lactide monomers generates an *atactic* polymer, Rac-PLA, which is completely amorphous. Moreover, *syndiotactic* PLA is obtained when D- and L- lactic acid units are placed alternatively along the chain whereas *heterotactic* chain architecture is attained when D- and L- lactide units are inserted alternatively on the polymer chain [30]. *Syndiotactic* PLA is a semicrystalline polymer exhibiting higher crystallization temperature (T_c) than isotactic PLA but lower T_m , whilst *heterotactic* PLA is amorphous [31]. Furthermore, the one-pot sequential addition polymerization method [32] of D- and L-lactide monomers yields *stereo-block* copolymers with blocks of opposite chirality, featuring melting temperatures 50°C higher than isotactic homopolymers (220°C) [7].

Besides, PLA displays different crystalline phases (α , α' , β , γ) established by the chain architecture and the specific crystallization mechanism or thermo-mechanical history imposed during its processing, which defines the properties of the final product [33] (**Figure 1.2**). The α -phase is the more stable PLA homo crystal structure that corresponds to an orthorhombic unit cell in which the helices are packed in a hexagonal fashion, containing two antiparallel chains per unit cell. The α -phase is normally obtained when isotactic PLLA or PDLA are crystallized from the melt above 130°C or by crystallization from solution, characterized by a melting temperature of around 170°C [34,35]. The α' -phase (or δ -phase) is the disordered form of the α -phase that is generated either from crystallization from the melt at temperatures below 110°C or by cold-crystallization after quenching PLA to the glassy state. The α' -phase is also organized in the orthorhombic crystallographic unit cell, however, it contains two parallel helices per unit cell which increases the lattice parameters when compared to the ordered α phase. Besides, a mixture of α - and α' -phases is obtained when PLA is crystallized between 110°C and 130°C, although the α' -phase recrystallizes into α -phase when heated near the T_m (150-160°C) [34]. Moreover, the β -phase is developed by stretching PLA fibres in the α -phase at high temperature (130°C-140°C) and high draw ratios as well as by casting thin films from solution [35,36]. The chain conformation of the β -phase is a threefold helix in a trigonal unit cell containing three chains per unit cell, and its T_m is ca. 10°C lower than α -phase T_m [37] [38]. In addition, the β -phase exhibits piezoelectricity that allows the interchange of mechanical and electrical energy [39], broadening its potential applications. Finally, the γ -phase is produced by epitaxial crystallization of PLA on hexamethylbenzene, forming two antiparallel threefold helices in an orthorhombic unit cell [40].

Furthermore, a new crystal structure, the stereocomplex (SC) phase, is formed from the co-crystallization of the two stereoisomers of PLA (PLLA and PDLA) that features a trigonal unit cell comprised of six threefold helices per unit cell. The structural peculiarity of the SC phase with the nearest neighbours of any stem being of a different polymeric chain provides

them easy access to the growth front for both enantiomeric species. In addition, the specific C-H...O-H hydrogen bonds within the crystal lattice that stabilize the structure [41] confirms stereocomplexes with a higher melting (220°C) as well as degradation temperature (220-260°C) [27]. The SC phase was first found by casting a mixed solution of both enantiomers [42] and since then, the SC phase has typically been obtained intentionally from the blend of both enantiomers in solution (in an appropriate solvent such as dichloromethane or chloroform at room temperature, and acetonitrile around boiling temperature [43]) or in the solid-state from the melt [10]. However, the SC crystallization of the blended enantiomers diminishes for high molecular weight (HMw) PLA, and enantiomeric homocrystals (HC) in the α -phase are obtained instead [11]. Additionally, the critical Mw to exclusively obtain SC crystallization is lower for blends obtained from the melt than from solution [44] which hampers its industrial application. The optical purities of the polymers and the mixing ratio of the isomeric chains also affect the obtained ratio of SC to HC crystallites and thus, the preparation of pure SC-PLA



T_g : glass transition temperature; T_c : crystallization temperature; T_m : melting temperature; ?: No information found. ^a[40] ^b[38] ^c[10] ^d[34] ^e[31].

Figure 1.2. Overview of the morphology attained by the different PLA derivatives depending on the processing conditions. Dimer refers to starting lactide dimer for ROP polymerizations.

requires meticulous specific conditions [45]. SC crystallites can also be generated through the synthesis of block copolymers by the one-pot sequential monomer addition to a truly living polymerization catalyst, which allows retaining the SC crystallization in HMw polymers [12,13].

The diverse synthetic approaches afford a wide range of chain architectures that can be generated through the different ratios of L- and D-Lactide monomers that offer the possibility

to tailor the properties of the final polymeric product depending on the intended application. Furthermore, understanding the advantages and drawbacks of the different synthetic processing methods to obtain PLA is crucial to tailoring the foreseen applications. Moreover, since PLA still exhibits performance drawbacks such as low mechanical properties, low thermal resistance and hydrophobicity that limit its applications in some biomedical fields, novel materials with unique properties can be obtained through the blend or copolymerization of PLA with other biodegradable or non-biodegradable polymers, such as polyethylene (PE), polypropylene (PP), Polyhydroxyalkanoates (PHA), PMMA, Poly(ethylene-*co*-vinyl acetate) (PEVA), etc. [5,46,47]. In addition, nanocomposites can be fabricated by mixing PLA with other complementary compounds such as silk [48], gelatin [49], collagen [50], tungsten disulfide [51–53], natural fibres (flax, jute, hemp,) [54], ceramics (ZnO, TiO₂) [55,56], etc. to enhance their performance.

1.3 Synthesis of PLA

PLA was first synthesized by polycondensation by Théophile-Jules Pelouze in 1845. In 1932, Wallace Hume Carothers developed a novel synthetic method based on the ring-opening polymerization (ROP) of the cyclic lactide monomer to synthesize PLLA. ROP was later patented by Du Pont in 1954 to synthesize vinyl fluoride (U.S. Patent No. 2674632, 1954). However, HM_w PLA by ROP on an industrial scale was only attained by the mid-1990s [26].

The lactic acid monomer can be converted to PLA through a polycondensation process by the reaction of the hydroxyl (-OH) and carboxylic acid (-COOH) groups with the removal of the detrimental by-products such as water. Generally, catalysts are added to polymerization to increase the reaction rate. The removal of water, enhanced under vacuum pressure, is critical to producing HM_w polymers due to the increased viscosity of the reaction mixture as the reaction proceeds. However, side reactions, such as transesterification, can also occur during the polycondensation of lactic acid, resulting in the formation of ring structures of different sizes, such as lactides. Transesterification reactions lower the overall M_w and the stereocontrol over the chain architecture, decreasing the physical properties of the PLA afforded as well as reducing the reaction yield [28]. The HM_w PLA is mainly synthesized by ROP due to the accurate chemical control in terms of molecular weight, polydispersity, polymer chain-ends, and tacticity. Moreover, ROP requires relatively mild conditions (130°C) when compared to polycondensation (180-200°C) [28,57]. Three reaction mechanisms have been proposed for ROP of lactide: anionic, cationic, and coordination-insertion mechanisms. In both anionic and cationic polymerizations, a monomer-activation mechanism occurs first that permits the catalyst to be independent of the propagating polymer, and thus, can be easily removed as the polymerization finishes. However, undesirable side and racemization reactions are likely to occur due to the highly activated monomers. On the contrary, coordination-insertion polymerization attains HM_w PLA with higher control over the M_w distribution [6,28]. Metal complexes of several metals have been widely employed as the catalysts for the ROP of lactides [28] of which the most studied are stannous 2-ethylhexanoate [Sn(Oct)₂], aluminium isopropoxide [Al(O i-Pr)₃], and zinc(II) lactate [Zn(Lact)₂] [57]. Sn(Oct)₂ is the catalyst utilized for the industrial synthesis of PLA, due to a large extent to be approved by the FDA for the use in medical (<20 ppm [58]) and food applications. Moreover, lauryl alcohol (1-dodecanol) is usually added as an initiator [28].

The polymerization is induced by a coordination-insertion three-step mechanism supported by the catalyst [57], which was first formulated in 1971 by Dittrich and Schulz [6] (**Figure 1.3**). Firstly, Sn(Oct)₂ reacts with the lauryl alcohol to form a tin alkoxide. Subsequently, the exocyclic carbonyl oxygen of lactide temporarily coordinates with the tin atom of the catalyst being in the alkoxide form. The formed coordination system enhances the nucleophilicity of the alkoxide part of the initiator as well as the electrophilicity of the lactide

carbonyl group that enables the reaction to each other. Finally, the acyl-oxygen bond of lactide is disrupted and the generated linear chain of the lactide turns into the alkoxide part of the catalyst, promoting the coordination with a new lactide molecule and thus, the polymerization propagation [28]. Finally, the active metal-alkoxide bond is hydrolyzed as the monomer is entirely consumed and the formation of a hydroxyl end-group occurs [57]. In the last stage of the propagation step, as the monomer concentration becomes significantly lower (~80%), both intra- and inter-molecular transesterification reactions occur and molecular weight distribution increases. However, the degrees of racemization and chain scrambling achieved

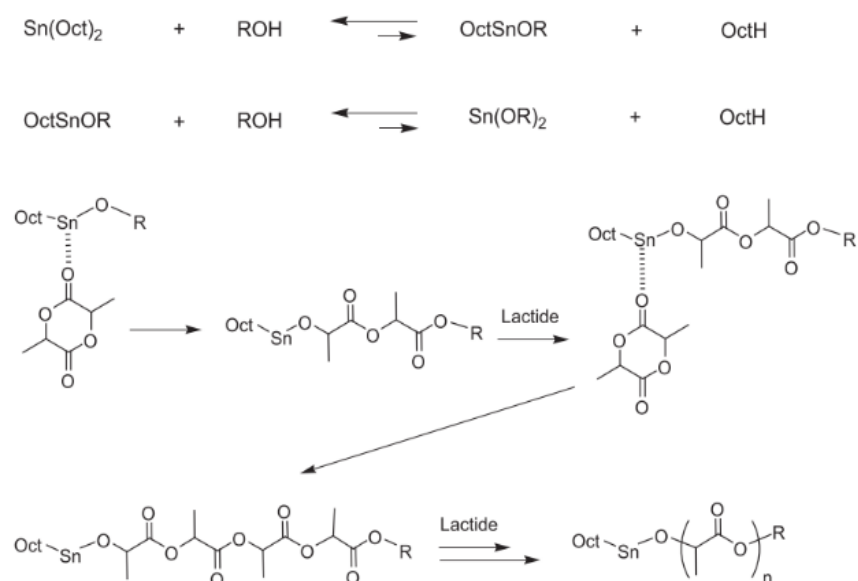


Figure 1.3. ROP of lactide by Sn(Oct)_2 by coordination-insertion mechanism. Reproduced from K. Masutani, Y. Kimura, *PLA Synthesis. From the Monomer to the Polymer*, in: A. Jiménez, M. Peltzer, R. Ruseckaite (Eds.), *Poly(Lactic Acid) Sci. Technol. Process. Prop. Addit. Appl.*, The Royal Society of Chemistry, Cambridge, 2015: pp. 3–36., with permission from The Royal Society of Chemistry.

by metal complexes that follow coordination-insertion mechanisms, are notably lower than those obtained by anionic or cationic catalysis [28]. The microstructure of the final polymers depends both on the initial monomers added to the reaction mixture (Figure 1.2) and the catalyst stereocontrol. The control exerted by the catalyst over the nanostructure of the PLA, and particularly to synthesize PLA stereo-block copolymers of HM_w , is essential to tailor the properties of the final product, and the synthesis of novel catalysts, particularly metal-based catalysts, for polymerization by the coordination-insertion mechanism has attracted much attention since the pioneering work of Kleine et al. in the 1950s [6,28,59,60]. However, several drawbacks to controlling the synthesis of HM_w stereo-block PLA have emerged since then, such as the decrease of the living character of the catalyst due to the increase in the reaction heterogeneity [61], the detrimental side reactions due to multiple nuclearities exhibited by the catalysts [62] as well as the long reaction time required to achieve the desired architectures and molecular weight [6]. Recently, novel catalysts that fulfil the synthetic requirements whilst

exhibiting low toxicity for the application of the PLA derivatives in the biomedical and pharmaceutical fields were just attained [13,63–65] which offers the possibility to design multiblock copolymers featuring simultaneously the PLA stereo-block to attain higher physicochemical properties with other complementary blocks to enhance the PLA limitations.

1.4 PLA processing

Once synthesized, PLA is usually manipulated into its final shape by the use of different processing techniques that apply diverse thermomechanical histories (**Figure 1.2**). Melt processing is a three-step process generally used to transform PLA into different commodity products at an industrial scale [66]. Firstly, the polymer is melted to subsequently be moulded into the desired shape which is then generally cooled to stabilize its dimensions. The industrial techniques such as extrusion and injection moulding are the two most common melt-based processes for manufacturing thermoplastic polymers. Besides, novel common additive manufacturing technologies with promising personalised biomedical applications such as fused deposition modelling follow a melt-based process [67]. Likewise, the tailoring of T_m of PLA is crucial for the performance of applications employing melt-based processing techniques as the process temperature must be above T_m to form a homogeneous melt although low enough to minimize thermal degradation [68]. In addition, the cooling rate during the third step will influence the properties of the final product which determine the crystallization conditions that dictate the crystallinity degree and crystalline phase. Particularly, quenching PLA from the melt at a high cooling rate ($>500^\circ\text{C}/\text{min}$, such as during injection moulding) will result in a highly amorphous polymer [69], whilst semicrystalline PLA is obtained when the cooling rate is reduced ($<30^\circ\text{C}/\text{min}$ [70]). The α -form is usually developed from PLLA or PDLA during typical melt processing, however, a mixture of α and α' phases is obtained when the cooling rate is higher than $2^\circ\text{C}/\text{min}$ since the α -form has very slow crystallization kinetics (pure α -phase is obtained at slower rates) [71]. Furthermore, post-production treatments such as annealing can be implemented to increase the thermal stability and mechanical properties of the final product. The α -phase develops completely from a melt-crystallized material exhibiting a mixture of α and α' when annealing at 140°C for 1h [71]. Additionally, obtaining only the SC phase from the melt from the equimolar blend of PLLA and PDLA enantiomers can be just achieved by restricted thermodynamic conditions such as the relatively low cooling rates ($20^\circ\text{C}/\text{min}$) to avoid the phase separation or from low molecular weight enantiomers ($\sim 20\text{kDa}$) [11] and the isothermal crystallization at temperatures above the T_m of homocrystals ($\sim 175^\circ\text{C}$) [44] as well as by melt-spinning under high tensile stress conditions [72] (**Figure 1.2**). However, PLA materials crystallized in the SC phase has not achieved the market yet [73].

Three-dimensional (3D) printing is an additive manufacturing technology, with the unique ability to produce personalized objects with complex designs at reduced costs and a high-resolution precision [74,75] that have already reached the market in the biomedical field such as the manufacturing of 3D scaffolds for studying the response of particular tissues to different stimuli [76]. In particular, PLA is the most-used polymer for 3D printing since the slow crystallization rate compared to polyolefins (i-PP or PET) avoids warping between layers [77]. «Classical» processing methods such as particulate leaching, gas foaming or solvent-

casting were used for tuning the internal architecture of 3D scaffolds due to their adequacy for replacing tissues with high regenerative capacity. However, 3D printing enables the required control over the scaffold architecture for less regenerative tissues, such as tendons or nerves [78]. Likewise, PLA 3D printed scaffolds have already been investigated for bone [79–84], neural [85] and musculoskeletal soft [86] tissue engineering. In addition, PLA nanofibers have also been used as part of a fibrous bioink for the 3D printing of a meniscus construct to study the proliferation of human adipose-derived stem cells that prove a higher cell proliferation and metabolic activity [86]. Recently, the assessment of PLA scaffold geometry effect on the orthopaedic applications [87] revealed that the presence of hydroxyapatite (HA) in the scaffold enables efficiently the mineralization as well as induces the crystallization of PLA after being 3D printed, whilst PLA without HA remained amorphous. The presence or absence of crystalline domains within the 3D printed PLA scaffold will invariably influence the hydrolysis degradation rate, which is crucial to controlling the optimum performance of the biomaterial. However, the usual lack of structural study for most of the reported 3D printed PLA scaffolds for biomedical applications impedes determining the relationship between the processing conditions, the crystalline structure and the biomedical performance.

Furthermore, in the biomedical industry, electrospinning has been considered a promising method to fabricate polymer nanofibers due to its simplicity and cost-effectiveness of the technique. Electrospinning, unlike drying spinning which relies on mechanical extrusion, uses the electrostatic force to spin the solution into fibres [69]. The fibres thus obtained have a nanometric diameter, producing materials with a high area/volume ratio, high flexibility, and superior mechanical properties compared with other materials formats [88]. Electrospun PLA usually exhibits either an amorphous structure or a semicrystalline structure, although with a very low crystallinity (~10%), due to the rapid solidification of the fibres during the process which entails post-processing thermal treatment between the T_g and the T_m to enhance the crystallinity by cold-crystallization in the α -phase [89,90]. Recently, the straightforward fabrication of PLA electrospun fibres exhibiting β -phase without further post-processing treatment was achieved [91], facilitating the development of PLA-based devices with piezoelectric properties for potential biomedical applications, as will be further discussed [92]. Furthermore, PLA fibres in the SC phase were also generated from the electrospinning of PLLA/PDLA blends resulting in more uniform fibres [93], however, an annealing post-processing step is usually required to obtain crystalline structures [94]. The large efforts dedicated to electrospun nanofibers in the biomedical field arise the possibility to mimic the extracellular matrix since the human tissues and organs are formed by nanofibrous scaffolds [95,96]. However, the industrial scale up production of PLA nanofibers has not been achieved yet, due to the low throughput of the technique, and the requirement of specific solvents [69]. Nevertheless, PLA nanofibers are a topic in continuous research due to their crucial role in several biomedical applications such as bone regeneration [97,98], drug delivery systems [99] and wound dressing [100].

Furthermore, PLA can be also processed into nanoparticles to generate drug delivery systems in which the drug release rate can be controlled by varying parameters such as the processing method, the microstructure of the starting polymer or its concentration in the organic solvent [101]. However, contradictory results are usually found when relating certain processing parameters to the final nanoparticle release kinetics [102–104], and hence, further studies based on the structure-property relationship are required to understand the mechanistic process occurring during nanoparticles formation to design drug nanocarriers with tailored drug release profiles [101] (**Figure 1.4**). Furthermore, the methods for preparing nanoformulations most commonly utilized at the laboratory scale, such as nanoprecipitation or emulsification-solvent evaporation, lack reproducibility between batches. However, novel approaches such as supercritical technology, electrospraying or premix membrane emulsification have emerged as methods more adapted for industrial production, enabling the scale-up process of nanoparticles [105].

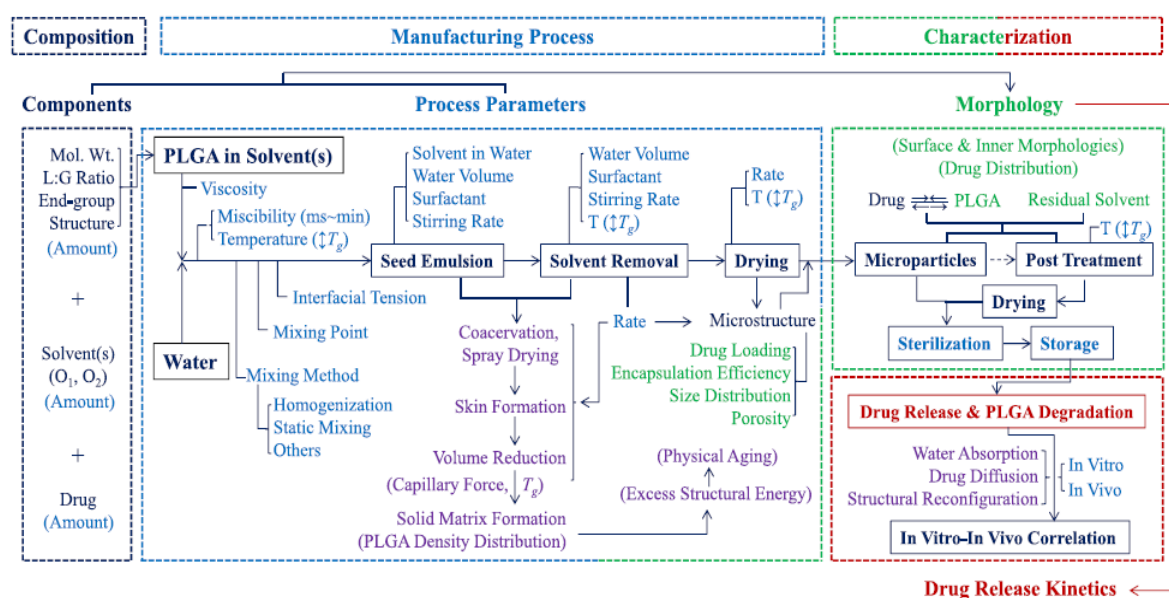


Figure 1.4. Manufacturing process of PLGA microparticles by emulsion methods and the parameters affecting the final properties of the formulation. Reprinted from K. Park, A. Otte, F. Sharifi, J. Garner, S. Skidmore, H. Park, Y.K. Jhon, B. Qin, Y. Wang, Formulation composition, manufacturing process, and characterization of poly(lactide-co-glycolide) microparticles, *J. Control. Release.* 329, Copyright 2021, with permission from Elsevier.

In addition, PLA is generally employed to afford hydrogels as is capable of absorbing a large amount of water that can be programmed to be expanded or shrunk due to external conditions changes [106]. Hydrogels are aqueous solutions that solidify by the decrease of polymer solubility in response to different physical and/or chemical stimuli, typically pH or temperature that are used to control the drug delivery systems [107]. PLA is usually copolymerized with a hydrophilic polymer to form associative micelles that constitute the gel in which the nanostructure and rheology can be tuned by varying the stereochemistry of the

PLA (L/D ratio) [108,109]. Moreover, PLA can also be part of hydrogel materials as a mechanically reinforcing and/or drug-eluting component [49,110,111]. PLA-based hydrogels studies are less common than PLA-based nanoparticles. However, a deeper structural characterization is usually accomplished.

1.5 PLA properties

When designing a PLA-based material for biomedical applications, physicochemical properties such as mechanical and thermal behaviour as well as the degradation degree under physiological conditions must be considered from the chain architecture synthesis together with the subsequent impact of the processing methods to correlate the structure-property relationship with the targeted application.

1.5.1 Mechanical properties

The mechanical properties of PLA are mainly associated with the crystalline phase and crystallinity degree [33] which must be tailored by controlling the stereocontrol exerted during the synthesis as well as by the subjected thermal history and pre-treatment conditions. The mechanical properties of PLA range from soft and elastic (amorphous PLA) to stiff and high strength (semicrystalline PLA) [1], and thus, semicrystalline PLA is preferred when robust mechanical properties are required. For amorphous PLA, the T_g is one of the most important parameters as below T_g amorphous PLA behaves like glass and its flexibility is drastically reduced, whilst above the T_g amorphous PLA behaves like a rubbery material. For semicrystalline PLA both, T_g and T_m , are important parameters since above the T_m the semicrystalline PLA behaves as a viscous liquid [66].

Amorphous PLA is typically obtained from rac-PLA as well as from isotactic PLA quenched from the melt (**Figure 1.2**). Semicrystalline PLA has a tensile strength of 60 MPa, flexural strength of 100MPa, and elongation at break of about 4%, whilst amorphous PLA has lower tensile and flexural strength (40MPa and 84MPa, respectively) and higher elongation at break (7,5%) [66]. The mechanical properties are also dependent on M_w [1] in particular, semicrystalline PLA is more affected compared to amorphous PLA [66] as the chain entanglements, which influence the crystallinity and hence the mechanical properties, increase as the M_w increases [112]. Likewise, the tensile strength increases by a factor of 10 when M_w is increased only by a factor of 4 [113]. Semicrystalline PLA presents higher mechanical properties than a few relevant commodity polymers such as PS, i-PP and PET but inferior thermal resistance [114]. PLA is then more susceptible to thermal degradation during processing, lowering its M_w and hence its final mechanical properties (M_w of PLA decreased 14-40% after injection moulding [115]).

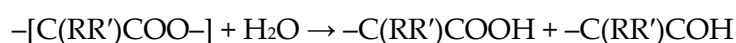
The mechanical properties of PLA as a function of crystal polymorphisms have also been investigated, although mainly for α - and α' -forms due to their abundant availability under industrial processing conditions. Likewise, heat deflection temperature of injected-moulded PLA materials was found to increase linearly with increasing crystallinity above ca. 35% - 40% as well as with the annealing temperature increase, which could be explained by the rise of the α/α' ratio [71,116]. Furthermore, PLLA materials crystallized in the α -phase by annealing after quenching feature a larger Young modulus, tensile strength and storage

modulus as well as lower elongation-at-break and water vapour permeability when compared to those crystallised in the α' - phase [116,117], which, may be attributed to the tighter molecular packing of PLA chains in the α -phase [117]. However, PLA crystallized from the melt showed a decrease in tensile strength, elongation at break, and unnotched impact strength as the temperature of crystallization increased (isothermally analysed between 100°C and 130°C) [118]. Moreover, the Young modulus increased as the temperature increased except for the PLA crystallized at 130°C (α -phase), which is associated with the formation of an aggregate between the amorphous and crystal region due to the formation of fewer nuclei [118]. The discrepancy between results may be attributed to the difference in spherulite density dependent on thermal treatment (annealing after quenching *vs.* crystallization from the melt) [119]. In addition, the tensile modulus and tensile strength of PLA also increase for the β phase compared to the α -phase [36]. Similarly, the tensile properties such as tensile strength, Young's modulus and elongation at break, as well as storage modulus, are also improved by stereocomplexation of PLA [120].

1.5.2 Degradation

Degradation is a crucial feature to be considered when designing PLA biomedical materials with tailored properties. The main factors that affect the mechanism and rate of PLA degradation depend either on the polymer characteristics such as the molecular weight, crystallinity and shape or/and size as well as physicochemical parameters related to the surrounding medium as temperature, pH or/and enzymes [121].

Commonly, PLA degradation is a multistep process that is initiated through a hydrolytic process followed by enzymatic action, since biotic attack only occurs when PLA reduces its M_w [122]. However, in the human body, only the hydrolytic process occurs, followed by the degradation of lactic acid in the Krebs cycle to finally yield water and oxygen. PLA hydrolysis follows the ester moiety cleavage from the polymeric backbone chain, decreasing the M_w :



Moreover, PLA hydrolysis is an autocatalytic process, as the chain scission increases the concentration of carboxylic acid end groups in the degradation medium, which possesses a catalytic action on the process (**Equation 1.1**) [123].

$$d[\text{COOH}]/dt = k[\text{COOH}][\text{H}_2\text{O}][\text{E}] \quad (1.1)$$

where $[\text{COOH}]$, $[\text{H}_2\text{O}]$, and $[\text{E}]$ are the concentrations of the carboxylic groups, water, and ester groups in the medium, respectively. The hydrolytic degradation of PLA typically occurs in a stepwise fashion. Firstly, water is diffused into the material that triggers the later hydrolysis of the chains in the amorphous region; subsequently, the diminution of M_w

proceeds as a result of the hydrolytic cleavage of ester bonds and the formation of water-soluble compounds; finally, the hydrolysis of the crystalline phase occurs [124].

1.5.2.1 Polymer factors

Hydrolytic degradation is inversely proportional to M_w below 4×10^4 g/mol, due to the higher mobility of chains and larger density of hydroxyl groups that enhance the probability of water-soluble oligomers formation, thus catalyzing PLA degradation [125]. However, the hydrolysis rate is no longer dependent on M_w above 8×10^4 g/mol since other parameters, such as total crystallinity have a higher effect on hydrolysis [126].

Besides, semicrystalline PLA is more resistant to hydrolytic degradation than amorphous polymeric chains, including the amorphous regions between crystalline parts. [121]. Hydrolysis of amorphous PLA showed a weight decrease of about 14% after 18 weeks, whilst semicrystalline PLA lost a similar weight after 20 months (at pH 3.4 and 37°C) [124]. However, accelerated hydrolysis in the early stages has been observed with increasing the initial polymer crystallinity (X_c) at pH 7.4 [127]. The higher density of hydrophilic terminal groups in the amorphous regions between the inter-crystalline areas accelerates the initial hydrolytic degradation of crystallized PLA regions by enhancing the diffusion of water molecules into the bulk material. Likewise, films formed by mainly amorphous PLA undergo hydrolytic degradation with a nearly constant hydrolysis rate constant (k_h) throughout the process, whilst films composed of predominantly semicrystalline PLA are subjected to a two-step hydrolytic degradation, initiated by a higher k_h stage, followed by a smaller k_h . Moreover, the degradation rate of the SC crystalline phase is smaller than that of the α -phase [128].

In addition, degradation is faster as the thickness of the object is increased [129]. The size is related to the hydrolytic degradation as a result of the solubility of the oligomers close to the surface that are drained into the solution as the ageing time increases. Besides, the solubilized oligomers within the matrix remain entrapped and contribute to the autocatalytic effect (Eq. 1.2). Likewise, the main PLA degradation mechanism was found to be dependent on several size regimes: bulk erosion for material thickness lower than 2mm, core-accelerated erosion between 2mm and 7.4 cm, and surface erosion for thickness higher than 7.4 cm [121].

1.5.2.2 Media factors

Furthermore, the main media factors that affect PLA hydrolysis are pH and temperature. Particularly, understanding the degradation kinetics dependence of PLA on pH is crucial to generating materials with tailored properties for biomedical applications due to the pH of the human body range from strongly acidic to almost neutral. Recent efforts have been focused on elucidating the effect of pH in the PLA hydrolysis mechanism of degradation. The pH dependence of the k_h was found to be described by the general rate constant equation (Equation 1.2) [130]:

$$k_h = k_o + k_H [H^+] + k_{OH} [OH^-] \quad (1.2)$$

where, k_o is the first-order rate constant degradation in water, and k_H and k_{OH} are the second-order rate constants catalysed by protons and hydroxyl ions respectively. A pH regime dependence described the hydrolysis mechanism, specifically hydroxyl-catalysed above pH 5 (**Figure 1.5**, the slope is ~ 1 in the plot of $\log k_h$ against pH) and specific proton catalysis occurs at pH values below pH 4 (**Figure 1.5**, slope ~ -1) whilst k_h is minimal at pH around 4.5 [130,131]. In addition, the dependence of the hydrolysis mechanism on pH was proved and the degradation under acidic conditions occurs through the split of the last lactic acid monomer after the nucleophilic attack by water [130–132]. However, the mechanism of PLA degradation in neutral or alkaline mediums is controversial, and the decomposition route is believed to follow either an intramolecular transesterification with the formation of lactide from the two end units of the oligomer [130] or a random ester cleavage degradation mechanism [131].

In addition, the effect of temperature on the hydrolytic degradation (T_h) was found to be differentiated into three thermal regimes related to the chain mobility: $T_h < T_g$, $T_g \leq T_h < T_m$ and $T_m \leq T_h$. The hydrolytic degradation rate increases when T_h is higher than T_g as a consequence of the higher chain mobility. Likewise, if T_h exceeds T_m , crystalline regions melt and disappear, and thus, the hydrolytic degradation in the melt occurs homogeneously, similarly to racemic PLA. However, when T_h is lower than T_m , the hydrolysis degradation causes a heterogeneous M_w reduction as a result of the lower water diffusion. Indeed, the activation energy of the hydrolytic degradation increases from 50.9 kJ/mol for the thermal range $T_m \leq T_h$, to 83 kJ/mol

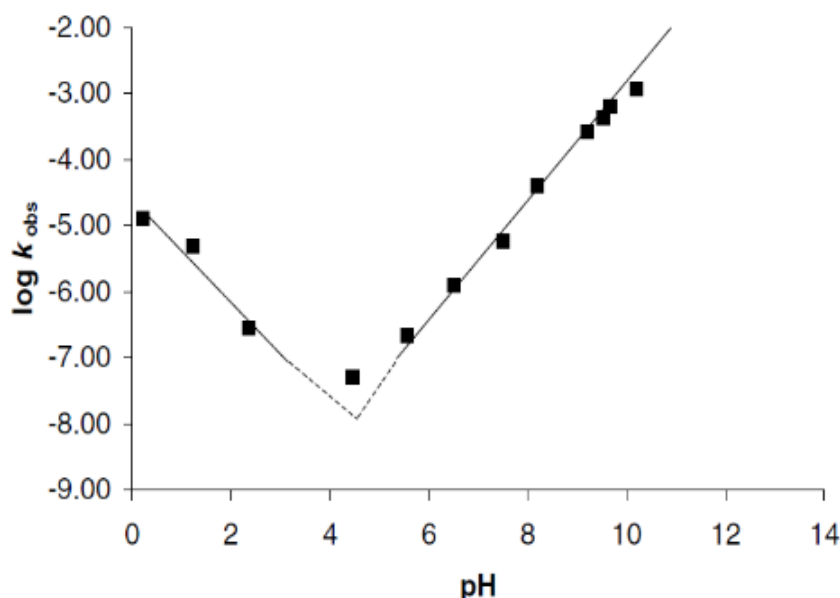


Figure 1.5. Dependence of hydrolytic degradation constant (k_{obs}) on pH. Reprinted from S.J. De Jong, E.R. Arias, D.T.S. Rijkers, C.F. Van Nostrum, J.J. Kettenes-Van Den Bosch, W.E. Hennink, New insights into the hydrolytic degradation of poly(lactic acid): Participation of the alcohol terminus, *Polymer (Guildf)*. 42 (2001) 2795–2802, copyright 2001, with permission from Elsevier.

for $T_h < T_g$, whilst intermediate activation energy of 69.9 kJ/mol is found for the temperature regime $T_g \leq T_h < T_m$ [121].

Moreover, the rate of degradation is also dependent on the magnitude and type of the applied stress that is crucial to designing biomedical materials employed in physiological conditions. Materials subjected to a static load experience a higher rate of degradation, which is further increased when a dynamic load is applied [133].

1.6 Medical applications

PLA and its copolymers are currently used at the clinical level in different pharmaceutical applications such as dermal fillers and drug delivery systems (DDS) as well as biomedical applications such as sutures or tissue engineering (TE) [134–137]. The first biomedical application of PLA at the clinical level, namely the suture Vycril® composed of glycolide and lactide components, dates from 1974. Since then, several sutures composed of different ratios of glycolide and lactide have reached the market, such as Polysorb®, Radik® or XLG® [134]. Moreover, Decapeptyl SR was the first pharmaceutical product based on PLGA microparticles approved in Europe in 1996 for the treatment of prostate cancer. Thereafter, more than 15 microparticles PLA-based products have been approved and marketed to control drug delivery [135] as well as a soft-tissue augmentation agent [136,137].

The recent trends of PLA in pharmaceutical and biomedical research will be addressed in the following section. The pharmaceutical section comprises the applications related to drug delivery such as nanoparticles whilst the biomedical section includes the applications related to tissue reparation, although the diffuse limit between both fields.

1.6.1 Pharmaceutical applications

1.6.1.1 Nanoparticles

PLA is among the biocompatible polymers the most frequently used as DDS (**Table 1.1**) due to the ease to tune the drug release profile from PLA formulations by modifying different architectural parameters such as polymer molecular weight, stereochemical composition or polymer crystallinity [138]. Nowadays, several PLA-based microparticles formulations have successfully reached the market [135], however, microsized DDS features inherent drawbacks to traverse biological barriers as well as their rapid clearance after systemic administration, limiting microparticles application to subcutaneous and intramuscular injections [139]. In contrast, nanosized DDS increase systemic circulation time and facilitate tissue penetration as well as sterilization via filtration [139]. PLA nanoparticles have been designed for the treatment of several pathologies such as cancer [140,141], Chagas disease [142], Alzheimer disease [143] or insulin-dependent diabetes [144]. Besides, the surface of PLA nanoparticles has been functionalized with antibodies [145] or cell-penetrating peptides [146,147] as a synthetic approach to target specific tissues or cells and both increase the therapeutic effect and decrease side effects. Moreover, the attachment of PLA nanoparticles to cells exhibiting blood barrier brain migratory properties (T lymphocyte) has also been proposed as a novel approach to drug delivery into the brain [148].

However, the unusual establishment of the correlation of the structure-property relationship of the PLA-based nanoparticles after formulation, such as the T_g , the crystallinity

Table 1.1 Summary of the PLA-derivative nanoparticles.

Material	Processing Technique	Polymer Structure	Molecular Weight (kDa)	Material Characterisation ¹	Studies ²	Ref.
Nanoparticles	Double emulsion-solvent evaporation	PLLA-PEG PLLA	85–160	Size, PDI, EE (%)	In vitro/in vivo	[140]
	Nanoprecipitation-solvent displacement	Rac-PLA	-	Size, PDI, Z-potential, LE (%), EE (%), Morphology (SEM)	In vitro/in vivo/clinical	[141]
	Interfacial deposition-solvent displacement	Rac-PLA-Peg	18–28	Size, PDI, Z-potential	In vivo	[142]
	Emulsion-solvent evaporation	Maleimide-PEG-PLA (no PLA specification)	PEG ₃ -PLA ₇₀	Size, Z-potential, Morphology (TEM)	In vivo	[143]
		Methoxy-PEG-PLA (no PLA specification)	PEG ₃ -PLA ₅₀			
	Emulsion-solvent evaporation	PLGA (75L:25G)	15	CE (%) complexation efficiency, Z-potential, morphology (SEM)	In vivo	[144]
	Nanoprecipitation-solvent displacement	Trastuzumab-PEIcoating-Rac-PLA	22	LE (%), EE (%), Morphology (TEM)	In vitro	[145]
	Emulsion-solvent evaporation	Maleimide-PEG-PLA (no PLA specification)	PEG _{3.4} -PLA ₃₄	Size, PDI, Z-potential, Morphology (TEM)	In vitro/In vivo	[146]
		Methoxy-PEG-PLA (no PLA specification)	PEG _{3.4} -PLA ₃₀			
	Emulsion-solvent evaporation	Maleimide-PEG-PLA (no PLA specification)	PEG _{3.4} -PLA ₃₄	Size, PDI, Z-potential, EE (%), LC (%), Morphology (TEM)	In vitro/In vivo	[147]
		Methoxy-PEG-PLA (no PLA specification)	PEG _{3.4} -PLA ₃₀			
	Nanoprecipitation-solvent displacement	Rac-PLA-OH	10.5	Size, Z-potential, Morphology (TEM)	In vitro	[148]
Rac-PLA-PEG-NH ₂		PLA _{4.5} -PEG _{3.5} -NH ₂				
Nanoprecipitation-solvent evaporation	PLA	-	Size, Z-potential, pH, EE(%), LE (%), Morphology (AFM, SEM), Molecular structure (FTIR)	In vitro	[149]	

or the physical ageing unable to understand the drug release mechanism from a nanoscopic scale. Particularly, the rearrangement of polymer chains during physical ageing, which typically occurs during the storage step and depends on the T_g , may increase water absorption leading to an initial burst release [150]. The control or the analysis of the polymeric

physicochemical parameters of the formulations is crucial to designing a specific degradation rate considering the influence of the conditions on the drug-release mechanism followed by the formulation: drug diffusion through water-filled pores, diffusion through the polymer matrix, osmotic pumping or surface and bulk erosion [139].

1.6.1.2 Hydrogels

PLA-based hydrogels that are formed through different external stimuli have already reached the clinical level. Particularly, Atridox® is a doxycycline formulation used for chronic periodontitis containing PLA and N-methyl-2-pyrrolidone mixtures that solidifies to a wax-like consistency upon contact with gingival crevicular fluids. Furthermore, OncoGel® is a paclitaxel formulation used for local tumour treatment based on PLGA-PEG-PLGA triblock copolymers that exhibit a sol-gel transition at body temperature [151]. The fabrication of PLA-hydrogels usually requires copolymerization with other polymers such as PEG, polyurethane and poly glycolic acid [152] as well as the blend with collagen and gelatin [49,50] to increase the hydrophilic character. Moreover, different physicochemical and mechanical properties, such as the drug release rate, can be modulated by varying the size of PEG, polymer concentration as well as the stereoisomery of PLA [153,154]. Likewise, a series of stereocomplexed PLA pentablock hydrogels were synthesized with tailored microstructure by varying the stereostructure, crystallization and stereocomplexation and their physical properties were thoroughly characterized (**Table 1.2**). The PLA hydrogels featuring symmetric pentablock copolymers exhibited higher gel-sol transition temperature, higher storage modulus and slower biodegradation and drug release compared to asymmetric pentablocks [155]. Recently, the synthesis of hydrophobic polymers, in particular PLA, to produce thermohydrogels has been achieved without the use of solvent, which enhances thermohydrogels biocompatibility [156]. Furthermore, a PLA-based hydrogel was designed that might be applied as a delivery vehicle with immediate release upon contact with reducing conditions, such as tumour microenvironments [157]. The polymer solution gelled between 32°C and 40°C due to the decrease of polymer solubility and collapsed upon exposure to strong reducing agents due to the cleavage of the disulphide bond incorporated in the polymer structure [157]. Likewise, a PLA-based hydrogel was recently designed for the treatment of chronic inflammatory diseases, such as rheumatoid arthritis, which fulfil an on-demand drug release depending on the severity of the disease by using nitric oxide (overproduced in inflammatory environments) as a hydrogel degradation agent [158]. PLA-based injectable hydrogels were also envisaged to be used for regenerative medicine requiring higher mechanical properties. Particularly, hydrogel composites comprising electrospun-PLA nanofibers and gelatin nanoparticles lead to a 15-fold increase of the storage modulus without compromising the injectability [159]. Moreover, the incorporation of PLA nanoparticles into a gelatin hydrogel also leads up to a 100-fold increase in the viscosity, without compromising the injectability [110].

Table 1.2 Summary of PLA-derivative hydrogels.

Material	Processing Technique	Polymer Structure	Molecular Weight (kDa)	Material Characterisation ¹	Studies ²	Ref.
Hydrogels	Temperature increase of solutions (RT --> 37 °C)	PLLA-Castor Oil	4.8	Viscosity, specific optical rotation, T _g , shear stress	-	[153]
		Rac-PLA-Castor Oil	4.6			
	Temperature increase of solutions (RT --> 37 °C)	PLLA	1.5	Sol-gel transition, micelles size, circular dichroism, morphology (TEM), nanostructure (XRD)	-	[160]
		Rac-PLA	1.5			
		PLLA-PEG	14.4			
Hydrogelation by concentration	PLLA-PEG-PLLA	11.5–15.5	Storage modulus, nanostructure (WAXD)	-	[161]	
	Rac-PLA-PEG-Rac-PLA					
Temperature increase of solutions (RT --> 37 °C)	OS-rac-PLA-PEG-rac-PLA-OS (olygomer serin)	~3	Sol-gel phase transition (depending on PEG M _w)	In vitro/In vivo	[154]	
"Click" reaction	DA-NOCCL + N ₃ + rac-PLA-PEG-N ₃ (NP)	~6	Aggregates size, morphology (Crio-SEM and TEM), mechanical properties	In vitro/In vivo	[158]	

1.6.1.3 Perspectives

1.6.1.3.1 Pharmaceutical design

The application of 3D printers for the customization and personalization of pharmaceuticals is one of the most revolutionary and powerful tools in the last decades [162,163]. The traditional « one-size-fits-all » treatment approach in the healthcare industry is ineffective in up to 70% of patients, according to the National Health Service, due to varied pharmacokinetic traits of different patients, creating the need to shift from mass production to personalized dosage medicine [164]. 3DP technologies have been used for the production of pharmaceuticals for pre-clinical animal models, due to the accuracy in producing dosage forms of appropriate geometry and size [165]. Besides, the Food and Drug Administration (FDA) approved in 2015 the first drug manufactured using 3DP technology, Spritam® [166,167], opening the scope of oral drug delivery using 3DP. Likewise, a five-in-one dose combination polypill was manufactured by three-dimensional extrusion with two independently controlled and well-defined release profiles [168], simplifying the drug therapy and potentially improving the adherence of patients to the prescribed treatment. Additionally, artificial intelligence machine learning techniques have been developed to predict key 3DP fabrication parameters and advance the 3DP fabrication process, reducing time, costs and resources normally invested in formulation development [74] (**Figure 1.6**). The current variety

of biomedical applications attained by PLA materials processed by 3D technology such as the oral formulation of solid dosage forms [169] and subcutaneous implants for prolonged drug delivery [170] by fused deposition modelling envisage their use increases as the 3D techniques advance and the utilisation of 3DP is expanded in the society.

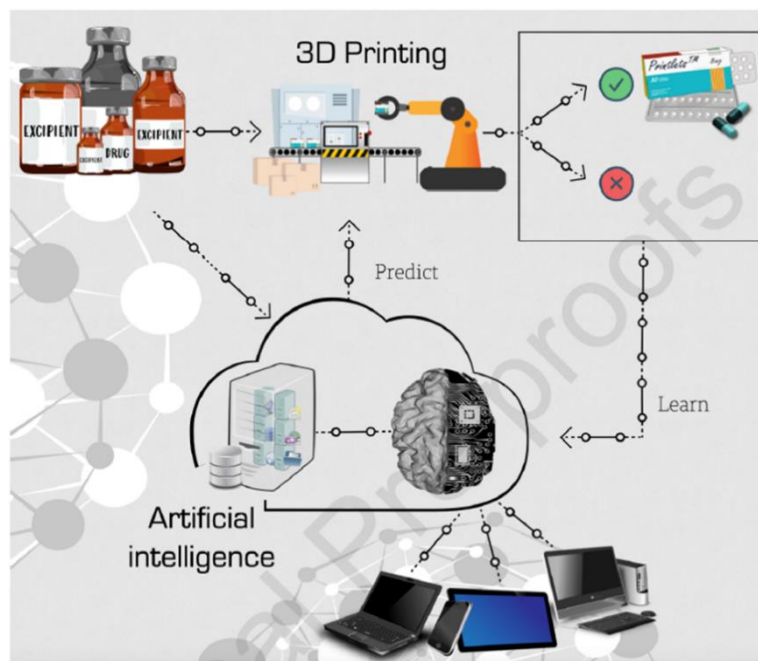


Figure 1.6. Machine learning approach for predicting the 3D printability of medicines (M3DISEEN). Reprinted from M. Elbadawi, B. Muñiz Castro, F.K.H. Gavins, J.J. Ong, S. Gaisford, G. Pérez, A.W. Basit, P. Cabalar, A. Goyanes, M3DISEEN: A novel machine learning approach for predicting the 3D printability of medicines, *Int. J. Pharm.* Copyright 2020, with permission from Elsevier.

1.6.1.3.2 Chiral drugs

The development of chiral drugs has recently become important for the pharmaceutical industry as frequently, the enantiomers of a racemic drug have different physiological activities and pharmacokinetic profiles (e.x. R-Thalidomide is a sedative, S-Thalidomide leads to birth deformity). However, the vast majority of drugs used clinically are still employed as racemates likely due to the difficulty in separating racemic compounds into enantiomerically pure isomers. The chirality of PLA enables its use for enantioselective drug delivery [171] as proved by the generation of chiral particles of PLLA and PDLA loaded with racemic naproxen which preferably releases S-naproxen isomer in ethanol and chloroform for both PLLA and PDLA particles. The enantioselective release of S-naproxen was found to result from a different distribution of R- and S- naproxen within the particle caused by enantioselective interaction [172] (**Figure 1.7**). Furthermore, the drug release of the designed drug nanocarrier

by chiral particles composed of two chiral helical polymers (PLA and the polymer-based on chiral acetylenic (PCM)) revealed that polymer chains with similar chirality (*S*-PCM/PLLA and *R*-PCM/PDLA) cooperated to release *R*-naproxen, while for *S*-PCM/PDLA and *R*-PCM/PLLA particles preferably released *S*-naproxen [173]. In addition, hetero-stereocomplexes were reported to form between poly-*D*-lactide and *L*-configured proteins [174], such as insulin [175], somatostatin [176] or leuprolide [177]. Particularly, different factors such as the increase of PDLA molecular weight or the Leuprolide/PDLA ratio increased the leuprolide release rate [178]. Furthermore, Leuprolide induced PDLA crystallization in a less stable crystal phase (β -phase) that recrystallizes into the α -phase upon further heating [179]. DNA-loaded PLA [180], as well as PLA-PEG [199,200] nanoparticles, were also recently developed where DNA acts as a nucleating agent due to the strong interactions between PLA/DNA molecules and which are primarily responsible for the sustained release of DNA. In addition, the DNA melting peak

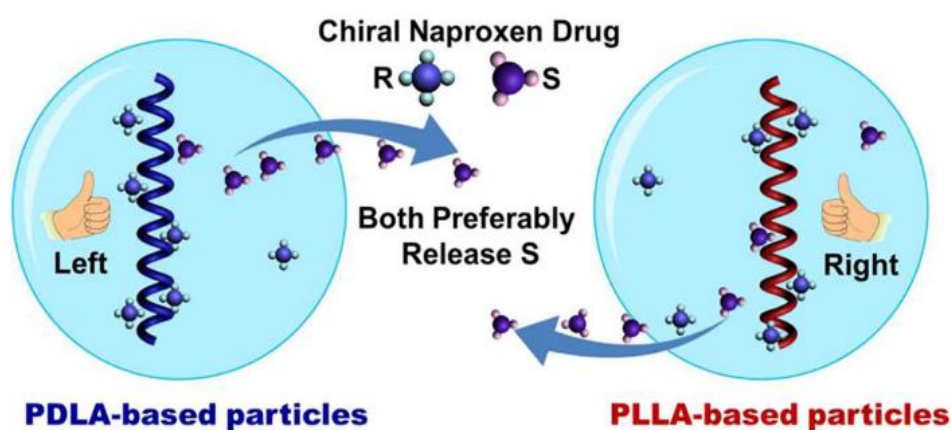


Figure 1.7. Polylactide-based chiral particles with enantio-differentiating release ability. Reprinted from J. Liang, B. Yang, J. Deng, Polylactide-based chiral particles with enantio-differentiating release ability, *Chem. Eng. J.* 344 (2018) 262–269., copyright 2018, with permission from Elsevier

shifted to a higher temperature in the PLA-DNA complex, suggesting the good protecting ability of the PLA matrix towards the incorporated DNA. Finally, the PLA-DNA complex exhibited a high transfection efficiency which is a crucial step to ensure the efficacy of the DNA molecule to be transcribed and translated. However, the PLGA nanoparticles exhibited higher gene transfection due to the higher DNA release [181]. Moreover, PLGA nanoparticles loaded with the correspondent antigen, stimulated robust mucosal IgA immunity after intranasal administration for both parainfluenza virus [182] and tuberculosis [183].

1.6.1.3.3 Antibacterial applications

Bacterial infections originated from implants and medical devices, are typically treated with antibiotics and their misuse has promoted their resistance to drugs. Multidrug-resistant bacteria is one of the main threats to health and food security worldwide, according to the World Health Organization, and alternative treatments mainly based on bacterial proliferation prevention need to be addressed [184]. Polymers usually do not exhibit intrinsic antibacterial properties, although antibacterial additives such as silver nanoparticles [185,186], titanium dioxide [187] or essential oils [188] can be used to develop nanocomposites exhibiting antimicrobial activity. Moreover, antibacterial PLA filaments for 3DP containing copper particles are already commercially available (PLACTIVE AN1 Copper3D [189], PLActive Red [190]) and antibacterial 3D prostheses have been developed to minimize skin disorders related to microbial infections [191]. PLA-based nanocomposites exhibiting antibacterial characteristics can be manufactured in a wide variety of architectures due to the capability of PLA to be processed by different techniques such as 3DP [192], electrospinning [193] (**Figure 1.8**), extrusion [194], spin coating [195], etc. that broads its applicability in the biomedical field.

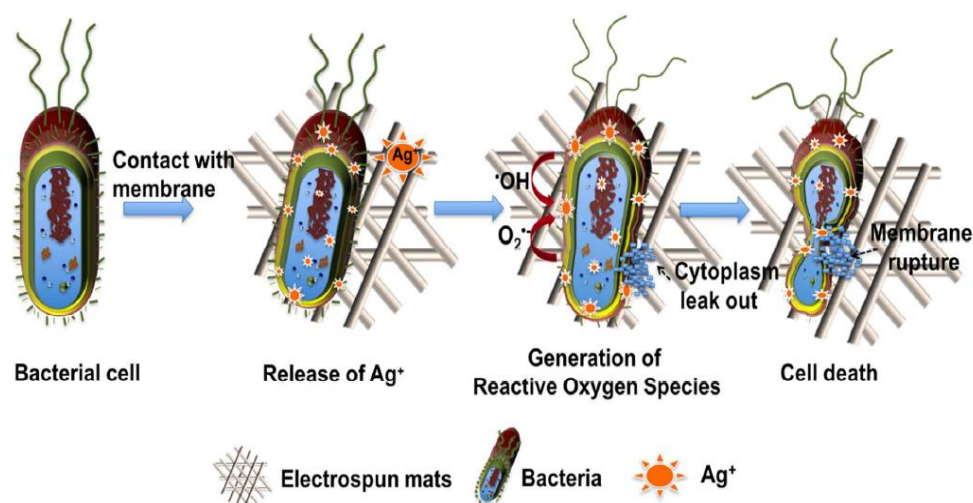


Figure 1.8. Schematic diagram of the release of Ag⁺ ions from AgNPs comprised in PLA electrospun membranes exhibiting antibacterial properties. Reprinted with permission from C. Liu, J. Shen, K.W.K. Yeung, S.C. Tjong, Development and Antibacterial Performance of Novel Polylactic Acid-Graphene Oxide-Silver Nanoparticle Hybrid Nanocomposite Mats Prepared by Electrospinning, ACS Biomater. Sci. Eng. 3 (2017) 471–486. Copyright 2017 American Chemical Society.

1.6.1.3.4 Polymer therapeutics

Polymer therapeutics is an alternative approach to conventional drug delivery systems which comprises polymer-drug/protein conjugates as well as polymers with a therapeutic effect by themselves (polymeric drugs). The lack of therapeutic activity featured by PLA has determined its use conjugated with drugs due to its higher stability, precise drug loading efficiency and sustained drug release compared to drug encapsulation systems [196,197].

Several synthetic methods have been proposed to conjugate PLA into different drugs (**Table 1.3**). Particularly, paclitaxel has been employed as an initiator for the ROP of rac-PLA through the reaction of the 2'OH of paclitaxel with lactide, ensuring the presence of paclitaxel at the chain termini [198]. In addition, paclitaxel has also been conjugated to rac-PLA throughout the PLA chain in a controlled way through an azide-alkyne click reaction which was found by in vitro cytotoxic analysis a higher therapeutic effect than the free drug [199]. Besides, antihypertensive drugs such as lisinopril have also been conjugated to PLA-PEG-PLA copolymers followed by micelle formulation exhibiting a more sustained release compared to physically loaded micelles [200]. Moreover, anti-inflammatory drugs such as indomethacin have also been covalently immobilized onto PLLA films as a potential metallic implant coating to avoid biofilms and blood clot formation [201]. However, the unusual nanostructure characterization of the PLA component of the polymer-drug conjugate which is typically based only on the molecular weight, morphological aspects as well as thermal properties (T_g , T_c , T_m , crystallinity), deter the understanding of the release kinetics [202].

Table 1.3 Summary of PLA-derivative polymer therapeutics.

Material	Processing Technique	Polymer Structure	Molecular Weight (kDa)	Material Characterisation ¹	Studies ²	Ref.
Polymer therapeutics	ROP mediated by Paclitaxel	PEG-RacPLA-Ptxl	~30	Structure (NMR), M_w (GPC)	-	[198]
	ROP mediated by Docetaxel	PEG-RacPLA-Dtxl				
	Azide-alkyne click reaction	Ptxl (23%)-RacPLA-PEG (25%)	~10–15	Size (DLS), structure (NMR), morphology (TEM), molecular weight (GPC)	In vitro	[199]
	Conjugation + micelles formulation	RacPLA-PEG-RacPLA-Lisinopril	~10	Size (DLS), morphology (AFM)	In vitro drug release	[200]
	Hot press film	PLLA-indomethacin	-	Conjugation (fluorescence, XPS), contact angle	-	[201]
	ROP	(PLLA) ₃ -Camptothecin [3-armed]	~30	Molecular weight (GPC), structure (NMR), morphology (AFM), thermal properties (TGA, DSC)	In vitro drug release and enzymatic degradation	[202]

1.6.2 Biomedical applications

1.6.2.1 Stents

Stents are medical devices placed in a lumen of the body, particularly blood vessels, to prevent its closure. Metal stents are typically used to treat coronary disease due to their flexibility, radial force, resistance to fracture, radiopacity, biocompatibility and low thrombogenicity. However, several late clinical complications including stent thrombosis, restenosis and neoatherosclerosis still exist [17]. Bioresorbable vascular scaffolds emerged as

Table 1.4 Summary of PLA-derivative stents.

Material	Processing technique	Polymer structure	Molecular weight (kDa)	Material characterization ¹	Studies ²	Ref
STENTS	Bought (REMEDY) ³	Rac-PLA	-	-	Clinical	[15]
	Desolve Cx ³	PLLA- Novolimus	-	In vitro/ in vivo degradation (Mw lost)	Clinical	[16]
	Mirage ³	PLLA (4% D- LA)-sirolimus	-	-	Clinical	[17]
	ABSORB V G2 ³	PLLA	-	-	Clinical trial (RENASCENT III)	[203]
	MAGNITUDE ³	PLLA- sirolimus	-	-	Clinical	[18]

a new technology in the field of percutaneous coronary intervention to provide temporary mechanical support and drug delivery followed by bioresorption of the scaffold in the vessel. The first biodegradable stent in the clinical setting was developed 30 years ago and was constituted by PLLA [15]. Subsequently, several drug-eluting stents mainly based on PLLA and Rac-PLA were developed and particularly BVS Absorb is the more spread [204]. BVS Absorb was approved in 2016 by the FDA based on non-inferiority test after 1 year of implantation compared to the corresponding “gold-standard”, namely the metallic everolimus-eluting stent [205]. However, compared with metallic stents, the BVS appears to be associated with both lower efficacy and higher thrombotic risk after 2 years on average [206] mainly due to scaffold discontinuity, malposition due to under expansion and neoatherosclerosis [207,208]. In addition, the current challenging generation of PLA-based scaffolds with equivalent radial strength and flexibility to their metallic stent counterparts [209] was recently faced by investigating the influence of the stent geometric parameters on the mechanical properties. The radial stiffness and peak compression force of the PLLA helical

stents were found to increase as both the initial pitch angle as well as the initial diameter decreased[210].

1.6.2.2 Tissue engineering

Tissue engineering (TE) is one of the main strategies of regenerative medicine that consists of the regeneration of neotissues by applying 3D scaffolds for cell attachment and growth [211]. The designed scaffolds must fulfil different criteria with ambivalent properties such as biocompatibility, and mechanical properties suitable for the intended application whilst supporting the normal functioning of cells and tissues. Polymers are the most popular materials for scaffold production due to their physicochemical characteristics and bioactivity [212]. Particularly, synthetic polymers have drawn large attention as an alternative to natural polymers such as peptides, nucleic acid and polysaccharides, due to their price and ease to be produced [213]. Among the synthetic polymers, PLA, PGA, poly-(ϵ -caprolactone) (PCL), polydioxane and poly-(trimethylene carbonate) are currently the most extensively used for tissue engineering applications [213] and the specific polymer selection is based on the structure-property relationship required for the targeted application. Likewise, PCL features high drug permeability and less acidic byproducts compared to other polyesters but a relatively slow degradation rate, limiting its usage to long term applications. In contrast, PLA presents a faster degradation rate compared to PCL, although still relatively slow. However, long degradation times coupled with the high crystallinity of the remained fragments might cause inflammatory reactions in the body. Likewise, the PLA is used frequently as *rac*-PLA to diminish detrimental health effects, being the latter rapidly degraded without the formation of crystalline fragments [14]. Besides, alternative approaches to circumvent the individual limitations of the single polymers such as synthetic co-polymers, the combination with natural polymers or/and the scaffold surfaces functionalization are frequently used to overcome the used manifested hydrophilicity, cell attachment and biodegradability issues [212].

However, 3D scaffolds generated from PLA and its copolymers [212] have already been evaluated for a wide variety of regenerative applications with different tissues such as bone [214], nerve [215], tendon [216] and cartilage which enlarge the applicability of conventional ceramic and metal solutions focussed on the orthopaedic field (**Table 1.5**). Particularly, polymers can be shaped into complex topologies for customised medical solutions with the advent of 3D printing technologies.

Table 1.5 Summary of PLA-derivative scaffolds.

Material	Processing technique	Polymer structure	Molecular weight (kDa)	Material characterization ¹	Studies ²	Ref
SCAFFOLDS	Freeze-drying, salt-leaching (3D scaffold)	PLGA (75L:25G)+ Silk +HA(Hidroxiapatite)	90-126	Structure (FTIR), Degradation temperature (TGA), Morphology (SEM), Swelling (%), water uptake (%), Mechanical properties	In vitro/ In vivo	[214]
	Wet-spinning (Microfilament)	P(L-co-rac-LA)(75:25)	200	Morphology (SEM)	In vivo	[215]
	Bought (kinnet filmanets)	PGA/PLA (2:1)	-	Morphology (SEM and TEM), Biomechanical properties	In vitro/In vivo	[216]
	Bought (forged composite sheets)	PLLA-PGA (88:12) + HA PLLA + HA	-	Morphology (SEM)	In vivo	[217]
	bought (OSTEOTRANS MX)	PLLA + HA	-	Molecular weight, Crystallinity, Morphology (SEM) [after surgery]	Clinical	[218]
	Bought (Plates)	PLLA/PGA PLLA/HA	-	-	Clinical	[219]
	Electrospinning	PLGA (85/15)	285	Morphology (SEM), Mechanical properties, Structure (FTIR)	In vitro	[220]
	Electrospinning	PLGA (85/15)	285	Morphology (SEM), Mechanical properties, Structure (FTIR)	In vitro	[221]
	Supercritical Emulsion extraction	PLGA carriers + fibrin hydrogel	38-54	Size, Morphology (SEM)	In vitro	[222]
	Electrospinning	PLGA + silk	-	Morphology (SEM), Mechanical properties	In vitro	[223]
Knitted fibers	PLGA (10/90)	-	Mechanical properties	In vivo	[224]	

	Four-armed PEG-(PLLA) ₄	PEG ₁₀ - PLLA ₁			
	Four-armed PEG-(PDLA) ₄	PEG ₁₀ - PDLA ₁	Size, Morphology (TEM), Nanostructure (FTIR, XRD), Thermal properties (DSC), mechanical properties	In vitro	[225]
Micelles in aqueous solution (hydrogel)	Four-armed PEG-(PLLA- Cho) ₄	PEG ₁₀ - PLLA ₁ - Chol			
	Four-armed PEG-(PDLA- Chol) ₄	PEG ₁₀ - PDLA ₁ - Chol			
Hydrogel by solution	PDLA-PLLA- PEG-PLLA- PDLA	~20	Specific optical rotation, Gel-sol transition, Physical gelation, Nanostructure (WAXS), Microstructure (SAXS)	In vitro drug release	[155]

1.6.2.2.1 Bone regeneration

Bone fracture is one of the more common injuries which is associated with treatment costs exceeding billions of dollars, societal productivity loss, and individual disability. Approximately 5 to 10% of fractured bone results in incomplete healing [226]. Currently, stainless steels and titanium-based bone plates remain dominant in bone fracture internal fixation [227]. However, metallic implants usually lead to health side complications, including bone atrophy and infection, and their subsequent removal can result in increased weakening and bone re-fracture due to the presence of the remained screw holes. Additionally, the organization and function of each bone are highly site-specific and related to its embryological origin [228].

In recent years, the use of biodegradable polymer plates for bone regeneration is gaining attention [14]. PLA and PGA are the biopolymers more commonly used due to the featured higher mechanical properties compared to other polyesters but a sufficiently low elastic modulus to avoid the stress shielding caused by metallic implants [227]. PLA was proposed as a potential substitute for titanium plates to heal bone fractures 30 years ago and several generations of PLA-based materials were developed since then, especially for the treatment of maxillofacial fractures [217]. The third generation materials composed of uncalcined hydroxyapatite and PLLA, have reached the market (FIXSORB MX or OSTEOTRANS MX) and several clinical studies have been conducted exhibiting promising results [217]. However, the titanium plates remain in daily clinical use due to the persistence of PLA properties drawbacks, in particular, the slow degradation rate which leads to a foreign

body reaction, and thus inflammation, after two years of implantation. Besides, the increase in the thickness of PLLA plates to match the strength of titanium plates increases the risk of exposure and patient discomfort [229], which might be improved by the fabrication of PLA plates in the SC phase to increase the strength avoiding the thickness increase. In addition, a fourth PLA-based material generation was recently developed which includes a small amount of PGA to overcome the slow degradation issue and its associated detrimental body inflammation [217,230,231]. PGA exhibits the highest initial mechanical properties, however, lessening strength very rapidly in the body due to its hydrolytic instability resulting in incomplete bone healing and high local acid concentration, causing inflammation [232], which turns the copolymer poly (lactide-*co*-glycolide) (PLGA) into the best option for bone regeneration. PLGA mechanical properties and degradation lifetime can be modified based on the PLA/PGA ratio (the lower the ratio PLA/PGA, the faster PLGA is expected to degrade). Moreover, silk [214], hydroxyapatite [233] or collagen [50] can be included in the scaffold to increase hydrophilicity, bone regeneration ability and tensile strength of the composite, respectively

Recently, the PLA applicability in bone tissue repair has advanced to tackle their characteristic limitations by the enhancement of the mechanical properties, degradation rate and the optimization of PLLA osteogenic activity [229]. Moreover, optimization of 3D printing parameters of PLA/Hydroxyapatite composites for bone plates has recently been developed, correlating the processing conditions with the final mechanical properties of the composite [234].

1.6.2.2 Tendon regeneration

PLA, and in particular its copolymer with PGA (PLGA) has also been employed for other tissue applications such as tendon regeneration. Tendinopathies represent about 30% of tendon-related injuries [220] and spontaneous tendon healing results in problematic restitution due to the low cellular and hypo-vascular nature of tendon tissue [221]. Biopolymeric 3D scaffolds provide an implement to both heal tendon injuries as well as to understand cell behaviour and differentiation in response to defined external biochemical and mechanical stimuli [222]. Particularly, a 2 cm partial resection of the Aquiles tendon was repaired in rabbits using a composite scaffold composed of an outer part of knitted PLGA, and an inner part of unwoven PGA fibres. The generated scaffold was incubated in adipose-derived stem cells culture and cell-seeded assemblies that formed a neo-tendon presenting a histological structure similar to native tendon 45 weeks after implantation [216]. PLGA has also been employed for tendon regeneration as a nanocarrier to ensure sustained and controlled delivery of human growth differentiation factor 5 [222], which is crucial for the expression of genes linked to the neo-tendon type. Similarly, stem cells with different origins were selected to understand the physiopathology of tendinopathy in which PLGA was always used as a 3D scaffold [223,224]. Recently, the influence of certain production parameters to

tailor the final nanofiber morphology such as the alignment and the fibre size were probed for an electrospun PLA scaffold on the differentiation of amniotic epithelial stem cells towards tenogenic lineage, concluding that highly aligned electrospun fibres [221] and smaller fibre diameter [220] enhanced cell differentiation and immunomodulation. Moreover, the mechanical properties of the electrospun scaffold were also influenced by the fibres alignment and its diameter, particularly, the scaffold featuring a higher diameter exhibited lower Young's modulus [220] and higher fracture strain whereas the alignment of the fibres increase the stress and strain values [221].

1.6.2.2.3 Nerve regeneration

Peripheral nerve injuries are the most common injury types affecting the nervous system and the posterior recovery of sensibility and motor functions is estimated to be less than 3% and 25%, respectively. Peripheral nerve injuries can be repaired by surgery, however, the use of grafts turns necessary when an important loss of physical substance occurs (>5mm) [235]. Synthetic conduits of PLA/PLDLA combined with longitudinal PLA filament scaffolds showed to enhance axon myelination in a rat sciatic nerve lesion model when compared to a silicone conduit [215]. In addition, the neural precursor cells which are an interesting source of cells for neural tissue regeneration, generate a high amount of detrimental reactive oxygen species during metabolism and the lactic acid degradation product released from PLA scaffolds has been shown to reduce the intracellular redox state that increases the proliferative capacity of the neural cell population [236]

1.6.2.2.4 Cartilage regeneration

Similarly to tendons, cartilage tissue exhibits little ability to self-repair due to the limited vascularity. The polymeric approaches were envisaged due to their versatility and the lack of current satisfactory solutions for cartilage tissue regeneration by other means [237,238]. Electrospun scaffolds based on PLA and gelatin loaded with the antioxidant resveratrol showed high specific surface area, slow drug release and thinner diameter to promote the repair of cartilage injury [239].

In addition, thermogels containing PEG-sc-PLA-Chol were evaluated as scaffolds for cartilage tissue engineering in which the cholesterol block enhanced the mechanical properties, enlarged the pore size and improved chondrocyte adhesion. The degradation cycle of the PLA scaffold was according to the regeneration of cartilage defects and in vivo results showed a good differentiation of the loaded chondrocytes in cartilage-like tissue [225]. The crystallization in the α - or SC- phase of the PLA block depending on the initial materials was evidenced by different techniques, however, only the stereocomplexed materials were analysed in vivo [225].

1.6.2.3 Perspectives

1.6.2.3.1 Piezoelectric activity

The β -phase of PLA [39] as well as the oriented α form of PLLA films fabricated by solution casting and uniaxial stretching [240] exhibit piezoelectric characteristics (Figure 1.9) that could enhance the functional complexity designed for therapeutic applications. Indeed, the piezoelectricity of PLA has already been explored for its biomedical application as a film sensor device [241,242].

Besides, the voltage gradient present in cells can trigger different cell types to change proliferation and differentiation by signalling across membranes. The potential for harnessing the electric fields in cells to enhance growth and differentiation has recently gained attention. Likewise, the piezoelectric properties of PLA are being evaluated from a biomedical perspective as the regeneration of damaged tissue is introduced by the growth and

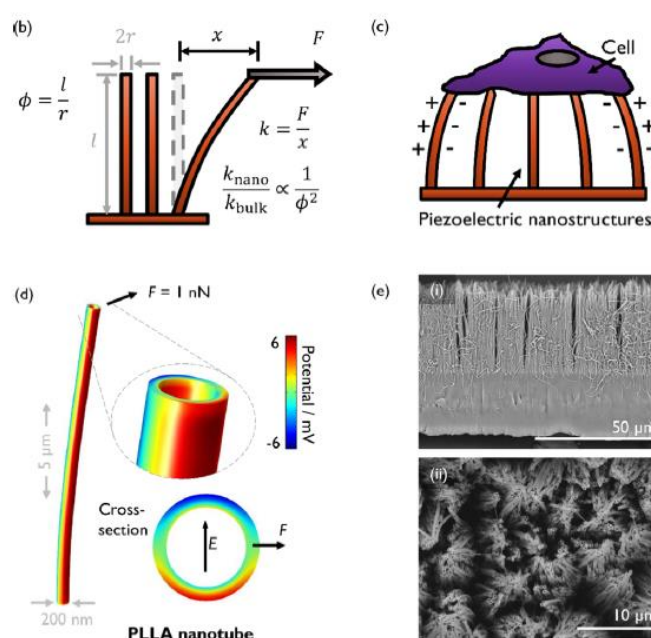


Figure 1.9. Piezoelectric activity of PLA. (b) Schematic of the bending mode of high aspect ratio structures with aspect ratio ϕ , which results in reduced effective stiffness by a factor of ϕ^2 with respect to the bulk material. (c) Proposed mechanism by which a cell can electromechanically stimulate itself by interacting with the piezoelectric nanostructures. (d) Simulation of a PLLA nanotube with axial polymer chain orientation, showing the potential developed in response to bending. Inset shows the opposing potentials developed across the tube diameter and the orientation of the corresponding electric field. (e) An example of the PLLA nanotube arrays produced via melt-press template wetting (i) in cross-section and (ii) in plan view. Adapted with permission from M. Smith, T. Chalklen, C. Lindackers, Y. Calahorra, C. Howe, A. Tamboli, D. V. Bax, D.J. Barrett, R.E. Cameron, S.M. Best, S. Kar-Narayan, Poly- L-Lactic Acid Nanotubes as Soft Piezoelectric Interfaces for Biology: Controlling Cell Attachment via Polymer Crystallinity, *ACS Appl. Bio Mater.* 3 (2020) 2140–2149. Copyright 2020 American Chemical Society.

proliferation of cells [243]. Particularly, PLLA nanotubes produced via the melt-press template wetting technique provided a soft piezoelectric surface for biological studies in which a cell can electromechanically stimulate itself by interacting with the piezoelectric nanostructure [244]. Moreover, cell attachment could be regulated by controlling the crystallinity of PLLA nanotubes since the surface potential of the nanotubes increases subtly upon crystallization [245].

Furthermore, a strong antibacterial effect due to the electric field generated by a piezoelectric PLLA yarn was recently observed, which could potentiate the applications of medical devices based on PLA [242].

1.6.2.3.2 Shape memory polymers

3D printing (3DP) is an additive manufacturing technology that allows mimicking the complex and multicomponent structure of human tissues at reduced costs [74,75,78].

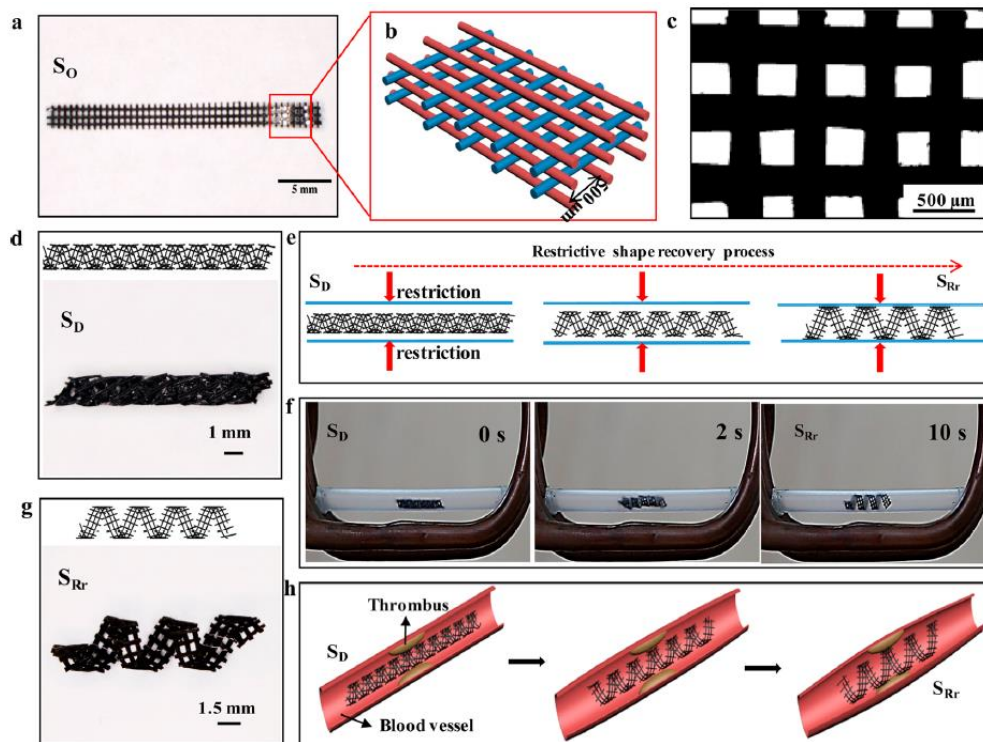


Figure 1.10. 4D scaffold of c-PLA/Fe₃O₄ ink and its potential biomedical application. (a) optical image of the multilayer scaffold; (b) schematic diagram of the detailed structure of the scaffold; (c) top view of the optical image of the printed scaffold; (d) deformation shape of the printed scaffold; (e) schematic of the restrictive shape recovery process; (f) demonstration of the restrictive shape recovery process triggered by a 30 kHz alternating magnetic field; (g) recovery shape under restrictive conditions; (h) potential application of the 4D scaffold as an intravascular stent. Reprinted with permission from H. Wei, Q. Zhang, Y. Yao, L. Liu, Y. Liu, J. Leng, Direct-write fabrication of 4D active shape-changing structures based on a shape memory polymer and its nanocomposite, *ACS Appl. Mater. Interfaces*. 9 (2017) 876–883. Copyright 2017, American Chemical Society.

Moreover, the 4D printing processing method has emerged as an extension of 3D printing in which printed objects exhibit the capability to self-transform over time, or in response to an external stimulus such as heat, light, pH, magnetic or electric forces [246]. Likewise, shape memory polymers (SMP) are capable of recovering their initial shape upon an external stimulus after being experienced a shape deformation [247] (Figure 1.10). PLA has already been used as a bio-ink for 4D printing applications. A spiral shape scaffold of a composite composed of PLA with magnetic iron oxide nanoparticles was printed to be used as an SMP. Iron oxide can be remotely heated and attracted by alternating magnetic fields demonstrating that it could be applied as a self-expandable stent with a minimally invasive intervention [247] as well as overcoming the lack of radial strength found for PLA stents compared to metallic stents. Similarly, porous tissue scaffolds attaining different internal structures based on PLA with embedded magnetic nanoparticles have recently been developed by 3D printing showing great cell attachment and proliferation ability [248].

1.7 Conclusions

PLA is a bio-based polymer that has attracted large interest due to its biodegradation capability and low price. PLA-derivatives attaining different architectures are obtained depending on both the starting lactide derivative and the polymerization method. The recently employed living polymerization assisted by a single-site catalyst allows affording PLA derivatives with high stereocontrol, high M_w and narrow polydispersity including the stereo-block copolymers. The availability of high M_w PLA stereo-block copolymers which feature enhanced physicochemical properties, expand the potential biomedical and pharmaceutical applications. In addition, the rich PLA nanostructure with diverse crystalline phases featuring different thermo-mechanical properties, as well as particular physico-chemical properties such as piezoelectricity, are obtained through several processing techniques such as electrospinning, 3D printing or nanoparticle formulation. Besides, the PLA crystalline domains degrade in physiological media at different rates depending either on the crystalline PLA phase as well as physicochemical and morphological parameters related to the surrounding medium, which must be considered when designing a biomedical device for a specific application.

Remarkably, PLA based materials have already attained the clinical level in both pharmaceutical and biomedical applications such as sutures, stents, microparticles and dermal fillers. In addition, PLA-based nanoparticles and 3D scaffolds are currently developed for drug delivery and tissue regeneration applications, respectively. Besides, the piezoelectricity and chirality exhibited by PLA enlarge the functionalities for potential biomedical devices. Likewise, the generation of bionanocomposites based on PLA affords the customisation of therapeutic materials with multifaceted capabilities. Furthermore, personalised therapeutic approaches have become feasible with the advent of 3D printing technology, designing specific pharmaceutical formulations for specific patients, pointing toward personalized medicine.

However, the current gap between the PLA structural characterisation and the performance of PLA in biomedical applications hinders the systematic conception of personalised biomedical solutions based on the correlation of the structure–property relationship with the required functionalities. The end-user requirements should be considered from an interdisciplinary approach from the genesis of PLA-based material to realistically reach the pharmaceutical/biomedical market. Likewise, the PLA-nanoparticles formulation has greatly advanced to attain drug carriers down to nanoparticles with a fair control; however, the nanostructure development during the polymer processing is frequently dismissed, which is key to tuning the drug release profile as well as diminishing the batch-to-batch variability usually obtained through conventional techniques that hamper the scalability of nanoparticle formulation to the industrial scale. Moreover, the comprehensive

nanostructure control achieved for a wide range of smart PLA-based hydrogels with specific functionalities must be followed by *in vitro* and *in vivo* studies to correlate the physicochemical properties with its performance under physiological conditions. In addition, the screening focus to develop new synthetic pathways to efficiently conjugate drugs to PLA should be also associated with a targeted PLA conjugate nanostructure in the applied medium in order to be translated reliably to both the release mechanism and the molecular recognition activity required to efficiently target the damaged tissue. Moreover, the tissue regeneration progress achieved from the materials approach requires a further understanding of the particular physicochemical and mechanical properties of each tissue, the alterations occurring under pathological conditions, and its evolution upon healing for designing materials according to the real requirements. Furthermore, the performance of the PLA-based stents suffers from structural stability due to the exhibited lack of radial strength that could be tackled by iterative structure-properties studies of novel multiblock copolymers. The mastering of novel polymer processing techniques, especially 3D techniques, should be achieved to generate customised materials with performing mechanical properties to attain consistently demanding applications.

1.8 Aims and objectives of the thesis

The main objective of this thesis is to establish from a global approach the structure-processing-properties relationship of tailored PLA-block copolymers to obtain personalised drug delivery systems.

Firstly, the synthesis of PLA-derivatives controlling the stereo-regularity of the polymeric chain architecture, particularly the long desired PLA-stereo-block copolymers will be described (**Chapter 2**). Moreover, the correlation of the structure-processing-properties relationship will be established, particularly the crystallization mechanism (**Chapter 3**) for the design of multifunctional bionanocomposites PLA-based with personalised drug release rates (**Chapter 4**).

The following chapters include a brief introduction of the subject, an enumeration of the specific objectives, a description and discussion of the main results as well as an enumeration of the main conclusions. The main experimental techniques won't be described in detail, but the specifications of each technique for the reproducibility of the results will be described after the conclusions (and not after the introduction), to maintain the narrative thread.

1.9 References

1. Farah, S.; Anderson, D.G.; Langer, R. Physical and Mechanical Properties of PLA , and Their Functions in Widespread Applications — A Comprehensive Review ☆. *Adv. Drug Deliv. Rev.* **2016**, *107*, 367–392, doi:10.1016/j.addr.2016.06.012.
2. Haider, T.P.; Völker, C.; Kramm, J.; Landfester, K.; Wurm, F.R. Plastics of the Future? The Impact of Biodegradable Polymers on the Environment and on Society. *Angew. Chemie - Int. Ed.* **2019**, *58*, 50–62, doi:10.1002/anie.201805766.
3. Castro-Aguirre, E.; Iñiguez-Franco, F.; Samsudin, H.; Fang, X.; Auras, R. Poly(Lactic Acid)—Mass Production, Processing, Industrial Applications, and End of Life. *Adv. Drug Deliv. Rev.* **2016**, *107*, 333–366, doi:10.1016/j.addr.2016.03.010.
4. Karamanlioglu, M.; Preziosi, R.; Robson, G.D. Abiotic and Biotic Environmental Degradation of the Bioplastic Polymer Poly(Lactic Acid): A Review. *Polym. Degrad. Stab.* **2017**, *137*, 122–130, doi:10.1016/j.polymdegradstab.2017.01.009.
5. Hamad, K.; Kaseem, M.; Ayyoob, M.; Joo, J.; Deri, F. Polylactic Acid Blends: The Future of Green, Light and Tough. *Prog. Polym. Sci.* **2018**, *85*, 83–127, doi:10.1016/j.progpolymsci.2018.07.001.
6. Dechy-cabaret, O.; Martin-vaca, B.; Bourissou, D. Controlled Ring-Opening Polymerization of Lactide and Glycolide. **2004**, 20–23.
7. Tsuji, H. Poly(Lactic Acid) Stereocomplexes: A Decade of Progress. *Adv. Drug Deliv. Rev.* **2016**, *107*, 97–135, doi:10.1016/j.addr.2016.04.017.
8. Stanford, M.J.; Dove, A.P. Stereocontrolled Ring-Opening Polymerisation of Lactide. *Chem. Soc. Rev.* **2010**, *39*, 486–494, doi:10.1039/b815104k.
9. Mehta, R.; Kumar, V.; Bhunia, H.; Upadhyay, S.N. Synthesis of Poly(Lactic Acid): A Review. *J. Macromol. Sci. - Polym. Rev.* **2005**, *45*, 325–349, doi:10.1080/15321790500304148.
10. Tsuji, H. Poly(Lactide) Stereocomplexes: Formation, Structure, Properties, Degradation, and Applications. *Macromol. Biosci.* **2005**, *5*, 569–597, doi:10.1002/mabi.200500062.
11. Pan, P.; Han, L.; Bao, J.; Xie, Q.; Shan, G.; Bao, Y. Competitive Stereocomplexation, Homocrystallization, and Polymorphic Crystalline Transition in Poly(L-Lactic Acid)/Poly(D-Lactic Acid) Racemic Blends: Molecular Weight Effects. *J. Phys. Chem. B* **2015**, *119*, 6462–6470, doi:10.1021/acs.jpcc.5b03546.
12. Ilaria D’Auria, Massimo Christian D’Alterio, Consiglia Tedesco, and C.P. Tailor-Made Block Copolymers of L-, D- and Raclactides and 3-Caprolactone via One-Pot Sequential Ring Opening Polymerization by Pyridylamidozinc(II) Catalysts. *RSC Adv.* **2019**, *9*, 32771–32779, doi:10.1039/C9RA07133D.
13. Rosen, T.; Goldberg, I.; Venditto, V.; Kol, M. Tailor-Made Stereoblock Copolymers of Poly(Lactic Acid) by a Truly Living Polymerization Catalyst. *J. Am. Chem. Soc.* **2016**, *138*, 12041–12044, doi:10.1021/jacs.6b07287.
14. Lasprilla, A.J.R.; Martinez, G.A.R.; Lunelli, B.H.; Jardini, A.L.; Filho, R.M. Poly-Lactic Acid Synthesis for Application in Biomedical Devices - A Review. *Biotechnol. Adv.* **2012**,

- 30, 321–328, doi:10.1016/j.biotechadv.2011.06.019.
15. Nishio, S.; Kosuga, K.; Igaki, K.; Okada, M.; Kyo, E.; Tsuji, T.; Takeuchi, E.; Inuzuka, Y.; Takeda, S.; Hata, T.; et al. Long-Term (>10 Years) Clinical Outcomes of First-in-Human Biodegradable Poly-L-Lactic Acid Coronary Stents: Igaki-Tamai Stents. *Circulation* **2012**, *125*, 2343–2352, doi:10.1161/CIRCULATIONAHA.110.000901.
 16. Mattesini, A.; Bartolini, S.; Dini, C.S.; Valente, S.; Parodi, G.; Stolcova, M.; Meucci, F.; di Mario, C. The DESolve Novolimus Bioresorbable Scaffold: From Bench to Bedside. *J. Thorac. Dis.* **2017**, *9*, S950–S958, doi:10.21037/jtd.2017.07.25.
 17. Tenekecioglu, E.; Bourantas, C.; Abdelghani, M.; Zeng, Y.; Silva, R.C.; Tateishi, H.; Sotomi, Y.; Onuma, Y.; Yilmaz, M.; Serruys, P.W. From Drug Eluting Stents to Bioresorbable Scaffolds; To New Horizons in PCI. *Expert Rev. Med. Devices* **2016**, *13*, 271–286, doi:10.1586/17434440.2016.1143356.
 18. R3 Vascular Inc. Magnitude Available online: <https://www.r3vascular.com/magnitude>.
 19. Cheng, Y.; Deng, S.; Chen, P.; Ruan, R. Polylactic Acid (PLA) Synthesis and Modifications: A Review. *Front. Chem. China* **2009**, *4*, 259–264, doi:10.1007/s11458-009-0092-x.
 20. Zheng, Y.; Pan, P. Crystallization of Biodegradable and Biobased Polyesters: Polymorphism, Cocrystallization, and Structure-Property Relationship. *Prog. Polym. Sci.* **2020**, *109*, 101291, doi:10.1016/j.progpolymsci.2020.101291.
 21. Tyler, B.; Gullotti, D.; Mangraviti, A.; Utsuki, T.; Brem, H. Polylactic Acid (PLA) Controlled Delivery Carriers for Biomedical Applications. *Adv. Drug Deliv. Rev.* **2016**, *107*, 163–175, doi:10.1016/j.addr.2016.06.018.
 22. Balla, E.; Daniilidis, V.; Karlioti, G.; Kalamas, T.; Stefanidou, M.; Bikiaris, N.D.; Vlachopoulos, A.; Koumentakou, I.; Bikiaris, D.N. Poly(Lactic Acid): A Versatile Biobased Polymer for the Future with Multifunctional Properties-from Monomer Synthesis, Polymerization Techniques and Molecular Weight Increase to PLA Applications. *Polymers (Basel)*. **2021**, *13*, doi:10.3390/polym13111822.
 23. DeStefano, V.; Khan, S.; Tabada, A. Applications of PLA in Modern Medicine. *Eng. Regen.* **2020**, doi:10.1016/j.engreg.2020.08.002.
 24. Singhvi, M.S.; Zinjarde, S.S.; Gokhale, D. V. Polylactic Acid: Synthesis and Biomedical Applications. *J. Appl. Microbiol.* 2019.
 25. Liu, S.; Qin, S.; He, M.; Zhou, D.; Qin, Q.; Wang, H. Current Applications of Poly(Lactic Acid) Composites in Tissue Engineering and Drug Delivery. *Compos. Part B Eng.* 2020.
 26. Groot, W.; van Krieken, J.; Sliemers, O.; de Vos, S. Production and Purification of Lactic Acid and Lactide. In *Poly(Lactic Acid): Synthesis, Structures, Properties, Processing, and Applications*; Auras, R., Lim, L.-T., Selke, S.E.M., Tsuji, H., Eds.; 2010; pp. 27–41 ISBN 9780470293669.
 27. Garlotta, D. A Literature Review of Poly (Lactic Acid). *J. Polym. Environ.* **2001**, *9*, 63–84.
 28. Masutani, K.; Kimura, Y. PLA Synthesis. From the Monomer to the Polymer. In

- Poly(lactic acid) Science and Technology: Processing, Properties, Additives and Applications*; Jiménez, A., Peltzer, M., Ruseckaite, R., Eds.; The Royal Society of Chemistry: Cambridge, 2015; pp. 3–36 ISBN 9781849738798.
29. Tsuji, H.; Ikada, Y. Crystallization from the Melt of Poly(Lactide)s with Different Optical Purities and Their Blends. *Macromol. Chem. Phys.* **1996**, *197*, 3483–3499, doi:10.1002/macp.1996.021971033.
 30. Pretula, J.; Slomkowski, S.; Penczek, S. Polylactides—Methods of Synthesis and Characterization. *Adv. Drug Deliv. Rev.* **2016**, *107*, 3–16, doi:10.1016/j.addr.2016.05.002.
 31. Tsuji, H.; Arakawa, Y. Synthesis, Properties, and Crystallization of the Alternating Stereocopolymer Poly(l-Lactic Acid-: Alt -d-Lactic Acid) [Syndiotactic Poly(Lactic Acid)] and Its Blend with Isotactic Poly(Lactic Acid). *Polym. Chem.* **2018**, *9*, 2446–2457, doi:10.1039/c8py00391b.
 32. Szwarc, M. © 1956 Nature Publishing. *Nature* **1956**, doi:10.1038/1781168a0.
 33. Di Lorenzo, M.L.; Androsch, R. Influence of A'-/ α -Crystal Polymorphism on Properties of Poly(l-Lactic Acid). *Polym. Int.* **2019**, *68*, 320–334, doi:10.1002/pi.5707.
 34. Righetti, M.C.; Gazzano, M.; Di Lorenzo, M.L.; Androsch, R. Enthalpy of Melting of A'- and α -Crystals of Poly(L-Lactic Acid). *Eur. Polym. J.* **2015**, *70*, 215–220, doi:10.1016/j.eurpolymj.2015.07.024.
 35. Takahashi, K.; Sawai, D.; Yokoyama, T.; Kanamoto, T.; Hyon, S.H. Crystal Transformation from the α - to the β -Form upon Tensile Drawing of Poly(L-Lactic Acid). *Polymer (Guildf)*. **2004**, *45*, 4969–4976, doi:10.1016/j.polymer.2004.03.108.
 36. Sawai, D.; Yokoyama, T.; Kanamoto, T.; Sungil, M.; Hyon, S.H.; Myasnikova, L.P. Crystal Transformation and Development of Tensile Properties upon Drawing of Poly(L-Lactic Acid) by Solid-State Coextrusion: Effects of Molecular Weight. *Macromol. Symp.* **2006**, *242*, 93–103, doi:10.1002/masy.200651015.
 37. Xue, J.; Yan, L.; Tian, X.; Huang, D.; Redyy, N.; Yang, Y. Chemical Structure of Poly(Lactic Acid). In *Poly(Lactic Acid): Synthesis, Structures, Properties, Processing, and Applications*; Auras, R., Lim, L.-T., Selke, S.E.M., Tsuji, H., Eds.; 2010.
 38. Lotz, B.A. Single Crystals of the Frustrated β -Phase and Genesis of the Disordered A'-Phase of Poly(l -Lactic Acid). *ACS Macro Lett.* **2015**, *4*, 602–605, doi:10.1021/acsmacrolett.5b00205.
 39. Lee, S.J.; Arun, A.P.; Kim, K.J. Piezoelectric Properties of Electrospun Poly(l-Lactic Acid) Nanofiber Web. *Mater. Lett.* **2015**, *148*, 58–62, doi:10.1016/j.matlet.2015.02.038.
 40. Cartier, L.; Okihara, T.; Ikada, Y.; Tsuji, H.; Puiggali, J.; Lotz, B. Epitaxial Crystallization and Crystalline Polymorphism of Polylactides. *Polymer (Guildf)*. **2000**, *41*, 8909–8919, doi:10.1016/S0032-3861(00)00234-2.
 41. Zhang, J.; Sato, H.; Tsuji, H.; Noda, I.; Ozaki, Y. Differences in the CH₃...O=C Interactions among Poly(L-Lactide), Poly(L-Lactide)/Poly(D-Lactide) Stereocomplex, and Poly(3-Hydroxybutyrate) Studied by Infrared Spectroscopy. *J. Mol. Struct.* **2005**, *735–736*, 249–257, doi:10.1016/j.molstruc.2004.11.033.

42. Ikada, Y.; Jamshidi, K.; Tsuji, H.; Hyon, S.-H. Stereocomplex Formation between Enantiomeric Poly(Lactides). *Am. Chem. Soc.* **1987**, 904–906.
43. Bertin, A. Emergence of Polymer Stereocomplexes for Biomedical Applications. *Macromol. Chem. Phys.* **2012**, 213, 2329–2352, doi:10.1002/macp.201200143.
44. Tsuji, H.; Ikada, Y. Stereocomplex Formation between Enantiomeric Poly(Lactic Acid)s. 9. Stereocomplexation from the Melt. *Macromolecules* **1993**, 26, 6918–6926.
45. Zhang, J.; Tashiro, K.; Tsuji, H.; Domb, A.J. Investigation of Phase Transitional Behavior of Poly(L-Lactide)/ Poly(D-Lactide) Blend Used to Prepare the Highly-Oriented Stereocomplex. *Macromolecules* **2007**, 40, 1049–1054, doi:10.1021/ma061693s.
46. Puthumana, M.; Santhana Gopala Krishnan, P.; Nayak, S.K. Chemical Modifications of PLA through Copolymerization. *Int. J. Polym. Anal. Charact.* **2020**, 25, 634–648, doi:10.1080/1023666X.2020.1830650.
47. Saini, P.; Arora, M.; Kumar, M.N.V.R. Poly(Lactic Acid) Blends in Biomedical Applications. *Adv. Drug Deliv. Rev.* **2016**, 107, 47–59, doi:10.1016/j.addr.2016.06.014.
48. Wang, S.; Zhang, Y.; Wang, H.; Yin, G.; Dong, Z. Fabrication and Properties of the Electrospun Polylactide/Silk Fibroin-Gelatin Composite Tubular Scaffold. *Biomacromolecules* **2009**, 10, 2240–2244, doi:10.1021/bm900416b.
49. Moya-Lopez, C.; Valcarcel, J.; Vázquez, J.A.; Bourson, P.; Chapron, D.; Solano, E.; Piñeiro, M.M.; Hermida-Merino, C.; Hermida-Merino, D. Biocompatibility Enhancement of PLA by the Generation of Bionanocomposites with Fish Collagen Derivatives. *Emergent Mater.* **2022**, 5, 695–702, doi:10.1007/s42247-021-00340-0.
50. Jin, S.; Sun, F.; Zou, Q.; Huang, J.; Zuo, Y.; Li, Y.; Wang, S.; Cheng, L.; Man, Y.; Yang, F.; et al. Fish Collagen and Hydroxyapatite Reinforced Poly(Lactide- Co-Glycolide) Fibrous Membrane for Guided Bone Regeneration. *Biomacromolecules* **2019**, 20, 2058–2067, doi:10.1021/acs.biomac.9b00267.
51. Naffakh, M.; Rica, P.; Moya-Lopez, C.; Castro-osma, J.A.; Alonso-moreno, C.; Moreno, D.A. The Effect of WS 2 Nanosheets on the Non- Isothermal Cold- and Melt-Crystallization Kinetics of Poly (L -Lactic Acid) Nanocomposites. **2021**, 1–19.
52. Naffakh, M.; Marco, C.; Ellis, G. Non-Isothermal Cold-Crystallization Behavior and Kinetics of Poly(L-Lactic Acid)/WS2 Inorganic Nanotube Nanocomposites. *Polymers (Basel)*. **2015**, 7, 2175–2189, doi:10.3390/polym7111507.
53. Naffakh, M.; Díez-Pascual, A.M.; Marco, C. Polymer Blend Nanocomposites Based on Poly(L-Lactic Acid), Polypropylene and WS2 Inorganic Nanotubes. *RSC Adv.* **2016**, 6, 40033–40044, doi:10.1039/c6ra05803e.
54. Usha Kiran Sanivada, Gonzalo Mármol, F. P. Brito, R.F. PLA Composites Reinforced with Flax and Jute. *Polymers (Basel)*. **2020**, 1–29.
55. Brounstein, Z.; Yeager, C.M.; Labouriau, A. Development of Antimicrobial PLA Composites for Fused Filament Fabrication. *Polymers (Basel)*. **2021**, 13, 1–18, doi:10.3390/polym13040580.

56. Eltouby, P.; Shyha, I.; Li, C.; Khaliq, J. Factors Affecting the Piezoelectric Performance of Ceramic-Polymer Composites: A Comprehensive Review. *Ceram. Int.* **2021**, doi:10.1016/j.ceramint.2021.03.126.
57. Dechy-Cabaret, O.; Martin-Vaca, B.; Bourissou, D. Polyesters from Dilactones. In *Handbook of Ring-Opening*; Dubois, P., Coulembier, O., Raquez, J.-M., Eds.; WILEY-VCH Verlag GmbH & C: Weinheim, 2009; pp. 255–286 ISBN 9783527317103.
58. Stjerndahl, A.; Wistrand, A.F.; Albertsson, A.C. Industrial Utilization of Tin-Initiated Resorbable Polymers: Synthesis on a Large Scale with a Low Amount of Initiator Residue. *Biomacromolecules* **2007**, *8*, 937–940, doi:10.1021/bm0611331.
59. Castro-Osma, J.A.; Alonso-Moreno, C.; Lara-Sánchez, A.; Otero, A.; Fernández-Baeza, J.; Sánchez-Barba, L.F.; Rodríguez, A.M. Catalytic Behaviour in the Ring-Opening Polymerisation of Organoaluminiums Supported by Bulky Heteroscorpionate Ligands. *Dalt. Trans.* **2015**, *44*, 12388–12400, doi:10.1039/c4dt03475a.
60. Otero, A.; Lara-Sánchez, A.; Fernández-Baeza, J.; Alonso-Moreno, C.; Castro-Osma, J.A.; Márquez-Segovia, I.; Sánchez-Barba, L.F.; Rodríguez, A.M.; Garcia-Martinez, J.C. Neutral and Cationic Aluminum Complexes Supported by Acetamidate and Thioacetamidate Heteroscorpionate Ligands as Initiators for Ring-Opening Polymerization of Cyclic Esters. *Organometallics* **2011**, *30*, 1507–1522, doi:10.1021/om1010676.
61. Yui, N.; Dijkstra, P.J.; Feijen, J. Stereo Block Copolymers of L- and D-Lactides. *Die Makromol. Chemie* **1990**, *191*, 481–488, doi:10.1002/macp.1990.021910303.
62. Thomas, C.M. Stereocontrolled Ring-Opening Polymerization of Cyclic Esters: Synthesis of New Polyester Microstructures. *Chem. Soc. Rev.* **2010**, *39*, 165–173, doi:10.1039/b810065a.
63. Moya-Lopez, C.; Bravo, I.; Castro-Osma, J.A.; Chapron, D.; Bourson, P.; Vagner, C.; Cochez, M.; Leon, N.; Alonso-Moreno, C.; Hermida-Merino, D. Synthesis of High Molecular Weight Stereo-Di-Block Copolymers Driven by a Co-Initiator Free Catalyst. *Polymers (Basel)*. **2022**, *14*, 1–16, doi:10.3390/polym14020232.
64. Rosen, T.; Goldberg, I.; Navarra, W.; Venditto, V.; Kol, M. Divergent $[\{\text{ONNN}\}\text{Mg}-\text{Cl}]$ Complexes in Highly Active and Living Lactide Polymerization. *Chem. Sci.* **2017**, *8*, 5476–5481, doi:10.1039/C7SC01514C.
65. D'Auria, I.; D'Alterio, M.C.; Tedesco, C.; Pellecchia, C. Tailor-Made Block Copolymers of l-, d- and: Rac -Lactides and ϵ -Caprolactone via One-Pot Sequential Ring Opening Polymerization by Pyridylamidozinc(II) Catalysts. *RSC Adv.* **2019**, *9*, 32771–32779, doi:10.1039/c9ra07133d.
66. Auras, R.; Lim, L.-T.; Selke, S.E.M.; Tsuji, H. *Poly (Lactic Acid). Synthesis, Structures, Properties, Processing and Applications*; 2010; ISBN 9780470293669.
67. Francis, L.F. Melt Processes. In *Materials Processing*; 2016; pp. 105–249 ISBN 9780123851321.
68. Le Marec, P.E.; Ferry, L.; Quantin, J.C.; Bénézet, J.C.; Bonfils, F.; Guilbert, S.; Bergeret,

- A. Influence of Melt Processing Conditions on Poly(Lactic Acid) Degradation: Molar Mass Distribution and Crystallization. *Polym. Degrad. Stab.* **2014**, *110*, 353–363, doi:10.1016/j.polymdegradstab.2014.10.003.
69. Lim, L.T.; Auras, R.; Rubino, M. Processing Technologies for Poly(Lactic Acid). *Prog. Polym. Sci.* **2008**, *33*, 820–852, doi:10.1016/j.progpolymsci.2008.05.004.
 70. Wang, Y.; Liu, C.; Shen, C. Crystallization Behavior of Poly(Lactic Acid) and Its Blends. *Polym. Cryst.* **2021**, *4*, 2–5, doi:10.1002/pcr2.10171.
 71. Tábi, T.; Hajba, S.; Kovács, J.G. Effect of Crystalline Forms (A' and α) of Poly(Lactic Acid) on Its Mechanical, Thermo-Mechanical, Heat Deflection Temperature and Creep Properties. *Eur. Polym. J.* **2016**, *82*, 232–243, doi:10.1016/j.eurpolymj.2016.07.024.
 72. Takasaki, M.; Ito, H.; Kikutani, T. Development of Stereocomplex Crystal of Polylactide in High-Speed Melt Spinning and Subsequent Drawing and Annealing Processes. *J. Macromol. Sci. - Phys.* **2003**, *42 B*, 403–420, doi:10.1081/mb-120021570.
 73. Im, S.H.; Im, D.H.; Park, S.J.; Chung, J.J.; Jung, Y.; Kim, S.H. Stereocomplex Polylactide for Drug Delivery and Biomedical Applications: A Review. *Molecules* **2021**, *26*, doi:10.3390/molecules26102846.
 74. Elbadawi, M.; Muñiz Castro, B.; Gavins, F.K.H.; Ong, J.J.; Gaisford, S.; Pérez, G.; Basit, A.W.; Cabalar, P.; Goyanes, A. M3DISEEN: A Novel Machine Learning Approach for Predicting the 3D Printability of Medicines. *Int. J. Pharm.* **2020**, *590*, 119837, doi:10.1016/j.ijpharm.2020.119837.
 75. Durga Prasad Reddy, R.; Sharma, V. Additive Manufacturing in Drug Delivery Applications: A Review. *Int. J. Pharm.* **2020**, *589*, 119820, doi:10.1016/j.ijpharm.2020.119820.
 76. Organovo Available online: <https://organovo.com/>.
 77. Srinivas, V.; van Hooy-Corstjens, C.S.J.; Rastogi, S.; Harings, J.A.W. Promotion of Molecular Diffusion and/or Crystallization in Fused Deposition Modeled Poly(Lactide) Welds. *Polymer (Guildf)*. **2020**, *202*, 122637, doi:10.1016/j.polymer.2020.122637.
 78. Bedell, M.L.; Navara, A.M.; Du, Y.; Zhang, S.; Mikos, A.G. Polymeric Systems for Bioprinting. *Chem. Rev.* **2020**, *120*, 10744–10792, doi:10.1021/acs.chemrev.9b00834.
 79. Chen, X.; Chen, G.; Wang, G.; Zhu, P.; Gao, C. Recent Progress on 3D-Printed Polylactic Acid and Its Applications in Bone Repair. *Adv. Eng. Mater.* **2020**, *22*, doi:10.1002/adem.201901065.
 80. Cheng, C.H.; Shie, M.Y.; Lai, Y.H.; Foo, N.P.; Lee, M.J.; Yao, C.H. Fabrication of 3d Printed Poly(Lactic Acid)/Polycaprolactone Scaffolds Using Tgf-B1 for Promoting Bone Regeneration. *Polymers (Basel)*. **2021**, *13*, 1–16, doi:10.3390/polym13213731.
 81. Ritz, U.; Gerke, R.; Götz, H.; Stein, S.; Rommens, P.M. A New Bone Substitute Developed from 3D-Prints of Polylactide (PLA) Loaded with Collagen i: An in Vitro Study. *Int. J. Mol. Sci.* **2017**, *18*, doi:10.3390/ijms18122569.
 82. Zhang, H.; Mao, X.; Du, Z.; Jiang, W.; Han, X.; Zhao, D.; Han, D.; Li, Q. Three

- Dimensional Printed Macroporous Polylactic Acid/Hydroxyapatite Composite Scaffolds for Promoting Bone Formation in a Critical-Size Rat Calvarial Defect Model. *Sci. Technol. Adv. Mater.* **2016**, *17*, 136–148, doi:10.1080/14686996.2016.1145532.
83. Sahvieh, S.; Oryan, A.; Hassanajili, S.; Kamali, A. Role of Bone Stem Cell–Seeded 3D Polylactic Acid/Polycaprolactone/Hydroxyapatite Scaffold on a Critical-Sized Radial Bone Defect in Rat. *Cell Tissue Res.* **2021**, *383*, 735–750, doi:10.1007/s00441-020-03284-9.
 84. Wang, C.; Zhao, Q.; Wang, M. Cryogenic 3D Printing for Producing Hierarchical Porous and RhBMP-2-Loaded Ca-P/PLLA Nanocomposite Scaffolds for Bone Tissue Engineering. *Biofabrication* **2017**, *9*, doi:10.1088/1758-5090/aa71c9.
 85. Yu, X.; Zhang, T.; Li, Y. 3D Printing and Bioprinting Nerve Conduits for Neural Tissue Engineering. *Polymers (Basel)*. **2020**, *12*, 1–27, doi:10.3390/POLYM12081637.
 86. Narayanan, L.K.; Huebner, P.; Fisher, M.B.; Spang, J.T.; Starly, B.; Shirwaiker, R.A. 3D-Bioprinting of Polylactic Acid (PLA) Nanofiber-Alginate Hydrogel Bioink Containing Human Adipose-Derived Stem Cells. *ACS Biomater. Sci. Eng.* **2016**, *2*, 1732–1742, doi:10.1021/acsbiomaterials.6b00196.
 87. Diez-Escudero, A.; Andersson, B.; Persson, C.; Hailer, N.P. Hexagonal Pore Geometry and the Presence of Hydroxyapatite Enhance Deposition of Mineralized Bone Matrix on Additively Manufactured Polylactic Acid Scaffolds. *Mater. Sci. Eng. C* **2021**, *125*, 112091, doi:10.1016/j.msec.2021.112091.
 88. Huang, Z.M.; Zhang, Y.Z.; Kotaki, M.; Ramakrishna, S. A Review on Polymer Nanofibers by Electrospinning and Their Applications in Nanocomposites. *Compos. Sci. Technol.* **2003**, *63*, 2223–2253, doi:10.1016/S0266-3538(03)00178-7.
 89. Ribeiro, C.; Sencadas, V.; Costa, C.M.; Gómez Ribelles, J.L.; Lanceros-Méndez, S. Tailoring the Morphology and Crystallinity of Poly(L-Lactide Acid) Electrospun Membranes. *Sci. Technol. Adv. Mater.* **2011**, *12*, doi:10.1088/1468-6996/12/1/015001.
 90. Gómez-Pachón, E.Y.; Sánchez-Arévalo, F.M.; Sabina, F.J.; Maciel-Cerda, A.; Campos, R.M.; Batina, N.; Morales-Reyes, I.; Vera-Graziano, R. Characterisation and Modelling of the Elastic Properties of Poly(Lactic Acid) Nanofibre Scaffolds. *J. Mater. Sci.* **2013**, *48*, 8308–8319, doi:10.1007/s10853-013-7644-7.
 91. Echeverría, C.; Limón, I.; Muñoz-Bonilla, A.; Fernández-García, M.; López, D. Development of Highly Crystalline Polylactic Acid with β -Crystalline Phase from the Induced Alignment of Electrospun Fibers. *Polymers (Basel)*. **2021**, *13*, doi:10.3390/polym13172860.
 92. Ribeiro, C.; Sencadas, V.; Correia, D.M.; Lanceros-Méndez, S. Piezoelectric Polymers as Biomaterials for Tissue Engineering Applications. *Colloids Surfaces B Biointerfaces* **2015**, *136*, 46–55, doi:10.1016/j.colsurfb.2015.08.043.
 93. Kang, Y.; Chen, P.; Shi, X.; Zhang, G.; Wang, C. Multilevel Structural Stereocomplex Polylactic Acid/Collagen Membranes by Pattern Electrospinning for Tissue Engineering. *Polymer (Guildf)*. **2018**, *156*, 250–260, doi:10.1016/j.polymer.2018.10.009.
 94. Feng, C.; Chen, Y.; Shao, J.; Hou, H. The Crystallization Behavior of Poly(L-Lactic

- Acid)/Poly(d -Lactic Acid) Electrospun Fibers: Effect of Distance of Isomeric Polymers. *Ind. Eng. Chem. Res.* **2020**, *59*, 8480–8491, doi:10.1021/acs.iecr.0c00625.
95. Al-Enizi, A.M.; Zagho, M.M.; Elzatahry, A.A. Polymer-Based Electrospun Nanofibers for Biomedical Applications. *Nanomaterials* **2018**, *8*, 1–22, doi:10.3390/nano8040259.
 96. Bhattarai, R.S.; Bachu, R.D.; Boddu, S.H.S.; Bhaduri, S. Biomedical Applications of Electrospun Nanofibers: Drug and Nanoparticle Delivery. *Pharmaceutics* **2019**, *11*, doi:10.3390/pharmaceutics11010005.
 97. Siqueira, L.; Passador, F.R.; Costa, M.M.; Lobo, A.O.; Sousa, E. Influence of the Addition of β -TCP on the Morphology, Thermal Properties and Cell Viability of Poly (Lactic Acid) Fibers Obtained by Electrospinning. *Mater. Sci. Eng. C* **2015**, *52*, 135–143, doi:10.1016/j.msec.2015.03.055.
 98. Holderegger, C.; Schmidlin, P.R.; Weber, F.E.; Mohn, D. Preclinical in Vivo Performance of Novel Biodegradable, Electrospun Poly(Lactic Acid) and Poly(Lactic-Co-Glycolic Acid) Nanocomposites: A Review. *Materials (Basel)*. **2015**, *8*, 4912–4931, doi:10.3390/ma8084912.
 99. Cui, W.; Li, X.; Zhu, X.; Yu, G.; Zhou, S.; Weng, J. Investigation of Drug Release and Matrix Degradation of Electrospun Poly(DL-Lactide) Fibers with Paracetamol Inoculation. *Biomacromolecules* **2006**, *7*, 1623–1629, doi:10.1021/bm060057z.
 100. Shahverdi, S.; Hajimiri, M.; Esfandiari, M.A.; Larijani, B.; Atyabi, F.; Rajabiani, A.; Dehpour, A.R.; Gharehaghaji, A.A.; Dinarvand, R. Fabrication and Structure Analysis of Poly(Lactide-Co-Glycolic Acid)/Silk Fibroin Hybrid Scaffold for Wound Dressing Applications. *Int. J. Pharm.* **2014**, *473*, 345–355, doi:10.1016/j.ijpharm.2014.07.021.
 101. Park, K.; Otte, A.; Sharifi, F.; Garner, J.; Skidmore, S.; Park, H.; Jhon, Y.K.; Qin, B.; Wang, Y. Formulation Composition, Manufacturing Process, and Characterization of Poly(Lactide-Co-Glycolide) Microparticles. *J. Control. Release* **2021**, *329*, 1150–1161, doi:10.1016/j.jconrel.2020.10.044.
 102. Song, X.; Zhao, Y.; Hou, S.; Xu, F.; Zhao, R.; He, J.; Cai, Z.; Li, Y.; Chen, Q. Dual Agents Loaded PLGA Nanoparticles: Systematic Study of Particle Size and Drug Entrapment Efficiency. *Eur. J. Pharm. Biopharm.* **2008**, *69*, 445–453, doi:10.1016/j.ejpb.2008.01.013.
 103. Slimane, M.; Gaye, I.; Ghoul, M.; Chebil, L. Mesoscale Modeling and Experimental Study of Quercetin Organization as Nanoparticles in the Poly-Lactic- Co-Glycolic Acid/Water System under Different Conditions. *Ind. Eng. Chem. Res.* **2020**, *59*, 4809–4816, doi:10.1021/acs.iecr.9b06630.
 104. Budhian, A.; Siegel, S.J.; Winey, K.I. Haloperidol-Loaded PLGA Nanoparticles: Systematic Study of Particle Size and Drug Content. *Int. J. Pharm.* **2007**, *336*, 367–375, doi:10.1016/j.ijpharm.2006.11.061.
 105. Ahlin Grabnar, P.; Kristl, J. The Manufacturing Techniques of Drug-Loaded Polymeric Nanoparticles from Preformed Polymers. *J. Microencapsul.* **2011**, *28*, 323–335, doi:10.3109/02652048.2011.569763.
 106. Ahmed, E.M. Hydrogel: Preparation, Characterization, and Applications: A Review. *J.*

- Adv. Res.* **2015**, *6*, 105–121, doi:10.1016/j.jare.2013.07.006.
107. Klouda, L. Thermoresponsive Hydrogels in Biomedical Applications A Seven-Year Update. *Eur. J. Pharm. Biopharm.* **2015**, *97*, 338–349, doi:10.1016/j.ejpb.2015.05.017.
 108. Yin, X.; Hewitt, D.R.O.; Quah, S.P.; Zheng, B.; Mattei, G.S.; Khalifah, P.G.; Grubbs, R.B.; Bhatia, S.R. Impact of Stereochemistry on Rheology and Nanostructure of PLA-PEO-PLA Triblocks: Stiff Gels at Intermediate l/d-Lactide Ratios. *Soft Matter* **2018**, *14*, 7255–7263, doi:10.1039/c8sm01559g.
 109. Yin, X.; Hewitt, D.R.O.; Preston, A.N.; Heroux, L.A.; Agamalian, M.M.; Quah, S.P.; Zheng, B.; Smith, A.J.; Laughlin, S.T.; Grubbs, R.B.; et al. Hierarchical Assembly in PLA-PEO-PLA Hydrogels with Crystalline Domains and Effect of Block Stereochemistry. *Colloids Surfaces B Biointerfaces* **2019**, *180*, 102–109, doi:10.1016/j.colsurfb.2019.04.031.
 110. Moya-Lopez, C.; Juan, A.; Donizeti, M.; Valcarcel, J.; Vazquez, J.A.; Solano, E.; Chapron, D.; Bourson, P.; Bravo, I.; Alonso-Moreno, C.; et al. Multifunctional PLA/Gelatin Bionanocomposites for Tailored Drug Delivery Systems. *Pharmaceutics* **2022**, *14*, 1138, doi:10.3390/pharmaceutics14061138.
 111. Wang, X.; Ronsin, O.; Gravez, B.; Farman, N.; Baumberger, T.; Jaisser, F.; Coradin, T.; Hélyary, C. Nanostructured Dense Collagen-Polyester Composite Hydrogels as Amphiphilic Platforms for Drug Delivery. *Adv. Sci.* **2021**, *8*, 1–16, doi:10.1002/advs.202004213.
 112. Bergström, J.S.; Hayman, D. An Overview of Mechanical Properties and Material Modeling of Polylactide (PLA) for Medical Applications. *Ann. Biomed. Eng.* **2016**, *44*, 330–340, doi:10.1007/s10439-015-1455-8.
 113. Van De Velde, K.; Kiekens, P. Biopolymers: Overview of Several Properties and Consequences on Their Applications. *Polym. Test.* **2002**, *21*, 433–442, doi:10.1016/S0142-9418(01)00107-6.
 114. Carrasco, F.; Pagès, P.; Gámez-Pérez, J.; Santana, O.O.; MasPOCH, M.L. Processing of Poly(Lactic Acid): Characterization of Chemical Structure, Thermal Stability and Mechanical Properties. *Polym. Degrad. Stab.* **2010**, *95*, 116–125, doi:10.1016/j.polymdegradstab.2009.11.045.
 115. Perego, G.; Cella, G.D.; Bastioli, C. Effect of Molecular Weight and Crystallinity on Poly(Lactic Acid) Mechanical Properties. *J. Appl. Polym. Sci.* **1996**, *59*, 37–43, doi:10.1002/(sici)1097-4628(19960103)59:1<37::aid-app6>3.0.co;2-n.
 116. Li, G.; Yang, B.; Han, W.; Li, H.; Kang, Z.; Lin, J. Tailoring the Thermal and Mechanical Properties of Injection-Molded Poly (Lactic Acid) Parts through Annealing. *J. Appl. Polym. Sci.* **2021**, *138*, 1–10, doi:10.1002/app.49648.
 117. Cocca, M.; Lorenzo, M.L. Di; Malinconico, M.; Frezza, V. Influence of Crystal Polymorphism on Mechanical and Barrier Properties of Poly(l-Lactic Acid). *Eur. Polym. J.* **2011**, *47*, 1073–1080, doi:10.1016/j.eurpolymj.2011.02.009.
 118. Ma, B.; Wang, X.; He, Y.; Dong, Z.; Zhang, X.; Chen, X.; Liu, T. Effect of Poly(Lactic Acid) Crystallization on Its Mechanical and Heat Resistance Performances. *Polymer (Guildf)*.

- 2021, 212, 1–9, doi:10.1016/j.polymer.2020.123280.
119. Tsuji, H. Properties and Morphologies of Poly(L-Lactide): 1. Annealing Condition Effects on Properties and Morphologies of Poly(L-Lactide). *Polymer (Guildf)*. **1995**, *36*, 2709–2716.
 120. Tsuji, H.; Ikada, Y. Stereocomplex Formation between Enantiomeric Poly(Lactic Acid)s. XI. Mechanical Properties and Morphology of Solution-Cast Films. *Polymer (Guildf)*. **1999**, *40*, 6699–6708, doi:10.1016/S0032-3861(99)00004-X.
 121. Tsuji, H. Hydrolytic Degradation. In *Poly(Lactic Acid): Synthesis, Structures, Properties, Processing, and Applications*; 2010; pp. 345–382 ISBN 9780470293669.
 122. Sin, L.T.; Tuenen, B.S. *Degradation and Stability of Poly(Lactic Acid)*; 2019; ISBN 9780128144725.
 123. Siparsky, G.L.; Voorhees, K.J.; Miao, F. Hydrolysis of Polylactic Acid (PLA) and Polycaprolactone (PCL) in Aqueous Acetonitrile Solutions: Autocatalysis. *J. Environ. Polym. Degrad.* **1998**, *6*, 31–41, doi:10.1023/A:1022826528673.
 124. Gorrasi, G.; Pantani, R. Hydrolysis and Biodegradation of Poly(Lactic Acid). In *Advances in Polymer Science*; Springer New York LLC, 2018; Vol. 279, pp. 119–151.
 125. Celikkaya, E.; Denkbaz, E.B.; Piskin, E. Poly(DL-Lactide)/Poly(Ethylene Glycol) Copolymer Particles. Preparation and Characterization. *J. Appl. Polym. Sci.* **1996**, *61*, 1439–1446.
 126. Saha, S.K.; Tsuji, H. Effects of Molecular Weight and Small Amounts of D-Lactide Units on Hydrolytic Degradation of Poly(L-Lactic Acid)s. *Polym. Degrad. Stab.* **2006**, *91*, 1665–1673, doi:10.1016/j.polymdegradstab.2005.12.009.
 127. Tsuji, H.; Mizuno, A.; Ikada, Y. Properties and Morphology of Poly(L-Lactide). III. Effects of Initial Crystallinity on Long-Term in Vitro Hydrolysis of High Molecular Weight Poly(L-Lactide) Film in Phosphate-Buffered Solution. *J. Appl. Polym. Sci.* **2000**, *77*, 1452–1464, doi:10.1002/1097-4628(20000815)77:7<1452::AID-APP7>3.0.CO;2-S.
 128. Tsuji, H. In Vitro Hydrolysis of Blends from Enantiomeric Poly(Lactide)s. Part 4: Well-Homo-Crystallized Blend and Nonblended Films. *Polymer (Guildf)*. **2000**, *41*, 3621–3630, doi:10.1016/S0142-9612(02)00365-4.
 129. Grizzi, I.; Garreau, H.; Li, S.; Vert, M. Hydrolytic Degradation of Devices Based on Poly(DL-Lactic Acid) Size-Dependence. *Biomaterials* **1995**, *16*, 305–311, doi:10.1016/0142-9612(95)93258-F.
 130. De Jong, S.J.; Arias, E.R.; Rijkers, D.T.S.; Van Nostrum, C.F.; Kettenes-Van Den Bosch, J.J.; Hennink, W.E. New Insights into the Hydrolytic Degradation of Poly(Lactic Acid): Participation of the Alcohol Terminus. *Polymer (Guildf)*. **2001**, *42*, 2795–2802, doi:10.1016/S0032-3861(00)00646-7.
 131. Schliecker, G.; Schmidt, C.; Fuchs, S.; Kissel, T. Characterization of a Homologous Series of D,L-Lactic Acid Oligomers; a Mechanistic Study on the Degradation Kinetics in Vitro. *Biomaterials* **2003**, *24*, 3835–3844, doi:10.1016/S0142-9612(03)00243-6.

132. Shih, C. Controlled Release Chain-End Scission in Acid Catalyzed Hydrolysis of Poly (D , L- Lactide) in Solution. **1995**, *34*, 9–15.
133. Hayman, D.; Bergerson, C.; Miller, S.; Moreno, M.; Moore, J.E. The Effect of Static and Dynamic Loading on Degradation of PLLA Stent Fibers. **2014**, *136*, 1–10, doi:10.1115/1.4027614.
134. Pillai, C.K.S.; Sharma, C.P. Review Paper: Absorbable Polymeric Surgical Sutures: Chemistry, Production, Properties, Biodegradability, and Performance. *J. Biomater. Appl.* **2010**, *25*, 291–366, doi:10.1177/0885328210384890.
135. Blasi, P. Poly(Lactic Acid)/Poly(Lactic-Co-Glycolic Acid)-Based Microparticles: An Overview. *J. Pharm. Investig.* **2019**, *49*, 337–346, doi:10.1007/s40005-019-00453-z.
136. Valantin, M.A.; Aubron-Olivier, C.; Ghosn, J.; Laglenne, E.; Pauchard, M.; Schoen, H.; Bousquet, R.; Katz, P.; Costagliola, D.; Katlama, C. Polylactic Acid Implants (New-Fill)® to Correct Facial Lipoatrophy in HIV-Infected Patients: Results of the Open-Label Study VEGA. *Aids* **2003**, *17*, 2471–2477, doi:10.1097/00002030-200311210-00009.
137. Fitzgerald, R.; Bass, L.M.; Goldberg, D.J.; Graivier, M.H.; Lorenc, Z.P. Physiochemical Characteristics of Poly-L-Lactic Acid (PLLA). *Aesthetic Surg. J.* **2018**, *38*, S13–S17, doi:10.1093/asj/sjy012.
138. Casalini, T.; Rossi, F.; Castrovinci, A.; Perale, G. A Perspective on Polylactic Acid-Based Polymers Use for Nanoparticles Synthesis and Applications. *Front. Bioeng. Biotechnol.* **2019**.
139. Kamaly, N.; Yameen, B.; Wu, J.; Farokhzad, O.C. Degradable Controlled-Release Polymers and Polymeric Nanoparticles : Mechanisms of Controlling Drug Release. **2015**, doi:10.1021/acs.chemrev.5b00346.
140. De Mattos, A.C.; Altmeyer, C.; Toyomi, T.; Maissar, N.; Mara, R. Polymeric Nanoparticles for Oral Delivery of 5- Fluorouracil: Formulation Optimization, Cytotoxicity Assay and Pre-Clinical Pharmacokinetics Study. *Eur. J. Pharm. Sci.* **2016**, *84*, 83–91, doi:10.1016/j.ejps.2016.01.012.
141. Estupiñán, Ó.; Niza, E.; Bravo, I.; Rey, V.; Tornín, J.; Gallego, B.; Casares, P.C.; Moris, F.; Ocaña, A.; Lorenzo, V.B.; et al. Mithramycin Delivery Systems to Develop Effective Therapies in Sarcomas. *J. Nanobiotechnology* **2021**, 1–21, doi:10.1186/s12951-021-01008-x.
142. Campos de Mello, C.G.; Branquinho, T.; Oliveira, T.; Milagre, M. Efficacy of Lychnopholide Polymeric Nanocapsules after Oral and Intravenous Administration in Murine Experimental Chagas Disease., doi:10.1128/AAC.00178-16.Address.
143. Zhang, C.; Wan, X.; Zheng, X.; Shao, X.; Liu, Q.; Zhang, Q.; Qian, Y. Dual-Functional Nanoparticles Targeting Amyloid Plaques in the Brains of Alzheimer’s Disease Mice. *Biomaterials* **2014**, *35*, 456–465, doi:10.1016/j.biomaterials.2013.09.063.
144. Sun, S.; Liang, N.; Piao, H.; Yamamoto, H.; Kawashima, Y.; Cui, F. Insulin-S.O (Sodium Oleate) Complex-Loaded PLGA Nanoparticles: Formulation, Characterization and in Vivo Evaluation. *J. Microencapsul.* **2010**, *27*, 471–478, doi:10.3109/02652040903515490.
145. Cimas, F.J.; Niza, E.; Juan, A.; Noblejas-López, M.D.M.; Bravo, I.; Lara-Sanchez, A.;

- Alonso-Moreno, C.; Ocaña, A. Controlled Delivery of Bet-Protacs: In Vitro Evaluation of MZ1-Loaded Polymeric Antibody Conjugated Nanoparticles in Breast Cancer. *Pharmaceutics* **2020**, *12*, 1–11, doi:10.3390/pharmaceutics12100986.
146. Xia, H.; Gao, X.; Gu, G.; Liu, Z.; Hu, Q.; Tu, Y.; Song, Q.; Yao, L.; Pang, Z.; Jiang, X.; et al. Penetratin-Functionalized PEG-PLA Nanoparticles for Brain Drug Delivery. *Int. J. Pharm.* **2012**, *436*, 840–850, doi:10.1016/j.ijpharm.2012.07.029.
147. Hu, Q.; Gao, X.; Gu, G.; Kang, T.; Tu, Y.; Liu, Z.; Song, Q.; Yao, L.; Pang, Z.; Jiang, X.; et al. Glioma Therapy Using Tumor Homing and Penetrating Peptide-Functionalized PEG-PLA Nanoparticles Loaded with Paclitaxel. *Biomaterials* **2013**, *34*, 5640–5650, doi:10.1016/j.biomaterials.2013.04.025.
148. Thomsen, T.; Reissmann, R.; Kaba, E.; Engelhardt, B.; Klok, H. Covalent and Noncovalent Conjugation of Degradable Polymer Nanoparticles to T Lymphocytes. **2021**, doi:10.1021/acs.biomac.1c00488.
149. de Freitas Oliveira, J.W.; da Silva, M.F.A.; Damasceno, I.Z.; Rocha, H.A.O.; da Silva Júnior, A.A.; Silva, M.S. In Vitro Validation of Antiparasitic Activity of PLA-Nanoparticles of Sodium Diethyldithiocarbamate against *Trypanosoma Cruzi*. *Pharmaceutics* **2022**, *14*, 1–15, doi:10.3390/pharmaceutics14030497.
150. Park, K.; Otte, A.; Sharifi, F.; Garner, J.; Skidmore, S.; Park, H.; Jhon, Y.K.; Qin, B.; Wang, Y. Potential Roles of the Glass Transition Temperature of PLGA Microparticles in Drug Release Kinetics. *Mol. Pharm.* **2021**, *18*, 18–32, doi:10.1021/acs.molpharmaceut.0c01089.
151. Jain, A.; Kunduru, K.R.; Basu, A.; Mizrahi, B.; Domb, A.J.; Khan, W. Injectable Formulations of Poly(Lactic Acid) and Its Copolymers in Clinical Use. *Adv. Drug Deliv. Rev.* **2016**, *107*, 213–227, doi:10.1016/j.addr.2016.07.002.
152. Basu, A.; Kunduru, K.R.; Doppalapudi, S.; Domb, A.J.; Khan, W. Poly(Lactic Acid) Based Hydrogels. *Adv. Drug Deliv. Rev.* **2016**, *107*, 192–205, doi:10.1016/j.addr.2016.07.004.
153. Sokolsky-Papkov, M.; Domb, A.J. Stereoisomeric Effect on in Vitro Drug Release from Injectable Poly(Lactic Acid Co Castor Oil) Polyesters. *Polym. Adv. Technol.* **2008**, *19*, 671–679, doi:10.1002/pat.
154. Le, T.M.D.; Nguyen, V.V.L.; Trinh, T.A.; Pham, N.S.; Lee, D.S.; Huynh, D.P. Sulfonamide Functionalized Amino Acid-Based PH- and Temperature-Sensitive Biodegradable Injectable Hydrogels: Synthesis, Physicochemical Characterization and in Vivo Degradation Kinetics. *J. Appl. Polym. Sci.* **2021**, *138*, 1–13, doi:10.1002/app.50488.
155. Mao, H.; Shan, G.; Bao, Y.; Wu, Z.L.; Pan, P. Thermoresponsive Physical Hydrogels of Poly(Lactic Acid)/Poly(Ethylene Glycol) Stereoblock Copolymers Tuned by Stereostructure and Hydrophobic Block Sequence. *Soft Matter* **2016**, *12*, 4628–4637, doi:10.1039/c6sm00517a.
156. Arun, Y.; Ghosh, R.; Domb, A.J. Biodegradable Hydrophobic Injectable Polymers for Drug Delivery and Regenerative Medicine. *Adv. Funct. Mater.* **2021**, *31*, 1–22, doi:10.1002/adfm.202010284.

157. Steinman, N.Y.; Domb, A.J. Instantaneous Degelling Thermoresponsive Hydrogel. *Gels* **2021**, *7*, doi:10.3390/gels7040169.
158. Kim, T.; Suh, J.; Kim, W.J. Polymeric Aggregate-Embodied Hybrid Nitric-Oxide-Scavenging and Sequential Drug-Releasing Hydrogel for Combinatorial Treatment of Rheumatoid Arthritis. *Adv. Mater.* **2021**, *33*, 1–12, doi:10.1002/adma.202008793.
159. Diba, M.; Polini, A.; Petre, D.G.; Zhang, Y.; Leeuwenburgh, S.C.G. Fiber-Reinforced Colloidal Gels as Injectable and Moldable Biomaterials for Regenerative Medicine. *Mater. Sci. Eng. C* **2018**, *92*, 143–150, doi:10.1016/j.msec.2018.06.038.
160. Joo, M.K.; Sohn, Y.S.; Jeong, B. Stereoisomeric Effect on Reverse Thermal Gelation of Poly(Ethylene Glycol)/Poly(Lactide) Multiblock Copolymer. *Macromolecules* **2007**, *40*, 5111–5115, doi:10.1021/ma070008u.
161. Sanabria-DeLong, N.; Agrawal, S.K.; Bhatia, S.R.; Tew, G.N. Controlling Hydrogel Properties by Crystallization of Hydrophobic Domains. *Macromolecules* **2006**, *39*, 1308–1310, doi:10.1021/ma052243n.
162. Elkasabgy, N.A.; Mahmoud, A.A.; Maged, A. 3D Printing: An Appealing Route for Customized Drug Delivery Systems. *Int. J. Pharm.* **2020**, *588*, 119732, doi:10.1016/j.ijpharm.2020.119732.
163. Trenfield, S.J.; Awad, A.; Goyanes, A.; Gaisford, S.; Basit, A.W. 3D Printing Pharmaceuticals: Drug Development to Frontline Care. *Trends Pharmacol. Sci.* **2018**, *39*, 440–451, doi:10.1016/j.tips.2018.02.006.
164. NHS England Improving Outcomes Through Personalised Medicine. **2016**, 1–18.
165. Seoane-Viaño, I.; Trenfield, S.J.; Basit, A.W.; Goyanes, A. Translating 3D Printed Pharmaceuticals: From Hype to Real-World Clinical Applications. *Adv. Drug Deliv. Rev.* **2021**, *174*, 553–575, doi:10.1016/j.addr.2021.05.003.
166. Hsiao, W.K.; Lorber, B.; Reitsamer, H.; Khinast, J. 3D Printing of Oral Drugs: A New Reality or Hype? *Expert Opin. Drug Deliv.* **2018**, *15*, 1–4, doi:10.1080/17425247.2017.1371698.
167. Aprecia Pharmaceuticals <https://www.spritam.com/>.
168. Khaled, S.A.; Burley, J.C.; Alexander, M.R.; Yang, J.; Roberts, C.J. 3D Printing of Five-in-One Dose Combination Polypill with Defined Immediate and Sustained Release Profiles. *J. Control. Release* **2015**, *217*, 308–314, doi:10.1016/j.jconrel.2015.09.028.
169. Gioumouxouzis, C.I.; Katsamenis, O.L.; Bouropoulos, N.; Fatouros, D.G. 3D Printed Oral Solid Dosage Forms Containing Hydrochlorothiazide for Controlled Drug Delivery. *J. Drug Deliv. Sci. Technol.* **2017**, *40*, 164–171, doi:10.1016/j.jddst.2017.06.008.
170. Stewart, S.A.; Domínguez-Robles, J.; McIlorum, V.J.; Mancuso, E.; Lamprou, D.A.; Donnelly, R.F.; Larrañeta, E. Development of a Biodegradable Subcutaneous Implant for Prolonged Drug Delivery Using 3D Printing. *Pharmaceutics* **2020**, *12*, doi:10.3390/pharmaceutics12020105.
171. Song, L.; Pan, M.; Zhao, R.; Deng, J.; Wu, Y. Recent Advances, Challenges and

- Perspectives in Enantioselective Release. *J. Control. Release* **2020**, *324*, 156–171, doi:10.1016/j.jconrel.2020.05.019.
172. Liang, J.; Yang, B.; Deng, J. Polylactide-Based Chiral Particles with Enantio-Differentiating Release Ability. *Chem. Eng. J.* **2018**, *344*, 262–269, doi:10.1016/j.cej.2018.03.076.
 173. Liang, J.; Deng, J. Chiral Particles Consisting of Helical Polylactide and Helical Substituted Polyacetylene: Preparation and Synergistic Effects in Enantio-Differentiating Release. *Macromolecules* **2018**, *51*, 4003–4011, doi:10.1021/acs.macromol.8b00580.
 174. Slager, J.; Domb, A.J. Biopolymer Stereocomplexes. *Adv. Drug Deliv. Rev.* **2003**, *55*, 549–583.
 175. Slager, J.; Domb, A.J. Stereocomplexes Based on Poly(Lactic Acid) and Insulin: Formulation and Release Studies. *Biomaterials* **2002**, *23*, 4389–4396.
 176. Bishara, A.; Domb, A.J. PLA Stereocomplexes for Controlled Release of Somatostatin Analogue. *J. Control. Release* **2005**, *107*, 474–483, doi:10.1016/j.jconrel.2005.05.026.
 177. Fraschini, C.; Jalabert, M.; Prud'homme, R.E. Physical Characterization of Blends of Poly(D-Lactide) and LHRH (A Leuprolide Decapeptide Analog). *Biomacromolecules* **2005**, *6*, 3112–3118, doi:10.1021/bm050439p.
 178. Slager, J.; Domb, A.J. Hetero-Stereocomplexes of D-Poly(Lactic Acid) and the LHRH Analogue Leuprolide. Application in Controlled Release. *Eur. J. Pharm. Biopharm.* **2004**, *58*, 461–469, doi:10.1016/j.ejpb.2004.04.017.
 179. Zhang, J.; Beshra, A.; Domb, A.J.; Ozaki, Y. D-Poly(Lactide) and LHRH Decapeptide Stereointeractions Investigated by Vibrational Spectroscopy. *Eur. Polym. J.* **2007**, *43*, 3016–3027, doi:10.1016/j.eurpolymj.2007.04.035.
 180. Senapati, S.; Upadhyaya, A.; Dhruw, S.; Giri, D.; Maiti, P. Controlled DNA Delivery Using Poly(Lactide) Nanoparticles and Understanding the Binding Interactions. *J. Phys. Chem. B* **2021**, *125*, 10009–10017, doi:10.1021/acs.jpcc.1c06520.
 181. Prabha, S.; Labhasetwar, V. Critical Determinants in PLGA/PLA Nanoparticle-Mediated Gene Expression. *Pharm. Res.* **2004**, *21*, 354–364, doi:10.1023/B:PHAM.0000016250.56402.99.
 182. Mansoor, F.; Earley, B.; Cassidy, J.P.; Markey, B.; Doherty, S.; Welsh, M.D. Comparing the Immune Response to a Novel Intranasal Nanoparticle PLGA Vaccine and a Commercial BPI3V Vaccine in Dairy Calves. *BMC Vet. Res.* **2015**, *11*, 1–11, doi:10.1186/s12917-015-0481-y.
 183. Zare, S.; Kabiri, M.; Amini, Y.; Najafi, A.; Mohammadpour, F.; Ayati, S.H.; Nikpoor, A.R.; Tafaghodi, M. Immunological Assessment of Chitosan or Trimethyl Chitosan-Coated PLGA Nanospheres Containing Fusion Antigen as the Novel Vaccine Candidates Against Tuberculosis. *AAPS PharmSciTech* **2022**, *23*, 1–14, doi:10.1208/s12249-021-02146-z.
 184. Olmos, D.; González-benito, J. Polymeric Materials with Antibacterial Activity: A

- Review. *Polymers (Basel)*. **2021**, *13*, 1–30, doi:10.3390/polym13040613.
185. Fortunati, E.; Rinaldi, S.; Peltzer, M.; Bloise, N.; Visai, L.; Armentano, I.; Jiménez, A.; Latterini, L.; Kenny, J.M. Nano-Biocomposite Films with Modified Cellulose Nanocrystals and Synthesized Silver Nanoparticles. *Carbohydr. Polym.* **2014**, *101*, 1122–1133, doi:10.1016/j.carbpol.2013.10.055.
 186. Fortunati, E.; Armentano, I.; Zhou, Q.; Iannoni, A.; Saino, E.; Visai, L.; Berglund, L.A.; Kenny, J.M. Multifunctional Bionanocomposite Films of Poly(Lactic Acid), Cellulose Nanocrystals and Silver Nanoparticles. *Carbohydr. Polym.* **2012**, *87*, 1596–1605, doi:10.1016/j.carbpol.2011.09.066.
 187. González, E.A.S.; Olmos, D.; Lorente, M. ángel; Vélaz, I.; González-Benito, J. Preparation and Characterization of Polymer Composite Materials Based on PLA/TiO₂ for Antibacterial Packaging. *Polymers (Basel)*. **2018**, *10*, 1–14, doi:10.3390/polym10121365.
 188. Salmieri, S.; Islam, F.; Khan, R.A.; Hossain, F.M.; Ibrahim, H.M.M.; Miao, C.; Hamad, W.Y.; Lacroix, M. Antimicrobial Nanocomposite Films Made of Poly(Lactic Acid)–Cellulose Nanocrystals (PLA–CNC) in Food Applications—Part B: Effect of Oregano Essential Oil Release on the Inactivation of *Listeria Monocytogenes* in Mixed Vegetables. *Cellulose* **2014**, *21*, 4271–4285, doi:10.1007/s10570-014-0406-0.
 189. <https://Filament2print.Com> Available online: <https://filament2print.com/es/pla-especial/994-plactive-copper3d-antibacteriano.html>.
 190. <https://Www.3djake.Es> Available online: <https://www.3djake.es/copper-3d/plactive-red>.
 191. Zuniga, J.M. 3D Printed Antibacterial Prostheses. *Appl. Sci.* **2018**, *8*, 1–10, doi:10.3390/app8091651.
 192. Alam, F.; Shukla, V.R.; Varadarajan, K.M.; Kumar, S. Microarchitected 3D Printed Polylactic Acid (PLA) Nanocomposite Scaffolds for Biomedical Applications. *J. Mech. Behav. Biomed. Mater.* **2020**, *103*, doi:10.1016/j.jmbbm.2019.103576.
 193. Liu, C.; Shen, J.; Yeung, K.W.K.; Tjong, S.C. Development and Antibacterial Performance of Novel Polylactic Acid-Graphene Oxide-Silver Nanoparticle Hybrid Nanocomposite Mats Prepared by Electrospinning. *ACS Biomater. Sci. Eng.* **2017**, *3*, 471–486, doi:10.1021/acsbomaterials.6b00766.
 194. Valerini, D.; Tamaro, L.; Villani, F.; Rizzo, A.; Caputo, I.; Paoletta, G.; Vigliotta, G. Antibacterial Al-Doped ZnO Coatings on PLA Films. *J. Mater. Sci.* **2020**, *55*, 4830–4847, doi:10.1007/s10853-019-04311-z.
 195. Yuan, Q.; Wu, J.; Qin, C.; Xu, A.; Zhang, Z.; Lin, S.; Ren, X.; Zhang, P. Spin-Coating Synthesis and Characterization of Zn-Doped Hydroxyapatite/Polylactic Acid Composite Coatings. *Surf. Coatings Technol.* **2016**, *307*, 461–469, doi:10.1016/j.surfcoat.2016.09.021.
 196. Duncan, R. Polymer Conjugates : Nanosized Medicines for Treating Cancer. **2006**, *24*, doi:10.1016/j.tibtech.2005.11.006.
 197. Duncan, R.; Vicent, M.J. Polymer Therapeutics-Prospects for 21st Century : The End of

- the Beginning ☆. *Adv. Drug Deliv. Rev.* **2013**, *65*, 60–70, doi:10.1016/j.addr.2012.08.012.
198. Tong, R.; Cheng, J. Drug-Initiated, Controlled Ring-Opening Polymerization for the Synthesis of Polymer – Drug Conjugates. **2012**.
 199. Yu, Y.; Chen, C.; Law, W.; Mok, J.; Zou, J.; Prasad, P.N.; Cheng, C. Well-Defined Degradable Brush Polymer – Drug Conjugates for Sustained Delivery of Paclitaxel. **2013**.
 200. Danafar, H.; Rostamizadeh, K.; Davaran, S.; Hamidi, M. Drug-Conjugated PLA–PEG–PLA Copolymers: A Novel Approach for Controlled Delivery of Hydrophilic Drugs by Micelle Formation. *Pharm. Dev. Technol.* **2017**, *22*, 947–957, doi:10.3109/10837450.2015.1125920.
 201. Sanchez-Bodon, J.; Ruiz-rubio, L.; Hernaez-Laviña, E.; Vilas-vilela, J.L.; Moreno-Benitez, M.I. -Lactide)-Based Anti-Inflammatory Responsive Surfaces for Surgical Implants. **2021**, 1–15.
 202. Plichta, A.; Kowalczyk, S.; Kamiński, K.; Wasyaeczko, M.; Wieckowski, S.; Oledzka, E.; Naecz-Jawecki, G.; Zgadzaj, A.; Sobczak, M. ATRP of Methacrylic Derivative of Camptothecin Initiated with PLA toward Three-Arm Star Block Copolymer Conjugates with Favorable Drug Release. *Macromolecules* **2017**, *50*, 6439–6450, doi:10.1021/acs.macromol.7b01350.
 203. Räber, L.; Onuma, Y.; Brugaletta, S.; Garcia-Garcia, H.M.; Backx, B.; Iñiguez, A.; Jensen, L.O.; Cequier-Fillat, À.; Pilgrim, T.; Christiansen, E.H.; et al. Arterial Healing Following Primary PCI Using the Absorb Everolimus-Eluting Bioresorbable Vascular Scaffold (Absorb BVS) versus the Durable Polymer Everolimus-Eluting Metallic Stent (XIENCE) in Patients with Acute ST-Elevation Myocardial Infarction: Ration. *EuroIntervention* **2016**, doi:10.4244/EIJY15M08_03.
 204. Abbott FDA Approves Abbott’s Absorb™ Bioresorbable Stent, the Only Fully Dissolving Heart Stent 2016.
 205. Ellis, S.G.; Kereiakes, D.J.; Metzger, D.C.; Caputo, R.P.; Rizik, D.G.; Teirstein, P.S.; Litt, M.R.; Kini, A.; Kabour, A.; Marx, S.O.; et al. Everolimus-Eluting Bioresorbable Scaffolds for Coronary Artery Disease. *N. Engl. J. Med.* **2015**, *373*, 1905–1915, doi:10.1056/nejmoa1509038.
 206. Sorrentino, S.; Giustino, G.; Mehran, R.; Kini, A.S.; Sharma, S.K.; Faggioni, M.; Farhan, S.; Vogel, B.; Indolfi, C.; Dangas, G.D. Everolimus-Eluting Bioresorbable Scaffolds Versus Everolimus-Eluting Metallic Stents. *J. Am. Coll. Cardiol.* **2017**, *69*, 3055–3066, doi:10.1016/j.jacc.2017.04.011.
 207. Yamaji, K.; Ueki, Y.; Souteyrand, G.; Daemen, J.; Wiebe, J.; Nef, H.; Adriaenssens, T.; Loh, J.P.; Lattuca, B.; Wykrzykowska, J.J.; et al. Mechanisms of Very Late Bioresorbable Scaffold Thrombosis: The INVEST Registry. *J. Am. Coll. Cardiol.* **2017**, *70*, 2330–2344, doi:10.1016/j.jacc.2017.09.014.
 208. Kraak, R.P.; Kajita, A.H.; Garcia-Garcia, H.M.; Henriques, J.P.S.; Piek, J.J.; Arkenbout, E.K.; van der Schaaf, R.J.; Tijssen, J.G.P.; de Winter, R.J.; Wykrzykowska, J.J. Scaffold Thrombosis Following Implantation of the ABSORB BVS in Routine Clinical Practice:

- Insight into Possible Mechanisms from Optical Coherence Tomography. *Catheter. Cardiovasc. Interv.* **2018**, *92*, E106–E114, doi:10.1002/ccd.27475.
209. Sakamoto, A.; Jinnouchi, H.; Torii, S.; Virmani, R.; Finn, A. V. Understanding the Impact of Stent and Scaffold Material and Strut Design on Coronary Artery Thrombosis from the Basic and Clinical Points of View. *Bioengineering* **2018**, *5*, 1–19, doi:10.3390/bioengineering5030071.
 210. Zhao, G.; Liu, J.; Liu, M.; Tian, Y.; Cheng, J.; Liu, W.; Ni, Z. Influence of Parameters on Mechanical Properties of Poly (L-Lactic Acid) Helical Stents. *J. Biomed. Mater. Res. - Part B Appl. Biomater.* **2022**, 1–8, doi:10.1002/jbm.b.35031.
 211. Litowczenko, J.; Woźniak-Budych, M.J.; Staszak, K.; Wieszczycka, K.; Jurga, S.; Tylkowski, B. Milestones and Current Achievements in Development of Multifunctional Bioscaffolds for Medical Application. *Bioact. Mater.* **2021**, *6*, 2412–2438, doi:10.1016/j.bioactmat.2021.01.007.
 212. Stratton, S.; Shelke, N.B.; Hoshino, K.; Rudraiah, S.; Kumbar, S.G. Bioactive Polymeric Scaffolds for Tissue Engineering. *Bioact. Mater.* **2016**, *1*, 93–108, doi:10.1016/j.bioactmat.2016.11.001.
 213. Tanaka, M.; Sato, K.; Kitakami, E.; Kobayashi, S.; Hoshihara, T.; Fukushima, K. Design of Biocompatible and Biodegradable Polymers Based on Intermediate Water Concept. *Polym. J.* **2015**, *47*, 114–121, doi:10.1038/pj.2014.129.
 214. Sheikh, F.A.; Ju, H.W.; Moon, B.M.; Lee, O.J. Hybrid Scaffolds Based on PLGA and Silk for Bone Tissue Engineering. *J. Tissue Eng. Regen. Med.* **2016**, *10*, 209–221, doi:10.1002/term.
 215. Cai, J.; Peng, X.; Nelson, K.D.; Eberhart, R.; Smith, G.M. Permeable Guidance Channels Containing Microfilament Scaffolds Enhance Axon Growth and Maturation. *J. Biomed. Mater. Res. - Part A* **2005**, *75*, 374–386, doi:10.1002/jbm.a.30432.
 216. Deng, D.; Wang, W.; Wang, B.; Zhang, P.; Zhou, G.; Zhang, W.J.; Cao, Y.; Liu, W. Repair of Achilles Tendon Defect with Autologous ASCs Engineered Tendon in a Rabbit Model. *Biomaterials* **2014**, *35*, 8801–8809, doi:10.1016/j.biomaterials.2014.06.058.
 217. Ngo, H.X.; Bai, Y.; Sha, J.; Ishizuka, S.; Toda, E.; Osako, R.; Kato, A.; Morioka, R.; Ramanathan, M.; Tatsumi, H.; et al. A Narrative Review of U-HA/PLLA, a Bioactive Resorbable Reconstruction Material: Applications in Oral and Maxillofacial Surgery. *Materials (Basel)*. **2022**, *15*, doi:10.3390/ma15010150.
 218. Sukegawa, S.; Kanno, T.; Katase, N.; Shibata, A.; Takahashi, Y.; Furuki, Y. Clinical Evaluation of an Unsintered Hydroxyapatite/Poly-L-Lactide Osteoconductive Composite Device for the Internal Fixation of Maxillofacial Fractures. *J. Craniofac. Surg.* **2016**, *27*, 1391–1397, doi:10.1097/SCS.0000000000002828.
 219. Kim, Y.M.; Lee, J.H. Clinical Courses and Degradation Patterns of Absorbable Plates in Facial Bone Fracture Patients. *Arch. Craniofacial Surg.* **2019**, *20*, 297–303, doi:10.7181/acfs.2019.00409.
 220. El Khatib, M.; Mauro, A.; Di Mattia, M.; Wyrwa, R.; Schweder, M.; Ancora, M.; Lazzaro,

- F.; Berardinelli, P.; Valbonetti, L.; Di Giacinto, O.; et al. Electrospun PLGA Fiber Diameter and Alignment of Tendon Biomimetic Fleece Potentiate Tenogenic Differentiation and Immunomodulatory Function of Amniotic Epithelial Stem Cells. *Cells* **2020**, *9*, 1–26, doi:10.3390/cells9051207.
221. Russo, V.; El Khatib, M.; di Marcantonio, L.; Ancora, M.; Wyrwa, R.; Mauro, A.; Walter, T.; Weisser, J.; Citeroni, M.R.; Lazzaro, F.; et al. Tendon Biomimetic Electrospun PLGA Fleeces Induce an Early Epithelial-Mesenchymal Transition and Tenogenic Differentiation on Amniotic Epithelial Stem Cells. *Cells* **2020**, *9*, doi:10.3390/cells9020303.
222. Ciardulli, M.C.; Marino, L.; Lovecchio, J.; Giordano, E.; Forsyth, N.R.; Selleri, C.; Maffulli, N.; Porta, G. Della Tendon and Cytokine Marker Expression by Human Bone Marrow Mesenchymal Stem Cells in a Hyaluronate/Poly-Lactic-Co-Glycolic Acid (PLGA)/Fibrin Three-Dimensional (3D) Scaffold. *Cells* **2020**, *9*, doi:10.3390/cells9051268.
223. Sahoo, S.; Toh, S.L.; Goh, J.C.H. A BFGF-Releasing Silk/PLGA-Based Biohybrid Scaffold for Ligament/Tendon Tissue Engineering Using Mesenchymal Progenitor Cells. *Biomaterials* **2010**, *31*, 2990–2998, doi:10.1016/j.biomaterials.2010.01.004.
224. Ouyang, H.W.; Goh, J.C.H.; Thambyah, A.; Teoh, S.H.; Lee, E.H. Knitted Poly-Lactide-Co-Glycolide Scaffold Loaded with Bone Marrow Stromal Cells in Repair and Regeneration of Rabbit Achilles Tendon. *Tissue Eng.* **2003**, *9*, 431–439, doi:10.1089/107632703322066615.
225. Wang, C.; Feng, N.; Chang, F.; Wang, J.; Yuan, B.; Cheng, Y.; Liu, H.; Yu, J.; Zou, J.; Ding, J.; et al. Injectable Cholesterol-Enhanced Stereocomplex Polylactide Thermogel Loading Chondrocytes for Optimized Cartilage Regeneration. *Adv. Healthc. Mater.* **2019**, *8*, 1–10, doi:10.1002/adhm.201900312.
226. Ghiasi, M.S.; Chen, J.; Vaziri, A.; Rodriguez, E.K.; Nazarian, A. Bone Fracture Healing in Mechanobiological Modeling: A Review of Principles and Methods. *Bone Reports* **2017**, *6*, 87–100, doi:10.1016/j.bonr.2017.03.002.
227. Li, J.; Qin, L.; Yang, K.; Ma, Z.; Wang, Y.; Cheng, L.; Zhao, D. Materials Evolution of Bone Plates for Internal Fixation of Bone Fractures: A Review. *J. Mater. Sci. Technol.* **2020**, *36*, 190–208, doi:10.1016/j.jmst.2019.07.024.
228. Felfel, R.M.; Ahmed, I.; Parsons, A.J.; Rudd, C.D. Bioresorbable Composite Screws Manufactured via Forging Process: Pull-out, Shear, Flexural and Degradation Characteristics. *J. Mech. Behav. Biomed. Mater.* **2013**, *18*, 108–122, doi:10.1016/j.jmbbm.2012.11.009.
229. Zan, J.; Qian, G.; Deng, F.; Zhang, J.; Zeng, Z.; Peng, S.; Shuai, C. Dilemma and Breakthrough of Biodegradable Poly-L-Lactic Acid in Bone Tissue Repair. *J. Mater. Res. Technol.* **2022**, *17*, 2369–2387, doi:10.1016/j.jmrt.2022.01.164.
230. Kawai, H.; Sukegawa, S.; Nakano, K.; Takabatake, K.; Ono, S.; Nagatsuka, H.; Furuki, Y. Biological Effects of Bioresorbable Materials in Alveolar Ridge Augmentation: Comparison of Early and Slow Resorbing Osteosynthesis Materials. *Materials (Basel)*. **2021**, *14*, doi:10.3390/ma14123286.

231. Ishizuka, S.; Dong, Q.N.; Ngo, H.X.; Bai, Y. Bioactive Regeneration Potential of the Newly Developed. **2021**.
232. Waris, E.; Konttinen, Y.T.; Ashammakhi, N.; Suuronen, R.; Santavirta, S. Bioabsorbable Fixation Devices in Trauma and Bone Surgery: Current Clinical Standing. *Expert Rev. Med. Devices* **2004**, *1*, 229–240, doi:10.1586/17434440.1.2.229.
233. Ngo, H.X.; Dong, Q.N.; Bai, Y.; Sha, J.; Ishizuka, S.; Okui, T.; Sukegawa, S.; Kanno, T. Bone Regeneration Capacity of Newly Developed Uncalcined/Unsintered Hydroxyapatite and Poly-L-Lactide-Co-Glycolide Sheet in Maxillofacial Surgery: An in Vivo Study. *Nanomaterials* **2021**, *11*, 1–22, doi:10.3390/nano11010022.
234. Aihemaiti, P.; Jiang, H.; Aiyiti, W.; Kasimu, A. Optimization of 3D Printing Parameters of Biodegradable Polylactic Acid/Hydroxyapatite Composite Bone Plates. *Int. J. Bioprinting* **2022**, *8*, 153–166, doi:10.18063/IJB.V8I1.490.
235. Fornasari, B.E.; Carta, G.; Gambarotta, G.; Raimondo, S. Natural-Based Biomaterials for Peripheral Nerve Injury Repair. *Front. Bioeng. Biotechnol.* **2020**, *8*, doi:10.3389/fbioe.2020.554257.
236. Lampe, K.J.; Namba, R.M.; Silverman, T.R.; Bjugstad, K.B. Impact of Lactic Acid on Cell Proliferation and Free Radical Induced Cell Death in Monolayer Cultures of Neural Precursor Cells. *Biotechnol. Bioeng.* **2009**, *15*, 1214–1223, doi:10.1002/bit.22352.Impact.
237. Tuan, R.S.; Chen, A.F.; Klatt, B.A. Cartilage Regeneration. *J. Am. Acad. Orthop. Surg.* **2013**, *21*, 303–311, doi:10.1142/9781848165595_0010.
238. Wu, J.; Chen, Q.; Deng, C.; Xu, B.; Zhang, Z.; Yang, Y.; Lu, T. Exquisite Design of Injectable Hydrogels in Cartilage Repair. *Theranostics* **2020**, *10*, 9843–9864, doi:10.7150/thno.46450.
239. Yu, F.; Li, M.; Yuan, Z.; Rao, F.; Fang, X.; Jiang, B.; Wen, Y.; Zhang, P. Mechanism Research on a Bioactive Resveratrol–PLA–Gelatin Porous Nano-Scaffold in Promoting the Repair of Cartilage Defect. *Int. J. Nanomedicine* **2018**, *13*, 7845–7858, doi:10.2147/IJN.S181855.
240. Du, X.; Zhao, C.; Zhang, J.; Ren, K. Study of Field-Induced Chain Conformation Transformation in Poly(L-Lactic Acid) Based Piezoelectric Film by Infrared Spectroscopy. *J. Appl. Phys.* **2016**, *120*, doi:10.1063/1.4965716.
241. Yoshida, T.; Imoto, K.; Tahara, K.; Naka, K.; Uehara, Y.; Kataoka, S.; Date, M.; Fukada, E.; Tajitsu, Y. Piezoelectricity of Poly(L-Lactic Acid) Composite Film with Stereocomplex of Poly(L-Lactide) and Poly(D-Lactide). *Jpn. J. Appl. Phys.* **2010**, *49*, doi:10.1143/JJAP.49.09MC11.
242. Ando, M.; Kawamura, H.; Kageyama, K.; Tajitsu, Y. Film Sensor Device Fabricated by a Piezoelectric Poly(L-Lactic Acid) Film. *Jpn. J. Appl. Phys.* **2012**, *51*, doi:10.1143/JJAP.51.09LD14.
243. Ning, C.; Zhou, Z.; Tan, G.; Zhu, Y.; Mao, C. Electroactive Polymers for Tissue Regeneration: Developments and Perspectives. *Prog. Polym. Sci.* **2018**, *81*, 144–162, doi:10.1016/j.progpolymsci.2018.01.001.

244. Smith, M.; Calahorra, Y.; Jing, Q.; Kar-Narayan, S. Direct Observation of Shear Piezoelectricity in Poly-L-Lactic Acid Nanowires. *APL Mater.* **2017**, *5*, doi:10.1063/1.4979547.
245. Smith, M.; Chalklen, T.; Lindackers, C.; Calahorra, Y.; Howe, C.; Tamboli, A.; Bax, D. V.; Barrett, D.J.; Cameron, R.E.; Best, S.M.; et al. Poly- l -Lactic Acid Nanotubes as Soft Piezoelectric Interfaces for Biology: Controlling Cell Attachment via Polymer Crystallinity. *ACS Appl. Bio Mater.* **2020**, *3*, 2140–2149, doi:10.1021/acsabm.0c00012.
246. Trenfield, S.J.; Awad, A.; Madla, C.M.; Hatton, G.B.; Firth, J.; Goyanes, A.; Gaisford, S.; Basit, A.W. Shaping the Future: Recent Advances of 3D Printing in Drug Delivery and Healthcare. *Expert Opin. Drug Deliv.* **2019**, *16*, 1081–1094, doi:10.1080/17425247.2019.1660318.
247. Wei, H.; Zhang, Q.; Yao, Y.; Liu, L.; Liu, Y.; Leng, J. Direct-Write Fabrication of 4D Active Shape-Changing Structures Based on a Shape Memory Polymer and Its Nanocomposite. *ACS Appl. Mater. Interfaces* **2017**, *9*, 876–883, doi:10.1021/acsami.6b12824.
248. Zhao, W.; Huang, Z.; Liu, L.; Wang, W.; Leng, J.; Liu, Y. Porous Bone Tissue Scaffold Concept Based on Shape Memory PLA/Fe₃O₄. *Compos. Sci. Technol.* **2021**, *203*, 108563, doi:10.1016/j.compscitech.2020.108563.

CHAPTER 2

Synthesis of high molecular weight stereo-diblock copolymers of PLA

CHAPTER 2

Table of contents

2.1 Introduction	71
2.2 Aims and objectives	73
2.3 Results and discussion	75
2.3.1 <i>Characterization and activity of the Initiator</i>	75
2.3.2 <i>Polymerization mechanism</i>	77
2.3.3 <i>Polymerization stereocontrol</i>	79
2.3.4 <i>Polymerization kinetics</i>	81
2.3.5 <i>Homochiral and Racemic Polymerization of Lactide</i>	83
2.3.6 <i>Stereo-Block Copolymerization by Sequential Monomer Addition</i>	84
2.4 Conclusions	87
2.5 Experimental section	89
2.5.1 <i>Materials</i>	89
2.5.2 <i>Synthesis</i>	89
2.5.2.1 <i>Synthesis of the Lig and 2,2-bis((3,5-dimethyl-pirazol-yl)-1-para-tolyloethoxide) (bpzteH)</i>	89
2.5.2.2 <i>Synthesis of the Initiator [Zn(Et)]-[2,2-bis((3,5-dimethyl-pirazol-yl)-1-para-tolyloethoxide)] (Zn(Et)(κ3-bpzteH))</i>	89
2.5.2.3 <i>Polymerizations of LA</i>	90
2.5.2.4 <i>Kinetic experiments</i>	90
2.5.3 <i>Instrumentation and measurements</i>	90
2.5.3.1 <i>¹H NMR, ¹³C NMR and homonuclear decoupled ¹H NMR</i>	90
2.5.3.2 <i>MALDI-TOF analysis</i>	91
2.5.3.3 <i>GPC analysis</i>	91
2.5.3.4 <i>Optical rotation</i>	91
2.5.4 <i>Computational methodology</i>	91
2.5.5 <i>Calculation of P_m values</i>	92
2.6 References	93

CHAPTER 2

2.1 Introduction

Previously, stereo-block-PLA derivatives have been achieved by the lengthening of building blocks on pre-polymers by a stepwise fashion [1], the extension of prepared PDLA and PLLA segments by reactive end-groups [2–4] or by solid state polycondensation [5–7]. However, limitations on the preciseness and complexity of the desired polymer architecture are the main drawbacks of the prepolymer extension synthetic approaches (asymmetric blocks, high molecular weight distributions, transesterification reactions, etc). Numerous efforts have been devoted over recent decades to the development of specific catalytic systems to promote the Ring-Opening Polymerization (ROP) of lactide (LA) attaining different tacticities under mild conditions to combine both the efficiency and polymerization control of ROP over polycondensation [8,9]. However, the slow advance of metalorganic catalysts for ROP that are able to retain the living character whilst assuring stereocontrol to avoid the common side reactions during the synthesis of HM_w polymers at mild experimental conditions has deterred the development of PLA derivatives with specific tacticities. Likewise, isotactic PLA synthesized from rac-LA by aluminium Schiff base catalytic systems has been obtained with a high stereoselectivity [10]. Furthermore, heterotactic and syndiotactic PLA were also afforded from rac- and meso-LA, respectively, by catalysts featuring specific ligand characteristics, such as bulky substituents or chiral components [8,11–13].

Numerous efforts have also been devoted to synthesize PLA stereo block copolymers (SBC) of HM_w following the one-pot sequential addition method. Particularly, the first PLA-SBC of medium molecular weight was attained in the 90 although the increase of the reaction heterogeneity was found to decrease the living character of the catalyst [14]. Besides, detrimental side reactions were later ascertained to occur during polymerizations with homoleptic catalysts due to multiple nuclearities exhibited by the catalysts, which resulted in broad molecular weight distributions and lack of stereocontrol over the polymerization [10]. PLA-SBC have also been achieved by the two-step polymerization of rac-LA combining stereo-selection and chiral ligand exchange [8], but requiring long polymerization times (up to 8h). Recently, achiral iron complexes has recently been introduced to initiate the ROP of rac-LA presenting relatively high heteroselectivity (92% isotacticity) and attaining medium molecular weight [15]. Moreover, monomeric and highly active Zn and Mg complexes have been introduced to initiate the ROP of homo-chiral lactides to synthesize by a pot sequential addition HM_w stereo-n-block copolymers in the presence of alcohol as an activator. PLA-SBC characterized with a high melting temperature (T_m) and enthalpy (ΔH_m) as well as very narrow polydispersities have been successfully synthesized by the one-pot sequential monomer addition method [16], suggesting the formation of desired SC crystals [17,18]. However, the development of novel robust catalysts able to attain HM_w PLA-SBC is still required to ascertain the mechanism of crystallization of the SC phase as well as to correlate the semicrystalline structure to its promising physicochemical properties, since previous studies exclusively

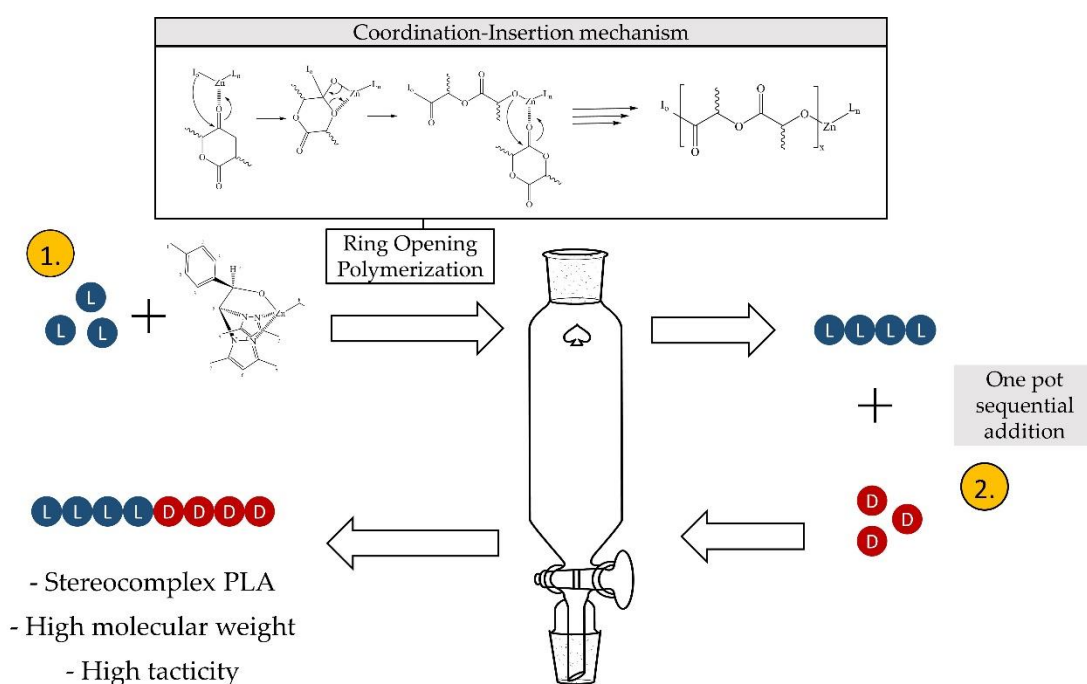
proved the presence of the SC-phase. Although, slight structural imperfections and modest chain-length distribution are tolerated when designing block polymers in benefit of the most synthetically economical approach, such as the dispensability of the activator [19].

A potential efficient metalorganic catalytic system to attain HM_w PLA-SBC by ROP should follow the coordination-insertion mechanism to avoid the termination step while maintaining a high activity for both L- and D-LA monomers during the synthesis as well as featuring a heteroleptic ligand to avoid transesterification reactions. In addition, a free-initiator catalyst will benefit the scalability of the synthesis to the industrial level since a more synthetically economical approach is achieved. Previously, a series of chiral scorpionate zinc alkyl complexes have been proved to catalyse as single-site living initiators through a truly living polymerization at mild conditions of both enantiopure L-LA and rac-LA monomers [20]. The high conversions and stereocontrol achieved during the ROP of lactide monomers assisted by the chiral scorpionate zinc alkyl complexes have encouraged us to synthesise stereodiblock-copolymers of PLA with HM_w due to their promising physicochemical properties.

2.2 Aims and objectives

The main objective of Chapter 2 is the synthesis of high molecular weight stereo-block copolymers of polylactide (HM_w PLA-SBC) by the ring-opening polymerization of lactide using a heteroscorpionate catalyst (**Scheme 2.1**). To accomplish the main objective, the following steps were followed in collaboration with the Faculty of Pharmacy, at the University of Castilla-La Mancha, in Spain:

- ✓ Synthesis and characterization of the **Initiator** [Zn(Et)(κ³-bpzteH)] (bpzteH = 2,2-bis(3,5-dimethylpyrazol-1-yl)-1-para-tolyloethoxide).
- ✓ Analysis of the **polymerization mechanism** followed by the Initiator.
- ✓ Analysis of the **polymerization kinetics** followed by the Initiator.
- ✓ Synthesis of **homo- and racemic- PLA**.
- ✓ Synthesis of **stereo-diblock PLA copolymers** attaining different molecular weight and tacticity.



Scheme 2.1. Ring-Opening polymerization of L- and D-lactide following the one-pot sequential addition method to synthesize high molecular weight stereo-diblock copolymers of polylactide. (1): The L-Lactide monomer is polymerized in solution following a coordination-insertion mechanism by the addition of the Initiator. (2): The D-lactide monomer is added to the reaction mixture when the first monomer has reached the maximum conversion and the PLA-SBC is obtained.

CHAPTER 2

2.3 Results and discussion

2.3.1 Characterization and activity of the Initiator

The bioinspiring structure of the previously synthesized Zn complexes with multifunctional ligands reproducing the active centre of the metalloproteins together with their low cost confer them as great candidates to generate feasible biocompatible polymers. The acid character of the Zn complexes enhances the polymerization of cyclic esters as facilitates the coordination of the LA monomer to the metal. Likewise, the functionalization of the scorpionate ligand to tailor the electronic environment and the steric hindrance confers stability to the metallic complex as well as directs specific molecular conformation to coordinate with other ligands. Among the scorpionate derivative zinc alkyl complexes, the Initiator $[\text{Zn}(\text{Et})(\kappa^3\text{-bpzteH})]$ (bpzteH = 2,2-bis(3,5-dimethylpyrazol-1-yl)-1-para-tolylolethoxide) (**Figure 2.1**), featuring an ethyl group as well as a scorpionate ligand with a tolyl ($p\text{-MeC}_6\text{H}_4$) substituent, was selected as a result of its potential higher activity aroused from the lower Zn-C bond, as well as the potential absence of hetero-enrichment due to the tolyl substituent [20]. The reactivity of the catalyst is crucial to one pot monomer sequential addition controlled by a living catalyst without the requirement of a co-initiator that potentially leads to detrimental chain transfer reactions [21]. However, the activity of the Initiator $[\text{Zn}(\text{Et})(\kappa^3\text{-bpzteH})]$ to ROP of LA remained undescribed in the previous work [20] as well as its mechanism of reaction.

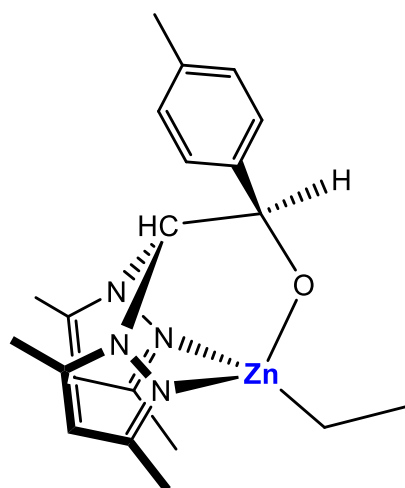


Figure 2.1. Chemical structure of the Initiator $[\text{Zn}(\text{Et})(\kappa^3\text{-bpzteH})]$.

Previously, an asymmetric dimeric conformation of the Initiator $[\text{Zn}(\text{Et})(\kappa^3\text{-bpzteH})]$ (**Figure 2.1**) featuring dinuclear complexes was found by X-ray diffraction analysis (XRD) in the solid state, whilst an equilibrium with the monomeric counterpart was not discarded in solution [20]. Furthermore, the existence of different enantiomers of Initiator was assessed by the addition of a chiral shift reagent (R)-(-)-(9-anthryl)-2,2,2-trifluoroethanol for ^1H NMR

solution experiment due to the existence of an asymmetric carbon in the ligand [20]. The presence in solution of only *meso*-enantiomer was confirmed by the appearance of only one signal for each proton. The crystalline structure manifested a tetrahedral arrangement for the metallic centre coordinated with a single pyrazol group and with a coordination κ -NN- μ -O to the ligand, whilst a distorted tetrahedral environment found for the Zn was found for a similar monomeric structure with a κ^3 -NNO coordination with the methyl group as alkyl substituent for the Zn complex [20]. The obtained ^1H NMR chemical shifts along with the crystal structure suggested a tetrahedral environment for the zinc atom with the two pyrazole rings in *cis*- and *trans*- conformation in reference to the *para*-tolyl group for the monomeric monalkyl Zn complex [20]. However, the ^1H NMR spectra is unable to ascertain the presence either the dimer or monomeric species in solution.

The synthesis of the ligand 2,2-bis((3,5-dimethyl-pirazol-yl)-1-*para*-tolylethoxide) (bpzteH) and the Initiator $[\text{Zn}(\text{Et})(\kappa^3\text{-bpzteH})]$ was accomplished following the previously published procedure [20], which is briefly described in the experimental section and its molecular structure was proved by ^1H NMR (**Figures A2.1** and **A2.2**, respectively). Moreover, the truly active species of the metal complex during polymerization and its stability with increasing temperature was analysed by variable temperature ^1H NMR (VT- ^1H NMR) of the catalyst in toluene (**Figure 2.2**) from 25 to 90 °C. Negligible multiplicity or width signal changes were observed upon heating, indicating the constant equivalence of all protons in solution. However, ethyl signals (δ 1.9 and 0.95) and *p*-tolyl methyl signal (δ 1.8) slightly shifted downfield and upfield (0.1 ppm) (**Figures 2.2** and **A2.3**), respectively, as the temperature increased, consistent with minor changes in the solvent–catalyst interactions or/and the molecular conformation of the ethyl substituent of the catalytic centre. The ^1H NMR shifts at high temperature might suggest the monomeric species at high temperature.

In addition, Density Functional Theory (DFT) theoretical calculations were performed to provide an overall interpretation of the coexistence of monomeric and dimeric forms of the Initiator. Both the dimeric and monomeric conformations of the Initiator were optimized and the energy profile of the most stable geometries in the process of rupture of the dimeric species was obtained (**Figure A2.4**). The yielded Gibbs free energy showed that the monomeric form was significantly more stable than the dimeric compound for both gas and solution (toluene) phases, affording ΔG of -5.36 and -14.51 kJ/mol, respectively, in agreement with VT- ^1H NMR analysis.

The key initiator parameters are the polymerization control and mechanism, the stereocontrol and rate [22]. Therefore, an analysis of the mechanism of reaction, tacticity and polymerization kinetics was accomplished.

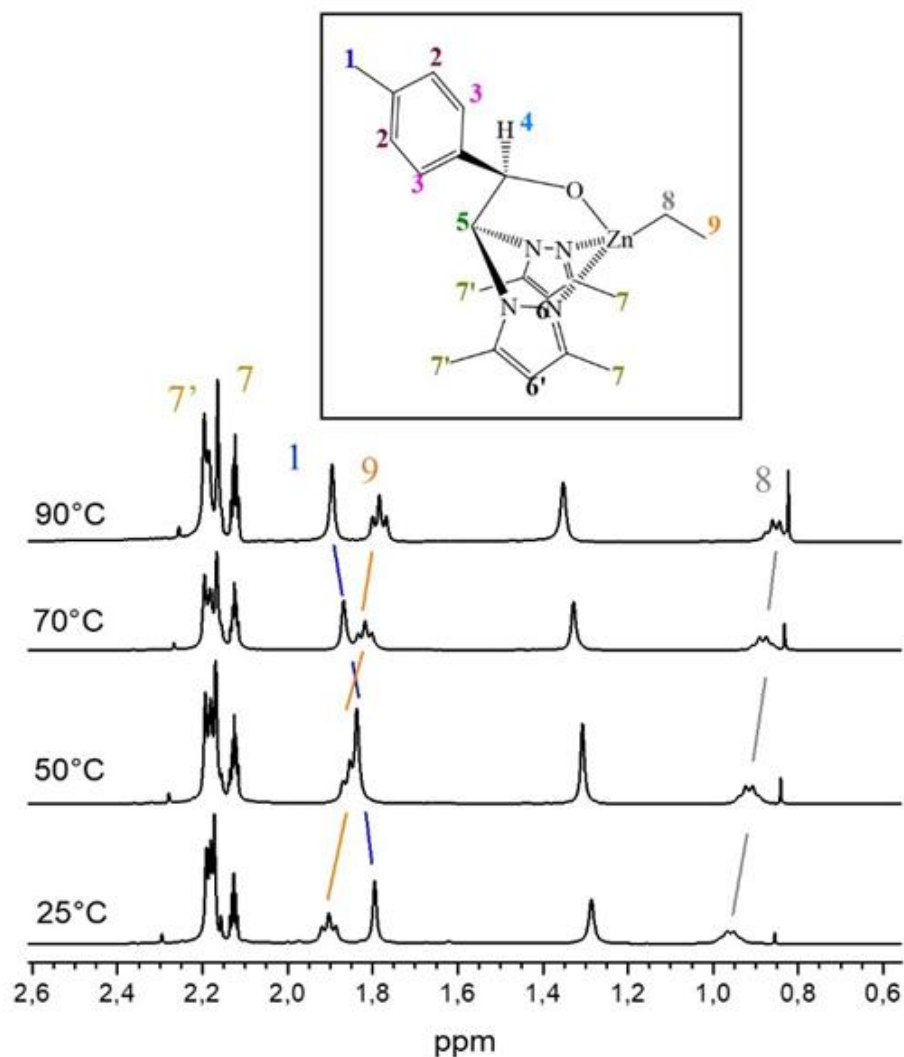


Figure 2.2. Variable temperature ^1H NMR (500 MHz, Tol-d₈, δ) spectra of the Initiator. ^1H NMR (CDCl_3 , 297 K): 1.88-1.91 (t, 3H, H₉); 1.79 (s, 3H, H₁); 0.95-0.96 (q, 2H, H₈).

2.3.2 Polymerization mechanism

The polymerization mechanism was assessed by following the ring-opening of the LA by the Initiator in a $[\text{LA}]/[\text{Zn}] = 1$ mixture, monitoring the key functional groups involved in the reaction by VT- ^1H NMR (**Figures 2.3** and **A2.5**). The coordination of the Zn atom to the carboxylic oxygen of LA and the subsequent insertion of the alkyl (Et) group formed an intermediate that was evidenced by the broadness of the ethyl signals (δ 1.9 and 0.95; blue and orange arrows) immediately after the addition of LA to the reaction mixture (δ 1.4 and 4.0–4; red box). Thereafter, the acyl–oxygen bond of LA is disrupted and the generated linear chain of LA turns into the alkoxide part of the catalyst (δ 1.2; green box), confirming the coordination–insertion mechanism.

Moreover, the degree of control exerted by an initiator is generally assessed by the fulfilment of the following criteria: linear increase of M_n with conversion, linear increase of M_n with increasing the ratio monomer/initiator, narrow PDI, the ability to undergo sequential

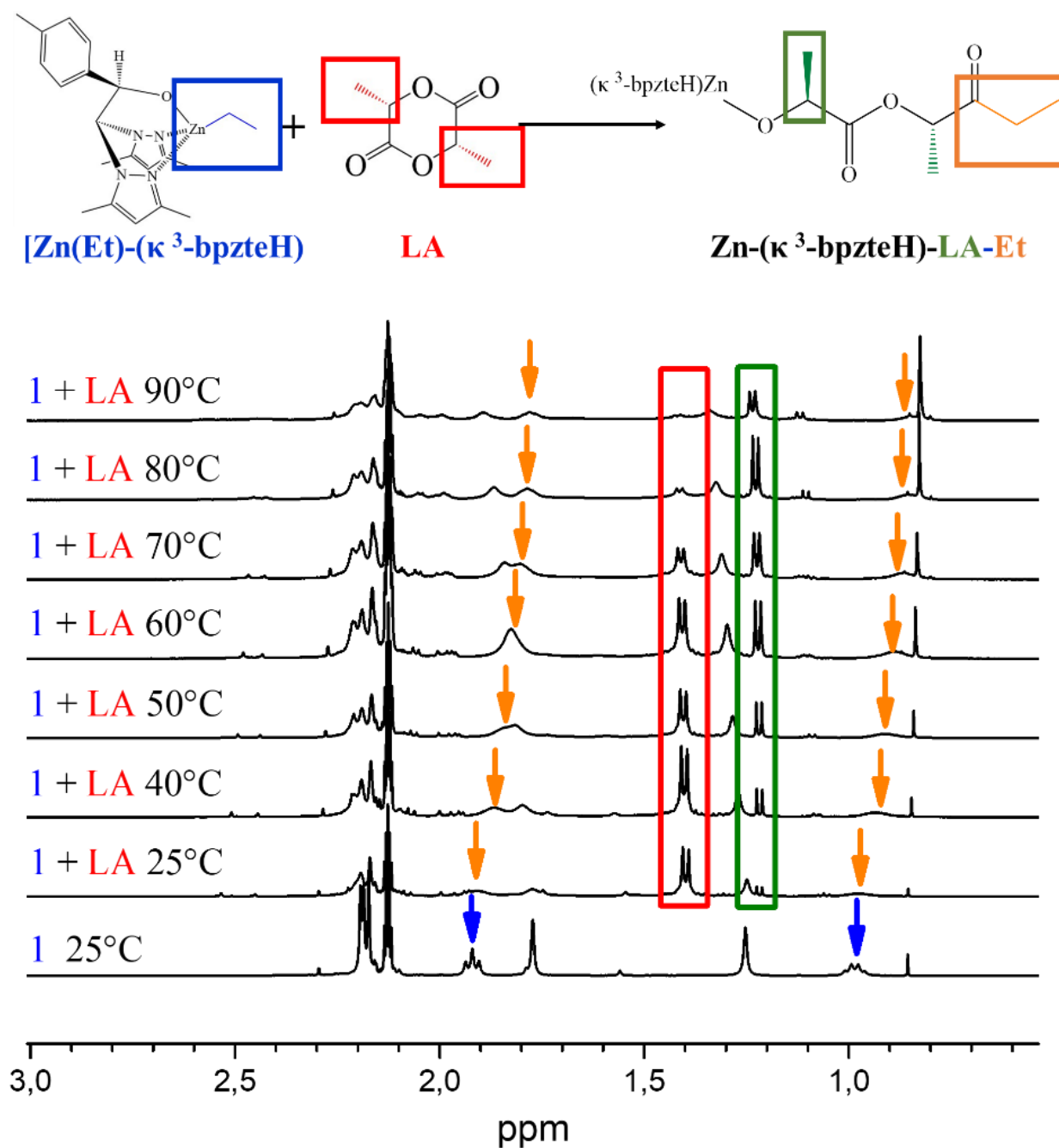


Figure 2.3. VT- ^1H NMR analysis of a $[\text{LA}]/[\text{Zn}]:1$ mixture.

monomer addition, and high $k_{\text{prop.}}/k_{\text{inic.}}$ and high $k_{\text{prop.}}/k_{\text{tr.}}$, where $k_{\text{prop.}}$ = propagation constant, $k_{\text{inic.}}$ =initiation constant and $k_{\text{tr.}}$ = transesterification constant [22]. The high level of chain control afforded by the Initiator was exemplified by the linear correlation between number average molecular weight (M_n) obtained by gel permeation chromatography (GPC) and the percentage of conversion ($R_2=0.9958$) that, along with the narrow molar mass distribution (PDI) observed, evidenced the living character of the Initiator (**Figure 2.4**). Moreover, the polymer chain architecture was evaluated by MALDI-TOF where a major population of linear polymers was found in a low weight average molecular weight (M_w) PLA derivative, with

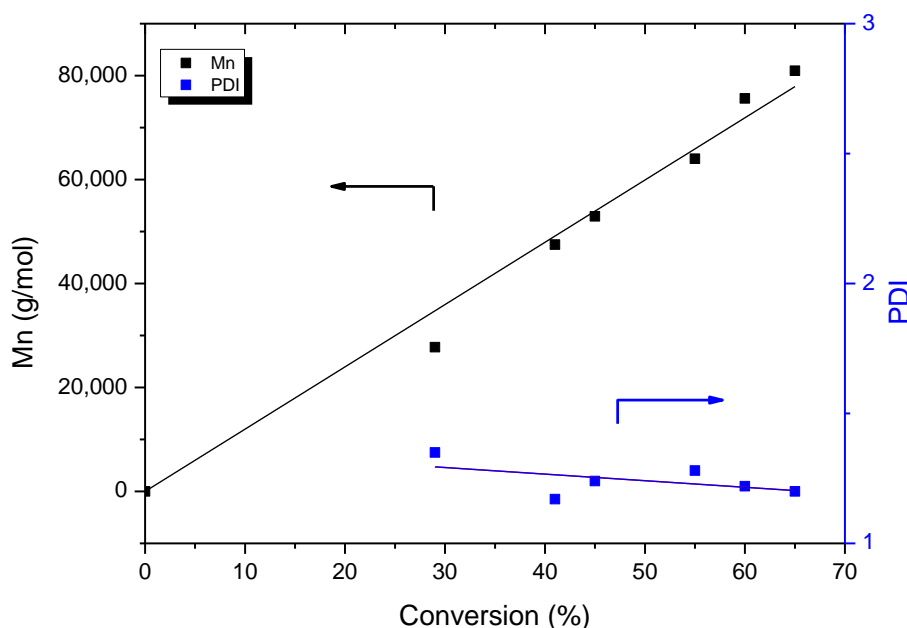


Figure 2.4. Plot of number average molecular weight (M_n) and molecular weight distribution values ($PDI=M_w/M_n$) obtained from gel permeation chromatography (GPC) as a function of monomer conversion (%). $[LA]_0/[Zn]_0 = 500$, toluene, 90 °C.

species separated by 144 Da and 72 Da (**Figure A2.6**). The formation of the shorter chain end (72Da) is generally ascribed to backbiting intramolecular transesterification reactions, although the occurrence during the sample treatment cannot be ruled out. In addition, the M_w of the chemical fragments observed by MALDI-TOF (**Figure A2.6**) revealed the existence of a single family of polymer chains capped by $-CH(CH_3)OH$ and $CH_3(CH_2)C(O)-$ termini, confirming that the ring-opening of LA occurs by the initial addition of the alkyl fragment to the LA monomer, following a nucleophilic route, with cleavage of the acyl–oxygen bond and subsequent monomer addition to the growing polymer chain. Likewise, the coordination–insertion mechanism proved by both VT- 1H NMR and MALDI-TOF analysis allows the desired chain architecture control required to obtain stereocomplex (SC)-PLA.

2.3.3 Polymerization stereocontrol

Furthermore, the stereocontrol exerted by Initiator was ascertained for the ROP of a racemic LA mixture by assessing the presence of either the hetero enrichment or random insertion by homonuclear decoupling 1H NMR of poly(rac-LA) using both Bernoullian and non-Bernoullian statistics. Likewise, the cis configuration of the relative orientation of two sequential alkyls of the diade is referred as i (“isotactic”) or m (“meso”), whilst the trans orientation is denoted as s (“syndiotactic”) or r (“racemic”). In this case, m and r notations are used. Thereby, five possible tetrad combinations are generated during the polymerization of rac-LA (**Table 2.1**). The stereocontrol achieved by a particular initiator is expressed in terms of probability to generate certain stereosequences. P_m is known as the probability of isotactic

enchainment while P_r is the probability of syndio/heterotactic enchainment [22]. Likewise, a random insertion is indicated when $P_m = 0.5$ whilst isotactic PLA is designated by $P_m = 1$, with the total probability expressed as $P_m + P_r = 1$ [30]. Stereocontrolled polymerization can be mediated by two distinct mechanisms, namely, chain-end control (CEC) and enantiomorphic site control (ESC). In the former case, the control of the chirality is known to be associated with the propagating chain end in which the transition state of the next monomer insertion defines the chirality of the next monomer unit to be incorporated into the growing

Table 2.1. Tetrad probabilities of ESC and CEC mechanisms based on non-Bernoullian and Bernoullian statistics.

Tetrad	Probability of ESC (non-Bernoullian)	Probability of CEC (Bernoullian)
mmm	$[P_m^2 + (1 - P_m)^2 + P_m^3 + (1 - P_m)^3]/2$	$P_m^2 + 0.5P_mP_r$
mmr	$[P_m^2(1 - P_m) + P_m(1 - P_m)^2]/2$	$0.5P_mP_r$
mmm	$[P_m^2(1 - P_m) + P_m(1 - P_m)^2]/2$	$0.5P_mP_r$
rmr	$[[P_m^2(1 - P_m) + P_m(1 - P_m)^2]/2]$	$0.5P_mP_r$
mrmm	$[P_m(1 - P_m)]$	$0.5(P_m^2 + P_mP_r)$

[rmr]= -LDDL- or -DLLD-

[rmm]= -LDDD- or -DLLL-

[mmr]= -LLLD- or -DDDL-

[mmm]= -LLLL- or -DDDD-

[mrm]= -LLDD- or -DDLL-

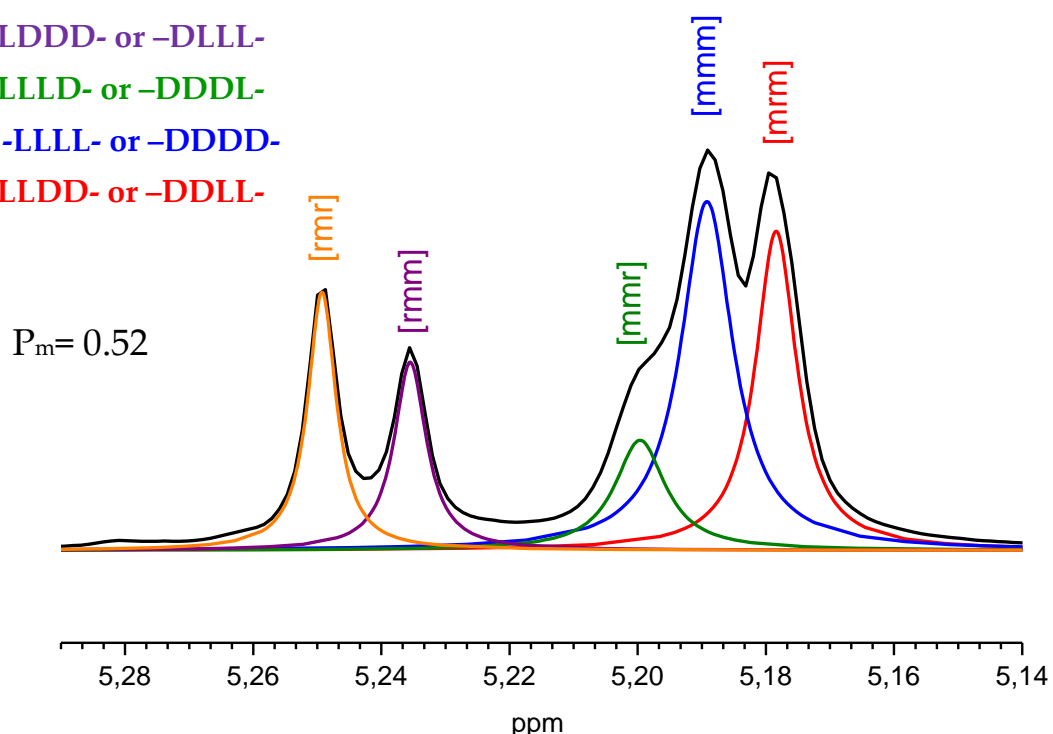


Figure 2.5. ^1H NMR spectra (500 MHz, 298 K, CDCl_3) of the homodecoupled CH resonance of poly(rac-lactide). r and m are the trans- and cis- configuration of the relative orientation of two sequential alkyls of the diade. [rmr] represents the probability of finding a sequence with the following stereochemistry -LDDL- or -DLLD-; [rmm]= -LDDD- or -DLLL-; [mmr]= -LLLD- or -DDDL-; [mmm]= -LLLL- or -DDDD- ; [mrm]= -LLDD- or -DDLL-.

chain. In contrast, for polymerizations mediated through an ESC mechanism, the chirality of the catalyst determines the chirality of the next monomer unit [30]. However, stereocontrol in the ROP of PLA is commonly achieved by CEC even when the initiator contains a chiral component. The deconvolution of the homodecoupled methine resonance of poly(rac-LA) derivative (Table A2.1, entry 14) revealed five signals in methine region (Figure 2.5), which were assigned to the five tetrads obtained from rac-LA polymerization [23] and were analysed by Bernoullian and non-Bernoullian statistics based on both CEC and ESC mechanism, respectively (Table A2.2). However, the probabilities calculated using non-Bernoullian statistics remained unresolved indicating that the stereocontrol exerted by Initiator follows a CEC mechanism. Likewise, the P_m obtained by CEC for poly (rac-LA) was 0.52, in agreement with a completely atactic polymer. The homodecoupled methine resonance employing a CEC mechanism was applied to the afforded PLA derivatives to elucidate the tacticity values.

2.3.4 Polymerization kinetics

Polymerization rate constants were determined by solution kinetic studies of a $[LA]_0/[Zn]_0=400$ polymerization at three different temperatures: 90, 75 and 60 °C. The order of reaction was calculated by plotting the $\ln([LA]_0/[LA]_t)$ versus reaction time where $[LA]_0$ is the initial LA monomer concentration and $[LA]_t$ is the LA concentration at a given time t (Figure 2.6A). The polymerization rate increased with increasing temperature, typical of Arrhenius systems (Table 2.2), with apparent rate propagation constants (k_{app}) of the polymerization

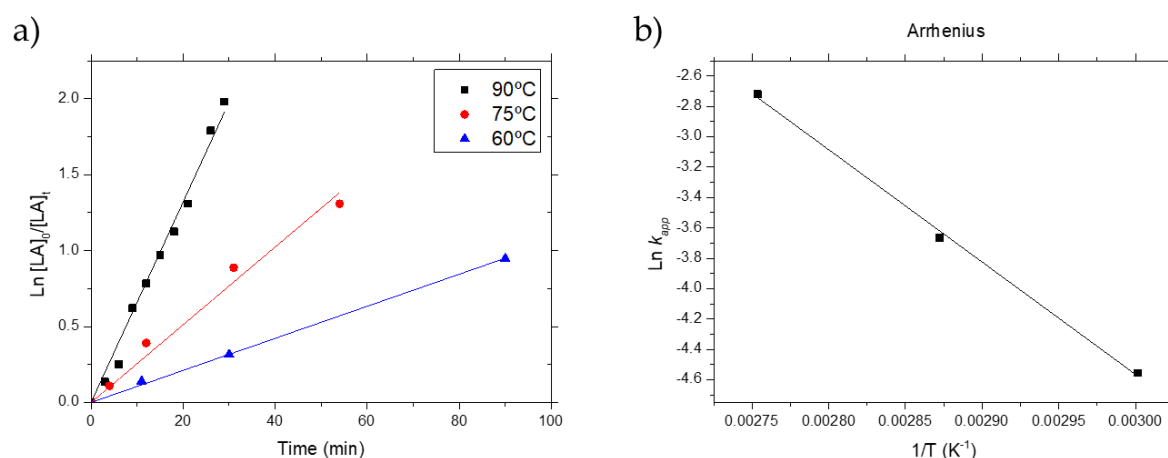


Figure 2.6. a) First-order kinetic plots of L-LA polymerization in toluene at different temperatures. $[LA]_0/[Zn]_0=400$; $[LA]_0= 400$ mM; $[Zn]_0= 1$ mM. b) Plot of $\ln k_{app}$ versus T^{-1} for Initiator in toluene with $[LA]_0/[Zn]_0=400$; $[LA]_0= 400$ mM; $[Zn]_0= 1$ mM.

conducted in toluene one order higher than the k_{app} values found for polymerizations carried out in THF with the same family of initiators [20]. In addition, identical order of magnitude of k_{app} was found for polymerization previously performed in dichloromethane with other Zn-initiators [23]. The linearity of the plots corresponds to a first-order dependence with respect

to the LA monomer, evidencing that termination reactions did not occur during polymerization. From the k_{app} values determined at different temperatures, the activation energy (E_a) of the polymerization was deduced by fitting the $\ln k_{app}$ versus T^{-1} (**Figure 2.6b**) according to the Arrhenius equation (**Equation 2.1**):

$$\ln k_{app} = -\frac{E_a}{R} \left(\frac{1}{T}\right) - \ln A \quad (\text{Eq. 2.1})$$

where k_{app} is the apparent rate propagation constant (10^2 s^{-1}), E_a the activation energy (J mol^{-1}), R the gas constant ($R=8.314 \text{ J mol}^{-1} \text{ K}^{-1}$), T the temperature (K) and A the Arrhenius constant. The E_a for the LA polymerization obtained, $61.57 \text{ kJ mol}^{-1}$, was higher than the E_a data for organoaluminium initiators ($\sim 6.5 \text{ kJ mol}^{-1}$) [24], which explains the slower polymerization kinetics observed.

Table 2.2. Rate constants. ^a $[\text{LA}]_0/[\text{Zn}]_0=400$; $[\text{LA}]_0= 400 \text{ mM}$; $[\text{Zn}]_0= 1\text{mM}$. ^b $[\text{LA}]_0/[\text{Zn}]_0=500$; ^b $[\text{LA}]_0= 625 \text{ mM}$; $[\text{Zn}]_0=1.25\text{mM}$

Entry	Sample	T (°C)	$k_{app} \times 10^2 (\text{s}^{-1})$
1	^a PLLA400	90	$6,59 \pm 0,002$
2	^a PLLA400	75	$2,56 \pm 0,002$
3	^a PLLA400	60	$1,05 \pm 0,0002$
4	^b PLLA500	90	$5,61 \pm 0,003$
5	^b PDLA500	90	$4,71 \pm 0,001$

Moreover, the polymerization rate constant of both homopolymers, PLLA and PDLA (**Table 2.2**, entries 4 and 5), were compared to confirm the absence of hetero-enrichment yielded by the heteroscorpionate complexes counterparts previously described [20], which would be evidenced by a significant higher rate constant for one of the enantiomers. Generally, a catalyst featuring a chiral carbon will invariably result in stereocontrol of polymerization exerted by an ESC mechanism. However, the CEC mechanism becomes predominant in polymerizations using a chiral catalyst under harsh reaction conditions (i.e. high temperature and monomer concentration). In addition, a slight difference in the activation energy barrier between L- and D-LA monomers to form the coordinated complex catalyst–monomer might influence certain kinetic parameters when the polymerization approaches equilibrium, such as the monomer concentration at equilibrium that potentially would control the stereochemistry of the generated polymer. Likewise, L- and D-LA monomer conversions during two independent homopolymer reactions were monitored by ¹H NMR, following the decrease in monomer concentration of both enantiomers during the PLA polymerizations.

The modelled polymerization kinetics manifested a slightly higher rate for L-LA polymerization over the D-LA (**Table 2.2**, entries 4 and 5) with a difference in monomer conversion of 10% after 45 min of reaction (85 and 95% for D- and L-LA, respectively). The similar polymerization rate constants for both D- and L-LA enantiomers obtained from

kinetics experiments exhibited that the Initiator is a potential catalyst for the synthesis of HM_w PLA stereo-diblock copolymers.

2.3.5 Homochiral and Racemic Polymerization of Lactide

The ROP reaction conditions (time, temperature, and solvent) were optimized (**Table 2.3** and **Table A2.1**, Entries 6–14) from previously generated conditions to attain HM_w PLA-derivatives [20]. Mild reaction conditions at low [LA]/[cat] with 100 eq. of L-LA in THF at 50 °C prevented the onset of the polymerization even after 2 h of reaction (**Table 2.3**, Entry 1). The solvent exchange by a lower polarity solvent as toluene increased the conversion only to 5%. Only under more extreme conditions was the Initiator able to promote the polymerization, converting 43 and 94% of monomer, in 1 h at 70 and 90 °C, respectively (**Table 2.3**, Entries 3–4). HM_w polymers obtained with monomer conversions of 94% were obtained after reaction with 500 eq. of L-LA at 70 and 90 °C, in 120 and 45 min, respectively (**Table 2.3**, Entries 5 and 7). Moreover, monomer conversions higher than 85% were achieved for D- and rac-LA in 2 h (**Table 2.3**, Entries 8–9).

Table 2.3. Polymerizations of L-, D- and rac-LA

Entry	Sample	[LA]/[cat]	Temperature (°C)	Time (min)	Conv. (%)	M _n (theor.) (Da) ^a	M _n (exp.) (Da) ^b	PDI	[α] ^c
1	PLLA100	100	50	120	0	0	-	-	
2	PLLA100	100	50	120	5	720	-	-	
3	PLLA100 (L1)	100	70	60	43	6.192	12.824	1,36	-159,4
4	PLLA100 (L2)	100	90	60	94	13.536	30.055	1,62	-171,4
5	PLLA500 (L3)	500	90	45	94	67.680	62.564	1,84	-172,2
6	PLLA500 (L4)	500	70	90	76	54.720	42.880	1,7	-162,7
7	PLLA500 (L5)	500	70	120	94	67.680	48.253	2,19	-168,4
8	PDLA500 (D1)	500	70	90	85	61.200	41.292	1,78	154
9	rac-PLA600 (Rac1)	600	70	120	90	64.800	40.754	1,59	-1,1

Polymerization conditions: 25 μmol of Initiator **1**, toluene as solvent except entry 1, 5 and 20 mL of solvent for [LA]/[cat]=100 and 500, respectively. ^aTheoretical M_n = (monomer/Initiator **1**) × (% conversion) × (M_w of LA). ^bDetermined by GPC relative to polystyrene standards in chloroform. ^cSpecific optical rotation. ([α]_{PLLA=173°}) [25].

The obtained molecular weights were in good agreement with the calculated values as the LA/Initiator ratio increased, confirming the living character of the polymerization as well as the single-site catalyst mechanism, apart from polymerizations at ratio [LA]/[cat] = 100 (L1 and L2), which are likely related to a high $k_{prop.}/k_{inic.}$ ratio. However, PLA-homopolymers L4 and D1 present similar M_n value whilst different conversions, which might be ascribed to an error in the conversion due to the heterogeneity of the reaction mixture ascribed to the high viscosity. Molecular weight distributions (PDI) obtained by GPC were found to be narrow, although slightly increased for HM_w PLA derivatives due to both the steric hindrance and viscosity rise in the reaction mixture. Furthermore, polymerization of L-LA and D-LA yielded stereochemically pure PLA (**Figures A2.7-A2.13**) indicating that epimerization of either the monomer or the polymeric derivative was absent under the polymerization conditions.

Likewise, the specific optical rotation (α) was evaluated from polarimetry measurements to corroborate the reaction stereocontrol (**Table 2.3**). The chiral purity may be estimated higher than 95% for all enantiopure derivatives (**Table 2.3**, Entries 1-8) based on calculations from the reported value of (α) = -173° at 598 nm for PLLA featuring perfect optical purity [25]. The specific optical rotation of poly(rac-LA) (**Table 2.3**, Entry 9) was close to 0°, in agreement with the previous P_m analysis by deconvolution of the homonuclear decoupled ^1H NMR spectrum.

2.3.6 Stereo-Block Copolymerization by Sequential Monomer Addition

Stereo-diblock PLA co-polymers exhibiting different M_w and tacticities were obtained by the one-pot sequential addition method (**Table 2.4** and **Figures A2.15-A2.36**), which consist on the addition of the second monomer to the reaction when the conversion of the first one has reached a certain percentage. The names of the PLA-SBC (**Table 2.4**) present the following structure: X123-Y123, were X and Y denote D and L, depending on the lactide chirality and 123 represent the length of the block measured in lactide units (also the monomer/catalyst ratio). The M_w was controlled by the monomer/catalyst ratio and the tacticity was controlled by changing the time at which the second monomer was added to the reaction, although the different between the experimental and theoretical M_n increase as the $[\text{LA}]/[\text{cat}]$ ratio increases probably due to the increase of the reaction mixture viscosity. The ^1H NMR monitored monomer consumption revealed conversions higher than 80% for both block sequences, which was in good agreement with the M_w determined by GPC. Likewise, the kinetic experiments of the addition of the second monomer yielded an equivalent k_{app} $6.2 \pm 0.002 \text{ s}^{-1}$ (**Figure A2.14**) with a first order of reaction, confirming the living character of polymerization upon the growth of the second block.

Table 2.4. Stereo-block copolymerizations of L-LA and D-LA.

Entry	Sample	[LA]/[cat]	Solvent	Temperature (°C)	Time (min) ^a	Conversion (%)	$M_n(\text{theor.})$ (Da) ^b	$M_w(\text{exp})$ (Da) ^c	$M_n(\text{exp.})$ (Da) ^c	PDI ^d	$[\alpha]^e$	P_m^f
1	(L115:D115)	250	Toluene	90	50	95	34.299	32.823	17.007	1,93	-2,47	0,96
2	(L220:D220)	500	Toluene	90	90	90	64.800	63.313	28.779	2,20	-5,09	0,88
3	(L250:D250)	600	Toluene	75	120	81	58.320	72.508	32.958	2,20	-2,67	0,92
4	(L275:D275)	600	Toluene	90	60	95	82.080	79.320	35.253	2,25	-1,07	0,9
5	(D275:L275)	600	Toluene	90	60	94	81.216	79.107	33.238	2,38	1,41	0,81
6	(L330:D330)	700	Toluene	90	60	84	72.576	94.181	44.636	2,11	-1,93	0,69
7	(L375:D375)	800	Toluene	90	100	97	97.776	107.912	63.853	1,69	-0,69	0,95
8	(L500:D500)	1100	Toluene	90	110	89	102.528	139.517	53.660	2,60	0,32	0,94
9	(L520:D520)	1200	Toluene	90	120	85	146.880	150.094	64.976	2,31	-1,65	0,92
10	(L1200:D300)	1600	Toluene	90	95	90	194.400	202.280	99.257	2,04	-87,7	0,93

Polymerization conditions: 25 μmol of Initiator, toluene as a solvent at 90°C. ^a30-60 min was maintained between each monomer addition, depending on the monomer loading. ^bTheoretical M_n = (monomer/Initiator 1) \times (% conversion) \times (M_w of LA). ^cDetermined by GPC relative to polystyrene standards in chloroform. ^dMolar mass distribution = M_w/M_n . ^eSpecific optical rotation ($[\alpha]_{\text{PLLA}} = -173^\circ$) [25] ^fProbability of finding dyads calculated from homonuclear decoupling ^1H NMR spectra after deconvolution; calculations are based on CEC statistics..

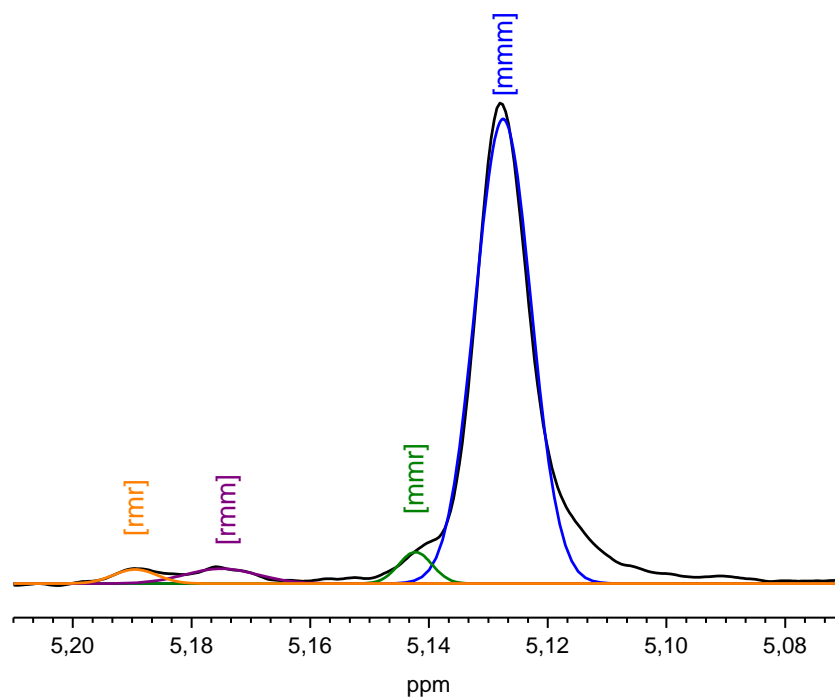


Figure 2.7. ^1H NMR spectra (500 MHz, 298 K, CDCl_3) of the homodecoupled CH resonance of stereodiblock copolymer 100L-b-100D (entry 2, Table 3).

Furthermore, the specific optical rotation (α) measured close to 0° for all samples, evidenced an L-LA/D-LA ratio of nearly one. The stereocontrol for the stereo-diblock copolymer formation was assessed by determining the tacticity of the copolymers obtained from deconvoluted homonuclear decoupled ^1H NMR spectra using Bernoullian statistics. The deconvoluted methine spectral regions of the homonuclear decoupled ^1H NMR spectrum of L375:D375 stereo-diblock co-polymer (**Figure 2.7** as a representative example) were assigned to the appropriate tetrads following previous reports [37], and a Bernoullian statistical model was applied to the deconvoluted spectra. The obtained P_m values for the series of stereo-diblock copolymers (**Table 2.2**, Entries 1-4 and 7-9) confirmed the high stereocontrol achieved in the ROP for both blocks (>0.88), evidencing the almost full consumption of the two LA enantiomers as well as the isotactic stereo-diblock microstructure nature of the polymeric derivatives. Moreover, the P_m value of two stereo-diblock copolymers (**Table 2.2**, Entries 5-6) was lower than 0.81 due to the addition of the second monomer before the total consumption of the first one, increasing the number of stereoerrors in the second block, hence decreasing its tacticity. Finally, an ultra-high molecular weight asymmetric block copolymer was synthesized (**Table 2.2**, Entry 10) by increasing the L-LA/D-LA ratio to 6. The high tacticity of the asymmetric block copolymer was confirmed by the P_m value obtained of 0,93 and the specific optical rotation measurement confirmed the presence of 80% and 20% of L-LA and D-LA, respectively.

CHAPTER 2

2.4 Conclusions

PLA stereocomplexation has typically been achieved by the blend of the PLA enantiomers with detrimental phase separation at high molecular weight that diminishes the promising physicochemical properties featured by the SC phase. In Chapter 2, the synthesis of high molecular weight stereo-diblock copolymers of PLA that might potentially fully crystallize in the SC phase has successfully been achieved.

- ✓ The first organometallic Initiator able to generate high molecular weight stereo-diblock copolymers of PLA without the use of a co-initiator has been reported.
- ✓ The Initiator follows a **coordination-insertion** polymerization mechanism.
- ✓ Kinetic experiments confirm the **living character** of the initiator, the **first-order reaction** and similar rate constant of the polymerization for each block.
- ✓ The reaction conditions have been optimized to attain homo-, racemic- and **stereocomplex-PLA** exhibiting **high molecular weight** and relatively **narrow PDI**.
- ✓ The PLA-derivatives tacticities and specific optical rotations values confirmed the fine **stereocontrol** achieved and minimal transesterification reactions on both symmetric and asymmetric PLA-SBC.

In Chapter 3, the characterization of the crystallization mechanism of the PLA stereo-diblock copolymers will be accomplished.

2.5 Experimental section

2.5.1 Materials

Solvents and reagents were commercially acquirable from Sigma-Aldrich (St. Louis, MO, USA) apart from L-lactide (L-LA) and D-lactide (D-LA) monomers that were purchased from Rex scientific. The lactide monomers were purified three times by sublimation and then stored in a glovebox at 4 °C. Toluene and tetrahydrofuran (THF) were pre-dried over sodium wire as well as distilled under nitrogen from sodium and subsequently stored over molecular sieves (3Å) in a glovebox.

2.5.2 Synthesis

All the synthetic manipulations were performed under nitrogen, using standard Schlenk techniques.

The synthesis of the Initiator followed the previously published procedure [24].

2.5.2.1 Synthesis of the Ligand *2,2-bis((3,5-dimethyl-pirazol-yl)-1-para-tolylethoxide) (bpzteH)*

The ligand (bpzteH) was synthesized via the following procedure: In a 250 mL Schlenk tube, Bis 3,5-(dimethyl-pirazol-yl)-methylene (bpm) (3 g, 14.7 mmol) was dissolved in dry THF (70 mL) and then cooled to -78°C. A 2.5 M solution of Bu_nLi (6.47 mL, 16.17 mmol) in hexane was added to the bpm solution and stirred for 1h. The resulting mixture was added dropwise to a cooled (-10°C) solution of p-tolyl (1.86 g, 15.43 mmol). The reaction mixture was allowed to warm up to ambient temperature and was stirred for 1h. The obtained product was hydrolyzed with saturated aqueous NH₄Cl (15 mL). The organic layer was extracted, dried over MgSO₄, filtered, and the solvent was removed in vacuum to yield the product as a yellow oil, which was titrated with hexane to afford the pure product as a yellow solid (1.54 g, 75%). ¹H NMR (500 MHz, CDCl₃, 297 K): δ 7.25-7.23 (d, 2H, H3), 6.91-6.88 (d, 2H, H2), 6.28-6.26 (d, 1H, H6), 5.90-5.89 (d, 1H, H6), 5.59 (s, 1H, H4), 5.44 (d, 1H, H5), 2.14-1.55 (m, 12H, H7), 1.44 (s, 3H, H1).

2.5.2.2 Synthesis of the Initiator [Zn(Et)]-[2,2-bis((3,5-dimethyl-pirazol-yl)-1-para-tolylethoxide)] (Zn(Et)(κ³-bpzteH)

The catalyst (Zn(Et)(κ³-bpzteH) was synthesized by the following procedure: The ligand (bpzteH) was dissolved in dry toluene and Zn(Et)₂ was added through a cannula to the solution placed on ice-bath (0°C). The resulted solution was stirred for 2h at room temperature and the solvent was removed in vacuum. Yield : 1,54g, 75%. ¹H NMR (500 MHz, CDCl₃, 297 K): δ 6.97-6.95 (d, 2H, H3), 6.89-6.87 (d, 2H, H2), 5.90-5.88 (d, 2H, H6), 5.68 (d, H, H4), 5.41 (d, 1H, H5), 2.34-2.24 (s, 12H, H7), 1.52 (s, 3H, H1), 1.40-1.36 (t, 3H, H9), 0.45-0.39 (q, 2H, H8).

2.5.2.3 Polymerizations of LA

Ring-opening polymerizations (ROP) were performed on a Schlenk line in a dried Schlenk flask equipped with a magnetic stirrer. The Schlenk tubes were loaded in the glovebox with the required amount of LA and Initiator 1, separately, and dissolved in the appropriate amount of solvent (**Table A2.1**). Both LA and initiator Schlenk flasks were attached to the vacuum line and temperature equilibrium was ensured by stirring the solutions for 15 min in an oil bath. Monomer and catalyst solutions were poured together by a glass bent adaptor and polymerization onset times were measured from that point. Stereo-diblock copolymerizations were achieved by the addition of the second monomer upon the first monomer high conversion that was probed by monitoring reaction aliquots by ^1H NMR. Methanol was used to terminate the reaction and precipitate out the polymer synthesized. The obtained polymer was collected by filtration, dried at room temperature, exposed to vacuum over 24 h in the Schlenk line, and stored upon characterization. The polymer derivatives experimental details and their respective characterization is detailed in the Appendix 2 (Figures **A2.7-A2.13** for homopolymers and **A2.15-A2.38** for PLA-SBC). Moreover, the names of the PLA-SBC present the following structure: X123-Y123, where X and Y are D and L, depending on the lactide chirality and 123 is the length of the block measured in lactide units.

2.5.2.4 Kinetic experiments

Reaction kinetic studies were conducted on the polymerizations of PLLA400 ($[\text{LA}]_0/[\text{Zn}]_0 = 400$; $[\text{LA}]_0 = 400$ mM; $[\text{Zn}]_0 = 1$ mM) at 90, 75 and 60 $^\circ\text{C}$, PLLA and PDLA500 ($[\text{LA}]_0/[\text{Zn}]_0 = 500$; $[\text{LA}]_0 = 625$ mM; $[\text{Zn}]_0 = 1.25$ mM) at 90 $^\circ\text{C}$, as well as L200:D200 ($[\text{LA}]_0/[\text{Zn}]_0 = 400$; $[\text{LA}]_0 = 400$ mM; $[\text{Zn}]_0 = 1$ mM) at 90 $^\circ\text{C}$, to establish the reaction constant rate of each homopolymer enantiomer (Table S1, entries 1–6). The polymerization procedure was followed as previously described and aliquots were collected using a glass pipette at appropriate time intervals. All the volatiles in the aliquots were removed, and the residue was subjected to monomer conversion determination that was monitored by integration of methine resonances and its subsequent monomer against polymer ratio calculation in ^1H NMR (CDCl_3).

2.5.3 Instrumentation and measurements

2.5.3.1 ^1H NMR, ^{13}C NMR and homonuclear decoupled ^1H NMR

Spectra were recorded at room temperature on a Varian Inova FT-400/500 spectrometer and referenced to the standard in the deuterated solvent with the relaxation time fixed to 4 s. The polymeric derivatives were dissolved in CDCl_3 for the synthetic characterization as well as homonuclear decoupled ^1H NMR and Toluene- d_8 for variable temperature ^1H NMR, respectively.

Homonuclear decoupled ^1H NMR spectroscopic analysis was conducted by applying the decoupling into the methyl region ($\delta = 1.5$). The global spectrum deconvolution technique was performed when the multiplicity of the proton associated with the CH group of the

polymer backbone corresponded to the tetrad signal ($\delta = 5.00\text{--}5.20$), using both non-Bernoullian and Bernoullian statistics, further experimental calculations in Supplementary Information.

2.5.3.2 MALDI-TOF analysis

Matrix-assisted laser desorption/ionization-time of flight (MALDI-TOF) spectra were acquired using a Bruker Autoflex II TOF/TOF spectrometer using dithranol (1,8,9-trihydroxyanthracene) and NaI as the matrix and the cationisation reagent, respectively. Samples co-crystallised with the matrix mixture in a ratio 100:1 on the probe were ionized in the positive reflector mode. External calibration was performed by using Peptide Calibration Standard II (covered mass range: 700–3200 Da) and Protein Calibration Standard I (covered mass range: 5000–17,500 Da).

2.5.3.3 GPC analysis

Molecular weight (M_n , M_w), as well as polydispersity index (PDI) of the afforded polymer derivatives, were determined from Gel permeation chromatography (GPC) using chloroform as eluent. The molecular weight characterization was performed with a Shimadzu Prominence-I LC-2030 equipped with a Shodex GPC KF-805L column (Shodex, Tokyo, Japan) and a Shimadzu RID-20A detector (Shimadzu, Kyoto, Japan). Analytical grade CHCl_3 was used as the mobile phase at 40 °C, with a flow rate of 1 mL/min. GPC samples were prepared by dissolving ca. 5 mg of the corresponding polymer in 1.5 mL of solvent and left overnight under constant agitation. Thereafter, the samples were filtered over a 0.2 μm polytetrafluoroethylene (PTFE) syringe filter prior to its injection. Polystyrene with a molecular weight of 172 kDa was used as a reference to determine the overall molecular weight of the samples.

2.5.3.4 Optical rotation

The specific optical rotation (α) was measured in dichloromethane (DCM) at a concentration of 1mg/mL and 25 °C by a JASCO P-2000 WI using a beam wavelength of 589 nm.

2.5.4 Computational methodology

Computational Simulations were conducted by using Gaussian09 (Rev. C.01) software package (Gaussian 09). The theoretical calculations employed a hybrid density functional B3LYP method to minimise the geometries of all species involved. 6-31G (d) basic set was used to represent all atoms except Zinc (Zn). For Zn, LANL2DZ has successfully been applied to describe the geometry of complexes [26,27]. Besides, the solvent (toluene) was simulated using the Polarizable Continuum Model (PCM) methodology implemented in Gaussian09 package [28]. The initial estimations for the different intermediates were generated from the crystallographic structures of the dimer. Geometry at the selected level of theory was

optimized for dimer structure, and then monomeric species were generated from them. Subsequently, an initial conformation analysis was carried out for all species to obtain the lowest energy conformation. The nature of the stationary points was assessed using the normal vibration frequencies calculated from the analytical second derivatives of the energy. The first-order saddle points –which are related to transition states– must show an imaginary value for the frequency associated with the eigenvector primarily describing the product formation step, whereas the real minima of the potential energy hypersurface –which are related to stable species– have to show positive real values for all the vibrational frequencies. Gibbs free energies used were obtained as the sum of electronic and thermal free energy at 298.15 K

2.5.5 Calculation of P_m values

Homodecoupled ^1H NMR spectra were obtained for racemic and stereo-diblock copolymers of PLA.

The methane region was deconvoluted and the curves were integrated using Origin software. The five tetrad dyads of the racemic spectrum were assigned according to literature [23] and probability of each dyad was obtained after normalizing by the total area. Both, Bernoullian and non-Bernoullian statistics based on chain-end control mechanism (CEC) and enantiomorphic site control mechanism (ESC), respectively, were applied. For CEC mechanism, P_r was firstly obtained from

$$[rmr] = 0.5 P_r^2 \quad (1)$$

to finally calculate P_m from

$$[mmm] = P_m^2 + 0.5 P_m P_r \quad (2)$$

For ESC mechanism, P_m was directly obtained from

$$[mmm] = [P_m^2 + (1-P_m)^2 + P_m^3 + (1 - P_m)^3]/2 \quad (3)$$

Since the probabilities calculated using non-Bernoullian statistics remained unresolved, Bernoullian statistic was applied to the afforded stereo-diblock copolymers for calculation of P_m .

2.6 References

1. Hirata, M.; Kobayashi, K.; Kimura, Y. Synthesis and Properties of High-Molecular-Weight Stereo Di-Block Polylactides with Nonequivalent D/L Ratios. *J. Polym. Sci. Part A Polym. Chem.* **2010**, *48*, 794–801, doi:10.1002/pola.23827.
2. Ma, Y.; Li, W.; Li, L.; Fan, Z.; Li, S. Stereocomplexed Three-Arm PPO-PDLA-PLLA Copolymers: Synthesis via an End-Functionalized Initiator. *Eur. Polym. J.* **2014**, *55*, 27–34, doi:10.1016/j.eurpolymj.2014.03.018.
3. Masutani, K.; Lee, C.W.; Kimura, Y. Synthesis and Thermomechanical Properties of Stereo Triblock Poly lactides with Nonequivalent Block Compositions. *Macromol. Chem. Phys.* **2012**, *213*, 695–704, doi:10.1002/macp.201100683.
4. Masutani, K.; Lee, C.W.; Kimura, Y. Synthesis and Properties of Stereo Di- and Tri-Block Poly lactides of Different Block Compositions by Terminal Diels-Alder Coupling of Poly-L-Lactide and Poly-D-Lactide Prepolymers. *Polym. J.* **2013**, *45*, 427–435, doi:10.1038/pj.2012.161.
5. Fukushima, K.; Kimura, Y. An Efficient Solid-State Polycondensation Method for Synthesizing Stereocomplexed Poly(Lactic Acid)s with High Molecular Weight. *J. Polym. Sci. Part A Polym. Chem.* **2008**, *46*, 3714–3722, doi:10.1002/pola.22712.
6. Fukushima, K.; Kimura, Y. A Novel Synthetic Approach to Stereo-Block Poly(Lactic Acid). *Macromol. Symp.* **2005**, *224*, 133–144, doi:10.1002/masy.200550612.
7. Fukushima, K.; Furuhashi, Y.; Sogo, K.; Miura, S.; Kimura, Y. Stereoblock Poly(Lactic Acid): Synthesis via Solid-State Polycondensation of a Stereocomplexed Mixture of Poly(L-Lactic Acid) and Poly(D-Lactic Acid). *Macromol. Biosci.* **2005**, *5*, 21–29, doi:10.1002/mabi.200400121.
8. Dechy-cabaret, O.; Martin-vaca, B.; Bourissou, D. Controlled Ring-Opening Polymerization of Lactide and Glycolide. **2004**, 20–23.
9. Dechy-Cabaret, O.; Martin-Vaca, B.; Bourissou, D. Polyesters from Dilactones. In *Handbook of Ring-Opening*; Dubois, P., Coulembier, O., Raquez, J.-M., Eds.; WILEY-VCH Verlag GmbH & C: Weinheim, 2009; pp. 255–286 ISBN 9783527317103.
10. Thomas, C.M. Stereocontrolled Ring-Opening Polymerization of Cyclic Esters: Synthesis of New Polyester Microstructures. *Chem. Soc. Rev.* **2010**, *39*, 165–173, doi:10.1039/b810065a.
11. Garcés, A.; Sánchez-Barba, L.F.; Fernández-Baeza, J.; Otero, A.; Lara-Sánchez, A.; Rodríguez, A.M. Studies on Multinuclear Magnesium Tert-Butyl Heteroscorpionates: Synthesis, Coordination Ability, and Heteroselective Ring-Opening Polymerization of Rac-Lactide. *Organometallics* **2017**, *36*, 884–897, doi:10.1021/acs.organomet.6b00934.
12. Sánchez-Barba, L.F.; Garcés, A.; Fernández-Baeza, J.; Otero, A.; Alonso-Moreno, C.; Lara-Sánchez, A.; Rodríguez, A.M. Stereoselective Production of Poly(Rac-Lactide) by ROP with Highly Efficient Bulky Heteroscorpionate Alkylmagnesium Initiators. *Organometallics* **2011**, *30*, 2775–2789, doi:10.1021/om200163t.

13. Char, J.; Brulé, E.; Gros, P.C.; Rager, M.N.; Guérineau, V.; Thomas, C.M. Synthesis of Heterotactic PLA from Rac-Lactide Using Hetero-Bimetallic Mg/Zn-Li Systems. *J. Organomet. Chem.* **2015**, *796*, 47–52, doi:10.1016/j.jorganchem.2015.02.038.
14. Yui, N.; Dijkstra, P.J.; Feijen, J. Stereo Block Copolymers of L- and D-Lactides. *Die Makromol. Chemie* **1990**, *191*, 481–488, doi:10.1002/macp.1990.021910303.
15. Marin, P.; Tschan, M.J.L.; Isnard, F.; Robert, C.; Haquette, P.; Trivelli, X.; Chamoreau, L.M.; Guérineau, V.; del Rosal, I.; Maron, L.; et al. Polymerization of Rac-Lactide Using Achiral Iron Complexes: Access to Thermally Stable Stereocomplexes. *Angew. Chemie - Int. Ed.* **2019**, *58*, 12585–12589, doi:10.1002/anie.201903224.
16. Szwarc, M. © 1956 Nature Publishing. *Nature* **1956**, doi:10.1038/1781168a0.
17. D’Auria, I.; D’Alterio, M.C.; Tedesco, C.; Pellecchia, C. Tailor-Made Block Copolymers of l-, d- and: Rac -Lactides and ϵ -Caprolactone via One-Pot Sequential Ring Opening Polymerization by Pyridylamidozinc(II) Catalysts. *RSC Adv.* **2019**, *9*, 32771–32779, doi:10.1039/c9ra07133d.
18. Rosen, T.; Goldberg, I.; Venditto, V.; Kol, M. Tailor-Made Stereoblock Copolymers of Poly(Lactic Acid) by a Truly Living Polymerization Catalyst. *J. Am. Chem. Soc.* **2016**, *138*, 12041–12044, doi:10.1021/jacs.6b07287.
19. Bates, F.S.; Hillmyer, M.A.; Lodge, T.P.; Bates, C.M.; Delaney, K.T.; Fredrickson, G.H. Multiblock Polymers: Panacea or Pandora’s Box? *Science (80-.)*. **2012**, *336*, 434–440, doi:10.1126/science.1215368.
20. Otero, A.; Fernández-Baeza, J.; Sánchez-Barba, L.F.; Tejeda, J.; Honrado, M.; Garcés, A.; Lara-Sánchez, A.; Rodríguez, A.M. Chiral N, N, O-Scorpionate Zinc Alkyls as Effective and Stereoselective Initiators for the Living ROP of Lactides. *Organometallics* **2012**, *31*, 4191–4202, doi:10.1021/om300146n.
21. Sin, L.T.; Tuen, B.S. *Synthesis and Production of Poly(Lactic Acid)*; 2019; ISBN 9780128144725.
22. Platel, R.H.; Hodgson, L.M.; Williams, C.K. Biocompatible Initiators for Lactide Polymerization. *Polym. Rev.* **2008**, *48*, 11–63, doi:10.1080/15583720701834166.
23. Ovitt, T.M.; Coates, G.W. Stereochemistry of Lactide Polymerization with Chiral Catalysts: New Opportunities for Stereocontrol Using Polymer Exchange Mechanisms. *J. Am. Chem. Soc.* **2002**, *124*, 1316–1326, doi:10.1021/ja012052+.
24. Castro-Osma, J.A.; Alonso-Moreno, C.; Lara-Sánchez, A.; Otero, A.; Fernández-Baeza, J.; Sánchez-Barba, L.F.; Rodríguez, A.M. Catalytic Behaviour in the Ring-Opening Polymerisation of Organoaluminiums Supported by Bulky Heteroscorpionate Ligands. *Dalt. Trans.* **2015**, *44*, 12388–12400, doi:10.1039/c4dt03475a.
25. Huang, S.J.; Onyari, J.M. Multicomponent Polymers of Poly(Lactic Acid) Macromonomers with Methacrylate Terminal and Copolymers of Poly(2-Hydroxyethyl Methacrylate). *J. Macromol. Sci. - Pure Appl. Chem.* **1996**, *33*, 571–584, doi:10.1080/10601329608010879.
26. Psciuk, B.T.; Lord, R.L.; Winter, C.H.; Schlegel, H.B. Can Metallapyrimidines Be

- Aromatic? A Computational Study into a New Class of Metallacycles. *J. Chem. Theory Comput.* **2012**, *8*, 4950–4959, doi:10.1021/ct3006979.
27. Laine, A.; Linnolahti, M.; Pakkanen, T.A.; Severn, J.R.; Kokko, E.; Pakkanen, A. Comparative Theoretical Study on Homopolymerization of α -Olefins by Bis(Cyclopentadienyl) Zirconocene and Hafnocene: Elemental Propagation and Termination Reactions between Monomers and Metals. *Organometallics* **2010**, *29*, 1541–1550, doi:10.1021/om900843h.
28. Tomasi, J.; Mennucci, B.; Cammi, R. Quantum Mechanical Continuum Solvation Models. *Chem. Rev.* **2005**, *105*, 2999–3093, doi:10.1021/cr9904009.

CHAPTER 3

Characterization of the mechanism of crystallization of PLA stereo-di block copolymers

Table of contents

3.1 Introduction	101
3.2 Aims and objectives	105
3.3 Results and discussion	107
3.3.1 Thermal degradation of SBC-PLA.....	107
3.3.2 Effect of Mw in the PLA-SBC crystallization	109
3.3.3 Spherulite growth rate of stereo-block copolymers (PLA-SBC) and PLLA and PDLA enantiomers (PLA-HP)	111
3.3.4 Isothermal crystallization	115
3.3.4.1 Avrami model.....	122
3.3.5 Non-isothermal crystallization	126
3.3.5.1 Avrami modified model.....	131
3.3.5.2 Ozawa model.....	133
3.3.5.3. Avrami-Ozawa model	133
3.3.6 Crystallization of SBC with nucleating agents	135
3.3.6.1 Nucleating agent efficacy survey	136
3.3.6.1.1 BHET	136
3.3.6.1.2 OXA.....	137
3.3.6.2 Morphology of the crystallized NA/SC-PLA derivatives.....	140
3.4 Conclusion	151
3.5 Experimental section	153
<i>Materials</i>	153
<i>Methods</i>	153
Polymerizations.....	153
Films preparation.....	153
<i>Instrumentations and measurements</i>	153
Thermogravimetric analysis (TGA).....	153
Gel permeation chromatography (GPC).....	153
Polarized Optical Microscopy (POM)	154
Differential Scanning Calorimetry (DSC)	154
Modulated-Differential Scanning Calorimetry (M-DSC)	155
Wide-Angle X-Ray Scattering (WAXS) and Small-Angle X-Ray Scattering (SAXS).....	155
Scanning X-ray micro-diffraction (micro-beam)	156
Nanocalorimeter.....	156
3.6 References	159

3.1 Introduction

The mechanism of crystallization of a semicrystalline polymer is well accepted to involve two main steps: the nucleation and subsequent growth [1]. The nucleation step can proceed homogeneously or heterogeneously. Homogeneous nucleation consists on the separation of a crystal nucleus from the amorphous phase by an interfacial surface. Below the melting temperature, a thermodynamic competition between the energy gain in the nuclei and the energy loss in the surface occurs, until a critical nucleus size is formed and the free energy barrier is exceeded. In heterogeneous nucleation an additive such as a nucleating agent (NA) is added, which already constitutes the surface where the polymer starts the crystallization [2], reducing the energy barrier required to form a stable nucleus. Subsequently, during the growth step and accordingly to the Lauritzen-Hoffman theory [3,4], the polymer chain folds back and forth into crystal stems to form lamellas, which are ca. 10-20 nm thick platelets with the growth axis that advance perpendicularly to the polymer chain [5]. Thereafter, the crystal growth continues with the stacking of the lamellas that growth radially from the nucleus to form the spherulite crystal structure (>1000 nm) which continues advancing with larger radius until impingement occurs [6]. The nucleation (i) and growth rate (g) can be determined by the application of the Lauritzen-Hoffman theory to the spherulites growth rate (G) determined by polarized optical microscopy (POM):

$$G = G_0 e^{\left[\frac{-U^*}{R(T_c - T_\infty)}\right]} e^{-K_g/(T_c \Delta T f)} \quad (\text{Eq. 3.1})$$

where G_0 is a constant known as front factor, U^* is the activation energy for local motion, R is the gas constant, T_c is the crystallization temperature, T_∞ is the temperature at which motion associated with viscous flow ceases (typically the glass transition temperature, T_g), ΔT is the undercooling and f is a factor that account the change in heat of fusion with temperature. K_g is the nucleation constant, which is given by:

$$K_g = \frac{ab\sigma\sigma_e T_m^0}{k\Delta H_m} \quad (\text{Eq. 3.2})$$

where a is a constant that depend on the crystallization regime (2 for regime II and 4 for regime I and III), b is the surface nucleus thickened, σ is the lateral surface free energy, σ_e is the fold surface free energy, T_m^0 is the equilibrium melting temperature, ΔH_m is the heat of fusion for 100% crystallinity and k is the Boltzmann constant [1].

Moreover, three regimes are identified in the Lauritzen-Hoffman theory depending on the limiting factor to the growth rate. At low undercooling (Regime I) the chain mobility to crystallize is high and the limiting factor is the nucleation rate. At high undercooling (Regime III) the nucleation rate is high but the chain mobility is reduced, limiting the overall growth rate. In middle undercooling (Regime II), the combination of a higher nucleation rate and still enough chain mobility usually prompt the highest growth rates. Both, nucleation and growth

processes, are influenced by the temperature, molecular weight, chemical structure, thermal history, etc [1]. Moreover, crystallization can be studied from solution, that provides isolable polymer crystals that can be precisely studied, and from the melt, that is closer to the realistic industrial conditions but additional degree of difficulty is added to the fundamental structural studies, that will affect the nucleation and growth of a crystal [7].

Poly lactide (PLA) is a semicrystalline polymer that can be arranged in different crystalline phases (**Table 3.1**). The α -phase is the more stable PLA homo crystal (HC) structure normally obtained when isotactic PLLA or PDLA are crystallized from the melt above 130°C or by crystallization from solution, characterized by a melting temperature of around 170°C [8,9]. The α' -phase (or δ -phase) is the disordered form of the α -phase and is generated either from crystallization from the melt at temperatures below 110°C or by cold-crystallization after quenching PLA to the glassy state. Besides, a mixture of α - and α' -phases is obtained when PLA is crystallized between 110°C and 130°C, although the α' -phase recrystallizes into α -phase when heated near the T_m (150-160°C) [8]. Moreover, the β -phase is developed by stretching PLA fibres in the α -phase at high temperature (130°C-140°C) and high draw ratios as well as by casting thin films from solution [9,10], and its T_m is ca. 10°C lower than α -phase T_m [11,12]. Finally, the γ -phase is produced by epitaxial crystallization of PLA on hexamethylbenzene, forming two antiparallel threefold helices in an orthorhombic unit cell [13]. Moreover, 11 lactate units are needed for PLLA to nucleate [14], the spherulite growth rate (G) and nucleation constant (Kg) of homopolymer (HP) PLLA varies from 2 to 10 $\mu\text{m}/\text{min}$ and from 1.85×10^5 to 5.97×10^5 , respectively, depending on the crystallization temperature [15], and the PLLA lamellar thickness is approximately 24 nm [16].

Table 3.1. Crystalline phases of PLA.

Crystalline phase	T_c	T_m	Unit cell	Obtention
α	130	175	Orthorhombic	From the melt above 130°C
α' or δ	110	150	Orthorhombic	From the melt below 110°C
β	135	160	?	Stretching the α -phase at 130°C
γ	140	?	Orthorhombic	Epitaxial crystallization on hexamethylbenzene
Stereocomplex	155	210-220	Trigonal	Homoenantiomeric blend of PLLA and PDLA

T_c : crystallization temperature; T_m : melting temperature.

The main drawback of PLA to replace polyolefins as materials for commodity products is the slow crystallization rate that hampers its processability under industrial conditions [17]. The slow PLA crystallization rate is mainly due to the presence of an oxygen atom in the polymer backbone that increase its flexibility with a nearly free rotation around the O-C bond, which implies less extended chains and a higher entropy barrier to crystallize [18]. Different strategies have proved to increase the crystallization rate of PLA such as stretching in the melt that promotes the polymeric chains orientation along the drawn direction that accelerates the nucleation of PLA [19–21], the use of nucleating agents to reduce the nucleation barrier of PLA [22,23] as well as the stereocomplexation between PLLA and PDLA, that decrease the free energy of the system compared to the HC counterpart [24,25] due to specific C-H...O-H hydrogen bonds within the crystal lattice that stabilize the structure [26] and confirms stereocomplexes with a higher melting (220°C) as well as degradation temperature (220-260°C) [27].

The stereocomplexation of PLA was first reported to occur by precipitation from a solution containing both enantiomers, PLLA and PDLA [28]. Several parameters affect the stereocomplexation of PLLA and PDLA, such as the mixing ratio of enantiomers, the annealing time and temperature [29] as well as the molecular weight, which is a crucial factor since exclusive stereocomplexation from the melt is only achieved for PLA-enantiomers exhibiting M_w lower than ~20 kDa [29,30]. During the crystallization of physically blended enantiomers featuring higher molecular weight (HM_w), a competition between stereocomplexation and homocrystallization occurs [30], since the stereocomplex (SC) formation suffers from a larger kinetic barrier despite its higher thermodynamic preference.

The mechanism of crystallization in the SC-phase of the enantiomeric blends has been largely investigated [31,32]. The formation of HC crystals during crystallization from the melt occurs after the SC formation instead of simultaneously [30], whilst the homocrystallization occurs before stereocomplexation during cold crystallization [33]. Moreover, the formation of helical pairs (PLLA and PDLA) below 220°C was observed by FTIR previously to the formation of a mesophase below 190°C that conclude with the stereocomplexation below 150°C [34]. However, the helical pairs are formed in the melt at relatively low cooling rates such as 2.5K/s which are suppressed at 3000K/s [35], leading to the appearance of the 10_3 helix conformation, characteristic of the α -phase. Although, the 10_3 helix undergoes a conformational transformation to the 3_1 helix, characteristic of the SC phase, upon isothermal crystallization above the T_g [36].

Moreover, the phase separation usually occurring in enantiomeric blends of HM_w has successfully been avoided by different approaches, such as the cold crystallization above the melting temperature of HC [37], the crystallization from solution at a high evaporation rate (such as in spin coating or solution casting) [38], the decrease of the entanglements during the solution blending by decreasing the polymer concentration in solution [39], the miscible

polymer blending with hydrogen bond interactions, such as poly(vinyl phenol) [40] or poly(ethylenglycol) [41], by a pickering emulsion approach followed by the reinforcing of the structure with cellulose [42] as well as the use of nucleating agents such as nanocrystals [43] and nanofibers [44] of cellulose. However, strategies to obtain full stereocomplexation from the melt with high crystallinity values of HM_w PLA-derivatives in a relatively short processing time, such as the crystallization of PLA stereo-block copolymer (PLA-SBC), are still required to adapt to the processing conditions at the industrial scale.

3.2 Aims and objectives

In Chapter 2, a series of PLA-SBC with different molecular weight and tacticities were synthesized, particularly, the largely desired HM_w PLA-SBC, to avoid the usually occurring phase separation when crystallizing the homoenantiomeric physical blend. In this Chapter, the crystallization mechanism from the melt of the PLA-SBC will be analysed and a summary of the samples that will be used in each section of the chapter is depicted in **Table 3.2** based on both, adequacy and availability.

- ✓ Firstly, a brief analysis of the thermal degradation of all the symmetric PLA-SBC as a function of the molecular weight will be accomplished by Thermogravimetric Analysis (TGA). Moreover, the methodology to verify the M_w /tacticity decrease of the PLA-SBC after the thermal treatments, particularly by DSC, will be explained using the MM_w -HPm as PLA-SBC model.
- ✓ Subsequently, the effect of the M_w in the crystallization of the PLA-SBC will be discussed, since it is a crucial parameter that determines the HC/SC ratio when stereocomplexation occurs from the enantiomeric blend. A series of PLA-SBC with similar tacticity (P_m higher than 0,9) and in 44-134kDa M_w range will be used in this section.
- ✓ Then, the spherulite growth of PLA-SBC, particularly the L520:D520 as a HM_w model, will be analysed and compared to both the corresponding homopolymer counterparts (L5 and D1), as well as to literature of stereocomplex formed from the enantiomeric blend.
- ✓ Moreover, an in-depth analysis of the crystallization mechanism under isothermal and non-isothermal conditions will be addressed, and a series of mathematical models will be applied to understand the kinetics of crystallizations. The effect of the M_w and tacticity on the crystallization mechanism will be addressed by selecting three PLA-SBC with different M_w and tacticity.
- ✓ Finally, the efficiency of different nucleating agents on the crystallization of PLA-SBC will be discussed to analyse if the crystallization rate of PLA can increase by both strategies, stereocomplexation and the use of NA.

Table 3.2. Summary of the PLA derivatives selected to accomplish the crystallization analysis.

<i>SAMPLE</i>	Code	Thermal degradation (3.3.1)	Effect of M_w (3.3.2)	Spherulites growth rate (3.3.3)	Iso and non-isothermal crystallization (3.3.4-3.3.5)	Effect of nucleating agents (3.3.6)
L115:D115		X	X			
L220:D220		X				
L250:D250		X				
L275:D275		X	X			
D275:L275		X				
L330:D330	MMw-LPm	X			X	
L375:D375	MMw-HPm	X	X		X	X
L500:D500	HMw-HPm	X	X		X	X
L520:D520		X	X	X		
L1100:D300	Asymmetric					X
L500	PLLA			X		
D500	PDLA			X		

3.3 Results and discussion

3.3.1 Thermal degradation of PLA-SBC

The understanding of thermal degradation/stability of the synthesized PLA-SBC (Table 2.3) is crucial to underpin the crystallization studied from the melt as involves the thermal treatment at high temperatures that might induce their degradation.

The onset of the stereocomplex-PLA (SC-PLA) degradation is at ca. 220-260°C [27] and thus, most of the calorimetry analyses reported in the literature erase the thermal history of SC-PLA by heating up to 230°C-260°C [30,34,41,45]. Likewise, the thermal degradation of the PLA-SBC derivatives was analysed by following the loss mass during a 5°C/min heating ramp from room temperature to 650°C by TGA (Figure 3.1). The PLA-SBC of low molecular weight

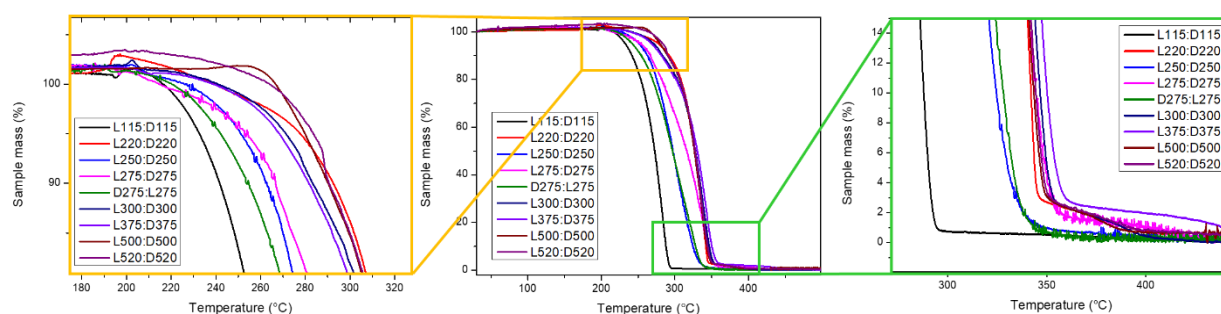


Figure 3.1. TGA thermograms of the PLA-SBC (middle) and extension of the start (left) and end (right) of the degradation curve.

(LM_w) (L115:D115; L220:D220; L250:D250; L275:D275) started to degrade at ca. 220°C whilst the onset HM_w PLA-SBC (L300:D300; L375:D375; L500:D500; L520:D520) degradation temperature shifted to ca. 240°C, which is in the range of the reported SC-PLA degradation [27]. In addition, the lower M_w PLA-SBC (L115:D115) was completely degraded at 300°C whilst the higher M_w PLA-SBC completely degraded between 350 and 400°C, which is higher than the temperature of degradation reported for the HP counterparts [27,46] and in agreement with the degradation temperature previously reported for blended SC-PLA [47,48]. The higher degradation temperature of the SC-PLA compared to the homopolymer-PLA (HP-PLA) is ascribed to the endurance of the hydrogen bonds that stabilize the stereocomplex crystal phase during the melt at temperatures below ca. 260°C [34,48].

Moreover, PLA degrades upon thermal processing due to undesirable reactions that occur at or above the melting temperature (T_m), such as hydrolysis, transesterification reactions, etc. [49,50], that can affect the molecular weight distribution of the isotactic HP-PLA (PLLA or PDLA). However, transesterification reactions occurring in the PLA-SBC derivatives can also affect the stereochemistry of the polymeric chain, which might modify the crystallization mechanism.

Besides, the degradation or transesterification degree at which the polymer is subjected upon the analysis of the crystallization mechanism from the melt, depends on the duration of the thermal step at or above T_m , typically varying from 1 to 5 minutes [30,34,41]. Likewise, the molecular weight (M_w) diminishing and crystallization temperature (T_c) variation as a function

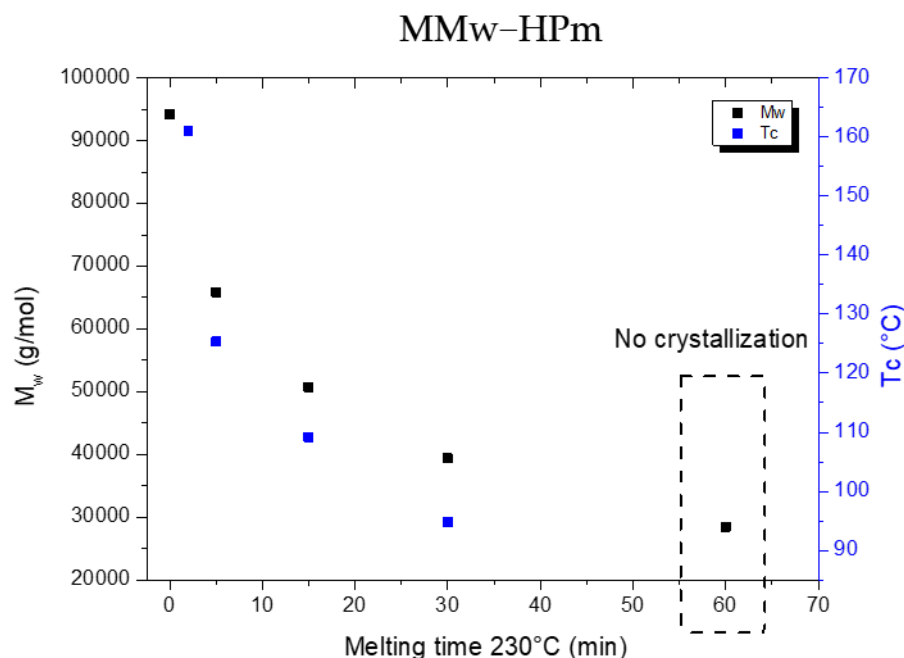


Figure 3.2. Molecular weight and crystallization temperature of the L375:D375 as a function of the holding time at 230°C.

of the holding time at 230°C was analysed by differential scanning calorimetry (DSC, **Figure 3.2**) and the subsequent M_w controlled by Gel Permeation Chromatography (GPC), of one of the HM_w PLA-SBC derivatives as model compound to the rest of the family due to featured HM_w , the MMw-HPm. A decrease of 30% in the M_w and T_c of the MMw-HPm was observed after 5 minutes at 230°C. Furthermore, the decrease of both M_w and T_c continued proportionally with the increase of the duration of the thermal step at T_m until the crystallization was impeded when the M_w decreased more than 60% after 60 minutes at 230°C, similarly to the decrease of M_w found for PLLA after thermal processing [50]. Interestingly, the T_c of both the HP-PLLA [17] and SC-PLA formed from the blend [30] increases as the M_w decrease, due to an increase of the molecular mobility. Moreover, SC-PLA presenting M_w similar to the PLA-SBC after 60 minutes at 230°C (~28.000 g/mol) is able to crystallize upon cooling at 10°C/min [30], suggesting that the observed decrease of T_c as a function of the holding time at 230°C (**Figure 3.2**) might be consequence of the transesterification reactions that changed the stereochemistry of the stereoblock copolymer rather than the decrease in M_w . However, Raman or Fourier-Transformed Infrared Spectroscopy analysis are required to confirm the stereochemistry of the polymeric chain after the thermal treatment.

Therefore, the thermal protocols imposed to the PLA-SBC derivatives were firstly introduced by a dwell step at 230°C for 2 minutes to erase the thermal history of the HM_w PLA-SBC for the analysis of the crystallization mechanism from the melt. In addition, the M_w/tacticity stability was controlled after subjecting the polymer to a thermal treatment in the melt by evaluating the T_c in a supplementary cooling ramp to draw conclusions with unequivocal polymer architectures.

3.3.2 Effect of M_w in the PLA-SBC crystallization

The effect of M_w in the mechanism of the stereocomplex crystallization was studied due to its crucial impact to determine the stereocomplexation/homocrystallization (SC/HC) ratio obtained in the competitive crystallization of the PLA enantiomeric blends. The crystallization behaviour under cooling from the melt of PLA-SBC synthesized with different M_w was analysed by DSC by applying thermal protocols with cooling and heating rates of 10°C/min (the complete protocol is specified in the experimental section) (Table 3.3). Herein, only the PLA-SBC derivatives presenting P_m values higher than 0,9 were considered for further discussion and are highlighted in Table 3.3 (Figure 3.3), although the crystallization from the melt of all the PLA-SBC was analysed by DSC (Figure A3.1 and Table 3.3).

The crystallization and melting behaviour of PLA-SBC were found to depend strongly on M_w, similarly to enantiomeric blends although with an inverse effect [41]. The T_c of the PLA-

Table 3.3. Thermal characterization by DSC of the PLA-SBC.

Sample	M _w (g/mol)	T _c ^{On} (°C)	T _c ^P (°C)	ΔH _c (J/g)	X _c (%)	T _g (°C)	T _{cc} ^P (°C)	ΔH _{cc} (J/g)	T _m ^{on} (°C)	T _m ^P (°C)	ΔH _m (J/g)	X _c (%)	P _m
L115:D115	18.381	143	106	37,5	26,4	41	82	2,2	160	187	39,8	28,0	0,96
L220:D220	35.445	119	102	20,0	14,1	53	91	9,0	17	190	35,2	24,8	0,88
L250:D250	40.604	125	105	22,2	15,6	52	91	9,5	178	195	40,0	28,8	0,92
L275:D275	44.419	118	100	28,3	19,9	46	87	8,2	168	190	42,6	30,0	0,90
D275:L275	44.300	157	126	38,3	26,9	49	90	3,3	169	190	41,9	29,0	0,81
L330:D330	94.181	137	119	51,1	35,9	49	-	-	188	202	50,7	34,7	0,69
L375:D375	107.912	163	144	62,9	44,3	56	-	-	205	209	61,8	43,5	0,95
L500:D500	130.951	182	170	66,1	46,6	52	-	-	202	210	66,1	46,5	0,94
L520:D520	150.095	144	125	48,à	33,8	56	-	-	206	208	47,2	33,3	0,92

M_w, Averaged-molecular weight; T_c^{on}, onset crystallization temperature; T_c^P peak crystallization temperature; ΔH_c, crystallization enthalpy; X_c, crystallinity obtained from crystallization; T_g, glass transition; T_{cc}, cold-crystallization temperature; ΔH_{cc}, cold-crystallization enthalpy; T_m^{on}, onset melting temperature; T_m^P, peak melting temperature; ΔH_m, melting enthalpy; $X_{c-m} = \frac{\Delta H_m}{\Delta H_m^0} \times 100$ avec ΔH_m⁰ = (142 J/g, crystallinity¹); P_m, probability of finding meso-dyads.

SBC derivatives increased as the M_w increased (**Figure 3.3A**) and further rheological analysis are needed to determine the entanglement degree before crystallization and its relationship with the PLA-SBC molecular weight since generally, the T_c of polymers decrease as M_w increase. However, the T_c decreased for the highest M_w PLA-SBC derivative (L520:D520) that might be ascribed to the decrease of chain mobility due to higher entanglement [17]. Similarly, the T_c of the low M_w PLA-SBC derivative (L115:D115) slightly increased, due to an increase of chain mobility. However, a decrease of the crystallization rate as the M_w decreased was

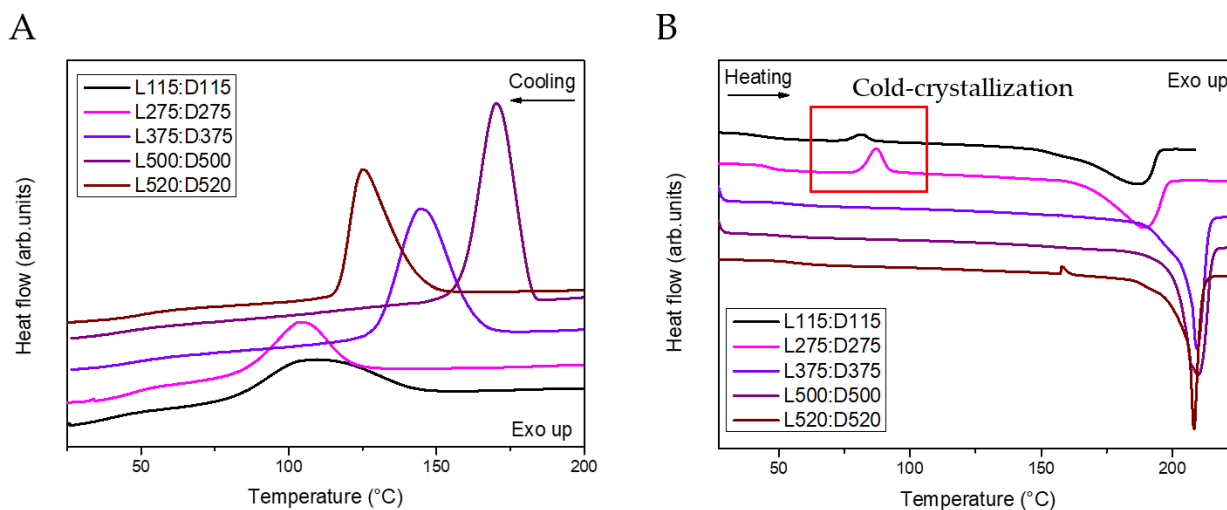


Figure 3.3. (A) Cooling and (B) heating ramps at 10°C/min of the PLA-SBC under analysis monitored by DSC.

suggested by the cold crystallization observed upon the subsequent heating of the lower M_w PLA-SBC derivatives (L115:D115; L275:D275) (**Figure 3.3B**, red square).

Moreover, the T_m of the PLA-SBC decreased as the M_w decreased, similarly to both HP-PLA [51] and SC-PLA formed from the enantiomeric blend [45]. In addition, the T_g of the PLA-SBC occurred between 41 and 56°C without a clear dependence on the M_w whilst the crystallinity values obtained from the melting enthalpy (X_{c-m}) increased from 28,02% (L115:D115) to 46,58% (L500:D500) with increasing M_w .

The low and medium M_w enantiomeric blends typically crystallize completely in the SC phase, with a decrease of the SC/HC ratio as the M_w increases, exhibiting a clear HC melting endotherm transition [30,52]. However, the HM_w PLA-SBC (L375:D375; L500:D500; L520:D520) fully crystallized in the SC phase upon cooling from the melt, as evidenced by the single endotherm at ca. 210°C and the absence of cold-crystallization upon heating (**Figure 3.3B** and **Table 3.3**).

Moreover, the crystal patterns of the PLA-SBC derivatives under study (with P_m values higher than 0,9) obtained by Wide Angle X-Ray Scattering (WAXS) upon crystallization from the melt at 10°C/min confirmed the presence of exclusively the stereocomplex phase in all the

PLA-SBC derivatives, independently of the M_w , as evidenced by the reflections (110), (300)/(030) and (220) ($q \text{ (nm}^{-1}\text{)} = 8.5, 14.7 \text{ and } 16.9$) (**Figure 3.4**).

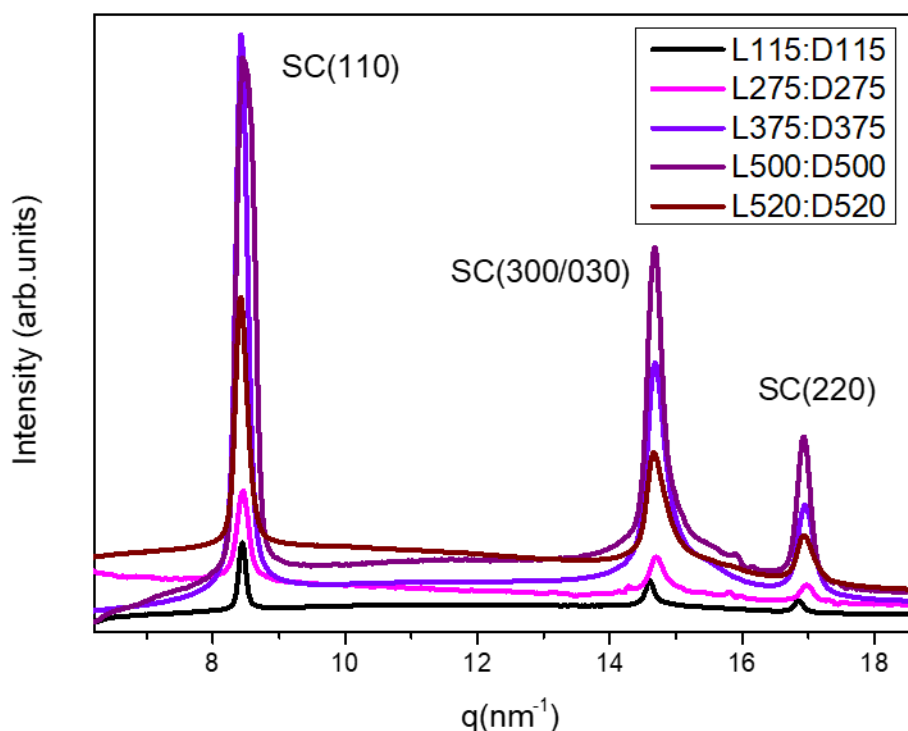





Figure 3.4. Wide-Angle X-Ray Scattering (WAXS) patterns of the PLA-SBC after cooling from the melt at $10^\circ\text{C}/\text{min}$

3.3.3 Spherulite growth rate of stereo-block copolymers (PLA-SBC) and PLLA and PDLA enantiomers (PLA-HP)

The spherulite growth rate of the M_w stereo-block copolymers was studied by polarized optical microscopy (POM) for the PLA-SBC (L520:D520) derivative as model compound for the rest of the family due to featured higher M_w , under both non-isothermal and isothermal conditions and compared to the HP-counterparts of slightly lower molecular weight (PLLA500 (L5) and PDLA500 (D1) **Table 2.2**), summarized in **Table 3.4**, to understand

Table 3.4. Abbreviations of the PLA derivatives used in this section.

Sample	Name	Color	M_w (g/mol)	P_m
PDLA500	PDLA		73.499	1
PLLA500	PLLA		105.674	1
L520:D520	L520:D520		150.094	0,92

the kinetics of nucleation and growth of the PLA-SBC as well as the crystal morphology developed upon cooling from the melt.

Firstly, the thermal history was erased by applying an isothermal step at the T_m during 2 minutes (200°C and 230°C for HP and SBC, respectively) and subsequently were cooled down to 30°C at a constant cooling rate of 5°C/min while acquiring POM images periodically. The HP crystallization of both enantiomers (PLLA and PDLA) started at ca. 135°C while the PLA-SBC crystallization started 25°C before, at ca. 160°C (**Figure 3.5**, yellow arrows). The T_c of the HP-PLA derivatives was similar to commercial PLA of similar M_w crystallized under the same conditions [23,53] and the PLA-SBC T_c was 30°C higher than the crystallization temperature of enantiomeric blends of similar M_w studied by POM [54].

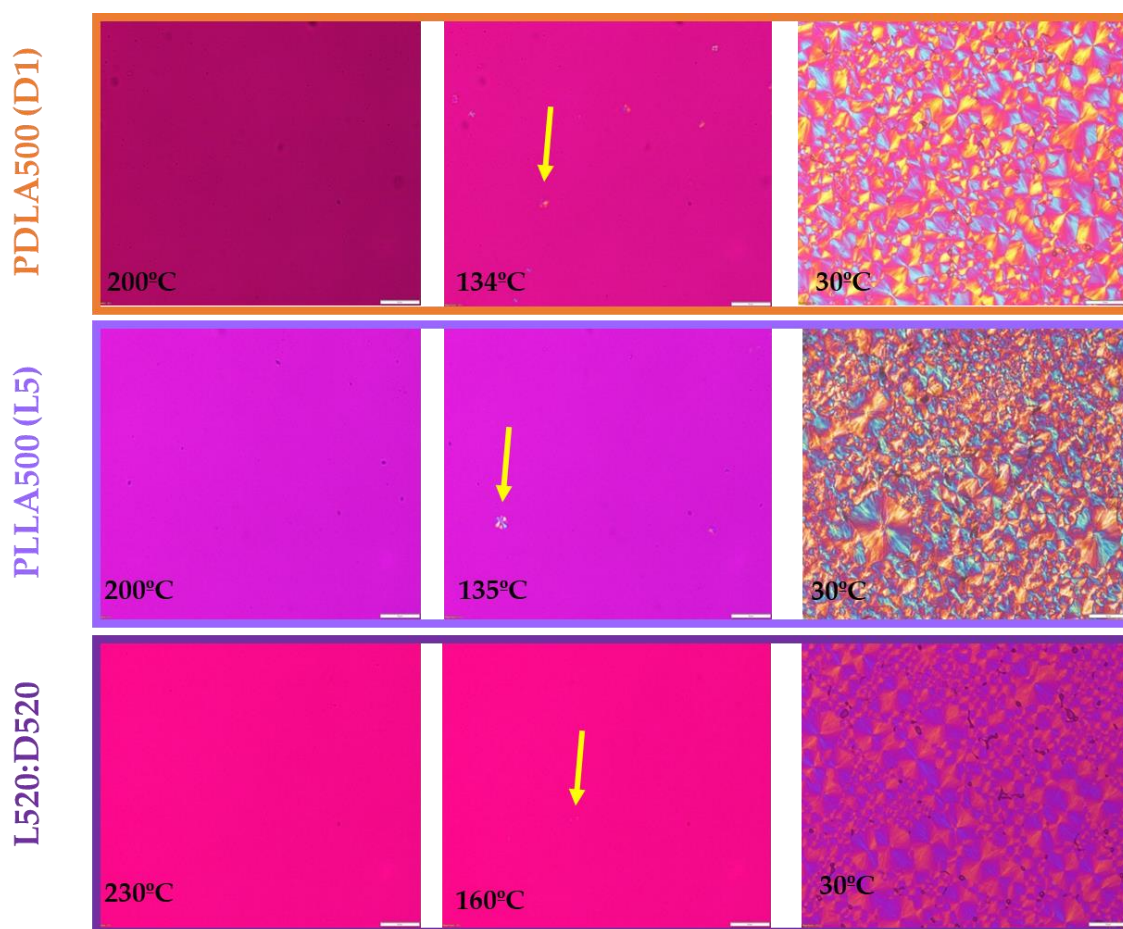


Figure 3.5. Optical microscopy images of PDLA500, PLLA500 and L520:D520 obtained upon cooling from the melt at 5°C/min. The size reference found at the right bottom of the images represents 50μm.

Moreover, heterogeneity in spherulite size was found for both HP-PLA and PLA-SBC upon cooling to 30°C (**Figure 3.5**) that might be ascribed according to Hoffman-Lauritzen theory to the transition from Regime II to Regime III, as in regime II both nucleation and

posterior growth contribute equally to the total growth rate whilst the Regime III is dominated by nucleation, since the reduction of chain mobility impedes the growth of spherulites.

The crystallization kinetics were also analysed under isothermal conditions. After erasing the thermal history, the PLA derivatives under study (PLLA, PDLA and L520:D520) were cooled down at 30°C/min to the isothermal-crystallization temperature (T_{i-c}) and hold during 60 minutes. The T_{i-c} were selected based on the crystallization temperature (T_c) found during the non-isothermal treatment, $\pm 10/15$ °C around the T_c , (summarized in **Figure 3.6** and **Table 3.5**). However, the comparison of crystallization among the PLA-derivatives must be accomplished carefully due to the difference in T_{i-c} for both HP-PLA and PLA-SBC. The three PLA-derivatives presented spherulites with obvious Maltese crosses and boundaries well defined in contrast with the observations found for PLA-enantiomeric blends of M_w higher than 32 kg mol⁻¹, in which the Maltese crosses were indistinctly observed and the boundaries were undefined [52]. Moreover, the presence of a periodical lamellar twisting was previously observed for PLLA and PDLA whilst disturbed lamella were found for the PLA-SC formed from enantiomeric blends [55]. However, both the HP-PLA and PLA-SBC exhibited a

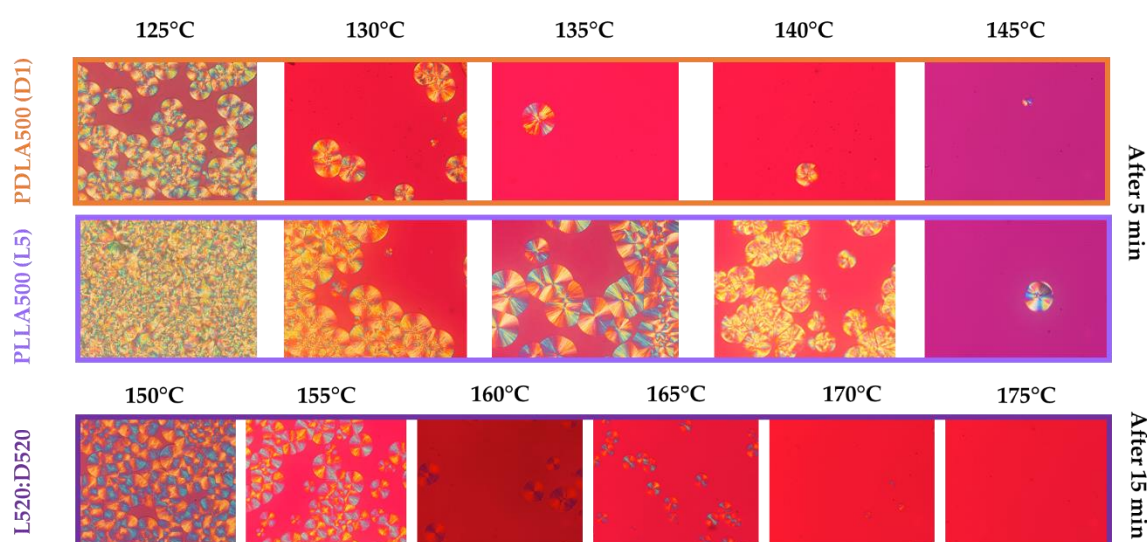


Figure 3.6. Optical images obtained by POM after 5 and 15 minutes at the isothermal crystallization temperature indicated above for HP-PLA (PLLA500 and D500) and SBC (L520:D520) respectively.

disturbed lamellar twisting morphology across the film area under study (**Figure A3.2**) although it can be ascribed to a high twisting distance that was unseeable at the spherulite size grown in the samples.

The three PLA-derivatives under study (PLLA, PDLA and L520:D520) exhibited lower spherulites density as the T_{i-c} increased, as previously reported for PLLA [17,56] due to the decrease of the nucleation rate with temperature. However, the spherulites density featured

by PLA-SBC was higher than for HP-PLA, considering the difference of the T_{i-c} analysed among the PLA derivatives, as previously determined for enantiomeric blends [57].

Likewise, the spherulite radius (r) of the three PLA-derivatives (PLLA, PDLA and L520:D520) was measured as a function of time (t) (**Figure A3.3**) to calculate the crystal growth rates (G) from its slope (**Table 3.5**). The G values obtained from the HP-PLA are equivalent to analogous PLA derivatives previously studied under the identical conditions (T_{i-c} and M_w) [58,59]. However, the crystal growth rate determined for the PLA-SBC was lower compared to lower M_w blended stereocomplex PLA [57] that might be due to the decrease of the chain mobility as the molecular weight increases.

The maximum G was obtained at 130°C (5,803 $\mu\text{m}/\text{min}$) and 135°C (6,3 $\mu\text{m}/\text{min}$) for PDLA and PLLA respectively (see orange and violet arrows in **Figure 3.7A**), which is in agreement with previously crystallization mechanism for similar PLA-derivatives [59,60]. In

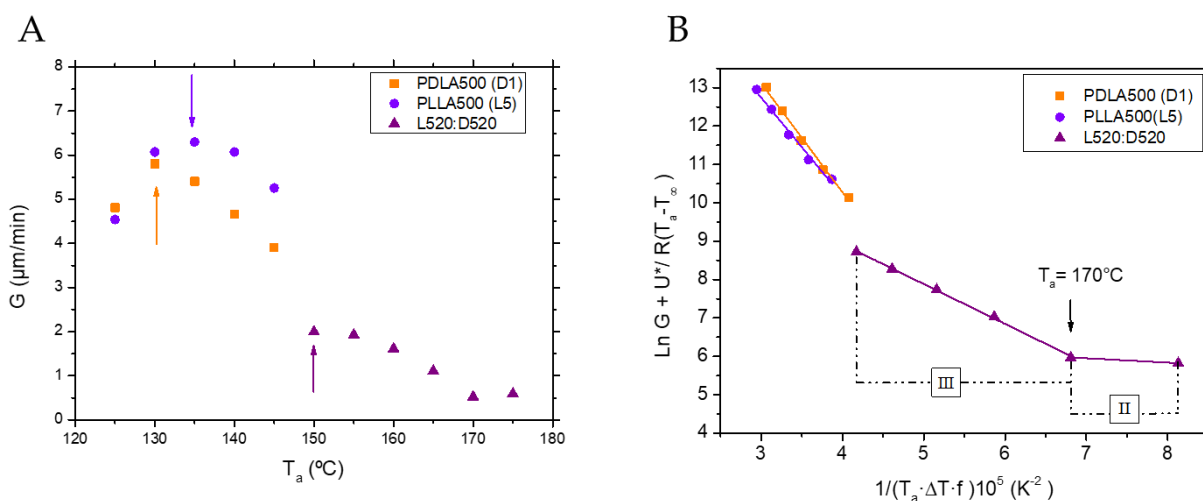


Figure 3.7. (A) Spherulite growth rate as a function of T_a and (B) Logarithmic plot of the Lauritzen-Hoffman equation for PDLA500, PLLA500 and L520:D520.

addition, the PLA-SBC exhibits its maximum G at $T_{i-c}=155^{\circ}\text{C}$. However, a higher G at lower T_{i-c} cannot be discarded, which is experimentally unattainable as the high crystallization rate produces the impingement of spherulite to be able to measure their radius.

The spherulite growth rate data obtained from POM were further analysed using the Lauritzen-Hoffman equation (**Eq 3.1**), from which the nucleation factor (K_g) and front factor (G_0) can be obtained from the slope and the intercept (**Figure 3.7B**) of the logarithmic plot (**Eq.3.3** summarized in **Table 3.3**).

$$\ln G + \frac{U^*}{R(T_{i-c} - T_{\infty})} = \ln G_0 - \frac{K_g}{(T_{i-c} \cdot \Delta T \cdot f)} \quad (\text{Eq.3.3})$$

by using the following parameter values: $U^* = 1500 \text{ cal mol}^{-1}$ and $T_{\infty} = T_g$ and $R = 1,987 \text{ cal K}^{-1} \text{ mol}^{-1}$ [61].

Table 3.5. Values of growth rate (G), nucleation factor (K_g) and front factor (G_0) for PDLA500, PLLA500 and L520:D520.

Symbol	Sample	T_{i-c} (°C)	G ($\mu\text{m}/\text{min}$)	K_g (K^2)	G_0 ($\mu\text{m}/\text{min}$)
■	PDLA	125	4,812	$2,84 \cdot 10^{-5}$	$2,501 \cdot 10^9$
		130	5,802		
		135	5,406		
		140	4,662		
		145	3,912		
●	PLLA	125	4,542	$2,57 \cdot 10^{-5}$	$5,034 \cdot 10^8$
		130	6,2551		
		135	6,3		
		140	6,072		
		145	5,256		
▲	L520:D520	150	1,998	$1,03 \cdot 10^{-5}$	$1,341 \cdot 10^5$
		155	1,926		
		160	1,614		
		165	1,11	$0,11 \cdot 10^{-5}$	845,56
		170	0,522		
		175	0,594		

The HP-PLA followed a single linear trend, whilst the PLA-SBC crystallization proceeded in two different linear regimes, although analysis at higher T_{i-c} should be accomplished. Hence, the crystallization of the PLA-SBC derivative might begin in the regime II for temperatures higher than 170°C and continued in regime III at temperatures lower than 170°C, in agreement with the transition temperature reported for PLA-SC formed from the enantiomeric blend (165°C [62] and 185°C [63]).

All the HP-PLA-derivatives exhibited a similar G_0 , and in the same order of magnitude to previously found for equivalent HP-PLA[17,64]. Interestingly, the PLA-SBC featured a slightly lower K_g , which might be related to the difference of the T_{i-c} selected to analyse the crystallization kinetics of the HP-PLA and PLA-SBC, since the nucleation rate decreases as the temperature increase [65].

3.3.4 Isothermal crystallization

The crystallization mechanism of merely the PLA-SBC was firstly probed at isothermal conditions for three PLA-SBC upon two different structural parameters such as M_w and tacticity (P_m), namely L500:D500, L375:D375 and L330:D330, which will be referred from now

on as high molecular weight and high tacticity (HMw-HPm), medium molecular weight and high tacticity (MMw-HPm) and medium molecular weight and low tacticity (MMw-LPm), respectively (represented by a black square, a red circle and a blue triangle, respectively, **Table 3.6**).

Table 3.6. Abbreviations of the PLA-SBC used in the following sections.

Sample	Name	Symbol	M_w (g/mol)	P_m
L500:D500	HMw-HPm	■	130.951	0,94
L375:D375	MMw-HPm	●	107.912	0,95
L330:D330	MMw-LPm	▲	94.181	0,69

HMw: high molecular weight; MMw: medium molecular weight; HPm: High tacticity; LPm: Low tacticity; Mw; weight-averaged molecular weight; Pm: probability of finding meso-diads.

The isothermal protocol (**Figure 3.8**) consisted of a first heating ramp at 10 °C/min from 25 °C to 230 °C and held for 2 min at the melt to erase thermal history. Samples were then cooled down to the isothermal-crystallization temperature (T_{i-c}) at 50°C/min, hold 60 minutes and cooled down to 25°C at 2°C/min. Subsequently, the samples were heated at 10°C/min to 230°C and cooled down again to 25°C at 10°C/min to analysed the melting behaviour of the isothermally crystallized PLA-SBC and verify the M_w /tacticity stability, respectively.

The crystallization temperatures for isothermal crystallization (T_{i-c}) were selected based on the crystallization temperature (T_c) found in the preliminary experiments under non-

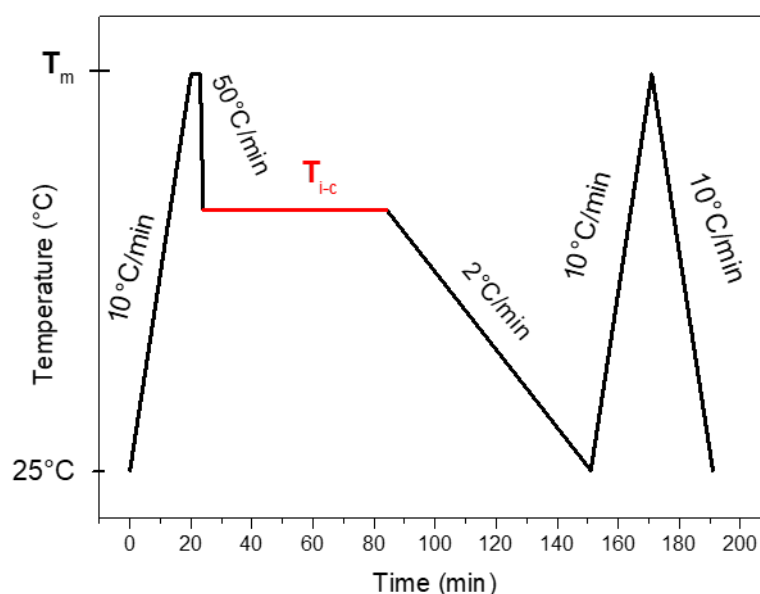


Figure 3.8. Isothermal protocol conducted by DSC.

isothermal conditions previously reported (**Figure 3.3 and Table 3.3**) resulting in different T_{i-c} for each PLA-SBC derivative (**Table 3.6**).

Likewise, the crystallization mechanism from the melt was firstly analysed by DSC at several temperatures revealing distinct difference among the PLA-SBC derivatives on the thermograms of the isothermal step (**Figure 3.9**). Moreover, the thermodynamic parameters extracted from the isothermal crystallization and subsequent cooling and melting ramps are presented in **Tables A3.1-A3.3**, in the appendix A3. However, it must be considered that the enthalpy of crystallization and the relative crystallinity (signed with a * symbol in **Tables A3.1-A3.3**), at certain T_{i-c} , might be inaccurate due to both an onset of the crystallization before reaching the T_{i-c} (unable experimentally to quench it fast enough) as well as an incomplete crystallization during the isothermal step, which impede the correct integration of the thermal peaks.

All the PLA-SBC exhibited a progressive increase of the crystallization time peak (the time at which the heat flow reach its maximum [66,67]) as the T_{i-c} increased. The crystallinity degree obtained from the enthalpy of crystallization (X_{c-c}) were c.a. 40%, 41% and 43% for MMw- LPm, HMw-HPm and MMw-HPm, respectively, independently of the T_{i-c} , whilst the enantiomeric blend of similar M_w PLA-derivatives exhibited crystallinity index lower than 10% under identical thermal conditions [30]. However, similar crystallinity values were obtained for HMw enantiomeric PLA blends in which a pre-treatment to decrease the entanglement was applied [39].

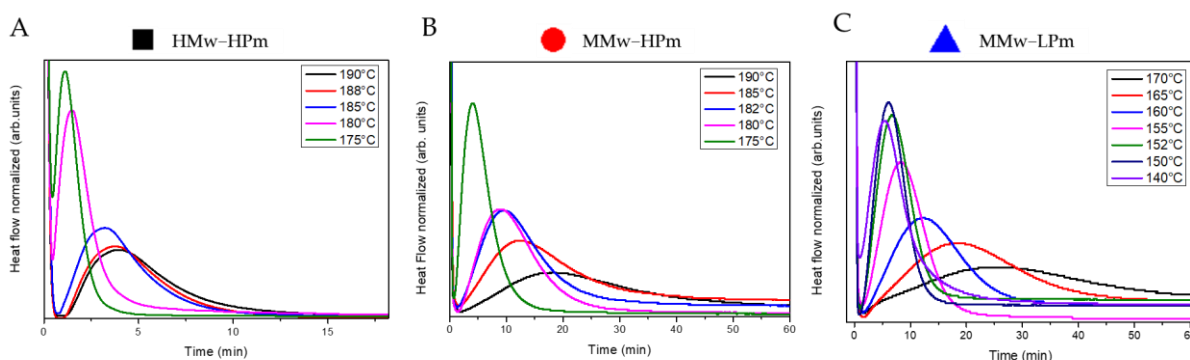


Figure 3.9. DSC plots of the isothermal steps at different annealing temperatures for L500:D500 (A), L375:D375 (B) and L330:D330 (C).

The stereo-diblock copolymers were further cooled down to room temperature to verify if the total crystallinity was attained for the PLA-derivatives during the isothermal step and particularly, the PLA-SBC crystallised at high T_{i-c} could further crystallize upon cooling, exhibiting higher crystallization enthalpy for the highest T_{i-c} (**Tables A3.1-A3.3**), indicating that the crystallization was incomplete during the isothermal step. The T_g of the high tacticity stereo-diblock copolymers (HMw-HPm and MMw-HPm) was c.a. 50°C independently of the

T_{i-c} , whilst the low tacticity PLA derivate exhibited a slightly lower T_g , at c.a. 44-48°C (Tables A3.1-A3.3), which is lower than the values previously reported for the SC-phase (65-72°C)[25].

Subsequently, the stereo-diblock copolymers were heated to 230°C to analyse the melting behaviour of the crystallites formed under isothermal conditions and the following cooling (Figure 3.10 and Tables A3.1-A3.3). The HMw-HPm stereodiblock copolymer

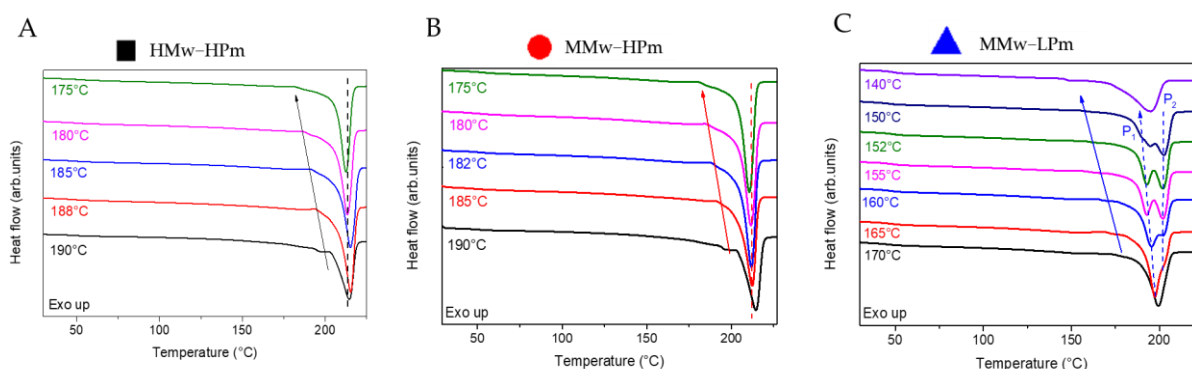


Figure 3.10. DSC plots of the heating ramp after the isothermal step and subsequent cooling for (A) L500:D500, (B) L375:D375 and (C) L330:D330

exhibited a melting temperature endotherm at 212-216°C and crystallinity degree (obtained from the melting enthalpy) c.a. 48%, whilst similar M_w SC-PLA formed from the enantiomeric blend exhibits a HP-PLA melting endotherm at 170°C, and a secondary SC-PLA melting endotherm at 220°C [30]. The MMw-HPm stereo-diblock copolymer exhibited a slightly lower melting temperature (~210-214°C) and similar X_c index for low T_{i-c} (175-182°C) and X_c c.a. 40% for high T_{i-c} (185-190°C). The X_c values of the high tacticity polymers are in agreement with similar X_c values obtained previously for HM_w PLA-SBC (41[68]-55%[69]). Moreover, both HPm stereo-diblock copolymers exhibited a slight increase of T_m as T_{i-c} increased, probably ascribed to the formation of more perfect crystals/bigger crystals at higher temperatures [70,71] due to an increase of the polymer chains mobility. Furthermore, an exotherm/endotherm was observed prior to the melting peak of both HPm stereo-diblock copolymers that might be attributed to the recrystallization of defective crystals formed during the isothermal crystallization and/or subsequent cooling. The exotherm/endotherm events prior to the melting peak gradually shift to lower temperatures as the T_{i-c} decrease (black and red arrows), since the T_m of the defective crystals decrease as the T_{i-c} decrease.

Finally, the MMw-LPm exhibited a significantly lower melting temperature (~200°C) compared to the HPm PLA-SBC counterparts. In addition, the T_m of the MMw-LPm significantly changed with T_{i-c} . The MMw-LPm crystallized at 170°C exhibited exclusively a narrow-distributed endotherm centred at 200°C that splits in two (P1 and P2) as the T_{i-c} decreases, probably due to the formation of a lower size crystal and/or lower crystal perfection population [70,71]. The P2 remains constant in temperature with a further decrease of T_{i-c} ,

whilst P1 shifts to lower temperature until it splits again at T_{i-c} 150°C. P1 can be ascribed to the melting of crystals developed during the isothermal crystallization or subsequent cooling and P2 is ascribed to the melting of crystals formed in the recrystallization upon heating [30]. However, the melting of the MMw-LPm crystallized at T_{i-c} 140° is represented again with a single endotherm, centred at 195°C but with a much wider distribution.

A second isothermal protocol (**Figure 3.11**) was conducted to discard the crystallization during the cooling ramp after the isothermal step that will influence the melting behaviour. The MMw-LPm derivative was crystallized isothermally at 160°C, as a model temperature, and subsequently heated to the melt.

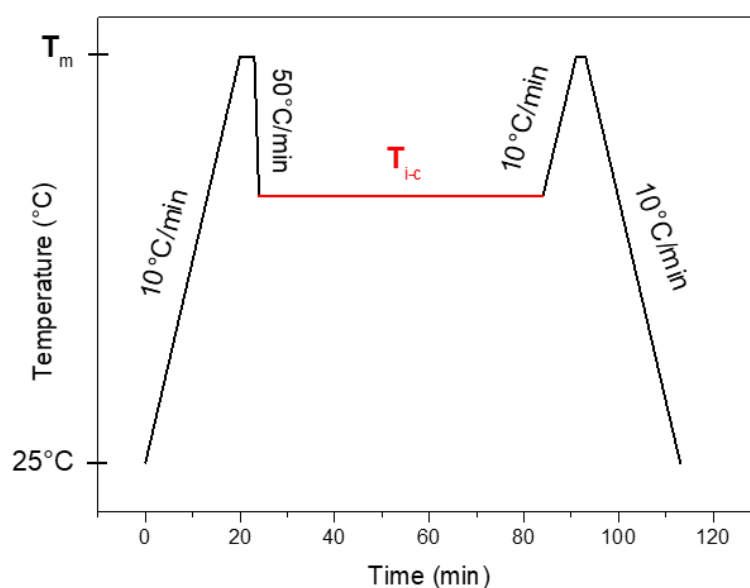


Figure 3.11. Second isothermal protocol conducted by DSC

A similar T_m and ΔH_m was obtained for the second protocol (**Figure 3.12 A**) suggesting that the multiple melting endotherms observed in the PLA-SBC derivatives isothermally crystallized that might be ascribed to a recrystallization of imperfect crystals, might be originated during the isothermal step rather than during the subsequent cooling to room temperature. In addition, identical protocol was performed by modulated DSC (MDSC, **Figure 3.12 B**) to confirm that the endo-/exothermic transitions observed prior to the main melting peak correspond to the recrystallization process that accounts for 13,2 J/g (non-rev. heat flow) whilst the total melting enthalpy (rev. heat flow) is 64,2J/g.

The nanostructure obtained during the isothermal crystallization from the melt was also investigated by simultaneous SAXS/WAXS experiments. The evolution of the intensity of the SAXS and WAXS patterns as surface plots during the isothermal step and the subsequent cooling to room temperature is included in the Appendix A3 for the sake of clearness (**Figures A3.4-A3.15**). The PLA-SBC derivatives crystallized in the SC phase and stacked in lamellae

crystals after 60 minutes at the T_{i-c} as observed by WAXS and SAXS patterns (**Figures 3.13-3.14**), respectively, except at high T_{i-c} (200°C and 175°C for HPm and LPm PLA-SBC, respectively) that only crystallized upon cooling to room temperature, as previously found for SC-PLA.

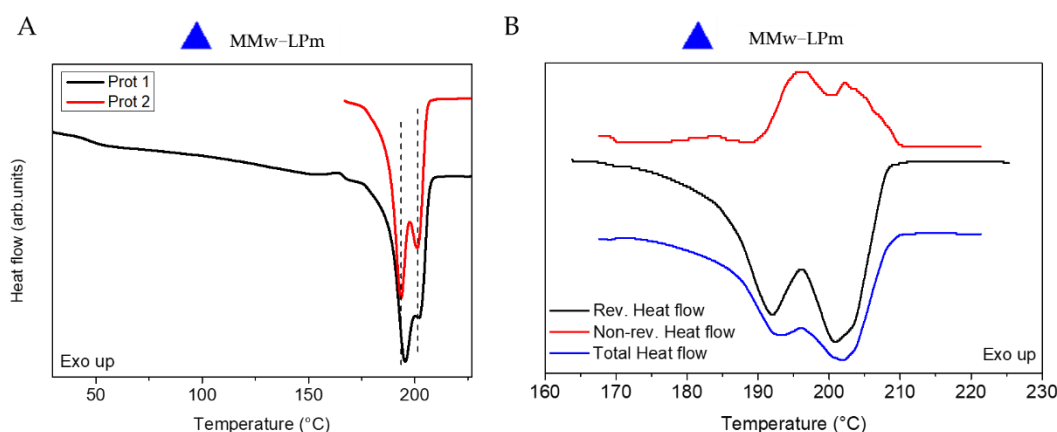


Figure 3.12. (A) DSC plot of the heating ramp after isothermal protocol 1 and 2 and (B) M-DSC plot of the heating ramp of L330:D330 at $T_a=160^\circ\text{C}$

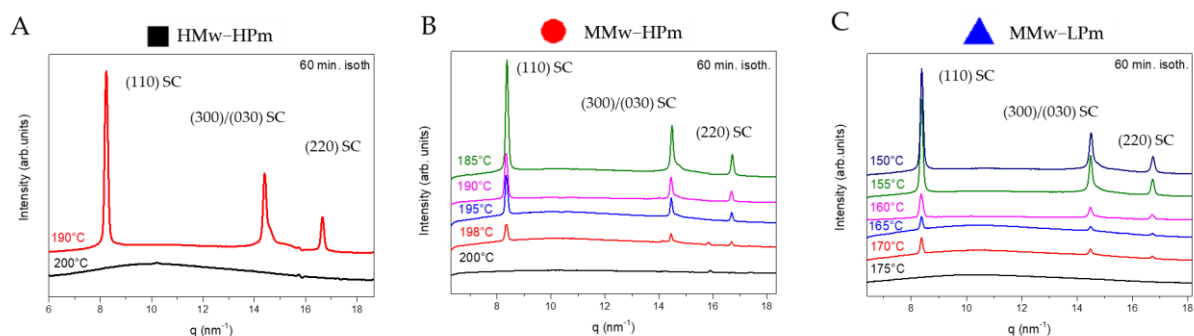


Figure 3.13. WAXS patterns of (A) HMw-HPm or L500:D500, (B) MMw-HPm or L375:D375 and (C) MMw-LPm or L330:D330 after 60 minutes isothermally crystallized at the temperatures indicated.

The PLA-SBC presented a single scattering peak in SAXS profiles that correspond to the SC crystallites (**Figure 3.14**). The HMw-HPm only featured SAXS scattering peak at $T_{i-c}=190^\circ\text{C}$, although lamellar stack at higher crystallization temperature cannot be discarded. The MMw-HPm only featured SAXS scattering peak when isothermally crystallized at temperatures lower than 198°C , although at 198°C the WAXS crystalline pattern appears slightly with a low crystallinity value of 8.8%. However, the lamellae were unable to stack and thus, the distance between crystals was too high to be measured with the q range selected.

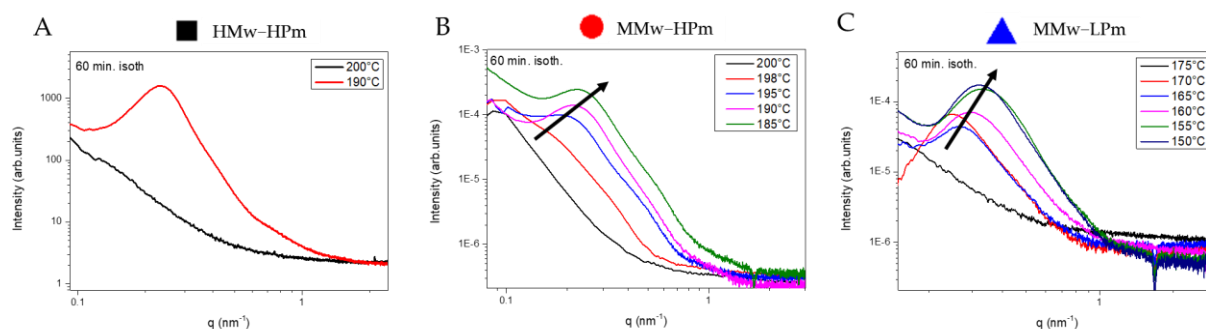


Figure 3.14. SAXS profiles of (A) HMw; HPm or L500:D500, (B) MMW; HPm or L375:D375 and (C) MMW; LPm or L330:D330 after 60minutes isothermally crystallized at the temperatures indicated.

The crystallinity degree (X_c) was obtained by the WAXS pattern deconvolution and integration and the Long period (L_p) was obtained by the Bragg equation ($L=2\pi/q_{max}$), where q_{max} correspond to the peak position in the Lorentz corrected SAXS profile.

The X_c at the end of the isothermal step increased and the L_p decreased as the T_{i-c} decreased (**Figure 3.15**). Furthermore, the PLA-SBC derivatives under study further crystallized upon cooling to room temperature (**Figure 3.15**) attaining a crystallinity degree ca. 40-60% independently of the T_{i-c} , confirming that crystallization during the isothermal step was incomplete, in agreement with DSC results. The crystallinity values were higher for the high tacticity PLA-SBC (HMw-HPm and MMw-HPm) compared to the low tacticity PLA-SBC (MMw-LPm).

The L_p of the HMw-HPm after the isothermal step at 190°C was ca. 24 nm and decreased to 18 upon cooling to room temperature. Moreover, the stack of lamellas of the HMw-HPm after the isothermal step at 200°C was undetectable, and featured ca. 15 nm upon cooling to room temperature. Moreover, the L_p of the MMw-HPm at the end of the isothermal step decrease from 28 nm to 24 nm as the T_{i-c} decrease from 195°C to 180°C, suggesting either an increase of the crystal thickness as the T_{i-c} increases or a bigger amorphous phase between crystals since the crystallinity decreased with increasing the T_{i-c} , as obtained by WAXS analysis. In addition, the L_p drastically decreased upon cooling to room temperature, to a constant values of 15-17 nm independently of the T_{i-c} , which is significantly higher than the L_p of SC-PLA formed from the enantiomeric blend of similar M_w PLA-derivatives (10-15 nm) [30], and slightly lower to block copolymers with significantly lower M_w (8.000 g/mol) crystallized between 70 and 170°C ($L_p = 7-21$ nm) [72].

The MMw-LPm stereo-diblock copolymer possessed long spacing when crystallized at temperatures lower than 170°C that become slightly lower at the end of the isothermal step and was lower than the L_p of the MMw-HPm stereo-diblock copolymer, between 22 and 16 nm. Similarly, the L_p increased also as the T_{i-c} increased, probably due to the increase of the

amorphous interphase between crystalline domains since the crystallinity degree decreased as the T_{i-c} increase, as observed by WAXS. Likewise, the L_p drastically decreased upon cooling reducing to constant values of 13-15 nm, independently of the T_{i-c} , which is still slightly higher than the L_p found for the SC-PLA formed from the blend [72], although the tacticity of the PLA-SBC is lower.

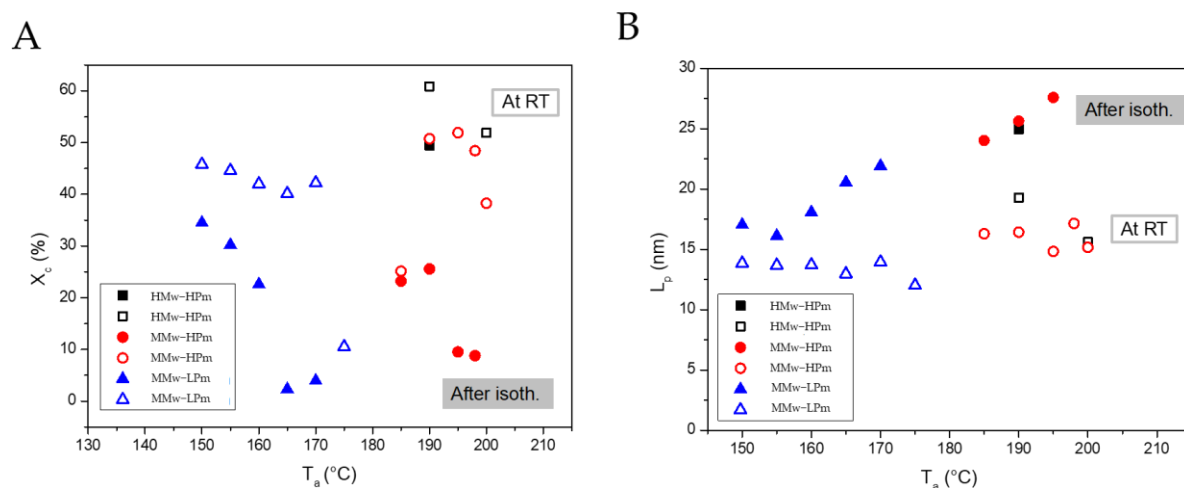


Figure 3.15. (A) Crystallinity values obtained from the deconvolution of the WAXS patterns and (B) long period obtained from the Lorentz-corrected SAXS profiles after the isothermal step (full symbols) and subsequent cooling to room temperature (empty symbols).

3.3.4.1 Avrami model

The crystallization mechanism at isothermal conditions was further analysed by modelling the kinetics of the PLA-SBC crystallization by the Avrami model. The Avrami equation (Eq. 3.3) is expressed as:

$$1 - V_c(t) = \exp(-kt^n) \quad (3.3)$$

where: V_c is the relative volumetric transformed fraction, n is the Avrami index and k the overall crystallization rate constant, that involves both, nucleation and growth. The evolution of V_c obtained from DSC with time is slower when increasing T_{i-c} for the stereo-diblock PLA copolymers under study (Figure A3.16). The linearization of the Avrami equation 3.4 permits to both determine the Avrami index and the crystallization rate by:

$$\text{Log} [-\text{Ln} [1 - V_c(t)]] = \text{Log} k + n \text{Log} (t) \quad (3.4)$$

The plotting (Figure 3.14) of $\text{Log} [-\text{Ln} [1 - V_c(t)]]$ vs $\text{Log} (t)$ and the subsequent linear regression of the experimental data is conducted to extract the Avrami index n and the overall crystallization rate k from the slope and the intercept, respectively (Table 3.7).

In addition, the Avrami index “ n ” (Eq. 3.5) is considered to be composed of two terms:

$$n = n_d + n_n \quad (3.5)$$

where n_d represent the dimensionality of the growing crystals with values 1, 2 or 3 for the corresponding 1-, 2- and 3-dimensional crystals ($n_d= 2$ or 3, for polymers). The time dependence of nucleation is represented by n_n that indicates either instantaneous/homogeneous nucleation when $n_n=0$ or sporadic/heterogeneous nucleation which is designated by $n_n=1$, although a mixture of both nucleation mechanisms might lead to no integer n values [73]. Moreover, the crystallization half time ($t_{1/2}$), defined as the period from the onset of crystallization to the time at which V_c is 50%, was obtained from k and n

Table 3.7. Avrami parameters obtained from DSC and WAXS for the three PLA-SBC under study.

AVRAMI							
Technique	Symbol	Sample	Temperature (°C)	b	K (min ⁻¹)	n	t _{1/2} (min)
DSC	■	HMw-HPm	185	-1,1917	0,0643	2,30	2,80
			188	-1,3939	0,0404	2,41	3,24
			190	-1,6596	0,0219	2,74	3,51
	●	MMW-HPm	180	-2,4283	0,0037	2,41	8,67
			182	-2,486	0,0033	2,44	8,95
			185	-2,3149	0,0048	1,81	15,51
	▲	MMw-LPm	150	-2,1489	0,0071	2,65	5,59
			152	-2,2366	0,0058	2,58	6,34
			155	-2,804	0,0016	3,07	7,23
			160	-2,6355	0,0023	2,26	12,41
			165	-2,8887	0,0013	2,29	8,44
			170	-2,8811	0,0013	1,81	31,41
WAXS	●	MMW-HPm	185	-0,693	0,2028	1,86	1,93
			190	-1,46	0,0347	1,44	7,95
			195	-1,999	0,0100	1,98	8,49
	▲	MMw-LPm	150	-3,9213	0,0001	2,77	22,71
			155	-3,4669	0,0003	2,61	18,44
			160	-3,5004	0,0003	2,07	41,01

b: slope of the logarithmic avrami equation; k: overall crystallization rate constant; n: Avrami index; t_{1/2}: half-time crvstallization

values (Eq. 3.6, Table 3.7), to study the kinetics of the crystallization under isothermal conditions:

$$t_{1/2} = [(-\ln(0.5))/k]^{1/n} \quad (3.6)$$

However, several parameters should be considered to minimise errors during the application of the model [74], such as the correct establishment of the onset of crystallization and the baseline, that together with a narrow crystallization window limit the Avrami model applicability to few T_{i-c}. Herein, the Avrami equation was applied to all the T_{i-c} but only the T_{i-}

t_c at which the onset of crystallization was clearly observed were considered for further discussion [74] (highlighted in **Table 3.7**).

The Avrami plots are almost parallel to each other (**Figure 3.16**) for the PLA-SBC derivatives under study for $V_c=3-20\%$ [74], indicating that the isothermal crystallization of the stereo-diblock copolymers is well described by the Avrami model. The n values obtained for the HPm stereo-diblock copolymers are c.a. 2.3-2.4 whilst for the LPm stereo-diblock copolymer are 2.5-3 suggesting a similar mechanism of crystallization independently of molecular weight and tacticity. Moreover, the n values indicate a 2-dimensional crystal growth (lamellar) and a mix of instantaneous and sporadic nucleation, which is in agreement with the Avrami index found for SC-PLA formed from the blend, at similar temperatures but with slightly lower molecular weight [43]. However, the POM images obtained during isothermal crystallization in thin films (**Figure 3.17**) exhibit the typical 3D crystal spherulite morphology for the PLA-SBC under study and in disagreement with the Avrami modelling of the bulk DSC studies.

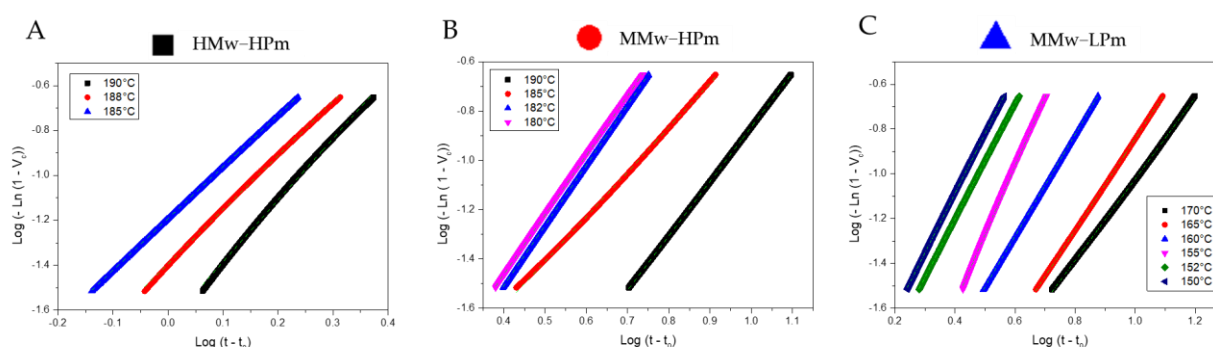


Figure 3.16. Avrami plots obtained from DSC analysis for PLA-SBC isothermally crystallized at different T_{i-c} (A) HMw-HPm (L500:D500), (B) MMw-HPm (L375:D375) and (C) MMw-LPm (L330:D330).

Furthermore, the crystallization rate constant k is significantly higher for HMw-HPm ($0,040-0,064 \text{ min}^{-1}$) followed by MMw-LPm ($0,007 \text{ min}^{-1}$). However, the fair difference in T_{i-c} for the experiments conducted for the LPm derivatives compared to the HPm counterparts in the stereo-diblock copolymers study limits the study of the effect of the molecular weight on the crystallization rate to the later. Interestingly, SC-PLA formed from the enantiomeric blend of PLA-derivatives of similar M_w and crystallized under identical conditions, featured $t_{1/2}$

values three-times higher (30 min vs 10 min) compared to the HPm stereo-diblock copolymers [30,39].

The Avrami model was also applied to the WAXS data obtained under the same thermal protocol than for DSC. Similarly, the V_c (Eq. 3.7) value was assumed to be the crystallinity obtained after the deconvolution and integration of the 1D WAXS patterns, calculated as follows:

$$V_{c(WAXS)} = \frac{A_{cryst}}{A_{cryst} + A_{amorph}} \times 100 \quad (3.7)$$

where A_{cryst} and A_{amorph} are the area of the crystalline and amorphous reflections respectively. Likewise, the V_c increase during the isothermal step at 190°C of the HMw-HPm was imminent and the Avrami model couldn't be applied. Moreover, the V_c evolution during the isothermal step of the MMw-LPm (Figure A3.17) followed a sigmoidal function at T_{i-c} 150°C and 155°C, indicating that was fully crystallized during the isothermal step following an Arrhenius behaviour, whilst at 160°C followed a much more linear function, suggesting an incomplete crystallization during the isothermal step, similar to the MMw-HPm at 195, 190 and 185°C.

The linear Avrami plots of the obtained from WAXS were almost parallel to each other (Figure 3.18), similar to Avrami plots obtained from DSC thermograms. The obtained n values of 2.6 for MMw-LPm are similar to n values calculated from DSC, however the $t_{1/2}$ were much higher (Table 3.7). Conversely, MMw-HPm presented n values slightly lower than the obtained from DSC and slightly lower $t_{1/2}$ (Table 3.7).

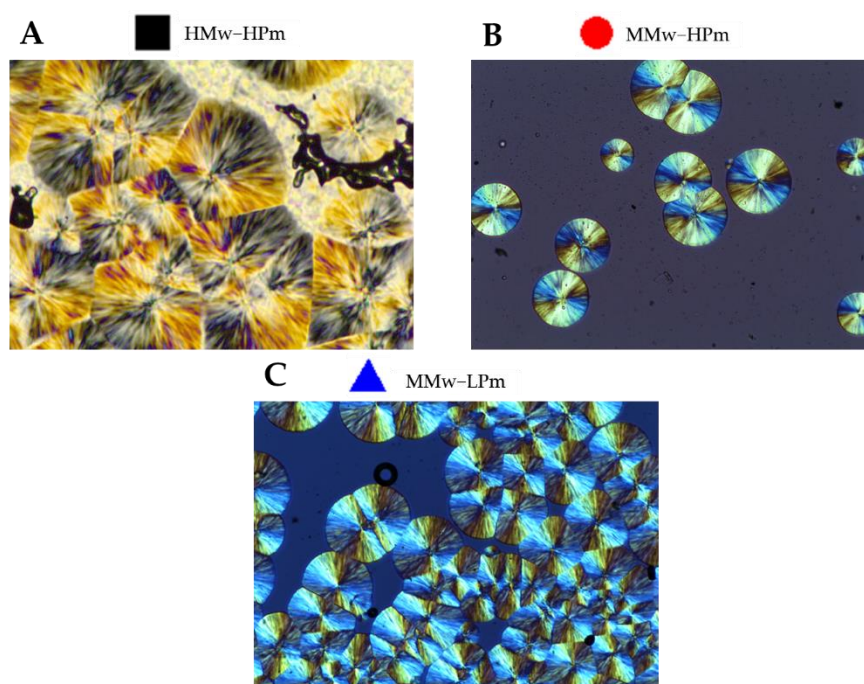


Figure 3.17. Optical images for (A) HMw-HPm at $T_{i-c} = 175^\circ\text{C}$, (B) MMw-HPm at $T_{i-c} = 170^\circ\text{C}$ and (C) MMw-LPm at $T_{i-c} = 152^\circ\text{C}$

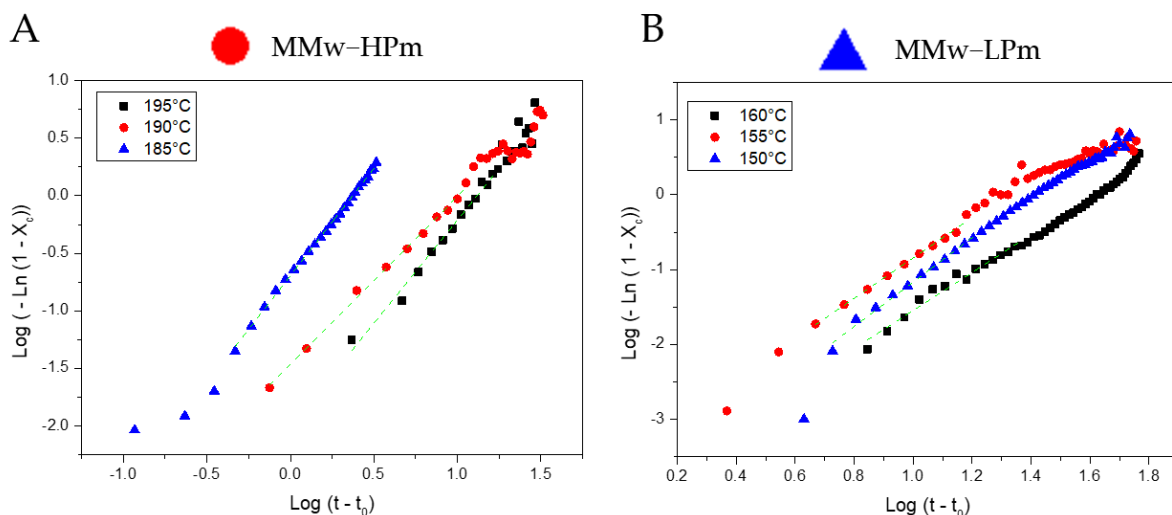


Figure 3.18. Avrami plots obtained from WAXS analysis for PLA-SBC isothermally crystallized at different T_{c-i} (A) MMw-HPm (L375:D375) and (B) MMw-LPm (L330:D330).

3.3.5 Non-isothermal crystallization

The crystallization mechanism of the PLA-SBC under non-isothermal conditions was investigated to elucidate the effect of M_w and tacticity upon crystallization from the melt under industrial conditions. Firstly, the PLA-SBC were analysed by DSC and the protocol (**Figure 3.19**) consisted of a first heating ramp at $10\text{ }^\circ\text{C}/\text{min}$ from $25\text{ }^\circ\text{C}$ to $230\text{ }^\circ\text{C}$ and held for 2 min at the melt to erase thermal history. Samples were then cooled to $25\text{ }^\circ\text{C}$ at different cooling rates,

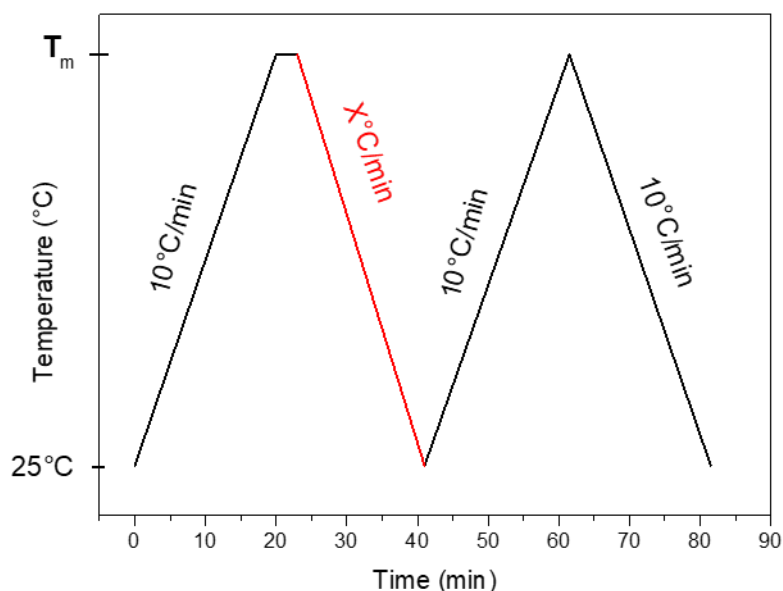


Figure 3.19. Non-isothermal protocol accomplished by DSC.

namely 5, 10, 15, 20, 30 and 50°C/min. Subsequently, the samples were heated to 230°C and cooled down to 25°C at 10°C/min to verify the M_w /tacticity stability.

The T_c , obtained from the maximum heat flow during the exothermal peak, and the crystallinity values (X_{c-c}), obtained from the crystallization enthalpy, are plotted in **Figure 3.20** as a function of cooling rate and the corresponding cooling thermograms and the thermodynamic values obtained from the thermograms in **Figures A3.18-A3.20** and **Tables A3.4-A3.6**, respectively. The T_c of the PLA-SBC under study decreased with increasing cooling rate (**Figure 3.20A**) and the exothermic curves became wider (**Figure A3.18-A3.20** and **Tables A3.4-A3.6**), since at low cooling rates the PLA derivatives are maintained at high temperatures for longer times, the nucleation and growth can be completed at higher temperatures that might assist to form more ordered and smaller distributed-size crystallites.

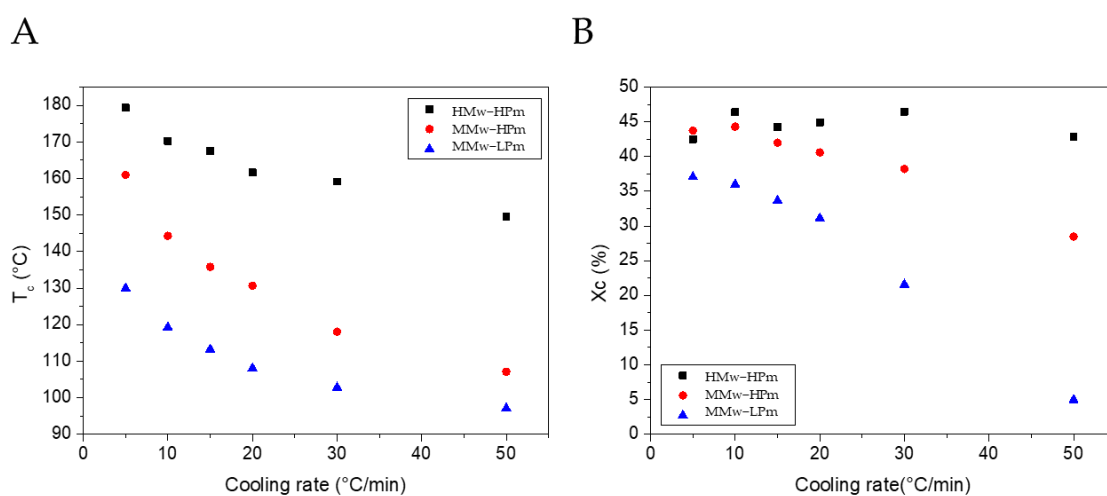


Figure 3.20 Crystallization temperature (A) and crystallinity degree obtained from the crystallization enthalpy (B) as a function of cooling rate for the SBC-PLA crystallized under non-isothermal conditions from the melt.

The obtained T_c were found higher for HMw-HPm, followed by MMw-HPm, which is probably ascribed to the higher molecular weight, in disagreement with the decrease of the T_c previously reported for similar SC-PLA formed from the enantiomeric blend, in which the HC- and SC- phases separated, decreasing the T_c [30]. Moreover, the T_c for HMw-HPm is 70°C higher compared to T_c values found for SC-PLA formed from the blend of homoenantiomers [30] and 30°C higher than T_c values of stereo-diblock copolymers exhibiting similar molecular weight and at similar cooling rates [75].

Furthermore, HMw-HPm polymer exhibited a crystallinity degree upon cooling of c.a. 44% independently of the cooling rate whilst the crystallinity of both MMw-HPm and MMw-LPm significantly decreased at 30°C and 50°C/min, (**Table A3.4-A3.6**) mainly due to an incomplete crystallization upon cooling at high cooling rates, as evidenced by the cold-crystallization exhibited upon subsequent heating (**Figure A3.19-A3.20**), suggesting a lower

crystallization rate for both MMw derivatives, being the slower the MMw-LPm. Besides, the X_{c-c} of the PLA-SBC exhibiting high tacticity (HMw-HPm and MMw-HPm) are slightly higher (5% over 100% of crystallinity) than similar SC-PLA derivatives formed from the blend (~40%) [75]. Furthermore, the HMw-HPm fully crystallized upon cooling even at high cooling rates such as 50°C/min, which to the best knowledge of the authors has never been reported, that increase its applicability as commodity product as the polymer processing at industrial scale typically imply high cooling rates.

Likewise, the PLA-SBC were subsequently heated to 230°C to analyse the melting behaviour of the crystallites formed under non-isothermal conditions (**Figure 3.21** and **A3.18-A3.20**). Firstly, the T_g was found to be dependent on the tacticity, shifting from 54-56°C for the HPm stereo-diblock copolymers to 50°C for the low tacticity stereo-diblock copolymers, probably due to the lower crystallinity obtained upon cooling. Moreover, the heating ramps

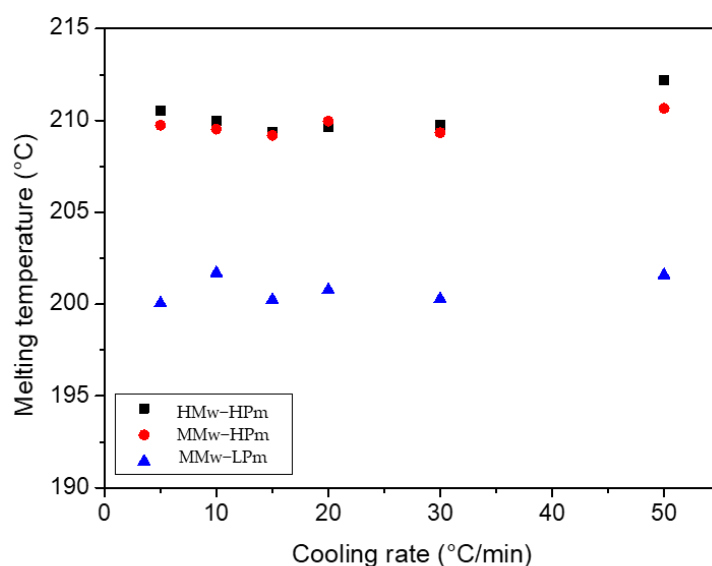


Figure 3.21. Melting temperature as a function of cooling rate for the SBC-PLA crystallized under non-isothermal conditions from the melt.

of both MMw PLA-SBC derivatives, the HPm and the LPm, suggested a lower crystallization rate compared to the HMw stereo-diblock copolymer due to the presence of cold-crystallization after cooling at 50 as well as 30 and 50°C/min, respectively. The melting temperatures of the HPm stereo-diblock copolymers (**Figure 3.21**) was c.a. 210°C whilst the low tacticity PLA-SBC (MMw-LPm) exhibited a melting temperature 10°C lower, similarly to the T_m after isothermal conditions. In addition, the melting endotherms of the high tacticity PLA-SBC exhibited a well mono distributed form independently of the cooling rate, whilst the low tacticity PLA-SBC showed a wide distributed melting endotherm for the crystallized derivative at 50°C/min, that becomes more defined as the cooling rate decreased, probably due

to the formation of more perfect crystals that decrease the enthalpy of the recrystallization process.

Similarly, the non-isothermal crystallization from the melt of the PLA-SBC was also investigated by simultaneous WAXS-SAXS analysis (**Figures 3.22 and 3.23**).

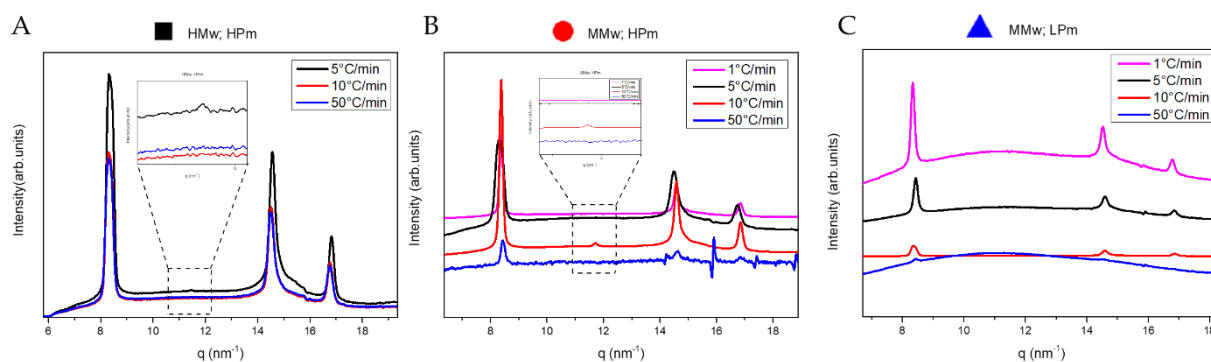


Figure 3.22. WAXS patterns of (A) HMw–HPm or L500:D500, (B) MMw–HPm or L375:D375 and (C) MMw–LPm or L330:D330 at room temperature crystallized from the melt at different cooling rates

The evolution of the intensity of the SAXS and WAXS patterns as surface plot during cooling ramp is included in the Appendix A3 for the sake of clearness (**Figures A3.21–A3.30**). Likewise, the PLA-SBC derivatives under study crystallized in the SC-phase and stacked in lamellae crystals independently of the M_w and tacticity, although the crystallization of the MMw-LPm PLA-SBC derivative was impeded at high cooling rate (50°C/min), similarly to the results obtained by DSC. Interestingly, the HMw–HPm and MMw–HPm PLA-SBC featured a low-intensity diffraction peak at q (nm^{-1}) = 12, upon cooling at 5 and 10°C/min, respectively, which correspond to the more intense peak of the α -phase ((110)/(200)), and that were developed at c.a. 110°C.

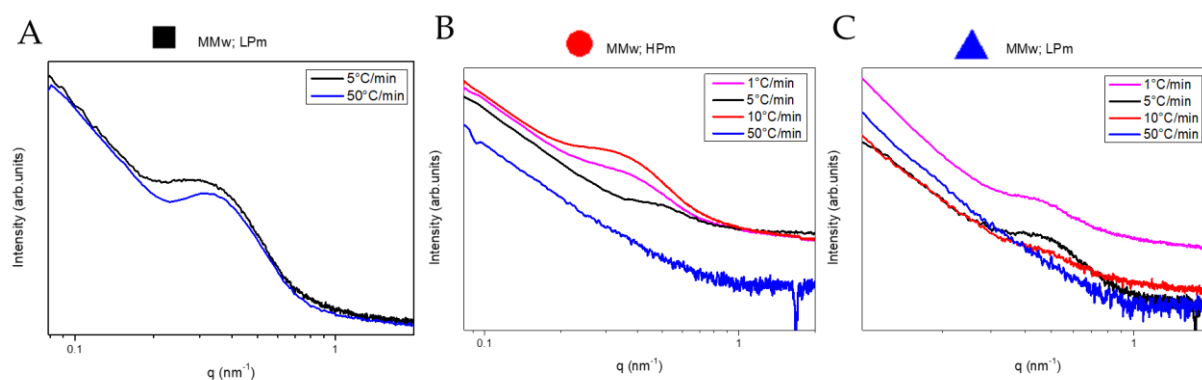


Figure 3.23. SAXS profiles of (A)HMw–HPm or L500:D500, (B) MMw–HPm or L375:D375 and (C) MMw–LPm or L330:D330 at room temperature crystallized from the melt at different cooling rates

Moreover, the PLA-SBC under study presented a single scattering peak in the SAXS profiles that correspond to SC crystallites (**Figure 3.23**). The MMw PLA-SBC derivatives, both HPm and LPm, only featured SAXS scattering peak when crystallized at cooling rates lower than 50°C/min, although crystallization was found by WAXS for the MMw-HPm PLA-SBC derivative upon cooling down at 50°C/min.

The crystallinity degree (X_{c-WAXS}) was obtained by the deconvolution and integration of the WAXS pattern and the Long period (L_p) was obtained by the Bragg equation ($L=2\pi/q_{max}$), where q_{max} correspond to the peak position in the Lorentz corrected SAXS profile. The HMw-HPm PLA-SBC attained a crystallinity degree higher than 50% independently of the cooling rate, in agreement with the X_{c-DSC} . Moreover, the L_p was constant at 16,6 nm indicating that the crystal thickness was similar independently of the cooling rate. The crystallinity degree of the MMw-HPm PLA-SBC at 1 and 10°C/min was close to 45% whilst decreased to 25% at 50°C/min that might be due to the uncompleted crystallization of the PLA-SBC upon cooling in agreement with the decrease of crystallinity obtained by DSC. Moreover, the crystallinity degree and L_p values observed for the MMw-HPm upon cooling at 5°C/min (**Figure 3.24** square boxes) did not followed the trend observed by DSC, which might be ascribed to an increase of the erasing thermal history temperature due to different experimental conditions, which typically modified the thermal behaviour of the SC-PLA formed from the blend [76].

Finally, the X_c and L_p of the MMw-LPm were lower than the HPm counterparts, indicating that the decrease of tacticity decrease both the crystallinity of the PLA-SBC and the crystal thickness.

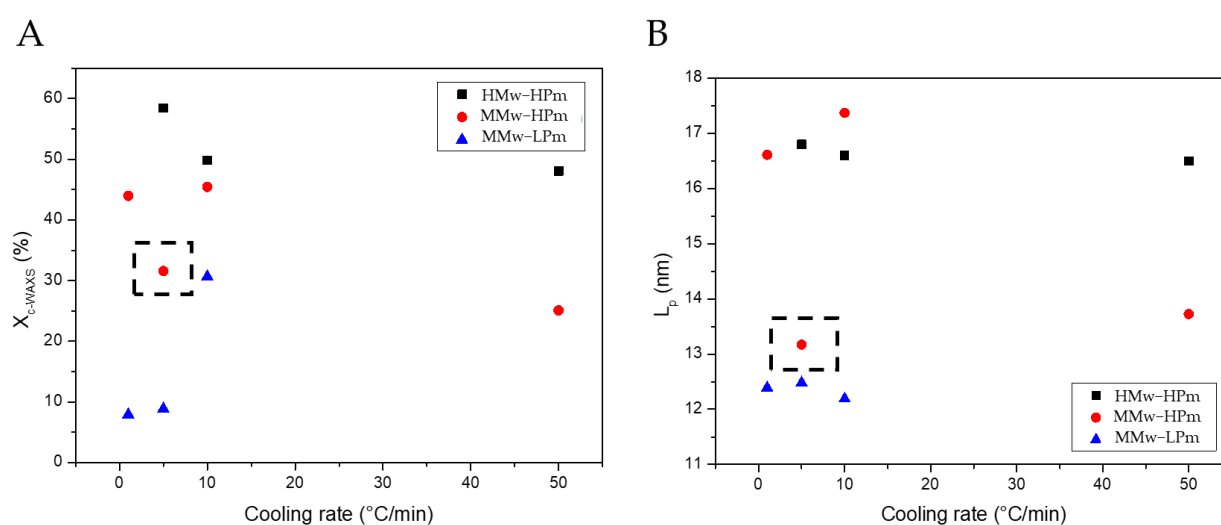


Figure 3.24. Crystallinity (A) and Long period (B) of the PLA-SBC derivative under study obtained from WAXS and SAXS experiments, respectively.

In addition, different theoretical models have been applied to the thermograms obtained upon cooling at different cooling rates to obtain further insights about the non-isothermal crystallization kinetics of the different PLA derivatives.

3.3.5.1 Avrami modified model

The Avrami equation modified by Jeziorny [66,67] is frequently applied to analyse the non-isothermal crystallization kinetics of polymers, according to which the relative degree of crystallinity (X_t) as a function of the crystallization time (**Figure A3.4**) can be expressed as **eq. 3.8**:

$$1 - X(t) = \exp[-Z_t t^n] \quad (3.8)$$

where n denotes the Avrami exponent which is dependent on the crystals nucleation and growth, and Z_t is a temperature-dependent constant related to the cooling rate with its linear form being **eq. 3.9**:

$$\log[-\ln(1 - X_t)] = \log Z_t + n \log(t) \quad (3.9)$$

However, during non-isothermal crystallization the temperature continues changing constantly and the relation between the crystallization time t and the temperature T needs to be applied, such as the **eq. 3.10**:

$$t = (T_0 - T)/\Phi \quad (3.10)$$

where Φ is the cooling rate. Moreover, the crystallization rate constant should also be corrected by the cooling rate, and the modified crystallization rate constant (Z_c) is expressed as **eq. 3.11**:

$$\log Z_c = \log Z_t/\Phi \quad (3.11)$$

The linearization of the Avrami modified equation by the logarithmic (**Eq. 3.9**, **Figure 3.25**) exhibited a linear behaviour in the early stage of crystallization, followed by a deviation at longer crystallization times, ascribed to the secondary crystallization due to spherulite

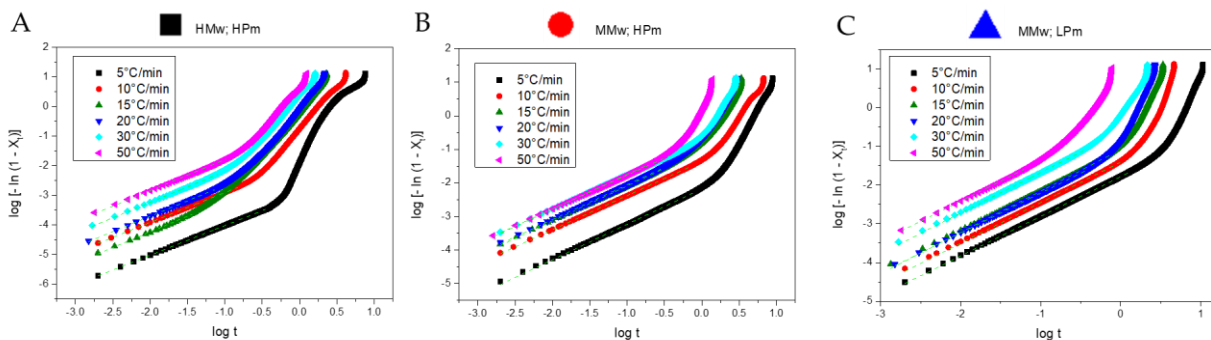


Figure 3.25. Logarithmic plot (Eq. 3.9) of the Avrami modified equation for (A) HMw-HPm or L500:D500, (B) MMw-HPm or L375:D375 and (C) MMw-LPm or L330:D330

impingement. Furthermore, the linear behaviour areas are almost parallel to each other, indicating that the nucleation mechanism and crystal growth geometries are similar for the primary crystallization at all the cooling rates investigated which shifted to longer time with decreasing cooling rate. The Avrami exponent n determined from the slope was found c.a. 1 for the PLA-SBC under study independently of the cooling rate, which are significantly different (between 2.1 and 2.8) for SC-PLA of similar M_w formed from physical blend of enantiomers [43] as well as for neat PLA, with values close to 2 (**Table 3.8**) [77]. Moreover, the obtained Z_c between 0.25 and 0.98 is in agreement with previous kinetics studies for HP-PLA

Table 3.8. Parameters of the Avrami modified model obtained by DSC for the PLA-SBC.

Cooling rate (°C/min) Φ	■ HMw-HPm			● MMw-HPm			▲ MMw-LPm		
	n	Z_t	Z_c	n	Z_t	Z_c	n	Z_t	Z_c
5	1	147,911	0,250	1,056	147,911	0,368	1,026	58,884	0,443
10	1,008	22,909	0,647	1,017	22,909	0,731	1,048	25,119	0,724
15	1,061	10,965	0,724	1,043	10,965	0,852	1,069	12,050	0,847
20	1,036	10,233	0,829	1,036	10,233	0,890	1,028	14,928	0,874
30	1,04	5,623	0,915	1,009	5,623	0,944	1,05	4,159	0,954
50	1,046	5,129	0,966	1,033	5,129	0,968	1,035	2,183	0,985

n : Avrami exponent. Z_t : temperature-dependent constant. Z_c : modified crystallization rate constant

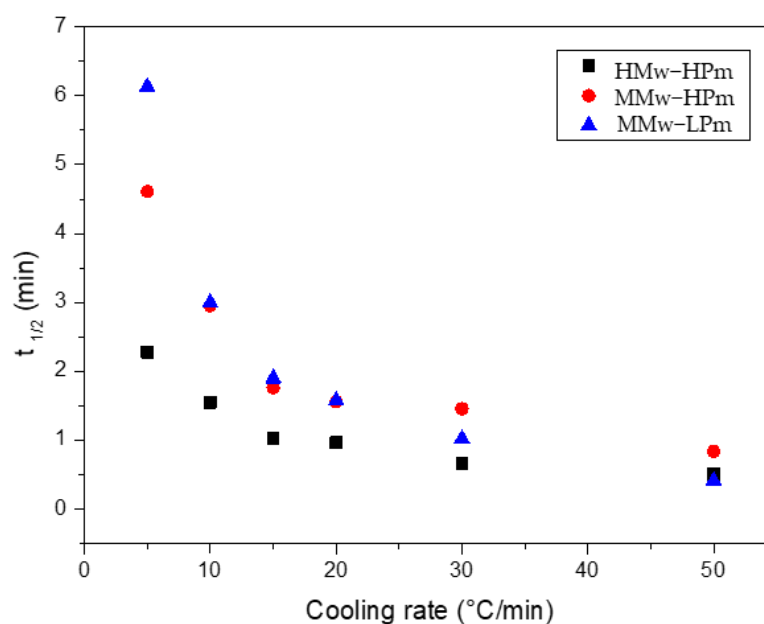


Figure 3.26. Half-crystallization time obtained from the application of the Avrami modified model on the SBC-PLA non-isothermally crystallized from the melt.

[77] and SC-PLA blends with similar M_w [43]. In addition, the Z_c were found to increase for the PLA-SBC derivatives under study as the cooling rate increases, since the transition process from the melt to the crystalline state is faster when the cooling rate was higher (Table 3.8) [43]. Furthermore, the $t_{1/2}$ decreased as the cooling rate was increased (Figure 3.26) in the PLA-SBC derivatives under study whereas at low cooling rates (5-20°C/min) the $t_{1/2}$ was higher for the MMw-LPm, followed by the MMw-HPm, which can be ascribed to the lower tacticity and lower molecular weight, respectively. At higher cooling rates, 30-50°C/min, the $t_{1/2}$ values of the PLA-derivatives should not be compared since the crystallization process was incomplete and errors have probably been introduced in the model, similarly to Avrami model applied to isothermal crystallization [74].

3.3.5.2 Ozawa model

Ozawa modified the Avrami equation and considered the non-isothermal process by incorporating the cooling rate factor as follows (Eq. 3.12):

$$1 - C(T) = \exp\left[-\frac{K(T)}{\phi^m}\right] \quad (3.12)$$

where $C(T)$ is the relative crystallinity, $K(T)$ is the Ozawa crystallization rate constant and m is the Ozawa exponent. The linearization of the Ozawa equation by applying the logarithms to the eq. 3.12 (Figure 3.27) (Eq. 3.13) should follow a linear behaviour if the model describes accurately the non-isothermal crystallization process.

$$\text{Log} [-\ln(1 - C(T))] = \log K(T) - m \text{Log } \phi \quad (3.13)$$

However, the logarithmic plot of the Avrami modified equation appears as relatively straight lines at small temperature ranges and with a R^2 lower than 0.98, indicating that the model is not describing the crystallization kinetics of our PLA derivatives.

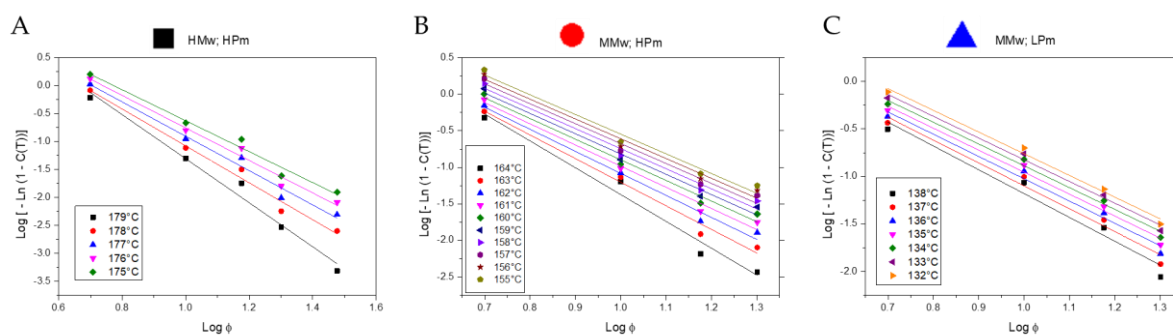


Figure 3.27. Logarithmic plot of the Ozawa model of the SBC-PLA non-isothermally crystallized from the melt.

3.3.5.3 Avrami-Ozawa model

A new crystallization model was proposed to study the non-isothermal crystallization behaviour by combining the Avrami and Ozawa equation [66,67]. The relation between

cooling rate and crystallization time could be used to describe a given crystallinity as the crystallinity is related to a cooling rate and a crystallization time by the following equation:

$$\text{Log}\Phi = \log F(T) - \alpha \log t \quad (3.14)$$

where the parameter $F(T)$ follows:

$$F(T) = \left[\frac{K(T)}{Z_t}\right]^{1/m} \quad (3.15)$$

which refers to the value of cooling rate selected at unit crystallization time, when the system reaches certain degree of crystallinity, and α is a ratio between the Avrami exponent n and the Ozawa exponent m . The plot of the eq. 3.14 (Figure 3.28) shown a linear range at a certain degree of crystallinity which permits to calculate the kinetic parameter $F(T)$ and the exponent

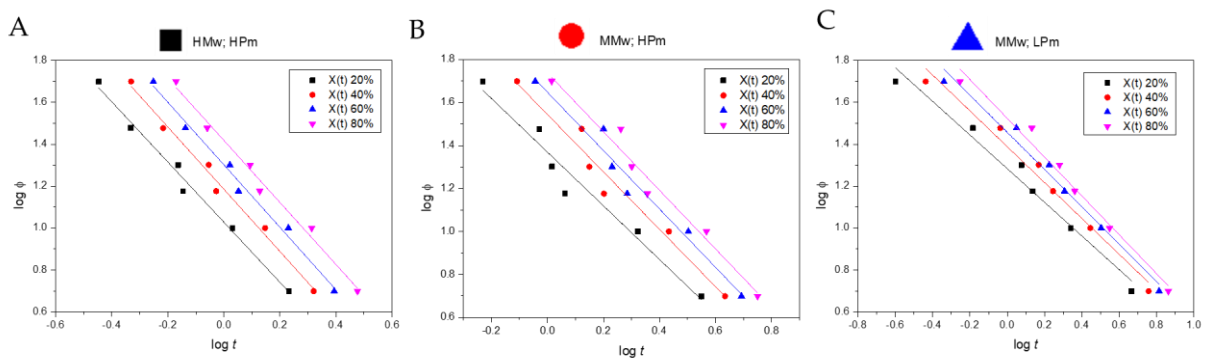


Figure 3.28. Logarithmic plot of the Avrami-Ozawa model of the SBC-PLA non-isothermally crystallized from the melt.

α from the intercept and slope, respectively (Table A3.7-A3.9). The increase of $F(T)$ with increasing the relative crystallinity in the PLA-SBC under study indicates that at unit crystallization time, a higher cooling rate is required to obtain a higher degree of crystallinity. Moreover, the trend of the obtained $F(T)$ with the lower value for HMw-HPm followed by MMw-LPm suggests that MMw-HPm requires a higher cooling rate to approach an identical degree of crystallization and thus, a lower crystallization rate [78]. The α values are in agreement with previous obtained for the SC-PLA obtained from the enantiomeric blend [79] as well as their featured tight range between 0.8-1.5 indicates that the Avrami-Ozawa equation describes well the non-isothermal crystallization kinetics of PLA-SBC.

The Avrami-Ozawa model approach has been used to describe the non-isothermal crystallization kinetics of different polymers, such as PLA or PEEK [22,78–80]. However, the Avrami-Ozawa model is still controversial since the two equations used to obtain the model are derived from the Avrami equation with different assumptions such as in the Ozawa equation, a constant cooling rate is assumed whilst in the Evans-Avrami equation, isothermal conditions are implied by a constant growth rate [81].

3.3.6 Crystallization of SBC with nucleating agents

One of the strategies to increase the crystallization rate of polymers and particularly of PLA consists of the addition of nucleating agents (NA) to reduce the energetic barrier to nucleate [82,83]. Likewise, the nucleation efficiency of three organic NA for the HM_w PLA-SBC was assessed to tackle one of the major disadvantages of PLA to substitute polyolefins at the industrial scale and in particular, with the advent of novel processing technologies such as 3D where the control of crystallization is key to tailor the properties of the final material [84]. Besides, melt-soluble bio-organic NA are generally preferred to conventional inorganic compounds as are designed to dissolve in the polymer melt and crystallize prior to the polymer on cooling, achieving higher nucleation efficiency due to the homogenous dispersion in the polymer matrix while preserving the biocompatibility of the afforded composites[23]. Likewise, the effect on the PLA-SBC crystallization of a series of low molecular weight NA featuring similar molecular groups with hydrogen bonding capability but differing on the structural rigidity and numbering of moieties was assessed. Therefore, the nucleation efficiency was assessed for *N,N'*-Bis(2-hydroxyethyl) terephthalamide [85] as well as 5,6,11,12-tetraoxo-4,7,10,13-tetraazahexadecane-1,16-dioate and diethyl 5,6,13,14-tetraoxo-4,7,12,15-etrazaoctadecane-1,18-dioate [23] with a series of PLA-SBC derivatives (**Table 3.8**) featuring different M_w as well as an PLA-SBC derivative with an asymmetric block to evaluate structural parameters on the kinetics mechanism.

Table 3.8. PLA-SBC derivatives and the corresponding code under study with the nucleating agent.

Sample	Name	M _w (g/mol)	P _m	%D-LA
Rac-PLA	Rac-PLA	84.022	0,52	48,0
L500	PLLA	105.673	1	0
D500	PDLA	73.500	1	100
L520:D520	SHM _w -HP _m	150.094	0,92	43,1
L375:D375	MM _w -HP _m	107.912	0,95	46,2
L500:D500	HM _w -HP _m	130.951	0,94	49,4
L1120:D180	A-UHM _w -HP _m	202.280	0,93	20,1

M_w: Molecular weight; P_m: Probability of finding meso-dyads; Rac-PLA: racemic Polylactide; PLLA: Poly (L-lactide); PDLA: Poly (D-lactide); SHM_w: Super-high molecular weight; HP_m: high tacticity; MM_w: Medium molecular weight; HM_w: High molecular weight; A-UHM_w: Asymmetric-Ultra high molecular weight.

Firstly, the nucleating capacity of the organic NA was assessed to identify the optimal conditions to then investigate the kinetics and morphology of crystallization in the different PLA-SBC derivatives at fixed nucleating agent concentration.

3.3.6.1 Nucleating agent efficacy survey

3.3.6.1.1 BHET

The efficiency of a terephthalic acid-based NA, the *N,N'*-Bis(2-hydroxyethyl) terephthalamide (BHET) (**Figure 3.29**) on the crystallization of SHMw-HPm was assessed. BHET was previously reported [85] to increase the crystallization temperature of PLLA from 100°C to 120°C and the crystallization enthalpy from 34.0 to 48.3 J/g by increasing the concentration

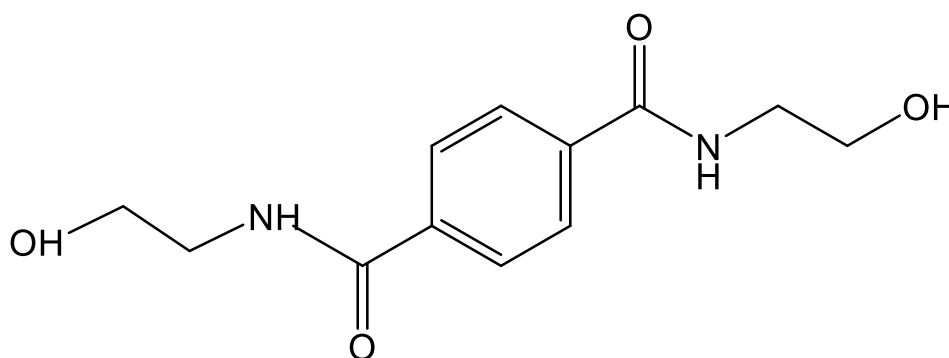


Figure 3.29. Chemical Structure of Compound *N,N'*-Bis(2- hydroxyethyl)terephthalamide (BHET)

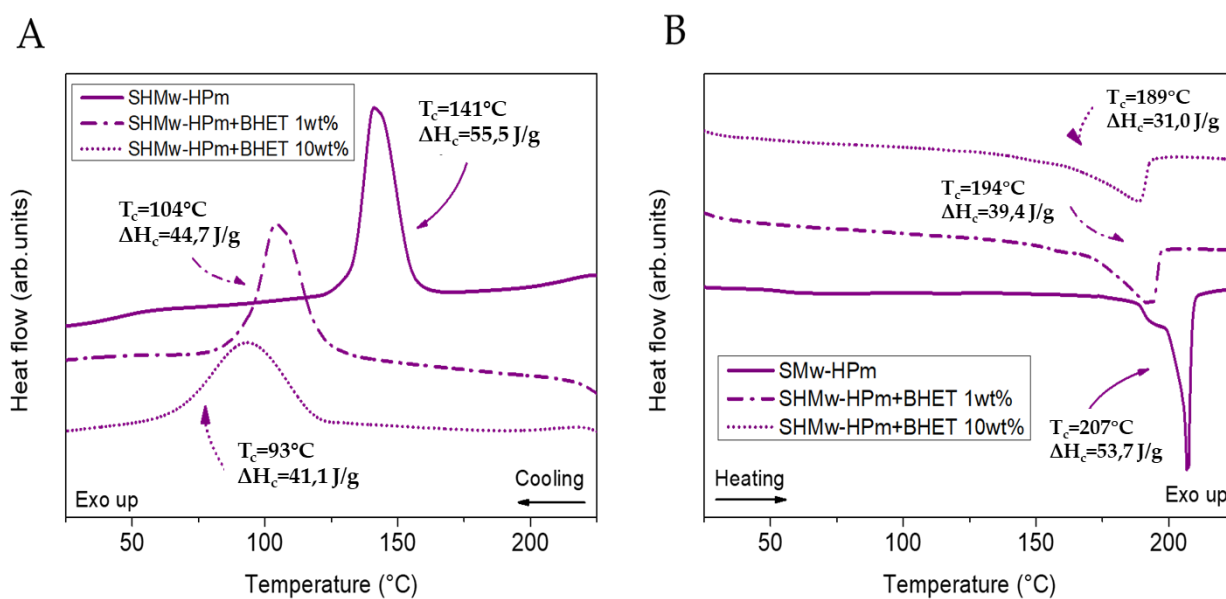


Figure 3.30. (A) Cooling and (B) heating thermograms of the PLA-SBC SHMw-HPm with 0, 1 and 10%wt of the nucleating agent BHET.

of BHET from 0 to 1.5% wt, respectively. Moreover, PLLA crystallized from the melt at 190, 170 and 140°C, at concentrations of 2.0, 1.5 and 1.0 % wt, respectively. The crystallization of films prepared with SHMw-HPm and different concentrations of BHET (0, 1 and 10% wt) was studied by DSC at fixed cooling and heating rates of 10°C/min (**Figure 3.30**, and the corresponding summary of the transitions in **Table 3.9**). The addition of 1 and 10%wt of BHET to the PLA-SBC decreased the crystallization temperature by 40 and 50°C, respectively. Moreover, the crystallization enthalpy decreased by 11 and 14 J/g, respectively, whilst the melting temperature diminished 13 and 18°C as well as the melting enthalpy decreased 14 and 22 J/g respectively, in contrast to the nucleation effect observed in PLLA at the identical cooling rate [85]. The decrease in the thermal transition temperatures and enthalpies can be ascribed

Table 3.8. Thermodynamic parameters obtained from the thermal analysis by DSC of the SHMw-HPm PLA-SBC with BHET.

Sample	BHET (%)	T _g (°C)	T _{cc} (°C)	ΔH _{cc} (J/g)	T _c (°C)	ΔH _c (J/g)	X _{c-c} (%)	T _m (°C)	ΔH _m (J/g)	X _{c-m} (%)
SHMw-HPm	-	52	-	-	144	55,5	39,1	207	53,7	37,8
SHMw-HPm	1	29	-	-	104	44,7	31,5	194	39,4	27,8
SHMw-HPm	10	33	-	-	93	41,1	28,9	189	31,0	21,8

T_g, glass transition; T_{cc} cold crystallization temperature; ΔH_{cc}, cold-crystallization enthalpy; T_c, crystallization temperature; ΔH_c, crystallization enthalpy; X_{c-c}, crystallinity obtained from crystallization; T_m, melting temperature; T_m^p, ΔH_m, melting enthalpy; X_{c-m} = $\frac{\Delta H_m}{\Delta H_m^0} \times 100$ avec ΔH_m⁰ = (142 J/g, crystallinity¹).

to the impingement of the BHET crystallization in the PLA-SBC melt, that in turn acts as a plasticizer, increasing the molecular mobility of the PLA-SBC and thus, decreasing its crystallization rate. Moreover, the heat capacity change during the glass transition decreased in presence of the BHET and shifted to a lower temperature (**Table 3.8**) confirming its plasticizing effect in the PLA-SBC matrix [86].

3.3.6.1.2 OXA

The efficiency of NA based on oxalamide to the enhancement of the crystallization rate of PLA-SBC was also tested due to melt solubility and higher crystallization temperature [87].

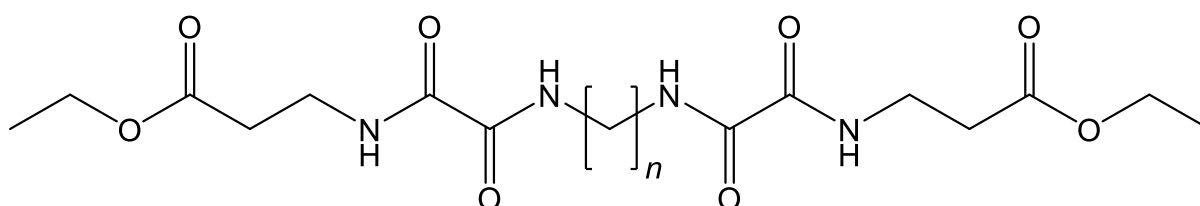


Figure 3.31. Chemical structure of the OBOCs used in this study, abbreviated based on the number of methylene groups in-between the oxalamide units. OXA-2: n=2 ; OXA-4: n=4.

Oxalamide-based organic compounds (OBOC) (**Figure 3.31**) are an example of melt-soluble organic NA in which the end groups stimulate dissolution in the polymer matrix at elevated temperatures due to their structural similarity, reducing the viscosity of the polymer at melt, while the hydrogen bonding between the oxalamide moieties provides the driving force for crystallization from the polymer melt upon cooling, that could potentially act both as plasticizers at the melt and nucleating agents upon cooling. Interestingly, the nucleation efficiency of the OBOCs increases at high cooling rates whilst preserving the biocompatibility of PLA due to its harmless effect [87].

Films of PLA-SBC, MMw-HPm, were produced containing several concentrations (0.5, 1 and 2%) of two OBOCs, OXA-4 and OXA-2. The dissolution and crystallization of the NA in the PLA derivative matrix were clearly observed by POM. The PLA-SBC containing OXA-4 crystallized above 140°C following homogeneous nucleation (**Figure 3.32A**), whilst the OXA-4 crystals appeared later than PLA spherulites, yielding also heterogeneous nucleation (**Figure 3.32 B**, see arrow). In addition, OXA-2 crystals were formed above 200°C allowing the onset of the nucleation of PLA-SBC around 170°C (**Figure 3.32 C-D**).

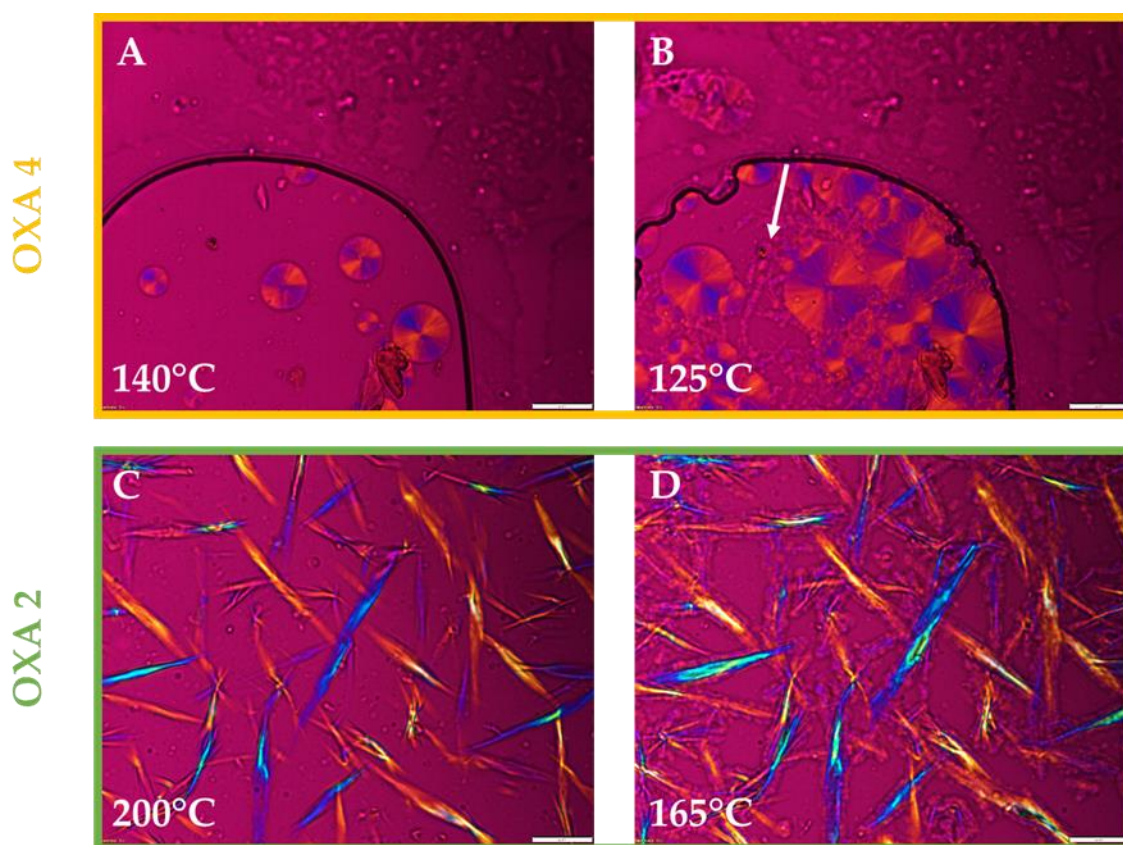


Figure 3.32. Polarized optical microscopy images of PLA film containing 2 wt % of OXA-4 (A,B) and OXA-2 (C,D).

The nucleation efficiency difference between the OBOCs might be ascribed to the increase of the molecule flexibility by the increase of the number of methylene groups in-

Table 3.9. Thermodynamic parameters obtained from the thermal analysis by DSC of the MMw-HPm PLA-SBC with OXA-2.

Sample	OXA-2 (%)	T _g (°C)	T _{cc} (°C)	ΔH _{cc} (J/g)	T _c (°C)	ΔH _c (J/g)	X _{c-c} (%)	T _m (°C)	ΔH _m (J/g)	X _{c-m} (%)
MMw-HPm	0	49	120	17	85	12,9	9,1	204,9	46,2	32,6
MMw-HPm	0,5	48	-	-	117	44,9	31,6	204,7	49,1	34,6
MMw-HPm	1	42	-	-	142	57,3	40,3	204,4	50,2	35,3
MMw-HPm	2	41	-	-	150	57,6	40,6	205,3	49,4	34,8

T_g, glass transition; T_{cc} cold crystallization temperature; ΔH_{cc} cold-crystallization enthalpy; T_c crystallization temperature; ΔH_c crystallization enthalpy; X_{c-c} crystallinity obtained from crystallization; T_m, melting temperature; T_m^p, ΔH_m, melting enthalpy; X_{c-m} = $\frac{\Delta H_m}{\Delta H_m^0} \times 100$ avec ΔH_m⁰ = (142 J/g, crystallinity¹).

between oxalamide units. The higher flexibility increases the rotation freedom, increasing the energy to nucleate. Interestingly, an increase in both crystallinity and crystallization temperature was observed by DSC with increasing the content of OXA-2 (Figure 3.33A and Table 3.9). Moreover, films containing 1 and 2% of OXA-2 exhibited a double melting peak (Figure 3.33B), which might be due to a competition between stereocomplexation and homoenantiomeric crystallization.

Furthermore, the crystal phase of the MMw-HPm film containing 2%wt of OXA-2 was also analysed by WAXS upon cooling from the melt at 30°C/min (Figure 3.34) to elucidate the origin of the double melting peak. The onset of the crystallization in the SC-phase was

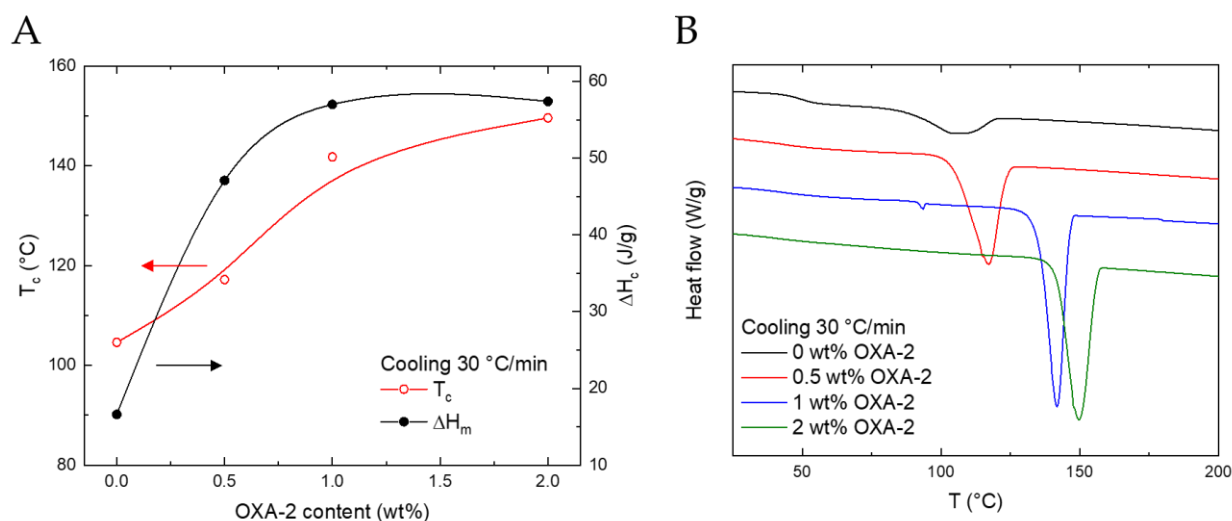


Figure 3.33. (A) Crystallization temperature and enthalpy of MMw-HPm films as a function of the OXA-2 content and (B) subsequent heating thermograms at 10°C/min.

observed at 160°C by the reflections ((110), (300))/(030) and (220) ($q \text{ (nm}^{-1}\text{)} = 8.5, 14.7 \text{ and } 16.9$)), and a low-intensity signal centred at $q(\text{nm}^{-1})=12$ appeared at 100°C (**Figure 3.34B**) corresponding to the more intense peak of the α -phase of the homocrystallization ((110)/(200)), in agreement with the stereocomplexation occurring before homocrystallization in isothermal crystallization as previously found for similar SC-PLA formed from the enantiomeric blend [30].

Likewise, the development of the α -phase upon cooling is in agreement with the double melting peak observed by DSC, however, it melts at 75°C (**Figure 3.33C-D**) which is in contradiction to the α -phase melting temperature (ca. 175°C). The nanostructure of the OXA-2 was analysed to discard the correspondence of the $q(\text{nm}^{-1})=12$ signal to a diffraction peak of the NA, but the more intense peaks of the OXA-2 appeared at q higher than 13 nm^{-1} (**Figure A3.31**). Likewise, further analyses are required to understand the origin of diffraction reflection to the α -phase as well as its melting at 75°C.

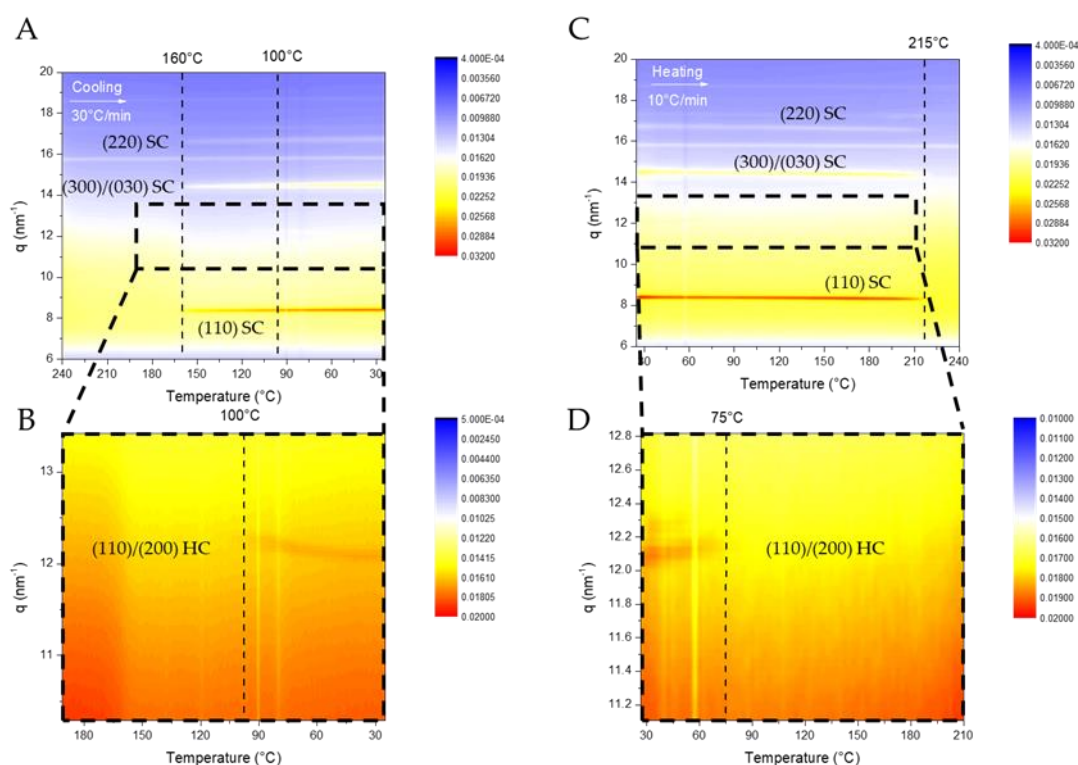


Figure 3.34. WAXS pattern of the L375:D375 film containing 2%wt of OXA-2 upon cooling (A) at 30°C/min and heating (C) at 10°C/min. (B) and (D) are zoom.

3.3.6.2 Morphology of the crystallized NA/SC-PLA derivatives

The influence of the nucleating agent and the attained crystallization kinetics on the morphology of the PLA-SBC under study (**Table 3.8**) was also investigated to understand the mechanism of crystallization. Moreover, the crystallization from the melt of the PLA-SBC was also analysed by DSC at a cooling rate of 30°C/min to compare the crystallization in bulk and

in film (**Table A3.10**). In addition, the tailoring of the crystallised morphology is a key parameter to customise their physicochemical properties such as the mechanical behaviour. Likewise, the differences in morphology of thin films crystallised both isothermally and under constant cooling from the melt were probed by POM and WAXS using a microbeam to enlarge the length scale under study.

The morphology of the crystallization of the OXA-2 within the PLA matrix was initially studied with an amorphous PLA derivative, Rac-PLA, to assess the OXA-2 crystal growth and morphology without the influence of the PLA crystallization as well as its distribution across the film area (**Figure 3.35**). The generated morphology by POM confirmed the needle-like growth that tends to form a branched network due to the likely concentration gradient provoked by the diffusion through the PLA melt as well as the depression of the crystallization temperature as previously observed [23].

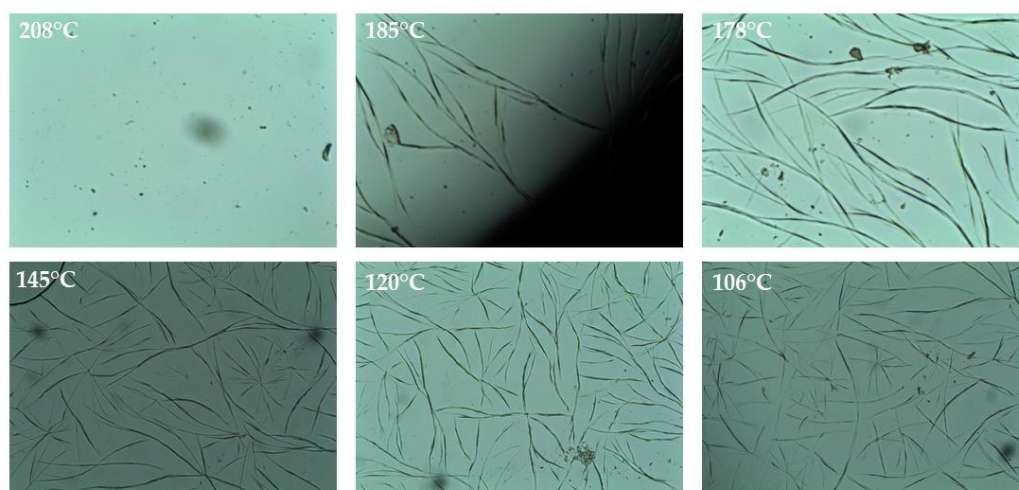


Figure 3.35. POM images of the thin film of Rac-PLA containing 2 wt% of OXA-2 non-isothermally crystallized from the melt at 20°C/min.

Likewise, the isothermal crystallization temperatures were then selected by screening the crystallization from the melt of the PLA-SBC derivatives under study. Therefore, the generated PLA-SBC thin films with and without OXA-2 were cooled from the melt at a constant rate of 20°C/min due to the technical limitations of the heating stage coupled to POM (highest cooling rate attainable) to visually determine the crystallization temperature (as shown for the MMw-HPm derivative, **Figure 3.36** and for the rest of the PLA-SBC derivatives under study in Appendix A3 Figures **A3.32-A3.33** and **Table 3.10**). The addition of OXA-2 to the PLA derivatives under study has produced the inverse effect on the crystallization temperature of the PLA derivatives compared to the OXA-2. Particularly, a general slight increase of the T_c was observed for the PLA derivatives at the applied cooling rate whilst the crystallization of OXA-2 proceeded at lower temperatures. However, the depression of the T_c

of OXA-2 is likely related to differences in molecular weight of the PLA derivatives which were blended.

The minor increase in the T_c of enantiomer PLLA derivatives generated by OXA-2 was previously [23] associated with the thickening of the OXA-2 and OXA-4 crystals together with the perfection of the crystal surface which diminishes the surface roughness, reducing the surface/volume ratio availability for HC-PLA. The later crystallization of OXA-2 crystals at higher supersaturation conditions with smaller crystal sizes and higher surface roughness

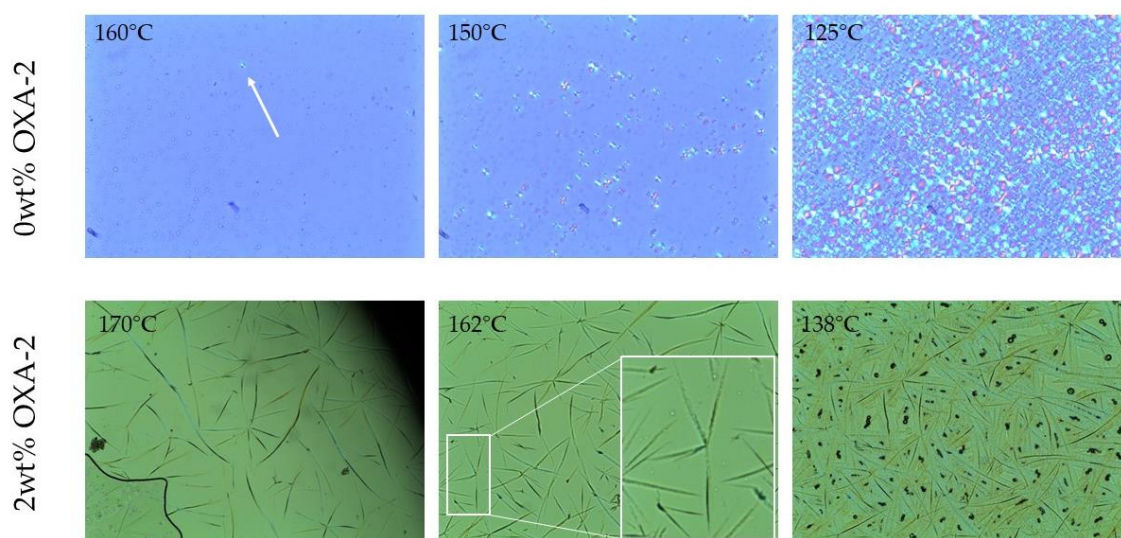


Figure 3.36. POM images of the thin films of MMw-HPm containing 0 wt% and 2 wt% of OXA-2 non-isothermally crystallized from the melt at 20°C/min.

promoted the crystallization on the needle-like crystals of spherulitic-like PLLA crystals which are consistent with the herein obtained PLLA and PDLA homocrystals (**Figure A3.34-A3.35**).

Furthermore, the OXA-2 crystal growth was proved to apply a local stress enough to generate shear-enhanced crystallization. The estimated Weissenberg number for PLLA derivatives of fairly comparable M_w to the herein studied PLLA and PLA-SBC derivatives suggests the shear exerted by OXA-2 crystal development affords the orientation of the PLA chains around the OXA-2 crystals. However, the proposed orientation chain effect would dictate the PLA crystal growth orientation, in contradiction with the observed spherulitic growth for the HC of both PLLA and PDLA herein studied (**Figure A3.34-A3.35**). Although, the crystallization of the PLA-SBC derivatives has consistently shown crystal morphologies in line with row nucleation on the previously formed OXA-2 crystals despite the differences in T_c between the OXA-2 and PLA-SBC crystals. The row nucleation crystallization could be aroused by a selective crystal influence of the PLA-SBC on the OXA-2 crystals that might suggest epitaxy growth, however, a likely chiral effect on the matching of PLA and OXA-2 crystals is discarded by the similar spherulitic morphologies observed by POM for both PLLA and PDLA derivatives (**Figure A3.34-A3.35**). Besides, the morphological analysis of the

isothermally crystallized PLA derivatives by POM (**Figure A3.36-A3.39**) has revealed the significant acceleration of the crystallization rate for the PLA derivatives under study which confirms the OXA-2 impact on the crystallization kinetics.

Likewise, the differences in morphology of native thin films isothermally crystallized for 20 minutes are compared to the 2% OXA-2 counterparts (**Table 3.10**) prior to being cooled down to room temperature at 20°C/min to assess the crystal growth at equilibrium conditions.

Table 3.10. Summary of the crystallization temperatures of the OXA-2 as well as PLA-SBC derivatives together with the corresponding selected isothermal crystallization selected for the study.

Sample	OXA-2 (%wt)	Code	Non-isothermal crystallization		Isothermal crystallization parameters	
			OXA-2 T_c (°C)	PLA T_c (°C)	T_{i-c} (°C)	Time at T_i (min)
MMw-HPm	2	MMw-HPm-2%OXA	175	162	170	20
HMw-HPm	2	HMw-HPm-2%OXA	176	160	170	20
A-UHMw-HPm	2	A-UHMw-HPm-2%OXA	153	105	150	20
MMw-HPm	0	MMw-HPm-0%OXA	-	160	170	20
HMw-HPm	0	HMw-HPm-0%OXA	-	155	170	20
A-UHMw-HPm	0	A-UHMw-HPm-0%OXA	-	111	120	20

However, the final cooling step allows probing the crystallization upon decreasing the temperature of the remained PLA. The crystalline morphology was probed at several length scales by correlating the microstructure visualised by POM to the crystal structure at the nanoscale by WAXS, scanning the observed morphology across the film with an X-Ray microbeam (2.5 microns beam with 5 microns steps, the footprint of the beam is evident after the scan, **Figure 3.37**, yellow region).

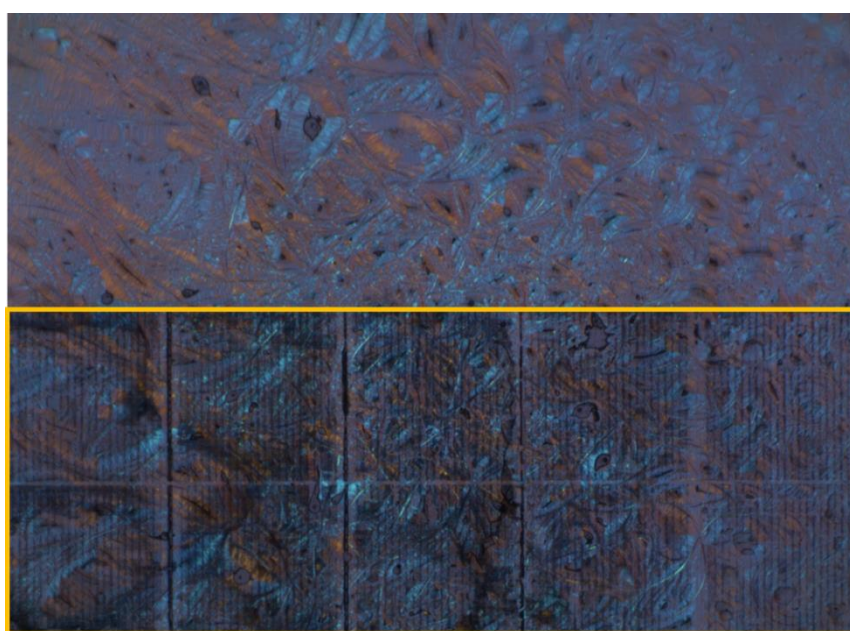


Figure 3.37. POM image of the MMw-HPm film after X-Ray microbeam.

The morphology of the medium molecular weight PLA-SBC derivative with high tacticity, MMw-HPm-0%OXA, along with the 2wt% OXA-2 counterpart, MMw-HPm-2%OXA, revealed by POM the mixed crystalline domains related to both thermal protocols (isothermal and cooling step, **Figure 3.38**). The crystallization mechanism during the isothermal step (highlighted in yellow in **Figures 3.38 A and B**) was dominated by the growth step for the MMw-HPm derivative, as evidenced by the low nucleation density, compared to the nucleation dominance imposed during the subsequent cooling ramp (highlighted in red in both **Figure 3.38 A and B**). Furthermore, the addition of OXA-2 at 2wt% increased the crystallinity (**Figures A3.36-A3.37** at 20 min) as well as modified the mechanism from

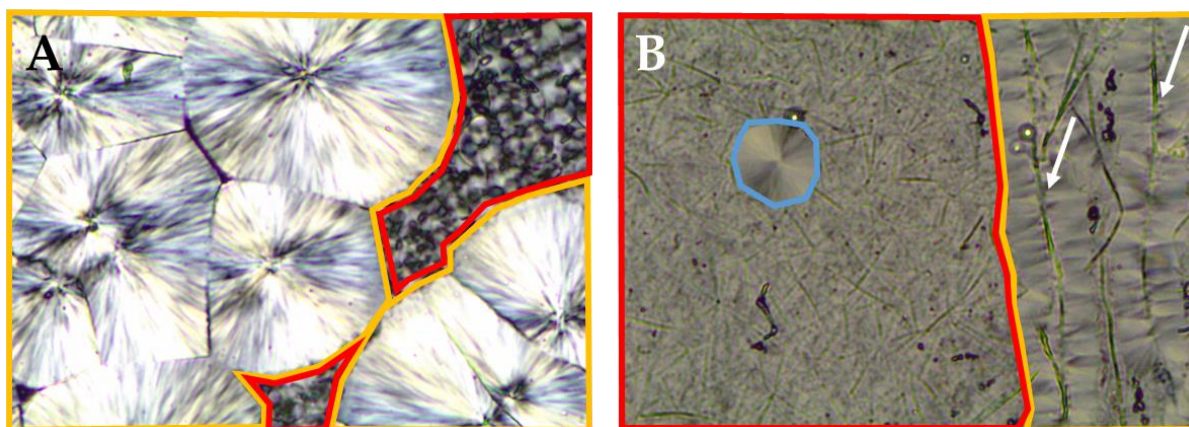


Figure 3.38. POM images of the thin films of MMw-HPm containing (A) 0 wt% and (B) 2wt% of OXA-2 isothermally crystallized at 170°C.

homogeneous to heterogeneous nucleation (**Figure 3.38B**), although a few homogenous nucleation events occurred sporadically as well in presence of the NA (**Figure 3.38B**, blue region) which are likely due to the lack of OXA-2. Moreover, the MMw-HPm-0%OXA exhibited standard spherulite growth with radial orientation (**Figure 3.38A**) whilst the MMw-HPm-2%OXA presented row nucleation from the needles-like crystals formed by the nucleating agent (**Figure 3.38B**, white arrow) that ended up with perpendicular orientation growth, suggesting a possible epitaxial growth.

The likely crystal phase distribution suggested previously by WAXS in bulk was probed by microbeam (**Figure 3.39**). The SC- phase across the film was represented as a measure of the more intense diffraction plane ((110), **Figure 3.39 A and B**) to probe the nanostructure across the film, where yellow and black colours represent high and low intensities, respectively. The intensity of the stereocomplex (110) plane plotted in 2D reproduced the morphology obtained by POM, where the crystal growth direction of the MMw-HPm-2%OXA was perpendicular to the needle-like crystals formed by the nucleating agent, evidenced by the intensity of the (110) plane SC diffraction in the region close to the nucleating agent (**Figure 3.39B**). Interestingly, the absence of homophase was indicated in both films by the only presence of the stereocomplex diffraction signals by the micro-WAXS

experiments, in disagreement with the suggested homophase observed previously by WAXS (Figure 3.39), that could be related to the material state either as bulk or thin films.

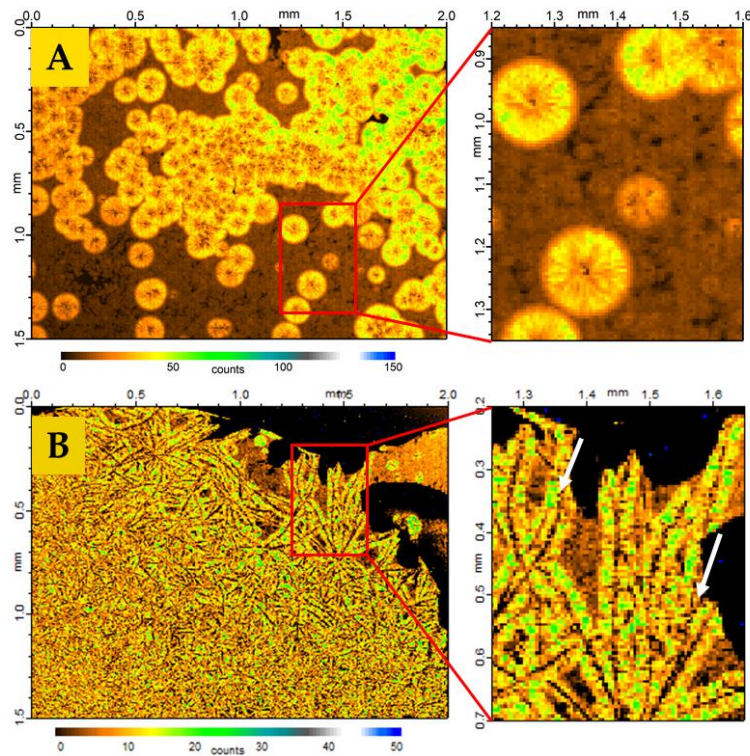


Figure 3.39. X-Ray micro beam images of MMw-HPm thin films with (A) 0wt% and (B) 2wt% of OXA-2 crystallized isothermally at 170°C, where yellow and black colours represent high and low intensities of the (110) SC plane.

Remarkably, the MMw-HPm-2%OXA morphology driven by the row nucleation on the OXA-2 offers the possibility to orient the OXA-2 needles crystals upon external forces such as shear to modify the PLA properties such as the mechanical behaviour.

Furthermore, the azimuthal integration of the (110) SC crystallographic reflection which define the growth direction (Figure 3.40) confirms the radial orientation of the MMw-

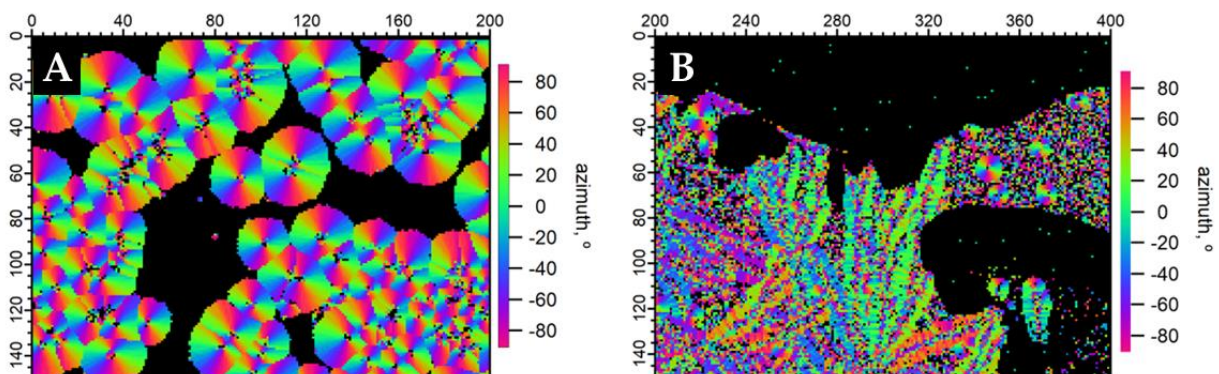


Figure 3.40. Azimuthal integration of (110) SC crystallographic reflection of MMw-HPm thin films with (A) 0wt% and (B) 2wt% of OXA-2 crystallized isothermally at 170°C.

HPm-0%OXA derivative spherulites whereas the perpendicular orientation to the OXA-2 needle crystals for the MMw-HPm-2%OXA indicates either an epitaxy growth or a geometric effect imposed by the high nucleation density on the OXA-2 crystals that impede the standard growth of the spherulites.

Similarly, the addition of OXA-2 to the PLA-SBC derivative with higher molecular weight, HMw-HPm-2%OXA, yielded a crystalline morphology dominated by row nucleation in contrast to the expected spherulitic structure without OXA-2, HMw-HPm-0%OXA probed by both POM (Figure 3.41) and micro-WAXS (Figure 3.42). However, larger crystalline domains are observed and in particular, higher branched morphology is obtained to the OXA-2 needle-like crystals. Although, the film thickness heterogeneity leads to films areas with different crystallization mechanisms. Likewise, the thinner film areas exhibit lower nucleation rate as it depends on the volume and thereby, the crystallization is dominated by crystal growth which depends on the temperature, yielding larger crystalline domains. In addition a likely gradient concentration of OXA-2 across the film should be expected due to the larger

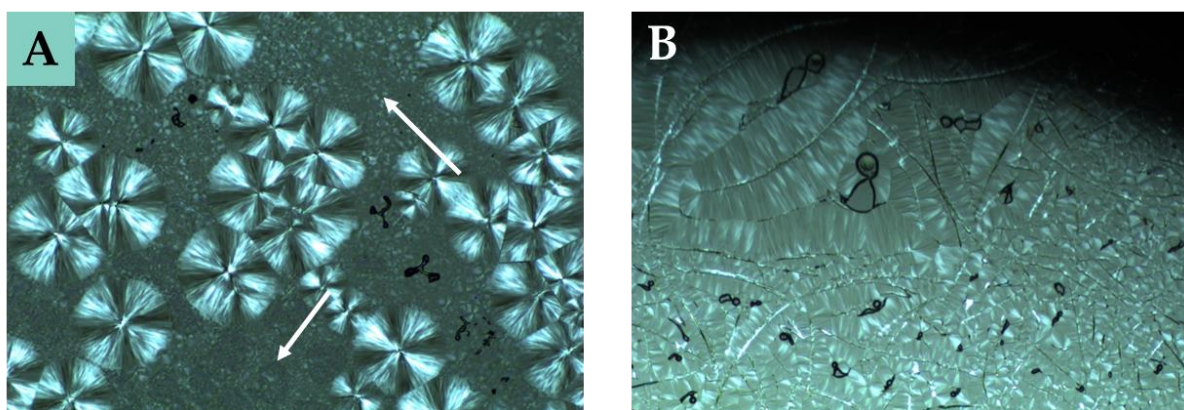


Figure 3.41. POM images of the thin films of HMw-HPm containing (A) 0 wt% and (B) 2wt% of OXA-2 isothermally crystallized at 170°C.

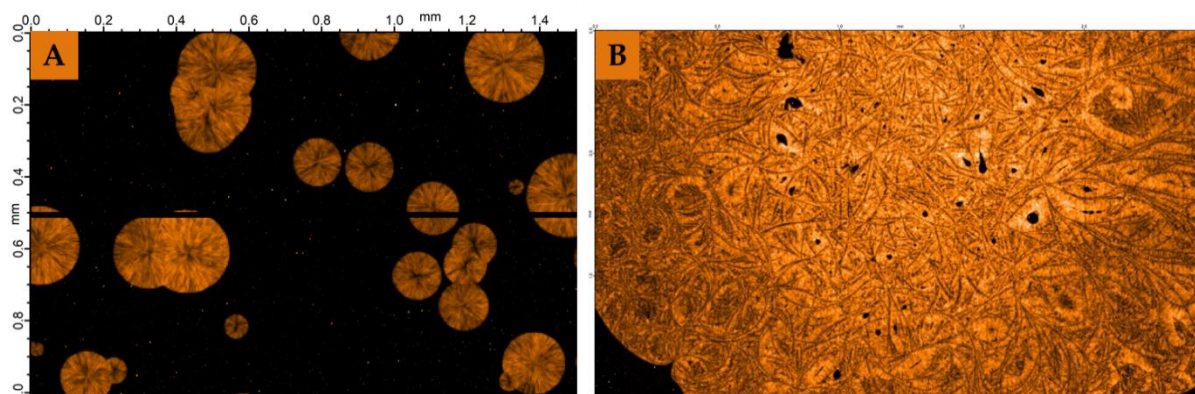


Figure 3.42. X-Ray micro beam images of MMw-HPm thin films with (A) 0wt% and (B)2wt% of OXA-2 crystallized isothermally at 170°C, where yellow and black colours represent high and low intensities of the (110) SC plane.

viscosity of the HMw-HPm derivative that will results on the branching of the OXA-2 crystals (**Figure 3.41**).

Moreover, the efficiency of OXA-2 as nucleating agent in the crystallization from the melt of the HMw-HPm PLA-SBC derivative was probed by DSC at 30°C/min (**Table A3.10**) as well as at high crystallization rates by coupling an optical microscope with a nanocalorimeter. The addition of OXA-2 to the PLA-SBC derivative enabled the crystallization at cooling rates up to 400°C/min, whilst the crystallization of the neat polymer was impede at cooling rates higher than 300°C/min (**Figure 3.43**).

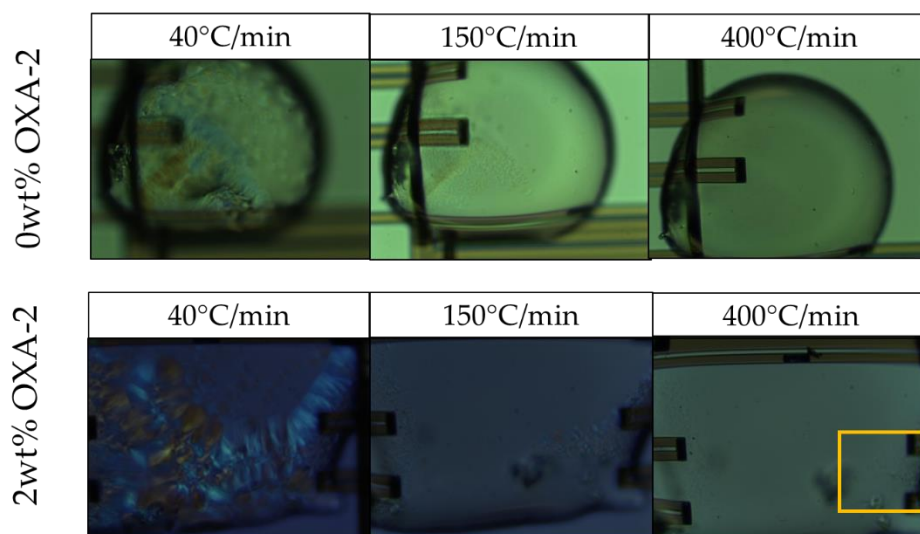


Figure 3.43. POM images obtained at room temperature of the HMw-HPm PLA-SBC derivative with 0 and 2wt% of OXA-2 crystallize from the melt in a nanocalorimeter.

Likewise, the efficiency of the OXA-2 as a nucleating agent was evaluated in the crystallization of an asymmetric PLA stereoblock copolymer (A-UHMw-HPm-0%OXA) that crystallizes from the melt at lower temperature, 105°C, as evidenced by the exothermic signal monitored by DSC during a cooling ramp at 5°C/min (**Figure A3.40**). Moreover, the DSC thermograms suggest that the neat A-UHMw-HPm-0%OXA crystallizes in both HC- and SC-phase as well as in their defective crystal forms (α' - and SC' - phases) as evidenced by the multiple and continuous melting endotherms monitored upon heating (**Table A3.10** and **Figure 3.40**). Likewise, the asymmetric blend of PLLA/ PDLA enantiomers was found to exhibit two well-defined endothermic signals representing both the HC and SC phases [82,83].

In addition, the crystallization temperature of the A-UHMw-HPM upon cooling from the melt was revealed 55°C lower than the MMw-HPm by DSC (**Figure A3.40**), which could be ascribed to the asymmetry as well as the lower chain mobility due to the higher molecular weight of the asymmetric PLA-SBC. Similarly to symmetric PLA-SBC, the T_c of the A-UHMw-HPM remained similar with the addition of OXA-2 as revealed by POM (**Figure A3.41**). Likewise, thin films of asymmetric PLA-SBC prepared at 0 and 2wt% of OXA-2, namely

UHMw-HPm-0%OXA and UHMw-HPm-0%OXA, respectively, were isothermally crystallized from the melt at 120°C and 150°C, respectively, as these were the temperatures at which the crystals were large enough to be later analysed with the X-ray microbeam. The nucleation density of the neat asymmetric UHMw-HPm-0%OXA was found significantly higher than the symmetric PLA-SBC-0wt%, probably due to the lower crystallization temperature (**Figure 3.44**).

Likewise, the morphology of the UHMw-HPm-2%OXA thin film crystallized at 150°C

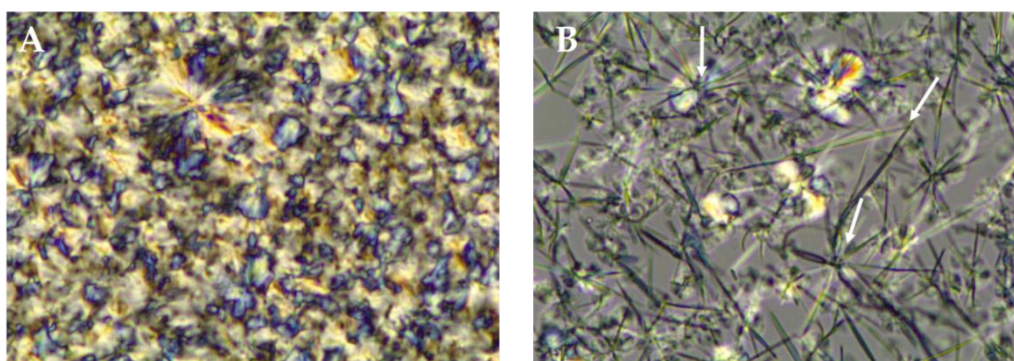


Figure 3.44. POM images of the thin films of A-UHMw-HPm containing (A) 0 wt% and (B) 2wt% of OXA-2 isothermally crystallized at 120°C and 150°C, respectively.

has shown that the nucleating agent formed a homogeneously distributed network with a similar needle dimension. In addition, mainly heterogeneous nucleation was found for the asymmetric UHMw-HPm-2%OXA with a standard radial spherulitic growth across the film, in contrast to the perpendicular orientation observed for the symmetric SC-PLA derivatives (MMw-HPm-2%OXA and HMw-HPm-2%OXA) during the isothermal step, suggesting lower nucleation along the needles like crystals formed by the nucleating agent that enable the growth of spherulites in all directions.

The homocrystal and stereocomplex phase distribution suggested by DSC was also probed by microWAXS in the thin films of both A-UHMw-HPm-0%OXA and A-UHMw-HPm-2%OXA. The A-UHMw-HPm-0%OXA presented a macroscopic phase separation upon crystallization from the melt, as revealed by the intensity distribution of both the (110)SC (**Figure 3.45A**) and (110)HC plane (**Figure 3.45B**). The macroscopic phase separation might be ascribed to the survival of the stereocomplex hydrogen bonds interactions in the melt that assist the phase separation upon high undercooling.

However, the nucleating agent, OXA-2, prevented the macroscopic phase separation observed in the UHMw-HPm-0%OXA and both HC- and SC-phases were homogeneously distributed across the film (**Figure 3.46**). Moreover, the stereocomplexation occurred firstly upon reaching 20-30µm of diameter (**Figure 3.46A**) followed by the homocomplexation in the

external part of the spherulites (**Figure 3.46B**), yielding a core shell structure as monitored by the X-Ray scattering microbeam.

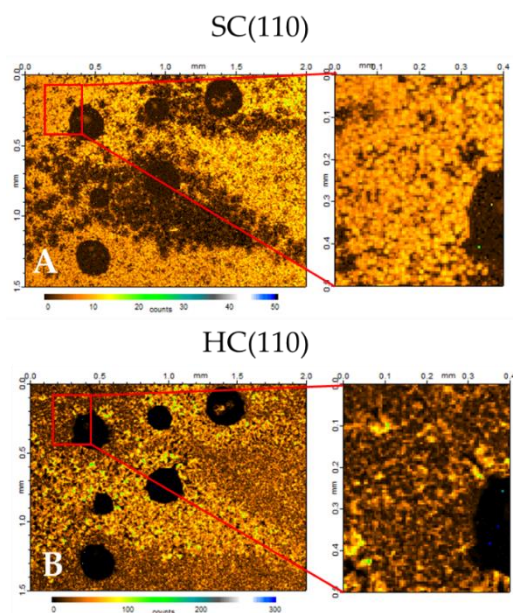


Figure 3.45. X-Ray micro beam images of A-UHMw-HPm thin films with 0xt% OXA-2 crystallized isothermally at 120°C, where yellow and black colours represent high and low intensities of the (110) SC plane (A) and the (110)HC plane.

Furthermore, the analysis of the (110) planes position of both the SC- and the HC-phases revealed a bimodal distribution of both phases, one crystal population a higher q values (represented by bluish spots in **Figure 3.47** and as 1 in the bottom right part of **Figure 3.47A and B**) that correspond to “perfect” crystals, and a second crystal population a lower q values (represented by greenish spots in **Figure 3.47** and as 0 in the bottom right part of **Figure 3.47 A and B**) that correspond to “defective” crystals, in agreement with the continuous melting endotherm revealed by DSC. In addition, the distribution of the “perfect” and “defective” crystals seemed heterogeneous across the film region analysed, where the “perfect” crystals distribution of one phase (blue region for the perfect SC-phase in **Figure 3.47**) overlaps with the “defective” crystals distribution of the second phase (**Figure 3.47B**, orange region for the phase), suggesting that stereocomplexation in a perfect crystal lattice leads homocomplexation in the α' -phase, whilst a disturbed SC-crystal lattice leads to defective HC to homocomplexation in the α -phase.

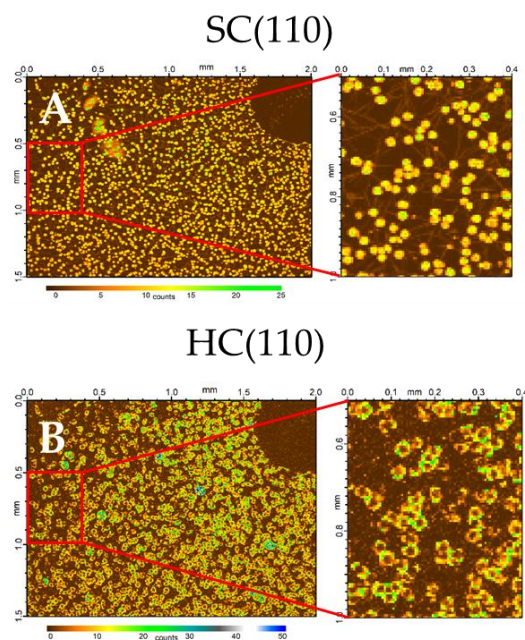


Figure 3.46. X-Ray micro beam images of A-UHMw-HPm thin films with 2wt% OXA-2 crystallized isothermally at 150°C, where yellow and black colours represent high and low intensities of the (110) SC plane (A) and the (110)HC plane (B).

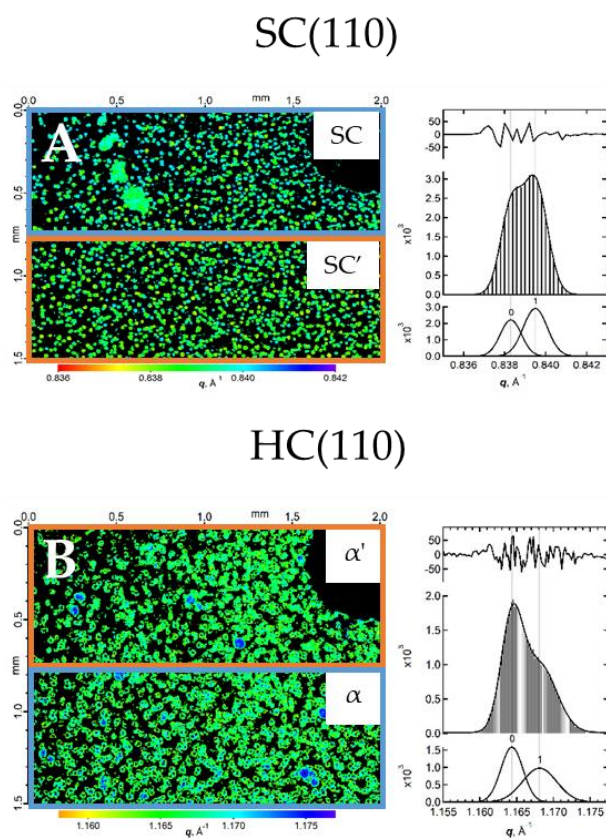


Figure 3.47. Peak position analysis of the X-Ray micro beam images of A-UHMw-HPm thin films with 2wt% OXA-2 crystallized isothermally at 150°C. (A) (110) SC plane and (B) (110)HC plane.

3.4 Conclusion

The investigation of the mechanism of crystallization of the novel PLA-SBC have revealed that:

- ✓ The increase of the M_w of PLA-SBC from 20kDa to 150kDa shifts the degradation temperature start from 220° to 240°C. Moreover, the increase of the elapsed time at the T_m to erase the thermal history of the PLA-SBC decreases both the M_w and the T_c , which might be ascribed to transesterification reactions.
- ✓ Both the T_c and T_m increases as the M_w increases. Importantly, the typical phase separation occurring in the SC-PLA formed from the blend as the molecular weight increases is absent in the high molecular weight PLA-SBC derivatives.
- ✓ The T_c obtained from the crystallization from the melt of the PLA-SBC was higher compared to both the enantiomeric counterparts (PLLA and PDLA) and the SC-PLA formed from the blend, as observed by POM. Moreover, the maximum spherulite growth rate of the HP-PLA and the PLA-SBC was found at ca. 130°C and 155°C, respectively, and a transition from the crystallization regime II to regime III was found at 170°C for the PLA-SBC, in line with previous experiments for both HP-PLA and SC-PLA formed from the blend.
- ✓ The crystallinity degree obtained from the PLA-SBC isothermally crystallized from the melt was ca. 10% higher than the enantiomeric blend of similar M_w PLA-derivatives. Moreover, the T_g of the PLA-SBC was slightly lower than the values reported for the SC-phase, suggesting a less rigid structure for the PLA-SBC compared to the enantiomeric blend.
- ✓ The PLA-SBC crystallize only in the SC- phase, as evidenced by WAXS analysis. However, the decrease of tacticity of the PLA-SBC derivatives (P_m value) from ca. 0,93 to 0,7 decrease the T_m from 210°C to 200°C, which might be ascribed to the formation of a “defective” SC-phase due to the stereoerrors along the polymeric chain.
- ✓ The mechanism of crystallization at isothermal conditions of the PLA-SBC is fairly well described by the Avrami model using the crystallization parameters obtained by both DSC and WAXS experiments, although the dimensional growth of the crystals obtained by the Avrami index n are in disagreement with the 3D crystal spherulite observed by POM.
- ✓ Moreover, the crystallization rate constant of the PLA-SBC is significantly higher than the SC-PLA formed from the enantiomeric blend, as observed by the three-times lower $t_{1/2}$ value obtained for the PLA-SBC.
- ✓ The crystallinity degree of the HM_w and high tacticity PLA-SBC was 44% at high cooling rates such as 50°C/min, increasing is suitability for industrial processing.

- ✓ Similarly, the Avrami modified model reproduced the kinetics of the PLA-SBC under non-isothermal conditions, although the Avrami index contradicted the values previously found for the SC-PLA formed from the blend and the dimensional growth of the crystals found by POM. Moreover, the crystallization rate at low cooling rates (5-20°C/min) decreases as the molecular weight and tacticity decreases.
- ✓ The Ozawa model might not described the crystallization kinetics of the PLA-SBC and the Avrami-Ozawa model results are in agreement with the Avrami results, which claimed that crystallization rate increases with increasing molecular weight and tacticity.
- ✓ The BHET molecule acts as plasticizer in the PLA-SBC matrix, as observed by the decrease of the T_c and T_g of the PLA-SBC derivative.
- ✓ The OXA-2 molecule acts as nucleating agent in the PLA-SBC matrix by increasing the crystallization rate of the PLA-SBC derivatives, as observed by DSC and POM analysis. Moreover, the efficiency of the OXA-2 as nucleating agent is higher for the PLA-SBC derivatives than for the homopolymer counterparts, which might be ascribed to an epitaxial crystallization of the PLA-SBC from the nucleating agent. In addition, OXA-2 changes the PLA-SBC crystal morphology from spherulite-like crystals to row nucleation, which could be useful for tailoring the mechanical properties of the PLA-SBC.

3.5 Experimental section

Materials

Solvents and reagents were acquired from Sigma-Aldrich. L- and D-lactide dimers were purchased from Rex scientific. The lactide dimers were purified three times by sublimation and then stored in a glovebox at 4°C. Toluene and tetrahydrofuran (THF) were pre-dried over sodium wire as well as distilled under nitrogen from sodium and subsequently stored over molecular sieves (3Å) in a glovebox. The *N,N'*-Bis(2-hydroxyethyl) terephthalamide (BHET) and the Oxalamide based organic compounds, OXA-4 and OXA-2, were kindly offered by the University of Maastricht [23,85].

Methods

Polymerizations

Polymerizations were performed as described previously in Chapter 2 [88].

Films preparation

Films containing PLA derivatives and the nucleating agents, BHET, OXA-4 and OXA-2, were prepared by solution cast. Briefly, individual 10wt% solutions in chloroform of the PLA derivatives and the nucleating agents were prepared by stirring during 1h. Subsequently, the nucleating agent solution was added to the PLA solution in different volumes to obtain the desired concentrations and the final solution was stirred for 1h. The solutions were solvent cast in a petri dish and the solvent was evaporated at room temperature. Finally, the films obtained were dry in vacuum at 80°C during 24h to eliminate all the solvent of the film.

Instrumentations and measurements

Thermogravimetric analysis (TGA)

The mass loss of the symmetric PLA-SBC was analysed by TGA with a Labsys evo instrument with a range temperature from 25°C to 1150°C. Briefly, 8-20 mg of the corresponding polymer was loaded in the TGA pans and heated from 30°C to 650°C at a constant heating rate of 5°C/min.

Gel permeation chromatography (GPC)

Molecular weight (M_n , M_w), as well as polydispersity index (PDI) of the afforded polymer derivatives, were determined from GPC using chloroform as eluent. The molecular weight characterization was performed with a Shimadzu Prominence-I LC-2030 equipped with a Shodex GPC KF-805L column (Shodex, Tokyo, Japan) and a Shimadzu RID-20A detector (Shimadzu, Kyoto, Japan). Analytical grade CHCl_3 was used as the mobile phase at 40 °C, with a flow rate of 1 mL/min. GPC samples were prepared by dissolving ca. 5 mg of the corresponding polymer in 1,5 mL of solvent and left overnight under constant agitation.

Thereafter, the samples were filtered over a 0,2 μm polytetrafluoroethylene (PTFE) syringe filter prior to its injection. Polystyrene with a molecular weight of 172 kDa was used as a reference to determine the overall molecular weight of the samples.

Polarized Optical Microscopy (POM)

The morphological development during the crystallization of the samples was monitored using polarized optical microscopy on an Olympus BX53 (x20 or x50 objective) microscope mounted with an Olympus DP26 camera and a Linkam heating stage (between cross-polarisers and using a wavelength of 530 nm). The samples were heated to 200°C and 230°C, for Homopolymers and stereoblock copolymers, respectively, and held at this temperature for 3 minutes. Non-isothermal crystallization was monitored by cooling down to room temperature at 5°C/min. Moreover, isothermal crystallization was monitored during 60 minutes after cooling to the desired isothermal crystallization temperature (T_{i-c}) at 30°C/min.

Differential Scanning Calorimetry (DSC)

DSC measurements. Differential scanning calorimetry (DSC) were performed using a DSC Discovery 250 (TA Instruments, New Castle, DE, USA) under nitrogen atmosphere. Temperature, heat flow and baseline were calibrated by using indium as a standard. DSC samples were prepared by loading around 5-7 mg of the polymer derivatives in Tzero Hermetic Aluminium pans (TA Instruments, New Castle, DE, USA). The thermal transitions and their corresponding enthalpies such as the temperature and enthalpy of crystallization upon cooling (T_c , ΔH_c), temperature and enthalpy of cold crystallization upon heating (T_{cc} , ΔH_{cc}), melting temperature and enthalpy of melting (T_m , ΔH_m) as well as the glass transition temperature (T_g) were calculated from the obtained thermograms.

The thermal degradation protocol consisted of a first heating ramp at 10 °C/min from 25 °C to 230 °C and held for 2, 5, 15, 30 and 60 min. Samples were then cooled down to 25 °C at a constant rate of 10 °C/min, heated to 230°C at 10°C/min and cooled down again at 10°C/min. The melting behaviour of all samples was observed by a new heating and cooling at 10°C/min.

The non-isothermal protocol consisted of a first heating ramp at 10 °C/min from 25 °C to 230 °C and held for 2 min at the melt to erase thermal history. Samples were then cooled to 25°C at different cooling rates (1, 10, 15, 20, 30 and 50°C/min).

The isothermal protocol 1 consisted of a first heating ramp at 10 °C/min from 25 °C to 230 °C and held for 2 min at the melt to erase thermal history. Samples were then cooled to the isothermal crystallization temperature (T_{i-c}) at 50°C/min, held 60 minutes and cooled down to 25°C at 2°C/min. Subsequently, the samples were heated at 10°C/min to 230°C and cooled down again to 25°C at 10°C/min. A variation of this protocol (isothermal protocol 2) was implemented by heating to 230°C right after the isothermal crystallization at the T_{i-c} .

Modulated-Differential Scanning Calorimetry (M-DSC)

M-DSC analysis were performed using a DSC Discovery 250 (TA Instruments, New Castle, DE, USA) under nitrogen atmosphere. The heat capacity signals were calibrated using the sapphire standard. M-DSC samples were prepared by loading around 5-7 mg of the polymer derivatives in Tzero Hermetic Aluminium pans (TA Instruments, New Castle, DE, USA). The isothermal protocol 2 was applied and modulation of the heat flow was applied to the heating ramp after the isothermal step, with 120s period, 1°C/min heating rate.

Wide-Angle X-Ray Scattering (WAXS) and Small-Angle X-Ray Scattering (SAXS)

SAXS/WAXS experiments were conducted both at DUBBLE (bm26) ESRF in Grenoble (France) and b111 NCD-SWEET at ALBA, Cerdanyola del Vallès (Spain) with an X-ray wavelength of 12 Kev. The WAXS patterns were recorded with a Pilatus 300 kw (1472 × 195 pixels configuration) with a pixel size of 172 μm² × 172 μm² in DUBBLE, whereas a Rayonix LX255-HS characterized by a pixel size of 40 μm² × 40 μm² and active area of 85 mm² × 255 mm² (h × v) was used at NCD-SWEET. The SAXS patterns were collected with a Pilatus 1M with a detector size (981 × 1043) with a pixel size of 172 μm × 172 μm at a sample to detector distance of ca. 2.5 m. The calibration of the scattering angular was performed with either α-Al₂O₃ (alumina) for the WAXS scattering angles or AgBe for the SAXS scattering angle range. The measured intensity in the 2D detectors was reduced to 1D intensity profiles using bubble [21] as a function of the scattering vector ($q = 4\pi/\lambda\sin\theta$) and reported in arbitrary units by correcting by the incident intensity and background subtraction.

The thermal protocol was performed with a Linkam stage DSC 600 with a 0,7x3 mm window.

The isothermal protocol was similar to the isothermal protocol 1 performed by DSC without the last heating and cooling ramps (due to the limited beamtime available). The non-isothermal protocol was also similar to the DSC non-isothermal protocol, with only one heating and cooling ramp.

The deconvolution of the 1D WAXS profile between 6 and 20 nm⁻¹ was accomplished with Lorentzian functions for the crystalline plane reflections and two pseudo-Voigt functions for the amorphous halo, as previously described for stereocomplexed PLA [34]. Moreover, the crystallinity values from the 1D WAXS patterns were obtained by the equation XX:

$$X_c = \frac{A_{crystalline}}{A_{crystalline} + A_{amorphous}} \times 100$$

where $A_{crystalline}$ and $A_{amorphous}$ are the area under the curve of the Lorentz and pseudo-voigt equations.

Furthermore, the SAXS intensity was corrected with the Lorentz correction function ($q^2I(q)$) and the Long period (L_p) was obtained with the position of the correlation peak, q_{\max} . The L_p , defined as the distance between crystalline lamellas, can be obtained from the equation:

$$L_p = \frac{2\pi}{q} = L_c + L_a$$

Where L_c and L_a represent the thickness of the crystalline and amorphous fraction, respectively. An approximation of the lamellar thickness can also be obtained from the equation:

$$L_c = L_p X_c$$

Scanning X-ray micro-diffraction (micro-beam)

Scanning X-ray micro-diffraction experiments were carried out using the microbeam facility at the ID13 beamline of the European Synchrotron Radiation Facility (ESRF) (Grenoble, France). The micron sized X-ray beam was focused to a spot size of $2 \times 2 \mu\text{m}^2$ in along both directions, (H x V), using compound Beryllium lenses. X-ray photons with energy of 13 keV were used in the experiments. 2D diffraction data were collected using an Eiger4M. The scanning of the samples was done in transmission geometry with the sample surface normal to the X-ray beam. After identification of the region of interest in the film sample by help of an on-axis optical microscope, the sample was using a high precision XYX gantry scanned in continuous mode. In this mode the sample is moved continuously through the beam focus of the X-ray beam while after each line scan the sample was vertically offset by an increment for the next line scan. The size of the illuminated sample volume is defined by the counting time of the acquisition scheme and the vertical displacement increment. The parameters were chosen to achieve a resolution in the two dimensional scan of $5 \times 5 \mu\text{m}^2$. The measurement geometry including the norm of the scattering vector q , where $|q| = 4\pi \sin(\theta)/\lambda$, was calibrated using several diffraction peaks of alpha-alumina using the PyFAI package available at the ESRF including data reduction and integration. The data analysis and visualization 2D diffractograms were done using home-built routines designed in Igor Pro software (Wavemetrics Ltd.).

Nanocalorimeter

A custom-built ultrafast microelectromechanical systems (MEMS)-based nanocalorimeter instrument [89] was used to study the crystallization of PLA-SBC from the melt a high cooling rates. Briefly, 30-40 ng of the PLA-SBC were positioned within the active area of the nanocalorimeter sensor using a micromanipulator. PLA-SBC derivative samples were heated to 230°C and cooled down to room temperature at cooling rates from 1000°C/min

to 40°C/min. The crystallization of the PLA-SBC derivative was evaluated visually by a polarized optical microscopy coupled to the nanocalorimeter sensor.

3.6 References

1. Muthukumar, M. Shifting Paradigms in Polymer Crystallization. In *Progress in understanding of polymer crystallization*; 2007; pp. 1–18.
2. Schick, C.; Androsch, R. Nucleation-Controlled Semicrystalline Morphology of Bulk Polymers. *Polym. Cryst.* **2018**, *1*, 1–15, doi:10.1002/pcr2.10036.
3. Hoffman, J.D.; Lauritzen, J.I. Crystallization of Bulk Polymers With Chain Folding : Theory of Growth of Lamellar Spherulites. *J. Res. Natl. Bur. Stand. Phys. Chem.* **1961**, *65*, 297–336.
4. Nakajima, A.; Hayashi, S.; Nishimura, H. Change in Lamellar Thickness of Polyethylene Single Crystal during Isothermal Annealing in Bulk. *Kolloid-Zeitschrift Zeitschrift für Polym.* **1969**, *229*, 107–116, doi:10.1007/BF01552703.
5. Hu, W. The Physics of Polymer Chain-Folding. *Phys. Rep.* **2018**, *747*, 1–50, doi:10.1016/j.physrep.2018.04.004.
6. Crist, B. Structure of Polycrystalline Agregates. In *Handbook of polymer crystallization*; Piorkowska, E., Rutledge, G.C., Eds.; 2013; pp. 73–121.
7. Zhang, M.C.; Guo, B.H.; Xu, J. *A Review on Polymer Crystallization Theories*; 2017; Vol. 7; ISBN 8610627845.
8. Righetti, M.C.; Gazzano, M.; Di Lorenzo, M.L.; Androsch, R. Enthalpy of Melting of A'- and α -Crystals of Poly(L-Lactic Acid). *Eur. Polym. J.* **2015**, *70*, 215–220, doi:10.1016/j.eurpolymj.2015.07.024.
9. Takahashi, K.; Sawai, D.; Yokoyama, T.; Kanamoto, T.; Hyon, S.H. Crystal Transformation from the α - to the β -Form upon Tensile Drawing of Poly(L-Lactic Acid). *Polymer (Guildf)*. **2004**, *45*, 4969–4976, doi:10.1016/j.polymer.2004.03.108.
10. Sawai, D.; Yokoyama, T.; Kanamoto, T.; Sungil, M.; Hyon, S.H.; Myasnikova, L.P. Crystal Transformation and Development of Tensile Properties upon Drawing of Poly(L-Lactic Acid) by Solid-State Coextrusion: Effects of Molecular Weight. *Macromol. Symp.* **2006**, *242*, 93–103, doi:10.1002/masy.200651015.
11. Xue, J.; Yan, L.; Tian, X.; Huang, D.; Redyy, N.; Yang, Y. Chemical Structure of Poly(Lactic Acid). In *Poly(Lactic Acid): Synthesis, Structures, Properties, Processing, and Applications*; Auras, R., Lim, L.-T., Selke, S.E.M., Tsuji, H., Eds.; 2010.
12. Lotz, B.A. Single Crystals of the Frustrated β -Phase and Genesis of the Disordered A'-Phase of Poly(L-Lactic Acid). *ACS Macro Lett.* **2015**, *4*, 602–605, doi:10.1021/acsmacrolett.5b00205.
13. Cartier, L.; Okihara, T.; Ikada, Y.; Tsuji, H.; Puiggali, J.; Lotz, B. Epitaxial Crystallization and Crystalline Polymorphism of Polylactides. *Polymer (Guildf)*. **2000**, *41*, 8909–8919, doi:10.1016/S0032-3861(00)00234-2.
14. Jong, S.J. De; Bosch, J.J.K. Den; Schuyl, P.J.W.; Hennink, W.E. Monodisperse Enantiomeric Lactic Acid Oligomers: Preparation, Characterization, and Stereocomplex Formation. *Macromolecules* **1998**, *31*, 1–6.

15. Di Lorenzo, M.L. Crystallization Behavior of Poly(l-Lactic Acid). *Eur. Polym. J.* **2005**, *41*, 569–575, doi:10.1016/j.eurpolymj.2004.10.020.
16. Pyda, M. Melting. In *Handbook of polymer crystallization*; Piorkowska, E., Rutledge, G.C., Eds.; Wiley, Hoboken, 2013; pp. 265–285.
17. Saeidlou, S.; Huneault, M.A.; Li, H.; Park, C.B. Poly(Lactic Acid) Crystallization. *Prog. Polym. Sci.* **2012**, *37*, 1657–1677, doi:10.1016/j.progpolymsci.2012.07.005.
18. Hoffman, J.D.; Millerr, R.L.; Marand, H.; Roitman, D.B. Relationship between the Lateral Surface Free Energy and the Chain Structure Ofmelt-Crystallized Polymers. *Macromolecules* **1992**, *25*, 2221–2229.
19. Yamazaki, S.; Itoh, M.; Oka, T.; Kimura, K. Formation and Morphology of “Shish-like” Fibril Crystals of Aliphatic Polyesters from the Sheared Melt. *Eur. Polym. J.* **2010**, *46*, 58–68, doi:10.1016/j.eurpolymj.2009.09.003.
20. Zhou, C.; Li, H.; Zhang, W.; Li, J.; Huang, S.; Meng, Y.; De Claville Christiansen, J.; Yu, D.; Wu, Z.; Jiang, S. Thermal Strain-Induced Cold Crystallization of Amorphous Poly(Lactic Acid). *CrystEngComm* **2016**, *18*, 3237–3246, doi:10.1039/c6ce00464d.
21. Cong, Y.; Liu, H.; Wang, D.; Zhao, B.; Yan, T.; Li, L.; Chen, W.; Zhong, Z.; Lin, M.C.; Chen, H.L.; et al. Stretch-Induced Crystallization through Single Molecular Force Generating Mechanism. *Macromolecules* **2011**, *44*, 5878–5882, doi:10.1021/ma201249y.
22. Nanocomposites, P.L.; Naffakh, M.; Rica, P.; Moya-lopez, C.; Castro-osma, J.A.; Alonso-moreno, C.; Moreno, D.A. The Effect of WS 2 Nanosheets on the Non-Isothermal Cold- and Melt-Crystallization Kinetics Of. *Polymers (Basel)*. **2021**, *13*, 2214.
23. Roy, M.; Zhelezniakov, M.; de Kort, G.W.; Hawke, L.G.D.; Leoné, N.; Rastogi, S.; Wilsens, C.H.R.M. On the Nucleation of Polylactide by Melt-Soluble Oxalamide Based Organic Compounds. *Polymer (Guildf)*. **2020**, *202*, doi:10.1016/j.polymer.2020.122680.
24. Tsuji, H. Poly(Lactic Acid) Stereocomplexes: A Decade of Progress. *Adv. Drug Deliv. Rev.* **2016**, *107*, 97–135, doi:10.1016/j.addr.2016.04.017.
25. Tsuji, H. Poly(Lactide) Stereocomplexes: Formation, Structure, Properties, Degradation, and Applications. *Macromol. Biosci.* **2005**, *5*, 569–597, doi:10.1002/mabi.200500062.
26. Zhang, J.; Sato, H.; Tsuji, H.; Noda, I.; Ozaki, Y. Differences in the CH₃…O=C Interactions among Poly(L-Lactide), Poly(L-Lactide)/Poly(D-Lactide) Stereocomplex, and Poly(3-Hydroxybutyrate) Studied by Infrared Spectroscopy. *J. Mol. Struct.* **2005**, *735–736*, 249–257, doi:10.1016/j.molstruc.2004.11.033.
27. Garlotta, D. A Literature Review of Poly (Lactic Acid). *J. Polym. Environ.* **2001**, *9*, 63–84.
28. Ikada, Y.; Jamshidi, K.; Tsuji, H.; Hyon, S.-H. Stereocomplex Formation between Enantiomeric Poly(Lactides). *Am. Chem. Soc.* **1987**, 904–906.
29. Tsuji, H.; Ikada, Y. Stereocomplex Formation between Enantiomeric Poly(Lactic Acid)s. 9. Stereocomplexation from the Melt. *Macromolecules* **1993**, *26*, 6918–6926.
30. Pan, P.; Han, L.; Bao, J.; Xie, Q.; Shan, G.; Bao, Y. Competitive Stereocomplexation, Homocrystallization, and Polymorphic Crystalline Transition in Poly(L-Lactic

- Acid)/Poly(D-Lactic Acid) Racemic Blends: Molecular Weight Effects. *J. Phys. Chem. B* **2015**, *119*, 6462–6470, doi:10.1021/acs.jpcc.5b03546.
31. Luo, F.; Fortenberry, A.; Ren, J.; Qiang, Z. Recent Progress in Enhancing Poly (Lactic Acid) Stereocomplex Formation for Material Property Improvement. *Front. Chem.* **2020**, *8*, 1–8, doi:10.3389/fchem.2020.00688.
 32. Bai, H.; Deng, S.; Bai, D.; Zhang, Q.; Fu, Q. Recent Advances in Processing of Stereocomplex-Type Polylactide. *Macromol. Rapid Commun.* **2017**, *1700454*, 1–12, doi:10.1002/marc.201700454.
 33. Lv, T.; Zhou, C.; Li, J.; Huang, S.; Wen, H.; Meng, Y.; Jiang, S. New Insight into the Mechanism of Enhanced Crystallization of PLA in PLLA/PDLA Mixture. *J. Appl. Polym. Sci.* **2018**, *135*, doi:10.1002/app.45663.
 34. Yang, C.F.; Huang, Y.F.; Ruan, J.; Su, A.C. Extensive Development of Precursory Helical Pairs Prior to Formation of Stereocomplex Crystals in Racemic Polylactide Melt Mixture. *Macromolecules* **2012**, *45*, 872–878, doi:10.1021/ma2026995.
 35. Li, Z.; Zhang, M.; Fan, X.; Ye, X.; Zeng, Y.; Zhou, H.; Guo, W.; Ma, Y.; Shao, J.; Yan, C. Hydrogen Bonding Assists Stereocomplexation in Poly(l-Lactic Acid)/Poly(d-Lactic Acid) Racemic Blends. *J. Polym. Sci. Part B Polym. Phys.* **2019**, *57*, 83–88, doi:10.1002/polb.24756.
 36. Zhang, M.; Fan, X.; Guo, W.; Zhou, H.; Li, Z.; Ma, Y.; Yan, C.; Dufresne, A. Insights into Stereocomplexation of Poly (Lactic Acid) Materials : Evolution of Interaction between Enantiomeric Chains and Its Role in Conformational Transformation in Racemic Blends. *ACS Appl. Polym. Mater.* **2022**, doi:10.1021/acsapm.2c00781.
 37. López-Rodríguez, N.; Martínez De Arenaza, I.; Meaurio, E.; Sarasua, J.R. Efficient Stereocomplex Crystallization in Enantiomeric Blends of High Molecular Weight Polylactides. *RSC Adv.* **2015**, *5*, 34525–34534, doi:10.1039/c4ra16994h.
 38. Liu, J.; Qi, X.; Feng, Q.; Lan, Q. Suppression of Phase Separation for Exclusive Stereocomplex Crystallization of a High-Molecular-Weight Racemic Poly (L - Lactide)/ Poly (D - Lactide) Blend from the Glassy State. *Macromolecules* **2020**, doi:10.1021/acs.macromol.0c00112.
 39. Sun, C.; Zheng, Y.; Xu, S.; Ni, L.; Li, X.; Shan, G.; Bao, Y.; Pan, P. Role of Chain Entanglements in the Stereocomplex Crystallization between Poly(Lactic Acid) Enantiomers. *ACS Macro Lett.* **2021**, doi:10.1021/acsmacrolett.1c00394.
 40. Pan, P.; Bao, J.; Han, L.; Xie, Q.; Shan, G.; Bao, Y. Stereocomplexation of High-Molecular-Weight Enantiomeric Poly(Lactic Acid)s Enhanced by Miscible Polymer Blending with Hydrogen Bond Interactions. *Polymer (Guildf).* **2016**, *98*, 80–87, doi:10.1016/j.polymer.2016.06.014.
 41. Xie, Q.; Guo, G.; Lu, W.; Sun, C.; Zhou, J.; Zheng, Y.; Shan, G.; Bao, Y.; Pan, P. Polymorphic Homocrystallization and Phase Behavior of High-Molecular-Weight Poly(L-Lactic Acid)/Poly(D-Lactic Acid) Racemic Mixture with Intentionally Enhanced Stereocomplexation Ability via Miscible Blending. *Polymer (Guildf).* **2020**, *201*, 122597, doi:10.1016/j.polymer.2020.122597.

42. Zhang, Y.; Wang, Y.; Wang, B.; Feng, X.; Ma, B.; Sui, X. Exclusive Formation of Poly(Lactide) Stereocomplexes with Enhanced Melt Stability via Regenerated Cellulose Assisted Pickering Emulsion Approach. *Compos. Commun.* **2022**, *32*, 101138, doi:10.1016/j.coco.2022.101138.
43. Feng, Y.; Lv, P.; Jiang, L.; Ma, P.; Chen, M.; Dong, W.; Chen, Y. Enhanced Crystallization Kinetics of Symmetric Poly (L -Lactide)/ Poly (D - Lactide) Stereocomplex in the Presence of Nanocrystalline Cellulose. *Polym. Degrad. Stab.* **2017**, *146*, 113–120, doi:10.1016/j.polymdegradstab.2017.10.002.
44. Ren, Q.; Wu, M.; Weng, Z.; Zhu, X.; Li, W.; Huang, P.; Wang, L.; Zheng, W.; Ohshima, M. Promoted Formation of Stereocomplex in Enantiomeric Poly(Lactic Acid)s Induced by Cellulose Nanofibers. *Carbohydr. Polym.* **2022**, *276*, 118800, doi:10.1016/j.carbpol.2021.118800.
45. Shao, J.; Xiang, S.; Bian, X.; Sun, J.; Li, G.; Chen, X. Remarkable Melting Behavior of PLA Stereocomplex in Linear PLLA/PDLA Blends. *Ind. Eng. Chem. Res.* **2015**, *54*, 2246–2253, doi:10.1021/ie504484b.
46. Coulembier, O.; Moins, S.; Raquez, J.; Meyer, F.; Mespouille, L.; Duquesne, E.; Dubois, P. Thermal Degradation of Poly (L -Lactide): Accelerating Effect of Residual DBU-Based Organic Catalysts. *Polym. Degrad. Stab.* **2011**, *96*, 739–744, doi:10.1016/j.polymdegradstab.2011.02.014.
47. Feng, L.; Bian, X.; Li, G.; Chen, X. Thermal Properties and Structural Evolution of Poly(l -Lactide)/Poly(d -Lactide) Blends. *Macromolecules* **2021**, *54*, 10163–10176, doi:10.1021/acs.macromol.1c01866.
48. Shyr, T.W.; Ko, H.C.; Wu, T.M.; Zhu, M. Effect of Storage Conditions on the Thermal Stability and Crystallization Behaviors of Poly(L-Lactide)/Poly(d-Lactide). *Polymers (Basel)*. **2021**, *13*, 1–14, doi:10.3390/polym13020238.
49. Tsuji, H. Hydrolytic Degradation. In *Poly(Lactic Acid): Synthesis, Structures, Properties, Processing, and Applications*; 2010; pp. 345–382 ISBN 9780470293669.
50. Carrasco, F.; Pagès, P.; Gámez-Pérez, J.; Santana, O.O.; MasPOCH, M.L. Processing of Poly(Lactic Acid): Characterization of Chemical Structure, Thermal Stability and Mechanical Properties. *Polym. Degrad. Stab.* **2010**, *95*, 116–125, doi:10.1016/j.polymdegradstab.2009.11.045.
51. Pan, P.; Kai, W.; Zhu, B.; Dong, T.; Inoue, Y. Polymorphous Crystallization and Multiple Melting Behavior of Poly(L-Lactide): Molecular Weight Dependence. *Macromolecules* **2007**, *40*, 6898–6905, doi:10.1021/ma071258d.
52. Shao, J.; Guo, Y.; Xiang, S.; Zhou, D.; Bian, X.; Sun, J.; Li, G.; Hou, H. The Morphology and Spherulite Growth of PLA Stereocomplex in Linear and Branched PLLA/PDLA Blends: Effects of Molecular Weight and Structure. *CrystEngComm* **2015**, *18*, 274–282, doi:10.1039/c5ce02017d.
53. Mathe, S.; Dimonie, D.; Cristea, M. Thermal Analysis and Polarized Light Microscopy as Methods to Study the Increasing of the Durability of PLA Designed for 3D Printing. *Int. J. Polym. Anal. Charact.* **2021**, *26*, 253–264, doi:10.1080/1023666X.2021.1880111.

54. Zhou, K. yu; Li, J. bo; Wang, H. xuan; Ren, J. Effect of Star-Shaped Chain Architectures on the Polylactide Stereocomplex Crystallization Behaviors. *Chinese J. Polym. Sci. (English Ed.)* **2017**, *35*, 974–991, doi:10.1007/s10118-017-1935-4.
55. Wang, H.F.; Chiang, C.H.; Hsu, W.C.; Wen, T.; Chuang, W.T.; Lotz, B.; Li, M.C.; Ho, R.M. Handedness of Twisted Lamella in Banded Spherulite of Chiral Polylactides and Their Blends. *Macromolecules* **2017**, *50*, 5466–5475, doi:10.1021/acs.macromol.7b00318.
56. Tsuji, H.; Ikada, Y. Crystallization from the Melt of Poly(Lactide)s with Different Optical Purities and Their Blends. *Macromol. Chem. Phys.* **1996**, *197*, 3483–3499, doi:10.1002/macp.1996.021971033.
57. Tsuji, H.; Tezuka, Y. Stereocomplex Formation between Enantiometric Poly(Lactic Acid)s. 12. Spherulite Growth of Low-Molecular-Weight Poly(Lactic Acid)s from the Melt. *Biomacromolecules* **2004**, *5*, 1181–1186, doi:10.1021/bm049835i.
58. Baratian, S.; Hall, E.S.; Lin, J.S.; Xu, R.; Runt, J. Crystallization and Solid-State Structure of Random Polylactide Copolymers: Poly(L-Lactide-Co-D-Lactide)S. *Macromolecules* **2001**, *34*, 4857–4864, doi:10.1021/ma001125r.
59. Di Lorenzo, M.L. Determination of Spherulite Growth Rates of Poly(L-Lactic Acid) Using Combined Isothermal and Non-Isothermal Procedures. *Polymer (Guildf.)* **2001**, *42*, 9441–9446, doi:10.1016/S0032-3861(01)00499-2.
60. De Santis, F.; Pantani, R.; Titomanlio, G. Nucleation and Crystallization Kinetics of Poly(Lactic Acid). *Thermochim. Acta* **2011**, *522*, 128–134, doi:10.1016/j.tca.2011.05.034.
61. Urbanovici, E.; Schneider, H.A.; Cantow, H.J. Some Considerations Concerning the Temperature Dependence of the Bulk Crystallization Rate. *J. Polym. Sci. part b Polym. Phys.* **1997**, *35*, 359–369.
62. Shyr, T.W.; Ko, H.C.; Wu, T.M.; Wu, T.M. Crystallisation and Spherulite Morphology of Polylactide Stereocomplex. *Polym. Int.* **2019**, *68*, 141–150, doi:10.1002/pi.5708.
63. Jiang, L.; Lv, P.; Ma, P.; Bai, H.; Dong, W.; Chen, M. Stereocomplexation Kinetics of Enantiomeric Poly(L-Lactide)/Poly(D-Lactide) Blends Seeded by Nanocrystalline Cellulose. *RSC Adv.* **2015**, *5*, 71115–71119, doi:10.1039/C5RA12586C.
64. Vasanthakumari, R.; Penning, A.J. Crystallization Kinetics of Poly (L-Lactic Acid). *Polymer (Guildf.)* **1983**, *24*, 175–178.
65. Okui, M.; Umemoto, S.; Kawano, R.; Mamum, A. Temperature and Molecular Weight Dependencies of Polymer Crystallization. In *Progress in understanding of polymer crystallization*; Reiter, G., Strobl, G.R., Eds.; 2007; pp. 392–423.
66. Liu, S.; Yu, Y.; Cui, Y.I.; Zhang, H.; Mo, Z. Isothermal and Nonisothermal Crystallization Kinetics of Nylon-11. *J. Appl. Polym. Sci.* **1998**, *70*, 2371–2380.
67. Liu, T.; Mo, Z.; Zhang, H. Nonisothermal Crystallization Behavior of a Novel Poly (Aryl Ether Ketone): PEDEK_mK. *J. Appl. Polym. Sci.* **1997**, *67*, 815–821.
68. Ilaria D’Auria, Massimo Christian D’Alterio, Consiglia Tedesco, and C.P. Tailor-Made Block Copolymers of L-, D- and Racemates and 3-Caprolactone via One-Pot Sequential

- Ring Opening Polymerization by Pyridylamidozinc(II) Catalysts. *RSC Adv.* **2019**, *9*, 32771–32779, doi:10.1039/C9RA07133D.
69. Rosen, T.; Goldberg, I.; Navarra, W.; Venditto, V.; Kol, M. Divergent $\{[\text{ONNN}]\text{Mg}-\text{Cl}\}$ Complexes in Highly Active and Living Lactide Polymerization. *Chem. Sci.* **2017**, *8*, 5476–5481, doi:10.1039/C7SC01514C.
 70. Jiang, Q.; Yang, C.C.; Li, J.C. Size-Dependent Melting Temperature of Polymers. *Macromol. Theory Simulations* **2003**, *12*, 57–60.
 71. Höhne, G.W.H. Another Approach to the Gibbs – Thomson Equation and the Melting Point of Polymers and Oligomers. *Polymer (Guildf)*. **2002**, *43*, 4689–4698.
 72. Li, L.; Zhong, Z.; De Jeu, W.H.; Dijkstra, P.J.; Feijen, J. Crystal Structure and Morphology of Poly(L-Lactide-b-D-Lactide) Diblock Copolymers. *Macromolecules* **2004**, *37*, 8641–8646, doi:10.1021/ma049077o.
 73. Müller, A.J.; Michell, R.M.; Lorenzo, A.T. Isothermal Crystallization Kinetics of Polymers. In *Polymer morphology*; 2016; pp. 181–203 ISBN 9781118452158.
 74. Lorenzo, A.T.; Arnal, L.; Albuerne, J.; Mu, A.J. DSC Isothermal Polymer Crystallization Kinetics Measurements and the Use of the Avrami Equation to Fit the Data : Guidelines to Avoid Common Problems. *Polym. Test.* **2007**, *26*, 222–231, doi:10.1016/j.polymertesting.2006.10.005.
 75. Han, L.; Shan, G.; Bao, Y.; Pan, P. Exclusive Stereocomplex Crystallization of Linear and Multi-Arm Star-Shaped High-Molecular-Weight Stereo Diblock Poly (Lactic Acid) s Exclusive Stereocomplex Crystallization of Linear and Multi-Arm Star-Shaped High-Molecular-Weight Stereo Diblock Poly (. *J. Phys. Chem. B* **2015**, *119*, 14270–14279, doi:10.1021/acs.jpcc.5b06757.
 76. Sun, J.; Yu, H.; Zhuang, X.; Chen, X.; Jing, X. Crystallization Behavior of Asymmetric PLLA / PDLA Blends. *J. Phys. Chem. B* **2011**, 2864–2869.
 77. Su, Z.; Guo, W.; Liu, Y.; Li, Q.; Wu, C. Non-Isothermal Crystallization Kinetics of Poly(Lactic Acid)/Modified Carbon Black Composite. *Polym. Bull.* **2009**, *62*, 629–642, doi:10.1007/s00289-009-0047-x.
 78. Li, C.; Dou, Q. Non-Isothermal Crystallization Kinetics and Spherulitic Morphology of Nucleated Poly (Lactic Acid): Effect of Dilithium Hexahydrophthalate as a Novel Nucleating Agent. *Thermochim. Acta* **2014**, *594*, 31–38.
 79. Li, Y.; Han, C.; Zhang, X.; Dong, Q.; Dong, L. Effects of Molten Poly (d , l -Lactide) on Nonisothermal Crystallization in Stereocomplex of Poly (l -Lactide) with Poly (d -Lactide). *Thermochim. Acta* **2013**, *573*, 193–199, doi:10.1016/j.tca.2013.09.035.
 80. Qiu, Z.; Mo, Z.; Zhang, H.; Sheng, S.; Song, C. Crystallization Behavior of a Novel Ether Ketone Polymer Containing Meta-Phenylene Linkage : PEKEKK (T / I) Crystallization Behavior of a Novel Ether Ketone Polymer Containing Meta -Phenylene Linkage : PEKEKK (T / I). *Macromol. Sci. Part B Phys.* **2000**, *39*, 373–385, doi:10.1081/MB-100100392.
 81. Piorkowska, E.; Galeski, A.; Haudin, J. Critical Assessment of Overall Crystallization

- Kinetics Theories and Predictions. *Prog. Polym. Sci.* **2006**, *31*, 549–575, doi:10.1016/j.progpolymsci.2006.05.001.
82. Hu, J.; Wang, J.; Wang, M.; Ozaki, Y.; Sato, H.; Zhang, J. Investigation of Crystallization Behavior of Asymmetric PLLA/PDLA Blend Using Raman Imaging Measurement. *Polymer (Guildf)*. **2019**, doi:10.1016/j.polymer.2019.03.049.
 83. Schmidt, S.C.; Hillmyer, M.A. Polylactide Stereocomplex Crystallites as Nucleating Agents for Isotactic Polylactide. *J. Polym. Sci. Part B Polym. Phys.* **2001**, doi:10.1002/1099-0488(20010201)39:3<300::AID-POLB1002>3.0.CO;2-M.
 84. Vaes, D.; Van Puyvelde, P. Semi-Crystalline Feedstock for Filament-Based 3D Printing of Polymers. *Prog. Polym. Sci.* **2021**.
 85. Leone, N.; Roy, M.; Saidi, S.; Kort, G. De; Hermida-merino, D.; Wilsens, C.H.R.M. Improving Processing, Crystallization, and Performance of Poly-L-Lactide with an Amide-Based Organic Compound as Both Plasticizer and Nucleating Agent. *ACS Omega* **2019**, *4*, 10376–10387, doi:10.1021/acsomega.9b00848.
 86. Bocqué, M.; Voirin, C.; Lapinte, V.; Caillol, S.; Robin, J.J. Petro-Based and Bio-Based Plasticizers: Chemical Structures to Plasticizing Properties. *J. Polym. Sci. Part A Polym. Chem.* **2016**, *54*, 11–33, doi:10.1002/pola.27917.
 87. Roy, M.; Zhelezniakov, M.; de Kort, G.W.; Hawke, L.G.D.; Leoné, N.; Rastogi, S.; Wilsens, C.H.R.M. On the Nucleation of Polylactide by Melt-Soluble Oxalamide Based Organic Compounds. *Polymer (Guildf)*. **2020**, *202*, doi:10.1016/j.polymer.2020.122680.
 88. Moya-Lopez, C.; Bravo, I.; Castro-Osma, J.A.; Chapron, D.; Bourson, P.; Vagner, C.; Cochez, M.; Leon, N.; Alonso-Moreno, C.; Hermida-Merino, D. Synthesis of High Molecular Weight Stereo-Di-Block Copolymers Driven by a Co-Initiator Free Catalyst. *Polymers (Basel)*. **2022**, *14*, 1–16, doi:10.3390/polym14020232.
 89. Rosenthal, M.; Melnikov, A.P.; Rychkov, A.A.; Doblaz, D.; Anokhin, D. V.; Burghammer, M.; Ivanov, D.A. Design of a Combined Setup for Simultaneous Measurements of the Microstructural and Thermo-Analytical Parameters of Nanogram-Size Samples. *Appl. Mech. Mater.* **2015**, doi:10.4028/www.scientific.net/amm.788.136.

CHAPTER 4

Multifunctional PLA/Gelatin Bionanocomposites for Tailored Drug Delivery Systems

Table of contents

4.1 Introduction	173
4.2 Aims and objectives	175
4.3 Results and discussion	177
4.3.1 <i>Selection and characterization of PLA-derivatives</i>	178
4.3.2 <i>Nanoparticles formulation</i>	181
4.3.3 <i>Nanoparticles characterization</i>	182
4.3.4 <i>Bionanocomposite formation</i>	186
4.3.5 <i>Rheological properties of the bionanocomposite</i>	189
4.3.6 <i>Drug release analysis</i>	191
4.4 Conclusions	193
4.5 Experimental section	195
4.5.1 <i>Materials</i>	195
4.5.2 <i>Methods</i>	195
4.5.2.1 <i>Gelatin extraction</i>	195
4.5.2.2 <i>Polymerizations</i>	195
4.5.2.3 <i>Nanoparticles formulations</i>	195
4.5.2.4 <i>Bionanocomposites generation</i>	196
4.5.3 <i>Instrumentation and measurements</i>	196
4.5.3.1 ^1H NMR	196
4.5.3.2 GPC analysis	196
4.5.3.3 <i>Optical rotation</i>	196
4.5.3.4 <i>DLS technique</i>	196
4.5.3.5 SEM	197
4.5.3.6 <i>Cryo-SEM</i>	197
4.5.3.7 <i>DSC measurements</i>	197
4.5.3.8 <i>Raman spectroscopy</i>	198
4.5.3.9 <i>Small-angle X-ray scattering (SAXS) and wide-angle X-ray scattering (WAXS)</i>	198
4.5.3.10 <i>Rheological experiments</i>	198
4.5.3.11 <i>Release studies</i>	199
4.6 References	201
 CHAPTER 4. APPLICATION	 171

4.1 Introduction

Nanoparticles (NP) emerged in the 1970s as a drug delivery system (DDS) approach to improve the stability and solubility of the encapsulated molecules, promote drug delivery across cellular membranes as well as enhance drug circulation duration, improving safety and efficacy [1]. The composition of the designed nanoparticles has ranged from natural materials such as chitosan, dextran and gelatin or inorganic materials such as gold, silica and Cd/Zn as well as synthetic polymeric NP [2]. In particular, polymeric NP have recently received great interest due to the possibility to tailor the drug release rate by varying polymeric architectural parameters such as crystallinity, hydrophilicity or glass transition temperature [3]. Polylactide (PLA) is among the most commonly used polymers for nanoparticle formulation development due to its biocompatibility. As described in Chapter 1, PLA is a bio-based and polymorphic polyester comprising a chiral carbon in its structure that yields a wide variety of nanostructured derivatives (isotactic, atactic, syndiotactic, stereo-complexed, etc.) [4–6] featuring different physicochemical properties. In addition, the processing conditions during the formation of the NP determine the kinetic trapped or thermodynamic state of the final material that affect significantly the final polymer characteristics such as crystallinity degree and crystalline phase (**Figure 1.2**, Chapter 1), which influence the drug release rate [3]. Particularly, polyesters exhibiting low glass transition temperature (T_g), melting temperature (T_m), and degree of crystallinity generally feature higher drug release [7,8]. Furthermore, amorphous PLA is characterized by soft and elastic mechanical properties, whilst semicrystalline PLA is stiff and robust [9], which will invariably define the drug release. Likewise, the drug release rate from PLA nanoparticles exhibiting stereocomplex (SC) phase is expected to decrease compared to the HP counterpart due to the stabilization by specific C-H...O-H hydrogen bonds of the crystalline phase that increases its hydrolytic resistance [10]. However, the impact of the processing parameters of the formation of the nanoparticles on the final nanoparticles release kinetics is generally found inconsistent due to the lack of mechanistic process control as well as the unusual analysis of the structure–properties relationship of the formulated nanoparticles. However, systematic studies correlating the structure-processing-properties relationship of nanoparticles formulation have been recently accomplished [3,11].

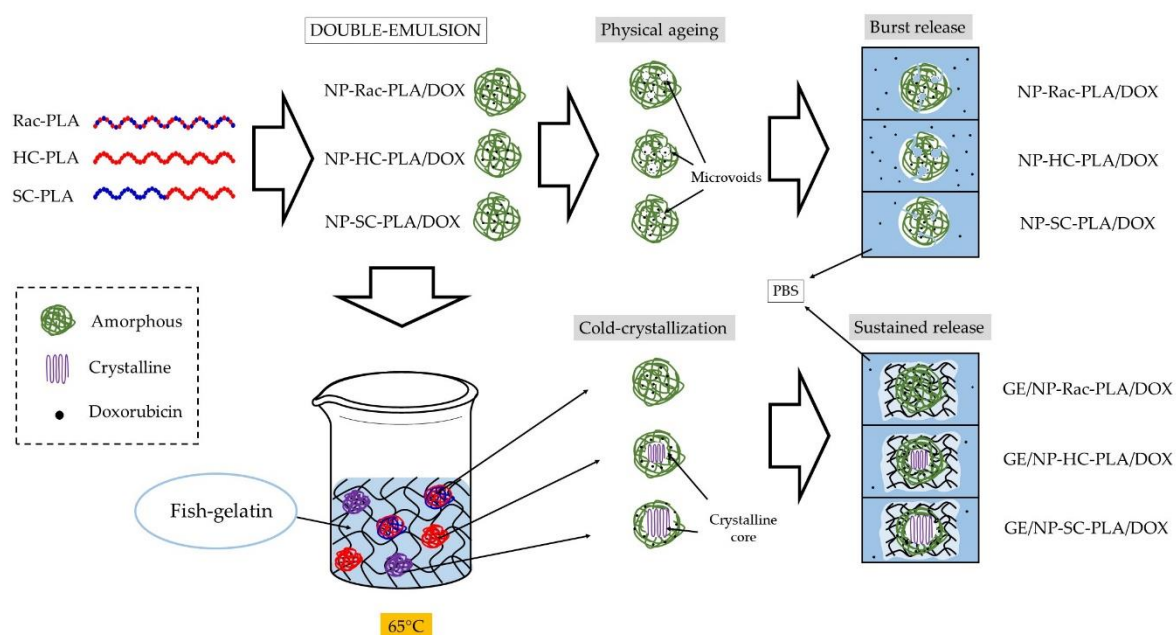
The hydrophobic character of PLA increases the contact angle with water, which diminishes the interaction with physiological fluids and cell adhesion, which is commonly faced by copolymerizing PLA with hydrophilic monomers such as polyethyleneglycol (PEG) or poly-glycolic acid (PGA) to afford block copolymers with enhanced biocompatibility [12–14]. Recently, nanoparticles generated from poly-L-lactide (PLLA)-3-ethylglycolide and poly-D-lactide (PDLA)-3-ethylglycolide were successfully formulated featuring the SC phase as well as attaining crystallinity degrees up to 50%. However, a long (7 days) stereocomplexation process from solution was required to obtain crystallized nanoparticles [15]. In addition, PLA

micelles crystallized in SC-phase were also achieved from PEG-PLLA-PDLA stereoblock copolymers by the nanoprecipitation method, which exhibited a slower drug release rate than the amorphous and isotactic counterpart [16]. However, the copolymerization of PLA with PGA or PEG usually deters the crystallization of the nanoparticles, limiting the physicochemical properties of the PLA-derivatives to the characteristic features of the amorphous phase [15] that neutralize the PLA chirality effect on the molecular mobility and the relaxation process [17]. Alternative processing methods are urged to favor the hydrophilicity of the PLA-based material whilst retaining the tunability of the physicochemical properties for the nanostructured PLA derivatives. Several bio-based materials have been previously used for the fabrication of bioscaffolds such as collagen, chitosan, alginate, gelatin, silk, etc. [18]. Alginate is an attractive material for biomedical applications due to its structural similarities to polysaccharides; however, it is unable to meet concomitantly the different required parameters for tissue engineering applications such as the degradation degree, the mechanical properties and bioactivity [19]. Similarly, collagen-based scaffolds for the regeneration of tissues such as nerves, bone, cartilage or skin were also developed with the detrimental low solubility in water that turns gelatin into a better candidate for tissue engineering [20]. Gelatin is a natural biopolymer obtained from the denaturation of collagen [21] that preserves key bioactive functions of collagen for biomedical applications, such as cell adhesion and proliferation [22]. Moreover, gelatin is widely used in the food and cosmetic industries, and particularly, fish gelatin is becoming increasingly used for biomedical applications due to a likely less intense immune reaction in the human body than mammalian gelatin [23] as well as an approach to revalorize the by-products from fish industrial processes [24]. Moreover, gelatin can be processed in several formats depending on the intended applications, such as electrospun matrices for wound healing [25], microspheres for being loaded with a growth factor for bone regeneration [26], nanoparticles as nanocarriers for anticancer therapeutic agents [27], protein, gene and vaccines delivery [28], DDS for regenerative medicine or three-dimensional scaffolds for drug screening [29]. PLA/gelatin-based scaffolds were frequently used as a matrix for tissue engineering or drug delivery. Recently, tetracycline-loaded PLLA microparticles embedded in a porous gelatin scaffold exhibited controlled release behavior, biocompatibility as well as antibacterial activity [30]. Furthermore, an electrospun composite scaffold of polycaprolactone and gelatin with curcumin-loaded PLA microparticles exhibited biocompatibility and good mechanical properties for wound-healing applications [31]. However, the design of bionanocomposites containing crystalline PLA nanoparticles was generally dismissed as an approach to tailor the drug delivery rate.

4.2 Aims and objectives

The main objective of Chapter 4 is the generation of a series of bionanocomposites composed of shark gelatin and PLA nanoparticles featuring different nanostructures to design multifunctional drug delivery systems with tailored release rates and local applicability (**Scheme 4.1**). To accomplish the main objective, the following steps were followed, in collaboration with the Universities of Vigo and Castilla-La Mancha, as well as The European Synchrotron Radiation Facility (ESRF):

- ✓ Selection of three PLA-derivatives described in Chapter 2 exhibiting different chain architecture and characterization of its nanostructure.
- ✓ Formulation and characterization of **PLA nanoparticles** with two different antitumoral compounds based on the three different PLA derivatives selected.
- ✓ **Blending of PLA nanoparticles with fish gelatin** at 65°C to generate the multifunctional bionanocomposite.
- ✓ Characterization of the **storage capability and the feasibility for local administration** of the bionanocomposite.
- ✓ **Drug release analysis** from both the PLA nanoparticles, gelatin hydrogel network and the bionanocomposite.



Scheme 4.1. Summary of the steps followed along the chapter to obtain the bionanocomposites.

4.3 Results and discussion

As state in the introduction, the discussion of the main results and the conclusion will be presented firstly and the experimental techniques will be briefly described at the end of the chapter. Moreover, some of the data herein described have already been discussed in Chapter 2 and 3, but they will be repeated for the sake of convenience and fluidity when comparing results. Furthermore, since the amount of nanoparticles obtained by the double emulsion method is limited, not all formulations could be analysed by all tests. However, triplicate measurements have been performed to ensure the reproducibility of the data. The correspondence between the abbreviated name of the samples and its compositions is described in **Table 4.1**.

Table 4.1. Correspondence between the abbreviated name and the composition.

NAME	GELATIN	PLA	BULK POLYMER/ NANOPARTICLE	DRUG
Rac-PLA	-	Racemic	Bulk	-
HC-PLA	-	Homopolymer	Bulk	-
SC-PLA	-	Stereoblock copolymer	Bulk	-
GE	Yes	-	-	-
GE/DOX	Yes	-	-	Doxorubicin
NP-Rac-PLA	-	Racemic	Nanoparticle	-
NP-HC-PLA	-	Homopolymer	Nanoparticle	-
NP-SC-PLA	-	Stereoblock copolymer	Nanoparticle	-
NP-Rac-PLA/DOX	-	Racemic	Nanoparticle	Doxorubicin
NP-HC-PLA/DOX	-	Homopolymer	Nanoparticle	Doxorubicin
NP-SC-PLA/DOX	-	Stereoblock copolymer	Nanoparticle	Doxorubicin
NP-Rac-PLA/DAS	-	Racemic	Nanoparticle	Dasatinib
NP-HC-PLA/DAS	-	Homopolymer	Nanoparticle	Dasatinib
NP-SC-PLA/DAS	-	Stereoblock copolymer	Nanoparticle	Dasatinib
GE/NP-Rac-PLA/DOX	Yes	Racemic	Nanoparticle	Doxorubicin

GE/NP-HC-PLA/DOX	Yes	Homopolymer	Nanoparticle	Doxorubicin
GE/NP-SC-PLA/DOX	Yes	Stereoblock copolymer	Nanoparticle	Doxorubicin

4.3.1 Selection and characterization of PLA-derivatives

Three PLA-derivatives with different nanostructures and medium molecular weight (M_n) were generated, namely racemic-PLA (PDLLA; rac-PLA), homopolymer-PLA (PLLA; HC-PLA) and in particular the long-desired stereo-diblock-PLA (PLLA-*b*-PDLA; SC-PLA), by Ring-Opening Polymerization (ROP) using our novel alkyl zinc organometallic heteroscorpionate initiator as previously described in Chapter 2 [32]. The selected PLA derivatives possess either amorphous or semicrystalline nanostructures with different crystalline phases. The molecular structure and M_n of the PLA derivatives were characterized by ^1H NMR and GPC, respectively (Table 4.2 and Figures A4.1–A4.3). Moreover, the L-LA/D-LA ratio was estimated to be higher than 98% for the HC-PLA and close to 50% for rac-PLA and SC-PLA, as analyzed by polarimetry measurements (Table 4.2). Furthermore, the P_m values, known as the probability of isotactic enchainment in which $P_m = 0.5$ is a random insertion whilst isotactic enchainment is designated by $P_m = 1$ [33], were obtained from deconvoluted homonuclear decoupling ^1H NMR spectra (Appendix A2) and confirmed the atactic character of the rac-PLA and the isotactic character of HC-PLA and SC-PLA (Table 4.2).

Table 4.2. Bulk polymer characterization.

Sample	Name	M_n (g/mol) ^a	PDI ^b	T_g (°C) ^c	T_c (°C) ^d	ΔH_c (J/g) ^e	T_m (°C) ^f	ΔH_m (J/g) ^g	X_c (%) ^h	P_m ⁱ	$[\alpha]$ ^j
PDLLA	Rac-PLA	59.594	1,77	24,12	-	-	-	-	-	0,52	-1,1
PLLA	HC-PLA	36.047	1,92	40,84	101,24	46,102	170,24	49,538	53,75	0,99	-159,4
(*)PLLA- <i>b</i> - PDLA	SC-PLA	35.253	2,25	41,28	113,83	44,767	193,93	46,91	33,03	0,90	-1,07

^a Molecular weight in number average obtained by GPC relative to polystyrene standards in chloroform. ^b PDI= M_w/M_n ; Polydispersity Index obtained by GPC. ^c Glass transition temperature. ^d Crystallization temperature. ^e Crystallization enthalpy. ^f Melting temperature. ^g Melting enthalpy. ^h Crystallinity $X_c = \frac{\Delta H_f}{\Delta H_f^0} \times 100$ with $\Delta H_{fHC}^0 = (93.7 \text{ J/g, } ^1)$ and $\Delta H_{fSC}^0 = (142 \text{ J/g})$. ⁱ Probability of isotactic enchainment calculated from homonuclear decoupling ^1H NMR spectra after deconvolution; calculations based on CEC statistics [34]. ^j Specific optical rotation ($(\alpha)_{\text{PLLA}} = -173^\circ$) [35]. (*) Same polymer as Entry 4 in Table 2.3.

Firstly, the nanostructure of the bulk polymer derivatives was characterized to understand the structure–properties relationship of the selected PLA derivatives to design different release rates. The thermal transitions of the bulk polymers were studied by DSC (Table 4.2 and Figure 4.1) to understand the crystallization mechanism that will determine the nanostructure generated at the formulation conditions. Rac-PLA exhibited a T_g at 24 °C, which was notably lower than values reported in the literature [36], which is likely due to the lower molecular weight [37], whilst isotactic PLA-derivatives, namely HC- and SC-PLA, exhibited a T_g c.a. 40 °C. Additionally, only the HC- and SC-PLA exhibited crystallization and melting transitions, as both the T_c and T_m of SC-PLA were 13 °C higher than those of HC-PLA (Figure 4.1A). Notably, the HC-PLA exhibited a double endothermic peak at 161 °C (P_{HC1}) and 167 °C

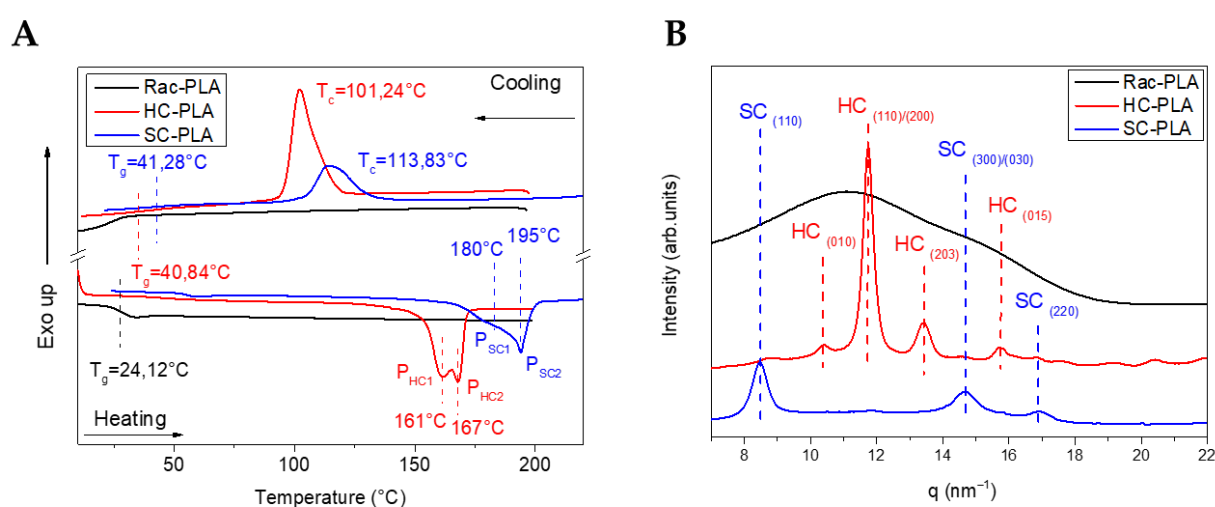


Figure 4.1. DSC thermogram (A) and WAXS patterns (B) of bulk polymer at room temperature.

(P_{HC2}), corresponding to the recrystallization of the α' - into the α -phase and the subsequent melting of the latter [38]. Moreover, the SC-PLA exhibited also a double melting peak (at 180 °C (P_{SC1}) and 195 °C (P_{SC2})) likely ascribed to the melt-recrystallization process of the α -phase into the stereocomplex (SC) phase [39]. The melting enthalpy for both HC- and SC-PLA was ca. 47 J/g. However, the crystallinity was 20% higher for the HC-PLA due to the lower ΔH_m° value.

Furthermore, the crystal phase of the bulk polymers was analyzed by Wide-Angle X-Ray Scattering (WAXS) (Figure 4.1B). Only an amorphous halo was found for rac-PLA in agreement with the atactic character obtained from the P_m value. The characteristic pattern of the α -phase at (010), (110)/(200), (203) and (015) (q (nm⁻¹)= 10.65, 11.9, 13.6 and 15.7) was observed for the HC-PLA, whilst the SC-PLA showed high-intensity reflections of the SC phase at (110), (300)/(030) and (220) (q (nm⁻¹) = 8.5, 14.7 and 17) and a low-intensity reflection at (110)/(200) characteristic of the α -phase. The presence of both α - and SC- phases on the SC-PLA, which is in agreement with the double-melting peak observed by DSC, is likely due to

the typical crystallization competition occurring between homo- and stereocomplexation [39] when a quenching process occurs, such as the precipitation with methanol after the synthesis.

In addition, Raman spectroscopy analysis of PLA bulk polymers (full spectrum in **Figure 4.2A**) was accomplished to identify the vibrational bands associated with phase variations (**Figure 4.2B–E** and **Table A4.1**). In particular, the ν C-COO stretching vibration band in the spectral range between 850 and 1000 cm^{-1} characterizes the helix conformation of the PLA polymer chain (**Figure 4.2B**). Likewise, the vibrational band assigned typically to ν C-COO stretching at 870 cm^{-1} was found to shift to a higher wavenumber, to 880 cm^{-1} , for SC-PLA as usually found for PLA in the stereocomplex phase [40]. Moreover, a second vibrational band of medium intensity, attributed to the coupling of the ν C-C backbone stretching mode with the CH_3 rocking mode, is observed either at 920 or 908 cm^{-1} for HC-PLA and SC-PLA, respectively, whilst it remained absent for the rac-PLA, reflecting that the PLA chain retains

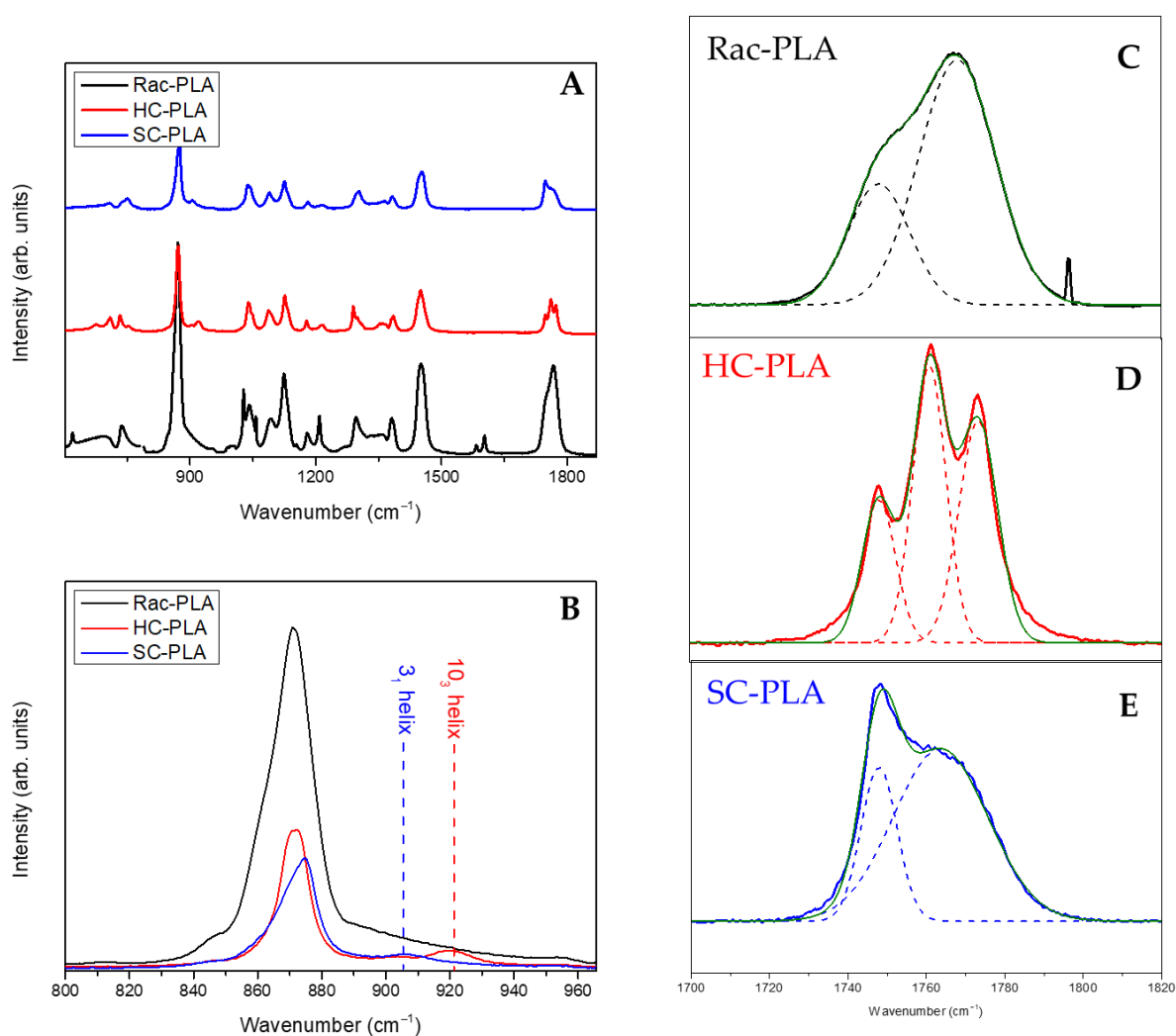


Figure 4.2. Full Raman spectrum of the bulk polymers (**A**), C-COO stretching Raman region of the bulk polymers (**B**) and carbonyl region of the Rac-PLA (**C**), HC-PLA (**D**) and SC-PLA (**E**)

either the 10_3 helix or the 3_1 helix conformation for the corresponding α - and SC- phases (**Figure 4.2B**). Furthermore, the vibrational band associated with the stretching of the PLA carbonyl (C=O) appears mainly at ca. 1770 cm^{-1} for the racemic PLA derivative [41] (**Figure 4.2C**), confirming its amorphous nature, whereas the HC-PLA carbonyl spectral region splits in three overlapping bands at 1755 , 1766 and 1777 cm^{-1} (**Figure 4.2D**), as reported previously for isotactic PLA. In addition, the carbonyl band of SC-PLA appeared centered with a strong and sharp band at 1752 cm^{-1} , which arose from the symmetric stretching vibrations [15], which are due to the stabilization of the stereocomplex crystalline phase by hydrogen bonds [10], and a broad shoulder at ca. 1770 cm^{-1} resulting from the vibration of the amorphous component (**Figure 4.2E**).

4.3.2 Nanoparticles formulation

Polymeric nanoparticles from the selected PLA derivatives (NP-PLA) were successfully formulated with two different antitumoral compounds by the double emulsion method and their size and morphology were characterized by DLS (**Table 4.3** and **A4.2**) and SEM (**Figures 4.3** and **A4.4**, as representative examples). Doxorubicin and dasatinib were selected to assess the loading capacity of the NP-PLA with two different model compounds that possess distinct structures either featuring a stiff structure imposed by the aromatic groups for the doxorubicin or a flexible chain structure for dasatinib.

Table 4.3 DLS characterization of PLA nanoparticles.

Particle	Average diameter (nm)	PDI	Z Potential (mV)
NP-Rac-PLA	231.52 ± 11.18	0.11 ± 0.02	-14.99 ± 2.02
NP-HC-PLA	239.64 ± 19.16	0.10 ± 0.03	-14.56 ± 3.62
NP-SC-PLA	256.80 ± 9.19	0.09 ± 0.03	-10.00 ± 2.60

An averaged unimodal hydrodynamic diameter of $254 \pm 22\text{ nm}$ with narrow PDI (0.10 ± 0.03) was obtained for all formulations by DLS. Furthermore, fairly spherical nanoparticles with a roundness index of 0.86 (being 1 perfectly round) and an average diameter of $104 \pm 4\text{ nm}$ were observed for the generated nanoparticle formulations by SEM. The size discrepancies observed by both techniques are related to shrinking effects during the freeze-drying and Au-shadowed treatment required for the SEM characterization, whilst DLS measurements were conducted in solution, resulting in NP swelling. In addition, the hydrodynamic diameter calculated by DLS arises from the diffusion coefficient of nanoparticles in suspension, in which small amounts of aggregates or dust are known to disturb the size determination [42,43]. Additionally, DLS analysis was performed at longer times to verify (PDI values remained constant with time) their stability in solution and thus the NP storage capability prior to their

incorporation into the gelatin hydrogel network (**Figure A4.5**). In addition, the nanostructure of the formulated NP-PLA was characterized to understand the effect of the processing conditions on the PLA crystallization mechanism and its correlation with the release profiles.

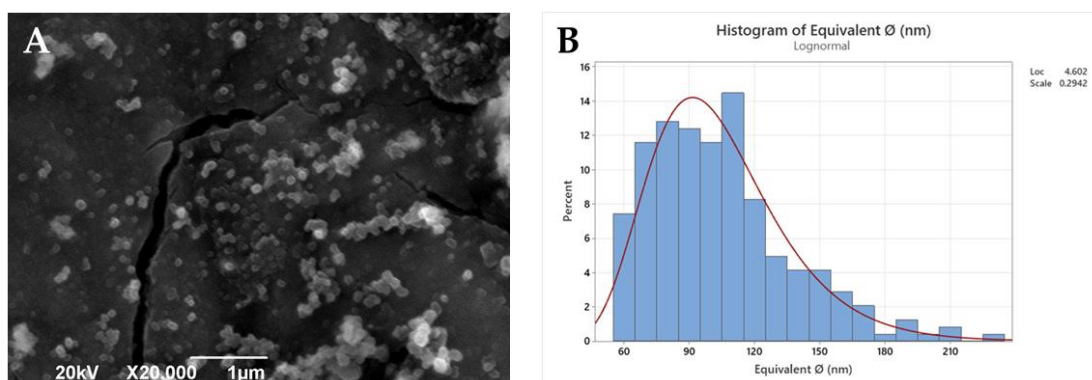


Figure 4.3. SEM image of NP-HC-PLA (A) and histogram of the statistical diameter analysis (B).

4.3.3 Nanoparticles characterization

The nanostructure of the formulated NP-PLA was characterized to understand the effect of the processing conditions on the PLA crystallization mechanism and its correlation with the release profiles. The nanostructure of the lyophilized NP-PLA with doxorubicin (NP-PLA/DOX) probed by WAXS evidenced the kinetically trapped state in the amorphous phase for the PLA derivatives (**Figure 4.4A**) during the NP formation, removing the targeted crystallinity of the designed semicrystalline PLA derivatives (NP-HC-PLA and NP-SC-PLA).

The amorphous structure obtained from the formulation conditions is likely related to the subjected short incubation time of the polymer solution during the water quenching

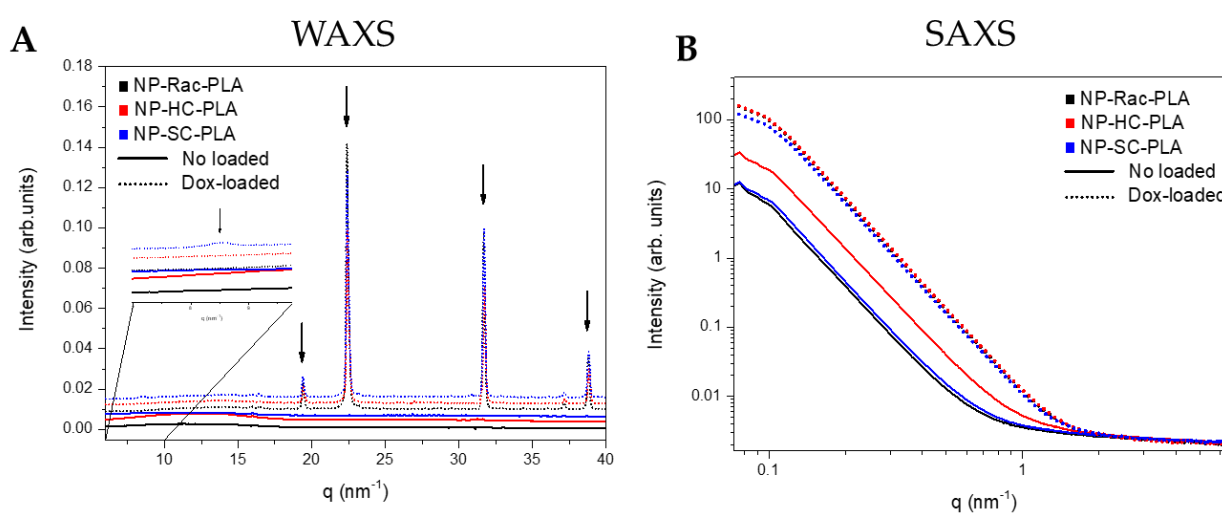


Figure 4.4. WAXS (A) and SAXS (B) of the Doxorubicin-loaded and no-loaded PLA nanoparticles at room temperature.

conducted to generate the NP-PLA that prevents the polymer chains to nucleate and form the polymer crystallites [15]. However, the WAXS profiles of the NP-PLA/DOX exhibited crystalline reflections at high q values (q (nm^{-1}) = 19.3, 22.4, 38.8 and 45, **Figure 4.4A**), corresponding to doxorubicin reflections [44], indicating that doxorubicin maintained its crystalline structure upon encapsulation in PLA nanoparticles. In addition, the NP-SC-PLA/DOX featured a crystalline structure (**Figure 4.4A**, zoom), which suggests the nucleating effect of doxorubicin. Likewise, the absence of the long period in the SAXS profile of the loaded nanoparticles confirms the quenching mechanism during the formation of the nanoparticles (**Figure 4.4B**).

Thermal treatment for the formulated NP-PLA was applied by annealing them at 65 °C, above the observed T_g at ca. 40 °C (**Figure 4.5**), for 1 h to modify the kinetically trapped nanostructure afforded upon formulation whilst selecting a temperature that will maintain the stability of the gelatin matrix. The thermal parameters obtained from the thermograms are summarized in **table 4.3**. The NP-PLA T_g at ca. 40°C was followed by an endothermic peak at ca. 55 °C that might correspond to an enthalpy relaxation that occurred due to physical ageing

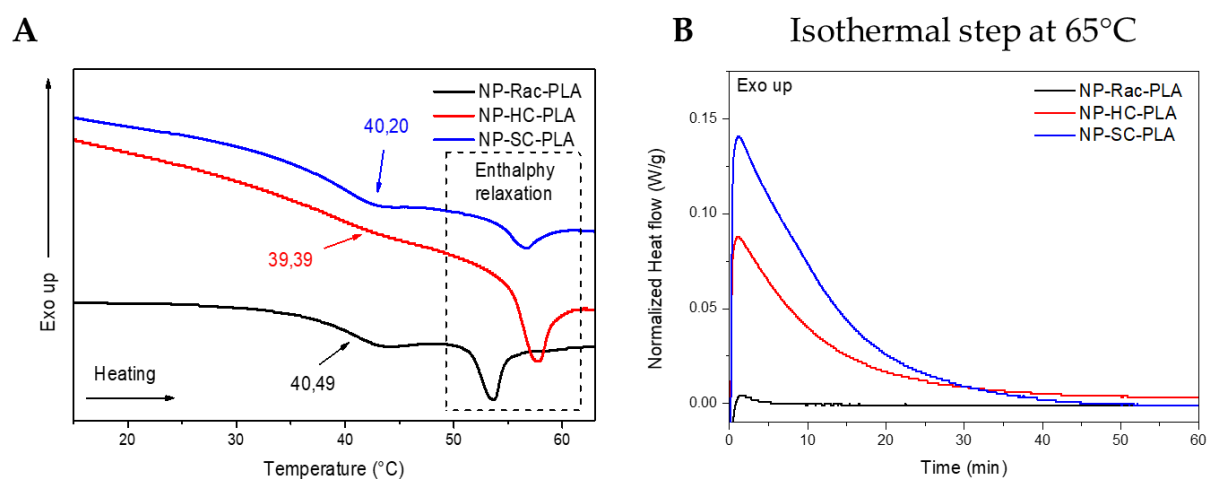


Figure 4.5. DSC thermograms of the no-loaded nanoparticles during heating step (A) and isothermal step at 65°C (B).

during the storage period before the thermal analysis (**Figure 4.5A**). Moreover, both NP-HC-PLA and NP-SC-PLA exhibited a cold crystallization during the isothermal annealing, confirming the quenched effect by the NP formation and discarding any degradation effect upon formulation (**Figure 4.5B**). NP-Rac-PLA did not crystallize upon heating in agreement with the bulk polymer structure. Additionally, upon further heating, NP-HC-PLA and NP-SC-PLA exhibited an endothermic peak at 165 °C and 200 °C, respectively, which is consistent with the melting of the α - and SC- phases, respectively, corroborating the crystallization of the semicrystalline PLA derivatives formulations during the annealing step (**Figure A4.6**). Notably, an exothermal peak is observed prior to the melting peak of NP-HC-PLA that can be

attributed to the recrystallization of the α' -phase into the α -phase [38], which is similar to the results obtained for the bulk polymer. Moreover, a double-melting peak was observed for the NP-SC-PLA, which was likely ascribed to the melt-recrystallization process of the α -phase into the SC phase, as found for the bulk polymer. The crystallinity (X_c) degrees obtained for NP-HC-PLA and NP-SC-PLA were around 23 and 31%, respectively.

Table 4.4. Thermal parameters obtained from DSC analysis of the Doxorubicin-loaded and non-loaded NP-PLA.

Sample	T_g (°C)	Enthalpy Relaxation (J/g)	ΔH_c (J/g) Annealing at 65°C
NP-Rac-PLA	40,49	1,172	-
NP-HC-PLA	39,39	1,438	57,984
NP-SC-PLA	40,20	1,061	111,76
NP-Rac-PLA/DOX	43,26/51,26	-	-
NP-HC-PLA/DOX	50,37	-	11,00
NP-SC-PLA/DOX	47,13	-	17,66

Furthermore, the doxorubicin-loaded nanoparticles revealed by DSC an increase of T_g upon heating (Table 4.4 and Figure 4.6A), which might be ascribed to the interaction of PLA with doxorubicin. Moreover, the isothermal treatment at 65 °C of the doxorubicin-loaded nanoparticles revealed the crystallization of both NP-HC-PLA/DOX and NP-SC-PLA/DOX (Figure 4.6B). However, a lower crystallization enthalpy was found with respect to the

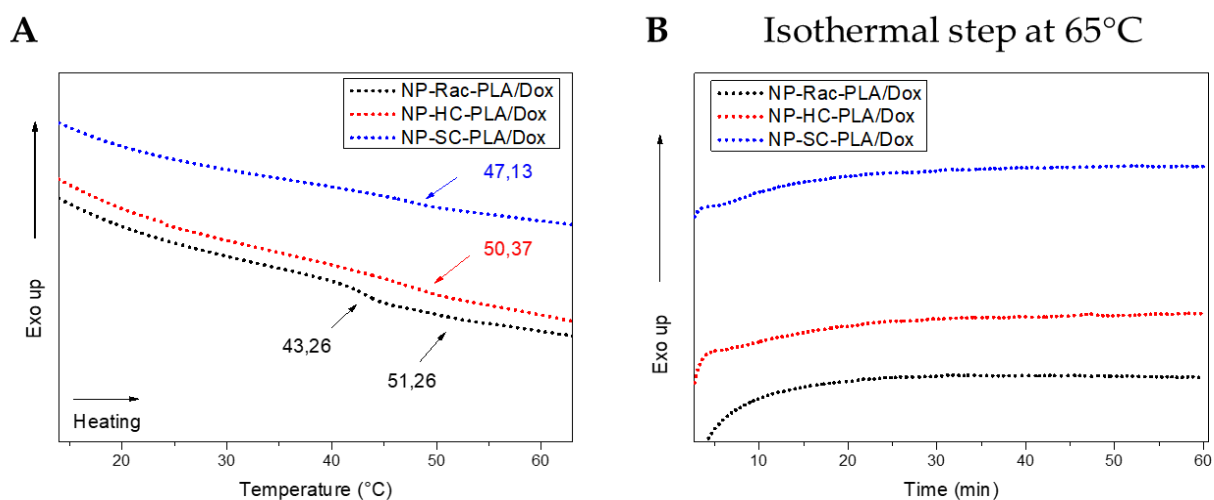


Figure 4.6. DSC thermograms of the Doxorubicin-loaded nanoparticles during heating step (A) and isothermal step at 65°C (B).

corresponding NP-HC-PLA and NP-SC-PLA counterparts (not drug-loaded), which is

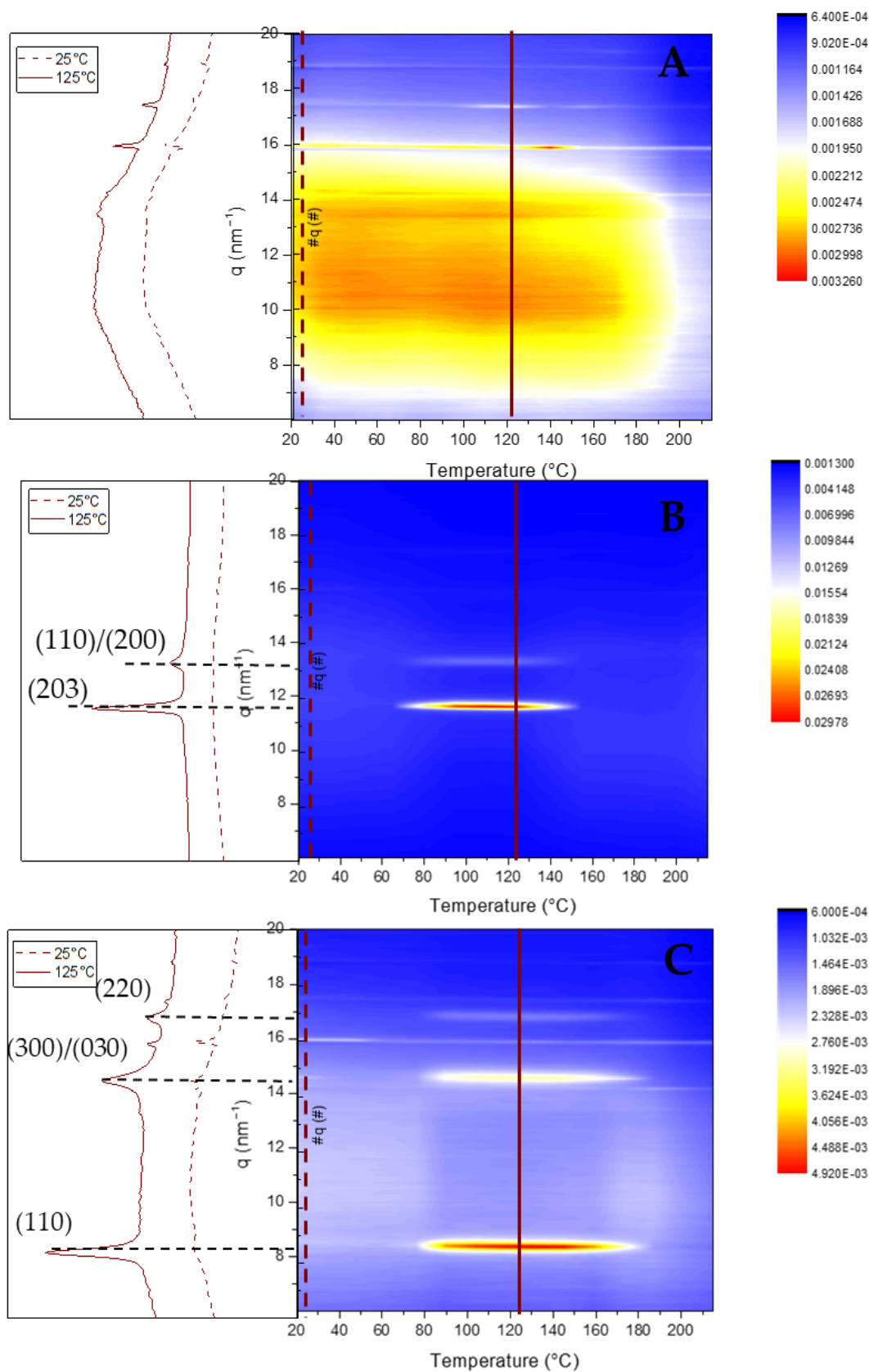


Figure 4.7. WAXS patterns of NP-Rac-PLA (A), NP-HC-PLA (B) and NP-SC-PLA (C) upon heating from room temperature to 215°C.

probably due to a partial crystallization of the NP upon formulation as a consequence of the nucleating effect of the doxorubicin, which is in agreement with WAXS analysis.

The nanoparticle nanostructures were subsequently monitored by WAXS measurements upon heating. NP-Rac-PLA retained the amorphous phase upon heating in agreement with the previous DSC analysis (**Figure 4.7A**). However, both NP-HC-PLA and NP-SC-PLA crystallized at 80 °C upon heating as evidenced by the development of WAXS reflections (**Figure 4.7B,C**) into the α -phase for the NP-HC-PLA ((110)/(200) and (203) (q (nm^{-1}) = 11.9 and 13.6)) and the SC-phase for the NP-SC-PLA ((110), (300)/(030) and (220) (q (nm^{-1}) = 8.5, 14.7 and 17)), indicating that the double-emulsion method did not impede the nanoparticles by possible degradation to further recrystallize upon heating.

However, the annealing step to crystallize the freeze-dried nanoparticles leads to aggregation, deleting the pharmaceutical advantages of the nanoparticles for drug delivery applications. A simple method to prevent the aggregation of the NP-PLA upon heating is to disperse them in a matrix, which should enhance their hydrophilicity and ideally promote cellular growth as well as endorsing the DDS with storage capability and easy applicability.

4.3.4 Bionanocomposite formation

Gelatin is a natural polymer featuring inherent biocompatibility, uniformly distributed interconnected porosity and appreciable mechanical strength that is ideal for drug delivery and tissue engineering applications. A bionanocomposite hydrogel formed by NP-HC-PLA and fish gelatin (GE/NP-HC-PLA) was formed upon cooling to room temperature of the homogenized gelatin solution by sonication at 65 °C as the gelatin hydrogel network is disrupted, allowing the NP-PLA dispersion and the concomitant cold crystallization of the PLA nanoparticles in the α -phase, as confirmed by WAXS measurements at room temperature (**Figure 4.8A, red line**). The development of the α -crystalline phase reflections was observed over the WAXS profile of the gelatin, which features a broad amorphous halo with the superimposed signals of the triple helix with the characteristic domain distances of 11–12.6 Å and mainly the single α -helices with repeat distance of 2.9 Å (**Figure A4.7A**). Furthermore, the NP-HC-PLA embedded in the gelatin hydrogels were isothermally annealed at 65 °C for 30 min, and the nanostructure development was probed by simultaneous SAXS/WAXS experiments (**Figure 4.8B-4.8D**). The crystallinity of the homo phase ((110)/(200) and (203) (q (nm^{-1}) = 11.9 and 13.6), respectively) further increased during the isothermal treatment (**Figure 4.8B**), whilst the α -helices of the gelatin diminishes (**Figure A4.7A**). Furthermore, the SAXS profile of the annealed bionanocomposite was exclusively sensible to the gelatin hydrogel nanostructure in the q range under study (**Figure A4.7B**) due to the large size of the NP-PLA. Likewise, the SAXS intensity is dominated by hydrogel nanostructure as a result of the likely low scattering of NP-PLA internal structure considering its low concentration (**Figure 8C-D**).

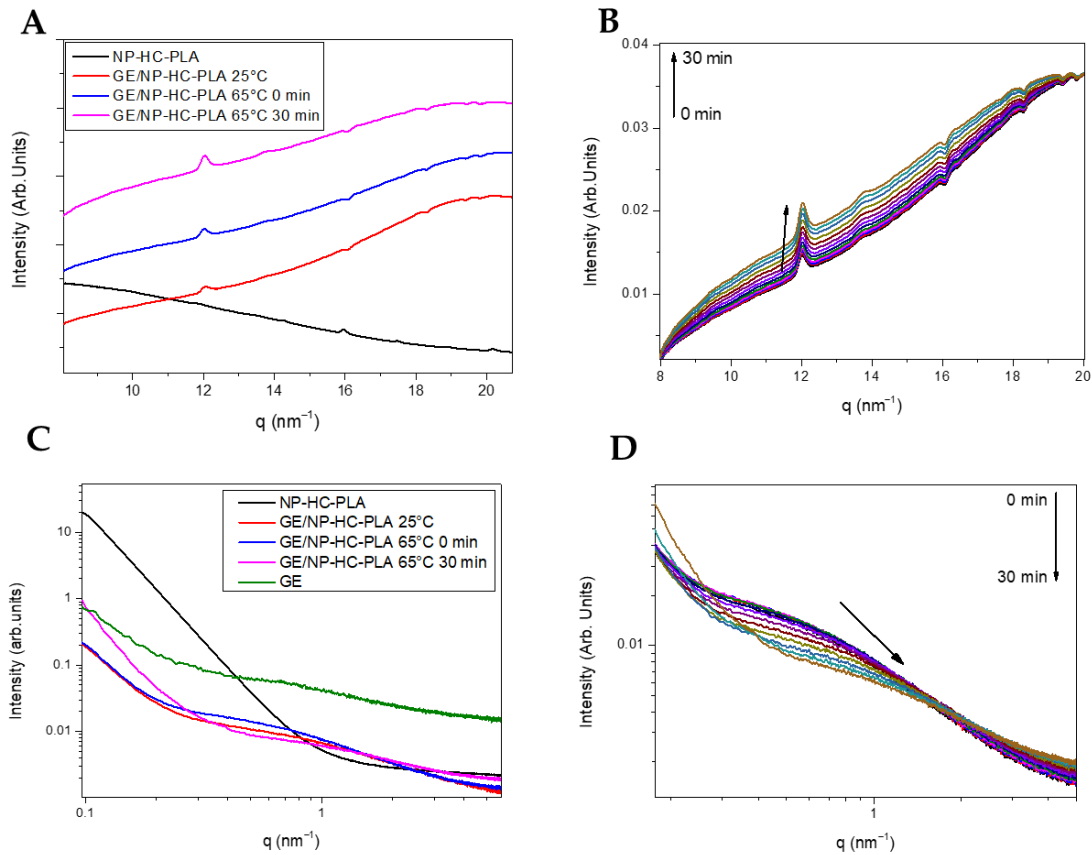


Figure 4.8. (A) WAXS pattern of NP-HC-PLA (black line), the bionanocomposite of NP-HC-PLA at room temperature (red line), 65 °C (blue line) and after 30 minutes at 65 °C (pink line). (B) WAXS pattern evolution during the isothermal at 65 °C. (C) SAXS pattern of NP-HC-PLA (black line), the gelatin (green line), the bionanocomposite of NP-HC-PLA at room temperature (red line), 65 °C (blue line) and after 30 minutes at 65 °C (pink line). (D) SAXS pattern evolution during the isothermal at 65 °C.

The measured SAXS profiles were fitted to fractal aggregates with a radius of gyration of ca. 1 nm and a fractal dimension of 1 with a correlation length of ca. 6 nm. In addition, the fibrillar structure of the triple helix undergoes a transition upon thermal treatment to a higher compact fractal cluster with a radius of gyration of firstly ca. 0.33 nm and then 0.65 with a fractal dimension of 2.5 and 3 and a correlation length of ca. 1 nm, indicating the transition of the gelatin chains to a random coil during the isothermal step at 65 °C (Table A4.2 and Figure A4.8A–C).

In addition, the effect of the nanoparticles embedded in the hydrogel thermal stability was assessed by DSC analyses. The sol–gel transition of the gelatin hydrogel network was shifted upon the incorporation of the NP-PLA from ca. 20 °C for the shark gelatin hydrogel to ca. 45–50 °C (Figure A4.9), which confirms that NP-PLA percolation throughout the hydrogel network reinforced the physical crosslinks, suggesting storage capability.

The morphology of the gelatin hydrogel as well as the corresponding bionanocomposites was analyzed by cryo-SEM to probe the effect of the annealing step on both the NP-SC-PLA and the gelatin hydrogel network (**Figure 4.9**). A porous network was found for both the shark gelatin hydrogel and the bionanocomposites in agreement with previous tuned gelatin hydrogel [27]. However, the size of the pores showed that the NP-SC-PLA promoted the development of a mesh with bimodal cavity distribution in which a second network features a finer pore dimension (**Figure A4.10**), whereas the gelatin hydrogel network (GE) presents a standard lognormal size distribution. Furthermore, the lack of NP-PLA

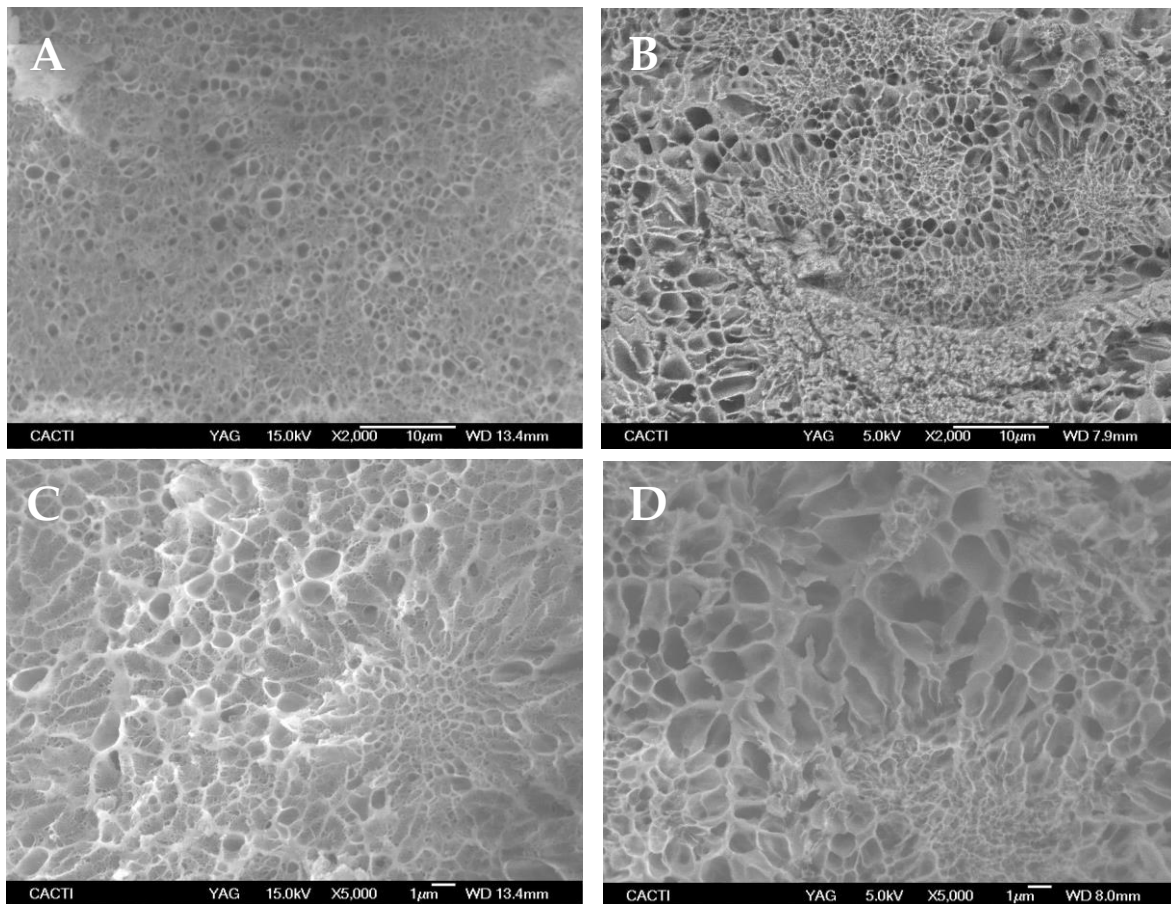


Figure 4.9. Cryo-SEM images of GE with (A-C) and without (B-D) NP-SC-PLA at x2000 (A-B) and x5000 (C-D) magnification

clusters within the gelatin hydrogel network proved the efficacy to avoid the NP agglomeration upon annealing by the gelatin matrix.

4.3.5 Rheological properties of the bionanocomposite

The extended rheological properties of DOX-loaded bionanocomposites (GE/NP-PLA/DOX) were examined to assess in detail their mechanical performance by evaluating their critical deformation and storage capability. The stability of the bionanocomposites in the linear viscoelastic region (LVR) was probed by subjecting the GE/NP-PLA/DOX to strain sweeps at 20 °C, in which the strain amplitude ranged from 0.1 to 1000% at a constant temperature and a frequency of 10 rad·s⁻¹ (**Figure 4.10A**). The strain sweeps were conducted to determine the region where the viscoelastic behavior of the gelatin network is independent of the applied

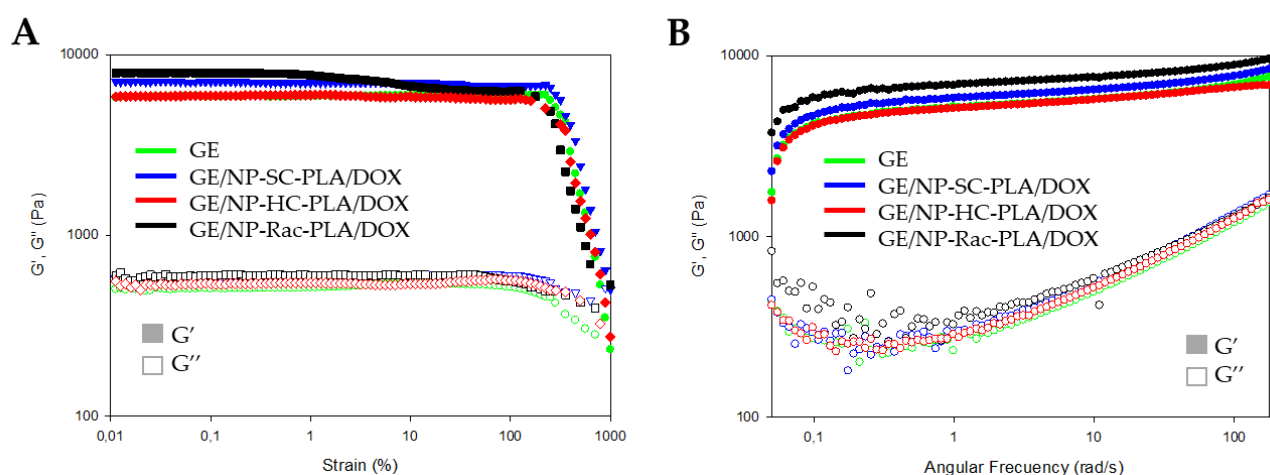


Figure 4.10. Strain and frequency sweep for GE (green color), GE/NP-SC-PLA/DOX (blue color), GE/NP-HC-PLA/DOX (red color) and GE/NP-Rac-PLA/DOX (black color). Storage (G' ; filled symbols) and loss moduli (G'' ; hollow symbols) depicted versus strain (**A**) and angular frequency (**B**) at 20 °C.

strain. Likewise, the strain sweeps of the GE/NP-PLA/DOX have shown that the viscoelasticity remains fairly linear up to a strain greater than 100% (**Figure 4.10A**) and with higher values for the GE/NP-PLA/DOX compared to the hydrogel of gelatin, which proves the enhanced mechanical stability of the GE/NP-PLA/DOX. In addition, frequency sweeps of the GE/NP-PLA/DOX were performed to understand the viscoelastic behavior as a function of the relaxation time scale to allow the prediction of the storage properties and process conditions during the application of the materials (**Figure 4.10B**). The elastic modulus component prevailed over the viscous in the entire region ($G' > G''$) under study [27], confirming its mechanical stability. The flow behavior of GE/NP-PLA/DOX indicates the increase in the elastic network, which is characteristic of complex gels that approach a solid-like trend. Both moduli increased with angular frequency, showing similar storage and loss modulus values between the studied gelatin networks, with GE/NP-Rac-PLA/DOX being the highest, followed by GE/NP-SC-PLA/DOX, indicating the greater stability of the gel.

In addition, the so-called “syringe test” [45] was conducted to evaluate the mechanical behavior of hydrogels during a local administration through a needle. The rheological response in terms of the apparent viscosity of the bionanocomposites was assessed with three different steps (two different shear rates and two different temperatures; see the Experimental section). The shark gelatin hydrogel (GE) was characterized by an initial viscosity of 10.1 ± 2.1 Pa·s ($p < 0.03$) at a shear rate of 0.1 s^{-1} (**Figure 4.11A**, blue box), whilst the addition of the nanoparticles into the GE increased the viscosity of the bionanocomposite to 219.6 ± 11.0 Pa·s, 488.6 ± 62.9 Pa·s and 1720 ± 115.58 Pa·s ($p < 0.03$) for GE/NP-Rac-PLA/DOX, GE/ NP-SC-PLA/DOX and GE/ NP-HC-PLA/DOX, respectively (**Figure 4.11B–D**, blue box), indicating that NP-PLA reinforced the three-dimensional network of the gelatin hydrogel and in agreement with the increase in the sol/gel transition upon the addition of the nanoparticles found by DSC. Subsequently, the shear rate was increased to 100 s^{-1} , and the temperature was gradually raised to $37 \text{ }^\circ\text{C}$ (**Figure 4.11A–D**, green box), simulating an injection through a needle of 0.9 mm in diameter and the temperature gradient (from 20 to $37 \text{ }^\circ\text{C}$) along the needle in contact with the human body. The viscosity of all hydrogels decreased below $5 \text{ Pa}\cdot\text{s}$ when the shear rate was

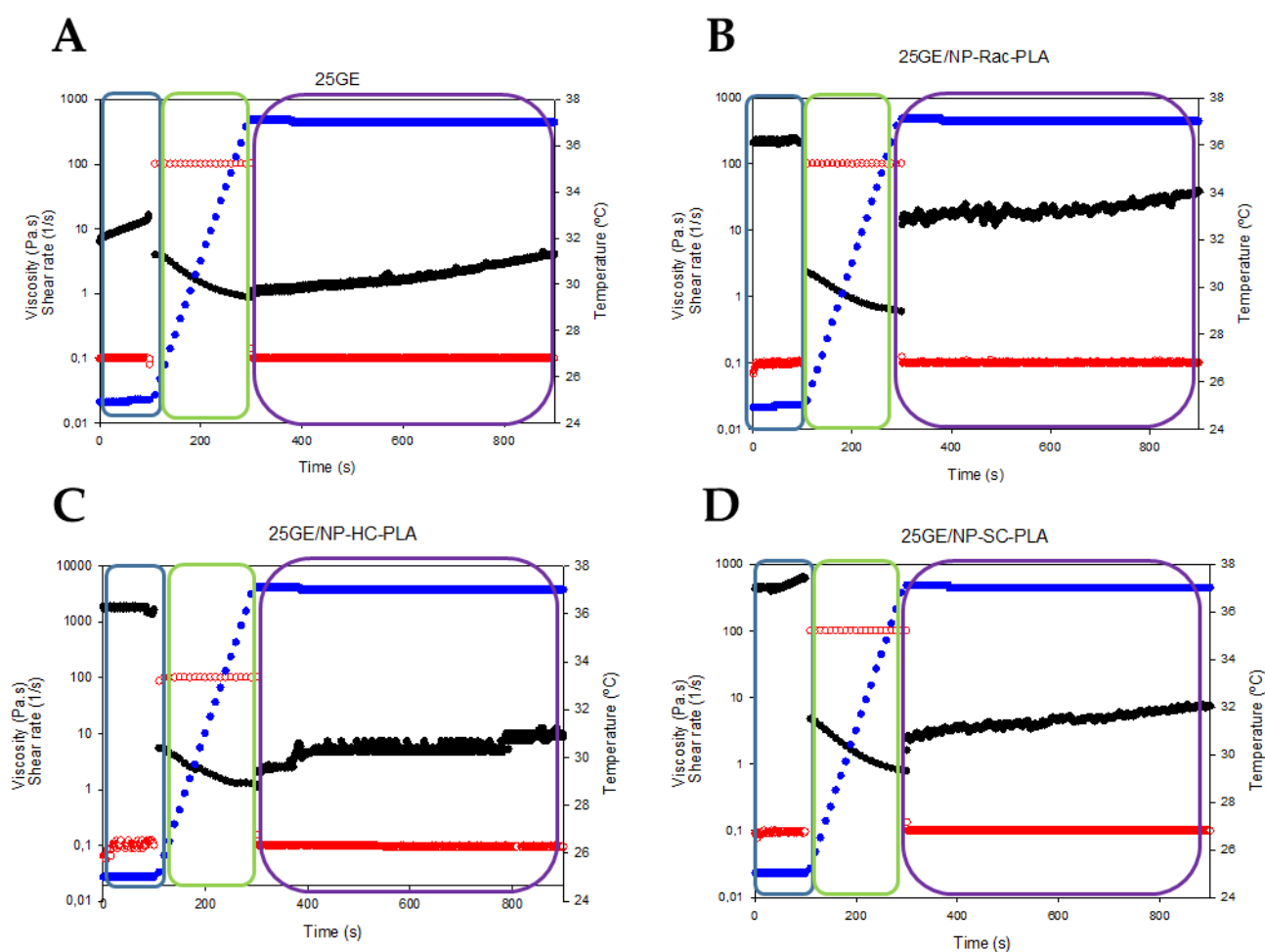


Figure 4.11. Syringe test results of gelatin hydrogel (A), GE/NP-Rac-PLA/DOX (B), GE/NP-HC-PLA/DOX (C) and GE/NP-SC-PLA/DOX (D). Viscosity (black color), shear rate (red color), temperature (blue color).

set to 100 s^{-1} , $1.9 \pm 1.1\text{ Pa}\cdot\text{s}$, $1.25 \pm 0.4\text{ Pa}\cdot\text{s}$, 1.9 ± 1.2 and $2.3 \pm 1.1\text{ Pa}\cdot\text{s}$ for GE, GE/NP-Rac-PLA/DOX, GE/NP-SC-PLA/DOX and GE/NP-HC-PLA/DOX, respectively, and it gradually further decreased upon the increase in temperature, indicating that all the gelatin-based hydrogels can be easily injected despite the initially high viscosity. Finally, the shear rate was set at 0.1 s^{-1} at a constant temperature of $37\text{ }^{\circ}\text{C}$, simulating physiological conditions (**Figure 4.9A–D**, purple box). The viscosity of the GE hydrogel slightly increased with time, whilst the GE hydrogels containing NP-PLA exhibited an immediate increase in viscosity upon reducing the shear rate followed by an increase upon time. The viscosity values of the bionanocomposites upon injection are close to the viscosity values of the human liver, $1.9 \pm 0.9\text{ Pa}\cdot\text{s}$, $21.3 \pm 3.8\text{ Pa}\cdot\text{s}$, 4.7 ± 1.2 and $5.7 \pm 1.6\text{ Pa}\cdot\text{s}$ for GE, GE/NP-Rac-PLA/DOX, GE/NP-SC-PLA/DOX and GE/NP-HC-PLA/DOX, respectively, turning the GE hydrogel containing NP into a potential biomaterial for liver tissue regeneration [46] as well as for the distribution into a complex anatomical human body area in particular after tumor resection where a combination of therapeutic agents is required to be administrated with low invasive techniques and that concomitantly promote the cellular growth.

4.3.6 Drug release analysis

Finally, the release of the loaded doxorubicin from the NP-PLA/DOX as well as from the GE/NP-PLA/DOX was monitored in PBS at $37\text{ }^{\circ}\text{C}$ by UV-Vis spectrometry (**Figure 4.12**). Shark gelatin absorption spectra present a UV-Vis band at 215 nm with a shoulder at 290 nm , whilst the doxorubicin and PLA main absorption bands are located at 490 nm and 231 nm , respectively [47], which permits the monitoring of the drug release profiles. All the NP-PLA/DOX (NP-HC, NP-SC and NP-rac) released completely the loaded doxorubicin within a few hours, with a significant burst release step during the first 2 h (98.9%, 60.9% and 51.6% for NP-HC, NP-Rac and NP-SC, respectively, **Figure 4.12**) that might be related to the formation of internal NPs microvoids due to heterogeneous structural relaxation during physical aging. The microvoids could be then filled with water when exposed to an aqueous solution that promotes the doxorubicin dissolution from the inner NP region [48]. Moreover, the enthalpy relaxation values related to physical aging found by DSC (1.44 J/g , 1.2 J/g and 1.06 J/g for NP-HC, NP-Rac and NP-SC, respectively, **Figure 4.5A**) are in agreement with the burst release differences between formulations, being both the enthalpy and the burst release higher for NP-HC followed by NP-Rac (**Figure 4.12**).

In contrast, the doxorubicin release from the GE/NP-PLA/DOX exhibited a sustained pattern similar to all the NP formulations ($\approx 5\%$ in 120 h) that was slower than the doxorubicin release from the gelatin network itself, confirming the tailoring of the drug release profiles. Moreover, GE/NP-SC-PLA/DOX exhibited slightly higher release, followed by GE/NP-HC-PLA/DOX and GE/NP-Rac-PLA/DOX, which might be related to the crystallinity difference found by DSC (**Figure 4.6B** and **Table 4.3**), since the doxorubicin molecule might interact

preferentially with the amorphous phase of the nanoparticles, resulting in a higher doxorubicin/amorphous phase ratio for the more crystalline NP, namely GE/NP-SC-PLA/DOX followed by GE/NP-HC-PLA/DOX, and hence, a slightly higher release rate (**Figure 4.12**)

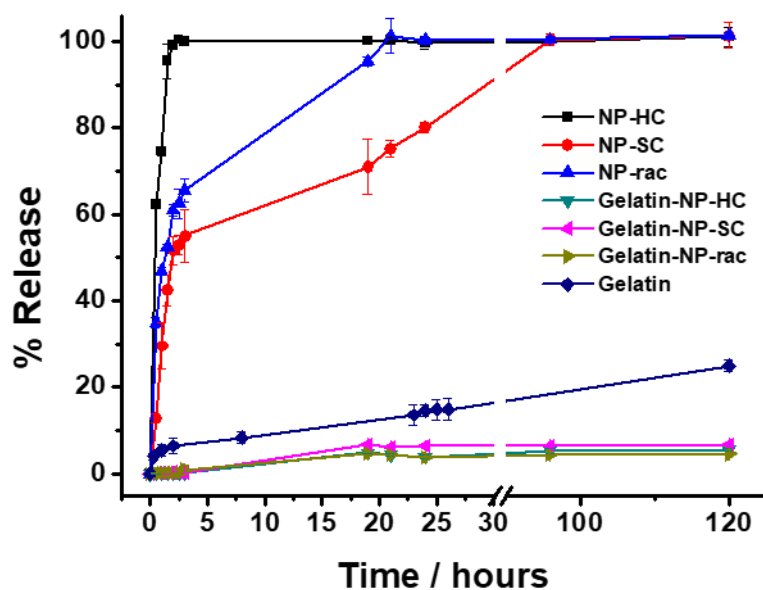


Figure 4.12. Release profiles of DOX from nanoparticles in suspension (NP-HC, NP-SC and NP-rac), gelatin (Gelatin) and nanoparticles embedded in gelatin (Gelatin-NP-HC, Gelatin-NP-SC and Gelatin-NP-Rac) in PBS pH 7.4 at 37 ° C. The drug releases were tested in three replicates. Error bars are 2 σ .

4.4 Conclusions

A straightforward methodology to anneal the PLA nanoparticles to customize the drug release rate was developed by generating bionanocomposites with shark gelatin hydrogels.

- ✓ The nanoparticles were successfully formulated with different PLA derivatives and loaded with two different antitumoral compounds but yielded amorphous PLA materials upon formulation, erasing the designed nanostructures.
- ✓ The dispersion of PLA nanoparticles in the gelatin hydrogel permits their thermal annealing and thus, their crystallization, without the detrimental agglomeration that diminishes their therapeutic effect.
- ✓ The SAXS and WAXS profiles as well as the cryo-SEM, DSC and rheological measurements of the bionanocomposites suggested the stability and reversibility of the hydrogel network upon the incorporation of the nanoparticles.
- ✓ The bionanocomposites generated were proved to feature storage capability at room temperature as well as being able to be injected by a syringe, which provides the possibility to be administrated locally.
- ✓ The generated bionanocomposites based on gelatin and comprising PLA nanoparticles with several nanostructures might have potential in the development of DDS for local release in soft tissue treatments requiring the administration of alternative drugs.

4.5 Experimental section

4.5.1 Materials

Solvents and reagents were acquired from Sigma-Aldrich. Blue Shark (BS, *Prionace glauca*) skin by-products were kindly provided by Propegal S.L. L- and D-lactide dimers were purchased from Rex scientific. The lactide dimers were purified three times by sublimation and then stored in a glovebox at 4°C. Toluene and tetrahydrofuran (THF) were pre-dried over sodium wire as well as distilled under nitrogen from sodium and subsequently stored over molecular sieves (3Å) in a glovebox.

4.5.2 Methods

4.5.2.1 Gelatin extraction

For the production of gelatin (GE), frozen skins of BS were cut in portions of around 5 × 5 cm and, after defrosting, were washed with water for 30 min under orbital agitation to remove impurities. Then, sequential chemical treatments were applied to skins, in all cases using a (1:4) solid: liquid ratio and continuous agitation (50 rpm). Each chemical stage was run for 30 min at 22 °C, intercalating water washings in between treatments. The first treatment of skins was performed with 0.05M NaOH, which was followed by acid processing using a solution of H₂SO₄ (0.02 M) and ending with another solution of citric acid (0.052 M). Thereafter, skins were soaked in water (1:2 ratio) at 45 °C for 16 h and gentle stirring to achieve the gelatin extraction in an aqueous medium. The obtained gelatin solution was then separated from skins by filtration (500 μm) and mixed with active charcoal (1.5%, *w/v*) for 3 h under constant agitation (100 rpm). Charcoal and impurities were removed by centrifugation (8000× *g*/20 min), and the gelatin was dried in an air-forced convection oven at 50 °C for 72 h.

4.5.2.2 Polymerizations

Polymerizations were performed as described previously in Chapter 2 [32].

4.5.2.3 Nanoparticles formulations

PLA nanoparticles (NP-PLA) were formulated from the three PLA derivatives, racemic-PLA (NP-rac-PLA), homopolymer-PLA (NP-HC-PLA) and stereo-diblock-PLA (NP-SC-PLA). In addition, all the PLA derivatives NP were loaded with the antitumoral doxorubicin and dasatinib as reference drugs [49–51]. Nanoparticles were prepared following the double emulsion methodology. Briefly, 10 mg of PLA was dissolved in 4 mL of CH₂Cl₂ and 1 mL of mQ water was added; then, the mixture was shaken in a Vortex and subsequently sonicated in an ice bath for 1 min to avoid emulsion overheating. The pre-emulsion generated was added to 10 mL of PVA (1%), shaken in a Vortex and sonicated for 5 min. The emulsion was allowed to evaporate organic solvent at room temperature for 45 min in a fume hood; then, it was centrifuged at 4 °C and 15k rpm for 20 min. Nanoparticles were collected and

dissolved in PBS pH = 7. Drug-encapsulated nanoparticles were prepared following the above-mentioned methodology. The amount of the drug (1 mg) was dissolved along with the polymer in 4 mL of CH₂Cl₂. The encapsulated drug in the NP-PLA is indicated at the end of the abbreviation name: NP-rac-PLA/DOX. The correspondence between the sample abbreviations and their compositions is summarized in Table 4.3.

4.5.2.4 Bionanocomposites generation

The bionanocomposites (GE/NP-Rac-PLA, GE/NP-HC-PLA, GE/NP-SC-PLA, GE/NP-Rac-PLA/DOX, GE/NP-HC-PLA/DOX, GE/NP-SC-PLA/DOX) were prepared by blending NP-PLA or NP-PLA/DOX with shark skin gelatin and tri-distilled water in a 0.4/25/74.6 *w/w* (NP/GE/H₂O) proportion under constant stirring in an ultrasound bath (SELECTA, 40 kHz, 125 W) at 65 °C for 30 min. Furthermore, a hydrogel of gelatin (GE) was prepared at the same ratio 25/75 (GE/H₂O) as a reference to compare the drug release [52]. Likewise, the corresponding sample abbreviation with its chemical composition is listed in the Supplementary Information (Table 4.3).

4.5.3 Instrumentation and measurements

4.5.3.1 ¹H NMR

Spectra were recorded at room temperature on a Varian Inova FT-400/500 spectrometer and referenced to the standard in the deuterated solvent with the relaxation time fixed to 4 s. The polymeric derivatives were dissolved in CDCl₃ for the synthetic characterization by ¹H NMR.

4.5.3.2 GPC analysis

The molecular weight and polydispersity index of the obtained PLA derivatives were determined by gel permeation chromatography (GPC) with a Shimadzu Prominence-I LC-2030 equipped with a Shodex GPC KF-805L column (Shodex, Tokyo, Japan) and a Shimadzu RID-20A detector (Shimadzu, Kyoto, Japan). CHCl₃ was used as the mobile phase at 40 °C, with 1mL/min as the flow rate. Then, 5 mg of the PLA derivatives was dissolved in 1.5 mL of solvent overnight in constant agitation. Subsequently, the PLA solutions were filtered through a 0.2 μm polytetrafluoroethylene (PTFE) syringe filter before injection. Polystyrene with a molecular weight of 172 kDa was used as a reference to determine the overall molecular weight of the samples.

4.5.3.3 Optical rotation

The specific optical rotation [α] was measured by a JASCO P-20000 WI using a beam wavelength of 598 nm, using dichloromethane as solvent at a concentration of 1 mg/mL.

4.5.3.4 DLS technique

The nanoparticle size and its polydispersity index were measured in a 0.5% *v/v* PBS solution by using DLS techniques in a Zetasizer Nano ZS instrument (Malvern instruments).

4.5.3.5 SEM

NP-PLA were freeze-dried and Au-shadowed before SEM images were recorded on a Jeol 6490LV electron microscope to evaluate the size and morphology of the particles.

The resulting images were analyzed using Digital Micrograph™ software from Gatan. Moreover, NP-PLA were quantified using ImageJ software [53]. Filters were applied to the images to normalize the contrast and highlight the edges of the nanoparticles. Then, a suitable threshold was used to binarize the images. A Watershed binary image segmentation was applied to separate touching particles. Particle agglomerates were generated in most cases, since sample preparation was complicated, individual particles were considered for sample characterization/quantification using image analysis, and large particle agglomerates were avoided as much as possible.

4.5.3.6 Cryo-SEM

The nanostructures of the GE/NP-HC-PLA, GE/NP-SC-PLA and GE/NP-Rac-PLA were evaluated in cryogenic mode. The hydrogels were mounted on the 13 mm gold sample holder and frozen at $-200\text{ }^{\circ}\text{C}$ with liquid nitrogen. Subsequently, the samples were transferred under liquid nitrogen in a cryogenic box to the Baltec equipment (MODEL, MED-020) and cut into 2–3 mm thickness slices. Finally, the samples were analyzed with an SEM (JEOL JSM-6700) at an acceleration voltage of 5 kV.

Cryo-SEM images at a magnification of $\times 2000$ were selected for the quantitative analysis due to the presence of a significant number of pores as statistically representative of the system. The coral-like porous structure in the micrographs was examined using ImageJ software [53]. Filters were applied in order to highlight the edges of the cells and be able to threshold and segment them. Several closing steps were applied also to clean artefacts in the images and only pores having an equivalent diameter bigger than $0.1\text{ }\mu\text{m}$ were quantified to plot the cell size distributions.

4.5.3.7 DSC measurements

Differential scanning calorimetry (DSC) analyses were performed using a Q2000 DSC (TA Instruments, New Castle, DE, USA). The calibration was performed by using indium as a standard ($T_m = 156.61\text{ }^{\circ}\text{C}$). DSC samples were prepared by sealing around 5 mg of the samples in Tzero Hermetic aluminum pans (TA Instruments, New Castle, DE, USA). The thermal protocol performed for bulk polymers consisted of a first heating ramp at $5\text{ }^{\circ}\text{C}/\text{min}$ from 10 to $200\text{ }^{\circ}\text{C}$ for Rac-PLA and HC-PLA, and from 25 to $220\text{ }^{\circ}\text{C}$ for SC-PLA, followed by a cooling ramp at $5\text{ }^{\circ}\text{C}/\text{min}$ to $10\text{ }^{\circ}\text{C}$ and $25\text{ }^{\circ}\text{C}$, respectively. Moreover, the thermal protocol performed for NP-PLA and bionanocomposites (Gelatin with NP) consisted of a first heating ramp at $5\text{ }^{\circ}\text{C}/\text{min}$ from 10 to $65\text{ }^{\circ}\text{C}$, followed by an isothermal step for 60 min. Samples were cooled down to $10\text{ }^{\circ}\text{C}$ at $5\text{ }^{\circ}\text{C}/\text{min}$ and further heated at $5\text{ }^{\circ}\text{C}/\text{min}$ to $200\text{ }^{\circ}\text{C}$ for the Rac and HC samples and

to 220 °C for the SC samples. The thermal transitions (T_g , T_c , and T_m) and their corresponding enthalpies (ΔH_c , ΔH_m) were calculated from the obtained thermograms.

4.5.3.8 Raman spectroscopy

Raman measurements were performed with a micro-Raman spectrometer LabRAM HR from Horiba Jobin with a laser at 532 nm. The spectral resolution was around 1 cm^{-1} and a 50× microscope objective was used.

4.5.3.9 Small-angle X-ray scattering (SAXS) and wide-angle X-ray scattering (WAXS)

SAXS/WAXS experiments were conducted both at DUBBLE (bm26) ESRF in Grenoble (France) and bl11 NCD-SWEET at ALBA, Cerdanyola del Vallès (Spain) with an X-ray wavelength of 12 Kev. The WAXS patterns were recorded with a Pilatus 300 kw (1472×195 pixels configuration) with a pixel size of $172 \mu\text{m}^2 \times 172 \mu\text{m}^2$ in DUBBLE, whereas a Rayonix LX255-HS characterized by a pixel size of $40 \mu\text{m}^2 \times 40 \mu\text{m}^2$ and active area of $85 \text{ mm}^2 \times 255 \text{ mm}^2$ (h × v) was used at NCD-SWEET. The SAXS patterns were collected with a Pilatus 1M with a detector size (981×1043) with a pixel size of $172 \mu\text{m} \times 172 \mu\text{m}$ at a sample to detector distance of ca. 2.5 m. The calibration of the scattering angular was performed with either $\alpha\text{-Al}_2\text{O}_3$ (alumina) for the WAXS scattering angles or AgBe for the SAXS scattering angle range. The measured intensity in the 2D detectors was reduced to 1D intensity profiles using bubble [21] as a function of the scattering vector ($q = 4\pi/\lambda\sin\theta$) and reported in arbitrary units by correcting by the incident intensity and background subtraction.

The reduced SAXS experimental data of the hydrogel derivatives were adjusted to a heterogeneous sphere with fractal structure defined with a radius of gyration Rg related to the fractal size as well as the fractal dimension D that represent their compactness [54] by an inhouse program [55,56] connected to the minimization routine used by the MINUIT [57] program conceived in CERN, and thus, the SAXS profile intensity ($I(q)$) was fitted to:

$$I(q) = \frac{(D-1) \sin((D-1) \tan^{-1}(q, \xi))}{(D-1)q\xi (1+q^2\xi^2)^{\frac{(D-1)}{2}}}$$

with

$$\xi^2 = \frac{2Rg^2}{D(D+1)}$$

ξ being the correlation length.

4.5.3.10 Rheological experiments

The mechanical properties were determined using a Physica MCR 101 rheometer (Anton Paar, Graz, Austria) able to control torques between $0.5 \mu\text{N}\cdot\text{m}$ and $125 \text{ mN}\cdot\text{m}$. Strain and sweep frequency sweeps for GE, GE/NP-Rac-PLA, GE/NP-SC-PLA and GE/NP-HC-PLA were performed using a cone-plate geometry (CP 25-1) with a constant space of 0.048 mm. The

temperature was controlled using a Peltier P-PTD 200, which was placed at the lower plate [58]. The rheological experiments were repeated three times to analyze the reproducibility of obtained results, and the deviations in (complex) viscosities between repetitions were lower than 3%.

The linear viscoelastic range was previously determined by performing a strain sweep experiment in the range from 0.1 to 1000% at a constant angular frequency of 10 rad/s at 20 °C. The storage modulus G' and the loss modulus G'' were determined in the linear strain range using a constant 0.1% strain. Frequency sweep measurements were conducted from 0.05 to 200 rad/s applying a constant strain of 0.1% at 20 °C. The solutions were preheated to 60 °C for 30 min for all rheological experiments to homogenize the samples and ensure adequate filling of the geometry as well as avoid air bubbles.

The so-called “syringe test” experiments were performed using a plate–plate geometry (PP25/S) with a plate diameter of 25 mm and a geometric gap of 0.1 mm. A three-step experiment [45] was performed to evaluate the response of the gelatin-based bionanocomposites to mimic the injection in the human body of the DDS. Firstly, samples were subjected to a constant shear rate of 0.1 s⁻¹ at room temperature, which simulates the resting state of the formulation under storage conditions and in the injection syringe. Subsequently, samples were heated up to 37 °C at a constant shear rate of 100 s⁻¹, which simulates an injection using a needle with a diameter equal to 0.9 mm, which was typically selected for the administration of hydrogel formulations. Finally, a shear rate of 0.1 s⁻¹ was imposed at 37 °C, simulating the rest state of the GE/NP-PLA hydrogel mixture in the human body.

4.5.3.11 Release studies

For NP-PLA/DOX, 10 mg of lyophilized DOX-loaded NPs were placed in the dialysis membrane (molecular weight cut-off: 3500 kDa) and incubated in 8 mL of phosphate-buffered saline (PBS, pH 7.4). The suspension was incubated at 37 °C with continuous stirring (50 rpm) in an IKA incubator shaker KS 3000. At different intervals of incubation, 1 mL of releasing medium was removed to measure the DOX absorbance in a UV-Vis Carey 100 spectrophotometer at 470 nm, and new PBS was added to maintain the volume constant.

For GE/NP-PLA/DOX, 1 mL of gelatin loaded with 5 mg of DOX-loaded NPs was placed in a dialysis membrane and released in the same method described above for the NP-PLA/DOX counterparts.

4.6 References

1. Mitchell, M.J.; Billingsley, M.M.; Haley, R.M.; Langer, R.; Wechsler, M.E.; Peppas, N.A. Engineering Precision Nanoparticles. *Nat. Rev. Drug Discov.* **2021**, doi:10.1038/s41573-020-0090-8.
2. De Jong, W.H.; Borm, P.J. Drug Delivery and Nanoparticles : Applications and Hazards. **2008**, *3*, 133–149.
3. Park, K.; Otte, A.; Sharifi, F.; Garner, J.; Skidmore, S.; Park, H.; Jhon, Y.K.; Qin, B.; Wang, Y. Formulation Composition, Manufacturing Process, and Characterization of Poly(Lactide-Co-Glycolide) Microparticles. *J. Control. Release* **2021**, *329*, 1150–1161, doi:10.1016/j.jconrel.2020.10.044.
4. Tsuji, H. Poly(Lactic Acid) Stereocomplexes: A Decade of Progress. *Adv. Drug Deliv. Rev.* **2016**, *107*, 97–135, doi:10.1016/j.addr.2016.04.017.
5. Stanford, M.J.; Dove, A.P. Stereocontrolled Ring-Opening Polymerisation of Lactide. *Chem. Soc. Rev.* **2010**, *39*, 486–494, doi:10.1039/b815104k.
6. Mehta, R.; Kumar, V.; Bhunia, H.; Upadhyay, S.N. Synthesis of Poly(Lactic Acid): A Review. *J. Macromol. Sci. - Polym. Rev.* **2005**, *45*, 325–349, doi:10.1080/15321790500304148.
7. Karavelidis, V.; Giliopoulos, D.; Karavas, E.; Bikiaris, D. Nanoencapsulation of a Water Soluble Drug in Biocompatible Polyesters. Effect of Polyesters Melting Point and Glass Transition Temperature on Drug Release Behavior. *Eur. J. Pharm. Sci.* **2010**, *41*, 636–643, doi:10.1016/j.ejps.2010.09.004.
8. Karavelidis, V.; Karavas, E.; Giliopoulos, D.; Papadimitriou, S.; Bikiaris, D. Evaluating the Effects of Crystallinity in New Biocompatible Polyester Nanocarriers on Drug Release Behavior. *Int. J. Nanomedicine* **2011**, *6*, 3021–3032.
9. Farah, S.; Anderson, D.G.; Langer, R. Physical and Mechanical Properties of PLA , and Their Functions in Widespread Applications — A Comprehensive Review ☆. *Adv. Drug Deliv. Rev.* **2016**, *107*, 367–392, doi:10.1016/j.addr.2016.06.012.
10. Zhang, J.; Sato, H.; Tsuji, H.; Noda, I.; Ozaki, Y. Differences in the CH₃...O=C Interactions among Poly(L-Lactide), Poly(L-Lactide)/Poly(D-Lactide) Stereocomplex, and Poly(3-Hydroxybutyrate) Studied by Infrared Spectroscopy. *J. Mol. Struct.* **2005**, *735–736*, 249–257, doi:10.1016/j.molstruc.2004.11.033.
11. Xie, W.; Jiang, C.; Yu, X.; Shi, X.; Wang, S.; Sun, Y.; Yin, M.; Wu, D. Stereocomplex-Induced Self-Assembly of PLLA-PEG-PLLA and PDLA-PEG-PDLA Triblock Copolymers in an Aqueous System. *ACS Appl. Polym. Mater.* **2021**, *3*, 6078–6089, doi:10.1021/acsapm.1c00879.
12. Hu, Q.; Gao, X.; Gu, G.; Kang, T.; Tu, Y.; Liu, Z.; Song, Q.; Yao, L.; Pang, Z.; Jiang, X.; et al. Glioma Therapy Using Tumor Homing and Penetrating Peptide-Functionalized PEG-PLA Nanoparticles Loaded with Paclitaxel. *Biomaterials* **2013**, *34*, 5640–5650, doi:10.1016/j.biomaterials.2013.04.025.
13. Almoustafa, H.A.; Alshawsh, M.A.; Chik, Z. Technical Aspects of Preparing PEG-PLGA

- Nanoparticles as Carrier for Chemotherapeutic agents by Nanoprecipitation Method. *Int. J. Pharm.* **2017**, *533*, 275–284, doi:10.1016/j.ijpharm.2017.09.054.
14. Xia, H.; Gao, X.; Gu, G.; Liu, Z.; Hu, Q.; Tu, Y.; Song, Q.; Yao, L.; Pang, Z.; Jiang, X.; et al. Penetratin-Functionalized PEG-PLA Nanoparticles for Brain Drug Delivery. *Int. J. Pharm.* **2012**, *436*, 840–850, doi:10.1016/j.ijpharm.2012.07.029.
 15. Scheuer, K.; Bandelli, D.; Helbing, C.; Weber, C.; Alex, J.; Max, J.B.; Hocken, A.; Stranik, O.; Seiler, L.; Gladigau, F.; et al. Self-Assembly of Copolyesters into Stereocomplex Crystallites Tunes the Properties of Polyester Nanoparticles. *Macromolecules* **2020**, *53*, 8340–8351, doi:10.1021/acs.macromol.0c01247.
 16. Ma, C.; Pan, P.; Shan, G.; Bao, Y.; Fujita, M.; Maeda, M. Core-Shell Structure, Biodegradation, and Drug Release Behavior of Poly(Lactic Acid)/Poly(Ethylene Glycol) Block Copolymer Micelles Tuned by Macromolecular Stereostructure. *Langmuir* **2015**, *31*, 1527–1536, doi:10.1021/la503869d.
 17. Varol, N.; Monnier, X.; Delbreilh, L.; Saiter, A.; Fatyeyeva, K.; Dargent, E. Highlight of Primary and Secondary Relaxations in Amorphous Stereocomplex Polylactides. *Express Polym. Lett.* **2020**, *14*, 48–62, doi:10.3144/expresspolymlett.2020.5.
 18. Nii, T. Biomaterial-Assisted Regenerative Medicine. **2021**, 1–18.
 19. Sun, J.; Tan, H. Alginate-Based Biomaterials for Regenerative Medicine Applications. *Materials (Basel)*. **2013**, *6*, 1285–1309, doi:10.3390/ma6041285.
 20. Dong, C.; Lv, Y. Application of Collagen Scaffold in Tissue Engineering: Recent Advances and New Perspectives. *Polymers (Basel)*. **2016**, *8*, 1–20, doi:10.3390/polym8020042.
 21. Coppola, D.; Oliviero, M.; Vitale, G.A.; Lauritano, C.; D'Ambra, I.; Iannace, S.; de Pascale, D. Marine Collagen from Alternative and Sustainable Sources: Extraction, Processing and Applications. *Mar. Drugs* **2020**, *18*, doi:10.3390/md18040214.
 22. Petros, S.; Tesfaye, T.; Ayele, M. A Review on Gelatin Based Hydrogels for Medical Textile Applications. *J. Eng. (United Kingdom)* **2020**, *2020*, doi:10.1155/2020/8866582.
 23. Cremer, M.A.; Ye, X.J.; Myers, L.K.; Brand, D.D.; Rosloniec, E.F.; Kang, A.H. T Cell Immunity to Type II Collagen in the Biobreeding Rat: The Identification and Characterization of RT1 u -Restricted T Cell Epitopes on A1(II) . *J. Immunol.* **2004**, *173*, 1795–1801, doi:10.4049/jimmunol.173.3.1795.
 24. Tabata, Y.; Ikada, Y. Protein Release from Gelatin Matrices. *Adv. Drug Deliv. Rev.* **1998**, *31*, 287–301, doi:10.1016/S0169-409X(97)00125-7.
 25. Gaspar-Pintilieșcu, A.; Stanciuc, A.M.; Craciunescu, O. Natural Composite Dressings Based on Collagen, Gelatin and Plant Bioactive Compounds for Wound Healing: A Review. *Int. J. Biol. Macromol.* **2019**, *138*, 854–865, doi:10.1016/j.ijbiomac.2019.07.155.
 26. Patel, Z.S.; Young, S.; Tabata, Y.; Jansen, J.A.; Wong, M.E.K.; Mikos, A.G. Dual Delivery of an Angiogenic and an Osteogenic Growth Factor for Bone Regeneration in a Critical Size Defect Model. *Bone* **2008**, *43*, 931–940, doi:10.1016/j.bone.2008.06.019.

27. Hermida-Merino, C.; Cabaleiro, D.; Lugo, L.; Valcárcel, J.; Vázquez, J.A.; Bravo, I.; Longo, A.; Salloum-Abou-Jaoude, G.; Solano, E.; Gracia-Fernández, C.; et al. Characterization of Tuna Gelatin-Based Hydrogels as a Matrix for Drug Delivery. *Gels* **2022**, *8*, 237, doi:10.3390/gels8040237.
28. Elzoghby, A.O. Gelatin-Based Nanoparticles as Drug and Gene Delivery Systems: Reviewing Three Decades of Research. *J. Control. Release* **2013**, *172*, 1075–1091, doi:10.1016/j.jconrel.2013.09.019.
29. Nii, T.; Makino, K.; Tabata, Y. Three-Dimensional Culture System of Cancer Cells Combined with Biomaterials for Drug Screening. *Cancers (Basel)*. **2020**, *12*, 1–24, doi:10.3390/cancers12102754.
30. Nooeaid, P.; Chuysinuan, P.; Pengsuk, C. Journal of Science : Advanced Materials and Devices Poly(lactic Acid) Microparticles Embedded Porous Gelatin Scaffolds with Multifunctional Properties for Soft Tissue Engineering. *J. Sci. Adv. Mater. Devices* **2020**, *5*, 337–345, doi:10.1016/j.jsamd.2020.07.002.
31. Saadipour, M.; Karkhaneh, A.; Nazarpak, M.H. An Investigation into Curcumin Release from PLA Particles Loaded in PCL-GELATIN Fibers for Skin Application. *Int. J. Polym. Mater. Polym. Biomater.* **2020**, *0*, 1–9, doi:10.1080/00914037.2020.1838520.
32. Moya-Lopez, C.; Bravo, I.; Castro-Osma, J.A.; Chapron, D.; Bourson, P.; Vagner, C.; Cochez, M.; Leon, N.; Alonso-Moreno, C.; Hermida-Merino, D. Synthesis of High Molecular Weight Stereo-Di-Block Copolymers Driven by a Co-Initiator Free Catalyst. *Polymers (Basel)*. **2022**, *14*, 1–16, doi:10.3390/polym14020232.
33. Orhan, B.; Tschan, M.J.; Wirotius, A.; Dove, A.P.; Coulembier, O.; Taton, D. Isolelective Ring-Opening Polymerization of Rac -Lactide from Chiral Takemoto ' s Organocatalysts: Elucidation of Stereocontrol. *ACS Macro Lett.* **2018**, *7*, 1413–1419, doi:10.1021/acsmacrolett.8b00852.
34. Ovitt, T.M.; Coates, G.W. Stereochemistry of Lactide Polymerization with Chiral Catalysts: New Opportunities for Stereocontrol Using Polymer Exchange Mechanisms. *J. Am. Chem. Soc.* **2002**, *124*, 1316–1326, doi:10.1021/ja012052+.
35. Huang, S.J.; Onyari, J.M. Multicomponent Polymers of Poly(Lactic Acid) Macromonomers with Methacrylate Terminal and Copolymers of Poly(2-Hydroxyethyl Methacrylate). *J. Macromol. Sci. - Pure Appl. Chem.* **1996**, *33*, 571–584, doi:10.1080/10601329608010879.
36. Zuza, E.; Ugartemendia, J.M.; Lopez, A.; Meaurio, E.; Lejardi, A.; Sarasua, J.R. Glass Transition Behavior and Dynamic Fragility in Polylactides Containing Mobile and Rigid Amorphous Fractions. *Polymer (Guildf)*. **2008**, *49*, 4427–4432, doi:10.1016/j.polymer.2008.08.012.
37. Zhang, X.J.; Yang, Q.S.; Liu, X.; Shang, J.J.; Leng, J.S. Atomistic Investigation of the Shape-Memory Effect of Amorphous Poly(L-Lactide) with Different Molecular Weights. *Smart Mater. Struct.* **2020**, *29*, doi:10.1088/1361-665X/ab471c.
38. Zhang, J.; Duan, Y.; Sato, H.; Tsuji, H.; Noda, I.; Yan, S.; Ozaki, Y. Crystal Modifications

- and Thermal Behavior of Poly(L-Lactic Acid) Revealed by Infrared Spectroscopy. *Macromolecules* **2005**, *38*, 8012–8021, doi:10.1021/ma051232r.
39. Pan, P.; Han, L.; Bao, J.; Xie, Q.; Shan, G.; Bao, Y. Competitive Stereocomplexation, Homocrystallization, and Polymorphic Crystalline Transition in Poly(L-Lactic Acid)/Poly(D-Lactic Acid) Racemic Blends: Molecular Weight Effects. *J. Phys. Chem. B* **2015**, *119*, 6462–6470, doi:10.1021/acs.jpcc.5b03546.
 40. Kister, G.; Cassanas, G.; Vert, M. Effects of Morphology, Conformation and Configuration on the IR and Raman Spectra of Various Poly(Lactic Acid)S. *Polymer (Guildf)*. **1998**, *39*, 267–273, doi:10.1016/S0032-3861(97)00229-2.
 41. Hu, J.; Wang, J.; Wang, M.; Ozaki, Y.; Sato, H.; Zhang, J. Investigation of Crystallization Behavior of Asymmetric PLLA/PDLA Blend Using Raman Imaging Measurement. *Polymer (Guildf)*. **2019**, *172*, 1–6, doi:10.1016/j.polymer.2019.03.049.
 42. Kim, A.; Ng, W.B.; Bernt, W.; Cho, N.J. Validation of Size Estimation of Nanoparticle Tracking Analysis on Polydisperse Macromolecule Assembly. *Sci. Rep.* **2019**, *9*, 1–14, doi:10.1038/s41598-019-38915-x.
 43. Bootz, A.; Vogel, V.; Schubert, D.; Kreuter, J. Comparison of Scanning Electron Microscopy, Dynamic Light Scattering and Analytical Ultracentrifugation for the Sizing of Poly(Butyl Cyanoacrylate) Nanoparticles. *Eur. J. Pharm. Biopharm.* **2004**, *57*, 369–375, doi:10.1016/S0939-6411(03)00193-0.
 44. Margaritis, A.; Manocha, B. Controlled Release of Doxorubicin from Doxorubicin/ γ -Polyglutamic Acid Ionic Complex. *J. Nanomater.* **2010**, *2010*, doi:10.1155/2010/780171.
 45. Cristiano, M.C.; Mancuso, A.; Giuliano, E.; Cosco, D.; Paolino, D.; Fresta, M. Etogel for Intra-Articular Drug Delivery: A New Challenge for Joint Diseases Treatment. *J. Funct. Biomater.* **2021**, *12*, doi:10.3390/JFB12020034.
 46. Asbach, P.; Klatt, D.; Hamhaber, U.; Braun, J.; Somasundaram, R.; Hamm, B.; Sack, I. Assessment of Liver Viscoelasticity Using Multifrequency MR Elastography. *Magn. Reson. Med.* **2008**, *60*, 373–379, doi:10.1002/mrm.21636.
 47. Costanzo, G.D.; Ribba, L.; Goyanes, S.; Ledesma, S. Enhancement of the Optical Response in a Biodegradable Polymer/Azo-Dye Film by the Addition of Carbon Nanotubes. *J. Phys. D. Appl. Phys.* **2014**, *47*, doi:10.1088/0022-3727/47/13/135103.
 48. Park, K.; Otte, A.; Sharifi, F.; Garner, J.; Skidmore, S.; Park, H.; Jhon, Y.K.; Qin, B.; Wang, Y. Potential Roles of the Glass Transition Temperature of PLGA Microparticles in Drug Release Kinetics. *Mol. Pharm.* **2021**, *18*, 18–32, doi:10.1021/acs.molpharmaceut.0c01089.
 49. Niza, E.; Ocaña, A.; Castro-Osma, J.A.; Bravo, I.; Alonso-Moreno, C. Polyester Polymeric Nanoparticles as Platforms in the Development of Novel Nanomedicines for Cancer Treatment. *Cancers (Basel)*. **2021**, *13*, doi:10.3390/cancers13143387.
 50. Niza, E.; Nieto-Jiménez, C.; Noblejas-López, M.D.M.; Bravo, I.; Castro-Osma, J.A.; de la Cruz-Martínez, F.; Buchaca, M.M. de S.; Posadas, I.; Canales-Vázquez, J.; Lara-Sanchez, A.; et al. Poly(Cyclohexene Phthalate) Nanoparticles for Controlled Dasatinib Delivery in Breast Cancer Therapy. *Nanomaterials* **2019**, *9*, 1–14, doi:10.3390/nano9091208.

51. Niza, E.; Castro-Osma, J.A.; Posadas, I.; Alonso-Moreno, C.; Bravo, I.; Garzón, A.; Canales-Vázquez, J.; Ceña, V.; Lara-Sánchez, A.; Albaladejo, J.; et al. Assessment of Doxorubicin Delivery Devices Based on Tailored Bare Polycaprolactone against Glioblastoma. *Int. J. Pharm.* **2019**, *558*, 110–119, doi:10.1016/j.ijpharm.2018.12.079.
52. Hermida-Merino, C.; Cabaleiro, D.; Lugo, L.; Calcarcel, J.; Vazquez, J.A.; Bravo, I.; Longo, A.; Salloum-Abou-Jaoude, G.; Gracia-Fernandez, C.; Piñeiro, M.M.; et al. Tuna Gelatin-Based Hydrogels as Drug Delivery Systems for Local Administration. *Gels* **2022**, Under revision.
53. Rasband, WS (U. S. National Institutes of Health, Bethesda, Maryland, U. Image J.
54. Beaumont, M.; Rosenfeldt, S.; Tardy, B.L.; Gusenbauer, C.; Khakalo, A.; Nonappa; Opietnik, M.; Potthast, A.; Rojas, O.J.; Rosenau, T. Soft Cellulose II Nanospheres: Sol-Gel Behaviour, Swelling and Material Synthesis. *Nanoscale* **2019**, *11*, 17773–17781, doi:10.1039/c9nr05309c.
55. Calandra, P.; Longo, A.; Liveri, V.T. Synthesis of Ultra-Small ZnS Nanoparticles by Solid-Solid Reaction in the Confined Space of AOT Reversed Micelles. *J. Phys. Chem. B* **2003**, *107*, 25–30, doi:10.1021/jp021223+.
56. Longo, A.; Calandra, P.; Casaletto, M.P.; Giordano, C.; Venezia, A.M.; Liveri, V.T. Synthesis and Physico-Chemical Characterization of Gold Nanoparticles Softly Coated by AOT. *Mater. Chem. Phys.* **2006**, *96*, 66–72, doi:10.1016/j.matchemphys.2005.06.043.
57. James, F. MINUIT Function Minimization and Error Analysis: Reference Manual Version 94.1 1994, 50 pages.
58. Hermida-Merino, C.; Perez-Rodríguez, M.; Pereiro, A.B.; Piñeiro, M.M.; Pastoriza-Gallego, M.J. Tailoring Nanofluid Thermophysical Profile through Graphene Nanoplatelets Surface Functionalization. *ACS Omega* **2018**, *3*, 744–752, doi:10.1021/acsomega.7b01681.

CONCLUSIONS AND PERSPECTIVES

The main objective of the thesis was to design novel materials for personalized pharmaceutical applications from a global approach by tailoring the PLA-block copolymers architecture to generate defined nanostructures with specific structure-processing-properties relationships required for the end-product performance. Particularly, the PLA stereocomplex phase, which is typically obtained from the physical blend of the PLA enantiomers, exhibits promising physicochemical properties such as higher melting temperature, hydrolysis resistance and mechanical performance compared to the enantiomeric counterparts. However, detrimental phase separation occurs with high molecular weight derivatives that deteriorate their physicochemical properties performance. The synthesis of high molecular weight PLA-stereoblock copolymer was long time desired to overcome the phase separation, however, sophisticated catalysts with high stereocontrol for both enantiomers are required that are extremely rare.

Herein, the synthesis of high molecular weight and high tacticity stereo-diblock copolymers of PLA (PLA-SBC) has successfully been achieved. The organometallic initiator employed for the PLA polymerization constitutes the first initiator able to generate the stereo-diblock copolymers without the use of a co-initiator, which represents an advantage for scalability to industrial production. The polymerization follows a coordination-insertion mechanism and the initiator features a living character with a first-order constant rate. In addition, a similar rate constant for both PLA enantiomers was found, which enables the synthesis of stereo-block copolymers in a relatively short time, as well as the racemic-PLA counterpart. The tacticity of the block-copolymers can be tailored by changing the time at which the second monomer is added to the reaction, although the decrease of the enantiomeric purity of each monomer might be also a solution to tailor the tacticity.

Subsequently, the characterization of the PLA-SBC mechanism of crystallization was studied from the melt, under different thermal conditions, at different length-scales by a multi-technique approach. Importantly, the typical phase separation occurring in the enantiomeric blend of PLA is avoided in the high molecular weight PLA-SBC derivatives even at high cooling rates such as 50°C/min, which increase the suitability of the PLA-SBC for its processing under industrial conditions. The temperature of degradation, melting and crystallization of the PLA-SBC increases as the molecular weight increases. Moreover, the decrease of tacticity of the PLA-SBC decreases the melting temperature from 210°C to 200°C which might be ascribed to the formation of a defective SC crystal phase. The crystallinity degree and the crystallization rate of the high molecular weight PLA-SBC are 10% higher and 3-times higher, respectively, than the SC-PLA formed from the enantiomeric blend. Furthermore, the addition of OXA-2 as the nucleating agent can further increase the crystallization rate enabling the crystallization at high cooling rates such as 400°C/min. Interestingly, the OXA-2 changes also

the PLA-SBC crystal morphology from spherulite-like crystals to oriented crystals due to the row nucleation on the OXA-2 crystals, which is key for tailoring the mechanical properties of the PLA-SBC.

Finally, a series of bionanocomposites composed of gelatin hydrogel and PLA nanoparticles featuring different nanostructures were designed to obtain multifunctional drug delivery systems with tailored drug release rates. PLA-derivatives nanoparticles were successfully formulated with two antitumoral drugs by the double emulsion method that yielded an amorphous structure independently of the chain architecture, erasing the designed nanostructure. However, post-formulation thermal annealing enabled the crystallization of the nanoparticles in the corresponding crystal phase, although detrimental nanoparticles agglomeration occurred that diminished their therapeutic effect. A straightforward methodology to anneal the nanoparticles and avoid aggregation was developed by the dispersion of the PLA nanoparticles in the gelatin hydrogel at 65°C. The gelatin serves as a mechanical support for the storage and local administration of the drug delivery system as well as a support to complementary drugs with different release profiles. However, the drug release profiles of the annealed PLA nanoparticles within the gelatin matrix were similar independently of the polymeric nanostructure, although long-term drug release analysis was unable due to the saturation of the UV-drug signal resulting from the disintegration of the gelatin.

The wide field covered by the herein thesis from the synthesis and the posterior full characterization to the application was evaluated from a multidisciplinary approach that limited the focus on a particular scope in return and thus, future lines of research are envisaged to enlarge the knowledge of the project.

The inorganic initiator employed for the synthesis enabled the polymerization of PLA derivative for the biomedical field due to biocompatibility of Zn. However, “greener” synthetic approaches might be considered by the use of organic initiator that excludes metals, such as 4-(dimethylamino)pyridine, which were already reported to successfully polymerize PLA, although the synthesis of stereo-block copolymers have not been achieved yet. Moreover, the control of the synthesis enables the polymerization of multiblock-PLA (tri-, tetra-, penta-, etc.) which will exhibit tailored properties, as well as hetero-block copolymers with complementary properties such as PEG, PGA, PCL. Furthermore, the yield of the polymerization at the laboratory scale was of few grams limiting certain properties analysis that required higher yield, such as the mechanical test. Therefore, scaling the synthesis process to obtain a greater amount of polymer per batch is required to continue the characterization of the PLA-SBC as well as its processing through new processing techniques such as 3D printing.

The analysis of the thermal stability assessment performed was mainly focused on the detection of likely degradation occurring during the thermal treatment during the analysis of

the mechanism of crystallization from the melt. However, a deeper analysis to understand the degradation process as well as to quantify the detrimental transesterification reactions occurring upon thermal treatment is necessary to establish the structure-processing-properties relationship. In addition, the data acquired to study the crystallization mechanism should be investigated further to describe the lamellar crystal thickness by the application of the correlation function to the SAXS profiles. In addition, the crystallization mechanism from the glass state or solution needs also to be addressed. Likewise, nano-beam analysis at the interface of the OXA-2 nucleating agent with PLA-SBC crystallized should be addressed to tackle the question of the higher nucleation efficiency of the PLA-SBC copolymer compared to the homopolymer counterpart. The analysis of the crystal phase orientation of the PLA-SBC on the OXA-2 crystal might clarify whether the row nucleation observed at the micro-scale is due to a geometric effect or an epitaxial growth.

Furthermore, the designed bionanocomposite drug delivery system should be studied with a different detection method to analyse the drug release at a longer time, such as high-performance liquid chromatography (HPLC), since the gelatin signal saturated the UV-drug detection. In addition, new methods to improve the crystallization of the nanoparticles upon formulation could be envisaged as well as a deeper analysis of the mechanistic governing the formulation of PLA nanoparticles from a thermodynamic point of view. Finally, the potential application of the PLA-SBC in the biomedical field includes the fabrication of stents, which have already been fabricated based on PLLA, although yielding devices with a lack of radial stress that might be overcome by the enhanced mechanical properties presented by the PLA stereocomplex phase.

APENDIX

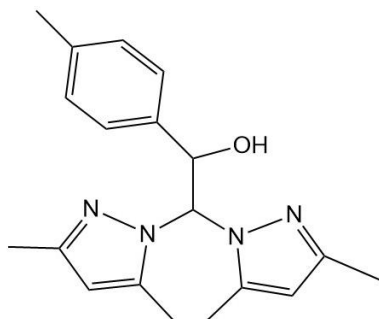
APENDIX A2

Entry	Sample	[LA]/[cat]	Solvent	Temperature (°C)	Time (min)	Conversion (%)	$M_n^{(theor.)}$ (Da) ^a	$M_n^{(exp.)}$ (Da) ^b	PDI	$[\alpha]^c$
1	PLLA400	400	Toluene	60	90	90	51.840	47.539	1,97	-
2	PLLA400	400	Toluene	75	50	89	51.264	33.861	1,78	-
3	PLLA400	400	Toluene	90	30	90	51.840	43.348	1,85	-
4	PLLA500	500	Toluene	90	45	68	48.960	62.564	1,84	-
5	PDLA500	500	Toluene	90	45	61	43.920	33.442	1,96	-
6	PLLA100	100	THF	50	120	0	0	-	-	-
7	PLLA100	100	Toluene	50	120	5	720	-	-	-
8	PLLA100 (L1)	100	Toluene	70	60	43	6.192	12.824	1,36	-159,4
9	PLLA100 (L2)	100	Toluene	90	60	94	13.536	30.055	1,62	-171,4
10	PLLA500 (L3)	500	Toluene	90	45	94	67.680	62.564	1,84	-172,2
11	PLLA500 (L4)	500	Toluene	70	90	76	56.880	42.880	1,77	-162,7
12	PLLA500 (L5)	500	Toluene	70	120	94	67.680	48.253	2,19	-168,4
13	PDLA500 (D1)	500	Toluene	70	90	85	61.200	41.292	1,78	154
14	rac-PLA600 (Rac1)	600	Toluene	70	120	90	64.800	40.754	1,59	-1,1
15	(L115:D115)	250	Toluene	90	50	95	34.200	17.007	1,93	-2,47
16	(L220:D220)	500	Toluene	90	90	90	64.800	28.779	2,20	-5,09
17	(L250:D250)	500	Toluene	75	120	81	58.320	32.958	2,20	-2,67
18	(L275:D275)	600	Toluene	90	60	95	82.080	35.253	2,25	-1,07
19	(D275:L275)	600	Toluene	90	60	94	81.216	33.238	2,38	1,41
20	(L330:D330)	600	Toluene	90	60	84	72.576	44.636	2,11	-1,93
21	(L375:D375)	700	Toluene	90	100	97	97.776	63.853	1,69	-0,69
22	(L500:D500)	1000	Toluene	90	110	89	102.528	53.660	2,60	0,32
23	(L520:D520)	1200	Toluene	90	120	85	146.880	64.976	2,31	-1,65
24	(L1200:D300)	1600	Toluene	90	95	90	194.400	99.257	2,04	-87,7

Table A2.1. Polymerizations catalysed by Initiator. Polymerization conditions: 25 μ mol of initiator. ^aTheoretical M_n = (monomer/initiator) x (% conversion) x (M_w of LA). ^bDetermined by GPC relative to polystyrene standards in chloroform. ^cSpecific optical rotation ($[\alpha]_{PLLA=-173^\circ}$) [30].

A2.1 Characterization and activity of the catalyst

A2.1.1 Synthesis of the 2,2-bis((3,5-dimethyl-pirazol-yl)-1-para-tolylolethoxide) (bpzteH)



The ligand (bpzteH) was synthesized via the following procedure: In a 250 mL Schlenk tube, Bis 3,5-(dimethyl-pirazol-yl)-methylene (bpm) (3 g, 14.7 mmol) was dissolved in dry THF (70 mL) and then cooled to -78°C . A 2.5 M solution of Bu_nLi (6.47 mL, 16.17 mmol) in hexane was added to the bpm solution and stirred for 1h. The resulting mixture was added dropwise to a cooled (-10°C) solution of p-tolyl (1.86 g, 15.43 mmol). The reaction mixture was allowed to warm up to ambient temperature and was stirred for 1h. The obtained product was hydrolyzed with saturated aqueous NH_4Cl (15 mL). The organic layer was extracted, dried over MgSO_4 , filtered, and the solvent was removed in vacuum to yield the product as a yellow oil, which was titrated with hexane to afford the pure product as a yellow solid (1.54 g, 75%). ^1H NMR (500 MHz, CDCl_3 , 297 K): δ 7.25-7.23 (d, 2H, H3), 6.91-6.88 (d, 2H, H2), 6.28-6.26 (d, 1H, H6), 5.90-5.89 (d, 1H, H6), 5.59 (s, 1H, H4), 5.44 (d, 1H, H5), 2.14-1.55 (m, 12H, H7), 1.44 (s, 3H, H1).

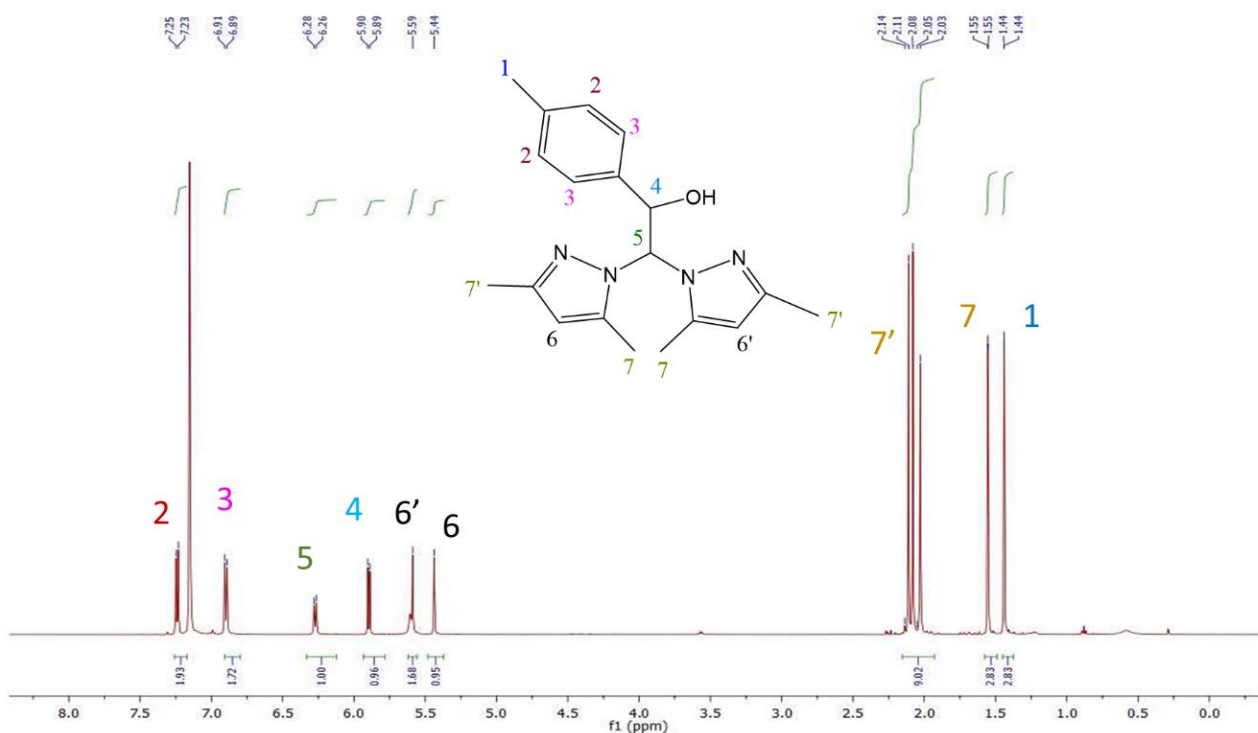
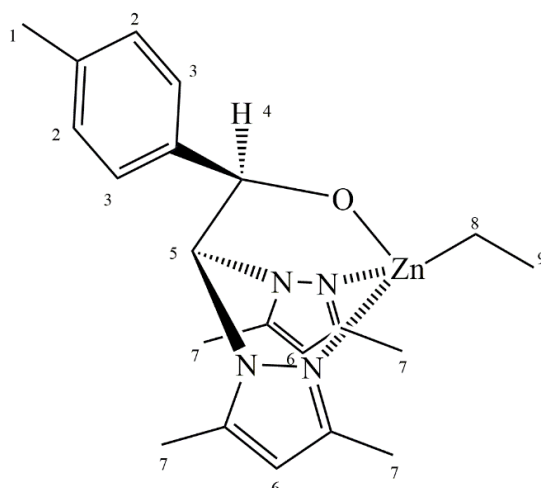


Figure A2.1: ^1H NMR spectrum (500 MHz, 298 K, CDCl_3) of the ligand 2,2-bis((3,5-dimethyl-pirazol-yl)-1-para-tolylolethoxide) (bpzteH): δ 7.25-7.23 (d, 2H, H3), 6.91-6.88 (d, 2H, H2), 6.28-6.26 (d, 1H, H6), 5.90-5.89 (d, 1H, H6), 5.59 (s, 1H, H4), 5.44 (d, 1H, H5), 2.14-2.11 (m, 12H, H7), 2.08 (m, 12H, H7), 2.05 (m, 12H, H7), 1.55 (s, 3H, H1), 1.44 (s, 3H, H1), 1.44 (s, 3H, H1).

A2.1.2 Synthesis of $[\text{Zn}(\text{Et})]\text{-}[2,2\text{-bis}((3,5\text{-dimethyl-pirazol-yl})\text{-1-para-tolylolethoxide})]$ ($\text{Zn}(\text{Et})(\kappa^3\text{-bpzteH})$)

The catalyst ($\text{Zn}(\text{Et})(\kappa^3\text{-bpzteH})$) was synthesized by the following procedure: The ligand (bpzteH) was dissolved in dry toluene and $\text{Zn}(\text{Et})_2$ was added through a cannula to the solution placed on ice-bath (0°C). The resulted solution was stirred for 2h at room temperature and the solvent was removed in vacuum. Yield : 1,54g, 75%. ^1H NMR (500 MHz, CDCl_3 , 297



K): δ 6.97-6.95 (d, 2H, H3), 6.89-6.87 (d, 2H, H2), 5.90-5.88 (d, 2H, H6), 5.68 (d, H, H4), 5.41 (d, 1H, H5), 2.34-2.24 (s, 12H, H7), 1.52 (s, 3H, H1), 1.40-1.36 (t, 3H, H9), 0.45-0.39 (q, 2H, H8).

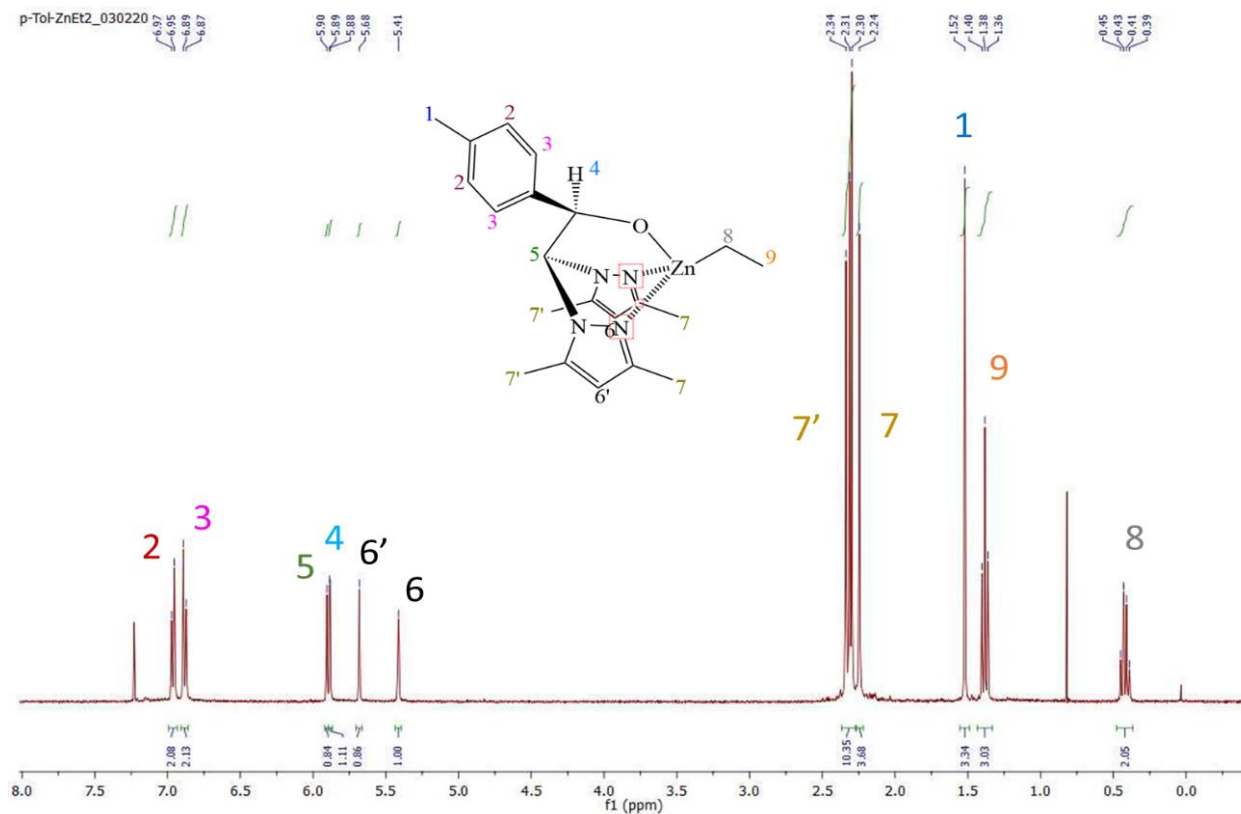


Figure A2.2: ¹H NMR spectrum (500 MHz, 298 K, CDCl₃) of (Zn(Et)(κ³-bpzteH)) δ 6.97-6.95 (d, 2H, H3), 6.89-6.87 (d, 2H, H2), 5.90-5.88 (d, 2H, H6), 5.68 (d, H, H4), 5.41 (d, 1H, H5), 2.34-2.24 (s, 12H, H7), 1.52 (s, 3H, H1), 1.40-1.36 (t, 3H, H9), 0.45-0.39 (q, 2H, H8).

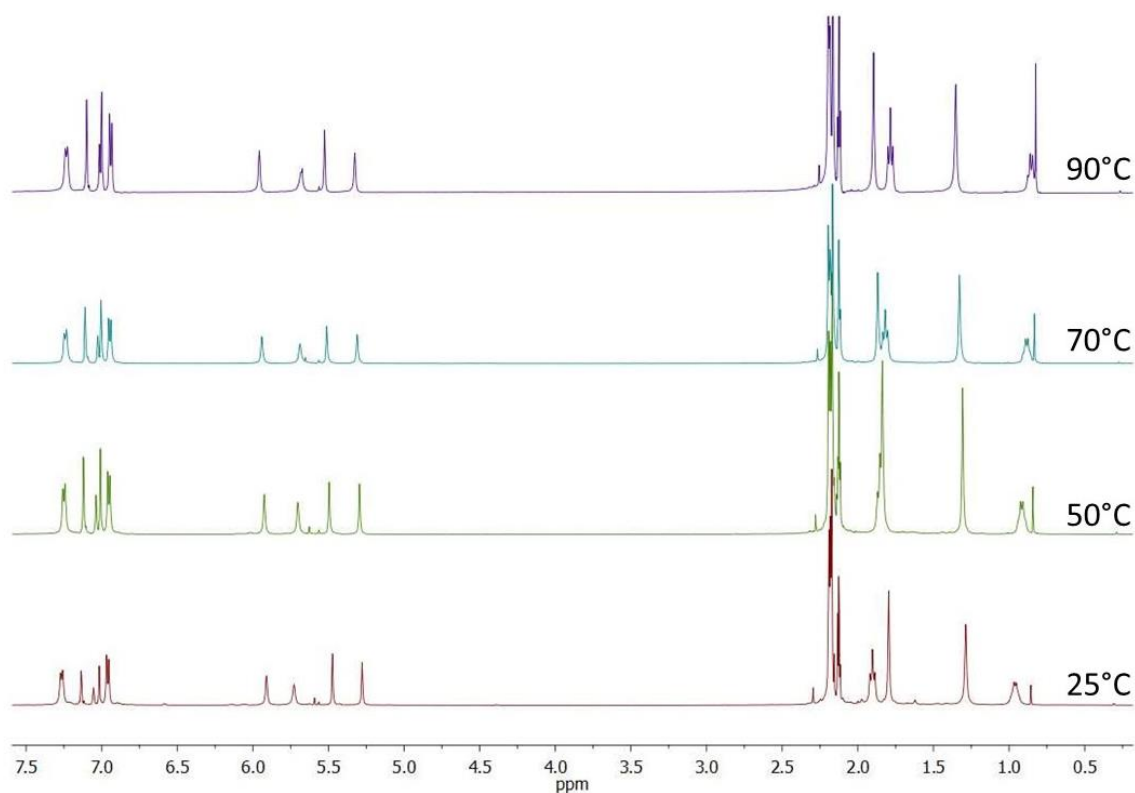


Figure A2.3. VT- ¹H NMR spectrum (500 MHz, 298 K, CDCl₃) of (Zn(Et)(κ³-bpzteH)). ¹H NMR (Told8, 298 K): δ 7.25-7.27 (d, 2H, H3), 6.95-6.96 (d, 2H, H2), 5.910 (s, 1H, H6'), 5.728 (s, 1H, H6), 5.473 (d, H, H4), 5.27 (d, 1H, H5), 2.11-2.19 (s, 12H, H7), 1.79 (s, 3H, H1), 1.88-1.91 (t, 3H, H9), 0.95-0.96 (q, 2H, H8). ¹H NMR (Told8, 348 K): δ 7.24-7.25 (d, 2H, H3), 6.94-6.96 (d, 2H, H2), 5.92 (s, 1H, H6'), 5.70 (s, 1H, H6), 5.49 (d, H, H4), 5.29 (d, 1H, H5), 2.05-2.25 (s, 12H, H7), 1.83 (s, 3H, H1), 1.85-1.87 (t, 3H, H9), 0.90-0.92 (q, 2H, H8). ¹H NMR (Told8, 368 K): δ 7.23-7.24 (d, 2H, H3), 6.94-6.95 (d, 2H, H2), 5.94 (s, 1H, H6'), 5.68 (s, 1H, H6), 5.51 (d, H, H4), 5.31 (d, 1H, H5), 2.11-2.19 (s, 12H, H7), 1.86 (s, 3H, H1), 1.80-1.81 (t, 3H, H9), 0.87-0.89 (q, 2H, H8). ¹H NMR (Told8, 388 K): δ 7.22-7.24 (d, 2H, H3), 6.93-6.94 (d, 2H, H2), 5.95 (s, 1H, H6'), 5.68 (s, 1H, H6), 5.52 (d, H, H4), 5.32 (d, 1H, H5), 2.11-2.25 (s, 12H, H7), 1.89 (s, 3H, H1), 1.76-1.80 (t, 3H, H9), 0.84-0.87 (q, 2H, H8).

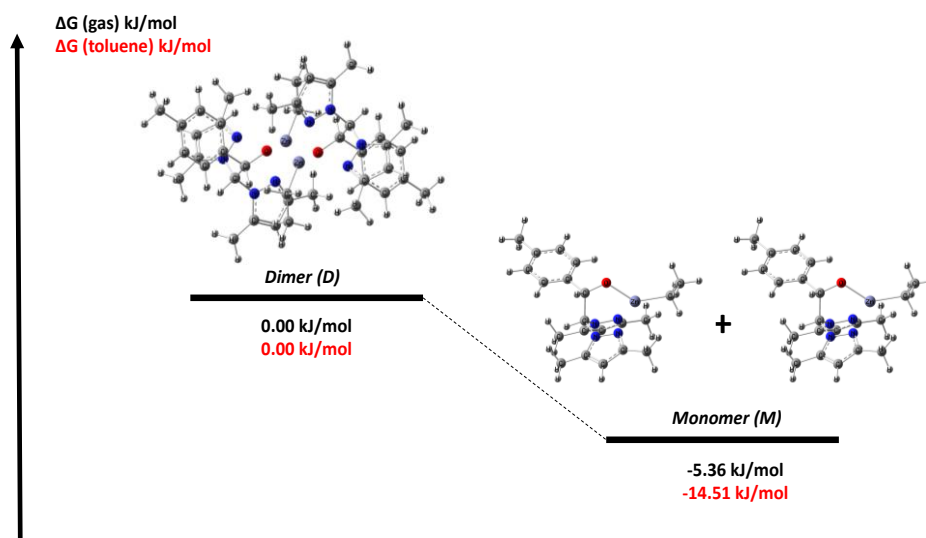


Figure A2.4. Energy profile for the dimeric and monomeric species. $\Delta G = 0$ for the dimer in gas and toluene

A2.2 Polymerization mechanism

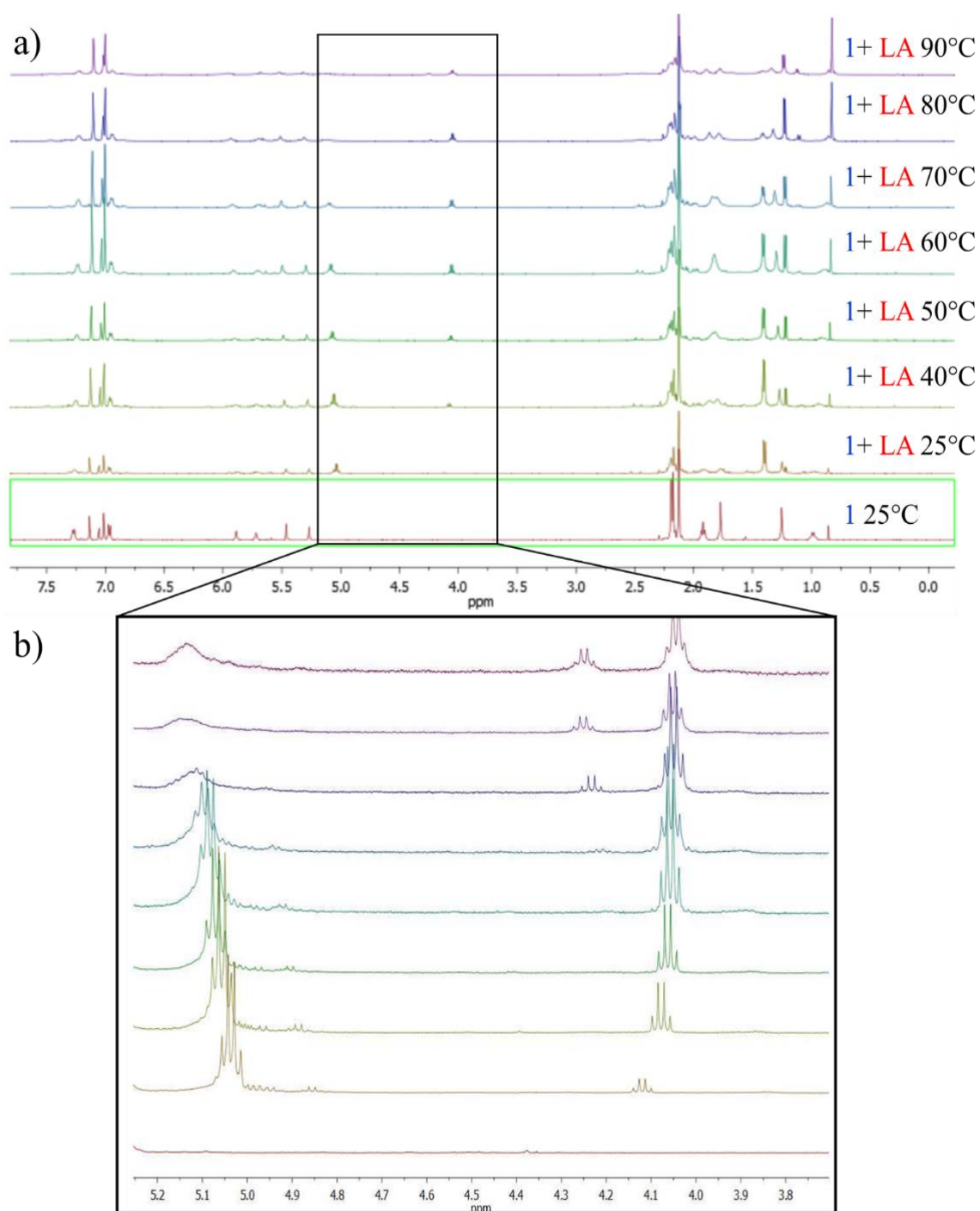


Figure A2.5. VT- ¹H NMR spectrum (500 MHz, 298 K, CDCl₃) of [LA]/[cat]=1. a) Full spectrum; b) CH region

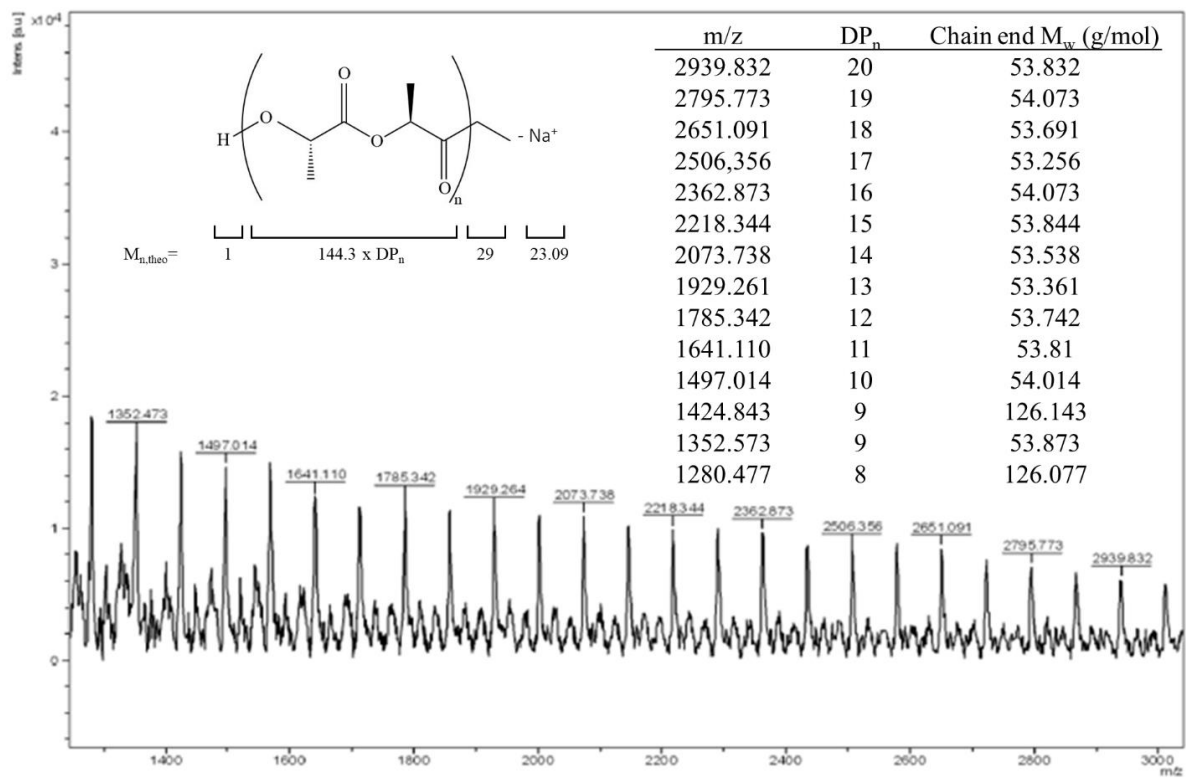


Figure A2.6. Selected area of MALDI-TOF mass spectrum of PLLA sample obtained with $[LA]/[cat]=20$, 79% conversion.

A2.3 Homochiral and racemic polymerization of lactide

A2.3.1 Synthesis of L1: Homopolymer synthesis

Two schlenk tubes were charged in the glovebox with 10.4 mg and 360 mg of catalyst and L-LA respectively, and 2 and 3 mL of solvent respectively. Both, LA and catalyst schlenks flasks were attached to the vacuum line and temperature equilibrium was ensured by stirring the solutions for 15 min in an oil bath pre-heated at 70°C. Monomer and catalyst solutions were poured together by a glass bent adaptor and polymerization times were measured from that point. Methanol was used to terminate the reaction and precipitate the polymer synthesized after 60 min. The obtained polymer was collected by filtration and dried at room temperature exposed to vacuum over 24h, obtaining a white powder (97 mg, 27%). ¹H NMR (500 MHz, CDCl₃, 297 K): δ 5.21-5.07 (q, 1H, CH(PLA)), 4.99-4.94 (q, 1H, CH(L-LA)), 1.62-1.60 (d, 3H, CH₃(L-LA)), 1.52-1.50 (d, 3H, CH₃(PLA)). GPC (CHCl₃): M_w=17440, M_n=12824, Đ=1.36.

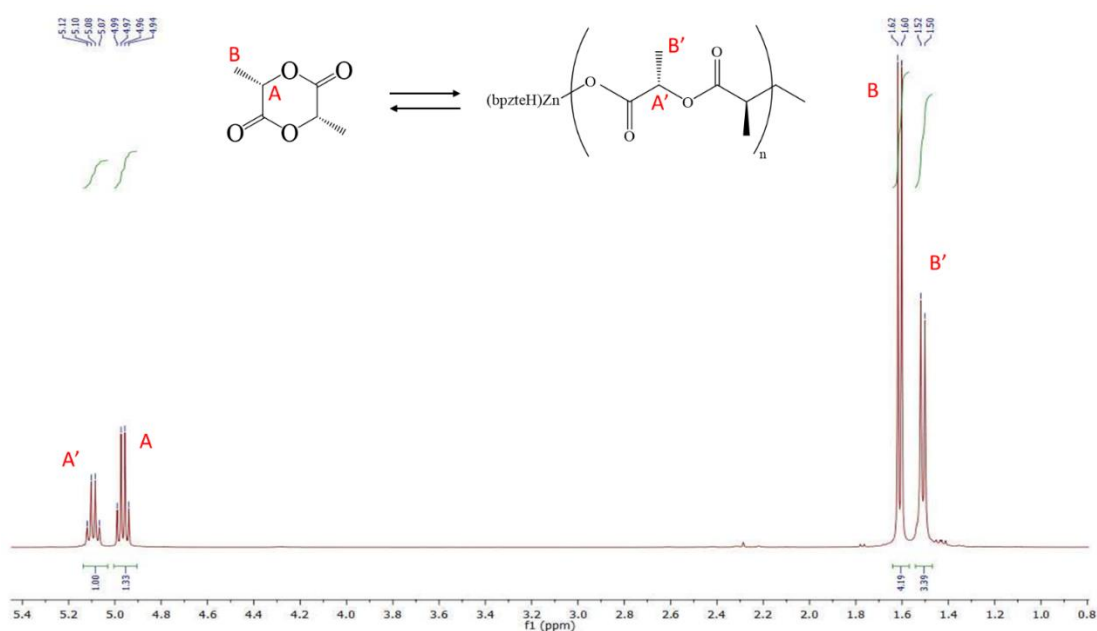


Figure A2.7: ¹H NMR spectrum (500 MHz, 298 K, CDCl₃) of L1.

A2.3.2 Synthesis of L2

The polymer L2 was synthesized following the procedure described for the L1 polymer, namely the homopolymer synthesis. Two schlenk tubes were charged in the glovebox with 10.4 mg and 360 mg of catalyst and L-LA respectively, and 2 and 3 mL of solvent, respectively. The oil bath was pre-heated at 90°C rather than 70°C. A white powder was obtained after 60 min (270mg, 75%). ^1H NMR (500 MHz, CDCl_3 , 297 K): δ 5.21-5.16 (q, 1H, $\text{CH}_{(\text{PLA})}$), 5.07-5.03 (q, 1H, $\text{CH}_{(\text{L-LA})}$), 1.71-1.70 (d, 3H, $\text{CH}_3(\text{L-LA})$), 1.61-1.59 (d, 3H, $\text{CH}_3(\text{PLA})$). GPC (CHCl_3): $M_w=48689$, $M_n=30055$, $D=1.62$.

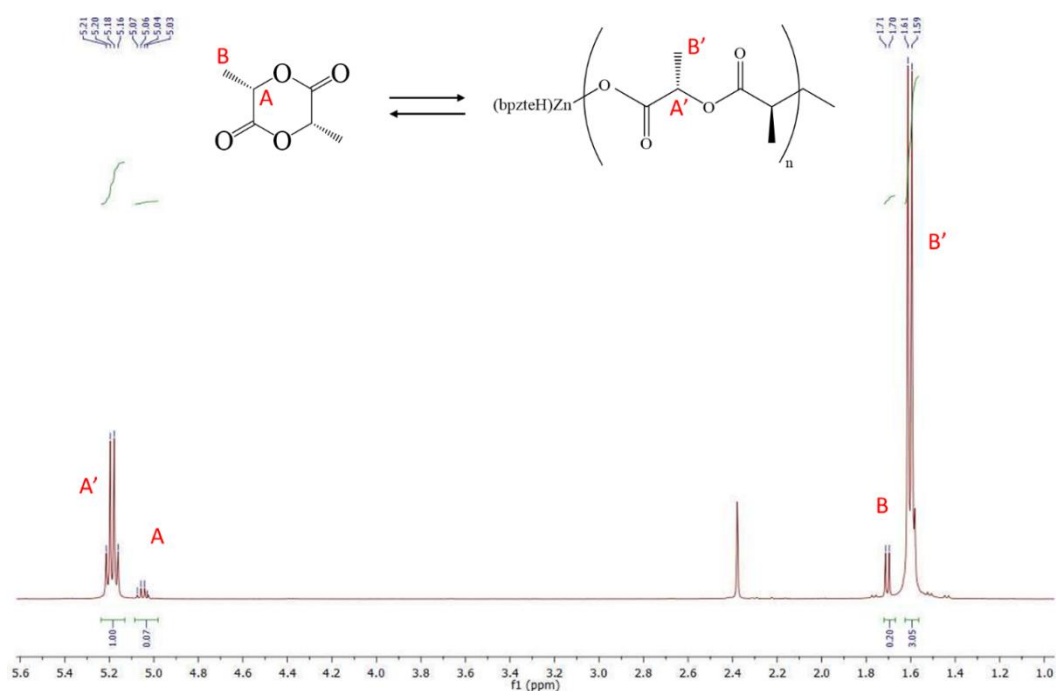


Figure A2.8: ^1H NMR spectrum (500 MHz, 298 K, CDCl_3) of L2.

A2.3.3 Synthesis of L3

The polymer L3 was synthesized following the procedure described for the L1 polymer, namely the homopolymer synthesis. Two schlenk tubes were charged in the glovebox with 10.4 mg and 1.8 g of catalyst and L-LA respectively, and 5 and 15 mL of solvent respectively. The oil bath was pre-heated at 90°C. A white powder was obtained after 45 min (1.44g, 80%). $^1\text{H NMR}$ (500 MHz, CDCl_3 , 297 K): δ 5.21-5.16 (q, 1H, $\text{CH}_{(\text{PLA})}$), 5.07-5.02 (q, 1H, $\text{CH}_{(\text{L-LA})}$), 1.71-1.70 (d, 3H, $\text{CH}_3(\text{L-LA})$), 1.61-1.59 (d, 3H, $\text{CH}_3(\text{PLA})$). GPC (CHCl_3): $M_w=115118$, $M_n=62564$, $D=1.84$.

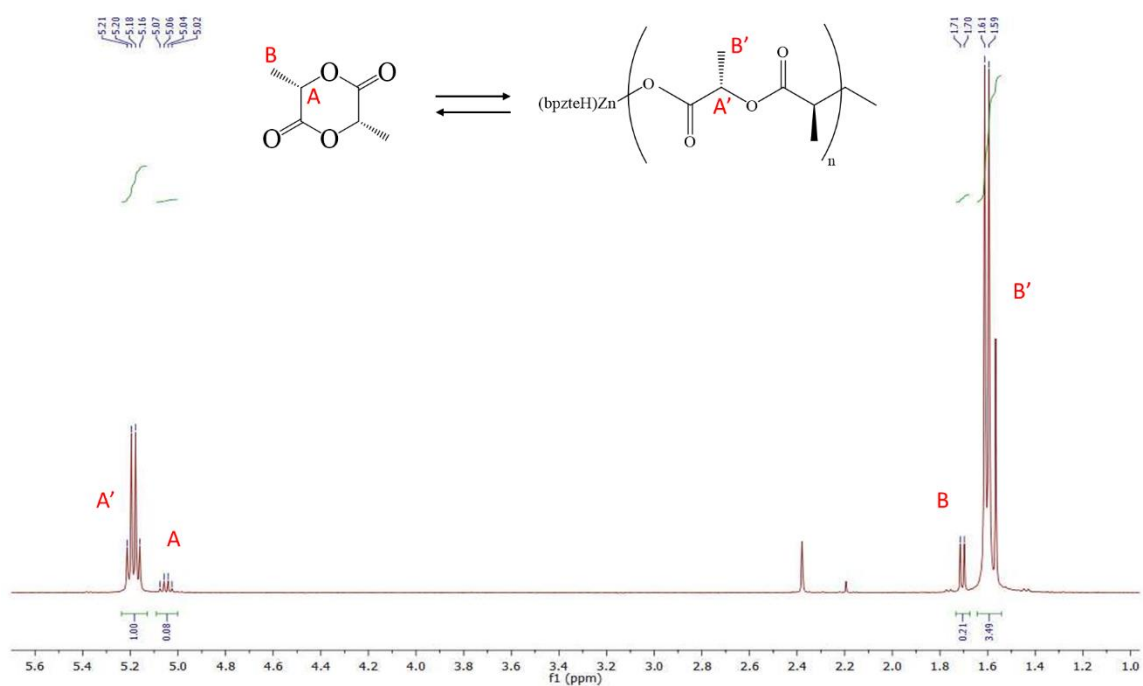


Figure A2.9: $^1\text{H NMR}$ spectrum (500 MHz, 298 K, CDCl_3) of L3.

A2.3.4 Synthesis of L4

The polymer L4 was synthesized following the procedure described for the L1 polymer, namely the homopolymer synthesis. Two schlenk tubes were charged in the glovebox with 10.4 mg and 1.8 g of catalyst and L-LA and 5 and 15 mL of solvent, respectively. A white powder was obtained after 90 min (1.20g, 66 %). ^1H NMR (500 MHz, CDCl_3 , 297 K): δ 5.21-5.16 (q, 1H, $\text{CH}_{(\text{PLA})}$), 5.07-5.02 (q, 1H, $\text{CH}_{(\text{L-LA})}$), 1.71-1.69 (d, 3H, $\text{CH}_3(\text{L-LA})$), 1.61-1.59 (d, 3H, $\text{CH}_3(\text{PLA})$). GPC (CHCl_3): $M_w=75898$, $M_n=42880$, $\text{D}=1.77$.

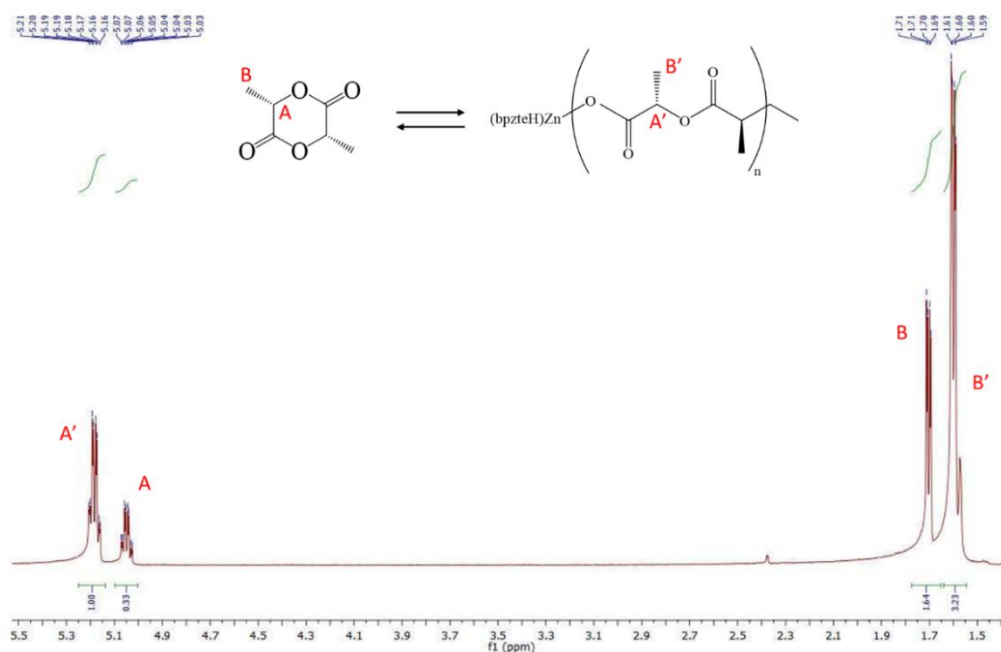


Figure A2.10: ^1H NMR spectrum (500 MHz, 298 K, CDCl_3) of L4.

A2.3.5 Synthesis of L5

The polymer L5 was synthesized following the procedure described for the L1 polymer, namely the homopolymer synthesis. Two schlenk tubes were charged in the glovebox with 10.4 mg and 1.8 g of catalyst and L-LA and 5 and 15 mL of solvent, respectively. A white powder was obtained after 120 min (1.55g, 86 %). $^1\text{H NMR}$ (500 MHz, CDCl_3 , 297 K): δ 5.12-5.06 (q, 1H, $\text{CH}_{(\text{PLA})}$), 4.98-4.93 (q, 1H, $\text{CH}_{(\text{L-LA})}$), 1.62-1.60 (d, 3H, $\text{CH}_3(\text{L-LA})$), 1.52-1.47 (d, 3H, $\text{CH}_3(\text{PLA})$). GPC (CHCl_3): $M_w=105673$, $M_n=48253$, $\text{Đ}=2.19$.

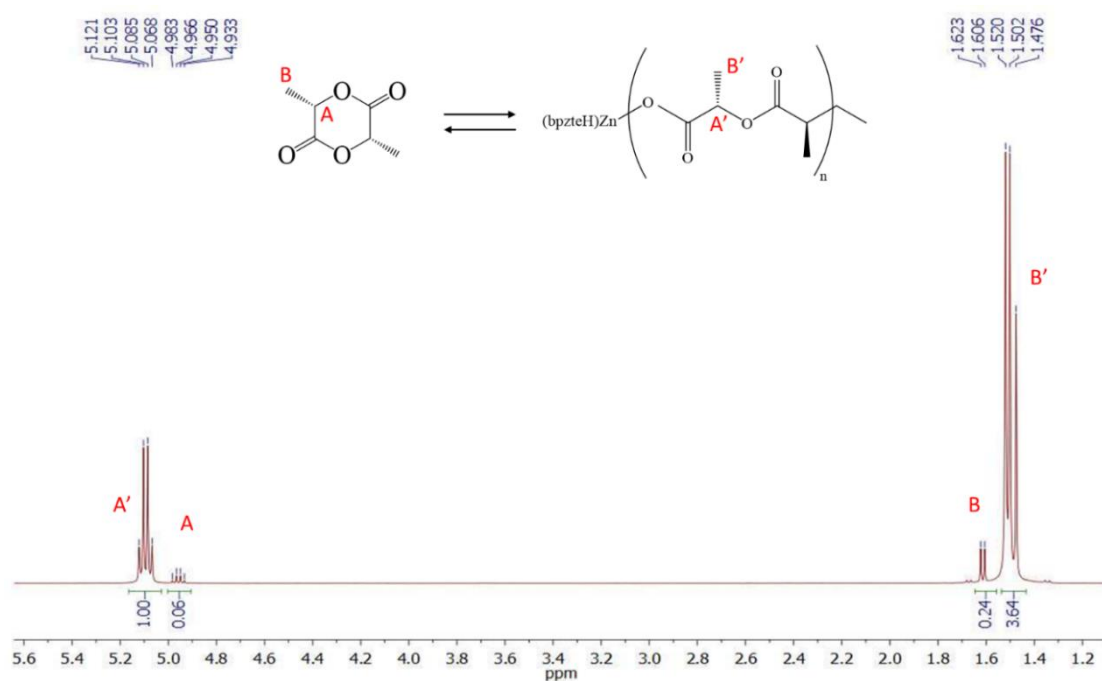


Figure A2.11: $^1\text{H NMR}$ spectrum (500 MHz, 298 K, CDCl_3) of L5.

A2.3.6 Synthesis of D1

The polymer D1 was synthesized following the procedure described for the L1 polymer, namely the homopolymer synthesis. D-LA was used rather the L-LA. Two schlenk tubes were charged in the glovebox with 10.4 mg and 1.8 g of catalyst and D-LA and 5 and 15 mL of solvent, respectively. A white powder was obtained after 90 min (1.30g, 72 %). $^1\text{H NMR}$ (500 MHz, CDCl_3 , 297 K): δ 5.19-5.15 (q, 1H, $\text{CH}_{(\text{PLA})}$), 5.06-5.02 (q, 1H, $\text{CH}_{(\text{L-LA})}$), 1.70-1.69 (d, 3H, $\text{CH}_3_{(\text{L-LA})}$), 1.61-1.58 (d, 3H, $\text{CH}_3_{(\text{PLA})}$). GPC (CHCl_3): $M_w=73500$, $M_n=41295$, $D=1.78$.

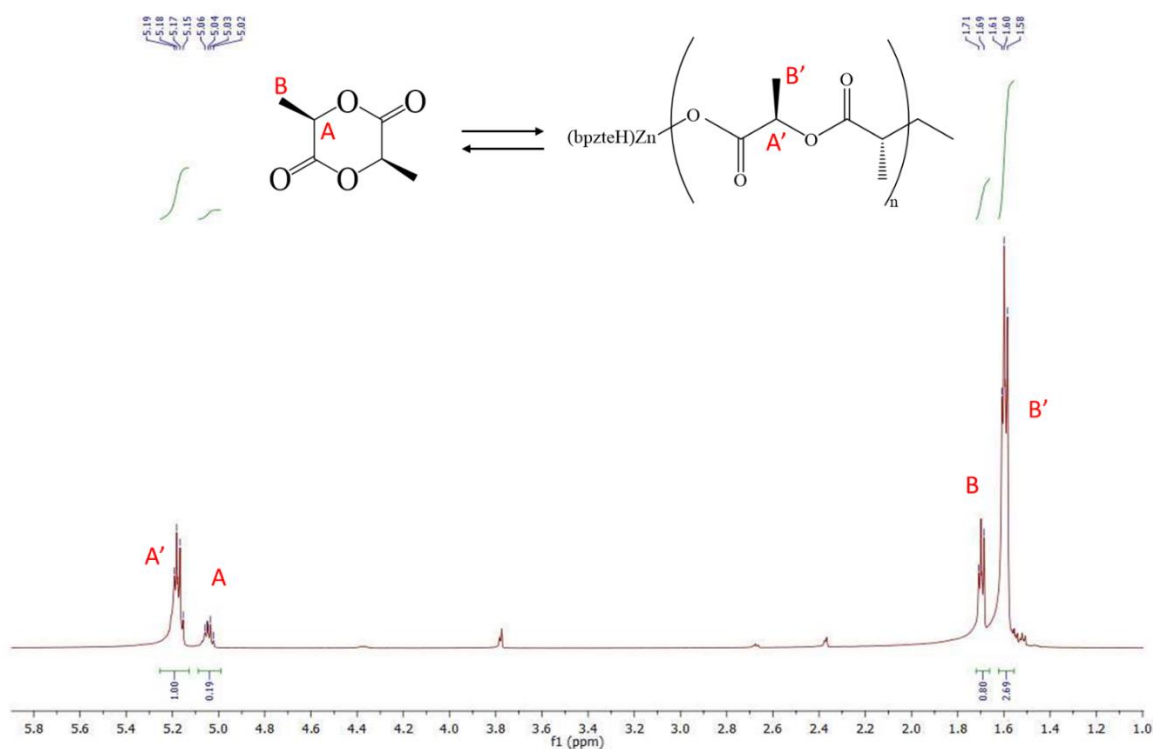


Figure A2.12: $^1\text{H NMR}$ spectrum (500 MHz, 298 K, CDCl_3) of D1.

A2.3.7 Synthesis of Rac1

The polymer Rac1 was synthesized following the procedure described for the L1 polymer, namely the homopolymer synthesis. Racemic-LA (L-LA and D-LA) was used rather than L-LA. Two schlenk tubes were charged in the glovebox with 10.4 mg and 1.8 g of catalyst and Rac-LA and 5 and 15 mL of solvent, respectively. A transparent and rubbery product was obtained after 120 min (650 mg, 36 %). ^1H NMR (500 MHz, CDCl_3 , 297 K): δ 5.25-5.17 (m, 1H, $\text{CH}_{(\text{PLA})}$), 5.16-5.05 (q, 1H, $\text{CH}_{(\text{L-LA})}$), 1.70-1.68 (d, 3H, $\text{CH}_3(\text{L-LA})$), 1.60-1.57 (m, 3H, $\text{CH}_3(\text{PLA})$). GPC (CHCl_3): $M_w=23592$, $M_n=14212$, $D=1.66$.

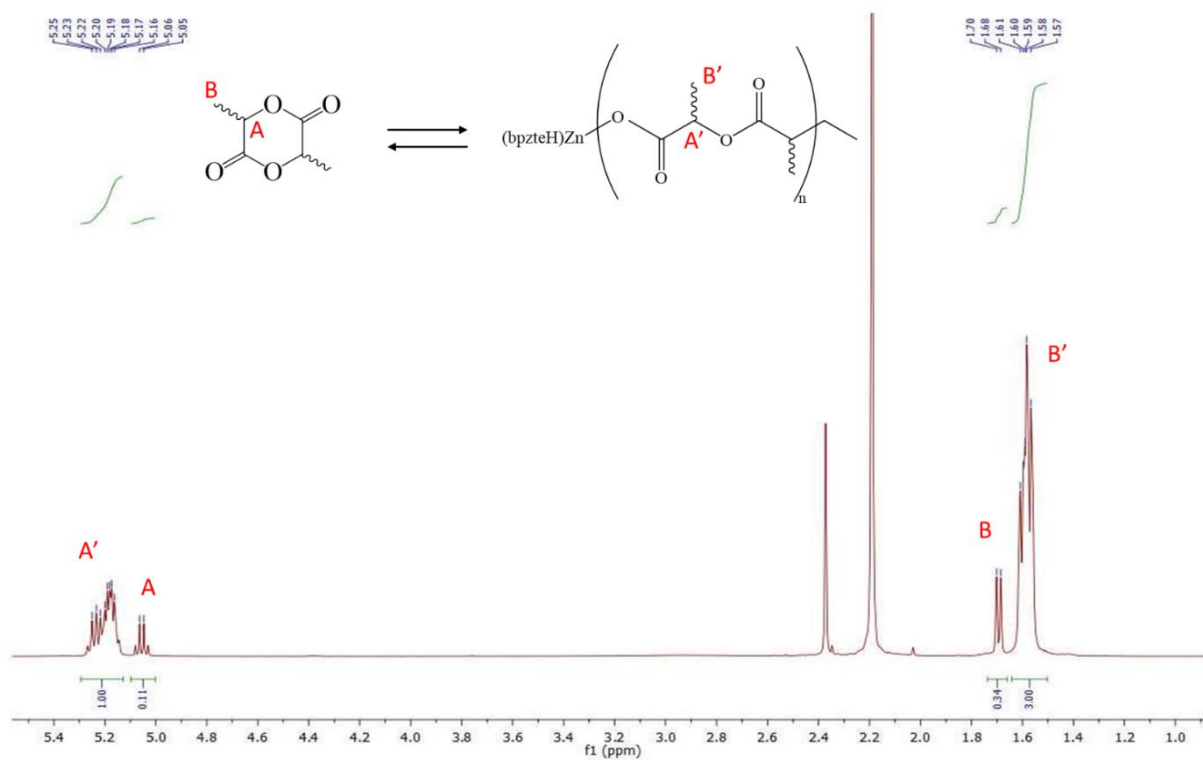


Figure A2.13. ^1H NMR spectrum (500 MHz, 298 K, CDCl_3) of Rac1.

A2.4 Stereo-Block Copolymerization by Sequential Monomer Addition

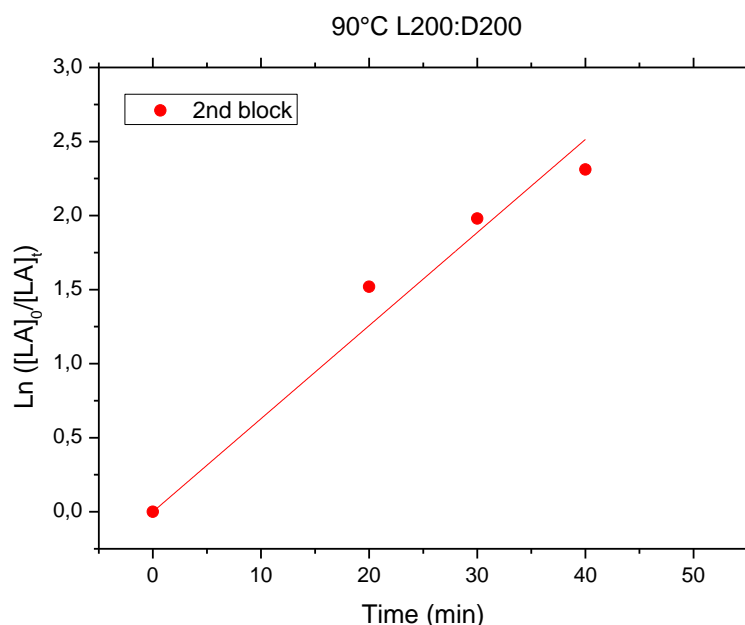


Figure A2.14. First-order kinetic plot of the second block polymerization reaction of L200:D200 at 90°C. $[D-LA]_0/[Zn]_0=200$; $[LA]_0= 200$ mM; $[Zn]_0= 1$ mM.

A2.4.1 Synthesis of L115:D115: one pot sequential addition

The block-copolymer L115:D115 was synthesized following the one-pot sequential addition. Three schlenk tubes were charged in the glovebox with 10.4 mg, 450 mg and 450 mg of catalyst, L-LA and D-LA, respectively. 2 ml, 3ml and 3ml were added to the schlenk flasks respectively. Catalyst, L-LA and D-LA schlenk flasks were attached to the vacuum line and temperature equilibrium was ensured by stirring the solutions for 15 min in an oil bath pre-heated at 90°C. L-LA monomer and catalyst solutions were poured together by a glass bent adaptor and polymerization times were measured from that point. D-LA monomer solutions was added to the polymerization reaction after 25min of L-LA polymerization. Methanol was used to terminate the reaction and precipitate the polymer synthesized after 50 min. The obtained polymer was collected by filtration and dried at room temperature exposed to vacuum over 24h, obtaining a white powder (603 mg, 67%). 1H NMR (500 MHz, $CDCl_3$, 297 K): δ 5.21-5.16 (q, 1H, $CH_{(PLA)}$), 5.07-5.03 (q, 1H, $CH_{(L-LA)}$), 1.71-1.70 (d, 3H, $CH_3_{(L-LA)}$), 1.61-1.59 (d, 3H, $CH_3_{(PLA)}$). ^{13}C NMR (500 MHz, $CDCl_3$, 297 K): δ 169.56 (CO), 68.95 (CH), 16.60 (CH_3). GPC ($CHCl_3$): $M_w=32823$, $M_n=17007$, $D=1.93$.

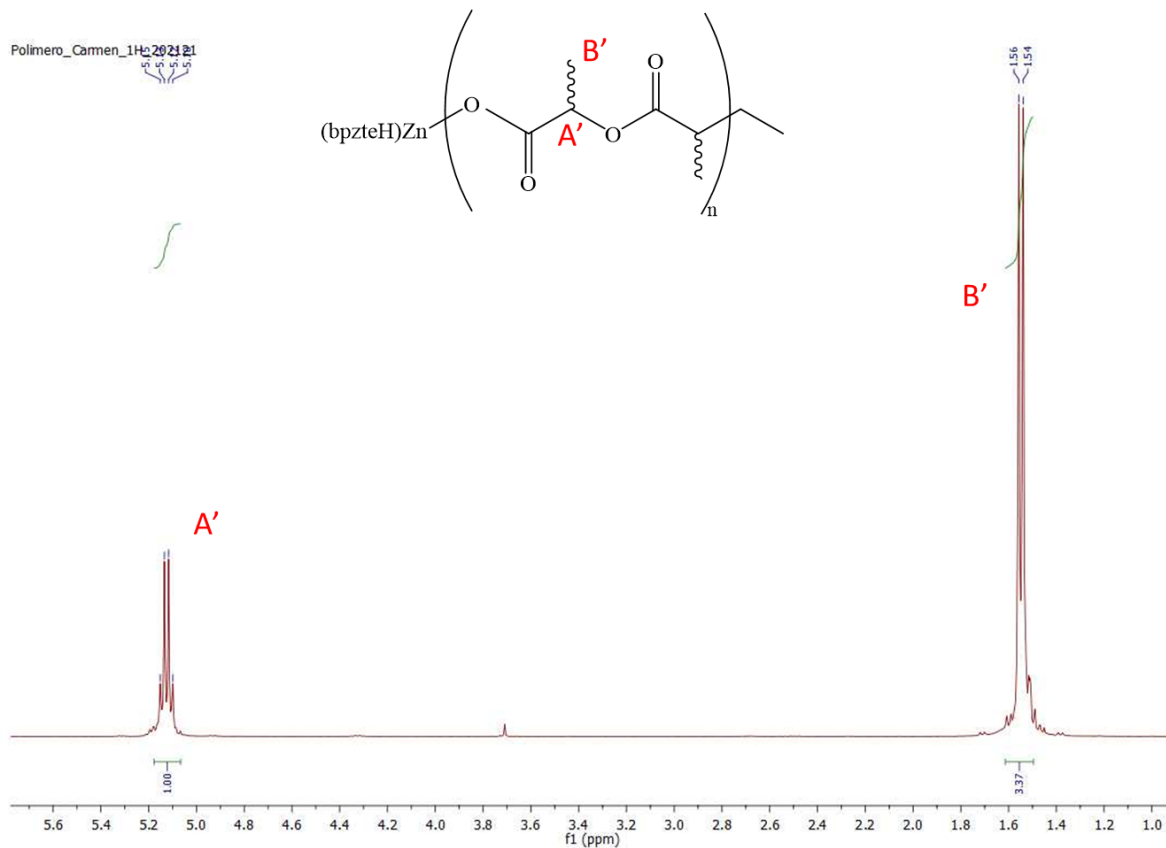


Figure A2.15: ¹H NMR spectrum (500 MHz, 298 K, CDCl₃) of L115:D115.

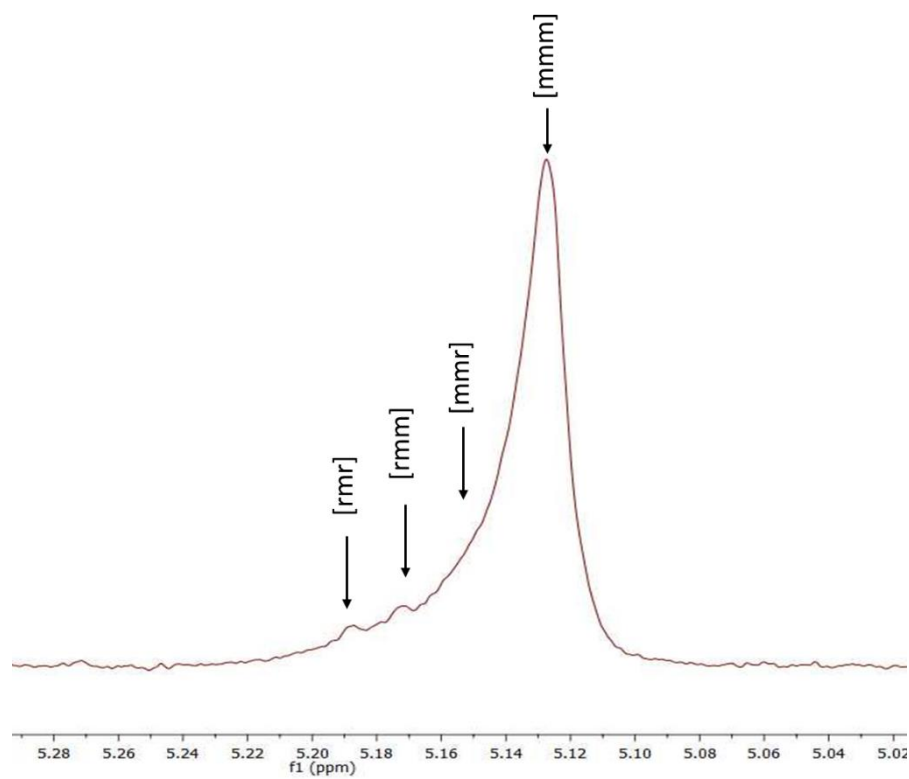


Figure A2.16: ¹H NMR spectrum (500 MHz, 298 K, CDCl₃) of the homodecoupled CH resonance of L115:D115.

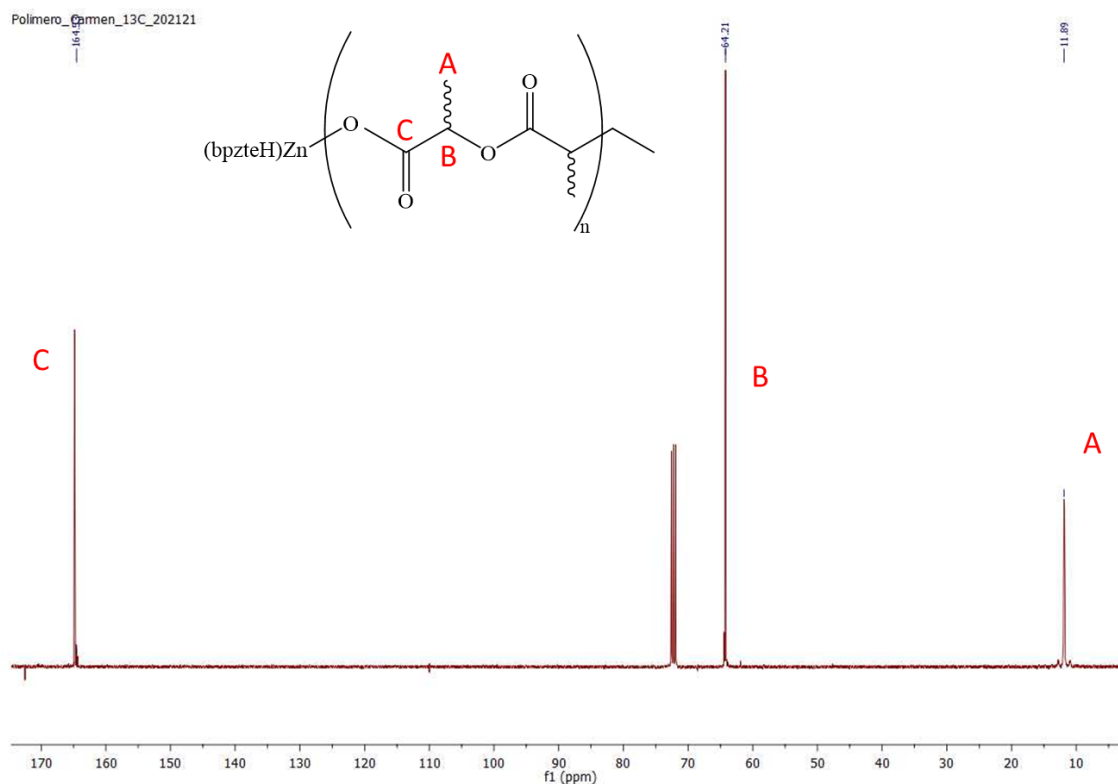


Figure A2.17: ^{13}C NMR spectrum (500 MHz, 298 K, CDCl_3) of L115:D115.

A2.4.2 Synthesis of L220:D220

The block-copolymer L220:D220 was synthesized following the one-pot sequential addition. Three schlenk tubes were charged in the glovebox with 10.4 mg, 900 mg and 900 mg of catalyst, L-LA and D-LA, respectively. 2 ml, 7ml and 7ml were added to the schlenk flasks respectively. Catalyst, L-LA and D-LA schlenks flasks were attached to the vacuum line and temperature equilibrium was ensured by stirring the solutions for 15 min in an oil bath pre-heated at 90°C . L-LA monomer and catalyst solutions were poured together by a glass bent adaptor and polymerization times were measured from that point. D-LA monomer solution was added to the polymerization reaction after 45min of L-LA polymerization. Methanol was used to terminate the reaction and precipitate the polymer synthesized after 90 min. The obtained polymer was collected by filtration and dried at room temperature exposed to vacuum over 24h, obtaining a white powder (1,152 mg, 64%). ^1H NMR (500 MHz, CDCl_3 , 297 K): δ 5.21-5.16 (q, 1H, $\text{CH}_{(\text{PLA})}$), 1.61-1.59 (d, 3H, $\text{CH}_3(\text{PLA})$). GPC (CHCl_3): $M_w=63.313$, $M_n=28.779$, $\text{D}=2,20$

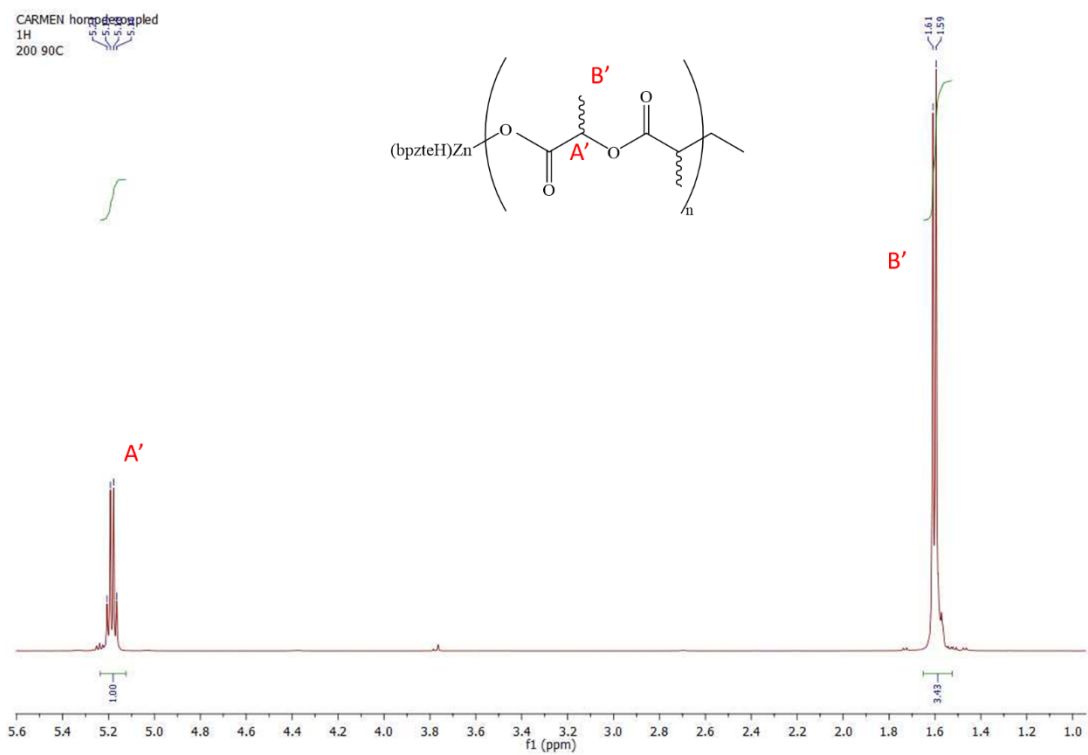


Figure A2.18: ^1H NMR spectrum (500 MHz, 298 K, CDCl_3) of L220:D220.

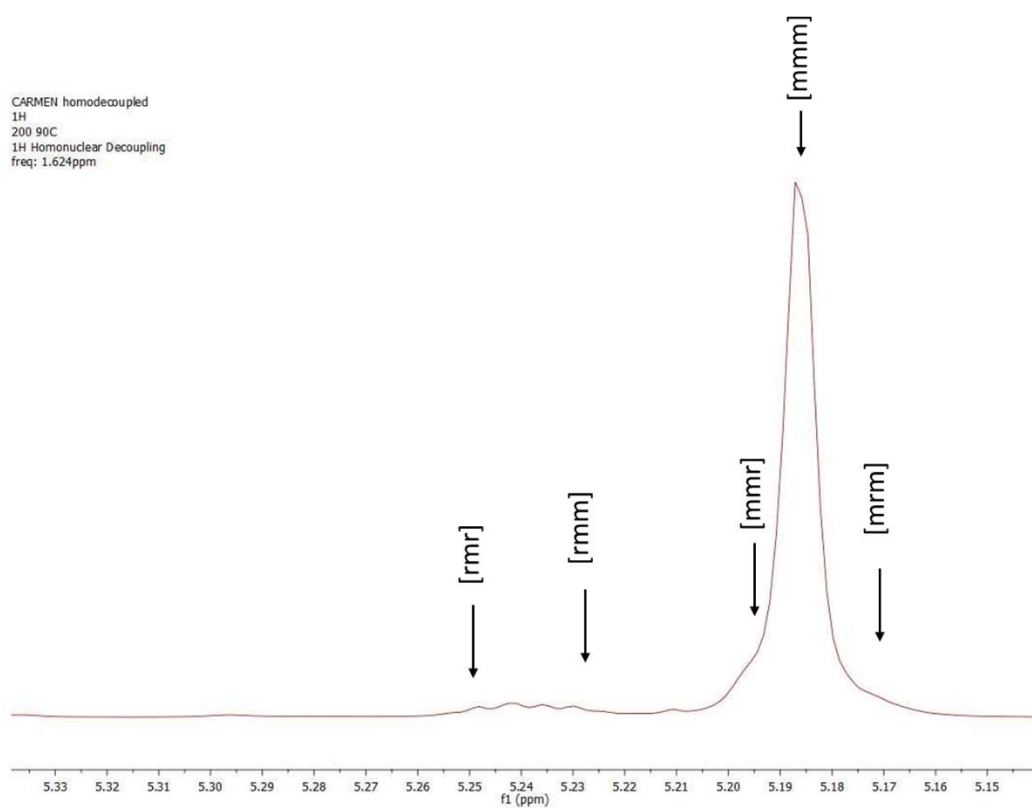


Figure A2.19: ^1H NMR spectrum (500 MHz, 298 K, CDCl_3) of the homodecoupled CH resonance of L220:D220.

A2.4.2 Synthesis of L250:D250

The block-copolymer L250:D250 was synthesized following the one-pot sequential addition. Three schlenk tubes were charged in the glovebox with 10.4 mg, 900 mg and 900 mg of catalyst, L-LA and D-LA, respectively. 2 ml, 7ml and 7ml were added to the schlenk flasks respectively. Catalyst, L-LA and D-LA schlenks flasks were attached to the vacuum line and temperature equilibrium was ensured by stirring the solutions for 15 min in an oil bath pre-heated at 75°C. L-LA monomer and catalyst solutions were poured together by a glass bent adaptor and polymerization times were measured from that point. D-LA monomer solutions was added to the polymerization reaction after 60min of L-LA polymerization. Methanol was used to terminate the reaction and precipitate the polymer synthesized after 120 min. The obtained polymer was collected by filtration and dried at room temperature exposed to vacuum over 24h, obtaining a white powder (1,224 g, 68%). ^1H NMR (500 MHz, CDCl_3 , 297 K): δ 5.21-5.16 (q, 1H, $\text{CH}_{(\text{PLA})}$), 1.61-1.59 (d, 3H, $\text{CH}_3(\text{PLA})$). GPC (CHCl_3): $M_w=72.508$, $M_n=32.958$, $\text{D}=2,20$.

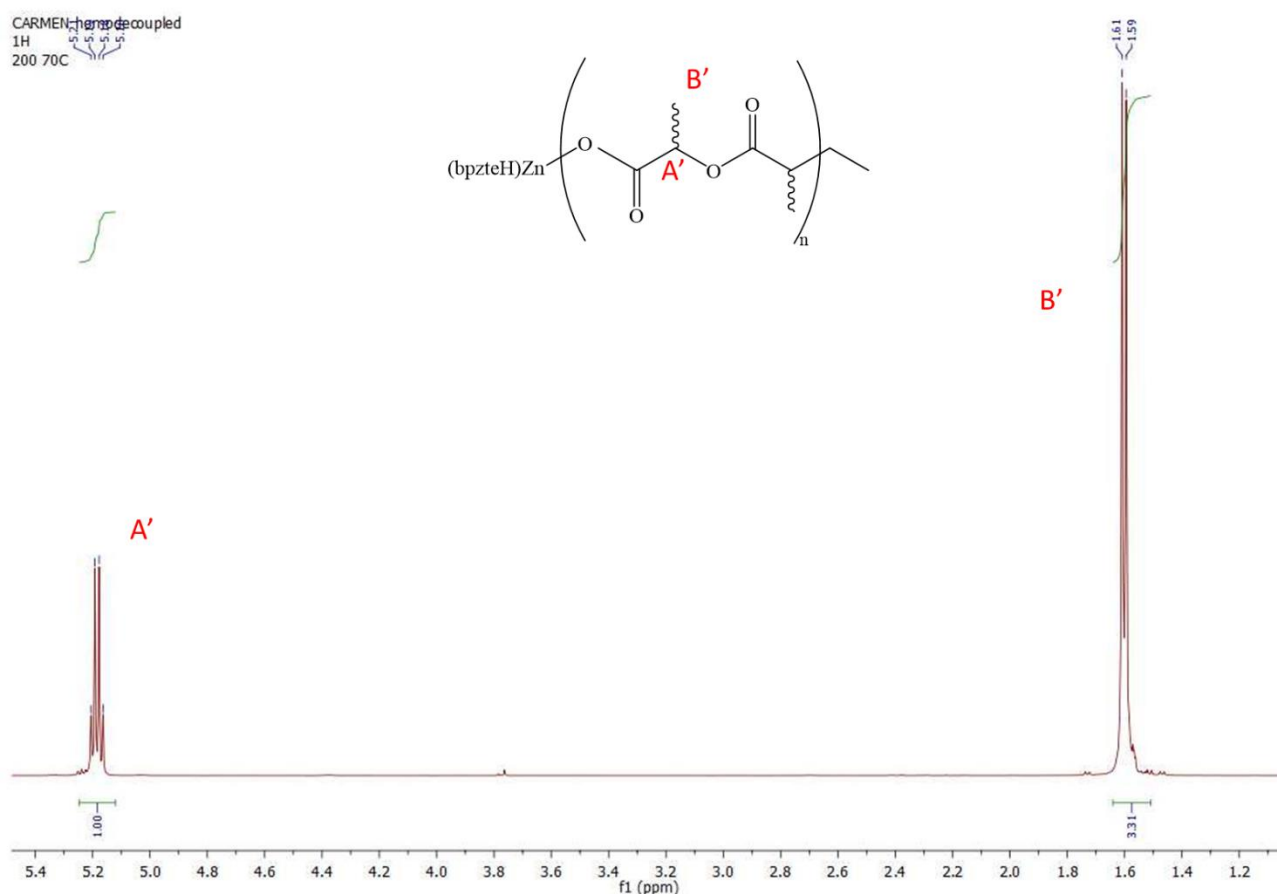


Figure A2.20: ^1H NMR spectrum (500 MHz, 298 K, CDCl_3) of L250:D250.

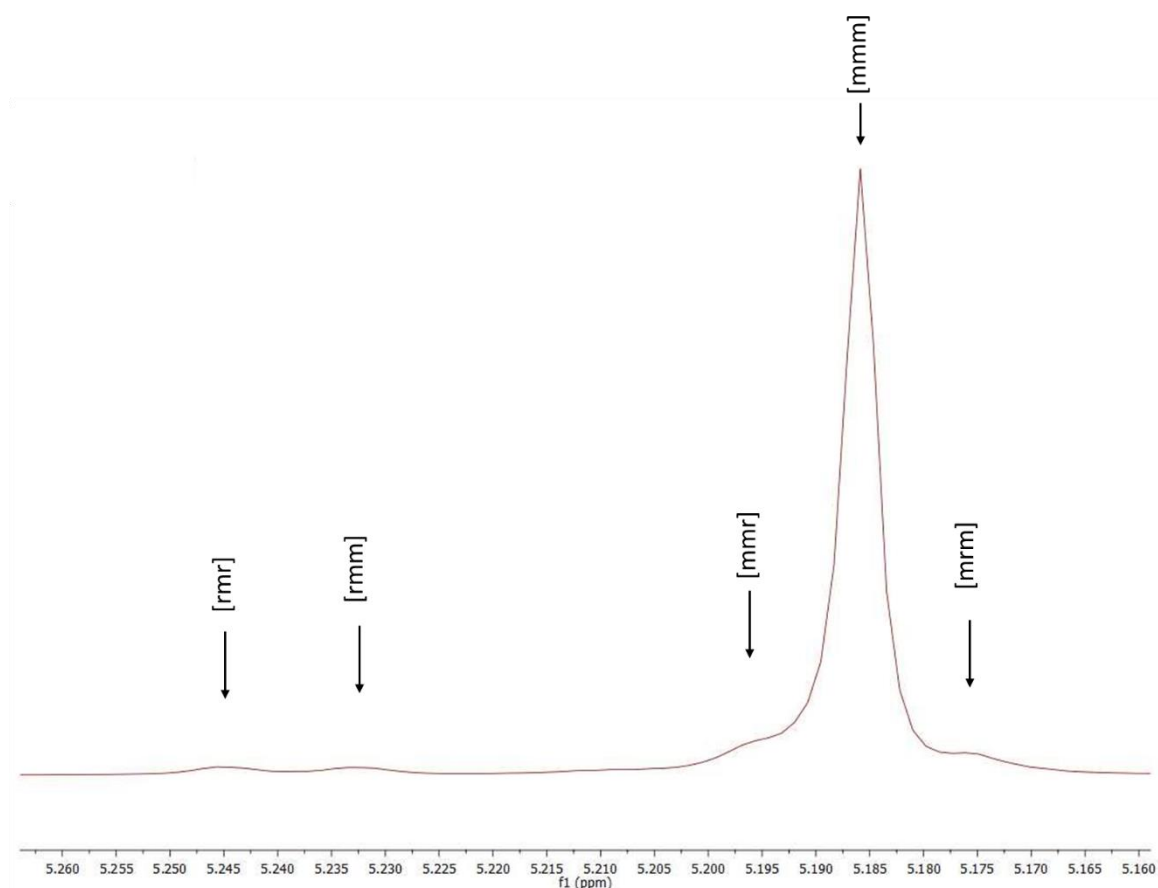


Figure A2.21: ^1H NMR spectrum (500 MHz, 298 K, CDCl_3) of the homodecoupled CH resonance of L250:D250.

A2.4.2 Synthesis of L275:D275

The block-copolymer L275:D275 was synthesized following the one-pot sequential addition. Three schlenk tubes were charged in the glovebox with 10.4 mg, 1,080 g and 1,080 g of catalyst, L-LA and D-LA, respectively. 5 ml, 10 ml and 10 ml were added to the schlenk flasks respectively. The second monomer solution (D-LA) was added after 30 min of L-LA polymerization. Methanol was used to terminate the reaction and precipitate the polymer synthesized after 60 min. The obtained polymer was collected by filtration and dried at room temperature exposed to vacuum over 24h, obtaining a white powder (1,826 mg, 83%). ^1H NMR (CDCl_3 , 297 K): δ 5,15-5,10 (q, 1H, $\text{CH}_{(\text{PLA})}$), 5,02-4,98 (q, 1H, $\text{CH}_{(\text{L-LA})}$), 1,66-1,64 (d, 3H, $\text{CH}_3_{(\text{L-LA})}$), 1,56-1,54 (d, 3H, $\text{CH}_3_{(\text{PLA})}$). ^{13}C NMR (CDCl_3 , 297 K): δ 169,56 (CO), 68,95 (CH), 16,60 (CH_3). GPC (CHCl_3): $M_w=79.320$, $M_n=35.253$, $\text{Đ}=2,25$.

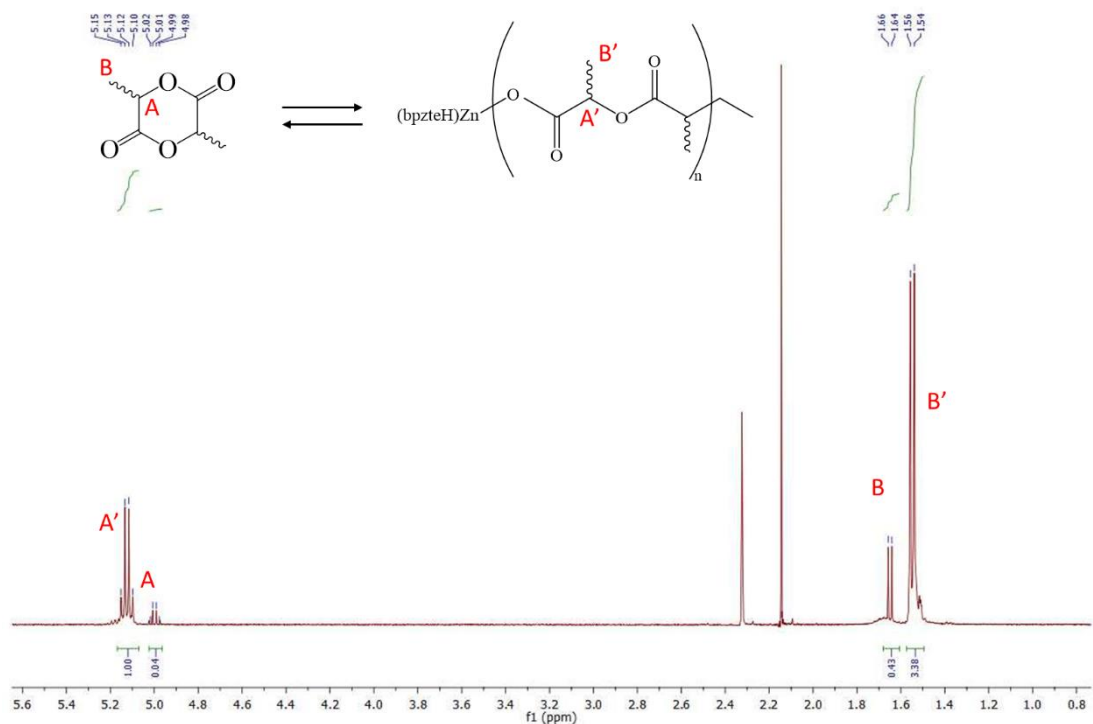


Figure A2.22: ^1H NMR spectrum (500 MHz, 298 K, CDCl_3) of L275:D275.

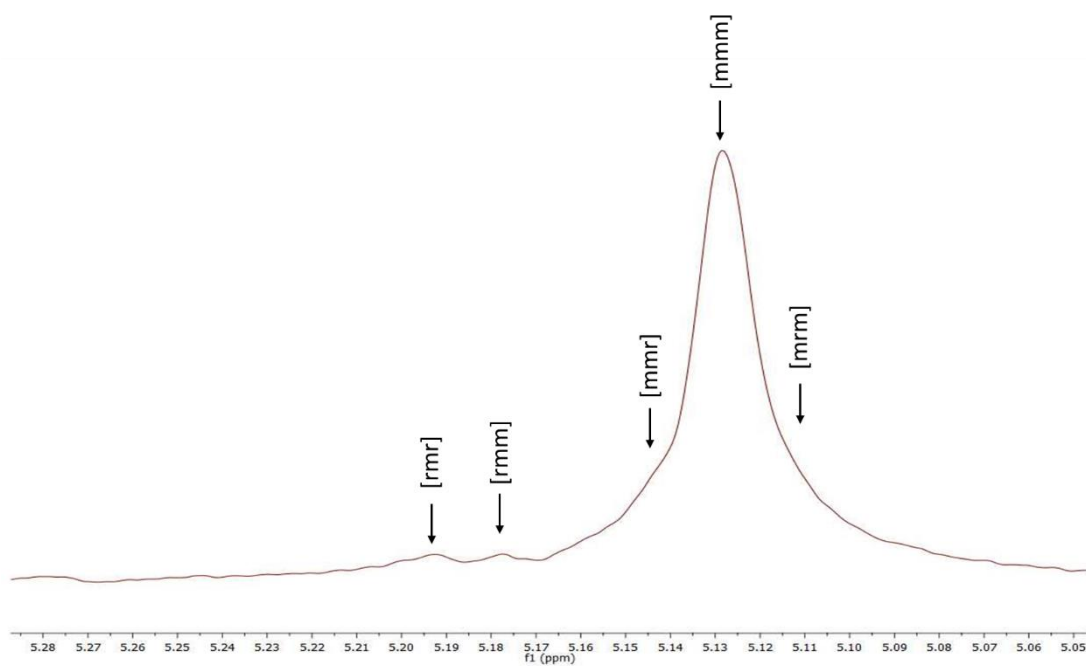


Figure A2.23: ^1H NMR spectrum (500 MHz, 298 K, CDCl_3) of the homodecoupled CH resonance of L275:D275.

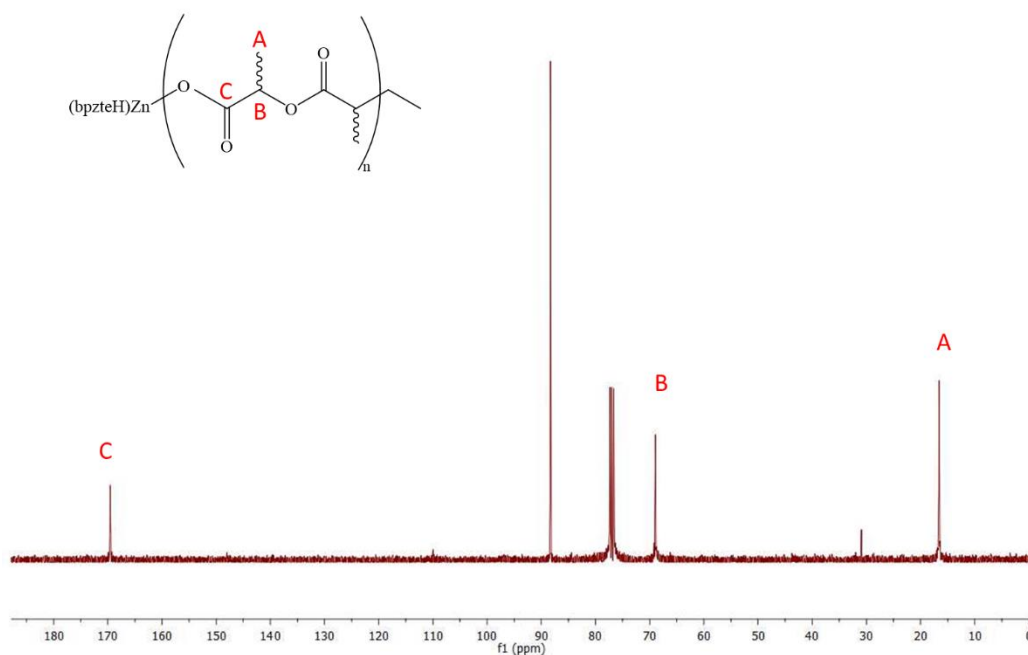


Figure A2.24: ^{13}C NMR spectrum (500 MHz, 298 K, CDCl_3) of L275:D275.

A2.4.2 Synthesis of D275:L275

The block-copolymer D275:L275 was synthesized following the one-pot sequential addition. Three schlenk tubes were charged in the glovebox with 10.4 mg, 1,080 g and 1,080 g of catalyst, L-LA and D-LA, respectively. 5 ml, 10 ml and 10 ml were added to the schlenk flasks respectively. The second monomer solution (L-LA) was added after 30 min of D-LA polymerization. Methanol was used to terminate the reaction and precipitate the polymer synthesized after 60 min. The obtained polymer was collected by filtration and dried at room temperature exposed to vacuum over 24h, obtaining a white powder (1,706 mg, 79%). ^1H NMR (CDCl_3 , 297 K): δ 5,15-5,10 (q, 1H, $\text{CH}_{(\text{PLA})}$), 5,02-4,98 (q, 1H, $\text{CH}_{(\text{L-LA})}$), 1,66-1,64 (d, 3H, $\text{CH}_3_{(\text{L-LA})}$), 1,56-1,54 (d, 3H, $\text{CH}_3_{(\text{PLA})}$). GPC (CHCl_3): $M_w=79.107$, $M_n=33.238$, $D=2,38$.

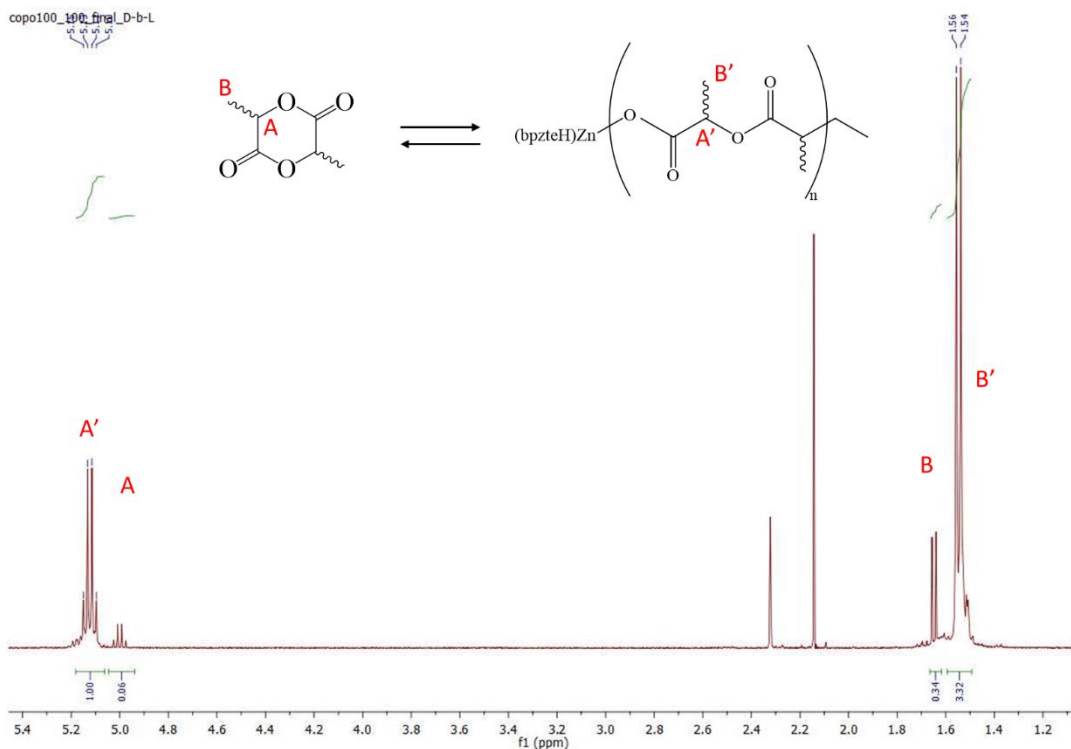


Figure A2.25: ^1H NMR spectrum (500 MHz, 298 K, CDCl_3) of D275:L275.

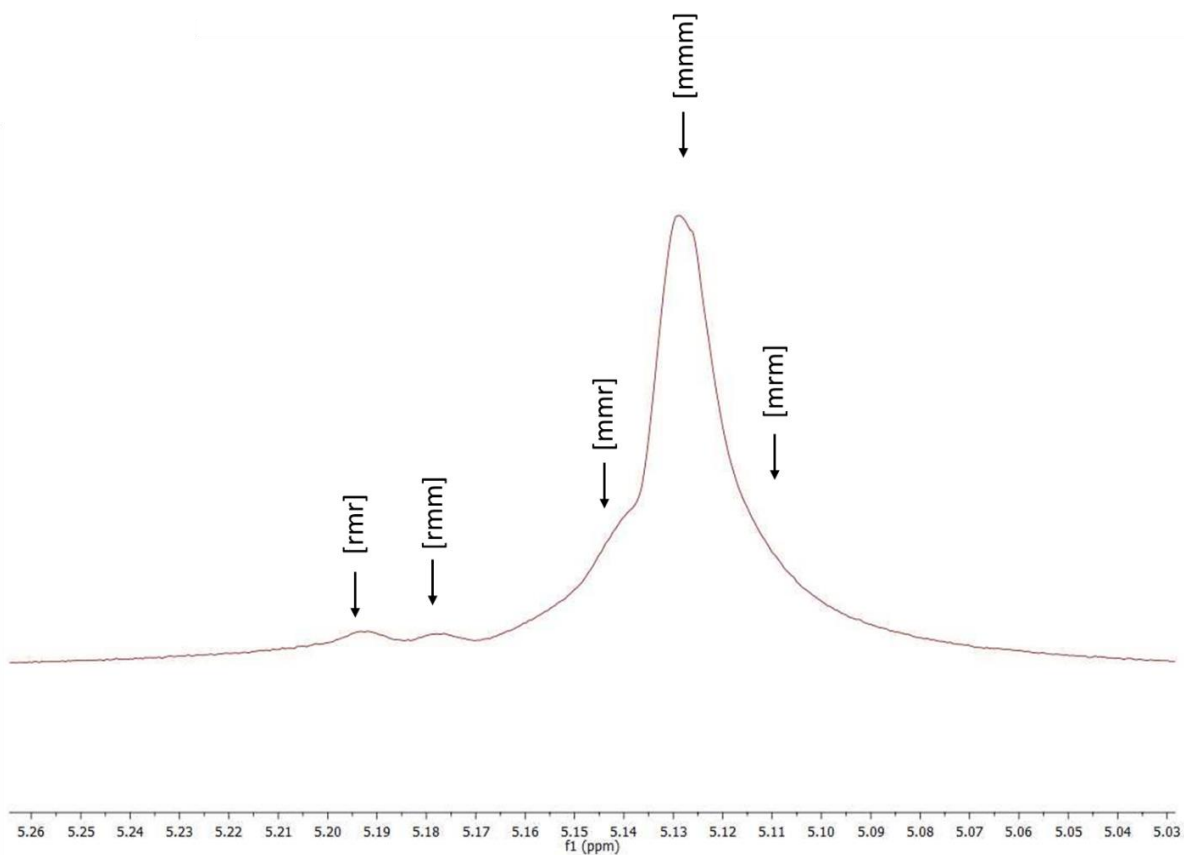


Figure A2.26: ^1H NMR spectrum (500 MHz, 298 K, CDCl_3) of the homodecoupled CH resonance of D275:L275.

A2.4.2 Synthesis of L330:D330

The block-copolymer L330:D330 was synthesized following the one-pot sequential addition. Three schlenk tubes were charged in the glovebox with 10.4 mg, 1,080 g and 1,080 mg of catalyst, L-LA and D-LA, respectively. 5 ml, 10ml and 10ml were added to the schlenk flasks respectively. The second monomer solution (D-LA) was added after 20 min of L-LA polymerization. Methanol was used to terminate the reaction and precipitate the polymer synthesized after 60 min. The obtained polymer was collected by filtration and dried at room temperature exposed to vacuum over 24h, obtaining a white powder (1,987 g, 92%). $^1\text{H NMR}$ (500 MHz, CDCl_3 , 297 K): δ 5,15-5,10 (q, 1H, $\text{CH}_{(\text{PLA})}$), 1,56-1,54 (d, 3H, $\text{CH}_3(\text{PLA})$). GPC (CHCl_3): $M_w=94.181$, $M_n=44.636$, $D=2,11$.

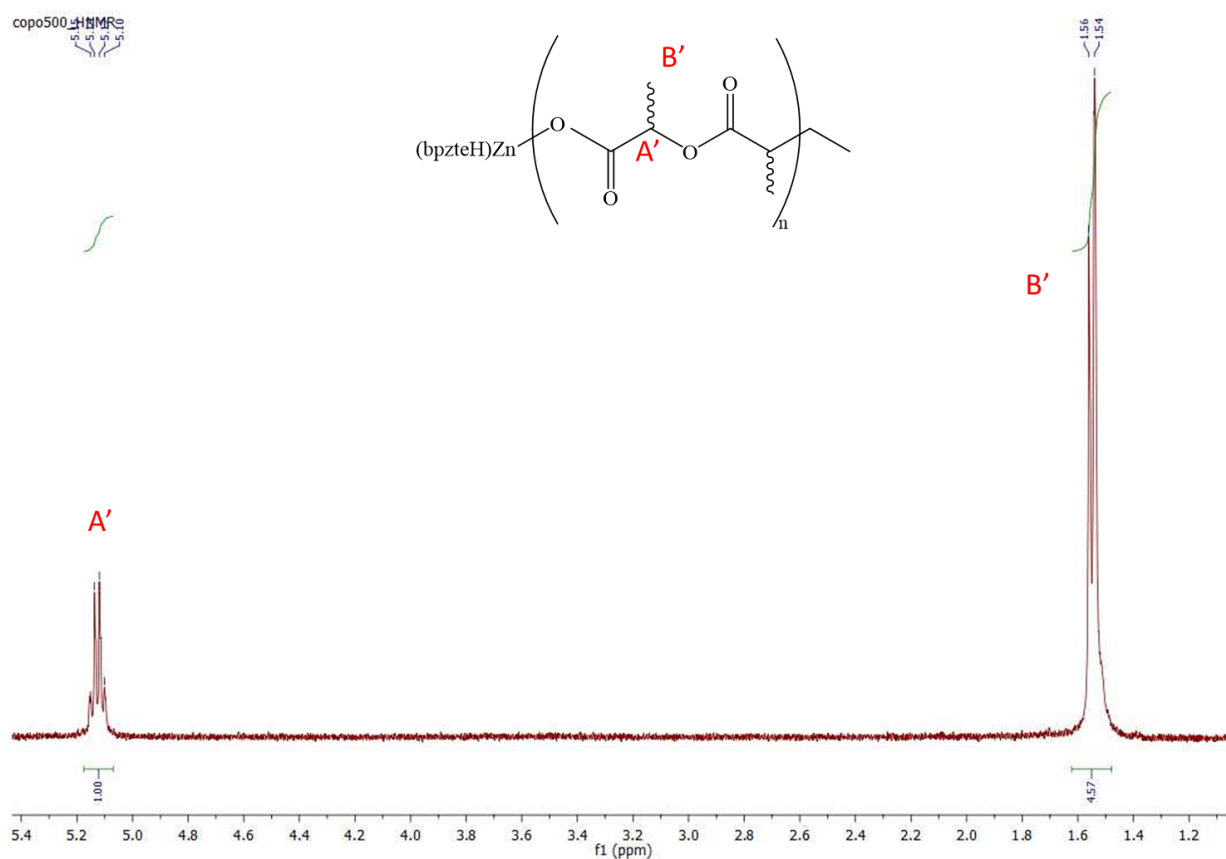


Figure A2.27: $^1\text{H NMR}$ spectrum (500 MHz, 298 K, CDCl_3) of L330:D330.

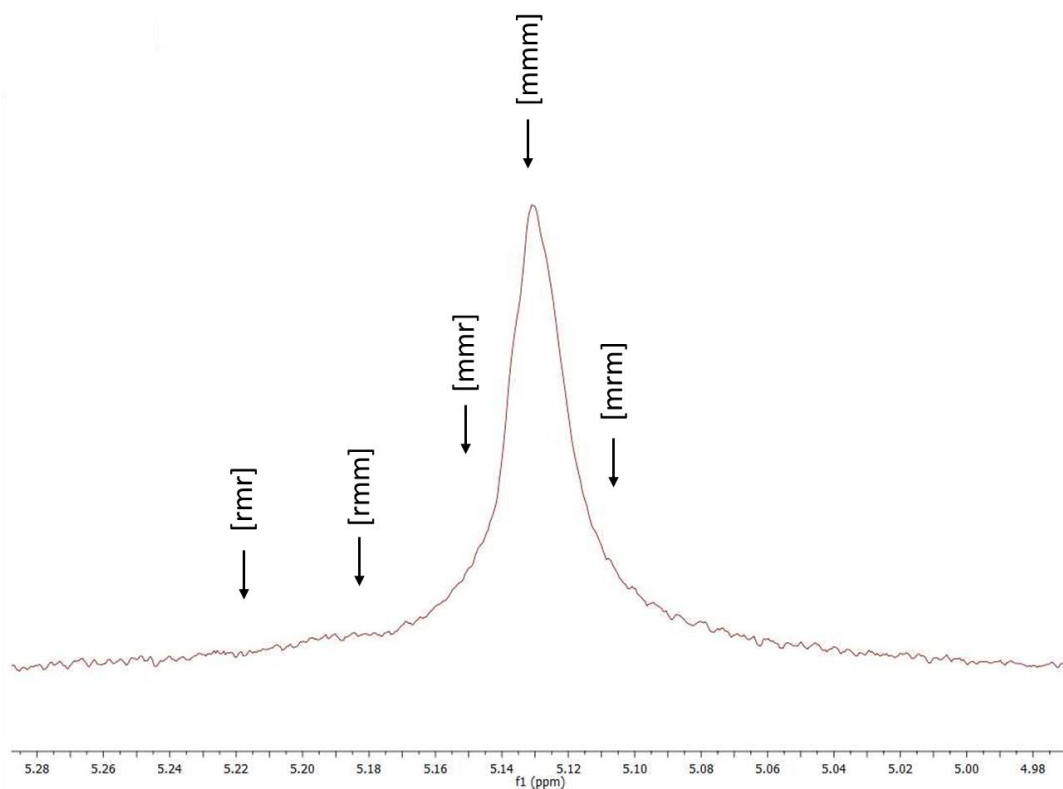


Figure A2.28: ^1H NMR spectrum (500 MHz, 298 K, CDCl_3) of the homodecoupled CH resonance of L330:D330.

A2.4.2 Synthesis of L375:D375

The block-copolymer L375:D375 was synthesized following the one-pot sequential addition. Three schlenk tubes were charged in the glovebox with 10.4 mg, 1.26 g and 1.26 g of catalyst, L-LA and D-LA, respectively. 5 ml, 12 ml and 12 ml were added to the schlenk flasks respectively. The second monomer solution (D-LA) was added after 50 min of L-LA polymerization. Methanol was used to terminate the reaction and precipitate the polymer synthesized after 100 min. The obtained polymer was collected by filtration and dried at room temperature exposed to vacuum over 24h, obtaining a white powder (2.318 g, 92%). ^1H NMR (500 MHz, CDCl_3 , 297 K): δ 5.15-5.10 (q, 1H, $\text{CH}_{(\text{PLA})}$), 5.02-4.98 (q, 1H, $\text{CH}_{(\text{L-LA})}$), 1.66-1.64 (d, 3H, $\text{CH}_3_{(\text{L-LA})}$), 1.56-1.54 (d, 3H, $\text{CH}_3_{(\text{PLA})}$). ^{13}C NMR (500 MHz, CDCl_3 , 297 K): δ 169.56 (CO), 68.95 (CH), 16.60 (CH_3). GPC (CHCl_3): $M_w=107.912$, $M_n=63.853$, $\text{D}=1.69$.

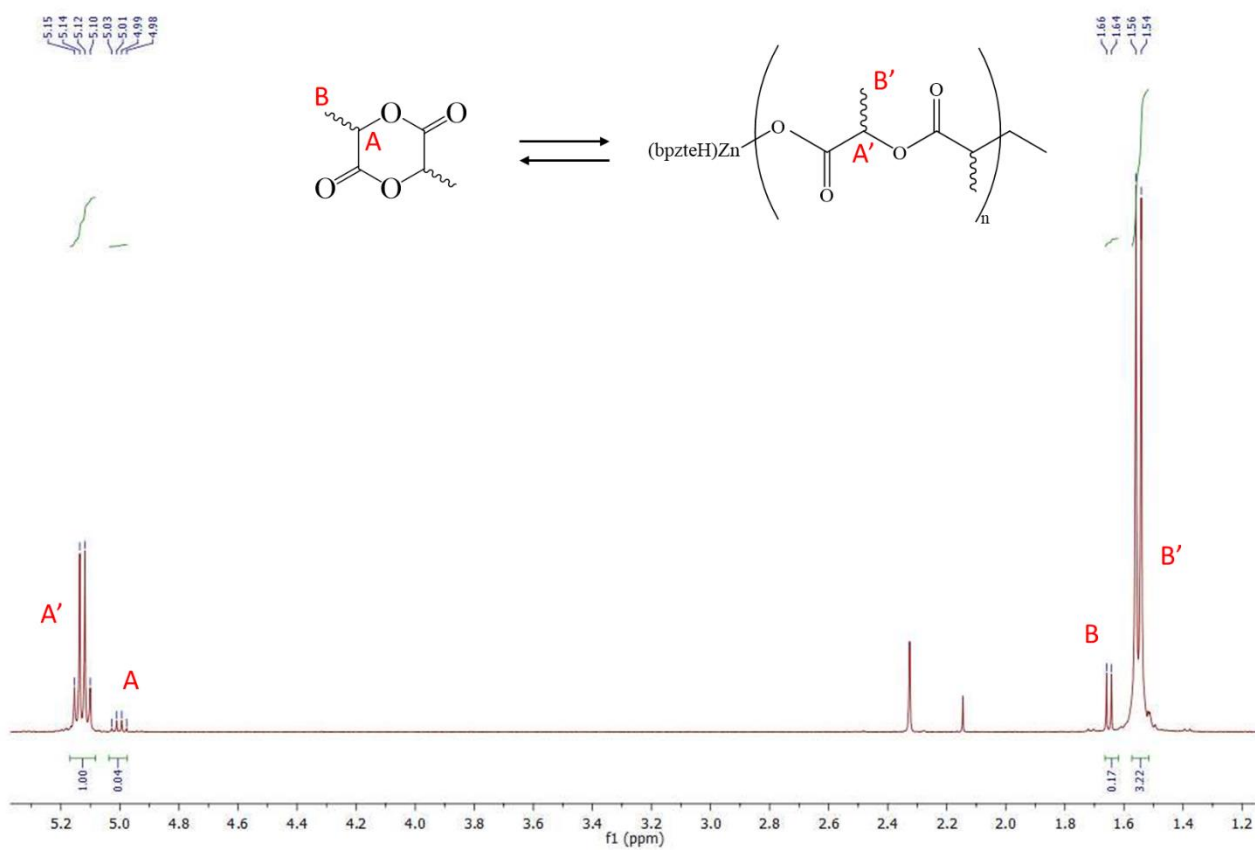


Figure A2.29: ^1H NMR spectrum (500 MHz, 298 K, CDCl_3) of L375:D375.

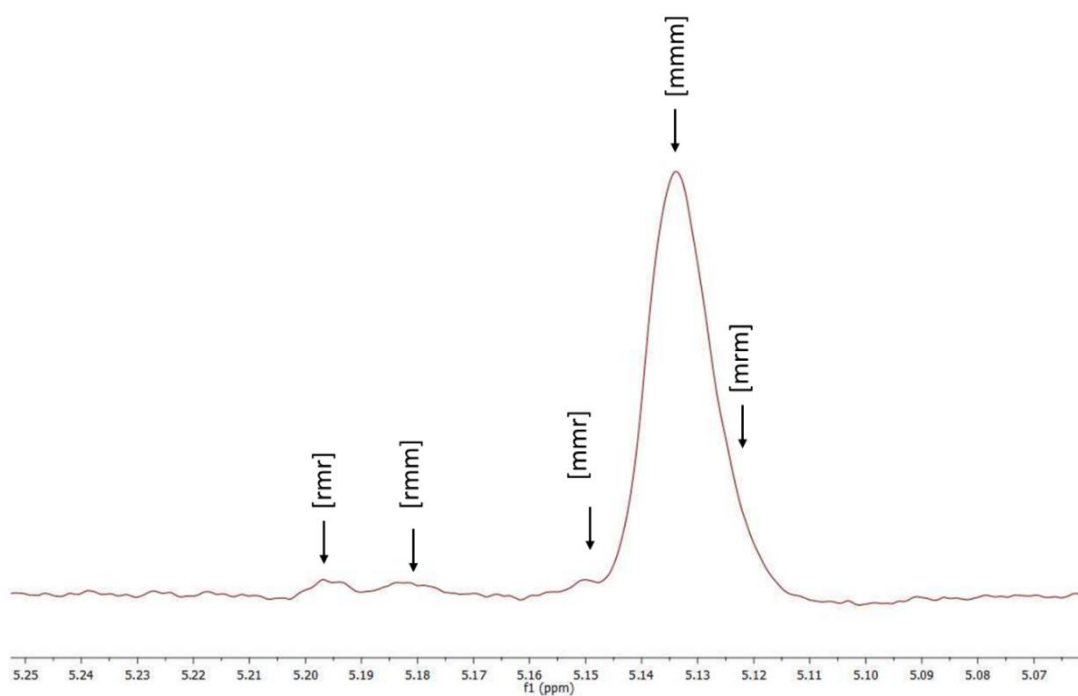


Figure A2.30: ^1H NMR spectrum (500 MHz, 298 K, CDCl_3) of the homodecoupled CH resonance of L375:D375.

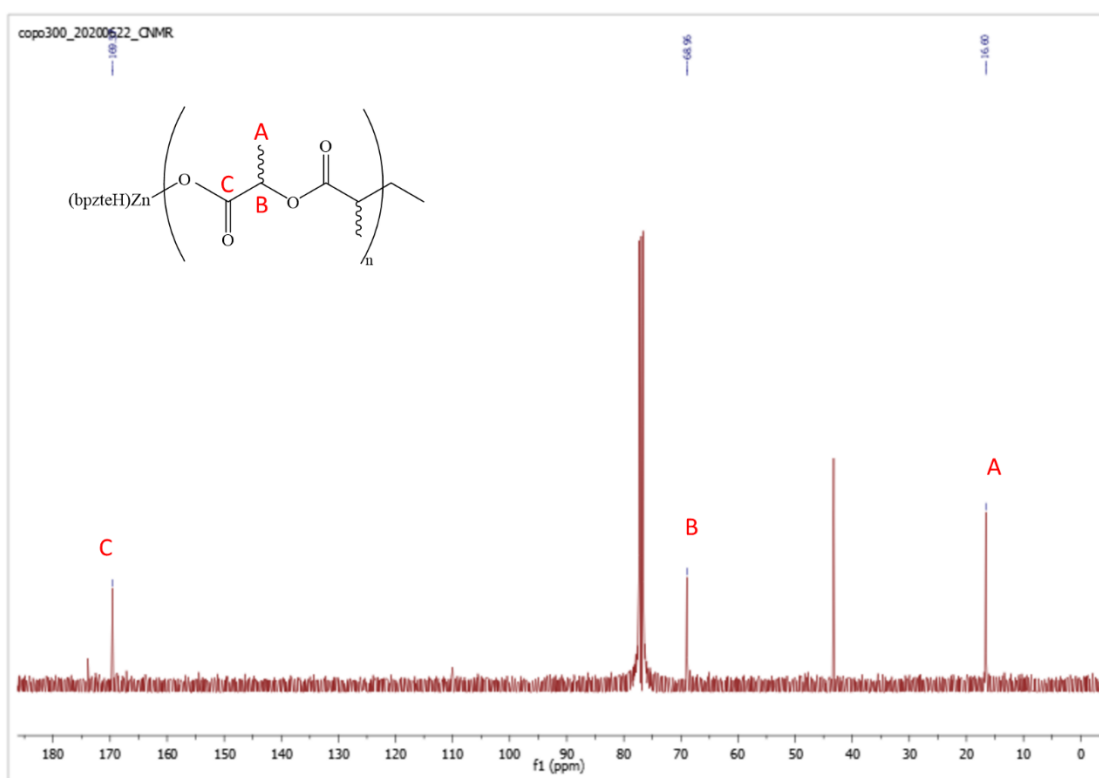


Figure A2.31: ^{13}C NMR spectrum (500 MHz, 298 K, CDCl_3) of L375:D375.

A2.4.2 Synthesis of L500:D500

The block-copolymer L500:D500 was synthesized following the one-pot sequential addition. Three schlenk tubes were charged in the glovebox with 10.4 mg, 1,8 g and 1,8 mg of catalyst, L-LA and D-LA, respectively. 5 ml, 15ml and 15ml were added to the schlenk flasks respectively. The second monomer solution (D-LA) was added after 60 min of L-LA polymerization. Methanol was used to terminate the reaction and precipitate the polymer synthesized after 110 min. The obtained polymer was collected by filtration and dried at room temperature exposed to vacuum over 24h, obtaining a white powder (2,7 g, 75%). ^1H NMR (500 MHz, CDCl_3 , 297 K): δ 5,16-5,10 (q, 1H, $\text{CH}_{(\text{PLA})}$), 1,56-1,54 (d, 3H, $\text{CH}_3(\text{PLA})$). GPC (CHCl_3): $M_w=139.517$, $M_n=53.660$, $D=2.6$.

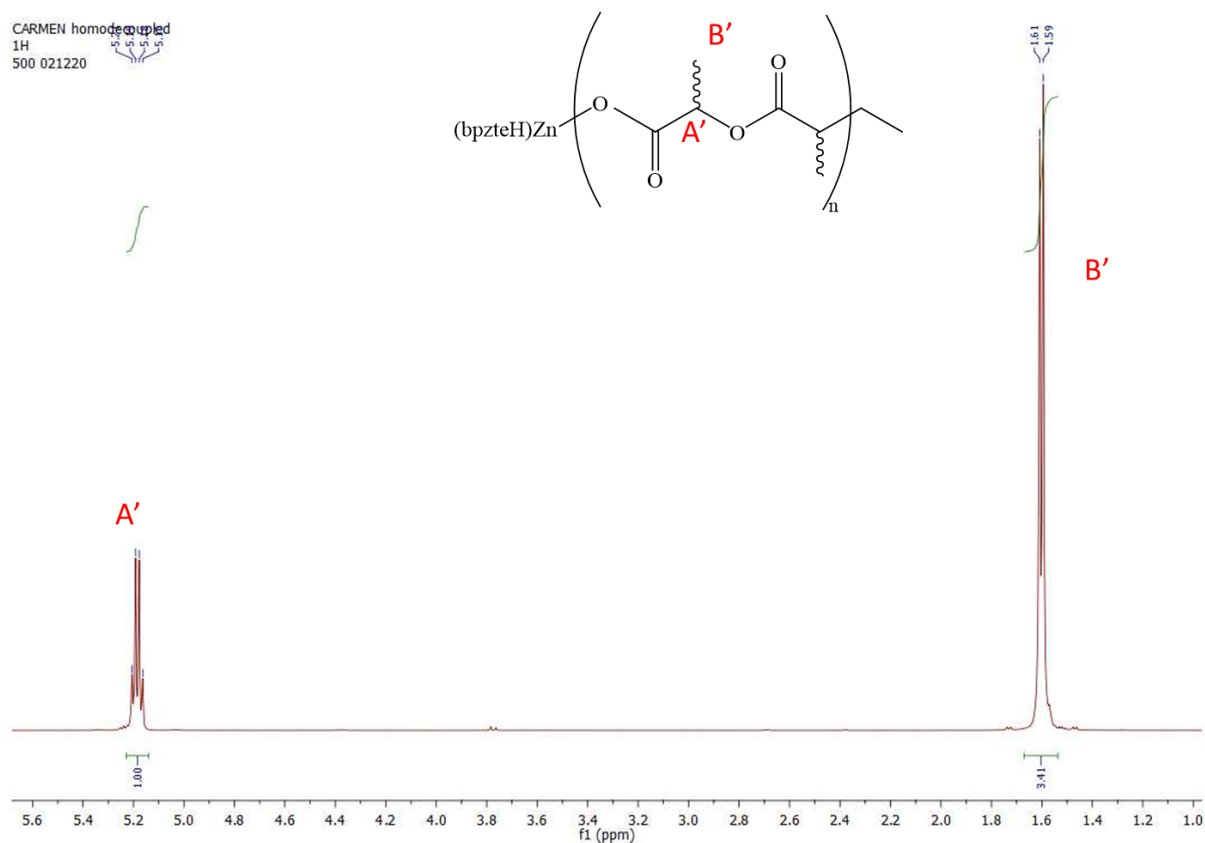


Figure A2.32: ^1H NMR spectrum (500 MHz, 298 K, CDCl_3) of L500:D500.

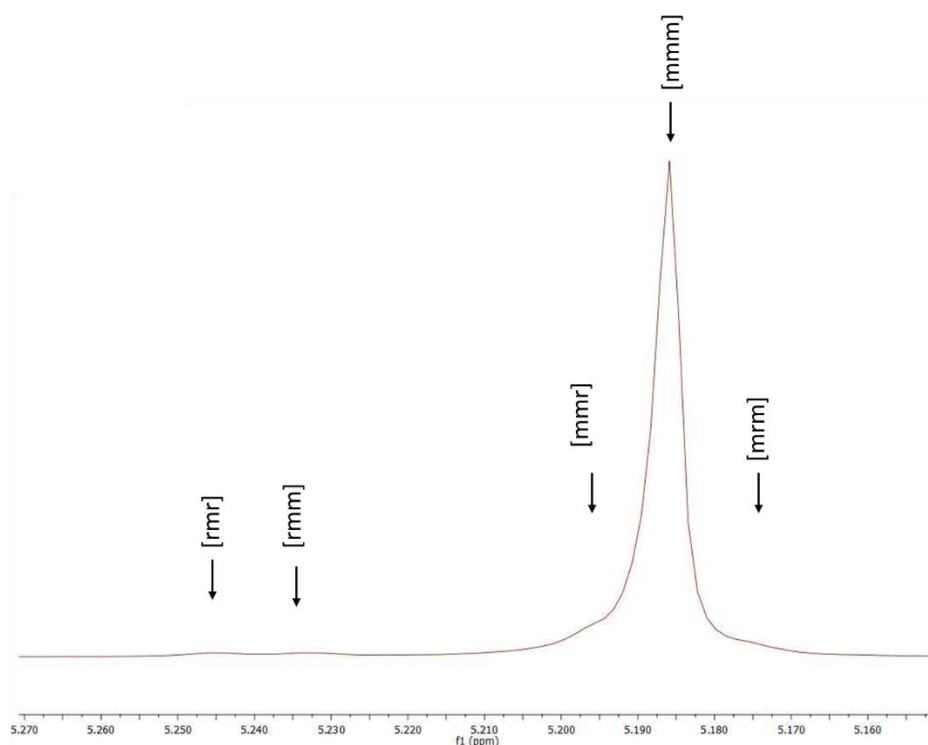


Figure A2.33: ^1H NMR spectrum (500 MHz, 298 K, CDCl_3) of the homodecoupled CH resonance of L500:D500.

A2.4.2 Synthesis of L520:D520

The block-copolymer L520:D520 was synthesized following the one-pot sequential addition. Three schlenk tubes were charged in the glovebox with 10.4 mg, 2,2 g and 2,2 mg of catalyst, L-LA and D-LA, respectively. 5 ml, 15ml and 15ml were added to the schlenk flasks respectively. The second monomer solution (D-LA) was added after 60 min of L-LA polymerization. Methanol was used to terminate the reaction and precipitate the polymer synthesized after 120 min. The obtained polymer was collected by filtration and dried at room temperature exposed to vacuum over 24h, obtaining a white powder (2,880 g, 80%). ^1H NMR (500 MHz, CDCl_3 , 297 K): δ 5,16-5,10 (q, 1H, $\text{CH}_{(\text{PLA})}$), 5,02-4,99 (q, 1H, $\text{CH}_{(\text{L-LA})}$), 1,66-1,64 (d, 3H, $\text{CH}_{3(\text{L-LA})}$), 1,56-1,54 (d, 3H, $\text{CH}_{3(\text{PLA})}$). ^{13}C NMR (500 MHz, CDCl_3 , 297 K): δ 169,56 (CO), 68,95 (CH), 16,60 (CH_3). GPC (CHCl_3): $M_w=150.094$, $M_n=64.976$, $D=2,31$.

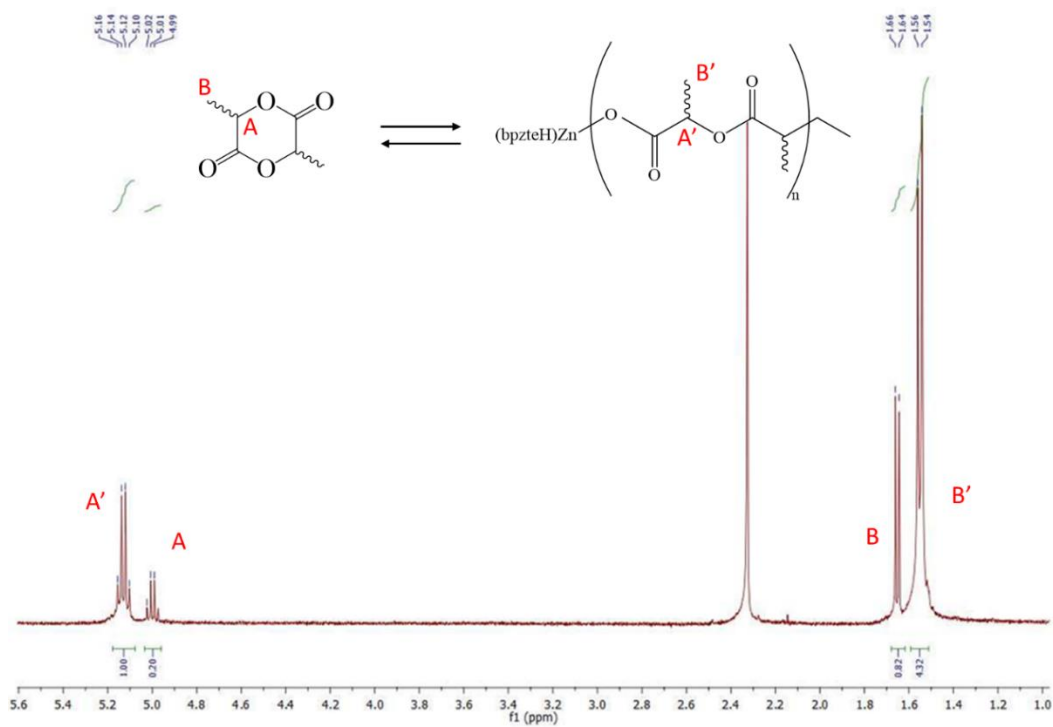


Figure A2.34: ^1H NMR spectrum (500 MHz, 298 K, CDCl_3) of L520:D520.

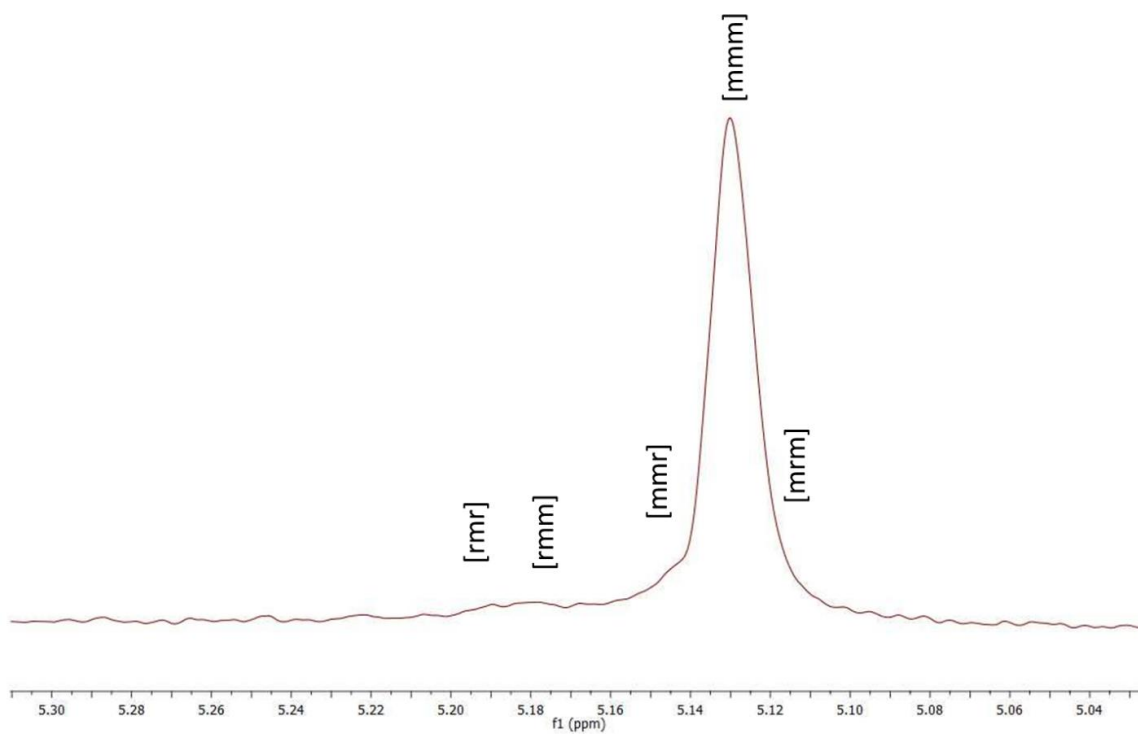


Figure A2.35: ^1H NMR spectrum (500 MHz, 298 K, CDCl_3) of the homodecoupled CH resonance of L520:D520.

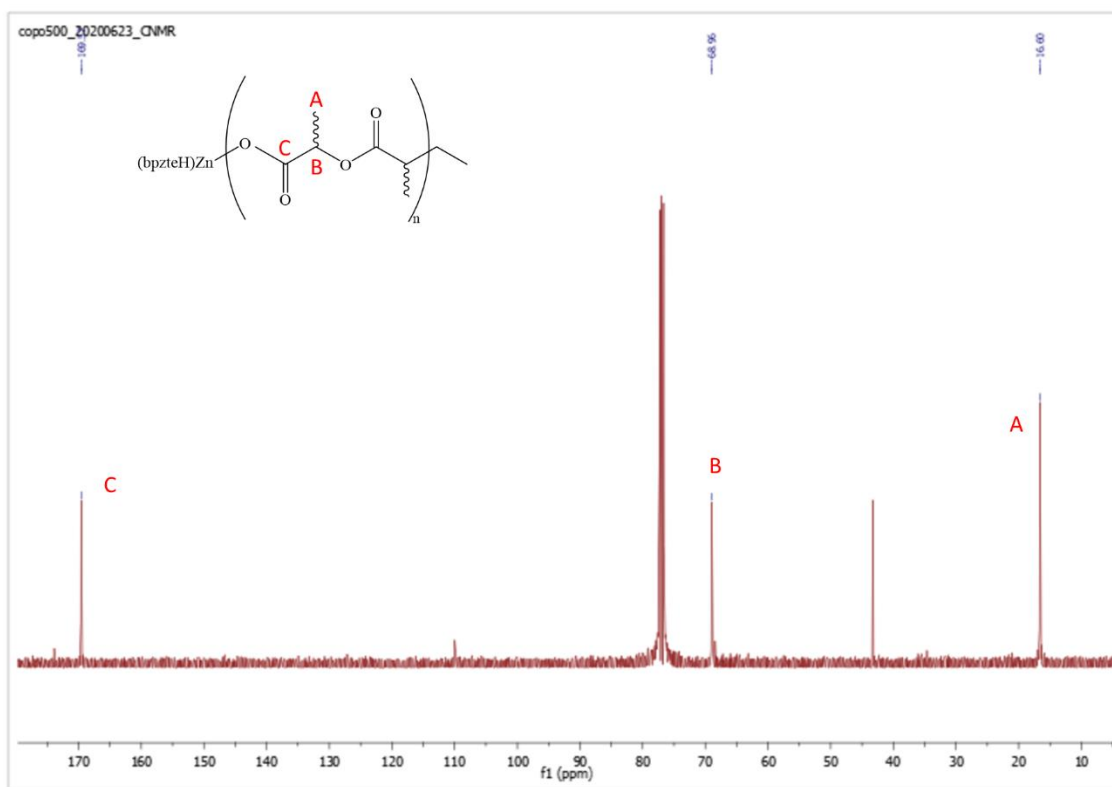


Figure A2.36. ¹³C NMR spectrum (500 MHz, 298 K, CDCl₃) of L520:D520.

A2.4.3 Synthesis of L1200:D300

The block-copolymer L1200:D300 was synthesized following the one-pot sequential addition. Three schlenk tubes were charged in the glovebox with 10.4 mg, 4.3 g and 1.1 g of catalyst, L-LA and D-LA, respectively. 5 ml, 30ml and 7ml were added to the schlenk flasks respectively. The second monomer solution (D-LA) was added after 70 min of L-LA polymerization. Methanol was used to terminate the reaction and precipitate the polymer synthesized after 95 min. The obtained polymer was collected by filtration and dried at room temperature exposed to vacuum over 24h, obtaining a white powder (3.51 g, 65%). ¹H NMR (500 MHz, CDCl₃, 297 K): δ 5.16-5.10 (q, 1H, CH_(PLA)), 1.56-1.54 (d, 3H, CH_{3(PLA)}). GPC (CHCl₃): M_w=202.280, M_n=99.257, Đ=2.04.

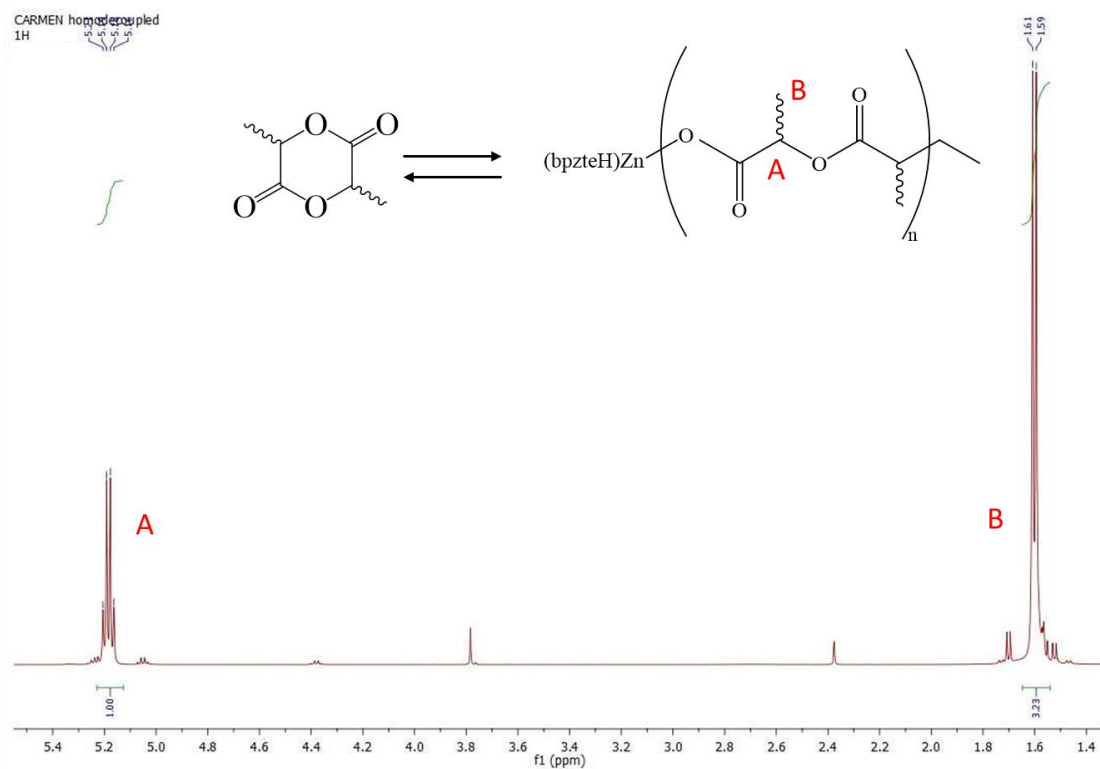


Figure A2.37. ^1H NMR spectrum (500 MHz, 298 K, CDCl_3) of L1200:D300.

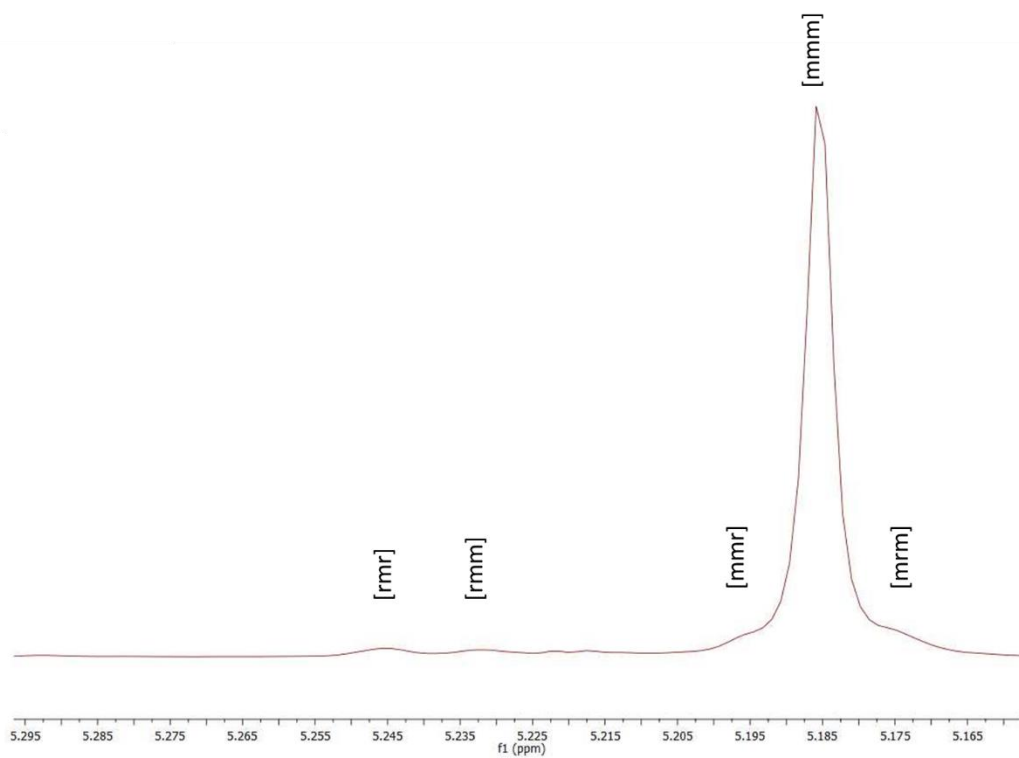


Figure A2.38. ^1H NMR spectrum (500 MHz, 298 K, CDCl_3) of the homodecoupled CH resonance of L1200:D300.

APENDIX A3

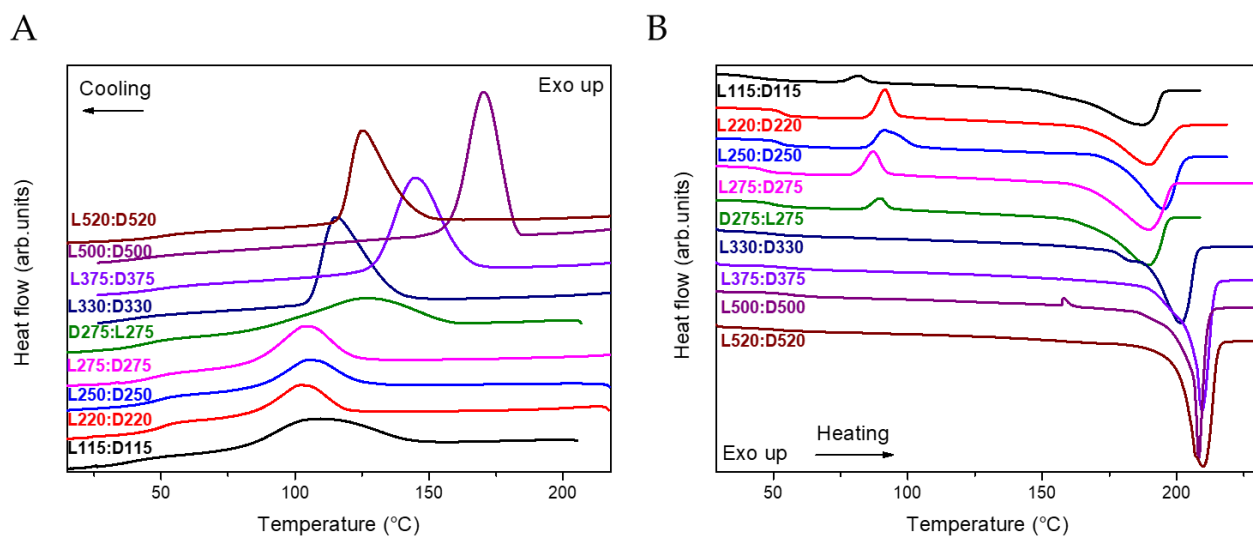


Figure A3.1. (A) Cooling and (B) heating ramps at 10°C/min of the PLA-SBC monitored by DSC.

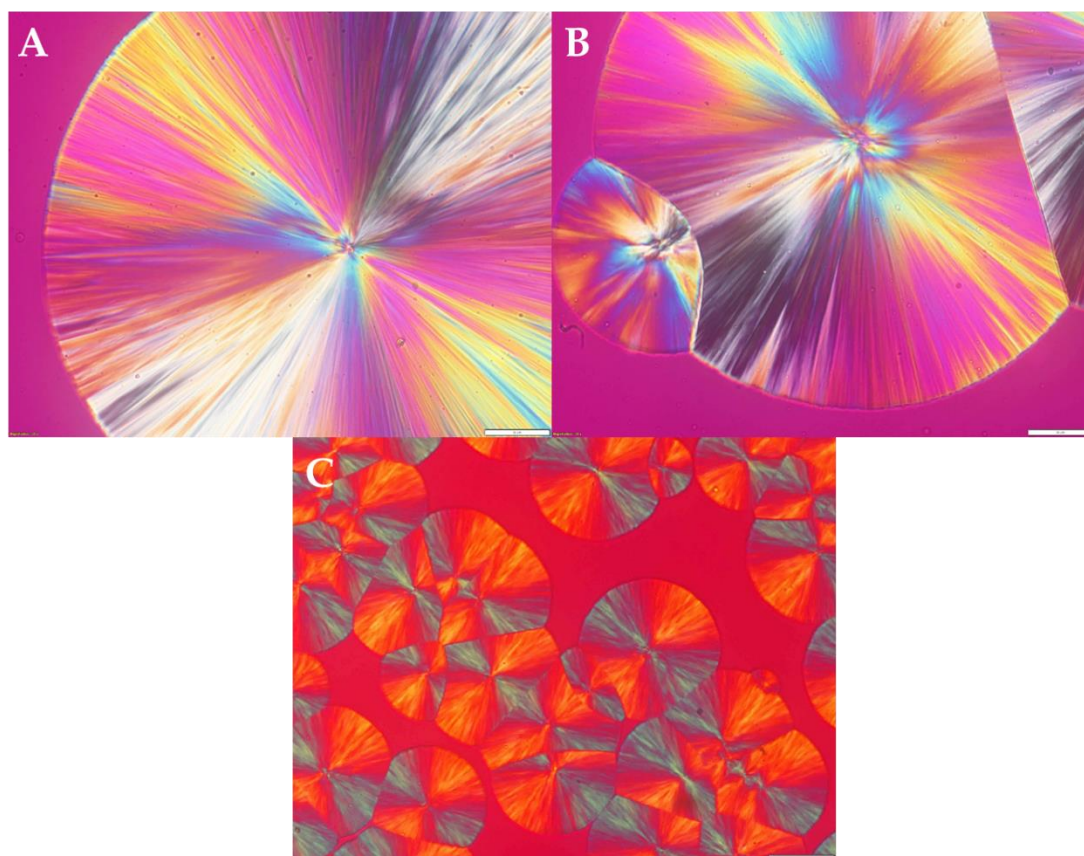


Figure A3.2. Polarized optical microscopy images of (A) PLLA500, (B) PDLA500 and (C) L520:D520 upon cooling from the melt at 10°C/min.

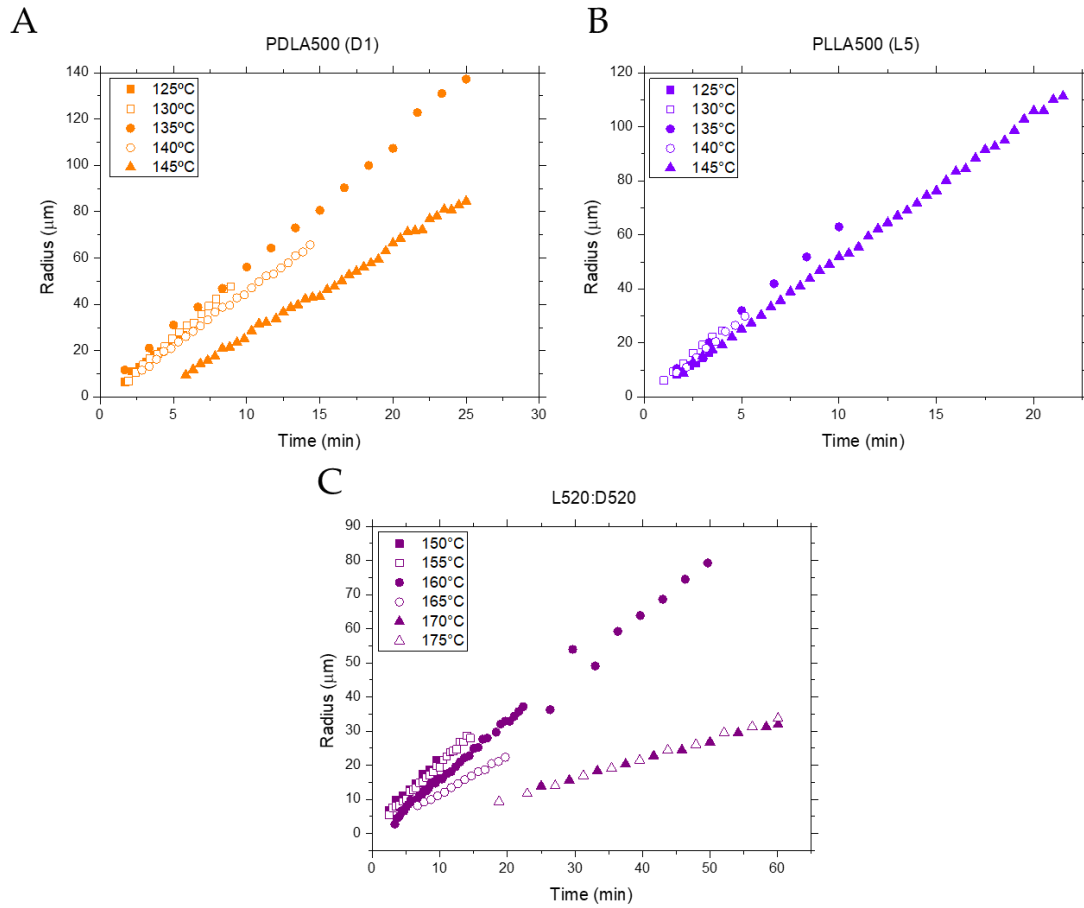


Figure A3.3. Spherulite radius as a function of time at different isothermal crystallization temperatures of (A) PDLA500, (B) PLLA500 and (C) L520:D520.

Table A3.1. Thermodynamic parameters of HMw-HPm PLA-SBC obtained during isothermal crystallization from the melt.

■ HMw-HPm										
T_{i-c} (°C)	t^P (min)	ΔH_{i-c} (J/g)	X_{C-ic} (%)	T_g (°C)	T_c (Y/N)	ΔH_c (J/g)	T_m^{on} (°C)	T_m^P (°C)	ΔH_m (J/g)	X_{C-m} (%)
190	4	59,3	41,7	49	Y	3,8	207	216	67,7	47,7
188	3,75	59,2	41,7	49	Y	2,1	208	215	68,1	47,9
185	3,21	58,4	41,1	51	Y	1,1	208	215	70,4	49,6
180	1,46	42,1*	29,6*	50	N	-	206	213	72,5	50,1
175	1,11	25,9*	18,3*	52	N	-	206	213	68,8	48,4

T_{i-c} , selected temperature of isothermal crystallization; t^P , peak crystallization time, obtained from the maximum heat flow; ΔH_{i-c} , enthalpy of crystallization obtained during the isothermal ramp; T_g , glass transition; T_c , crystallization upon cooling after the isothermal step, Y: Yes, N:No; ΔH_c , enthalpy of crystallization obtained during the cooling ramp after the isothermal step; T_m^{on} , onset melting temperature; T_m^P , peak melting temperature; ΔH_m , melting enthalpy; X_{C-m} , crystallinity obtained from melting: $X_{C-m} = \frac{\Delta H_m}{\Delta H_m^0} \times 100$ avec $\Delta H_m^0 = (142 \text{ J/g, crystallinity})$.

Table A3.2. Thermodynamic parameters of MMw-HPm PLA-SBC obtained during isothermal crystallization from the melt.

● MMw-HPm										
T_{i-c} (°C)	t^P (min)	ΔH_{i-c} (J/g)	X_{C-ic} (%)	T_g (°C)	T_c (Y/N)	ΔH_c (J/g)	T_m^{on} (°C)	T_m^P (°C)	ΔH_m (J/g)	X_{C-m} (%)
190	18,25	48,8*	34,3*	49	Y	16,3	204	214	52,9	37,2
185	12,35	62,1	43,7	50	Y	5,0	204	212	57,1	40,2
182	9,60	64,6	45,5	51	Y	4,2	205	212	67,8	47,8
180	8,92	62,2	43,8	50	Y	3,3	205	212	69,3	48,8
175	4,07	49,2*	34,6*	52	N	-	204	211	70,5	49,6

T_{i-c} , selected temperature of isothermal crystallization; t^P , peak crystallization time, obtained from the maximum heat flow; ΔH_{i-c} , enthalpy of crystallization obtained during the isothermal ramp: $X_{C-ic} = \frac{\Delta H_{i-c}}{\Delta H_m^0} \times 100$ with $\Delta H_m^0 = (142 \text{ J/g, crystallinity})$; T_g , glass transition; T_c , crystallization upon cooling after the isothermal step, Y: Yes, N:No; ΔH_c , enthalpy of crystallization obtained during the cooling ramp after the isothermal step; T_m^{on} , onset melting temperature; T_m^P , peak melting temperature; ΔH_m , melting enthalpy; X_{C-m} , crystallinity obtained from melting: $X_{C-m} = \frac{\Delta H_m}{\Delta H_m^0} \times 100$ avec $\Delta H_m^0 = (142 \text{ J/g, crystallinity})$.

Table A3.3 Thermodynamic parameters of MMw-LPm PLA-SBC obtained during isothermal crystallization from the melt.

▲ MMw-LPm										
T_{i-c} (°C)	t^P (min)	ΔH_{i-c} (J/g)	X_{C-ic} (%)	T_g (°C)	T_c (Y/N)	ΔH_c (J/g)	T_m^{on} (°C)	T_m^P (°C)	ΔH_m (J/g)	X_{C-m} (%)
170	25,52	50,8*	35,7*	47	Y	3,4	191	200	47,1	32,9
165	17,41	68,1*	47,6*	48	N	-	191	197	57,2	40,3
160	10,34	56,4	39,7	44	N	-	188	196	54,9	38,6
155	7,18	52,9	37,3	47	N	-	187	195	59,6	51,9
152	6,73	57,9	40,8	48	N	-	186	202	59,4	41,8
150	6,08	57,5	40,5	46	N	-	183	203	60,9	42,9
140	5,36	37,5*	26,4*	49	N	-	175	195	49,2	39,7

T_{i-c} , selected temperature of isothermal crystallization; t^P , peak crystallization time, obtained from the maximum heat flow; ΔH_{i-c} , enthalpy of crystallization obtained during the isothermal ramp: $X_{C-ic} = \frac{\Delta H_{i-c}}{\Delta H_m^0} \times 100$ with $\Delta H_m^0 = (142 \text{ J/g, crystallinity})$.; T_g , glass transition; T_c , crystallization upon cooling after the isothermal step, Y: Yes, N:No; ΔH_c , enthalpy of crystallization obtained during the cooling ramp after the isothermal step; T_m^{on} , onset melting temperature; T_m^P , peak melting temperature; ΔH_m , melting enthalpy; X_{C-m} , crystallinity obtained from melting: $X_{C-m} = \frac{\Delta H_m}{\Delta H_m^0} \times 100$ with $\Delta H_m^0 = (142 \text{ J/g, crystallinity})$.

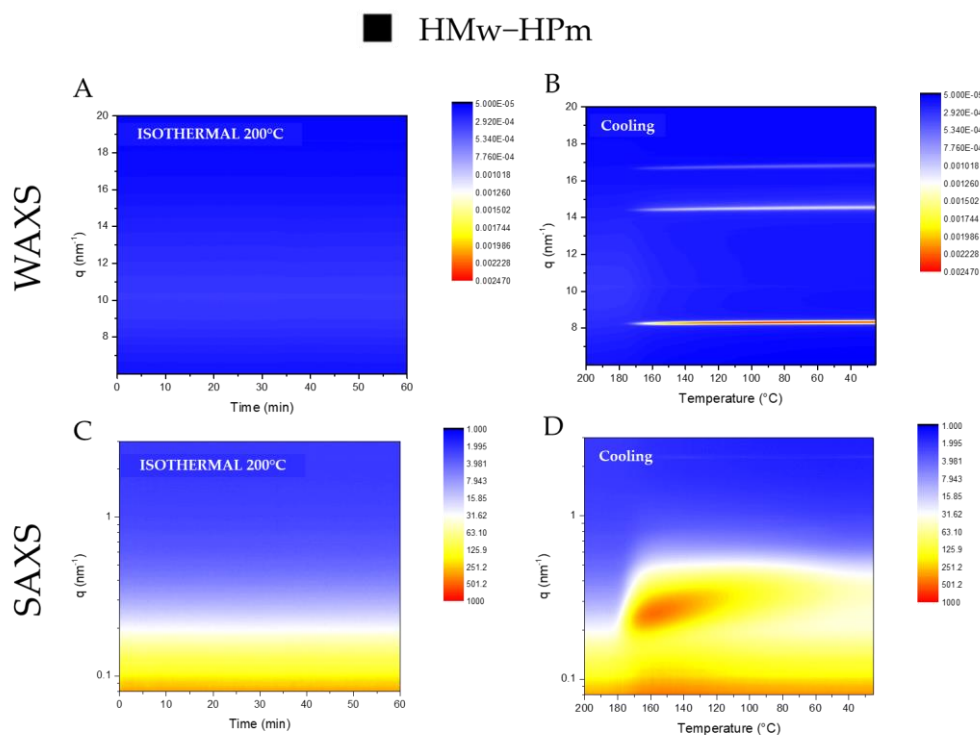


Figure A3.4. WAXS (A-B) and SAXS (C-D) patterns of the HMw-HPm isothermally crystallized from the melt at 200°C (A-C) and the subsequent cooling to room temperature (B-C).

■ HMw-HPm

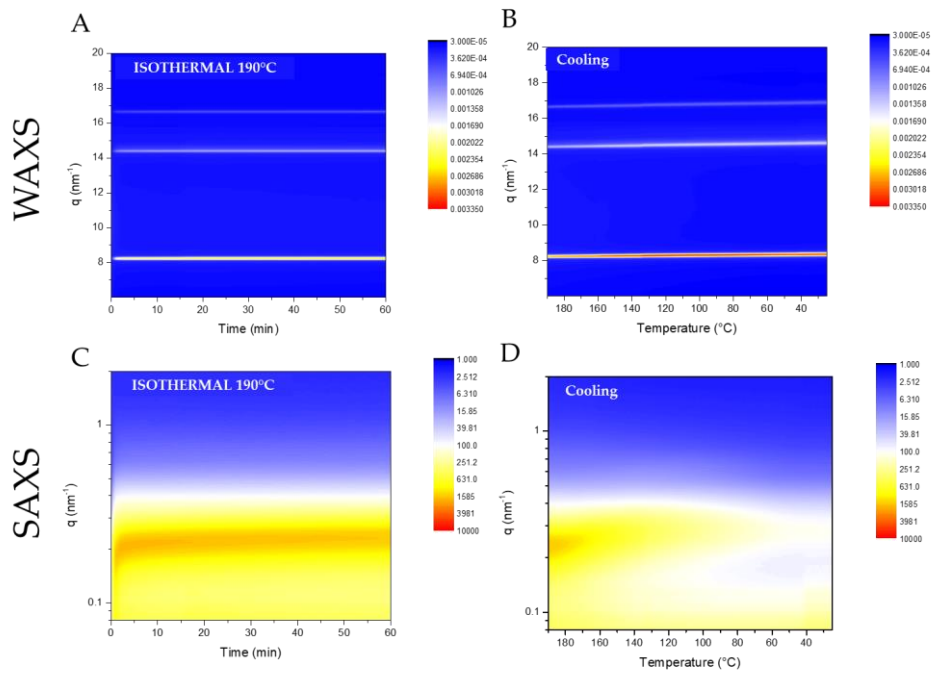


Figure A3.5. WAXS (A-B) and SAXS (C-D) patterns of the HMw-HPm isothermally crystallized from the melt at 190°C (A-C) and the subsequent cooling to room temperature (B-C).

● MMw-HPm

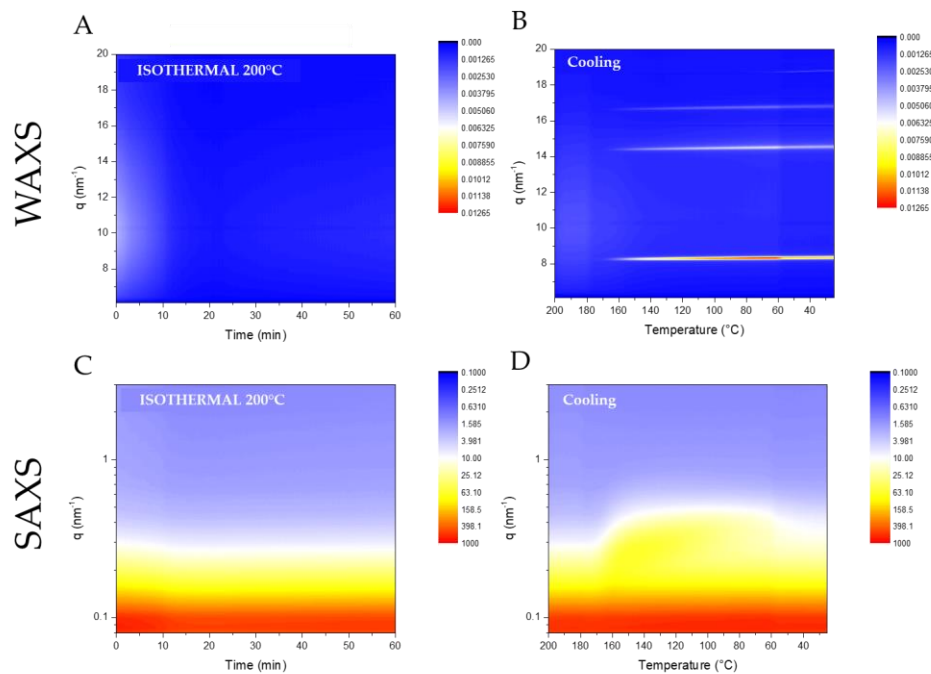


Figure A3.6. WAXS (A-B) and SAXS (C-D) patterns of the MMw-HPm isothermally crystallized from the melt at 200°C (A-C) and the subsequent cooling to room temperature (B-C).

● MMw-HPm

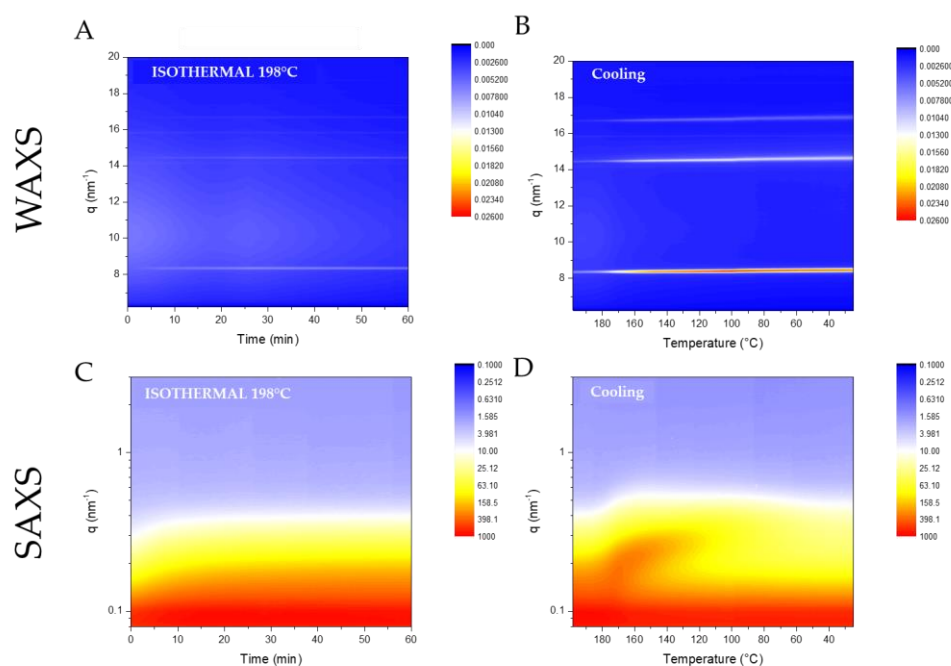


Figure A3.7. WAXS (A-B) and SAXS (C-D) patterns of the MMw-HPm isothermally crystallized from the melt at 198°C (A-C) and the subsequent cooling to room temperature (B-C).

● MMw-HPm

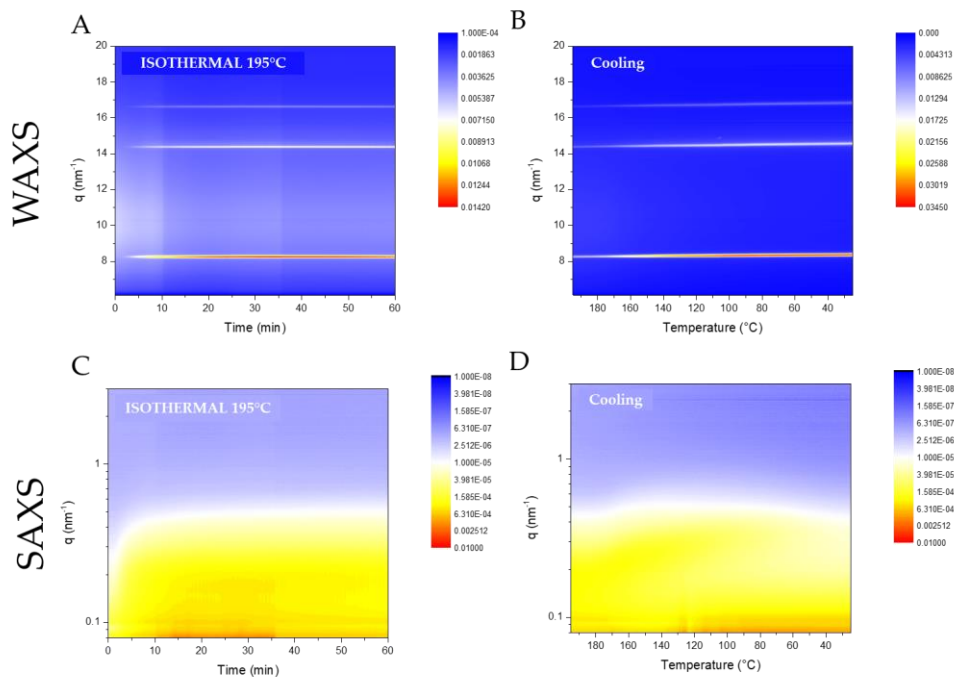


Figure A3.8. WAXS (A-B) and SAXS (C-D) patterns of the MMw-HPm isothermally crystallized from the melt at 195°C (A-C) and the subsequent cooling to room temperature (B-C).

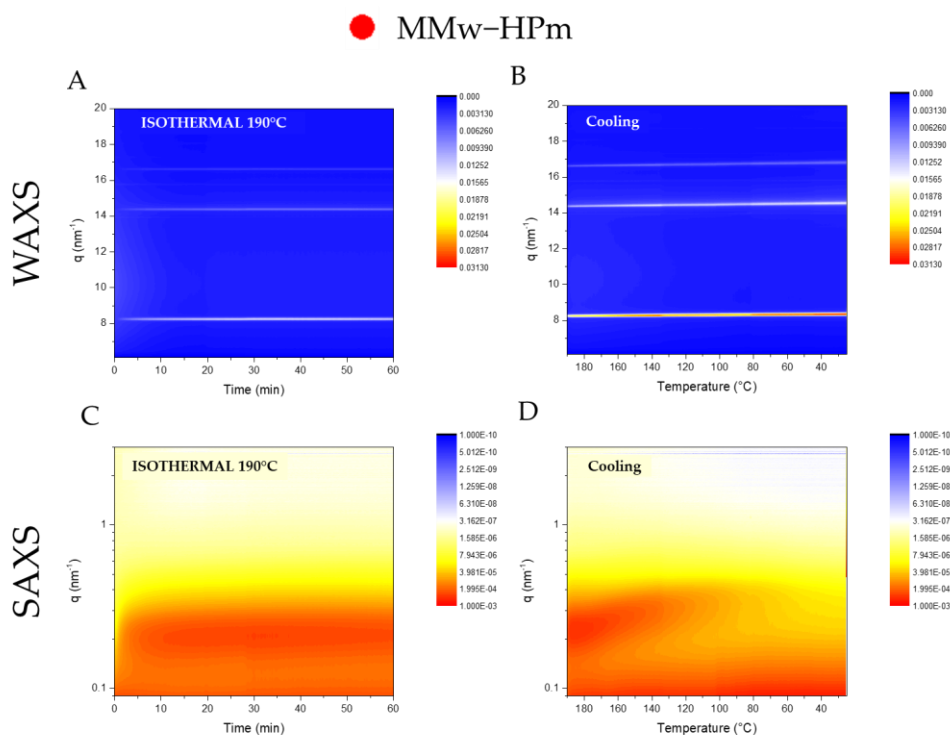


Figure A3.9. WAXS (A-B) and SAXS (C-D) patterns of the MMw-HPm isothermally crystallized from the melt at 190°C (A-C) and the subsequent cooling to room temperature (B-C).

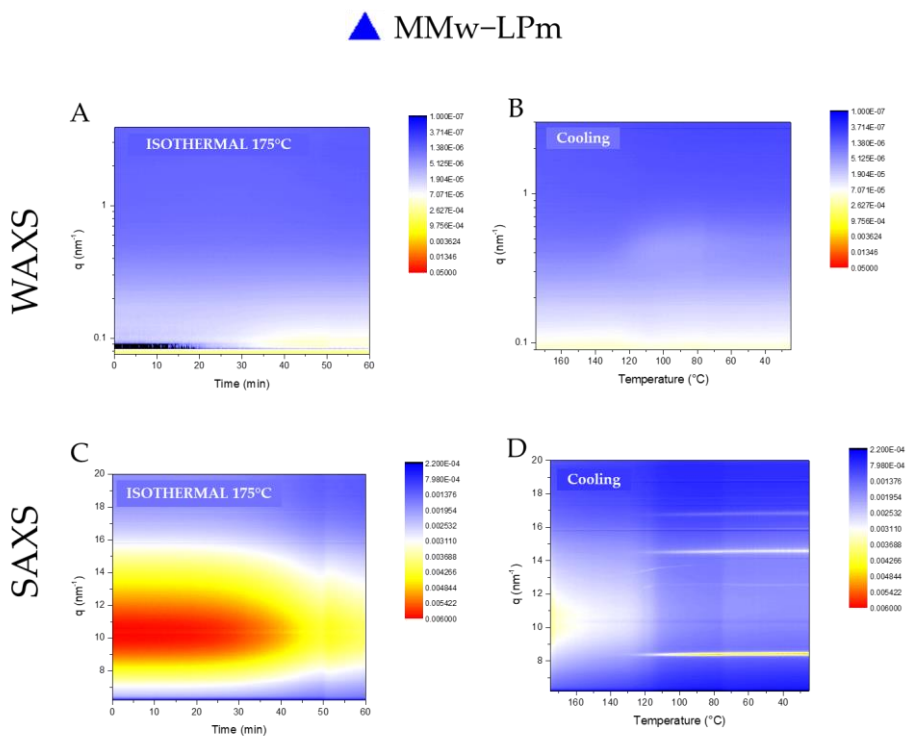


Figure A3.10. WAXS (A-B) and SAXS (C-D) patterns of the MMw-LPm isothermally crystallized from the melt at 175°C (A-C) and the subsequent cooling to room temperature (B-C).

▲ MMw-LPm

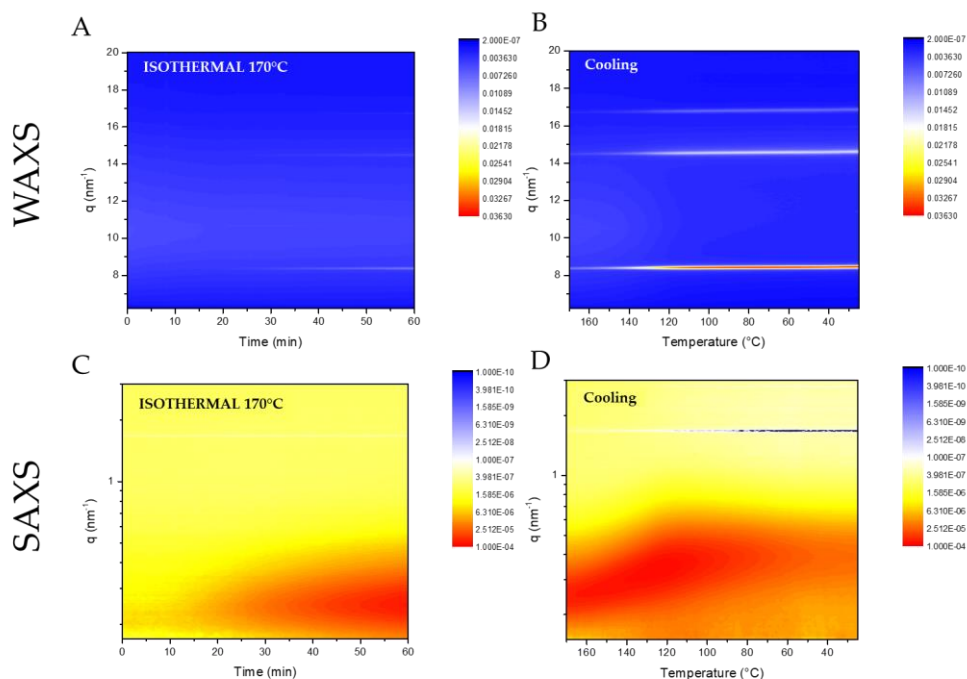


Figure A3.11. WAXS (A-B) and SAXS (C-D) patterns of the MMw-LPm isothermally crystallized from the melt at 170°C (A-C) and the subsequent cooling to room temperature (B-C).

▲ MMw-LPm

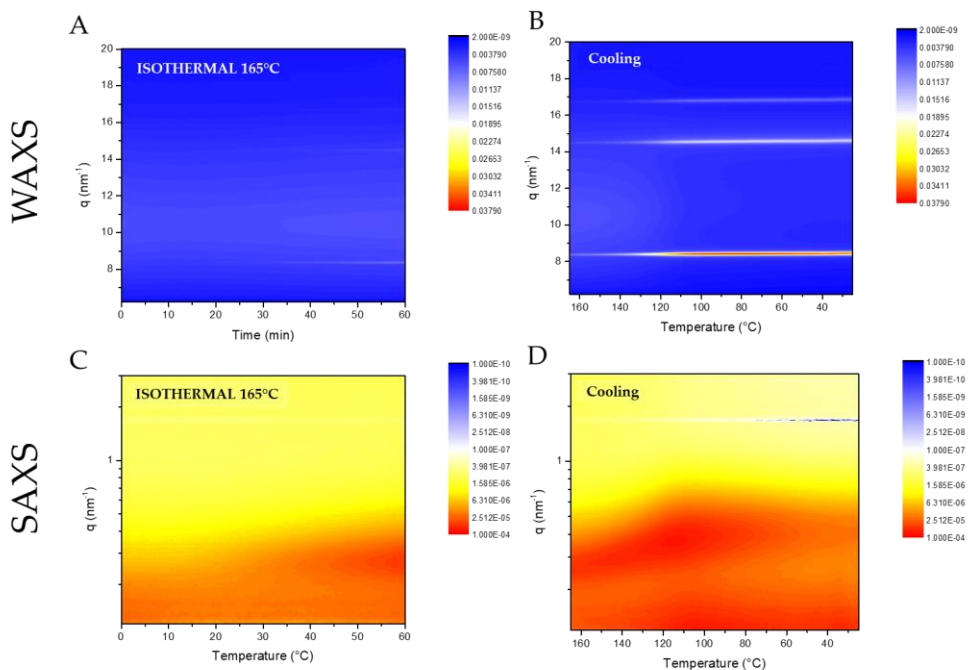


Figure A3.12. WAXS (A-B) and SAXS (C-D) patterns of the MMw-LPm isothermally crystallized from the melt at 165°C (A-C) and the subsequent cooling to room temperature (B-C).

▲ MMw-LPm

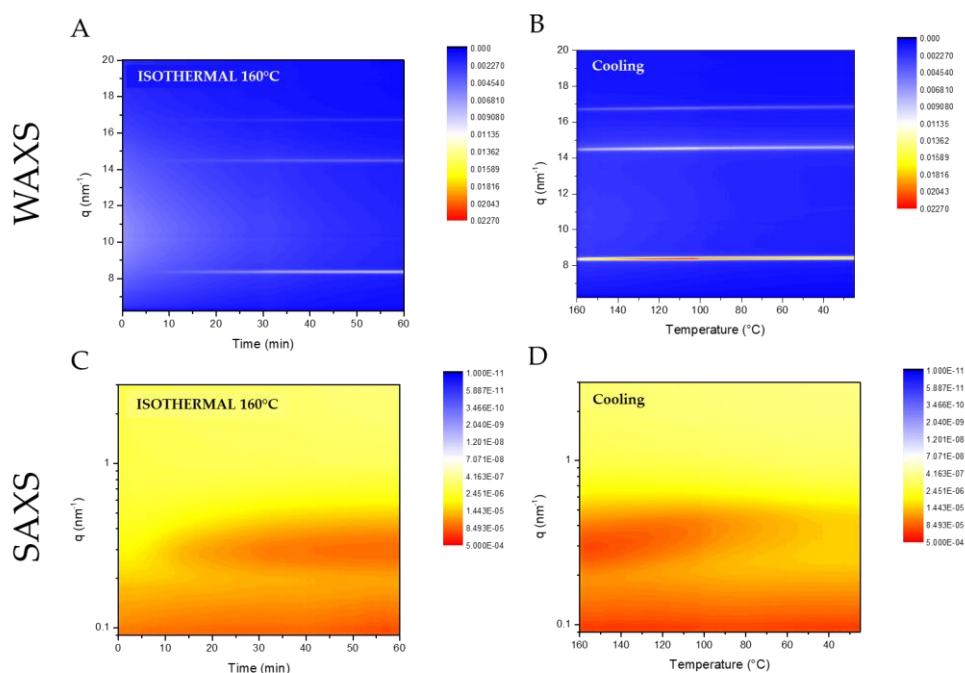


Figure A3.13. WAXS (A-B) and SAXS (C-D) patterns of the MMw-LPm isothermally crystallized from the melt at 160°C (A-C) and the subsequent cooling to room temperature (B-C).

▲ MMw-LPm

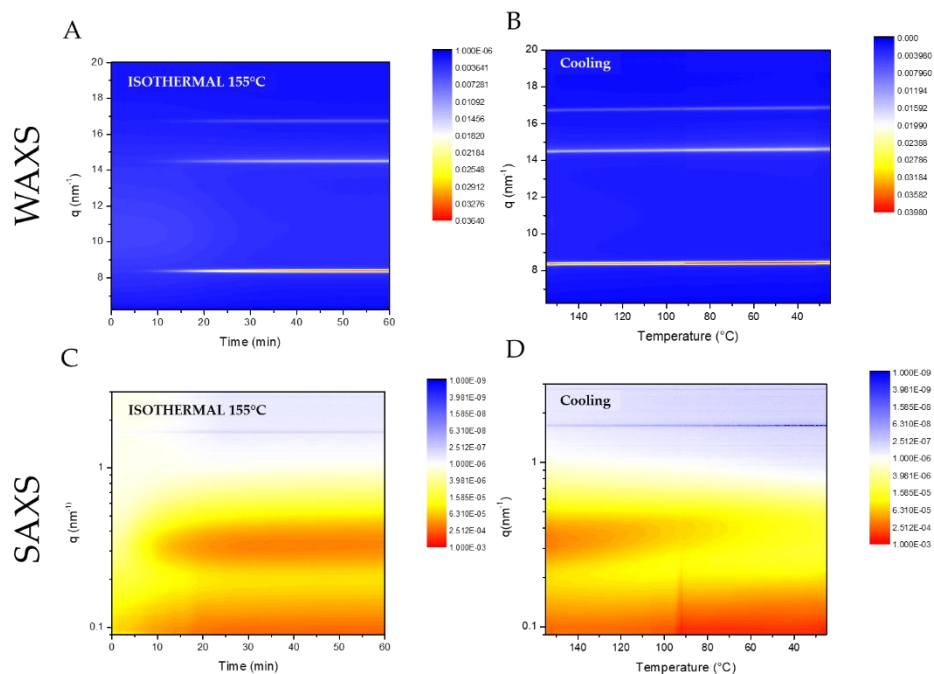


Figure A3.14. WAXS (A-B) and SAXS (C-D) patterns of the MMw-LPm isothermally crystallized from the melt at 155°C (A-C) and the subsequent cooling to room temperature (B-C).

▲ MMw-LPm

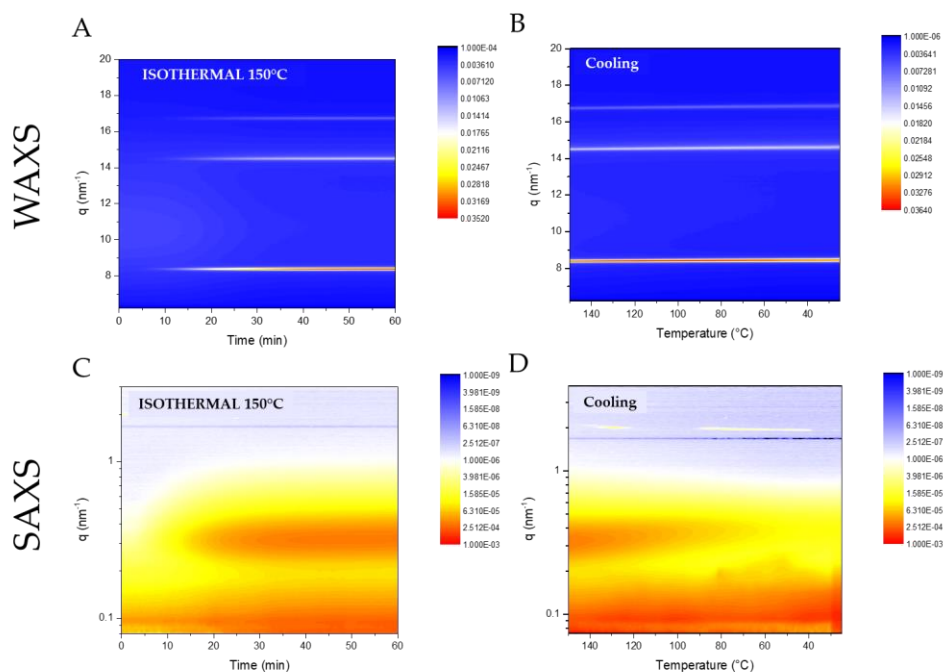


Figure A3.15. WAXS (A-B) and SAXS (C-D) patterns of the MMw-LPm isothermally crystallized from the melt at 150°C (A-C) and the subsequent cooling to room temperature (B-C).

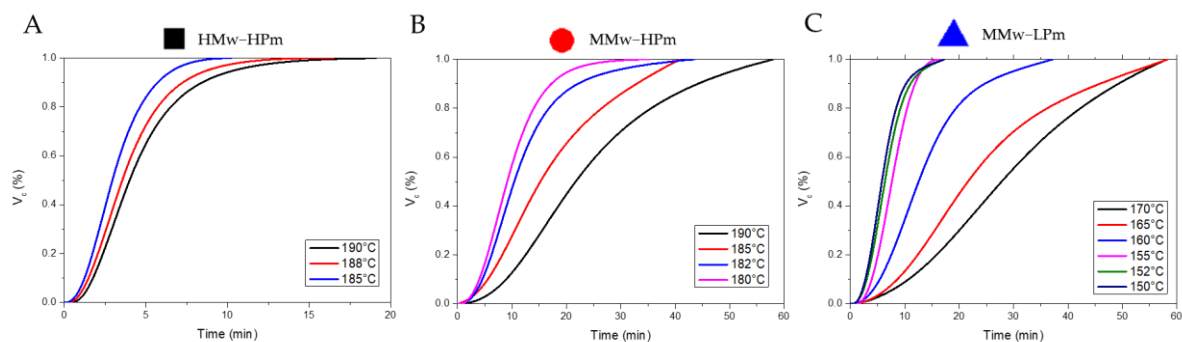


Figure A3.16. Crystallinity evolution (V_c) of (A) HMw-HPm, (B) MMw-HPm and (C) MMw-LPm during the isothermal ramps obtained by DSC.

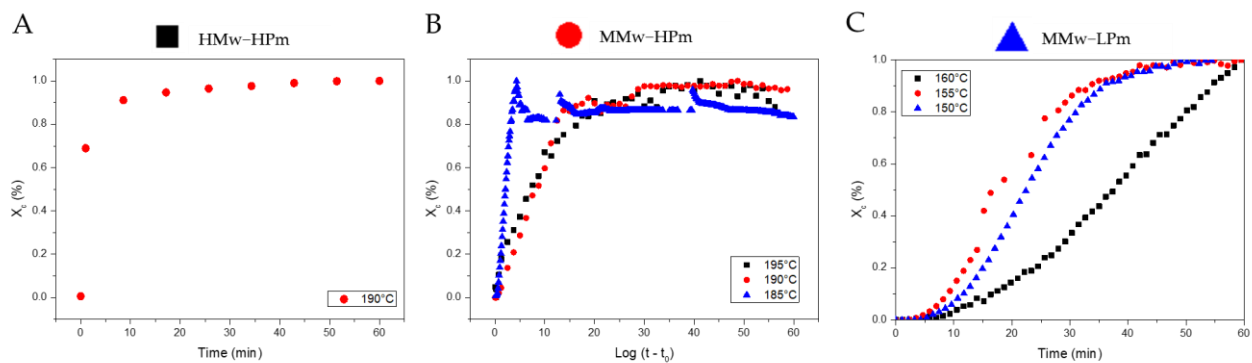


Figure A3.17. Crystallinity evolution (X_c) of (A) HMw-HPm, (B) MMw-HPm and (C) MMw-LPm during the isothermal ramps obtained by WAXS.

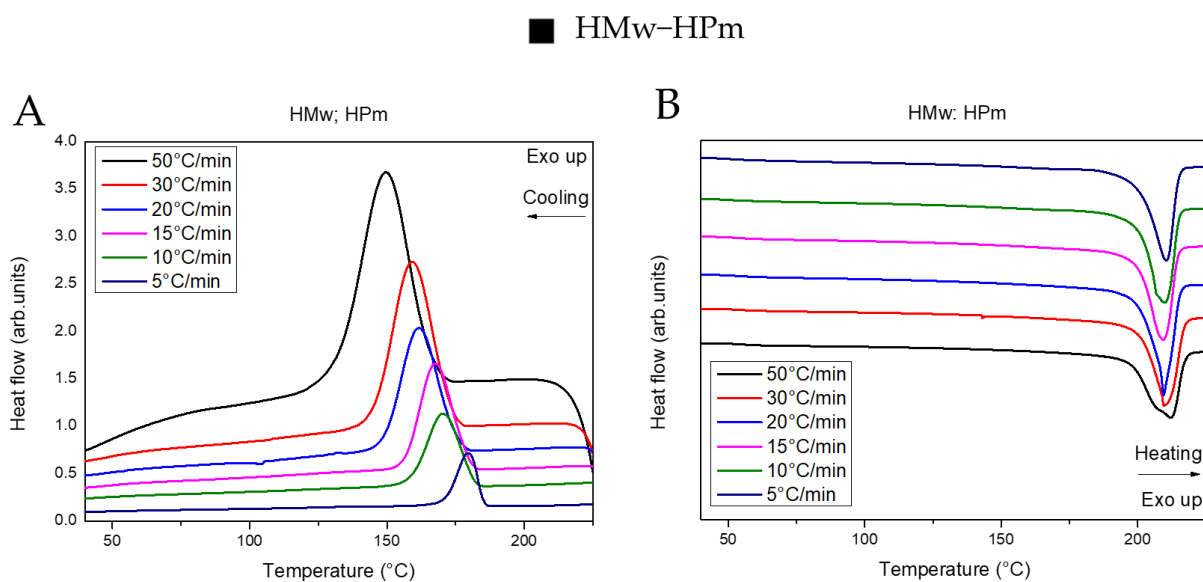


Figure A3.18. DSC thermograms of HMw-HPm upon non-isothermal crystallization from the melt at different cooling rates (A) and the subsequent heating at $10^\circ\text{C}/\text{min}$ (B).

● MMw-HPm

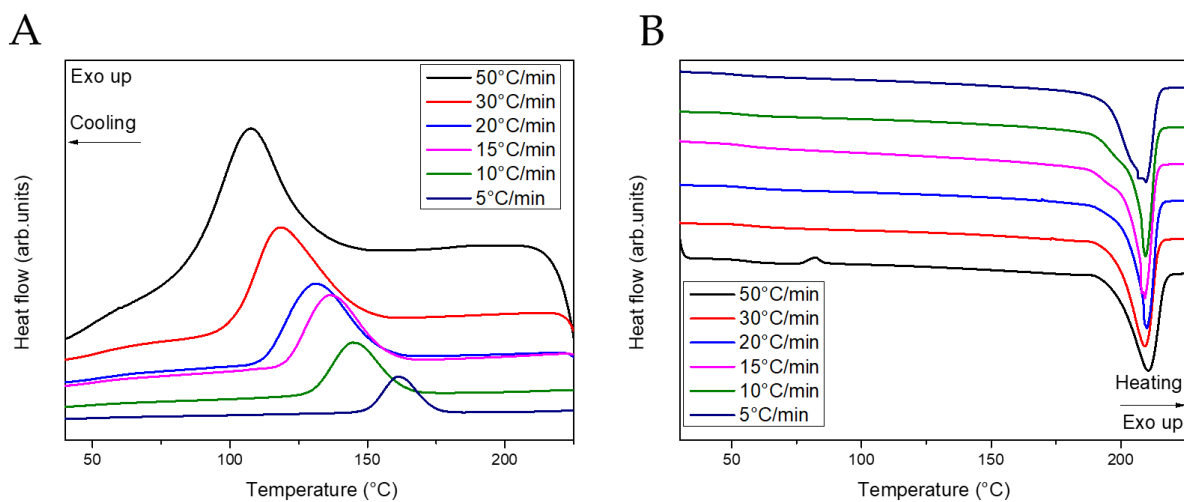


Figure A3.19. DSC thermograms of MMw-HPm upon non-isothermal crystallization from the melt at different cooling rates (A) and the subsequent heating at 10°C/min (B).

▲ MMw-LPm

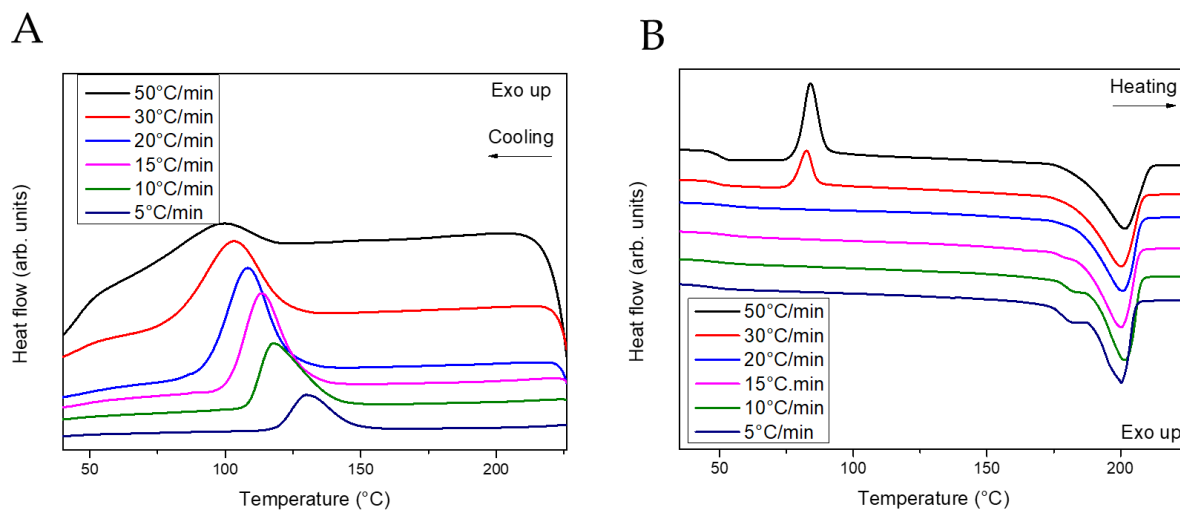


Figure A3.20. DSC thermograms of MMw-LPm upon non-isothermal crystallization from the melt at different cooling rates (A) and the subsequent heating at 10°C/min (B).

Table A3.4. Thermodynamic parameters of HMw-HPm PLA-SBC obtained during non-isothermal crystallization from the melt.

■ HMw-HPm											
Cooling rate	T_c^{on} (°C)	T_c^p (°C)	ΔH_c (J/g)	X_{c-c} (%)	T_g (°C)	T_{cc}^p (°C)	ΔH_{cc} (J/g)	T_m^{on} (°C)	T_m^p (°C)	ΔH_m (J/g)	X_{c-m} (%)
50°C/min	166	150	60,9	42,9	55	-	-	197	212	56,9	40,1
30°C/min	174	159	65,7	46,4	55	-	-	204	210	58,1	40,9
20°C/min	175	162	63,8	44,9	53	-	-	205	210	64,3	45,2
15°C/min	180	168	62,9	44,3	54	-	-	200	209	62,8	44,2
10°C/min	182	170	66,2	46,6	52	-	-	202	210	66,1	46,6
5°C/min	185	179	60,3	42,5	5	-	-	200	211	60,6	42,7

T_c^{on} , onset crystallization temperature; T_c^p , peak crystallization temperature; ΔH_c , enthalpy of crystallization obtained during the cooling ramp; X_{c-c} , crystallinity obtained from crystallization: $X_{c-c} = \frac{\Delta H_{c-c}}{\Delta H_m^0} \times 100$ with $\Delta H_m^0 = (142 \text{ J/g, crystallinity})$.; T_g , glass transition; T_{cc} , cold-crystallization temperature; ΔH_{cc} , enthalpy of cold-crystallization; T_m^{on} , onset melting temperature; T_m^p , peak melting temperature; ΔH_m , melting enthalpy; X_{c-m} , crystallinity obtained from melting: $X_{c-m} = \frac{\Delta H_m}{\Delta H_m^0} \times 100$ with $\Delta H_m^0 = (142 \text{ J/g, crystallinity})$.

Table A3.5. Thermodynamic parameters of MMw-HPm PLA-SBC obtained during non-isothermal crystallization from the melt.

● MMw-HPm											
Cooling rate	T_c^{on} (°C)	T_c^p (°C)	ΔH_c (J/g)	X_{c-c} (%)	T_g (°C)	T_{cc} (°C)	ΔH_{cc} (J/g)	T_m^{on} (°C)	T_m^p (°C)	ΔH_m (J/g)	X_{c-m} (%)
50°C/min	130	107	40,4	28,5	56	82	1,8	198	211	57,6	40,5
30°C/min	148	118	54,8	38,2	56	-	-	198	209	54,7	38,5
20°C/min	154	131	57,6	40,6	56	-	-	207	210	55,5	39,1
15°C/min	157	136	59,6	41,9	55	-	-	206	209	57,6	40,5
10°C/min	163	144	62,9	44,3	56	-	-	205	210	61,8	43,5
5°C/min	174	161	62,1	43,74	55	-	-	194	210	63,4	44,6

T_c^{on} , onset crystallization temperature; T_c^p , peak crystallization temperature; ΔH_c , enthalpy of crystallization obtained during the cooling ramp; X_{c-c} , crystallinity obtained from crystallization: $X_{c-c} = \frac{\Delta H_{c-c}}{\Delta H_m^0} \times 100$ with $\Delta H_m^0 = (142 \text{ J/g, crystallinity})$.; T_g , glass transition; T_{cc} , cold-crystallization temperature; ΔH_{cc} , enthalpy of cold-crystallization; T_m^{on} , onset melting temperature; T_m^p , peak melting temperature; ΔH_m , melting enthalpy; X_{c-m} , crystallinity obtained from melting: $X_{c-m} = \frac{\Delta H_m}{\Delta H_m^0} \times 100$ with $\Delta H_m^0 = (142 \text{ J/g, crystallinity})$.

Table A3.6. Thermodynamic parameters of MMw-HPm PLA-SBC obtained during non-isothermal crystallization from the melt.

▲ MMw-LPm												
Cooling rate	T_c^{on} (°C)	T_c^p (°C)	ΔH_c (J/g)	X_{c-c} (%)	T_g (°C)	T_{cc}^p (°C)	ΔH_{cc} (J/g)	T_m^{on} (°C)	T_m^p (°C)	ΔH_m (J/g)	X_{c-m} (%)	
50°C/min	119	97	7,1	4,9	50	84	22,1	184	202	47,3	33,3	
30°C/min	123	103	30,9	21,6	48	82	9,8	183	200	49,9	35,1	
20°C/min	123	108	45,6	32,1	54	-	-	185	201	46,3	32,6	
15°C/min	128	113	47,8	33,6	53	-	-	185	200	48,7	34,3	
10°C/min	137	119	51,1	35,9	49	-	-	188	202	50,7	35,7	
5°C/min	147	130	52,6	37,0	48	-	-	187	200	51,5	36,3	

T_c^{on} , onset crystallization temperature; T_c^p , peak crystallization temperature; ΔH_c , enthalpy of crystallization obtained during the cooling ramp; X_{c-c} , crystallinity obtained from crystallization: $X_{c-c} = \frac{\Delta H_{c-c}}{\Delta H_m^0} \times 100$ with $\Delta H_m^0 = (142 \text{ J/g, crystallinity})$; T_g , glass transition; T_{cc} , cold-crystallization temperature; ΔH_{cc} , enthalpy of cold-crystallization; T_m^{on} , onset melting temperature; T_m^p , peak melting temperature; ΔH_m , melting enthalpy; X_{c-m} , crystallinity obtained from melting: $X_{c-m} = \frac{\Delta H_m}{\Delta H_m^0} \times 100$ with $\Delta H_m^0 = (142 \text{ J/g, crystallinity})$.

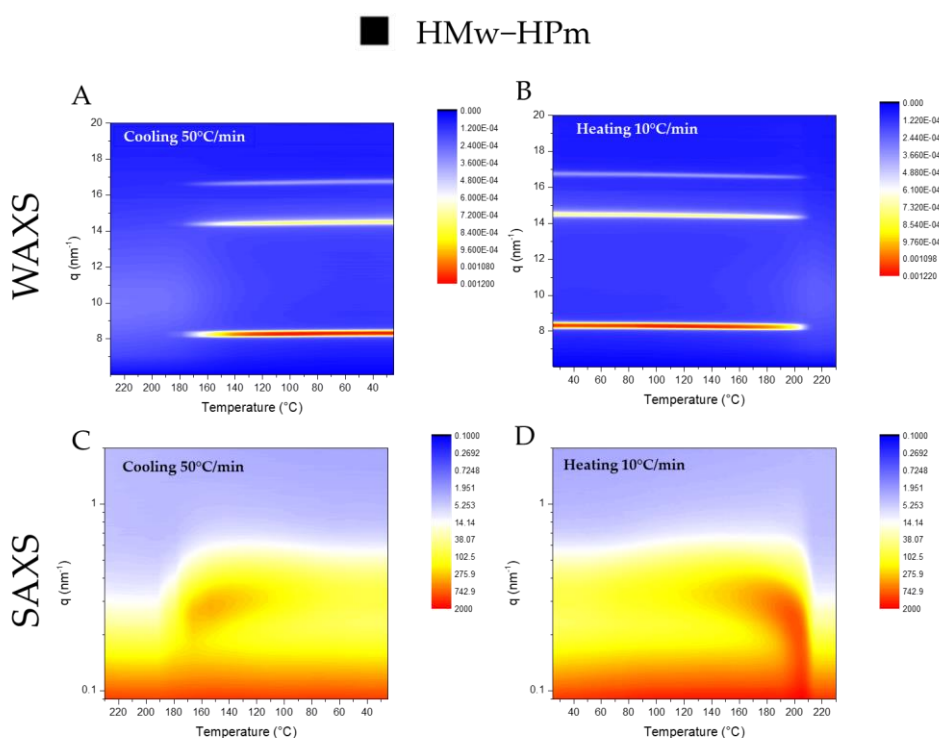


Figure A3.21. WAXS (A-B) and SAXS (C-D) patterns of the HMw-HPm non-isothermally crystallized from the melt at 50°C/min (A-C) and the subsequent heating at 10°C/min (B-C).

■ HMw-HPm

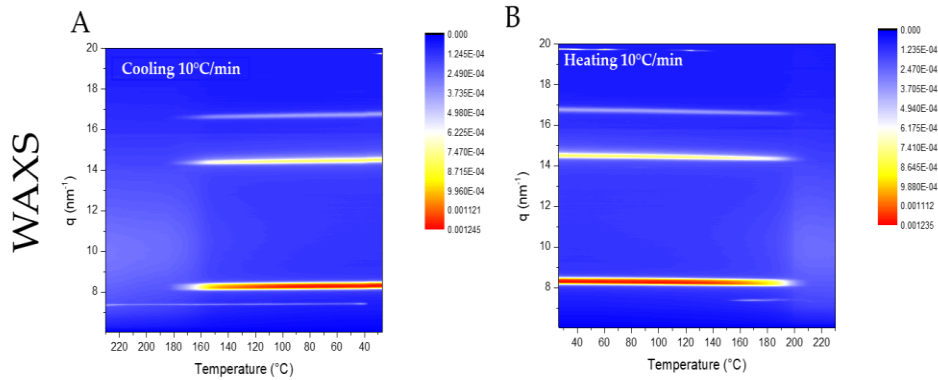


Figure A3.22. WAXS patterns of the HMw-HPm non-isothermally crystallized from the melt at 10°C/min (A) and the subsequent heating at 10°C/min (B).

■ HMw-HPm

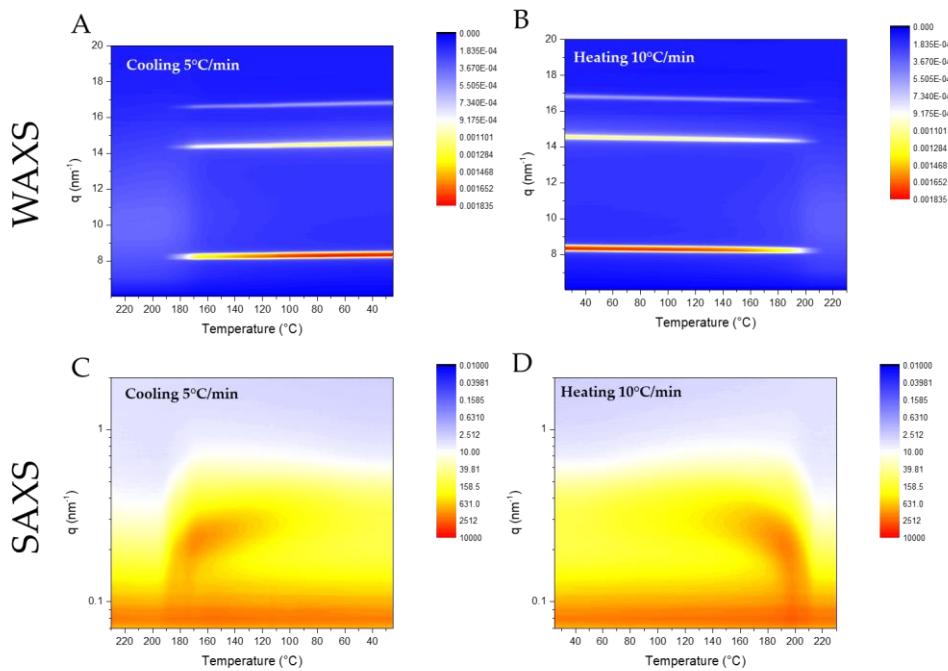


Figure A3.23. WAXS (A-B) and SAXS (C-D) patterns of the HMw-HPm non-isothermally crystallized from the melt at 5°C/min (A-C) and the subsequent heating at 10°C/min (B-C).

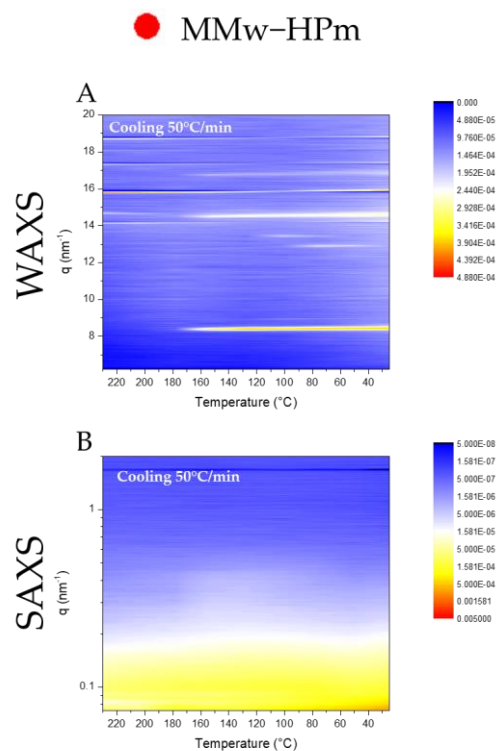


Figure A3.24. WAXS (A) and SAXS (B) patterns of the MMw-HPm non-isothermally crystallized from the melt at 50°C/min.

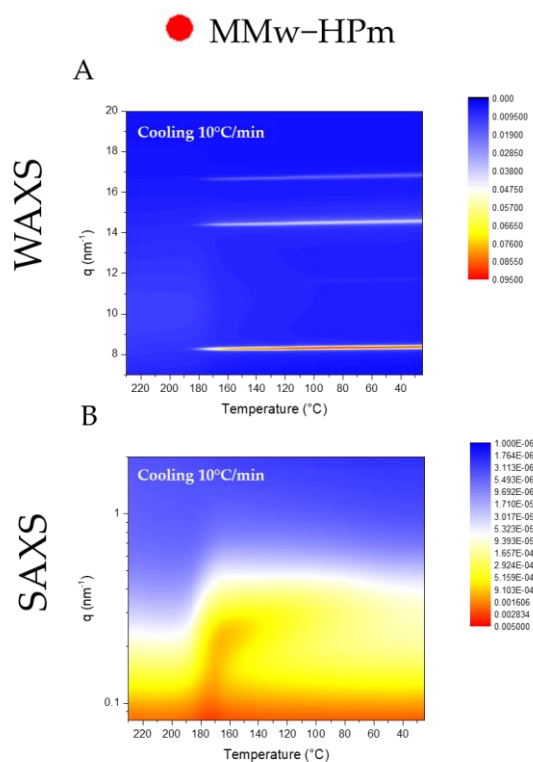


Figure A3.25. WAXS (A) and SAXS (B) patterns of the MMw-HPm non-isothermally crystallized from the melt at 10°C/min.

● MMw-HPm

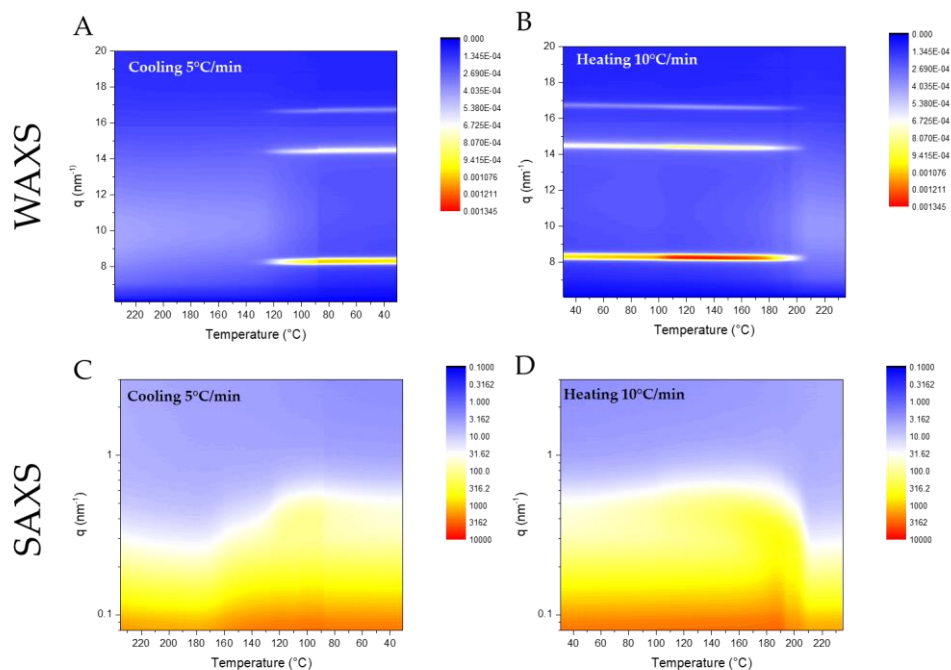


Figure A3.26. WAXS (A-B) and SAXS (C-D) patterns of the MMw-HPm non-isothermally crystallized from the melt at 5°C/min (A-C) and the subsequent heating at 10°C/min (B-C).

● MMw-HPm

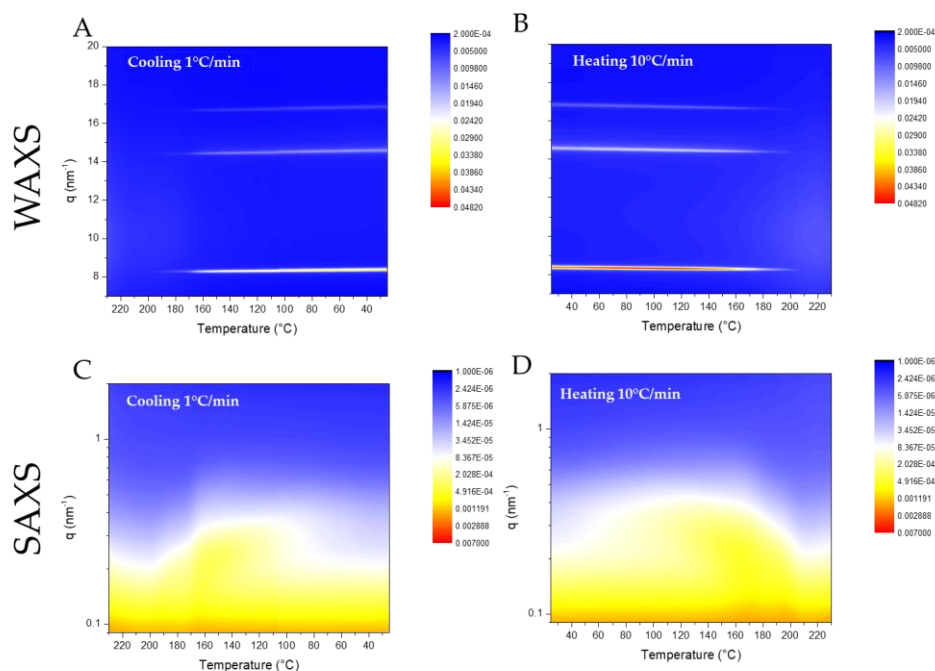


Figure A3.27. WAXS (A-B) and SAXS (C-D) patterns of the MMw-HPm non-isothermally crystallized from the melt at 1°C/min (A-C) and the subsequent heating at 10°C/min (B-C).

▲ MMw-LPm

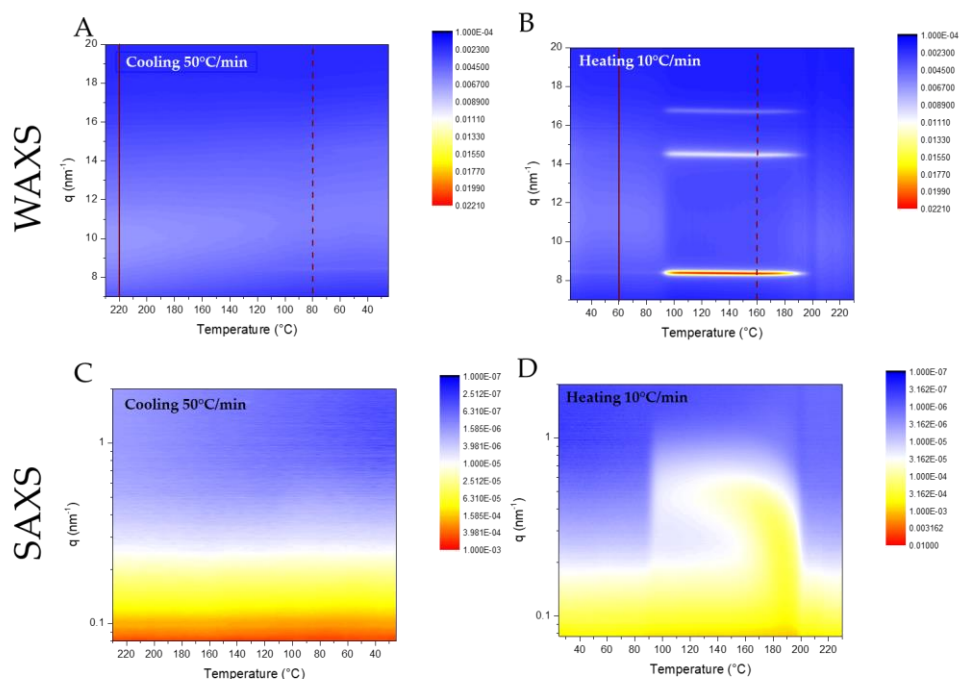


Figure A3.28. WAXS (A-B) and SAXS (C-D) patterns of the MMw-LPm non-isothermally crystallized from the melt at 50°C/min (A-C) and the subsequent heating at 10°C/min (B-C).

▲ MMw-LPm

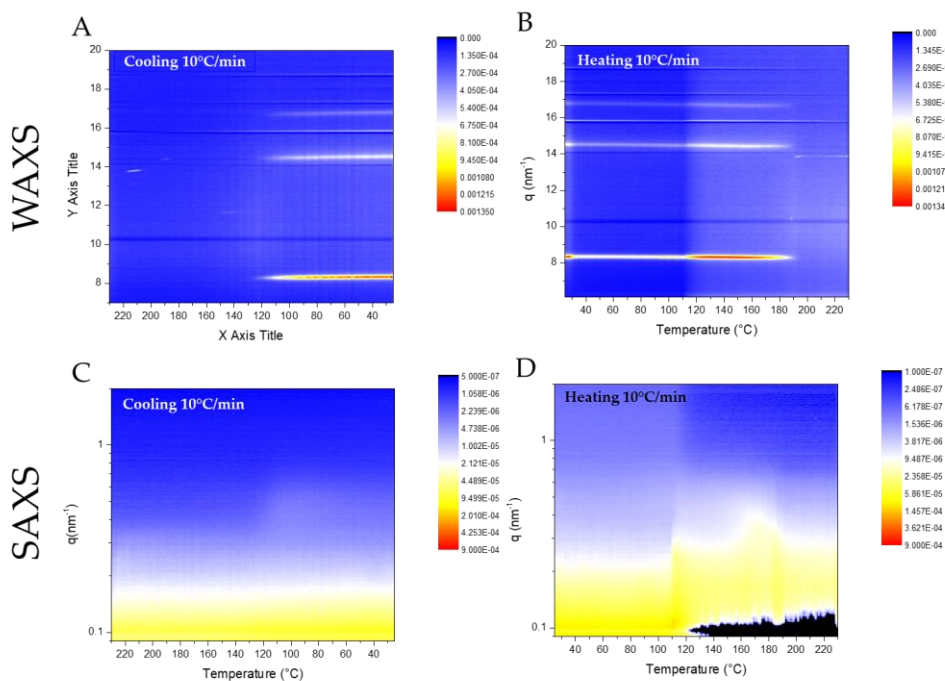


Figure A3.29. WAXS (A-B) and SAXS (C-D) patterns of the MMw-LPm non-isothermally crystallized from the melt at 10°C/min (A-C) and the subsequent heating at 10°C/min (B-C).

▲ MMw-LPm

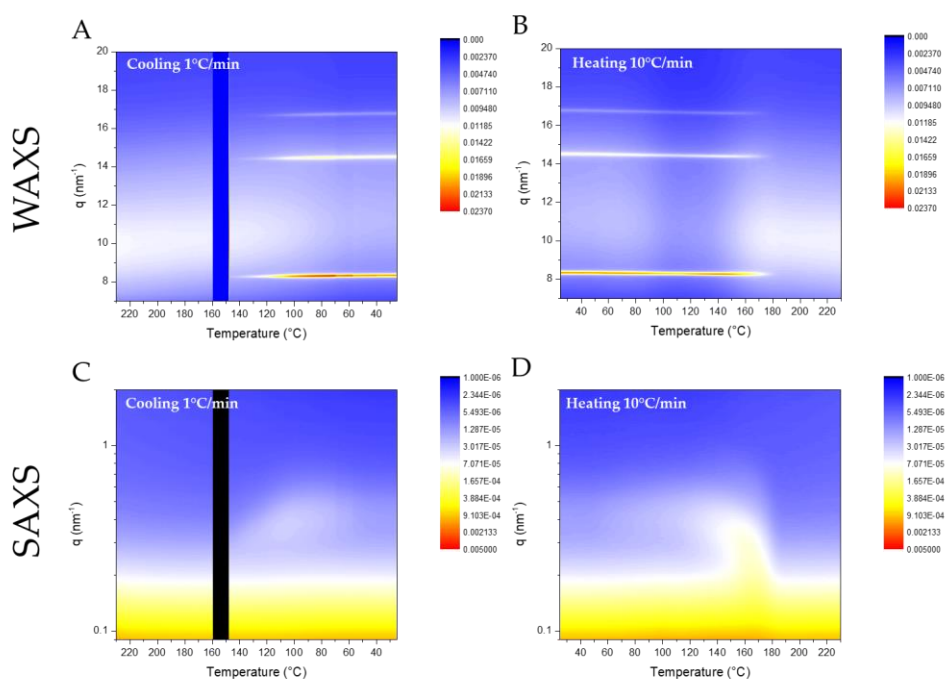


Figure A3.30. WAXS (A-B) and SAXS (C-D) patterns of the MMw-LPm non-isothermally crystallized from the melt at 5°C/min (A-C) and the subsequent heating at 10°C/min (B-C).

Table A3.7. Parameters of the Avrami-Ozawa modified model obtained by DSC for the HMw-HPm.

■ HMw-HPm				
Xt (%)	20	40	60	80
F(T)	10,666	15,311	20,045	26,182
α	1,435	1,484	1,491	1,48

Table A3.8. Parameters of the Avrami-Ozawa modified model obtained by DSC for the MMw-HPm.

● MMw-HPm				
Xt (%)	20	40	60	80
F(T)	23,388	34,995	44,463	54,576
α	1,248	1,335	1,358	1,363

Table A3.9. Parameters of the Avrami-Ozawa modified model obtained by DSC for the MMw-LPm.

▲ MMw-LPm				
Xt (%)	20	40	60	80
F(T)	19,187	24,434	28,576	33,343
α	0,802	0,855	0,89	0,926

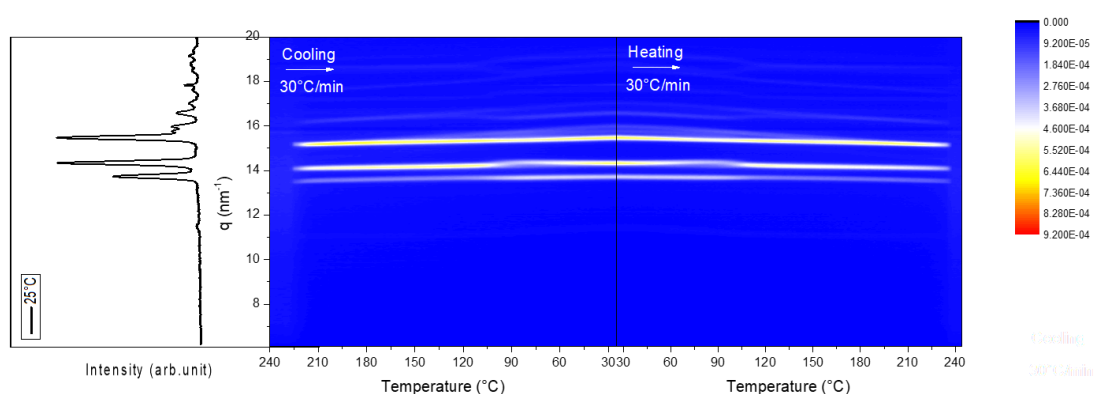


Figure A3.31. WAXS patterns of the OXA-2 non-isothermally crystallized from the melt at 30°C/min and the subsequent heating at 30°C/min.

Table A3.10. Thermodynamic parameters obtained from the thermal analysis by DSC of the PLA-SBC derivatives with OXA-2.

Sample	OXA-2 (%)	T _g (°C)	T _{cc} (°C)	ΔH _{cc} (J/g)	T _c (°C)	ΔH _c (J/g)	X _{c-c} (%)	T _m (°C)	ΔH _m (J/g)	X _{c-m} (%)
MMw-HPm	0	49	120	16,7	85	12,9	9,1	205	46,2	32,5
MMw-HPm	2	41	-	-	150	57,5	40,5	205	49,4	34,8
HMw-HPm	0	32	-	-	93	41,1	28,9	189	31,0	21,8
HMw-HPm	2	57	-	-	139	60,7	52,3	209	58,5	41,2
A-UHMw-HPm	0	33	80/103	16,9/4,8	82	1,1	?	147/163	45,6/1,8	48,6/1,3
A-UHMw-HPm	2	32	72/102	24,5/3,2	140/102	0,5/2,5	0,2/2,7	147/184	41,7/1,4	44,5/1

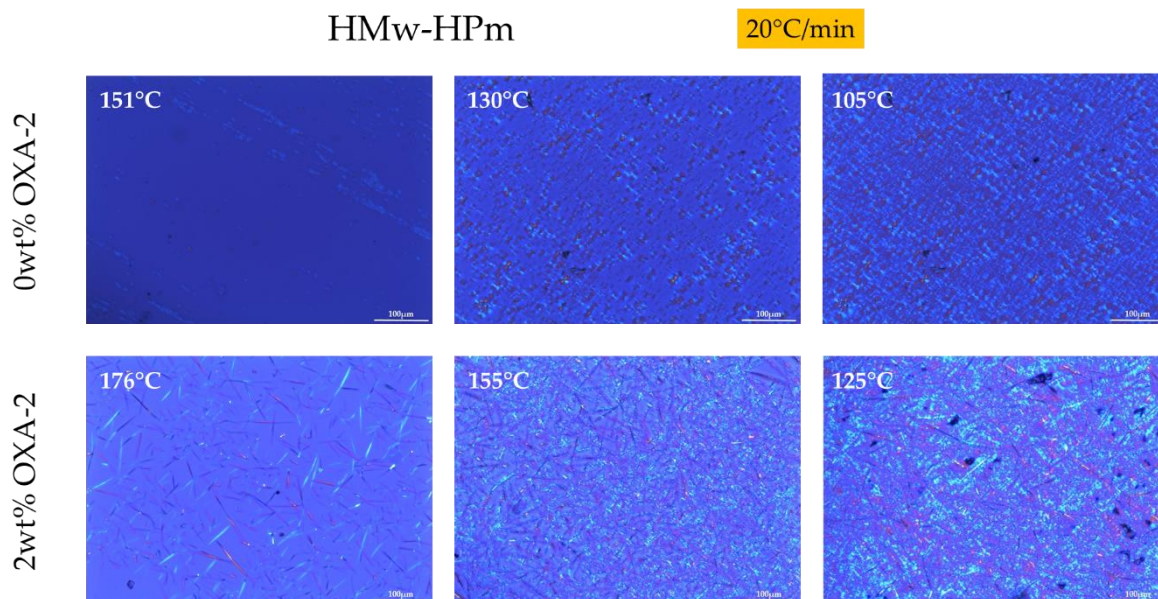


Figure A3.32. POM images of the thin films of HMw-HPm containing 0 wt% and 2 wt% of OXA-2 non-isothermally crystallized from the melt at 20°C/min.

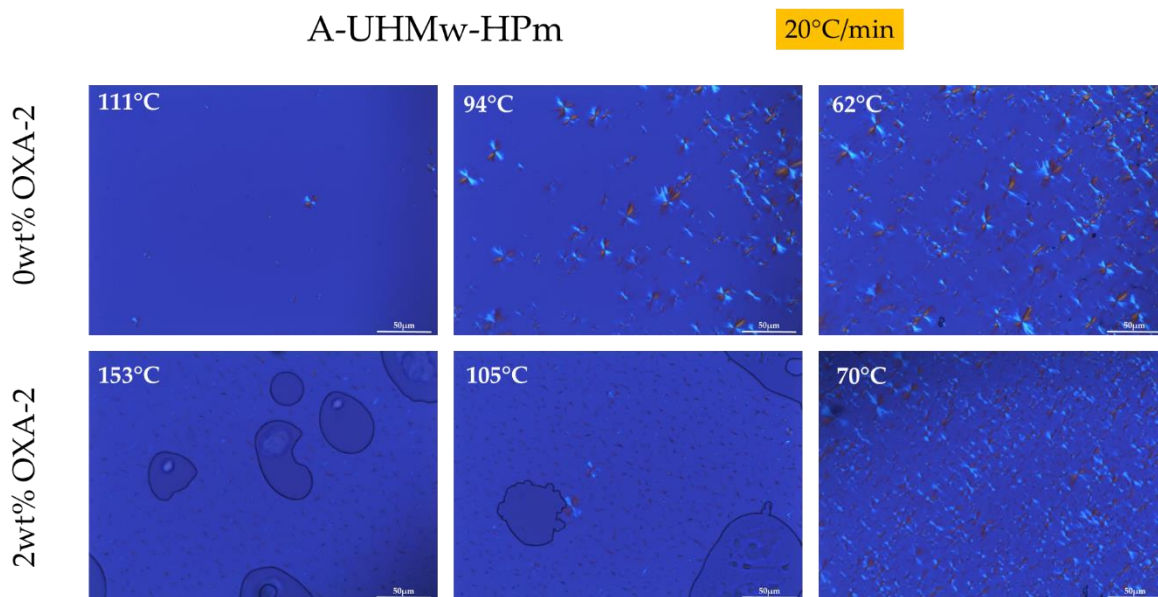


Figure A3.33. POM images of the thin films of A-UHMw-HPm containing 0 wt% and 2 wt% of OXA-2 non-isothermally crystallized from the melt at 20°C/min.

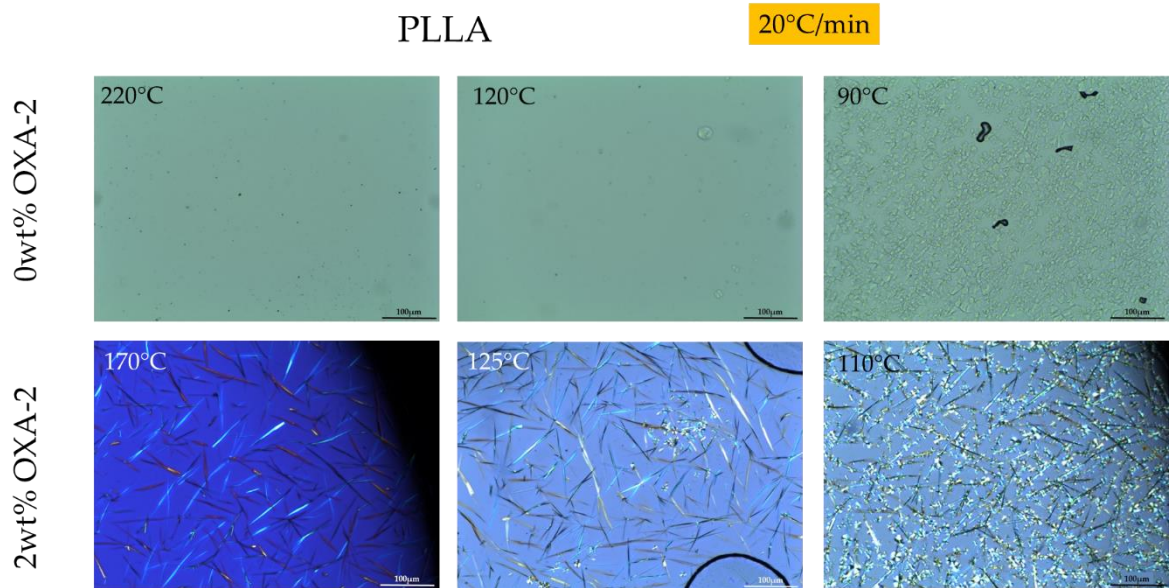


Figure A3.34. POM images of the thin films of PLLA containing 0 wt% and 2 wt% of OXA-2 non-isothermally crystallized from the melt at 20°C/min.

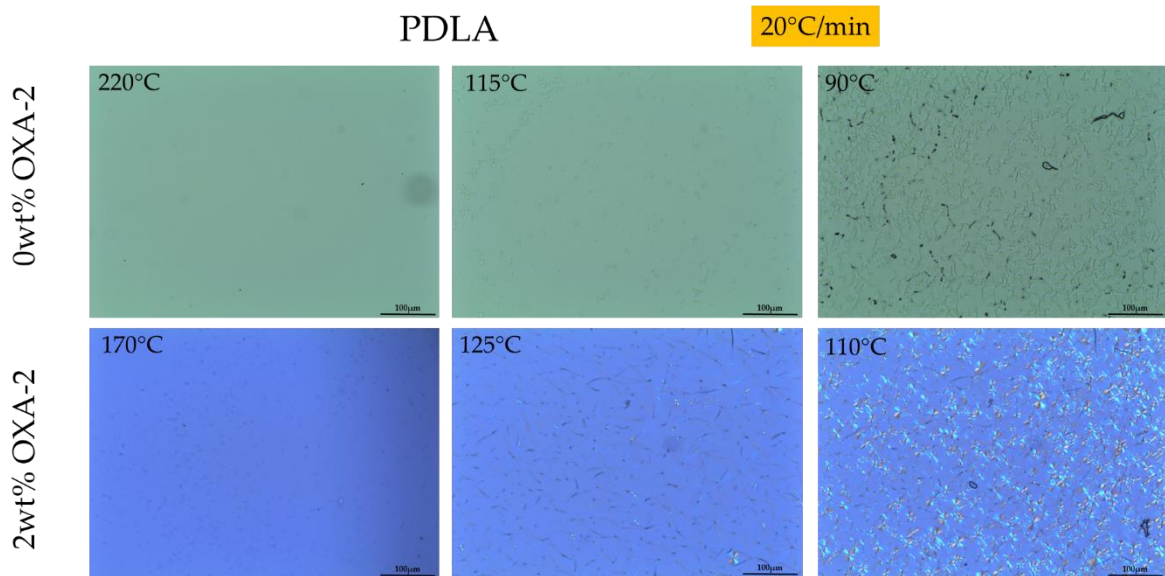


Figure A3.35. POM images of the thin films of PDLA containing 0 wt% and 2 wt% of OXA-2 non-isothermally crystallized from the melt at 20°C/min.

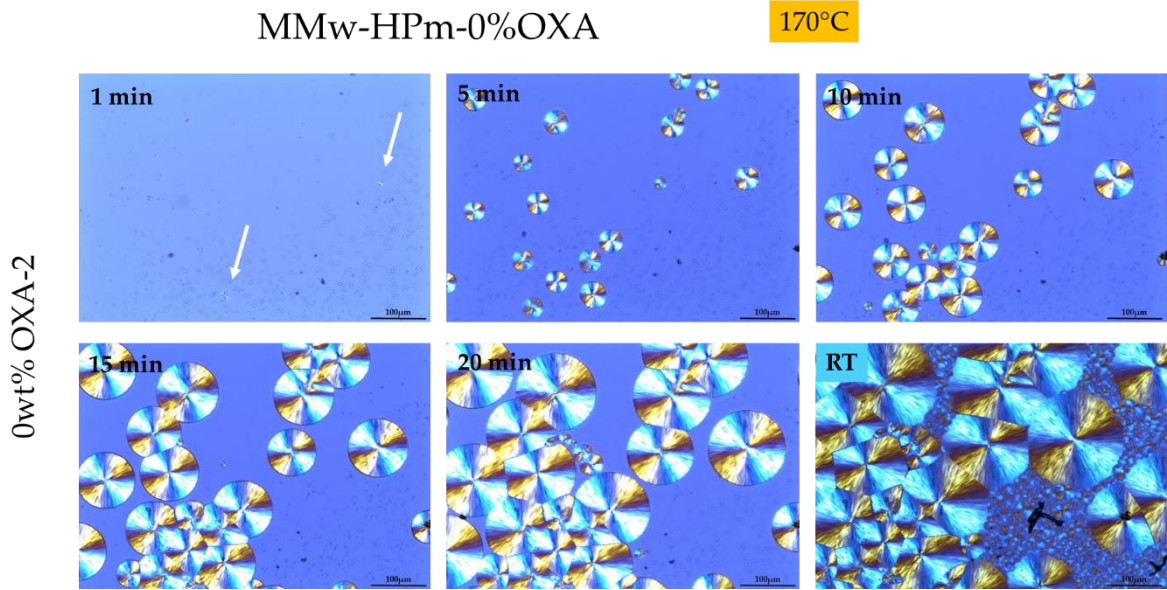


Figure A3.36. POM images of the thin films of MMw-HPm containing 0 wt% of OXA-2 isothermally crystallized from the melt at 170°C.

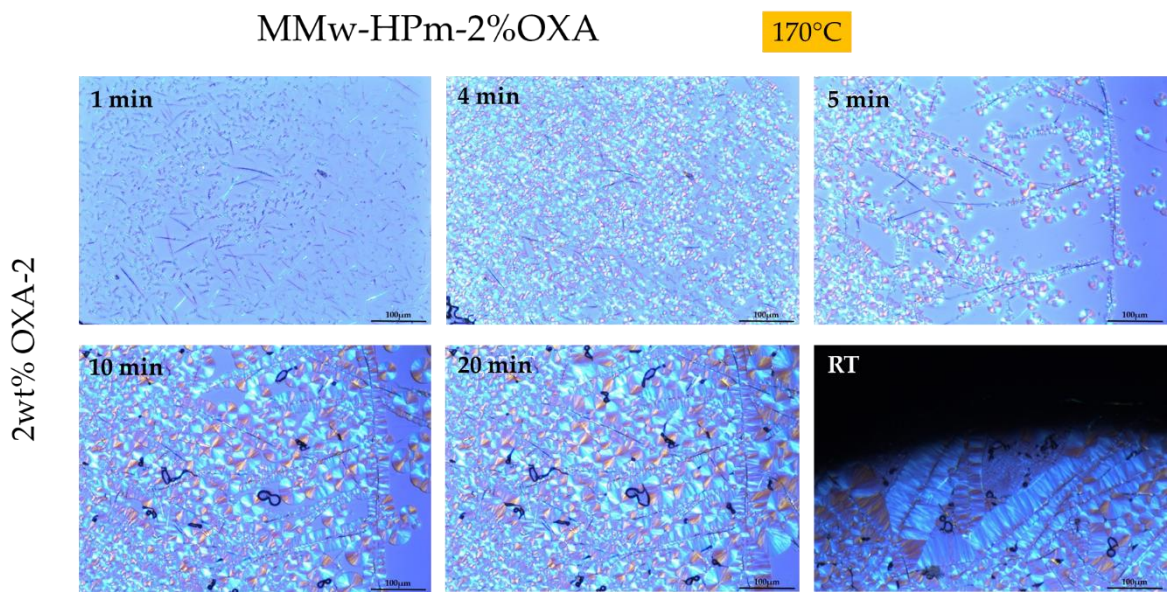


Figure A3.37. POM images of the thin films of MMw-HPm containing 2 wt% of OXA-2 isothermally crystallized from the melt at 170°C.

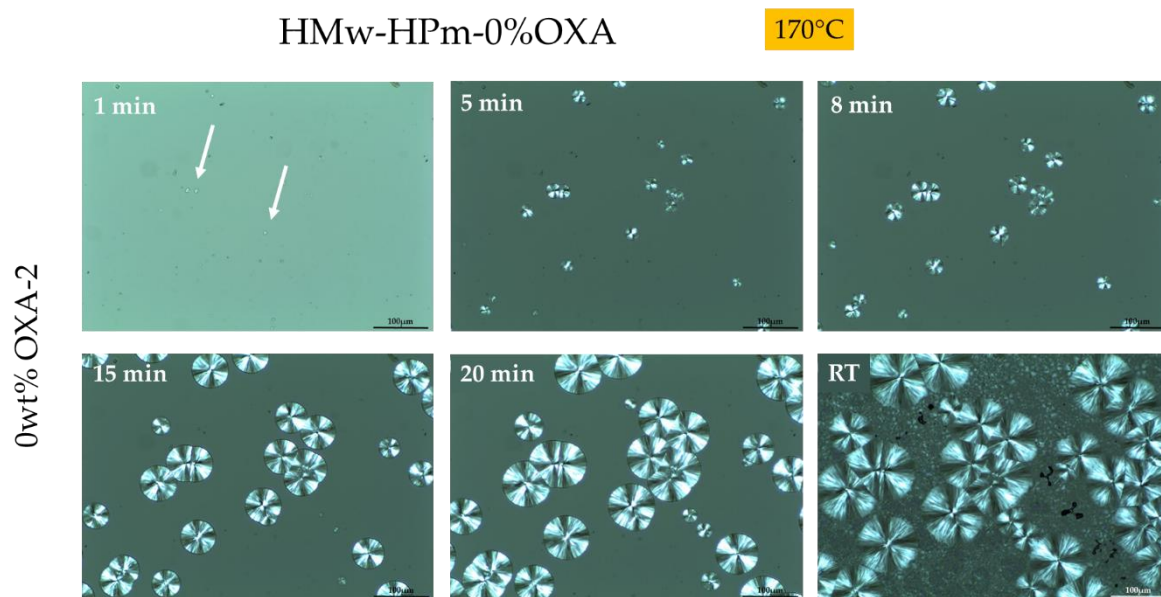


Figure A3.38. POM images of the thin films of HMw-HPm containing 0 wt% of OXA-2 isothermally crystallized from the melt at 170°C.

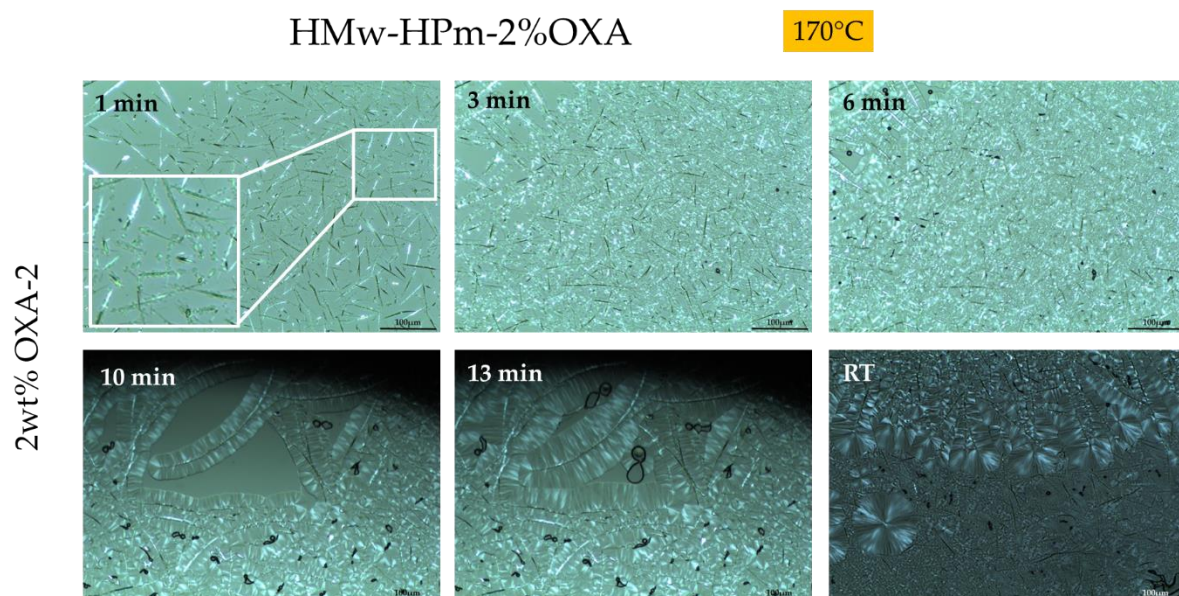


Figure A3.39. POM images of the thin films of HMw-HPm containing 2 wt% of OXA-2 isothermally crystallized from the melt at 170°C.

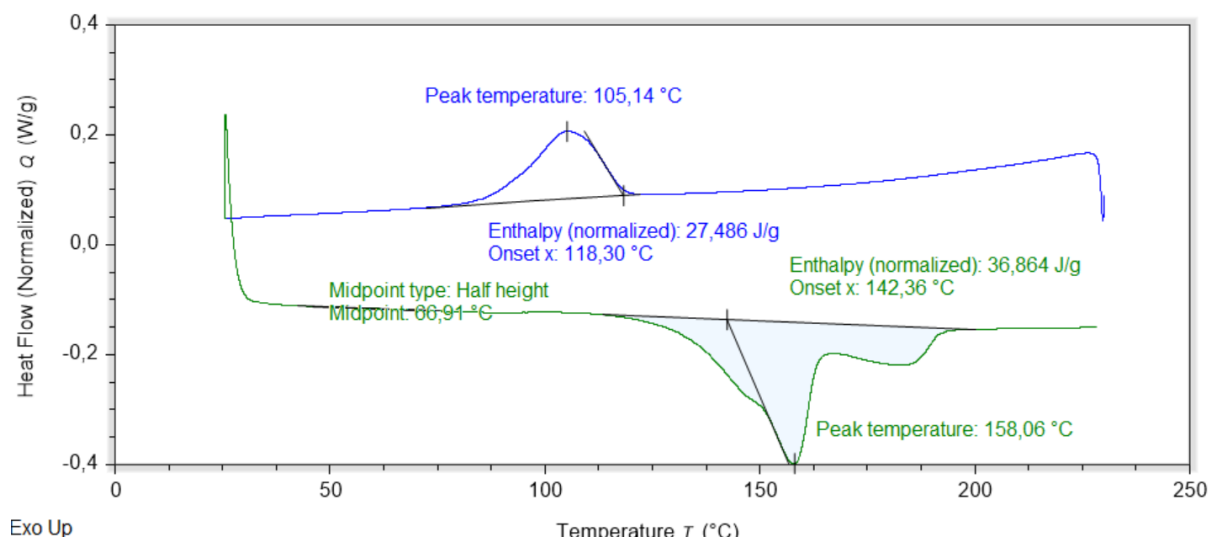


Figure A3.40. A-UHMw-HPm thermogram obtained by DSC upon cooling at 5°C/min and subsequent heating at 10°C/min.

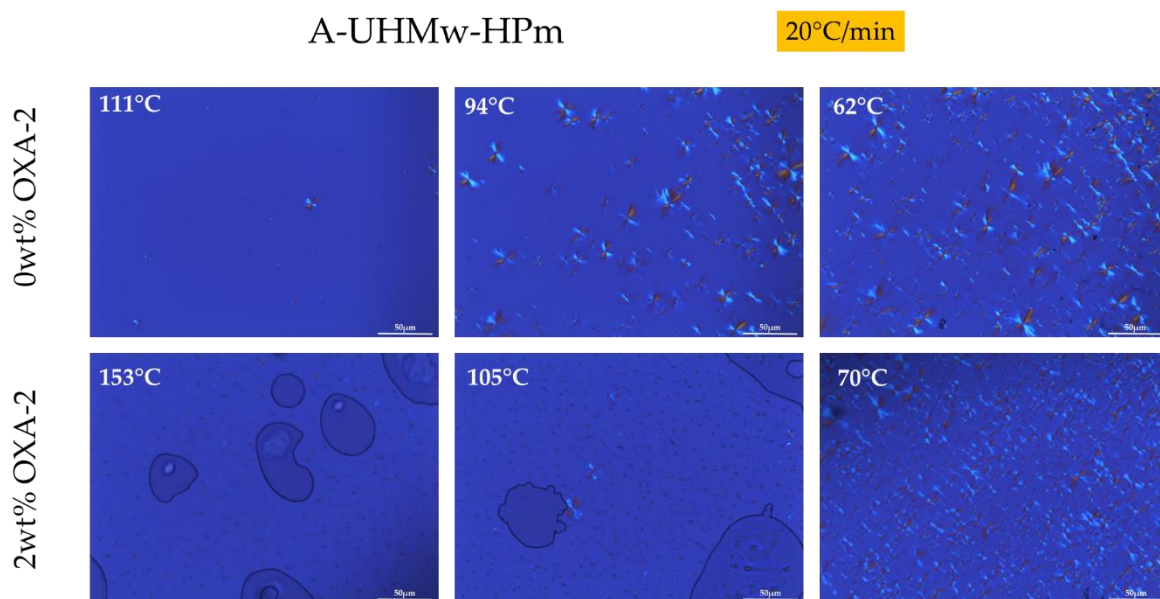


Figure A3.41. POM images of the thin films of A-UHMw-HPm containing 0 wt% and 2 wt% of OXA-2 non-isothermally crystallized from the melt at 20°C/min.

ANEXE A4

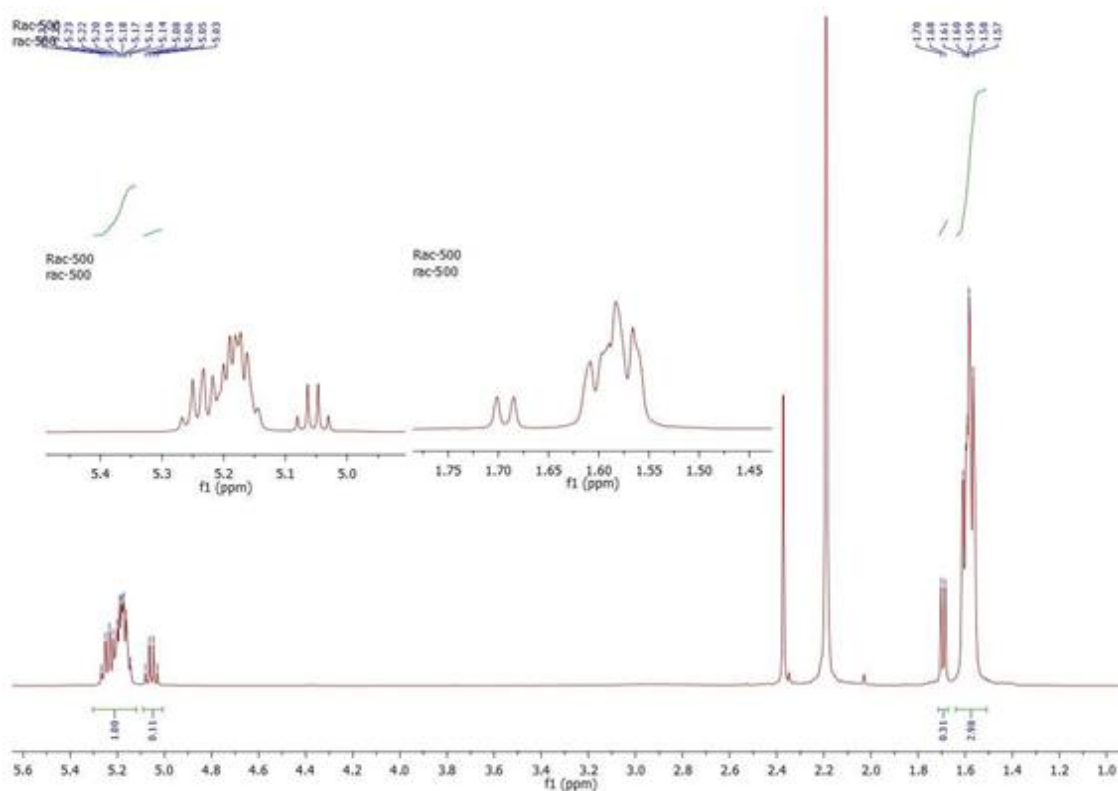


Figure A4.1. ¹H NMR spectrum (500 MHz, 298 K, CDCl₃) of Rac-PLA

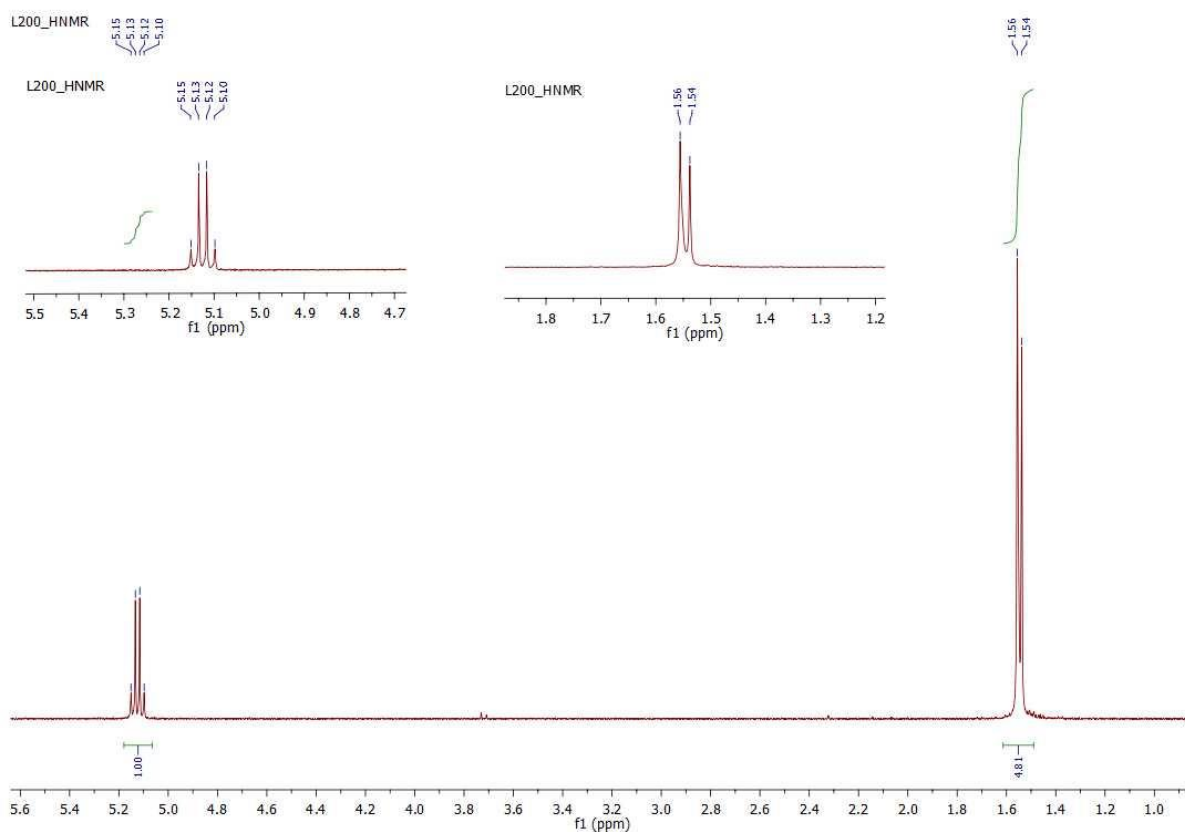


Figure A4.2. ¹H NMR spectrum (500 MHz, 298 K, CDCl₃) of HC-PLA

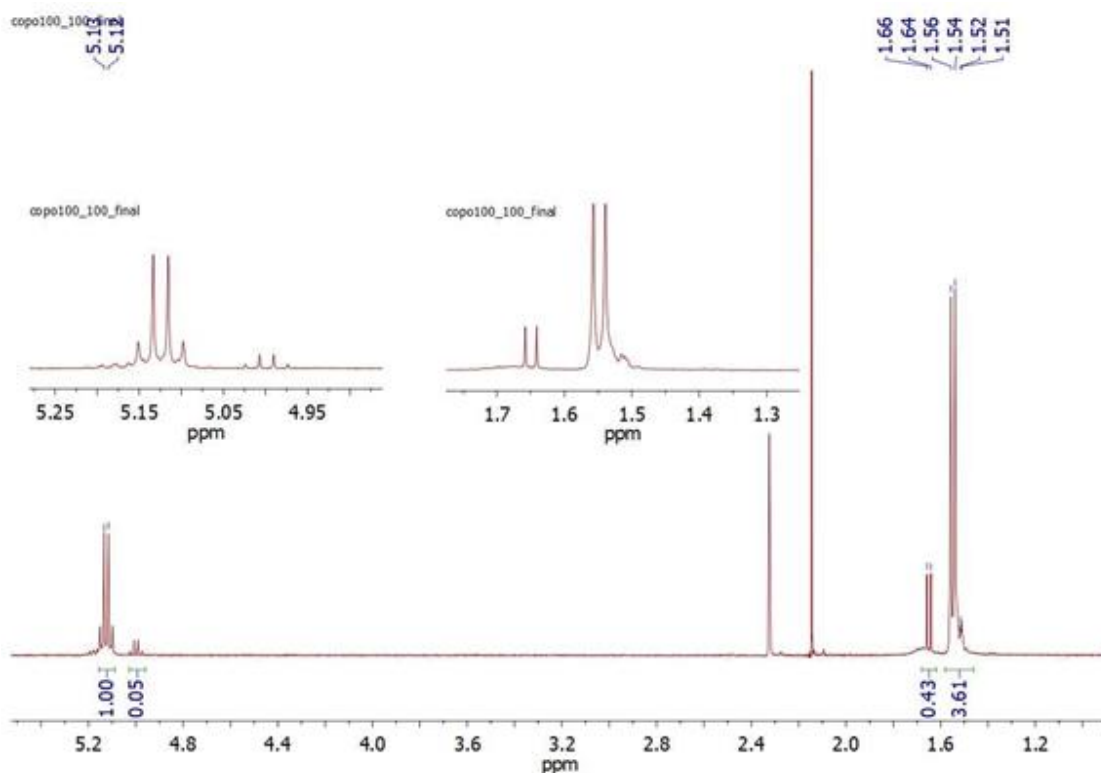


Figure A4.3. ^1H NMR spectrum (500 MHz, 298 K, CDCl_3) of SC-PLA

Sample	Vibrational bond	Raman shift (cm^{-1})
Rac-PLA	$\nu\text{C-COO}$	870
HC-PLA		870
SC-PLA		880
Rac-PLA	$\nu\text{C-C}$ (stretching) with CH_3 (rocking)	-
HC-PLA		908
SC-PLA		920
Rac-PLA	C=O	1770
HC-PLA		1755, 1766, 1777
SC-PLA		1752

Table A4.1. Raman shifts of the bulk polymers.

Particle	Average size (nm)	PDI	EE [%]
NP-Rac-PLA/DOX	286.35	0.17	0.3
NP-HC-PLA/DOX	214.8	0.18	0.24
NP-SC-PLA/DOX	270.0	0.17	0.18
NP-Rac-PLA/DAS	237.6	0.16	1.03
NP-HC-PLA/DAS	282.85	0.15	2.8
NP-SC-PLA/DAS	275.55	0.17	0.23

Table A4.2. DLS analysis of drug loaded nanoparticles

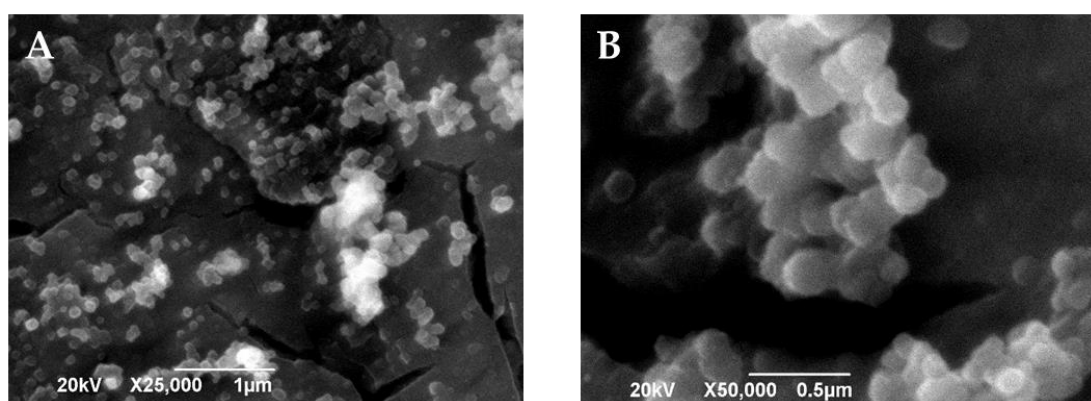


Figure A4.4. SEM images of NP-HC-PLA/DOX

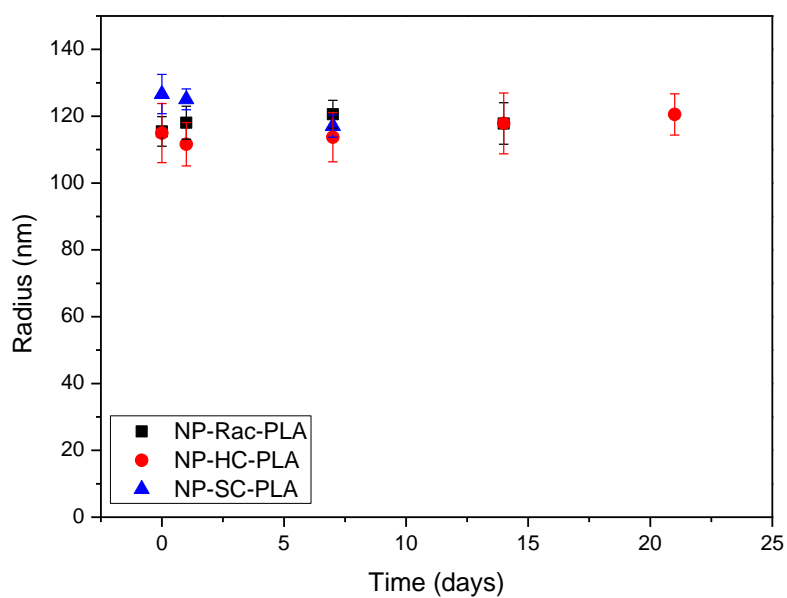


Figure A4.5. NP-PLA stability along time measured by DLS.

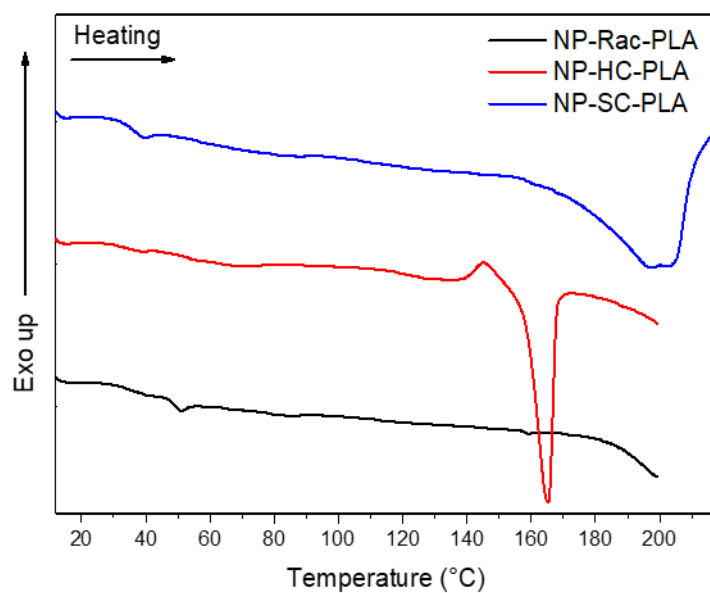


Figure A4.6. Heating ramp followed by DSC of the NP-PLA after the isothermal treatment at 65°C.

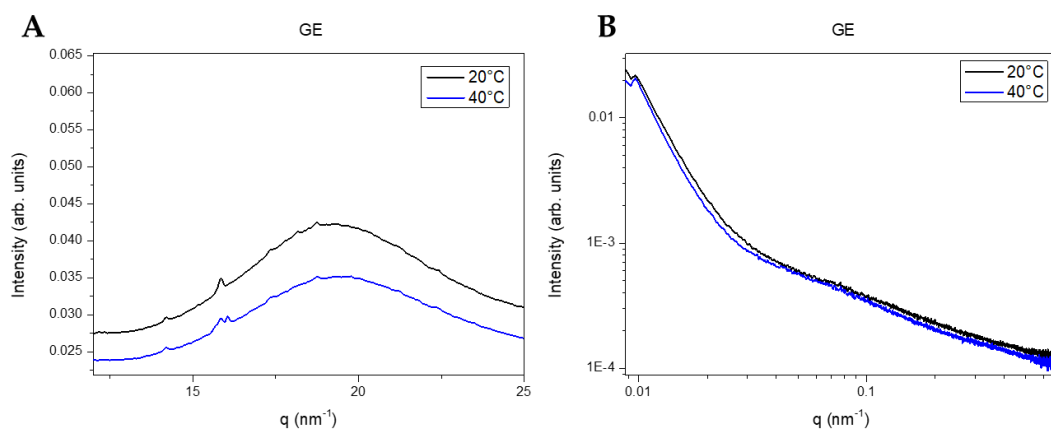


Figure A4.7. WAXS (A) and SAXS (B) of the gelatin hydrogel

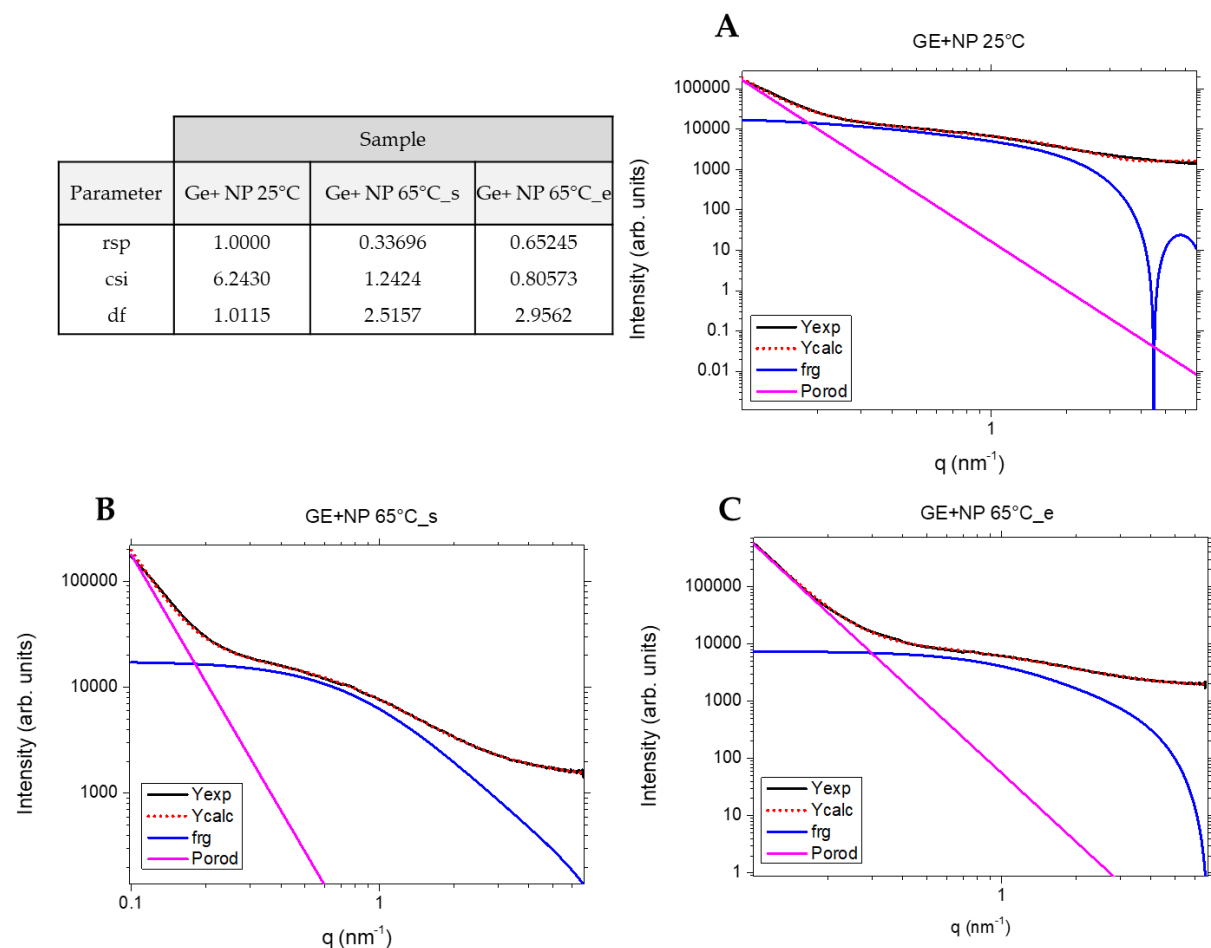


Figure A4.8. Table A4.2.SAXS fitting parameters and plots of GE/NP-HC-PLA at 25°C (A), 65°C (B) and after 30 min at 65°C (C).

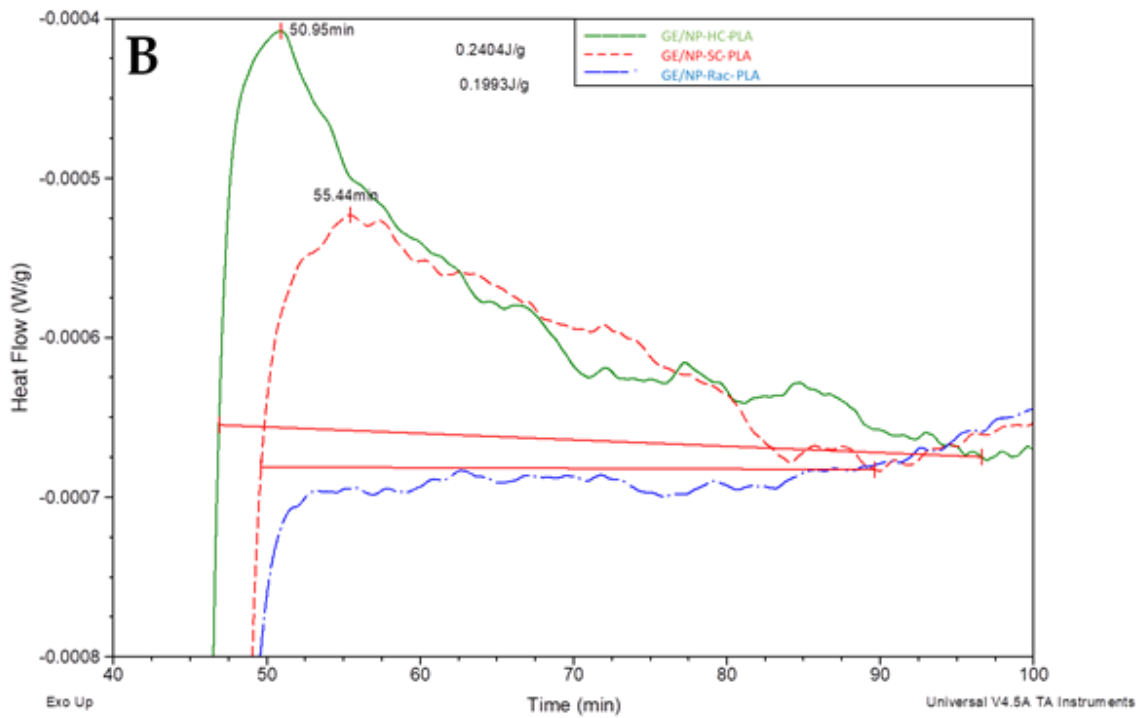
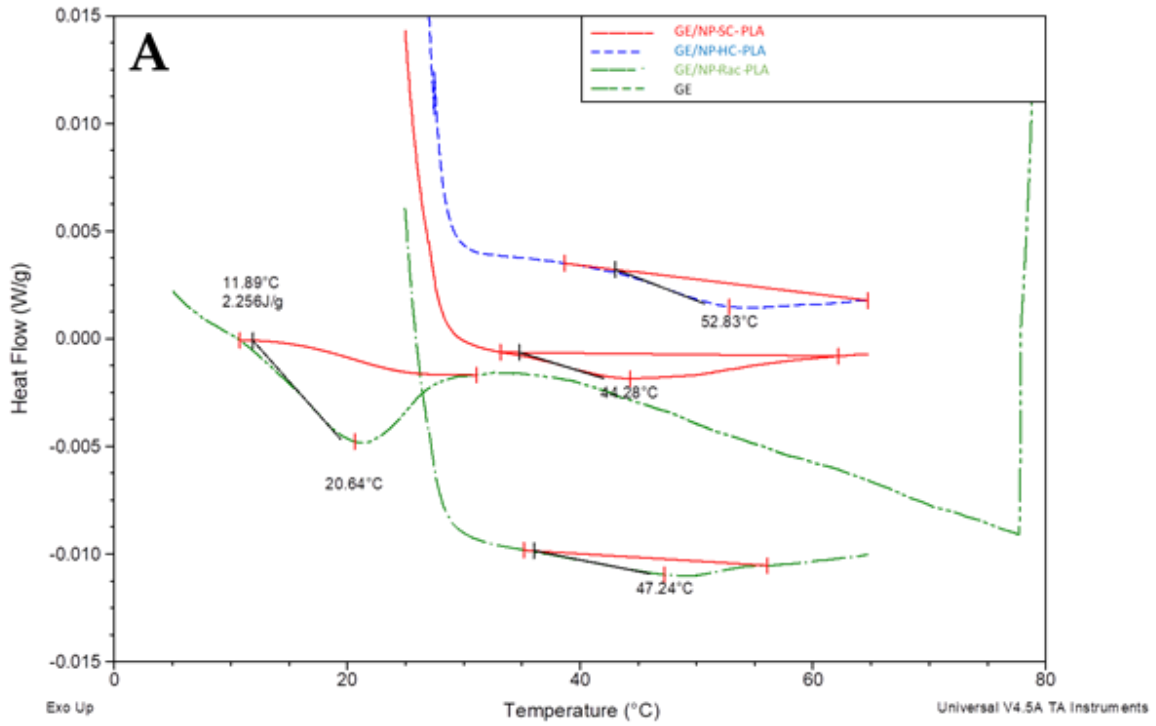
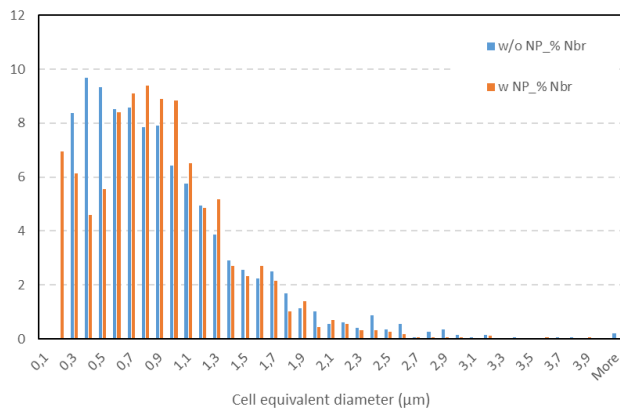


Figure A4.9. DSC thermograms of the Gelatin and NP-PLA bionanocomposites during the heating step from room temperature (**A**) and the isothermal step at 65°C (**B**).

A Percentage of cells



B Percentage of cells above a certain size

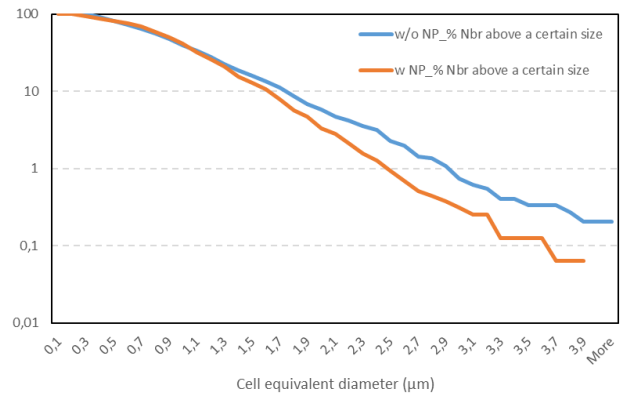


Figure A4.10. Histograms of the size cell (**A**) and the size cell above a certain size (**B**) of the x2000 magnification images for both GE without (w/o NP) and with PLA NPs (w NP).

**PLA STEREO-COMPLEXES A BLOC : DE LA
SYNTHESE AUX APPLICATIONS BIOMEDICALES**

Présentée par

Carmen Moya Lopez-Pelaez

LMOPS, Université de Lorraine

18 Novembre 2022 à Metz

INTRODUCTION

L'industrie pharmaceutique exige constamment le développement de systèmes d'administration de médicaments qui améliorent l'efficacité thérapeutique et réduisent les effets secondaires. La stratégie traditionnelle consistant à fabriquer des médicaments à dose médicamenteuse standardisée est inefficace pour 70 % des patients, créant le besoin de substituer la production en masse par une médecine personnalisée. En plus, les nanoparticules formulées normalement à partir de polymères permettent d'améliorer la stabilité et la solubilité des molécules encapsulées, ce qui favorise l'administration de médicaments à travers les membranes cellulaires et augmente la durée de circulation des médicaments, améliorant ainsi la sécurité et leur efficacité. Néanmoins, il existe un écart entre la caractérisation des propriétés physico-chimiques de nanoparticules polymériques et ses performances dans des conditions physiologiques qui entrave l'application au niveau clinique. L'acide poly-lactique (PLA) est un polyester aliphatique et synthétique obtenu à partir de sources renouvelables et biosourcées qui présente des caractéristiques biorésorbables grâce à son hydrolyse en milieu physiologique en produits non toxiques.

La richesse de la nanostructure du PLA, avec ses dérivés isotactiques, atactiques, syndiotactiques, etc., associée à sa nature polymorphe, offre la possibilité de modifier les propriétés physicochimiques souhaitées. En particulier, la phase stéréocomplexe (SC) a été largement visée en raison des propriétés physico-chimiques prometteuses qu'elle présente, notamment une température de fusion, des performances mécaniques et une résistance à l'hydrolyse plus élevées que celles de ses homologues énantiomères. De même, les applications biomédicales et pharmaceutiques ont été largement conçues avec des PLA stéréocomplexes, comme les systèmes d'administration de médicaments, ainsi que les applications industrielles et de commodité. Cependant, la cristallisation typique des SC par le mélange de dérivés énantiomères (PLLA et PDLA) diminue pour les PLA à haut poids moléculaire (HMw) et des homocristaux énantiomères (HC) sont obtenus à la place. En outre, la synthèse de copolymères stéréoblocs de PLA (PLA-SBC) présentant une masse moléculaire élevée et un contrôle stéréologique élevé nécessite des catalyseurs sophistiqués avec un contrôle stéréologique pour les deux énantiomères, qui sont extrêmement rares.

L'objectif principal de cette thèse était d'adapter des copolymères à blocs PLA avec des nanostructures définies, pour concevoir des matériaux avec une relation structure-traitement-propriétés spécifiques permettant d'obtenir des applications pharmaceutiques personnalisées (**Figure 1**). En particulier, la phase stéréocomplexe PLA, qui est généralement obtenue à partir du mélange physique des énantiomères PLA, présente des propriétés physicochimiques prometteuses telles qu'une température de fusion plus élevée, une résistance à l'hydrolyse et

des performances mécaniques par rapport aux homologues énantiomères. Cependant, une séparation de phase préjudiciable se produit à haut poids moléculaire, diminuant les propriétés physico-chimiques prometteuses. La synthèse de copolymères à blocs PLA constitue une solution possible pour surmonter la séparation de phase, cependant, un catalyseur sophistiqué avec un stéréocontrôle élevé pour les deux énantiomères est nécessaire qui sont extrêmement rapides.

Dans ce travail de thèse, l'état de l'art du PLA en tant que biomatériau pour son application médicale est passé en revue dans une approche globale en mettant en évidence les interconnexions entre les paramètres de la microstructure et les applications souhaitées. De plus, un accent particulier a été mis sur la phase stéréocomplexe et les problèmes rencontrés jusqu'à présent pour obtenir une phase stéréocomplexe « pure » (**Chapitre 1**) [1]. La synthèse du copolymère stéréo-dibloc long désiré-HMw de PLA (PLA-SBC) est décrite en utilisant un catalyseur hétéroscorpionate à base de Zn synthétisé par le groupe de chimie inorganique de l'Université de Castilla-La Mancha (UCLM), en Espagne. Cependant, dans ce chapitre, la synthèse de copolymères à blocs symétriques présentant différents poids moléculaires a été établie comme objectif principal (**Chapitre 2**)[2]. De plus, le mécanisme de cristallisation du bain de fusion du PLA-SBC sous différentes conditions thermiques est étudié à différentes échelles de longueur, en collaboration avec la ligne de lumière 26 de l'European Synchrotron Radiation Facility (ESRF), en France. De même, le mécanisme de cristallisation du PLA-SBC mélangé avec différents agents de nucléation (NA) est également analysé en collaboration avec l'Université de Maastricht, comme stratégie pour surmonter l'un des principaux inconvénients du PLA, le faible taux de cristallisation (**Chapitre 3**). La sélection d'un catalyseur à base d'oligo-éléments pour accomplir la synthèse de copolymères stéréoblocs de PLA visait à appliquer les dérivés de PLA dans le domaine biomédical. Au cours de mes études de pharmacie, j'ai été initiée au monde des nanopORTEURS grâce à la collaboration avec le groupe de recherche en neurosciences de la faculté de pharmacie de l'UCLM. Mais, il existe un écart entre la recherche sur les matériaux, les tests précliniques, les exigences cliniques et les aspects réglementaires qui entrave l'utilisation de ces recherches sur les nanoparticules de PLA au niveau clinique. C'est dans ce contexte que nous avons développée des systèmes de délivrance de médicaments à base de gélatine (DDS) contenant des nanoparticules formulées à partir de dérivés de PLA présentant différentes stéréorégularités de même que sont étudiés l'influence du taux de libération et l'applicabilité locale des bionanocomposites, ceci en collaboration avec les universités de Vigo et Castilla-La Mancha, en Espagne (**Chapitre 4**) [3].

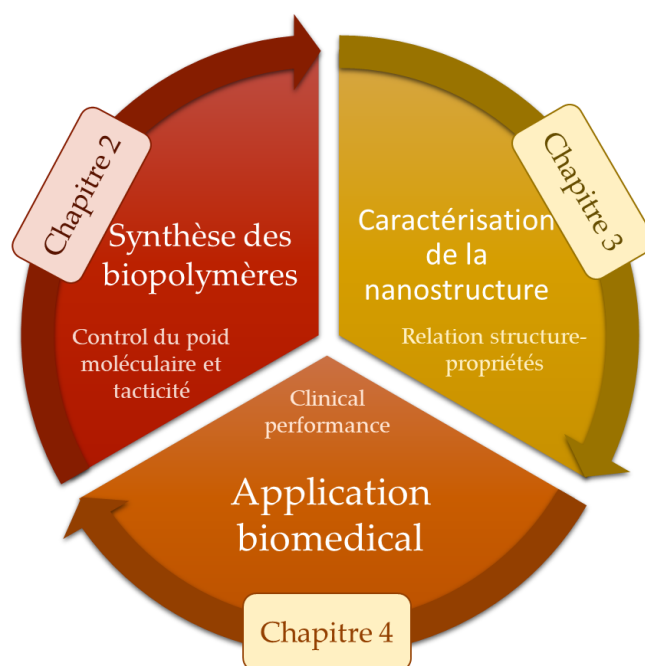


Figure 1. Résumé graphique de la thèse

MATERIAL ET METHODES

Une synthèse originale des dérivés de PLA a été réalisée par polymérisation par ouverture de cycle (ROP) en utilisant notre nouveau catalyseur dérivé de zinc [2], qui est biocompatible car à base d'un métal nécessaire à l'homme. De cette manière, la synthèse de PLA stéréocomplexe à bloc de poids moléculaire élevé et de haute tacticité a été synthétisée et caractérisé grâce à différentes techniques comme la Résonance magnétique nucléaire (RMN), Chromatographie par Perméation de Gel (GPC), et la Polarimétrie.

En plus, la caractérisation du mécanisme de cristallisation à différentes échelles du PLA stéréocomplexe à bloc a été faite avec différents techniques, notamment la Calorimétrie Différentielle à Balayage (DSC), la Microscopie Optique Polarisée (POM) et Diffusion de Rayons X (SAXS/WAXS)

Les nanoparticules de PLA ont été formulées par la méthode de la double émulsion. La gélatine a été extraite de la peau de requin et l'hydrogel formé avec celle-ci a été mélangé par sonication avec les nanoparticules de PLA pour former le bionanocomposite. En plus, les nanoparticules ont été caractérisées à différents échelles, du niveau moléculaire jusqu'au niveau microscopique, ainsi que les propriétés thermiques et mécaniques des polymères, des nanoparticules et des bionanocomposites. Ces mesures ont été réalisées en utilisant différentes

techniques : Résonance magnétique nucléaire (RMN), Chromatographie par Perméation de Gel (GPC), Polarimétrie, Calorimétrie Différentielle à Balayage (DSC), Diffusion de lumière dynamique (DLS), Spectroscopie électronique à Balayage (SEM), Spectroscopie Raman, Diffusion de Rayons X (SAXS/WAXS) et rhéologie.

RESULTATS ET CONCLUSIONS

Dans cette thèse, la synthèse de copolymères stéréo-diblocs de haut poids moléculaire et de haute tacticité de PLA a été faite avec succès (**Figure 2**). L'amorceur organométallique employé pour la polymérisation du PLA constitue le premier amorceur capable de générer les copolymères stéréo-diblocs longtemps désirés sans l'utilisation d'un co-amorceur, ce qui représente un avantage pour l'évolutivité vers la production industrielle. L'initiateur suit un mécanisme de coordination-insertion, présente un caractère vivant ainsi qu'une réaction cinétique de premier ordre. De plus, une constante de vitesse similaire pour les deux énantiomères PLA a été trouvée, ce qui permet la synthèse de copolymères stéréoblocs en un temps relativement court, ainsi que la synthèse de PLA racémique. La tacticité des copolymères séquencés peut être adaptée en modifiant le moment auquel le second monomère est ajouté à la réaction, bien que la diminution de la pureté énantiomérique de chaque monomère puisse également être une solution pour adapter la tacticité.

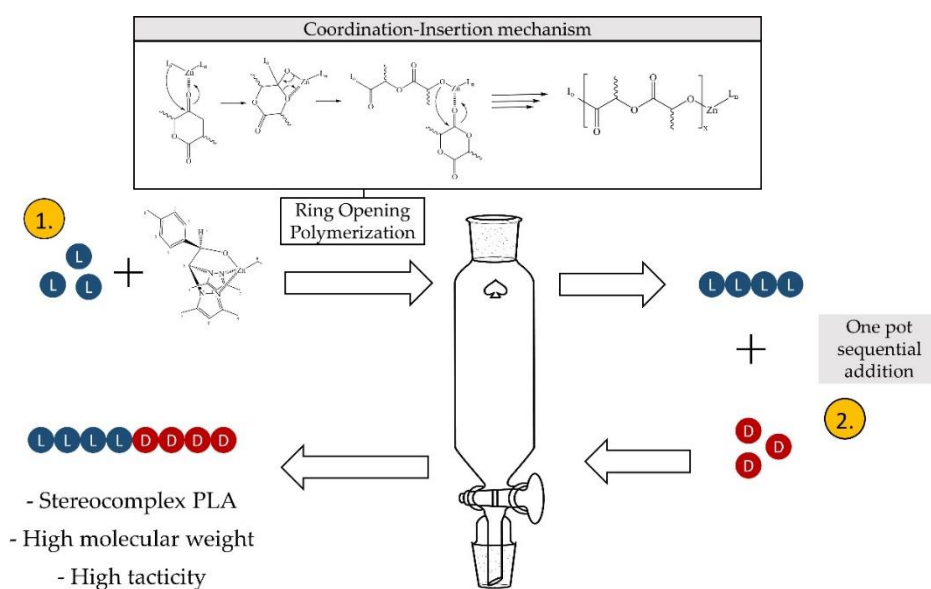


Figure 2. Résumé du procédé de synthèse

Par la suite, la caractérisation du mécanisme de cristallisation à partir de la masse fondue, sous différentes conditions thermiques, des copolymères stéréo-diblocs PLA a été réalisée à différentes échelles grâce à une approche multi-techniques. Il est important de noter que la séparation de phase typique se produisant dans le mélange énantiomère de PLA est

évitée dans les dérivés de PLA-SBC de poids moléculaire élevé, même à des vitesses de refroidissement élevées telles que 50 °C/min, ce qui augmente la pertinence du PLA-SBC pour son utilisation en conditions industrielles. La température de dégradation, de fusion et de cristallisation du PLA-SBC augmentent à mesure que le poids moléculaire augmente. De plus, la diminution de la tacticité du PLA-SBC diminue la température de fusion de 210°C à 200°C, ce qui pourrait être attribuée à la formation d'une phase cristalline stéréocomplexe « défectueuse ». Le degré de cristallinité et le taux de cristallisation du PLA-SBC de poids moléculaire élevé sont respectivement 10 % plus élevé et 3 fois plus élevé que le SC-PLA formé à partir du mélange énantiomère. En outre, l'ajout d'OXA-2 en tant qu'agent de nucléation peut encore augmenter la vitesse de cristallisation permettant la cristallisation à des vitesses de refroidissement élevées telles que 400°C/min. Fait intéressant, l'OXA-2 modifie la morphologie cristalline du PLA-SBC de cristaux de type sphérulite à une nucléation en rangée, ce qui pourrait être très utile pour adapter les propriétés mécaniques du PLA-SBC.

Enfin, une série de bionanocomposites composés d'hydrogel de gélatine et de nanoparticules de PLA présentant différentes nanostructures a été conçue pour obtenir des systèmes d'administration de médicaments multifonctionnels avec des taux de libération de médicaments sur mesure. Des nanoparticules de dérivés de PLA ont été formulées avec succès avec deux médicaments antitumoraux par la méthode de la double émulsion, mais produisant une structure amorphe indépendamment de l'architecture de la chaîne, effaçant la nanostructure conçue. Cependant, un recuit thermique post-formulation a permis la

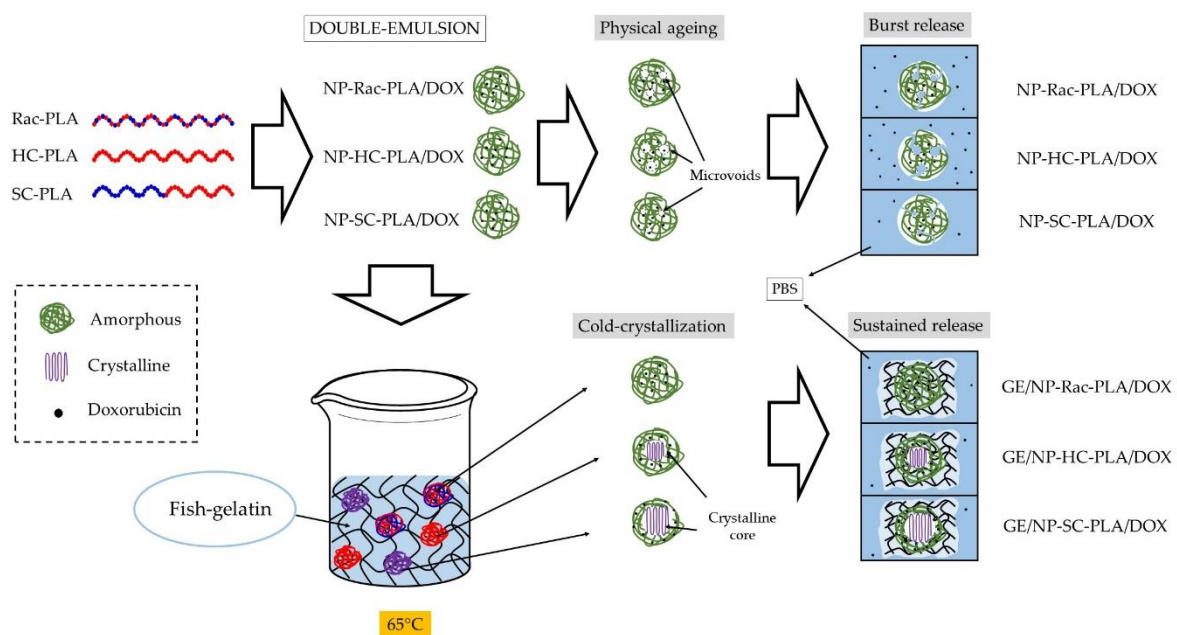


Figure 3. Résumé de la méthodologie suivie pour la fabrication de nanocomposites pour la libération contrôlée de médicaments.

crystallisation des nanoparticules dans la phase cristalline correspondante, mais produisant une agglomération des nanoparticules néfaste, diminuant l'effet thérapeutique. Une méthodologie simple pour recuire les nanoparticules et éviter l'agrégation a été développée par la dispersion des nanoparticules de PLA dans l'hydrogel de gélatine à 65°C. La gélatine sert de support mécanique pour le stockage et l'administration locale des systèmes d'administration de médicaments ainsi que de support aux médicaments complémentaires avec différents profils de libération. Cependant, les profils de libération de médicament des nanoparticules de PLA recuites dans la matrice de gélatine étaient similaires indépendamment de la nanostructure du polymère, bien que la libération de médicament à long terme n'ait pas pu être analysée en raison de la saturation du signal UV-médicament du fait de la désintégration de la gélatine.

PERSPECTIVES

L'initiateur inorganique utilisé pour la synthèse dans cette thèse constitue un bon candidat pour l'application future du dérivé PLA dans le domaine biomédical, puisque le Zn est un oligo-élément du corps humain. Cependant, des approches synthétiques «plus vertes» pourraient être envisagées en utilisant un initiateur organique qui exclut les métaux, tels que la 4-(diméthylamino)pyridine, qui ont déjà été signalés pour polymériser avec succès le PLA, mais pas encore les copolymères stéréoblocs. De plus, la maîtrise de la synthèse permet la polymérisation de multiblocs-PLA (tri-, tétra-, penta-, etc.) qui pourraient présenter des propriétés différentes, ainsi que des copolymères hétéro-blocs avec des matériaux présentant des propriétés complémentaires comme le PEG, le PGA, PCL, etc. De plus, le rendement de la polymérisation à l'échelle du laboratoire était de quelques grammes limitant certaines analyses de propriétés qui nécessitaient plus de matière, comme le test mécanique. Par conséquent, la mise à l'échelle du processus de synthèse pour obtenir une plus grande quantité de polymère par lot est nécessaire pour poursuivre la caractérisation du PLA-SBC ainsi que sa mise en forme par exemple grâce à de nouvelles techniques telles que l'impression 3D. L'analyse de la dégradation thermique réalisée dans cette thèse s'est principalement concentrée sur la détection d'éventuelles dégradations survenant au cours du traitement thermique lors de l'analyse du mécanisme de cristallisation à partir du bain de fusion. Cependant, une analyse plus approfondie pour comprendre le processus de dégradation ainsi que pour quantifier les réactions de transestérification nuisibles se produisant lors du traitement thermique est nécessaire pour établir la relation structure-traitement-propriétés. De plus, de nombreuses données présentées ici concernant le mécanisme de cristallisation peuvent être analysées plus en détail, telles que l'obtention de l'épaisseur du cristal lamellaire par l'application de la fonction de corrélation aux profils SAXS. Le mécanisme de cristallisation

à partir du verre ou de la solution doit également être abordé. De même, l'analyse par nano-faisceau à la surface de l'agent de nucléation OXA-2 avec du PLA-SBC cristallisé dessus est conseillée pour aborder la question de l'efficacité de nucléation plus élevée sur le copolymère PLA-SBC par rapport à l'homopolymère homologue. L'analyse de l'orientation de la phase cristalline du PLA-SBC sur le cristal OXA-2 pourrait être clarifié si la nucléation en rangée observée à l'échelle microscopique est due à un effet géométrique ou à une croissance épitaxiale.

Concernant le système de délivrance de médicament bionanocomposite conçu dans la dernière partie de cette thèse, une méthode de détection différente pourrait être utilisée pour analyser la libération de médicament sur une durée plus longue, comme la chromatographie liquide à haute performance (HPLC), puisque le signal de gélatine sature l'UV - détection de drogue. Enfin, de nouvelles méthodes pour améliorer la cristallisation des nanoparticules lors de la formulation pourraient être envisagées ainsi qu'une analyse plus approfondie du mécanisme régissant la formulation des nanoparticules de PLA d'un point de vue thermodynamique. L'application potentielle du PLA-SBC dans le domaine biomédical comprend la fabrication de stents, qui ont déjà été fabriqués à base de PLLA mais produisant des dispositifs sans contrainte radiale qui pourraient être surmontés par les propriétés mécaniques améliorées présentées par le stéréocomplexe PLA phase.

BIBLIOGRAPHIE

1. Moya-Lopez, C.; González-Fuentes, J.; Bravo, I.; Chapron, D.; Bourson, P.; Alonso-Moreno, C.; Hermida-Merino, D. Polylactide Perspectives in Biomedicine: From Novel Synthesis to the Application Performance. *Pharmaceutics* **2022**, *14*, 1673, doi:10.3390/pharmaceutics14081673.
2. Moya-Lopez, C.; Bravo, I.; Castro-Osma, J.A.; Chapron, D.; Bourson, P.; Vagner, C.; Cochez, M.; Leon, N.; Alonso-Moreno, C.; Hermida-Merino, D. Synthesis of High Molecular Weight Stereo-Di-Block Copolymers Driven by a Co-Initiator Free Catalyst. *Polymers (Basel)*. **2022**, *14*, 1–16, doi:10.3390/polym14020232.
3. Moya-Lopez, C.; Juan, A.; Donizeti, M.; Valcarcel, J.; Vazquez, J.A.; Solano, E.; Chapron, D.; Bourson, P.; Bravo, I.; Alonso-Moreno, C.; et al. Multifunctional PLA/Gelatin Bionanocomposites for Tailored Drug Delivery Systems. *Pharmaceutics* **2022**, *14*, 1138, doi:10.3390/pharmaceutics14061138.

Sapere aude